Electrochemical Probing of the Nanostructure of Non-Crystalline Nitrogenated Carbon Materials for Electrocatalysis

James A. Behan

A thesis submitted to The University of Dublin, Trinity College Dublin

for the Degree of Doctor of Philosophy

Trinity College Dublin, School of Chemistry

2019

Declaration

I declare that this thesis has not been submitted as an exercise for a degree at this or any other university and it is entirely my own work. Due acknowledgements or references are given to the contributions of others where they are included in the text.

I agree to deposit this thesis in the University's open access institutional repository or allow the Library to do so on my behalf, subject to Irish Copyright Legislation and Trinity College Library conditions of use and acknowledgement.

James A. Behan,

January 2019

Acknowledgements

I would like to acknowledge my supervisor, Prof. Paula Colavita, for her guidance and support over the past four years. Our collaboration began as a three month summer project in her lab more than five years ago, when I was an undergraduate with no research experience. I have learned many things since then, a good deal of which may be attributed to our long scientific discussions on the merits (and demerits) of some data set or other, whether it was my own work or a paper I plucked out of the literature in an attempt to make sense of my own work.

Prof. Colavita was always there to offer suggestions and feedback to keep the project moving forward, while simultaneously trusting my judgement in pursuing new experimental leads that arose in the course of the work. Without this freedom, chapters IV and V in this thesis would not exist as they are. I am also indebted to Prof. Max García-Melchor and Dr. Laia Vilella-Arribas, who introduced me to the world of DFT calculations and taught me how to think like a theoretician. Collaborating with them made me far more confident in my interpretation of the voltammetric data on catechol adsorption, although I now fear that I will never trust my scientific instincts again until I see the computational results…

The Colavita Group has been like a second family to me over these past years. I would not have been so happy to come to work every day if it wasn't for the friendship of my fellow PhD students and postdocs: Ronan, Dee, Dilushan, Daniela, Adam, Joana, Federico, Guido, Leticia, Serban, Suoyuan, Carlota, Stefano, Sam, Khairul, Swapnil and others. I am particularly grateful to Joana, who organised the group inside the lab and out, and Adam, for his friendship and boundless generosity.

I would like to thank all of the technical staff at the School of Chemistry for their hard work and assistance, particularly Patsy Greene for making my life as a JS lab demonstrator so much easier, Dr Manuel Ruether who trained me on countless instruments and Fred Cowzer who taught me the proper way to shift gas cylinders. I am also grateful to Dr Karsten Fleischer and Dr Cormac McGuinness for training me in XPS and Dr Dermot Daly for SEM training.

Outside of the lab, I was supported through all of the vicissitudes of research and protracted life as a student by my family and friends. I have to acknowledge in particular the support of my parents, Eva and Peter, and my girlfriend, Catríona. To all of my other friends, particularly: Kevin Daly, John Roche, Rhys Dunne, Johnathan Steps, Kevin Fogarty, I say: thank you for being my friends, thanks for being around, and thanks for the board games.

Summary

Carbon materials are ubiquitous in the field of electrochemistry. In fuel cells and electrolyzers; batteries, supercapacitors and biosensors, carbon materials are applied as metal-free electrocatalysts, catalyst support materials, and biocompatible probe materials. The prominence of carbon in these diverse applications may be attributed to its abundance, low cost, and versatility.

Carbon may be naturally found or synthesised as a variety of allotropes and nanoallotropes, all of which may be further modified by chemical treatments to introduce dopants or alter the carbon scaffold organisation. The electrochemical performance is generally also a complex function of the interfacial properties, such as surface termination, topography, wettability and specific surface area. The sheer number of variables which must be considered in the design and preparation of new carbon electrocatalyst materials is a major challenge for researchers.

The purpose of this thesis is to present a strategy for fundamental structure-activity studies of carbon electrode materials in a variety of electrochemical applications. The approach is based on the preparation of carbon model systems based on amorphous carbon film electrodes. Carbon model systems are carbon materials which possess properties amenable to fundamental studies with minimal interference from confounding variables. In the context of electrochemistry, carbon model systems possess a simple and reproducible morphology, smooth topography and well-defined chemical composition. They are also tuneable materials which have parameters such as dopant concentration, surface chemistry and carbon scaffold organisation that can be easily and independently varied in order to understand their effects on the electrochemical response.

Chapter I offers a brief review of the major carbon allotropes, including some discussion of their preparation and selected electrochemical applications. Nitrogen-incorporated carbons are then introduced in more detail as the main class of heteroatom-doped carbon investigated in the subsequent chapters. Various examples of carbon materials used as carbon model systems are then described, including glassy carbon and amorphous carbon film electrodes. Finally, the major redox probes used to electrochemically characterise the carbon model electrodes are introduced along with a brief description of the theory underlying heterogeneous charge transfer at the electrode-solution interface.

Chapter II briefly describes the DC magnetron sputtering technique used to prepare amorphous carbon and nitrogenated amorphous carbon film electrodes. The various experimental techniques used in this thesis to characterise the carbon model systems are also

described in some detail, including voltammetry, electrochemical impedance spectroscopy, spectroscopic ellipsometry, x-ray photoelectron spectroscopy and atomic force microscopy.

The characterisation of as-deposited amorphous carbon and nitrogenated amorphous carbon films is described in Chapter III, where the optoelectronic properties of electrodes determined through spectroscopic ellipsometry measurements are directly correlated to the charge transfer kinetics to outer-sphere redox probes. Nitrogen incorporation is found to improve the metallic character of the carbon material at low doping concentrations, but excessive nitrogenation disrupts the carbon scaffold through the introduction of defects and ultimately produces a heterogeneous CN-aggregate material with insulating properties.

Chapters IV and V introduce catechols as surface sensitive redox probes of the carbon nanostructure of graphitized amorphous carbon model electrodes prepared through thermal annealing of glassy carbon and as-deposited amorphous carbon films. A combination of voltammetry and computational studies is used to show that catechol adsorption at carbon surfaces is facilitated through non-covalent interactions between the redox probes and graphitic cluster domains at the carbon surface. The effects of N-doping and surface oxygenation of the model systems on the adsorption response are also investigated. N-doping is shown to enhance adsorption as long as it is not accompanied by the introduction of excessive defects in the carbon scaffold. Oxygen sites may be electrocatalytic towards catechol oxidation but do not facilitate adsorption in aqueous electrolytes.

The performance of two classes of nitrogenated carbon materials in the oxygen reduction reaction is studied in Chapter VI. The effects of surface nitrogenation through annealing with ammonia are compared with bulk nitrogenation through sputtering in terms of their effects on the onset potential of oxygen reduction, limiting current density and selectivity for the 4-electron reduction to water versus 2-electron reduction to hydroperoxide. The role of particular N-sites in electrocatalysing the reduction is also clarified through a comparison of the material performance as a function of pH. Results suggest that both surface and bulk nitrogenation can produce oxygen reduction electrocatalysts with good activity in terms of the onset potential, but the overall activity in terms of selectivity for the 4-electron reduction is strongly correlated to the degree of carbon scaffold disorder, irrespective of the particular doping method.

Finally, Chapter VII summarises the main conclusions of the thesis, briefly describes additional research carried out throughout the course of the project and describes possible future work.

Table of Contents

CHAPTER I

Introduction

Carbon materials showcase unrivalled structural variety and have found applications in a number of different fields of research. The most important applications of carbon materials in the modern, technologically-driven economy are in the field of electrochemistry, where they have been applied as materials for electrochemical energy conversion. In this introductory chapter some of the major allotropes of carbon materials are discussed with particular reference to their electrochemical applications. The properties of amorphous carbon (a-C) and nitrogenated amorphous carbon (a-C:N) materials in particular are described along with their application as model systems for structure-activity studies of electrochemical performance. Finally, the process of heterogeneous charge transfer is discussed with emphasis on how particular redox-active compounds may be used as model analytes for the characterisation of the surface chemistry and nanostructure of carbon materials.

The work in this chapter is adapted in part from the following book chapter:

Domínguez, C.,[1] Behan, J.A.,[1] Colavita, P.E. *Electrocatalysis at Nanocarbons: Model Systems and Applications in Energy Conversion* in Nanocarbon Electrochemistry, Edited by Nianjun Yang and John Foord, Wiley, 2018 *(In Press).*

[1]Authors contributed equally to this work.

1. The Ubiquity of Carbon

Carbon is all around us. Even if we set aside its fundamental role in the biochemistry of life, carbon has a unique resonance in our everyday experience and our popular culture: it is the draughtsman's graphite and charcoal, the coal and coke of the forge, and the diamond engagement ring. These manifestations of carbon are obvious to the layperson. However even a cursory look beyond these familiar examples confirms the unrivalled importance of carbon to a modern world which is increasingly dependent on technology. A Google Patents search returns thousands of results for industrial patents involving the use of graphite as a lubricant for industrial applications and in automotive brake friction materials. Protective carbon coatings have been used for some time in diverse applications including biomedical devices[1-2] and magnetic storage technology.[3]

The field of electrochemistry is arguably where the most significant applications of carbon materials are seen in the modern era. Li-ion batteries which, at the time of writing, serve as the main power source in our indispensable smart phones and other portable electronic devices, use graphite or some other form of graphitized carbon as the anode material.[4] Hydrogen-Oxygen fuel cells, already an extant technology in electric cars,[5] are widely considered to be the future of zero-emissions technology in transport. The current state of the art polymer electrolyte membrane fuel cell is based on platinum nanoparticles dispersed on a graphitized carbon support material.[6] Materials based on high specific surface area carbons are also the current standard for electrochemical capacitors, or supercapacitors.[7]

Carbon is therefore among the most important elements for both high-energy density and high-power density materials and for electrochemical energy transformation. This is in large part due to its low cost, its versatility in terms of the number of allotropes it may adopt and the different morphologies available, which include powders, fibres, and porous materials with high specific surface areas.[8] The following section will serve as a brief, but not exhaustive, overview of the diverse forms of carbon with reference to their history, their preparation and selected applications.

1.1 Classifying Carbon Allotropes and Nanoallotropes

Carbon atoms can form up to four bonds to one another and to other non-metal atoms in linear, trigonal or tetrahedral configurations, commonly referred to as sp, sp^2 and sp^3 hybridization respectively. The aforementioned structural versatility of carbon is in large part because of this variety in possible bonding arrangements, as is carbon's central role in organic chemistry and therefore in life.

A number of different classification methodologies exist for carbon materials. For instance, diamond and graphite may be distinguished from one another in terms of the bonding configuration, which is tetrahedral in the former and trigonal in the latter. Amorphous carbons can then be defined as carbon materials with some ratio of sp^3 and sp^2 carbon in the absence of long-range order, as will be discussed in a separate section.

Nanoallotropes such as nanodiamond and the fullerenes may be classified in a similar fashion, as they also differ fundamentally in terms of the predominant coordination

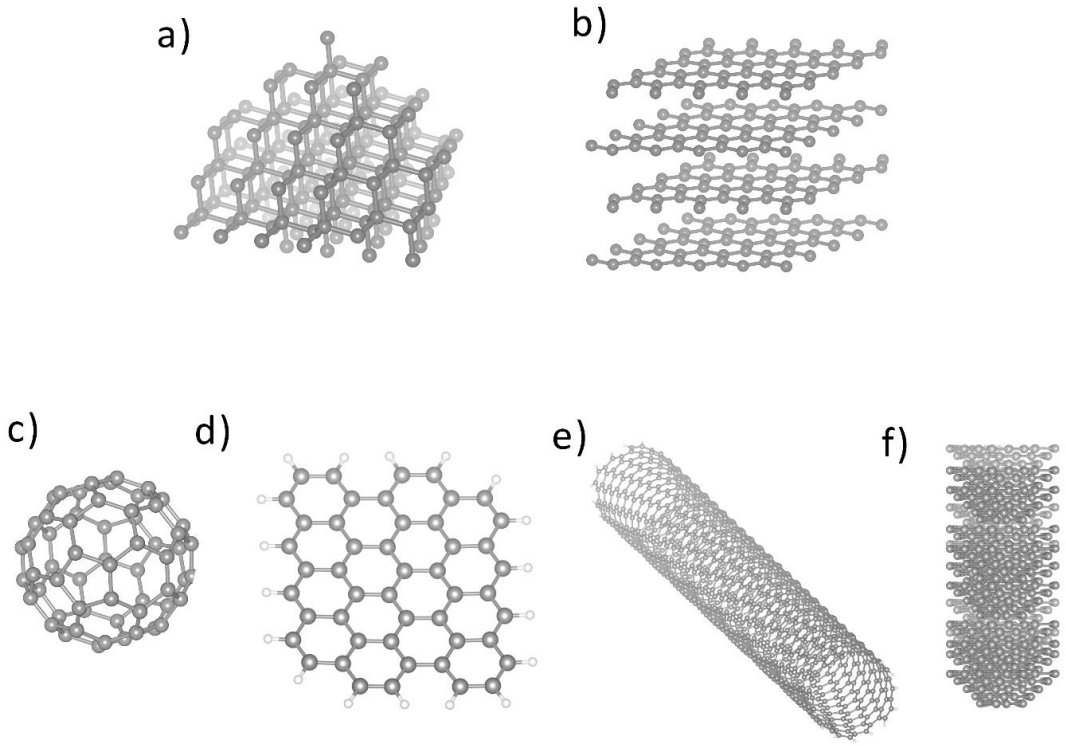

Figure 1.1. Schematic illustrating different carbon allotropes and nanoallotropes. a) Diamond b) Graphite c) C60 d) Graphene e) Single-Walled Carbon Nanotube f) Carbon Nanofibre.

configuration of the carbon atoms present in the material. However in electrochemical applications factors such as a material's morphology and the number of its dimensions not

confined to the nanoscale are also crucial considerations. As such the overview which follows in the next several sections will discuss nanocarbon materials according to their dimensionality, as defined in the classification scheme of Pokropivny and Skorohod[9] which was recently applied to carbon materials in particular in a review by Georgakilas et al.[10] Selected zero-dimensional (0D), one-dimensional (1D) and two-dimensional (2D) carbon materials will be discussed in turn, with brief reference to their history, synthetic methods for their preparation and some of their relevant applications. Three-dimensional (3D) materials, including carbon aerogels and foams, will be omitted from the discussion for the sake of brevity.

The review will emphasise developments in the use of carbon nanomaterials for electrochemical applications, most notably electrocatalysis, with a focus on the advancements in the use of metal-free electrocatalysts based on carbon nanomaterials. The role of incorporated heteroatoms, particularly nitrogen, in the carbon scaffold will be discussed in this context, as will nanostructural features of carbon materials such as the size of graphitic clusters and the density of reactive edge sites which are also highly relevant to the electrochemical performance.

Zero-Dimensional (0D) Carbon Materials

0D materials are those in which all dimensions fall within the nanoscale, *i.e.* < 100 nm. The category encompasses fullerenes, carbon dots (CDs), nanodiamonds, nanoonions and carbon nanospheres, among others. Fullerenes are the smallest of these; they are nanocage-shaped molecules with variable size (0.4-1.2 nm diameter)[10-11] depending on the number of C atoms that constitute the cage. The most famous member of this family is Buckminsterfullerene (C_{60}) which was first discovered in 1985.[12] Because of their tunable curvature, which allows for the controlled modulation of reactivity, and the ability to heteroatom-dope the carbon cage (*e.g.* azafullerenes) they are intriguing candidates as metal-free electrocatalysts for the oxygen reduction reaction (ORR), which is an ongoing area of research in the area of fuel cell technologies[11, 13-14]. However, due to factors such as low conductivity and issues with scalable synthesis and purification methods, their practical applications up to this point have been limited; other 0D materials, however, have been subject to experimental studies in electrocatalysis among other applications, as discussed in the following two sections.

Carbon Dots

Carbon dots (CDs) are 0D carbon nanostructures typically ranging from 2-10 nm in size. [15] CDs were first prepared accidentally in 2004 during the purification of single wall carbon nanotubes synthesized via arc discharge.[16] Numerous synthetic routes have since been developed, including the aforementioned arc-discharge, laser ablation,[17] and electrochemical etching of a macroscopic carbon source such as graphite.[18] Most studies have exploited their size-dependent fluorescence, which may be easily tuned by altering the preparation conditions and surface termination.[19] The earliest CDs had low photoluminescence efficiency, which was improved significantly by surface passivation with organic polymers[17] and, importantly, by the doping of the CD carbon scaffold with heteroatoms such as nitrogen.[20]

CDs have shown good biocompatibility and low cytotoxicity, making them promising candidates for *in vivo* bioimaging.[21-22] Hollow spherical CDs have also been prepared as bifunctional drug-delivery and bioimaging agents for cancer therapy.[23] CDs have also been studied as electrocatalysts, with the earliest reports CD electrocatalysis focusing on activity in the ORR.[24-27] Similar to the case of C_{60}, metal-free ORR with good activity was achieved for CDs through the incorporation of heteroatoms into the carbon scaffold. In many cases the CD material studied is actually a composite material and as such its electrocatalytic performance may only be evaluated by coupling them to conductive supports or to other nanocarbons such as carbon nanotubes or graphene, as reported in reference 25, to ensure conductivity. Finally, given that CDs display promising photophysical and electrocatalytic properties, their application in photoelectrochemical processes such as water splitting has also been reported recently.[28]

Carbon Blacks and Activated Carbons

'Carbon black' refers to graphitized carbon particles with average diameters < *ca.*50 nm. A variety of different carbon blacks exist and are typically referred to by their commercial names in the literature, e.g. Vulcan XC-72 and Ketjen Black. Since they are usually produced by combustion processes, carbon blacks often contain regions of amorphous carbon and numerous oxygen surface moieties. They may be prepared with high specific surface areas

ranging over 250-1400 m^2 g^{-1}, depending on the specific details of their processing. They are ubiquitous as conductive supports for nanoparticle electrocatalysts, although the modification of carbon blacks for applications in Pt-free catalysis of the ORR has also been studied.[29-30] Their predominance even in early electrocatalytic studies may be attributed to their low cost and wide commercial availability as a graphitized carbon source produced on an industrial scale.

O'Hayre and co-workers have recently reviewed some of the best electrocatalytic performances achieved through the modification of commercial carbon blacks such as Vulcan XC-72, Ketjen Black and Black Pearls 2000.[31] Modifications have aimed at incorporating heteroatoms, particularly N-sites, and earth-abundant metal centers such as Fe to replace precious metal nanoparticles. These studies are of particular significance to fuel cell technology, since the current state-of-the-art in the ORR is based on Pt nanoparticles dispersed on a carbon black support as has already been mentioned. Modifications of these materials therefore may serve the dual role of improving metal-support interactions and also utilizing the catalyst support as an electrocatalyst in its own right.

High Aspect Ratio (1D) Nanocarbons

1D nanomaterials are those in which only one of their dimensions is >100 nm. 1D carbons have generated tremendous interest since the discovery of carbon nanotubes – then referred to as 'helical microtubules of graphitic carbon' - by Iijima.[32] The two most studied members of the 1D nanocarbon family are carbon nanotubes (CNTs) and carbon nanofibers (CNFs), however other structures such as carbon nanohorns (CNHs) are also grouped among 1D materials due to their aspect ratio. Applications of 1D nanocarbons in electrocatalysis constitute a vast field of research. The following section will discuss the preparation and structure of CNTs and CNFs, as well as the incorporation of heteroatoms such as N into their carbon scaffold and the activity of the resulting doped materials in the ORR.

Carbon Nanotubes and Nanofibers

CNTs are a family of nanomaterials consisting of extremely high-aspect ratio graphitic tubular structures. The simplest CNTs may be described as a single graphene layer, folded over and with its edges sealed to form a cylinder with a continuous open channel of 0.4-2 nm in diameter. CNTs may be grown with lengths on the micron scale, yielding aspect ratios

of up to 10,000, with even higher values reported for ultralong CNTs in the literature. [33] CNTs can consist of a single wall (SWCNT, Figure 1.1 e) or of multiple walls (MWCNT), and non-covalent interactions between individual tubules often produce stable CNT 'bundles'. CNFs differ from CNTs in that the graphite planes of CNFs are aligned at an angle relative to the fiber axis (Figure 1.1 f), resulting in a high density of exposed graphitic edges. CNF diameters range over 50-200 nm and like CNTs may be up to several microns long. While both CNTs and CNFs are often paired together in discussions in the literature, CNFs are distinct in that they do not possess a continuous hollow channel as is the case with CNTs. CNTs and CNFs of similar aspect ratio also possess different degrees of exposed graphitic edges, which also leads to very different chemical properties.[10, 34]

CNTs and CNFs are most commonly synthesized via chemical vapor deposition (CVD).[35] The CVD process involves the decomposition of a carbon source such as acetylene followed by catalyzed re-assembly of carbon radicals and clusters into sp^2 carbon. Transition metals and their oxides such as Fe, Ni, and Al_2O_3 have been used as catalysts.[10, 36] Temperatures in the range of 800-1500 ^oC are typically needed for the growth of the sp^2 network. [37] A disadvantage of CVD is that it also results in samples that contain small amounts of metal impurities and residual amorphous carbon, both of which may have an impact on electrocatalytic performance. CNFs can also be prepared by electrospinning of polymer solutions such as polyacrylonitrile, followed by pyrolysis;[38] these CNFs tend to have larger diameters in the range 100-1000 nm.[39]

As was the case with 0D materials, CNTs and CNFs can be modified and functionalized to improve activity in electrocatalysis. The introduction of heteroatoms, most notably nitrogen, into the carbon matrix has been demonstrated for applications particularly in the ORR.[40-43] N-functionalized CNTs are among the most studied metal-free electrocatalysts for the ORR. Pioneering work in this area was carried out by Dai and co-workers[42]. Nitrogen-doped carbon nanofibers (N-CNFs) have also been investigated for electrocatalysis of the ORR albeit to a lesser extent relative to CNTs. The work of Stevenson and co-workers on N-CNFs prepared represents one of the earliest demonstrations of the beneficial role of N-incorporation into nanocarbons for electrocatalysis.[40, 44]

1.2 Two-dimensional (2D) Carbon Materials

2D nanomaterials are those in which only one dimension falls in the nanoscale domain. Graphene, its oxides and nanoribbons are the most famous examples of this category, [10, 45-46]

however the definition might also encompass carbon thin films, as these may easily be prepared with thickness < 100 nm using a variety of methods. 2D carbon nanomaterials can be prepared with properties well suited to fundamental structure-activity studies, such as a reproducible geometry and smooth topography. Both graphene and amorphous carbon thin films are discussed in this context in a later section on carbon model systems; here as in the previous sections of this overview the focus is on their preparation and selected applications.

Graphene and Graphene Nanoribbons

Graphene and graphene nanoribbons can be prepared via both 'top-down' and 'bottom-up' methods, with liquid exfoliation of graphite via ultrasonication being perhaps the most common example of the former.[47] Chemical exfoliation via oxidation to graphene oxide (GO) is a scalable route for generating large quantities of dispersible material;[48-49] the resulting GO is subsequently reduced either through thermal treatments or via the introduction of reductants in solution to form graphene nanoplatelets. Chemical oxidation typically results in a higher proportion of single layers, however reduced GO (rGO) is more defective than liquid-exfoliated graphene. [50]

Graphene nanoribbons are narrow sheets of graphene whose properties strongly depend on their edge structure and their chemical termination. They are occasionally categorized as 1D materials, depending on their aspect ratio.[51] Synthesis of nanoribbons can be achieved via "unzipping" of SWCNTs and MWCNTs using oxidative, thermal, photochemical or electrical treatments.[51] CVD growth has been extensively explored for these materials as well.[51-52] Chemical synthesis via condensation or on-surface coupling of polycyclic aromatics represents a promising bottom-up strategy that is expected to extend the applications of these materials, although the formation of a fully conjugated sp^2 network via the cross-coupling of oligomers remains a challenge.[51, 53]

Doping of these 2D materials has been extensively investigated for metal-free electrocatalysis. In 2010, Dai and co-workers[54] reported the first study of N-doped graphene as a metal-free catalyst for the ORR (Figure 1.2). N-graphene grown via CVD using NH_3 and CH_4 as gas sources was found to display a more positive onset potential than undoped graphene for the reduction of O_2 in alkaline solution. Numerous reports have focused on improving ORR activity since. Geng et al.[55] reported on a simple thermal treatment of graphene under NH_3 atmosphere, which resulted in very good ORR activity and high chemical stability in O_2-saturated 0.1 M KOH. In addition to doping, the importance of the

carbon scaffold organisation, particularly the lateral dimension of graphene clusters, has also been highlighted.[56-58]

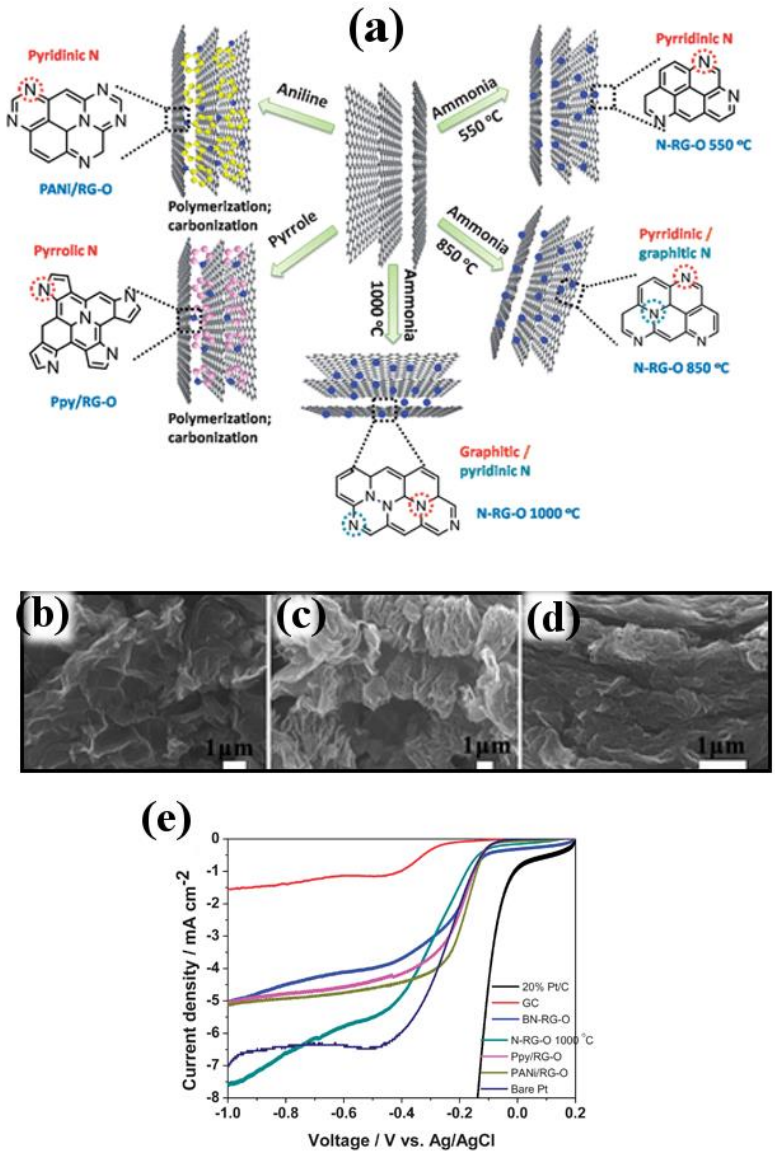

Figure 1.2. (a) Schematic diagram for preparation of N-doped graphene with different N-sites. N-reduced graphene oxide (N-RG-O) 550, 850, and 1000 °C were prepared by annealing GO powder at temperatures of 550 °C, 850 °C, and 1000 °C in NH_3. PANi/RG-O and Ppy/RG-O are prepared by annealing of PANi/G-O and Ppy/G-O composites at 850 °C. SEM images of (b) GO, (c) N-RG-O 850 °C and (d) N-RG-O 1000 °C. (e) Linear sweep voltammograms of catalysts studied, bare Pt and 20% Pt/C electrodes in O_2-saturated 0.1 M KOH at 2500 rpm and 10 mV s^{-1}. *Adapted from Lai et al. Energy Environ. Sci., 2012, 5, 7936-7942 with permission of The Royal Society of Chemistry*.[59]

Amorphous Carbon Materials

Amorphous carbon (a-C) broadly refers to carbon materials comprised of both trigonal and tetrahedral carbon domains arranged in the absence of long-range order. The 0D carbon black materials introduced in Section 1.1.1. also represent a form of amorphous carbon, since these materials are also disordered networks of carbon in different bonding configurations. Hence, the term a-C both in this section and throughout the body of this thesis refers to a-C films with thickness < 100 nm, which are classified as a 2D nanoallotrope of carbon.

Since their first description in previous decades[1, 60-62] a-C materials have found numerous applications in wear-resistant coatings due to their favourable mechanical and tribological properties,[63-65] *viz.* a low frictional coefficient,[3, 66-67] hardness ranging from 10 – 10 GPa[68-69] and a Young's Modulus ranging from 100 to >500 GPa.[70-71] a-C films have also been implemented in various biomechanical applications such as coronary artery stents, artificial heart valves and orthopaedic implants due to their biocompatibility, smoothness and good adhesive properties.[72-74]

Historically, the most common method of depositing a-C films has been through some form of magnetron sputtering[75-80] of high-purity graphite but a-C can also be prepared by a variety of other physical vapour deposition methods including the filtered cathodic vacuum arc technique[81], pulsed laser deposition (PLD)[82-83], as well as chemical vapour deposition (CVD) and plasma-enhanced CVD.[84]

Due to the presence of both three- and four-fold carbon bonding, a-C films display properties intermediate to those of diamond and graphite. Depending on the deposition technique and conditions, materials may be prepared with different ratios of sp^2 and sp^3 sites (Figure 1.3). The hardest and most chemically inert of the films typically have sp^3-bonded carbon contents >80% and are termed Diamond Like Carbon (DLC).[1, 61] DLC films may be heteroatom doped, as is the case with hydrogenated amorphous carbon (a-C:H) or N-doped diamond films. Undoped DLC with a high sp^3 content is referred to as tetrahedral amorphous carbon, ta-C, and is the preferred form of carbon overcoating in the read/write heads and hard disks used in magnetic storage technology due to their hardness, wear-resistance chemical inertness and atomic level smoothness even in ultrathin (< 2 nm) films. [85-86]

DLC films generally also possess a wide band gap and lower conductivity compared to more graphitic films, for which the optical and electronic properties are largely controlled by the sp^2 content and domain size. In general, sputtering produces softer films with narrower optical gaps and high sp^2 content; indeed, the use of DC magnetron sputtering has resulted in films with >80% sp^2 content as has been described in previous works from the Colavita group.[87-90]

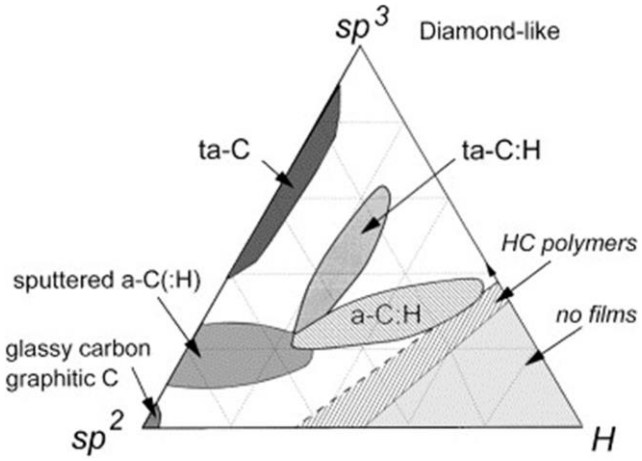

Figure 1.3.Ternary phase diagram for amorphous carbon materials including hydrogenated amorphous carbon (a-C:H), tetrahedral amorphous carbon (ta-C), and hydrogenated tetrahedral amorphous carbon (ta-C:H) prepared with different proportions of sp^2 and sp^3 carbon centers and via incorporation of H atoms. *Reprinted from Materials Science and Engineering: R: Reports, Volume 37, J. Robertson, Diamond-like amorphous carbon, Pages 129 - 281, Copyright 2002, with permission from Elsevier.* [1]

1.3 Nitrogen-Incorporated Amorphous Carbon (a-C:N)

A Brief History of Nitrogenated Carbons

Nitrogenated carbons have an eclectic history. The modern field of nitrogenated carbon chemistry may be traced back to investigations by 19th Century researchers into classes of compounds based on CN heterocycles.[91] Between 1834 and 1855 Justus Baron von Liebig, described a number of these compounds, including 'Melon', the by-product of heating mercuric thiocyanate $Hg(SCN)_2$, a compound first prepared by Berzelius, in air [92]. The resulting compound has a general formula $(HC_2N_3)_x$[93] and has the appearance of an amorphous and highly porous yellow solid. This reaction was for a time a source of great

amusement to the general public, for the decomposition into Melon resulted in the sudden and apparently miraculous emergence of plumes of the amorphous product from the reaction vessel, whose snake-like appearance led to the name 'Pharaoh's serpents.'

Other than a short-lived fad as a toy, (for which commercial 'reaction kits' of $Hg(SCN)_2$ were actually purchasable by the general public) the Pharaoh's serpents received little attention until nearly a century later, when Edward C. Franklin carried out a series of investigations into Melon and other so-called 'ammono-carbonic acids' – nitrogenous analogues of H_2CO_3 and related compounds.[93] Franklin speculated that the ultimate terminus of continued 'de-ammonation' reactions of Melon was a hypothetical H-free condensed product, C_3N_4, which Franklin termed 'carbonic nitride.' Attempts to synthesise C_3N_4 by heating Melon were unsuccessful, as the compound was more likely to decompose entirely rather than condensing along with elimination of ammonia.

Due to the efforts of Pauling and Sturdivant in studying some of Franklin's crystalline samples, [94] it was deduced that the structure of Melon and many related compounds was a carbon-nitrogen heterocycle built on heptazine units in a way analagous to the structure of benzene. It is the stability of these heptazine polymers along with their propensity to decompose with release of cyanogen $(CN)_2$ that frustrated Franklin's attempts to prepare pure carbon nitride[95] and indeed continues to thwart attempts to prepare C_3N_4 via this synthetic route to this day.

After the identification of heptazine as the building blocks of both Melon and C_3N_4, interest in carbon nitrides underwent a second large hiatus, this time until the 1980's. Motivated in large part by early predictions that carbon nitride, C_3N_4 would have super-hard properties surpassing those of diamond,[96-98] many researchers investigated new synthetic routes for the preparation of carbon nitrides. Later, the benefits of incorporating nitrogen into amorphous carbon films began to be explored in their own right due to the favourable mechanical properties imparted to the films following its incorporation, *viz.* improved durability,[99] substrate adhesion [100-101] and extremely high elastic recovery.[74]

Some of the earliest synthetic protocols for nitrogenated carbon materials relied upon the use of metal catalysts such as iron or cobalt in the presence of nitrogen-rich species such as phthalocyanine[102] and ammonia[103-104] with the metal catalysts subsequently removed via acid wash. Metal-free carbonisation in the presence of nitrogenous organic compounds has also been accomplished.[105] Many of the same methods used to prepare a-C films may also be used to prepare a-C:N, including CVD,[106] Pulsed Laser Arc Deposition,[107-108] and magnetron sputtering.[99, 109-114] The latter is advantageous as a fast, metal-free, single step

process which can easily be tuned by altering conditions within the deposition chamber such as the power, temperature and partial pressure of nitrogen gas.[115]

It is at this point that some clarifying statements regarding nomenclature need to be made. In the literature there are various references to 'carbon nitride' in reference to C_3N_4, but also

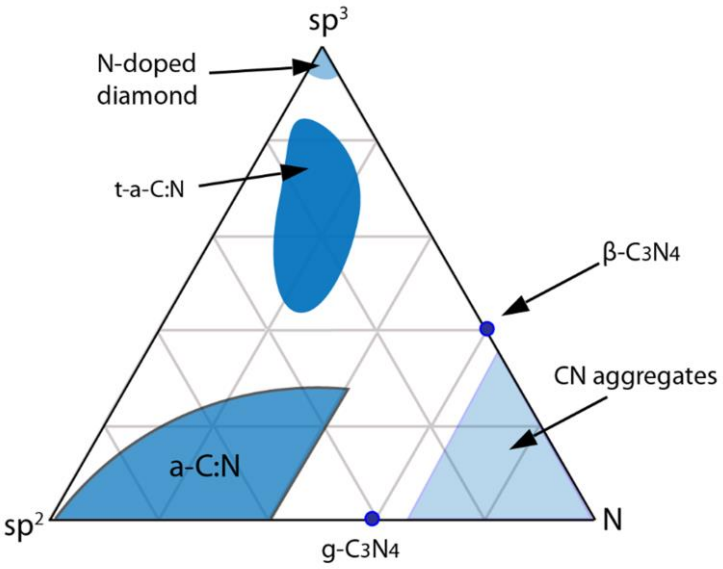

Figure 1.4. Ternary phase diagram for nitrogenated carbon materials including carbon nitride (β-C_3N_4), graphitic carbon nitride (g-C_3N_4) and tetrahedral nitrogenated amorphous carbon (t-a-C:N). Based on data from Reference 91, 149 and Chapter III of this thesis.

in the context of nitrogenated amorphous carbon. Some authors[116] refer to both nitrogenated amorphous carbon and indeed any general N-doped carbon material as a sub-species of 'carbon nitride' and refer to C_3N_4 in particular as 'graphitic' carbon nitride or g-C_3N_4. In order to avoid any connotations regarding specific stoichiometries of C and N as implied by the term 'carbon nitride', this thesis will instead use the term 'nitrogenated carbon' as the generic term for materials based on carbon incorporated with nitrogen. Carbon nitride is therefore a sub-group of nitrogenated carbons, as are particular materials such as N-doped diamond and nitrogenated amorphous carbon, a-C:N. This classification is summarised in Figure 1.4. Additionally, another commonly-used term for a-C:N, *viz.* 'amorphous carbon nitride' will also be avoided, again because it may easily be confused with C_3N_4.

Nitrogenating Carbon: Why Bother?

At the time of writing, nitrogenated carbon materials are the subject of intense research in the fields of electrocatalysis and energy storage, largely due to the discovery of the high

ORR activity of N-doped carbons. [24, 42, 54, 117-118] Stevenson et al. first reported the promising ORR activity of N-doped carbon nanofibers, [44, 119] whilst Dai et al. [24, 54] were the first to apply nitrogen incorporation to graphene for electrocatalysis. The incorporation of nitrogen has since been applied to the gamut of carbon materials discussed in Sections 1.1 and 1.2, whilst doping with other heteroatoms including boron, sulfur and phosophorus has also been studied.[120]

The main motivation for these studies is the need for precious metal-free electrocatalysts for important processes such as the oxygen reduction reaction (ORR) and oxygen evolution reaction (OER). At present these reactions are mainly catalysed by noble metal catalysts based on platinum and ruthenium, [121] creating issues pertaining to high costs and scarcity, as well as the susceptibility of metal centres to poisoning. [122]

Taking the example of the ORR, the reliance on platinum and other platinum group metals (PGM) presents a challenge for the commercialisation of H_2/O_2 fuel cells, which use these precious metal catalysts for both the oxidation of hydrogen and the reduction of oxygen. In order to reduce the costs associated with manufacturing fuel cells, both the Fuel Cell Commercialisation Conference of Japan (FCCJ) and the United States Department of Energy have stipulated that the 2020 target for platinum loadings in both the anode and cathode catalyst layers should be no more than 0.125 mg_{Pt} per square centimetre of area.[123] For vehicles powered by fuel cells, this loading translates to approximately 11.3 g_{Pt} in a midsize sedan vehicle, though other authors have proposed that the usage of Pt would need to be less than *ca.* 6 g_{Pt}/vehicle in order for fuel-cell electric vehicles to be commercially viable in the long term. [124]

Diminishing the usage of Pt and other precious metals is only a part of the challenge for H_2/O_2 fuel cells. Regardless of the Pt loading, there will be issues associated with the dispersal of nanoparticle catalysts on a support material. The current state-of-the-art Pt catalyst is dispersed on a carbon support, typically some form of carbon black. This arrangement suffers from a continuous loss of catalytically-active area due to sintering, Pt dissolution-redeposition and Ostwald ripening. [125-127] All of these processes are accelerated by the corrosion of the carbon support, which leads to the physical migration and coalescence of Pt nanoparticles as well as their detachment from the surface. [128] Carbon corrosion occurs during conditions where partial fuel starvation at the anode occurs, such as during start up and shut down, which results in high potentials at the cathode and subsequent carbon corrosion according to: [129-130]

$$C + 2H_2O \rightarrow CO_2 + 4H^+ + 4e^-$$

The incorporation of nitrogen into carbon support materials has been shown to promote Pt nanoparticle dispersion and improve long-term stability via favourable metal-support interactions. [104, 131-133] This point will be discussed in further detail in the discussion of carbon model systems in Section 1.4 of this chapter.

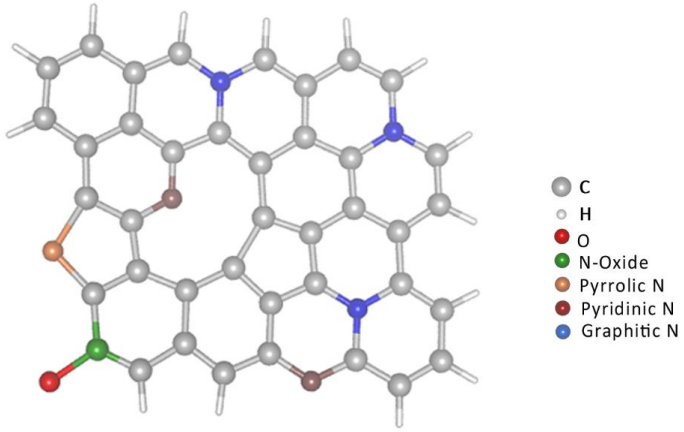

Figure 1.5. Schematic of a sputtered N-doped amorphous carbon fragment.

Many studies have examined the effects of nitrogen incorporation on the properties of amorphous carbon films. When the N atoms are inserted substitutionally into graphic clusters in the carbon scaffold, it may be considered as an n-type dopant,[99, 134-136] which has the effect of raising the Fermi level of the material and lowering the optical band gap.[59, 137] Doping also increases the degree of graphitisation of the films by inducing the formation of sp^2 clusters as confirmed by Raman Spectroscopy studies.[138]

Nitrogen incorporation can result in the formation of different types of sites in a-C:N films (Figure 1.5). Numerous XPS studies on a-C:N materials and carbon nanomaterials have identified four major nitrogen types in a-C:N: graphitic nitrogen, pyrrolic nitrogen, pyridinic nitrogen and pyridine n-oxides. [139] Additionally other types of N-sites such as amines and nitrile-like groups may be found; their abundance depends upon the method of preparation and their identification via XPS – by far the most common characterisation technique for determining the chemical composition of a-C:N materials - may be difficult due to spectral overlap.[140-141]

Applications of a-C:N in Electroanalysis

In recent years a-C:N materials have received much attention as electrode materials for electroanalytical applications due to the large (> 3 V) potential window and low background

current in aqueous solutions.[102, 108, 142] Nitrogen-incorporated carbons display potential windows exceeding even Boron-Doped Diamond (BDD), with the advantage of being cheaper and easier to synthesise: BDD requires high temperature CVD for long periods of time and is thus limited to few substrates;[143] by contrast a-C:N may be quickly and cheaply deposited via a variety of techniques as has already been described, on almost any substrate, allowing for much greater versatility in creating electrodes. Additionally, a-C:N films possess atomic level smoothness on average far superior to BDD.[102, 144]

The above favourable properties of a-C:N films have led to applications in the detection of heavy metals in solution[143] as well as the detection of biomolecules such as estrone, dopamine and ascorbate[144-146] with a low level of surface fouling. The latter application is extremely relevant for commercial biosensing as electrodes based on common disordered carbon such as vitreous (glassy) carbon are often rendered inactive by the presence of adsorbed intermediates created during the detection process. Glassy carbon is a graphitized form of carbon with a low porosity and high conductivity. Both its properties and its method of preparation are distinct from a-C/a-C:N materials as discussed in Section 1.4 of this chapter (*vide infra).* BDD electrodes also display excellent analytical stability but are more difficult to synthesise as explained above.

Nitrogen-incorporated carbons have found applications in the simultaneous detection of biologically relevant molecules which may otherwise be difficult to detect electrochemically due to the overlap of peak potentials in voltammograms. Various groups[147-149] have found that the introduction of nitrogen moieties into carbon-based materials allows for the voltammetric detection of dopamine in the presence of other important biomolecules such as ascorbic acid and uric acid. The nitrogen groups have been shown in many cases to accelerate the kinetics of electron transfer, resulting in greatly enhanced peak currents and/or a narrowing of the peak potential separation, ΔE.[148] The precise mechanism for this enhancement is unknown, but has been attributed to a combination of improved electronic properties in the material and interactions between the analyte molecules and surface groups introduced by nitrogen incorporation.[149]

Applications of a-C:N in Electrocatalysis

The incorporation of nitrogen into carbon surfaces alters both the surface and bulk properties of the material in several ways which are known to be beneficial in electrocatalytic applications. Nitrogen doping raises the Fermi level, E_F, of a-C:N relative to undoped a-C

and increases the density of states around E_F (Figure 1.6), improving its intrinsic electron transfer properties. [139] Doping also enhances the material's overall metallic character in terms of electrical conductivity, as long as a large number of defects are not formed.[135]

Nitrogen incorporation has also been correlated to the degree of exposed graphitic edges which is also associated with high reactivity in certain processes including ORR. [40, 44, 150-152] In addition to reactive edge sites, nitrogenous sites such as the aforementioned graphitic-N and pyridinic-N sites may be catalytically active themselves.[40, 44, 150-151, 153] Recently, it was also demonstrated that nitrogen incorporation affects the acid-base properties of the surface; due to the basicity and nucleophilicity of sites such as pyridinic sites and due to the greater electronegativity of N with comparison to C, a number of both positively and negatively charged surface sites may be created which in turn influences the electrocatalytic performance in the ORR. [154]

The favourable electrocatalytic properties of a-C:N and other nitrogen-incorporated carbons have found applications in, for example, the catalytic interconversion of Cl_2/Cl^-[142] and in the activation of the carbon-halogen bond in the reduction of organic halides;[155]

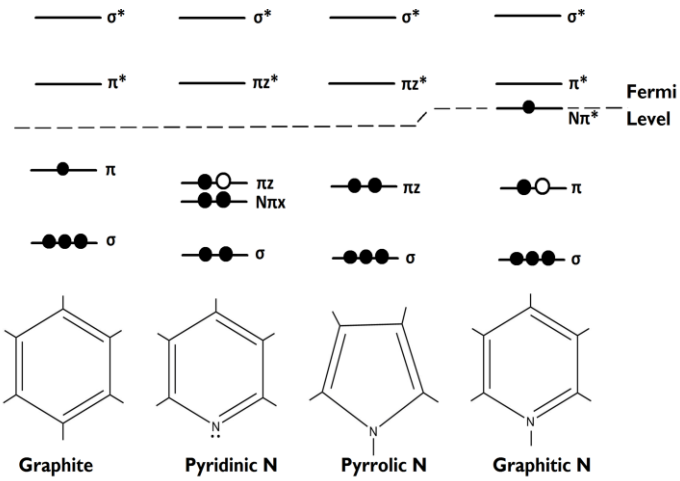

Figure 1.6. Simplified MO diagram showing different types of N sites in N-incorporated carbon materials. Graphitic N, unlike Pyridinic and Pyrrolic N, acts as a dopant. [Full circles = N electrons; Empty Circle = C electrons. Reproduced based on reference 139.

however the most important application of a-C:N as an electrocatalyst in recent years is for the ORR, since a-C:N materials may be candidates both as metal supports and as metal-free electrocatalysts in polymer electrolyte membrane (PEM) fuel cells[156-158].

Both the promising electrocatalytic activity of a-C:N and the electroanalytical applications of a-C:N discussed in the previous subsection are the result of a complex interaction between

incorporated heteroatom sites and the surrounding carbon matrix. As has been shown, nitrogenation of carbon materials produces both global and local changes in material properties by altering the bulk optoelectronic properties through doping and introducing specific N sites and surface defects. This interplay of different effects presents a significant challenge for researchers seeking to understand the fundamental properties of N-doped carbon materials for particular applications.

A further impediment to progress in such fundamental research is the confounding effects of variables such as surface topography, porosity, and the degree of disorder in the carbon scaffold. For example, comparisons of electrochemical activity between most of the N-doped 0D and 1D carbon nanoallotropes discussed in Section 1.1 can only be made somewhat meaningful if differences in electrochemically-accessible surface area (ESA) due to variations in the structure are controlled for.

A better approach for fundamental studies on the effects of N-doping (or indeed any particular heteroatom incorporation or chemical treatment) would utilise materials with smooth topographies and comparable levels of both surface roughness and disorder in the carbon scaffold. Some of the 2D nanoallotropes already introduced in Section 1.2 are ideal for such purposes. The next section will introduce the concept of carbon model systems for fundamental structure-activity studies for electrochemical performance in specific applications. Examples of such studies involving model systems based on carbon will be briefly reviewed, and both N-doped a-C:N and undoped a-C materials will be introduced as ideal candidates for carbon model systems due to their smooth topography and reproducible degree of scaffold disorder.

1.4 Carbon as a Model System for Electrochemical Studies

Carbon materials have found applications throughout the electrochemical disciplines for a number of reasons, chief of which being their low cost and their relative chemical inertness. The wide potential windows and low background currents achievable with carbon electrodes has resulted in their widespread use in the electroanalytical disciplines.[159] Other features such as the presence of reactive edge sites and the amenability to doping with heteroatoms such as nitrogen, phosphorous, sulphur and boron have been particularly important for the application of graphitized carbon in electrocatalytic processes including oxygen reduction and evolution, [117, 160-161] as outlined in the previous sections.

Carbon also owes its predominance in electrochemistry in part to its versatility, as discussed in Section 1.1. Being present in numerous allotropes and nanoallotropes including

graphite, graphene, carbon nanotubes, and amorphous carbon, carbon electrode materials may be synthesised with highly desirable properties tailored for particular applications. For instance, electrodes based on diamond doped with heteroatoms are often chosen for electroanalysis in order to achieve low background currents, [108, 145] whilst graphite serves as the anode material for Lithium ion batteries because the Li ions can reversibly intercalate between graphite planes. [162]

Graphitized carbon is the preferred catalyst support in the current state-of-the-art in hydrogen-oxygen fuel cells, due again to its low cost, good conductivity and its resistance to corrosion. Porous carbon structures including mesoporous carbon and ordered mesoporous carbon have also been explored as catalyst supports and supercapacitors due to their high specific surface areas and high density of reactive edge sites. [105, 163-166]

The highly divergent properties of carbon's various allotropes, combined with the variance in porosity, surface area, degree of graphitization, density of edge sites and the absence or presence of heteroatom dopants presents a significant challenge for researchers seeking to produce novel carbon-based materials for targeted applications. Research into metal-free ORR electrocatalysts, for instance, typically focuses on the creation of particular active sites via heteroatom incorporation and the correlation of the resulting ORR activity to these specific sites. Such an approach is complicated by the difficulties in preparing materials with different reactive sites *ceteris paribus*: there will almost inevitably be a distribution of chemical sites, along with changes in graphitic cluster size and concentration, defect densities, surface free energies and roughness.

Structure-activity studies are nonetheless required for the design of new metal-free electrocatalysts and catalyst support materials. One study design which has been utilized to great effect by numerous different research groups in recent years is the selection of carbon materials with well-defined and reproducible properties. Such materials will be called 'carbon model systems' (CMSs), the common features of which are generally an uncomplicated morphology, smooth topography, low (or no) porosity, and well-defined electronic properties. The use of CMSs both reduces the complexity of the system under study, allowing for the effects of a researcher's chosen parameters to be more likely to be isolated, as well as allowing for a greater ease of comparison to the work of other groups.

This section will focus mostly on four model systems which broadly fulfil the criteria just discussed, with minor references to other materials where appropriate. These CMSs are Highly Ordered Pyrolitic Graphite (HOPG), graphene, glassy carbon and amorphous carbon. Graphene has already been introduced in detail in Section 1.2, and in light of that discussion and the preceding paragraph it should be apparent that graphene readily fulfils the criteria of

a good CMS. HOPG is a synthetic form of graphite prepared via high temperature, high pressure pyrolysis. [167] Its suitability as a CMS is in large part due to its highly-ordered structure: HOPG has a graphitic cluster size (L_a) which typically exceeds 1 μm[168] whilst polycrystalline graphite may have $L_a < 100$ nm, in addition to these crystallites being randomly distributed. Natural single-crystal graphite is also 'ordered' on a scale comparable to HOPG, but it suffers from an abundance of transition metal impurities which are known to distort electrochemical results. [56]

HOPG also fulfils the topographic requirements of a CMS due to its smoothness, and from a pragmatic perspective the ease with which a 'fresh' HOPG surface may be prepared via peeling or cleaving of layers is attractive. As a 3D material, HOPG also presents a large density of edges along its c-axis which allows for the properties of reactive edge sites ('edge plane graphite') to be studied as well as the 'basal' or graphene plane. As will be shown, fundamental studies into the anchoring of nanoparticles on carbon surfaces have utilised HOPG in particular in order to isolate the effects of introducing physical defects, specific chemical sites, and alterations in surface roughness on supported nanoparticle size and morphology.

Glassy Carbon (GC) is also a synthetic form of graphitized carbon, prepared by the pyrolysis of organic polymers. In contrast to the highly ordered HOPG, it may be viewed as a disordered form of carbon material which nonetheless possesses a smooth and reproducible topography and low porosity. a-C has already been introduced in the previous two sections as any carbon material composed of sp^2- and sp^3-centers with no long-range order, only localized order in the form of graphitic clusters and diamond-like regions.[1, 60-62] Synthetic methods for the preparation of a-C can also easily be adapted to introduce heteroatoms in the a-C structure, (e.g. H, N, P, B and S).[115, 139, 169-174] The case of a-C nitrogenation is of particular relevance to this thesis as was discussed in Section 1.3. a-C films are therefore similar to both HOPG and Glassy Carbon in that both materials possess a planar geometry with a low roughness and porosity, meaning that structure-activity studies on a-C films also minimize the contribution of topography when studying surface chemistry is the primary consideration.

What makes a-C unique is its disordered nature, which is reflected in variations in sp^2/sp^3 ratios and the size of graphitic clusters as well as the manner in which they are packed in the carbon scaffold. These parameters can have an important effect in modulating charge transfer at interfaces and modulating specific interactions in surface-catalyzed processes, including the ORR, OER and HER. [24, 58, 175-176] Using a-C as a CMS in this context is useful, as these properties of a-C and related materials can be easily modulated both at the deposition

stage (by adjusting the deposition temperature and pressure and by introducing heteroatoms) and via post-deposition treatments including thermal annealing, plasma treatments and chemical modification of the surface.

Furthermore, it is worth noting that in real-world applications of carbon materials, both in metal-free electrocatalysis and nanoparticle supports, disorder is the norm rather than the exception. The carbon black supports employed in state-of-the-art Pt/C fuel cells are relatively disordered materials with a distribution of small crystallite sizes (L_a 1.5-3 nm and L_c 1.0-4.5 nm)[177] as well as varying porosity, specific surface area, particle size, surface chemistry and conductivity. A structure-activity study focusing on chemical effects such as heteroatom incorporation into disordered systems arguably calls for a CMS with a controlled, reproducible and tuneable level of disorder, but with a much simpler geometric arrangement; a-C films readily fulfil this role.

HOPG

Much of the electrocatalytic research in recent years into carbon materials concerns the role of carbon in fuel cell technology. Particular issues of concern include the need to minimize the loading of Pt and other precious metals, the need for the replacement of precious metal catalysts with non-precious metal catalysts and metal-free systems, and the requirement for longer operational lifetimes. The Pt/C cathode in the current generation of fuel cells is subjected to severe potentials during the start-up and shut down of the fuel cell, which results in the corrosion of the carbon support.[130] Such oxidation of carbon blacks is associated with Pt nanoparticle migration, coalescence and detachment, all of which are in turn associated with activity losses.[128] Some researchers have attempted to address these issues by searching for improved carbon materials with better corrosion resistance and stronger metal-support interactions, with the hope that the rate of catalyst sintering may be reduced if the nanoparticles are anchored more strongly to the support.

HOPG has been employed as a CMS to study the effects that heteroatom incorporation and the introduction of defects have on the interaction between metal and support. The work of O'Hayre and co-workers on controlled functionalization and defect generation in HOPG illustrates the strengths of the approach.[178] HOPG systems were subjected to ion bombardment experiments using both Ar and N_2 gas. The former was chosen to introduce a purely physical modification of the surface, as Ar^+ bombardment is expected to only introduce defects in the carbon lattice, whilst N_2^+ bombardment produced both N-sites and

N-free defects, including N-doping via substitutional nitrogen. Changes were investigated via a combination of capacitance studies and X-Ray Photoelectron Spectroscopy (XPS); it was shown that N-doping increases the nanoparticle dispersion and decreases the nanoparticle size compared to both unmodified HOPG and Ar^+-bombarded HOPG. They proposed that local donor states act as nucleation sites for the deposition of Pt nanoparticles and observed that Pt nanoparticle binding energy is also affected by the presence of N-sites, which indicates that Pt activity could be modulated by nitrogenation of the carbon support. These results therefore suggest that chemical modification, not defect introduction, might be the dominant reason for improved activity of nitrogenated Pt/C electrocatalysts.

Further studies from the same group showed that N-doping of HOPG results in greater durability following stress tests that deliberately subjected the model system to cycles at oxidative potentials; improved stability was attributed to specific chemical interactions between N-sites and Pt nanoparticles.[178] Their results demonstrated that increasing the density of both defects and N-sites resulted in greater dispersibility of Pt nanoparticles and in catalysts with similar morphologies. However, only N-site incorporation imparted high

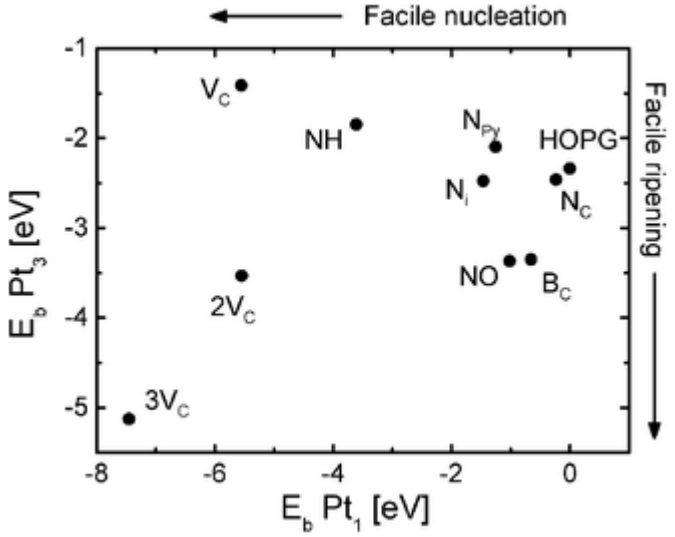

Figure 1.7. Summary of calculated binding energy (E_b) of Pt_1 and Pt_3 clusters at different defects on a basal plane: isolated and clustered vacancies (V_c, $2V_c$ and $3V_c$), substitutional-N (N_c), interstitial-N (N_i), pyridinic-N (N_{py}), N—O (NO), pyrrolic-NH (NH) and substitutional-B (B_c). The binding energy of Pt_3 was interpreted as a proxy for the ripening energy. *Reproduced from Holme et al. Phys. Chem. Chem. Phys., 2010, 12, 9461-9468 with permission of The Royal Society of Chemistry.*[179]

stability during cycling, thus indicating that structural defects, in the absence of nitrogenation, do not interact strongly enough with platinum to inhibit nanoparticle migration and aggregation.

Further studies using computational methods supported this conclusion.[179] Density functional theory (DFT) calculations simulating graphene and N-graphene fragments with

and without defects and their interaction with Pt atoms and Pt clusters (Pt_3 and Pt_4) confirmed that the ripening of Pt nanoparticles is hindered on nitrogenous defects, whilst large vacancies actually facilitate ripening (Figure 1.7). This study exemplifies one of the advantages offered by HOPG as a CMS, i.e. experimental results can be readily interpreted on the basis of computational results on graphitic clusters.

Further work by the group on HOPG systems has helped to study the effects of varying degrees of nitrogenation on the surface structure. For instance, XPS studies showed that greater levels of nitrogen incorporation result in significant disruption of the graphitic network as evidenced by the disappearance of the broad shake-up peak associated with the delocalized graphitic network.[180] 'Post-mortem' XPS and transmission electron microscopy (TEM) with electrochemical stress tests helped demonstrate that pyridine-like vacancies in particular are associated with increased nanoparticle stability.[180]

The value of a simplified planar geometry in the study of metal-support interactions may be illustrated by a comparison to a similar study on Pt- and Pd-support interactions on mesoporous carbon and on N-doped mesoporous carbon carried out by the Gennaro group.[104] The authors, as was the case in the above studies, also identified specific interactions between both Pt and Pd, and nitrogenated mesoporous carbon via XPS, and showed that this translated into superior ORR performance for N-modified materials. However, Pt nanoparticles on non-nitrogenated mesoporous carbon were found to have a higher stability than those deposited on the N-modified carbon. The authors attributed this to particle confinement effects, due to differences in porosity between the two materials. In this instance, the chemical effects of N-sites were confounded with geometrical considerations, thus illustrating the challenges involved in attributing activity enhancements to specific chemical effects in the absence of carbon morphology control.

The Gennaro group has also used HOPG as a model system to study the effects of chemical and physical modification of graphitic surfaces. Favaro et al. studied the effects of ion bombardment using Ar and N_2 on HOPG and correlated the results to the metal-free activity of the material in the ORR.[181] In this case the doped and undoped samples possessed essentially the same roughness after annealing, allowing for the effects of chemical modification on the electrochemical properties of each CMS to be directly compared.

The group also distinguished the physical effects of defect formation and surface amorphization; while both undoped and doped HOPG were found to be defective based on XPS studies, the ORR activity of the N-doped HOPG was superior to that of the Ar-bombarded HOPG. Both materials showcased improvement over the unmodified HOPG, illustrating another advantage of using HOPG as a CMS in electrocatalytic studies in

particular: unmodified HOPG has an extremely low ORR activity due to the inertness of the basal plane towards oxygen adsorption.[182] Any significant improvement in the ORR activity in CMSs based on HOPG is therefore both easy to detect and readily attributable to whatever modifications are being employed in the study.

Interest in metal-free carbon-based materials for energy applications has led many groups to carry out fundamental studies on heteroatom-doped carbons in particular to identify which chemical moieties are the most beneficial in terms of catalytic activity. In the case of nitrogenated carbons in ORR, much of the discussion has focused on which types of nitrogen functional groups constitute the active site, i.e. the site of O_2 adsorption. Since common nitrogenation protocols typically introduce a distribution of nitrogen sites, whilst also introducing differences in the sp^2/sp^3 ratio, crystallite size and carbon morphology, the unambiguous association of activity to one site in particular has posed a challenge to researchers.

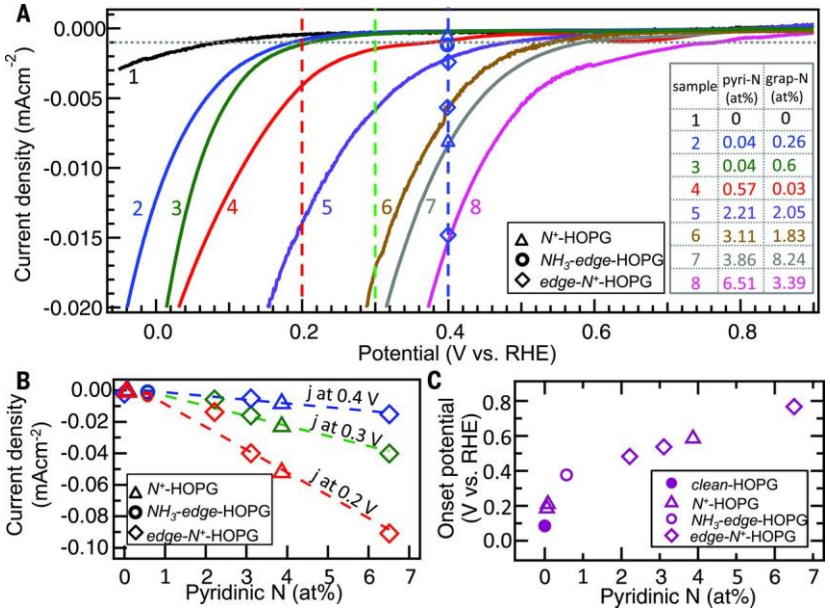

Figure 1.8. (A) Background corrected linear sweep voltammograms of model HOPG electrodes with different total concentrations (inset) of pyridinic-N (pryri-N) and graphitic-N (grap-N) in 0.1 M H_2SO_4 at 5 mV s^{-1}. (**B**) Comparison of cathodic current densities at 0.2, 0.3, and 0.4 V_{RHE} vs. pyridinic-N at.% content. (**C**) Onset potentials at 1 μA cm^{-2} vs. pyridinic-N concentrations. The markers indicate the sample preparation methods adopted to obtain the various model HOPG surfaces. *Reproduced from Guo et al. Science, 351, 361-365 with permission of Science.*[154]

The recent work of Guo et al.[154] has made a strong case that pyridinic-N sites produce active sites for the ORR under acidic conditions, specifically by introducing Lewis basicity into the adjacent carbon atoms. The researchers used a series of HOPG CMSs prepared using different nitrogen-incorporation techniques resulting in surfaces rich in different types of

nitrogen site. Importantly, each CMS was subjected to the same annealing temperature of 973 K in an attempt to ensure that each surface had a similar degree of graphitization. The effects of reactive edge sites were also studied in isolation to ensure that any observed activity was the result of the chemical effects of N-sites rather than the effect of edge-site creation. The results indicated that the HOPG CMS with predominantly pyridine-like N-sites had the highest ORR onset potential (Figure 1.8). The CMSs were also studied using temperature programmed desorption (TPD) experiments using CO_2 as a Lewis acid probe in vacuum; only the HOPG surface rich in pyridinic-N displayed enhanced adsorption of CO_2. This experiment further supported the idea that the Lewis basicity imparted by pyridinic-N might be responsible for the high ORR activity as this should also result in enhanced adsorption of O_2.

The use of CO_2 as a probe for Lewis basicity was also reported by Kiuchi et al. on a nitrogenated HOPG CMS.[183] The authors noted that the introduction of pyridinic-N may produce Lewis base sites in the HOPG surface, whilst also hypothesizing that the amorphization of the surface due to the nitriding process may itself produce Lewis basicity due to the creation of localised π-states just below the Fermi level. The CO_2 chemisorption observed on the N-HOPG surface – as opposed to mere physisorption on unmodified HOPG – was directly quantified using the assumption that controlled amounts of N-sites were created in the first graphitic plane of a smooth HOPG. Here once again the merits of using a CMS are evident as the quantitative approach adopted by the authors would not be possible on a highly complex carbon system with a large specific surface area and porosity.

Graphene

As a 2D nanocarbon material which may be considered as a single, continuous delocalised sp^2 network, graphene and materials derived from graphene are excellent CMSs and they have been frequently applied to fundamental studies on carbon materials for metal-free electrocatalysis. Groups studying graphene frequently pair experimental results with DFT calculations, making graphene the CMS for which theoretical studies have the closest correspondence to the actual material utilized in experiments. The effects of heteroatom incorporation as well as alterations to the carbon scaffold have both been studied in the context of metal-free electrocatalysis and metal-support interactions.[184]

Choi et al. carried out a fundamental study on the importance of graphitic domain size, N-doping and the presence of metallic impurities on the ORR activity of different graphene

oxides.[58] The issue of metallic impurities is important as powder catalysts are often formed through ball-milling which may introduce transition metal impurities such as Fe and Co.[56-57] Unmodified rGO as well as N-doped and ball-milled rGO were used to prepared three distinct graphene CMSs in their study. DFT calculations suggested that O_2 binding, which is proposed to be the first step in the ORR mechanism, may not be important for metal-free carbon catalysts based on graphene. This was ascribed to the dearth of suitable binding sites for O_2 other than at a particular minority of carbon edges which are found to be adjacent to graphitic N-sites. Instead a long range electron transfer mechanism was proposed which involved electron transfer to oxygen molecules located at the outer Helmholtz plane rather than to surface-bound O_2.

Experimental measurements on each CMS agreed with theoretical predictions; specifically, it was found that the major factor influencing the ORR kinetics was the position of the Fermi level, E_F, as electrode surfaces with a higher E_F would be expected to display a more reducing character and faster kinetics in long-range electron transfer reactions, where surface interactions are not at play. The introduction of N atoms into the carbon scaffold was found to have less of an effect on the ORR activity than the reduction of the graphitic cluster size induced by the ball milling process: the E_F was found to increase as the lateral dimension of the sp^2 network was reduced.

A study by Stamatin et al.[152] focused on the role that roughness and exposed defects have on the activity of graphene electrodes in the ORR. Thin layers of graphene were deposited via CVD on nanofiber supports resulting in undoped graphene electrode materials with negligible O-content, variable roughness and variable exposure of graphene layers to the electrolyte interface. The morphology of these graphene materials was remarkably different and could be controlled via the CVD growth process. Studies of ORR activity in alkaline conditions showed that, contrary to expectations, the morphologically smoothest fibers yielded the best ORR activity in terms of number of electrons and kinetic currents. Experiments using 4-nitrobenzylamine (4-NBA), which is proposed to intercalate at graphitic edge sites,[185] revealed that ORR activity correlated positively with the density of graphitic edges that are electrochemically active and available at the electrolyte interface. These results highlighted the importance of probing electrochemically relevant parameters when studying the correlation between structure/morphology and catalytic activity. Interestingly, conclusions from this study are in broad agreement with those by Choi et al.[58] regarding the role of edge density on ORR activity.

The majority of studies on the role of heteroatom doping focus on the effects arising from the introduction of nitrogen into the CMS's carbon scaffold. CMSs have also been used to

study the effects of other heteroatoms incorporated into graphene and related materials, including phosphorus,[186] boron[187-188] and sulphur.[189] Similar to the case of nitrogenation, graphene in these cases is an excellent CMS for studying the effects of heteroatom incorporation on electronic structure via a combination of DFT and optoelectronic techniques, and for the correlation of the resulting properties to electrocatalytic performance via standard electrochemical methods.

The beneficial effects of single dopants in carbon materials may be further enhanced by the use of co-doping strategies[190-191] where two or more heteroatoms are introduced into the scaffold together. The aim of such studies is generally to produce specific active sites through the combined effects of different heteroatoms. One such strategy is the use of boron and nitrogen co-doping, where the p- and n-type dopant effect of boron and nitrogen, respectively, may produce synergistic effects compared to the use of each dopant separately. [190, 192-193] The work of Zheng et al.[192] on B, N co-doped graphene CMSs demonstrated higher ORR onset potentials than singly-doped graphene. Furthermore,

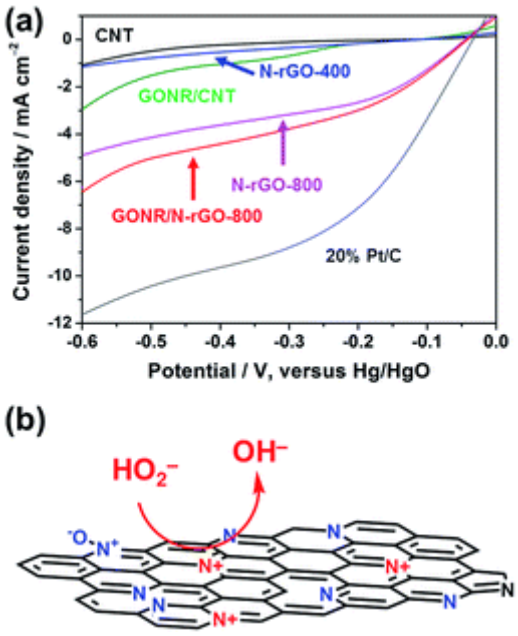

Figure 1.9. (a) Linear sweep voltammograms of CNTs, N-rGO prepared at 400 (N-rGO-400) and 800 °C (N-rGO-800), blends of GO nanoribbons with CNTs (GONR/CNT) and with N-rGO (GONER/N-rGO-800), and a 20% Pt/C standard catalyst; data collected in Ar-deaerated 0.1 M KOH electrolyte containing 20 mM H_2O_2. The nanocarbons with the highest activity towards H_2O_2 reduction are those that combine N-sites and O-sites in close association. (b) A simplified illustration of the proposed electrocatalytic role of active nitrogen sites (red) in N-rGO-800; other N-sites are displayed in blue. *Reproduced from Wu et al. J. Mater. Chem. A, 2017, 5, 3239-3248 with permission of The Royal Society of Chemistry.*

through DFT studies the group was able to propose a synergistic model for the improved

activity whereby an electron-withdrawing N-site located *meta* to a B-site activates the B-site and facilitates adsorption of O_2.

Another useful feature of graphene CMSs in contrast to a 3D material such as HOPG is that while the optoelectronic characterization of both materials may be carried out on single delocalized graphitic 'sheets', electrochemical studies on graphene can be carried out using powder catalysts. This feature allows for the blending of different functionalized graphene materials together into a single catalyst, as was done by Wu et al.[194] to study the cooperative effects of different pre-treatments on the same CMS. This work is distinct from the co-doping of a single CMS as each treatment is done separately, prior to mixing the catalysts together when producing an ink.

By studying three graphene-based systems, rGO containing defects and O-sites, H_2-treated rGO (H_2-rGO) with low O-content and H-terminated edges, and nitrogenated rGO (N-rGO), the authors showed that hydrogenation not only reduces ORR activity by passivating reactive edge sites and removing oxygenated edges, but it also appears to prevent the *in situ* production of new oxygenated edges. Hydrogenation of rGO inhibits hydrogen peroxide reduction to water at high overpotentials, thus suggesting that oxygenated moieties play a role in ensuring that the full $4e^-$ pathway for the reduction of O_2 proceeds at carbon surfaces (Figure 1.9).

N-rGO rich in graphitic-N and N-oxide type sites was found to have the highest onset potential and display an apparent $4e^-$ pathway at low overpotentials, however it also produced large peroxide yields at high overpotentials. The authors then showed that a catalyst that blended GO nanoribbons (GONR) with high O-site content and N-rGO resulted in both a high onset potential and a high rate of peroxide reduction at high overpotentials, thus supporting the role of cooperative effects between N-sites and O-sites in the ORR and offering mechanistic insights for future catalyst designs.

Glassy Carbon

Glassy carbon (GC), also known as vitreous carbon, is a carbon material first prepared in the 1960's by the thermal decomposition of organic polymers in inert atmosphere.[195] The material has its origins in the semiconductor processing industry, where it was first used as a crucible material. GC possesses numerous desirable properties including low porosity and smoothness, high chemical and thermal stability, and low thermal conductivity. For

industrial applications these properties are superior to crystalline graphite, which tends to flake off and absorb solution contaminants during processing.

The structure of GC may be described as hexagonal graphite 'packets' with no discernible graphitic orientation between the graphite layers. X-ray crystallographic measurements suggest that GC has a very small L_a of *ca.* 0.5 nm.[196] The porosity of GC has been determined to be less than 0.05%, compared to as high as 30% for graphite materials. As a graphitized form of carbon it is conductive, although its conductivity is less than that of pure graphite. It is therefore often described as a 'conductive ceramic,' owing to its intermediate properties between glasses and carbon materials.

For similar reasons to those discussed for HOPG, the low porosity and smoothness of GC suggests its utility as a model carbon material, particularly for electrochemical studies on disordered carbon materials. Important redox processes such as the ORR on normally take place on disordered carbon materials such as carbon blacks (see Section 1.1). GC may therefore be considered as a model system for disordered graphitized carbons with a reproducible surface morphology.

Figure 1.10. Advertisement for glassy carbon as a material for laboratory equipment, including crucibles and beakers. *Reproduced with permission from Cowlard et al. J. Mat. Sci., 1967, **2**, 507-512. Copyright © Springer Nature.*

The reactivity of GC materials is highly correlated to the compactness or hardness of the structure, which may depend on the specific details of the pyrolysis protocol. [197] The material

hardness is correlated to the number of free surface sites which may be functionalized with chemical moieties such as oxide groups which may modulate the reactivity. Electrochemical studies of the effects of carbon surface termination on reactivity in many redox processes have been published. Electrochemical pre-treatments to the surface of GC electrodes including anodization and cathodization were studied by Gunasingham et al. [197] and Engstrom et al.[198]

These studies attributed improved reactivity of GC towards many redox processes including ORR, Fe^{2+} oxidation and catechol oxidation to anodization treatments which introduce redox-mediating quinone groups into the surface and improve surface wettability. Factors such as surface roughening through chemical etching were excluded through SEM studies which showed no significant topographic changes after pre-treatment; the chemical inertness of GC allows it to serve as a robust model system for the study of harsh chemical pre-treatments without altering its morphology.

One disadvantage of GC electrodes is that they normally require some form of polishing protocol for their use as electrodes, in order to renew the electrode surface and remove contaminants. Polishing is typically accomplished with slurries of alumina or diamond on some form of cloth and often results in leftover polishing debris in the form of particles or organic binding agents, if the slurries are purchased commercially. Such debris can result in sluggish electron transfer kinetics by blocking surface sites or altering the surface wettability.[197] Fortunately, sonication with activated carbon in organic solvent[199] and electrochemical oxidation treatments have both been shown to allow for the removal of polishing debris to form a reproducible GC surface.[200]

Many studies of the effects of carbon surface chemistry on electrochemical reactivity with GC as a model surface have been carried out by McCreery et al. Examples include studies of electron transfer to redox probes such as $Fe^{2+/3+}$, $[Ru(NH_3)_6]^{2+/3+}$ and ascorbate.[201] Comparisons of oxidized GC surfaces with 'low-oxide' GC prepared via vacuum heat treatment allowed for the identification of carbonyl moieties in catalyzing charge transfer to $Fe^{2+/3+}$ in contrast to ascorbate, which was found to be sensitive to the surface termination but not to the specific presence of oxides.

Yang and McCreery also studied the effects of GC surface pre-treatment on the ORR.[202] In this study, a clean GC surface prepared by sonication in isopropanol/activated carbon was compared to GC covalently functionalized with a methylphenyl monolayer. Under alkaline conditions (pH > 10) the production of superoxide, $O_2^{\bullet-}$ from a $1e^-$ reduction of O_2 at the functionalized surface was demonstrated through voltammetry studies, whereas the $2e^-$ reduction of O_2 to peroxide was observed on the clean GC surface. The differences in

reactivity were specifically correlated to the surface termination: the organic layer on the functionalized GC allowed for electron tunneling to O_2 in solution to form superoxide, which then degraded in solution disproportionation.

By contrast, the clean GC surface was found to be highly active towards the adsorption of $O_2^{\bullet-}$ which the authors ascribed to the presence of numerous free binding sites such as dangling bonds at the electrode surface. These sites allowed for the formation of hydroperoxyl intermediates of the form $HO_2^{\bullet}$ at the surface which cannot occur on the functionalized surface due to the presence of the blocking organic monolayer. These results on GC are also likely applicable to O_2 reduction on nanocarbons in general, which often demonstrate the $2e^-$ reduction of O_2 as the sole reaction pathway.

Similar to the case of HOPG model systems, polished GC electrodes are often useful in electrocatalytic studies in particular because their intrinsic activity towards processes like the ORR and hydrogen evolution is typically poor. The effects of surface pre-treatments such as covalent functionalization and heteroatom doping on the electrocatalytic performance are therefore clearly contrasted when compared to unmodified GC. This feature of GC is also important when GC electrodes are used as the substrate for the deposition of other carbon materials, such as rGO and amorphous carbon on the GC surface for electrocatalytic studies, as discussed in the following section.

Amorphous Carbon

A frequent feature of studies on graphene is that they are not often carried out with pristine single layers, but more typically using electrodes prepared with multi-layer rGO. Interestingly, Pumera and co-workers[203] have shown that rGO displays extremely similar properties to a-C in terms of defect densities and graphitic cluster size, as determined via a combination of XPS and Raman spectroscopy. Whilst the authors argued that these parallels between the two materials implied that a-C might be an alternative choice of material to rGO for certain applications, it may also be argued that a-C constitutes a useful CMS in its own regard, particularly when the effects of disorder and the degree of graphitization are the parameters under study.

Like graphene, a-C materials have also been doped with nitrogen,[115, 139, 174] phosphorus,[169, 172] and boron.[170-171] a-C films may be easily prepared by an array of highly tunable physical vapour deposition methods, a fact that also holds true for the preparation of nitrogenated a-C:N films.[108-109, 111] Importantly, the ability to deposit these materials onto

standard electrodes in the form of a solid film presents two important advantages. Firstly, it enables the testing of the model carbon material in the absence of additives typically used to work with particle electrodes, such as Nafion®. Secondly, it enables fulfilment of all the requirements of hydrodynamic methods that use rotating disk electrodes, such as controlled and uniform material thickness and flat geometry, which are known to be sources of error that alter activity tests of carbon particle electrocatalysts, as discussed for example in work by Ozkan and co-workers[204] and Mayerhofer and co-workers.[205]

Work from the Colavita group utilized a-C and doped a-C materials for fundamental structure-activity studies focusing on correlating parameters such as the degree of graphitization and sp^2/sp^3 ratios to charge transfer kinetics at the interface.[87-88] Cullen et al. characterized a-C films with a high sp^2/sp^3 ratio and compared them to hydrogenated a-C (a-C:H) films with progressively higher sp^3 content and to glassy carbon using a combination of XPS, Raman spectroscopy, in situ infrared spectroscopy and a reactive aryldiazonium cation as a redox probe in solution.[87] The charge transfer properties of each CMS were studied using in situ real-time attenuated total internal reflectance Fourier transform infrared spectroscopy (ATR-FTIR) to monitor the covalent grafting of the aryldiazonium cation, which occurs via reductive dediazoniation.

Results indicated that grafting rates were highest for the undoped a-C with the highest sp^2/sp^3 ratio, and that increasing sp^3 content was negatively correlated with the rate of p-NBD attachement. Trends in the kinetics of reaction were found to be similar to those observed on CNTs by Strano and co-workers,[206-207] whereby increasing the metallic character of the carbon material correlated positively with grafting rates. Thus, an increased presence of sp^3 centres was found to directly impact electron transfer rates in these non-crystalline materials. Results were complemented by ex-situ voltammetric analysis of surfaces immersed in 4-nitrobenzylamine (4-NBA) which is proposed to intercalate at graphitic edge sites.[185] Undoped a-C also displayed higher coverages of 4-NBA than a-C:H films, which was attributed to passivation of edge sites in the latter materials by hydrogenation.

Therefore, both the sp^2/sp^3 and the abundance of defects could be compared between the different CMSs and correlated to their electrochemical performance. The presence of negligible roughness differences between the materials as determined by atomic force microscopy (AFM) measurements allowed for the chosen parameters of the materials to be studied without the confounding effects of differing surface areas or porosities. Moreover, the preparation of each CMS – in this case by DC magnetron sputtering – was easily facilitated by simply varying the Ar/H_2 gas mix during deposition.

Murphy et al. directly probed the effects of disorder in the carbon scaffold on charge transfer using two a-C CMSs and aryldiazonium salts as probes.[89] The results indicated that the post-deposition annealing of a-C at 700 °C produced a material with a greater degree of graphitization and greater metallic character than as-deposited a-C, as determined based on Raman, XPS and valence studies using ultraviolet photoelectron spectroscopy (UPS). The more metallic a-C electrode displayed faster charge transfer kinetics to the outer-sphere redox probe Hexaammine Ruthenium (III) as determined via impedance spectroscopy, as well as significantly faster spontaneous grafting rates of diazonium salts as quantified using in situ ATR-FTIR measurements.

Diazonium salts are not outer-sphere probes and the spontaneous grafting mechanism involves both an initial electron transfer and subsequent chemical steps;[89] their grafting rates are therefore expected to depend on the surface chemistry of the carbon electrode, including the density of graphitic edges which may serve as grafting sites. Indeed, this study found that the more graphitized carbon surface also possessed a higher edge plane density which may explain the higher overall diazonium grafting yield after graphitization. The effects of annealing on the bulk metallic character of the electrode are to increase the rate of the initial electron transfer step to the diazonium species in a similar fashion to which the electron transfer to Hexaammine Ruthenium (III) is enhanced. Subsequent steps in the mechanism such as chemical rearrangements or the binding of the reactive intermediates to edge sites may control the overall reaction rate. Nonetheless, this study illustrates the utility of a-C CMSs in structure-activity characterizations where the correlation between bulk material properties and charge transfer is of interest, a point which will be further explored in Chapter III of this thesis.

1.5 Probing the Structure and Reactivity of Carbon Materials Using Redox Processes

The choice of a good CMS for fundamental structure-activity studies of electrochemical performance is not the only factor to be considered by the good experimentalist. There is also the broad question of the electrochemical experiment itself, of which the electrode material forms but one aspect in addition to numerous others. These other variables include the choice of electrochemical instrumentation and cell arrangement, the solvent and any electrolyte dissolved therein, any electrochemical pre-treatments or surface cleaning protocols employed prior to the experiment proper, and the choice of redox active analyte

itself. The details of experimental techniques employed in this thesis will be discussed in Chapter II. This section will serve as a brief discussion of heterogeneous redox processes, *i.e.* electron transfer events occurring at the interface between a carbon electrode surface and the solution in which it is immersed.

A general overview of the electron transfer process will first be given, with reference to the early semi-quantitative model propounded by W.F. Libby in 1952[208] and the quantitative models which followed it in the works of R.A. Marcus[209-211]. This will be followed by a discussion of the chemistry of several important redox species with an emphasis on how these probes may be utilized as probes of the structure and surface chemical composition in carbon model systems.

The Marcus Theory of Electron Transfer

The earliest advances in treating the problem of electron transfer in aqueous media may be attributed to W.F. Libby,[208] who applied the Franck-Condon principle to the process. Libby reasoned that the different time scales for the motion of electrons in an electron transfer process and the motion of much heavier water molecules of the hydration sphere of the ion constituted a barrier to the charge transfer. Using the example of the ferrous-ferric ($Fe^{2+/3+}$) couple, an electron transferred to a ferric ion results initially in a ferrous ion with a ferric coordination sphere, before the slower reorientation of water molecules occurs. The energy barrier to the transfer is therefore proportional to the differences in hydration enthalpy between the ferrous and ferric ions and electron transfer occurs only if there is a similarity in geometrical arrangement between the reactant and product. When the hydration enthalpy is significantly different between the two ions, such a similarity may not be attainable within the amplitudes of the zero-point vibrations of the ground states, resulting in slow electron transfer.

Libby's approach explained why complex ions such as the ferro/ferricyanide redox couple underwent much more rapid electron transfer than for the simple ferrous/ferric couple. The complex ions consisted of a central $Fe^{2+/3+}$ ion with a fixed coordination sphere of cyanide ligands. This has the effect of reducing hydration enthalpies in general, thereby reducing the barrier to electron transfer, but more importantly the symmetry of the ferrocyanide and ferricyanide ions implies that a common spatial orientation is likely to be achieved by the vibrations of reactant and product complexes in their ground states.

The major lacuna in Libby's model was the lack of energy conservation, a fact that was recognized by Marcus when he first studied it. If an electron may only be transferred in a highly activated state analogous (but not identical) to the transition state in homogeneous chemical reactions, it obviously follows that energy is required in order to effect the transition. However, electron exchange reactions like the $Fe^{2+/3+}$ reaction by definition occur with no net change in the system's energy. This would not be a problem if the exchange were to be effected photochemically, but exchange reactions were known to occur in the dark and, in the particular case of complex ions, to occur rapidly. A more complete model was needed in order to explain quantitatively the factors affecting the rate of electron transfer whilst satisfying both the Franck-Condon principle and conserving the system's energy.

This model, expounded upon in a series of papers on the subject and ultimately culminating in Marcus' receipt of the Nobel Prize in Chemistry in 1992, is referred to as the Marcus Theory of electron transfer. At its core is the recognition that, owing to the differences in the solvent environment for ions with different valencies which Libby had described in his work, the intermediate state from which electron transfer occurs between reactant and product represents a non-equilibrium situation with the surrounding solvent molecules. This non-equilibrium state may be attained only through thermal fluctuations from the equilibrium state of the reactants. These fluctuations were envisioned by Marcus as changes of a vast multitude of coordinates: the positions of ions and solvent molecules, and their orientation (and therefore their dipole moments) relative to the redox species. Following attainment of the non-equilibrium state, the electron transfer may occur, and the system can then relax into a new orientation corresponding to equilibrium between the products and the solvent.

The problem in this sense is not dissimilar to activated complex theory and indeed one of the key predictions of Marcus theory is a rate constant for electron transfer with an exponential dependence on a free energy of activation in a similar fashion to the Eyring equation *(vide infra).* A quantitative treatment requires the computation of the system's potential energy, U, as a function of both the reacting ions and the vast array of solvent molecules surrounding them in the aforementioned state of non-equilibrium.

Marcus approached this problem by treating the reacting ions and their coordination sphere as charged spheres and the solvent beyond the reacting ions' inner sphere of coordinated molecules as a dielectric continuum with a particular value of polarization, P(r), which was a function of the position and orientation of the solvent molecules. He calculated the electrostatic free energy of the system, G, and thence derived P(r) in the state

corresponding to that in which the electron transfer may occur. This leads to an expression relating G and the amount of charge transferred, Δe, known as the Marcus formula:

$$G = \left(\frac{1}{2r_1} + \frac{1}{2r_2} - \frac{1}{R}\right) \cdot \left(\frac{1}{\mathcal{E}_0} - \frac{1}{\mathcal{E}_\infty}\right) \cdot (\Delta e)^2$$

In this formula, r_1 and r_2 are the radii of the ions involved in the charge transfer (including the inner-sphere solvent ligands), R is their separation, and ε_∞ and ε_0 are the static and high-frequency dielectric constants of the solvent respectively. The elegance of the Marcus formula is most evident in the fact that the many-coordinate problem of rearranging the solvent molecules into different orientations (due to the necessary differences in polarization because of the charge transfer) has been reduced to a relatively simple quadratic equation. This allows the free energy changes in the transition from reactant to product (and vice-versa) to be depicted as parabolic potential energy diagrams, as shown in Figure 1.11.

As shown in the figure, the reaction coordinate for the electron transfer process as parameterized through Δe involves an increase in the free energy of the reactants, which in this model is entirely due to the changes in polarization associated with the reorganization of the solvent.

The hypothetical scenario whereby the nuclear coordinates of the products are the same as the ground state of the charge distribution associated with the reactants is termed λ, the reorganization energy. The free energy of activation, $\Delta G^{\ddagger}$ may then expressed quantitatively in terms of λ, which may also be derived through simple simultaneous equation manipulations on the parabolas in Figure 1.11:

$$\Delta G^{\ddagger} = \frac{\left(\lambda + \Delta G^0\right)^2}{4\lambda}$$

This is qualitatively similar to the activation energy in Transition State Theory, but it must be stressed that the intersection point of the two parabolas in Figure 1.11 does not represent a unique nuclear configuration of reactants; outer-sphere redox reactions must only satisfy the condition that the reactant state and product state have equal energies and this is determined by the polarization state, P(r), of the solvent molecules, which is *not* a unique function of specific coordinates. Moreover, the ions and their coordination spheres are treated as non-deforming hard spheres which do not undergo alterations in bond lengths. Despite these differences from Transition State Theory, the approach leads to an analogous formula for the rate constant for electron transfer in terms of $\Delta G^{\ddagger}$:

$$k = Ae^{\left(-\frac{\Delta G^{\ddagger}}{k_B T}\right)}$$

With the pre-factor, A depending on the specific nature of the electron transfer and k_BT being the familiar product of the Boltzmann constant and the absolute temperature.

Marcus later modified his theory for exchange reactions in solution to include heterogeneous electron transfer at interfaces. He also extended his theory to include so-called 'inner-sphere' reactions which do involve significant alterations in the nuclear coordinates of the reactants themselves, including atom positions, bond lengths and alterations in the inner solvation shell.

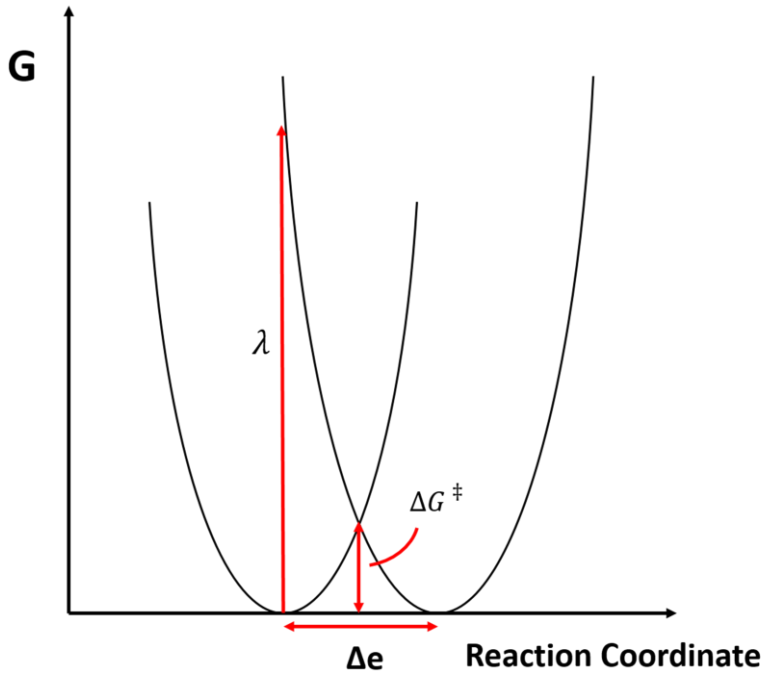

Figure 1.11. Free Energy – Reaction Coordinate diagram describing a charge transfer process between solvated ions according to the Marcus model. The reaction coordinate is parameterised in terms of the transfer of a quantity of charge, Δe, from one ion to the other in different solvation environments, as described by the Marcus equation. λ, the reorganisation energy for the process, as well as the activation energy $\Delta G^{\ddagger}$ are illustrated as arrows in the diagram.

In the following sections, some of the redox probes employed in this thesis will be discussed in the specific context of probing the properties of electrode materials. The convention used will be similar to the loose classification employed by Marcus himself in Reference 211. First, 'outer-sphere' redox probes will be discussed. They may be described as reactants whose reactivity may be adequately described by the outer-sphere theory that has just been introduced. In Marcus' convention, these are 'Class I' probes which are so categorized because of the absence of significant changes in the nuclear coordinates of the inner coordination sphere. In an analogous fashion Class II and III redox probes correspond to reactants which display slight and significant alterations in structure (*e.g.* in bond lengths

or ligand-ion distances) in their reduced and oxidized forms respectively. These will be grouped together in the present discussion as 'inner-sphere' probes.

Outer-Sphere Redox Compounds

Outer-sphere Redox compounds are those which do not show significant alterations in the inner solvation shell in the course of electron transfer reactions. An archetypal example which arguably aroused the interests of Libby in his original work is the Ferro/Ferricyanide couple, hexacyanoferrate (II)/(III), owing to its comparably rapid self-exchange kinetics when compared to hydrated Fe(II)/(III). Since the early work of Libby and Marcus, the kinetics of ferro/ferricyanide charge transfer have been found to be somewhat more complex than a simple outer-sphere redox probe in the context of electron transfer at interfaces. Accordingly, it is discussed in the following section.[215-216]

The near invariant nature of the inner coordination sphere of outer sphere redox compounds with respect to the oxidation state of the central ion implies that the only factors affecting the charge transfer process at the electrode-solution interface are, for a cathodic process, the overlap of the occupied states of the electrode material with the LUMO of the

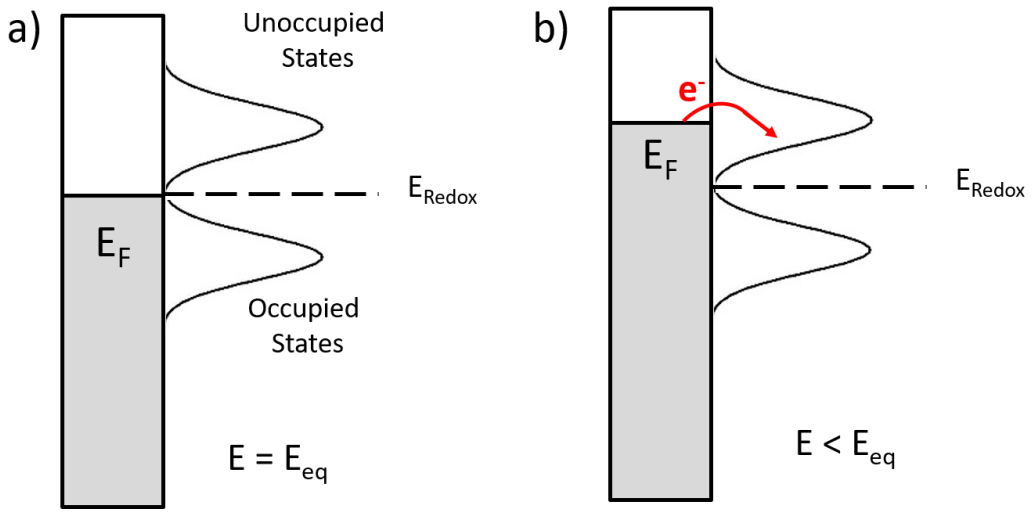

Figure 1.12. Energy level diagram illustrating an electrode in equilibrium with a solution containing a generic redox couple, O/R a) at the equilibrium potential, E_{eq} b) at a potential $E < E_{eq}$. The red arrow indicates charge transfer occurring from the electrode into the unoccupied states of the redox probe, corresponding to species O in solution.

redox probe. For an anodic process, the principle is identical, except the unoccupied states of the electrode and the HOMO of the probe are of interest. This is illustrated in Figure 1.12.

In this figure, the reduced and oxidized forms of a generic redox probe are depicted as O/R. Since both O and R may take on a variety of different states with different energies due to thermal fluctuations in the solvent orientations, the energy distribution is represented as a Gaussian curve around the equilibrium value.[212] The differences in the maxima of the O/R energy curves is proportional to the reorganization energy, λ, as described in the previous section. A smaller value of λ therefore implies a greater degree of overlap between the O/R states and therefore a faster rate of electron transfer.

Introducing an electrode into the solution of O and R induces a heterogeneous charge transfer at the interface until the electrode and the redox species in solution are in equilibrium. This is represented in Figure 1.12 as the point where the Fermi level, E_F, of the electrode is aligned with the energy levels of the solution species. At this point, no net charge transfer occurs and the system remains in equilibrium with an equilibrium potential difference (relative to the reference electrode) persisting at the interface. If the electrode is biased either positive or negative with respect to the solution energy levels, charge transfer is induced in order to restore the equilibrium condition, resulting in a change in the relative amounts of O and R to new equilibrium values. This process will be discussed in more detail in Chapter II.

For the present discussion, it suffices to say that an outer-sphere redox compound is expected to respond to changes in the potential difference at the interface in the manner just described without reference to the specific chemical nature of the interface. The low value of λ for the charge transfer implies that an approach of the analyte in solution to the surface is required only to effect the electron transfer, and no significant alterations (e.g. in bond lengths) are induced in the analyte by interactions at the surface. This is equivalent to stating that outer sphere redox compounds are unaffected by the presence of specific chemical moieties at the surface and are instead sensitive only to the material's bulk electronic properties, *viz.* the position of E_F and the density of states (DOS) around E_F.

A typical example of a Class I Redox couple is the Hexaammine Ruthenium (II)/(III) pair, $[Ru(NH_3)_6]^{2+/3+}$.[159, 213] The geometries of both oxidation states of the coordination complex are octahedral and the amine ligands which constitute the inner coordination sphere of the (II) and (III) ions do not show a dramatic alteration in bond lengths based on their infrared spectra, as expected for a Class I Redox Compound.[214] Due to its relative surface insensitivity, the $[Ru(NH_3)_6]^{2+/3+}$ couple is employed in Chapter III of this thesis for fundamental structure-activity studies on a-C:N electrodes where the bulk optoelectronic properties of the a-C:N are of primary interest.

Inner-Sphere Redox Compounds

The process of heterogeneous charge transfer between an electrode surface and an inner-sphere redox compound is governed by the same fundamental physical principles described in Figure 1.13 and the associated discussion in the previous section. The alteration of the electrode-solution potential away from its equilibrium value will also result in a net transfer of charge between the electrode and the solution until E_F and the redox levels in solution once again match. However, the distinguishing feature of an inner-sphere O/R couple is that it has a much larger value of λ than that expected for an outer-sphere couple, which serves as a significant energy barrier to charge transfer.

The main consequence of this higher energy barrier is that an inner-sphere probe can no longer be said to be sensitive only to an electrode's bulk properties. The physical interpretation of λ is that of a reorganization energy which may be associated with specific alterations in bond lengths in the inner coordination sphere as well as the requisite changes in the solvent environment discussed for outer-sphere processes. Accordingly, features of the electrode's surface chemistry may serve to expedite or impede charge transfer by facilitating or hindering this reorganization. The solvent can also have such an effect, as can the cations and anions of the supporting electrolyte.

Before discussing the redox probes of particular relevance to this thesis, it is worthwhile addressing some of the limitations of Marcus theory. When a reaction scheme involves multiple charge transfer steps (i.e. the reaction involves more than one heterogeneous electron transfer step), each with its own rate constant, *k*, the theory of Marcus is not applied to the final products with respect to the reactants, but may possibly be applied to the couple O and R involved in each individual step. Complex mechanisms involving processes such as the adsorption of analytes at the electrode surface or chemical reaction steps occurring in between electron transfer steps may also fall beyond the ambit of Marcus theory, but they still certainly constitute 'inner-sphere' processes in the most general meaning of the term and will also be discussed in this section.

Hexacyanoferrate (II)/(III) (Ferro/Ferricyanide)

Although it is the case that the fast rates of charge transfer associated with coordination complexes (as distinct from 'free' ions subject to hydration) inspired the work both Libby

and Marcus, it has since been determined that the hexacyanoferrate (II)/(III) couple, $[Fe(CN)_6]^{4-/3-}$, is not actually an outer-sphere redox probe even though it does display faster charge transfer kinetics than $Fe^{2+/3+}$. The resemblance between $[Fe(CN)_6]^{4-/3-}$ and the $[Ru(NH_3)_6]^{2+/3+}$ at many electrode surfaces is fortuitous. Firstly, the fast self-exchange of $[Fe(CN)_6]^{4-/3-}$ observed in many cases may actually be attributed to the presence of cations in solution from the supporting electrolyte.[215] It has been suggested that the highly charged complex $[Fe(CN)_6]^{4-/3-}$ ions are coupled via cation bridges, which would explain the observations of Peter et al. that the rate of charge transfer varies with cation size in the order $Li^+ << Na^+ < K^+ \cong Cs^+$.[215]

Swaddle et al. [216] demonstrated that in solutions containing potassium ions, the apparent rate constant for charge transfer in $[Fe(CN)_6]^{4-/3-}$, k_{app}, may actually be described as a function of the K^+ ion concentration:

$$k_{app} = k_0 + k_1[K^+]$$

the K^+ ions may serve as bridging ions between the complex anions, implying that the overall process is not actually outer-sphere but rather an inner-sphere process which is highly dependent upon both the size and abundance of cations. Indeed, experiments carried out by Swaddle et al. involving the sequestration of K^+ ions with crown ethers helped to demonstrate the catalytic effect of the cation and showed that k_0, the rate constant for the cation-independent electron transfer, displayed values consistent with those predicted by Marcus theory.

A further complicating factor in the use of $[Fe(CN)_6]^{4-/3-}$ is its sensitivity to the electrode surface. Beriet and Pletcher[217] demonstrated the aforementioned cation sensitivity with the addition of studies involving the Sr^{2+} ion, but also found that electron transfer to $[Fe(CN)_6]^{4/3-}$ is liable to be inhibited by the blocking of the surface with adsorbates. In particular, the decomposition of $[Fe(CN)_6]^{4-/3-}$ itself at the surface resulting in the attachment of cyanide ligands was proposed. Pre-adsorption of CN^- ions during surface preparation or via their introduction into the electrolyte was correlated to faster electron transfer, which the authors attributed to the inhibition of surface decomposition of $[Fe(CN)_6]^{4-/3-}$ and/or the prevention of interference from other adsorbates.

Further studies on Pt electrodes by Kitamura et al. confirmed that $[Fe(CN)_6]^{4-/3-}$ may dissociate at the surface, producing adsorbed species which may, depending on their orientation, either facilitate or inhibit electron transfer.[218] Intriguingly, the cation-dependence of $[Fe(CN)_6]^{4-/3-}$ was linked to its sensitivity to the electrode preparation by the authors, who posited that CN^- adsorbates facilitate electron transfer from/to $[Fe(CN)_6]^{4-/3-}$ by stabilizing adsorbed cations which serve as bridges to the heterogeneous

redox process in an equivalent fashion to their behavior in the homogeneous self-exchange process.

This result also explains the fast rates of electron transfer observed by Beriet and Pletcher following pre-adsorption of their electrodes with cyanide anions. Inhibition of charge transfer is expected for surfaces with surface moieties or blocking adsorbates which do not stabilize adsorbed cations which can then act as bridges for the electron transfer. Experimentation with the $[Fe(CN)_6]^{4-/3-}$ couple is therefore a relatively simple and accessible method for the characterization of an electrode's surface chemistry, as will be shown for a-C:N electrodes in Chapter III of this thesis.

Catechols

Catechol and its derivatives are important redox compounds with particular relevance to biology. 2-(3,4-Dihydroxyphenyl)ethylamine, better known as dopamine, is a catechol derivative which functions as a neurotransmitter. Aberrations in dopamine levels have been famously correlated to Parkinson's disease, as well as attention deficit hyperactivity disorder (ADHD) and schizophrenia.[148] Electrochemical methods for the detection of dopamine in biological media are highly desirable, but must be able to discriminate between it and co-analytes such as ascorbic acid which have similar redox potentials. [148-149]

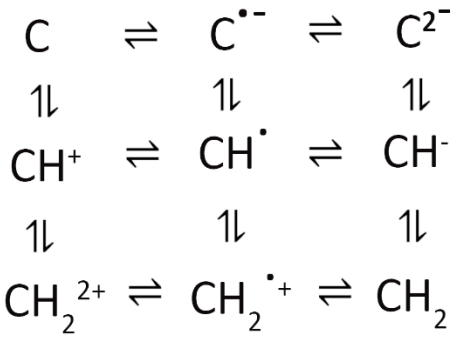

Figure 1.13. 'Scheme of Squares' describing a 2-electron, 2-proton oxidation of a catechol (CH_2).

The redox chemistry of catechols is highly complex. Disregarding for the moment any deviations introduced by the presence of different substituents on the dihydroxyphenyl core, the oxidation of catechol involves a net transfer of 2 electrons and 2 protons, which has been shown to be explicable as a 'scheme of squares'[219] (Figure 1.13). In this diagram, following the reaction scheme horizontally corresponds to an electron transfer step, whereas the vertical equilibria are proton transfer steps. The 'starting' point in any given experiment is

highly dependent on the pH, and the relative orders of electron and proton transfer have also been considered with reference to the pKa values of intermediates. For instance, the accepted pathway at low pH values is thought to be $e^- \rightarrow H^+ \rightarrow e^- \rightarrow H^+$.

Kinetic studies of dopamine oxidation in particular have been complicated by its sensitivity to the surface preparation. This point will be discussed in detail in Chapter IV, where this surface sensitivity is exploited as a means of characterizing the surface chemisty and nanostructure of nitrogenated carbon electrodes.

Oxygen

The oxygen reduction reaction (ORR) has already been discussed in previous sections of this chapter in the context of N-doped carbon nanomaterial electrocatalysis. This brief section will focus on the ORR in a more general sense by introducing the thermodynamics governing the reaction and commenting on the current challenge of overcoming its kinetic limitations. The ORR is a 4-electron, 4-proton process, making it the most complex redox process discussed thus far. The formal potential, $E^{0'}$, for the overall process is 1.229 V vs the Reversible Hydrogen Electrode, RHE:

$$O_2 + 4H^+ + 4e^- \rightarrow 2H_2O \qquad E°' = 1.229 \text{ V vs. RHE}$$

Any material capable of effecting the ORR at the thermodynamic potential of 1.229 V vs RHE would be a zero-overpotential ORR catalyst. However, this is not currently attainable even for the best catalysts currently known. Following the analysis of Marc Koper,[220] this is because ORR catalysis at surfaces requires the binding of oxygen or of its intermediates, and a balance in the magnitude of the adsorption free energy for each the intermediates (ΔG_{ads}) needs to be achieved. This is not currently possible due to strong correlation between the binding energies of the intermediates, as has been shown on metal surfaces.[221] For example, if for the sake of discussion the following mechanism is assumed:

$$O_2 + H^+ + e^- \rightarrow OOH^*$$
$$OOH^* + H^+ + e^- \rightarrow 2OH^*$$
$$2OH^* + 2H^+ + 2e^- \rightarrow 2H_2O$$

where asterisks denote species adsorbed at the electrode surface, the value of ΔG_{ads} for the OOH^* and OH^* intermediates are not independent of one another. One or more of these reaction steps is therefore expected to place a limitation on the ORR due to increases in the activation energy, $\Delta G^{\ddagger}$ with ΔG_{ads}, the so-called Bronsted-Evans-Polanyi postulate,[222] which implies that the strong binding of an intermediate will present a large activation barrier for its removal, and vice versa.

It is clear from this discussion that this result is independent of the exact mechanism: the optimal heterogeneous catalyst should always be one that binds oxygen (and any reaction intermediates derived from it) neither too strongly nor too weakly. It should also be apparent that most, if not all of the electron transfer steps in the ORR are inner-sphere processes which depend not only on specific surface sites which facilitate the binding of intermediates, but also the coverages of these intermediates and of any other blocking species which may also bind at the electrode surface. As a further complicating factor, the overall $4e^-$ reduction of O_2 may proceed as a $2 + 2\ e^-$ process with a hydrogen peroxide intermediate:

$$O_2 + H_2O + 2e^- \rightarrow HO_2^- + OH^- \qquad E°= 0.695\ V\ vs.\ RHE$$

Depending on the particular electrocatalyst, the above reaction may be the final product of O_2 reduction, particularly on undoped carbon surfaces.[202] The $2e^-$ pathway is often considered an inefficient and undesirable outcome compared to the full $4e^-$ reduction of oxygen to water.[223-224]

The sensitivity of the ORR to the electrode surface in the case of N-doped carbons has been studied both theoretically and experimentally by many groups.[24, 31, 115, 120, 153, 225-226] Many different N-sites have been implicated in promoting the ORR, as mentioned in Section 1.4, although at the time of writing, a clear consensus of which type and distribution of N site is desirable for promoting the process has not emerged. This problem is addressed in Chapter VI of this thesis, in which studies of the ORR performance of nitrogenated carbons derived from a-C and a-C:N films will be presented. The activity of the materials will be correlated to both their bulk properties and their surface chemistry. Keeping with the theme of using redox active compounds as probes of a material's structure, the use of oxygen in such studies can be considered as an extreme example of 'inner-sphere' probing, where the surface properties of the electrode are the most important factor in determining the electrochemical response.

1.6 Aim of this Thesis

In this chapter the numerous practical applications of carbon materials have been briefly reviewed, with a focus on their electrochemistry. N-doped carbon materials were also introduced as promising materials for electroanalysis and for metal-free electrocatalysis. Advances in both of these disciplines have been made by the judicious choice of carbon model systems for structure-activity studies, but there is still much to learn. The main aim of this thesis is therefore to prepare carbon model systems based on sputtered a-C:N films and to correlate their structural properties, both of the bulk and the surface, to their electrochemical performance. Real electrocatalytic systems frequently employ disordered carbon materials; the development of carbon model systems that incorporate disorder therefore allows the factors affecting electrocatalytic performance in practical systems to be systematically investigated.

The preparation of a-C:N films is discussed in Chapter III, where the effects of different levels of nitrogen-incorporation on the properties of the films are discussed. This includes a characterization of the bulk optoelectronic properties of the materials, the nitrogen content and N-site chemistry, film thickness, and surface roughness. This characterization is combined with electrochemical studies of a-C:N electrodes using the outer-sphere $[Ru(NH_3)_6]^{2+/3+}$ redox couple in order to focus on the bulk properties.

In Chapters IV-V, the electrochemistry of N-free and N-doped carbon model systems in solutions of catechol derivatives is studied. The electrochemical performance is correlated to the carbon scaffold nanostructure and N-site chemistry. The data obtained through experimentation are also complemented by density functional theory (DFT) calculations of catechol interactions with model carbon structures.

Chapter VI explores the ORR performance of different N-doped carbon model systems based on a-C:N films. The electrochemical activity is correlated to both the surface nanostructure and the N-site chemistry. Finally, results and conclusions from all of the work in Chapters III-VI are presented along with a brief discussion of side-projects undertaken throughout the course of this project and possible future work.

1.7 References

1. Robertson, J., Diamond-like amorphous carbon. *Materials Science and Engineering: R: Reports* **2002,** *37* (4–6), 129-281.

2. Grill, A., Diamond-like carbon coatings as biocompatible materials—an overview. *Diamond and Related Materials* **2003,** *12* (2), 166-170.

3. Jiang, J.; Arnell, R. D., The effect of sliding speed on wear of diamond-like carbon coatings. *Wear* **1998,** *218* (2), 223-231.

4. de las Casas, C.; Li, W., A review of application of carbon nanotubes for lithium ion battery anode material. *Journal of Power Sources* **2012,** *208*, 74-85.

5. Ehsani, M.; Gao, Y.; Longo, S.; Ebrahimi, K., *Modern electric, hybrid electric, and fuel cell vehicles*. CRC press: 2018.

6. Sui, S.; Wang, X.; Zhou, X.; Su, Y.; Riffat, S.; Liu, C.-J., A comprehensive review of Pt electrocatalysts for the oxygen reduction reaction: Nanostructure, activity, mechanism and carbon support in PEM fuel cells. *Journal of Materials Chemistry A* **2017,** *5* (5), 1808-1825.

7. Borenstein, A.; Hanna, O.; Attias, R.; Luski, S.; Brousse, T.; Aurbach, D., Carbon-based composite materials for supercapacitor electrodes: a review. *Journal of Materials Chemistry A* **2017,** *5* (25), 12653-12672.

8. Noked, M.; Soffer, A.; Aurbach, D., The electrochemistry of activated carbonaceous materials: past, present, and future. *Journal of Solid State Electrochemistry* **2011,** *15* (7), 1563.

9. Pokropivny, V. V.; Skorokhod, V. V., Classification of nanostructures by dimensionality and concept of surface forms engineering in nanomaterial science. *Materials Science and Engineering: C* **2007,** *27* (5), 990-993.

10. Georgakilas, V.; Perman, J. A.; Tucek, J.; Zboril, R., Broad Family of Carbon Nanoallotropes: Classification, Chemistry, and Applications of Fullerenes, Carbon Dots, Nanotubes, Graphene, Nanodiamonds, and Combined Superstructures. *Chemical Reviews* **2015,** *115* (11), 4744-4822.

11. Chen, X.; Chang, J.; Ke, Q., Probing the activity of pure and N-doped fullerenes towards oxygen reduction reaction by density functional theory. *Carbon* **2018,** *126*, 53-57.

12. Kroto, H. W.; Heath, J. R.; O'Brien, S. C.; Curl, R. F.; Smalley, R. E., C60: Buckminsterfullerene. *Nature* **1985,** *318*, 162.

13. Gao, F.; Zhao, G.-L.; Yang, S.; Spivey, J. J., Nitrogen-Doped Fullerene as a Potential Catalyst for Hydrogen Fuel Cells. *Journal of the American Chemical Society* **2013,** *135* (9), 3315-3318.

14. Noh, S. H.; Kwon, C.; Hwang, J.; Ohsaka, T.; Kim, B.-J.; Kim, T.-Y.; Yoon, Y.-G.; Chen, Z.; Seo, M. H.; Han, B., Self-assembled nitrogen-doped fullerenes and their catalysis for fuel cell and rechargeable metal-air battery applications. *Nanoscale* **2017,** *9* (22), 7373-7379.

15. Wu, Z. L.; Liu, Z. X.; Yuan, Y. H., Carbon dots: materials, synthesis, properties and approaches to long-wavelength and multicolor emission. *Journal of Materials Chemistry B* **2017,** *5* (21), 3794-3809.

16. Xu, X.; Ray, R.; Gu, Y.; Ploehn, H. J.; Gearheart, L.; Raker, K.; Scrivens, W. A., Electrophoretic Analysis and Purification of Fluorescent Single-Walled Carbon Nanotube Fragments. *Journal of the American Chemical Society* **2004,** *126* (40), 12736-12737.

17. Sun, Y.-P.; Zhou, B.; Lin, Y.; Wang, W.; Fernando, K. A. S.; Pathak, P.; Meziani, M. J.; Harruff, B. A.; Wang, X.; Wang, H.; Luo, P. G.; Yang, H.; Kose, M. E.; Chen, B.; Veca, L. M.; Xie, S.-Y., Quantum-Sized Carbon Dots for Bright and Colorful Photoluminescence. *Journal of the American Chemical Society* **2006,** *128* (24), 7756-7757.

18. Zhao, Q.-L.; Zhang, Z.-L.; Huang, B.-H.; Peng, J.; Zhang, M.; Pang, D.-W., Facile preparation of low cytotoxicity fluorescent carbon nanocrystals by electrooxidation of graphite. *Chemical Communications* **2008,** (41), 5116-5118.

19. Cao, L.; Wang, X.; Meziani, M. J.; Lu, F.; Wang, H.; Luo, P. G.; Lin, Y.; Harruff, B. A.; Veca, L. M.; Murray, D.; Xie, S.-Y.; Sun, Y.-P., Carbon Dots for Multiphoton Bioimaging. *Journal of the American Chemical Society* **2007,** *129* (37), 11318-11319.

20. Yang, Z.; Xu, M.; Liu, Y.; He, F.; Gao, F.; Su, Y.; Wei, H.; Zhang, Y., Nitrogen-doped, carbon-rich, highly photoluminescent carbon dots from ammonium citrate. *Nanoscale* **2014,** *6* (3), 1890-1895.

21. Li, Q.; Ohulchanskyy, T. Y.; Liu, R.; Koynov, K.; Wu, D.; Best, A.; Kumar, R.; Bonoiu, A.; Prasad, P. N., Photoluminescent carbon dots as biocompatible nanoprobes for targeting cancer cells in vitro. *The Journal of Physical Chemistry C* **2010,** *114* (28), 12062-12068.

22. Yang, S.-T.; Cao, L.; Luo, P. G.; Lu, F.; Wang, X.; Wang, H.; Meziani, M. J.; Liu, Y.; Qi, G.; Sun, Y.-P., Carbon dots for optical imaging in vivo. *Journal of the American Chemical Society* **2009,** *131* (32), 11308-11309.

23. Wang, Q.; Huang, X.; Long, Y.; Wang, X.; Zhang, H.; Zhu, R.; Liang, L.; Teng, P.; Zheng, H., Hollow luminescent carbon dots for drug delivery. *Carbon* **2013,** *59*, 192-199.

24. Li, Q.; Zhang, S.; Dai, L.; Li, L. S., Nitrogen-Doped Colloidal Graphene Quantum Dots and Their Size-Dependent Electrocatalytic Activity for the Oxygen Reduction Reaction. *Journal of the American Chemical Society* **2012,** *134* (46), 18932-18935.

25. Li, Y.; Zhao, Y.; Cheng, H.; Hu, Y.; Shi, G.; Dai, L.; Qu, L., Nitrogen-Doped Graphene Quantum Dots with Oxygen-Rich Functional Groups. *Journal of the American Chemical Society* **2012,** *134* (1), 15-18.

26. Zhu, C.; Zhai, J.; Dong, S., Bifunctional fluorescent carbon nanodots: green synthesis via soy milk and application as metal-free electrocatalysts for oxygen reduction. *Chemical Communications* **2012,** *48* (75), 9367-9369.

27. Hu, C.; Yu, C.; Li, M.; Wang, X.; Dong, Q.; Wang, G.; Qiu, J., Nitrogen-doped carbon dots decorated on graphene: a novel all-carbon hybrid electrocatalyst for enhanced oxygen reduction reaction. *Chemical Communications* **2015,** *51* (16), 3419-3422.

28. Huang, X.; Yang, L.; Hao, S.; Zheng, B.; Yan, L.; Qu, F.; Asiri, A. M.; Sun, X., N-Doped carbon dots: a metal-free co-catalyst on hematite nanorod arrays toward efficient photoelectrochemical water oxidation. *Inorganic Chemistry Frontiers* **2017,** *4* (3), 537-540.

29. Faubert, G.; Côté, R.; Guay, D.; Dodelet, J. P.; Dénès, G.; Bertrandc, P., Iron catalysts prepared by high-temperature pyrolysis of tetraphenylporphyrins adsorbed on carbon black for oxygen reduction in polymer electrolyte fuel cells. *Electrochimica Acta* **1998,** *43* (3), 341-353.

30. Faubert, G.; Lalande, G.; Côté, R.; Guay, D.; Dodelet, J. P.; Weng, L. T.; Bertrand, P.; Dénès, G., Heat-treated iron and cobalt tetraphenylporphyrins adsorbed on carbon black: Physical characterization and catalytic properties of these materials for the reduction of oxygen in polymer electrolyte fuel cells. *Electrochimica Acta* **1996,** *41* (10), 1689-1701.

31. Wood, K. N.; O'Hayre, R.; Pylypenko, S., Recent progress on nitrogen/carbon structures designed for use in energy and sustainability applications. *Energy & Environmental Science* **2014,** *7* (4), 1212-1249.

32. Iijima, S., Helical microtubules of graphitic carbon. *Nature* **1991,** *354*, 56.

33. Wang, X.; Li, Q.; Xie, J.; Jin, Z.; Wang, J.; Li, Y.; Jiang, K.; Fan, S., Fabrication of ultralong and electrically uniform single-walled carbon nanotubes on clean substrates. *Nano Letters* **2009,** *9* (9), 3137-3141.

34. Pham-Huu, C.; Ledoux, M.-J., Carbon nanomaterials with controlled macroscopic shapes as new catalytic materials. *Topics in Catalysis* **2006,** *40* (1), 49-63.

35. Hata, K.; Futaba, D. N.; Mizuno, K.; Namai, T.; Yumura, M.; Iijima, S., Water-Assisted Highly Efficient Synthesis of Impurity-Free Single-Walled Carbon Nanotubes. *Science* **2004,** *306* (5700), 1362-1364.

36. Pang, J.; Bachmatiuk, A.; Ibrahim, I.; Fu, L.; Placha, D.; Martynkova, G. S.; Trzebicka, B.; Gemming, T.; Eckert, J.; Rümmeli, M. H., CVD growth of 1D and 2D sp2 carbon nanomaterials. *Journal of Materials Science* **2016,** *51* (2), 640-667.

37. Terranova, M. L.; Sessa, V.; Rossi, M., The world of carbon nanotubes: An overview of CVD growth methodologies. *Chemical Vapor Deposition* **2006,** *12* (6), 315-325.

38. Kim, C.; Ngoc, B. T. N.; Yang, K. S.; Kojima, M.; Kim, Y. A.; Kim, Y. J.; Endo, M.; Yang, S. C., Self-sustained thin webs consisting of porous carbon nanofibers for supercapacitors via the electrospinning of polyacrylonitrile solutions containing zinc chloride. *Advanced Materials* **2007,** *19* (17), 2341.

39. Inagaki, M.; Yang, Y.; Kang, F., Carbon Nanofibers Prepared via Electrospinning. *Advanced Materials* **2012,** *24* (19), 2547-2566.

40. Maldonado, S.; Stevenson, K. J., Direct preparation of carbon nanofiber electrodes via pyrolysis of iron(II) phthalocyanine: Electrocatalytic aspects for oxygen reduction. *The Journal of Physical Chemistry B* **2004,** *108* (31), 11375-11383.

41. Huang, S.; Dai, L.; Mau, A. W. H., Patterned Growth and Contact Transfer of Well-Aligned Carbon Nanotube Films. *The Journal of Physical Chemistry B* **1999,** *103* (21), 4223-4227.

42. Gong, K.; Du, F.; Xia, Z.; Durstock, M.; Dai, L., Nitrogen-Doped Carbon Nanotube Arrays with High Electrocatalytic Activity for Oxygen Reduction. *Science* **2009,** *323* (5915), 760-764.

43. Domínguez, C.; Pérez-Alonso, F. J.; Abdel Salam, M.; Al-Thabaiti, S. A.; Obaid, A. Y.; Alshehri, A. A.; Gómez de la Fuente, J. L.; Fierro, J. L. G.; Rojas, S., On the relationship between N content, textural properties and catalytic performance for the oxygen reduction reaction of N/CNT. *Applied Catalysis B: Environmental* **2015,** *162*, 420-429.

44. Maldonado, S.; Stevenson, K. J., Influence of nitrogen doping on oxygen reduction electrocatalysis at carbon nanofiber electrodes. *The Journal of Physical Chemistry B* **2005,** *109* (10), 4707-4716.

45. Novoselov, K. S.; Fal′ko, V. I.; Colombo, L.; Gellert, P. R.; Schwab, M. G.; Kim, K., A roadmap for graphene. *Nature* **2012,** *490*, 192.

46. Solis-Fernandez, P.; Bissett, M.; Ago, H., Synthesis, structure and applications of graphene-based 2D heterostructures. *Chemical Society Reviews* **2017,** *46* (15), 4572-4613.

47. Hernandez, Y.; Nicolosi, V.; Lotya, M.; Blighe, F. M.; Sun, Z.; De, S.; McGovern, I. T.; Holland, B.; Byrne, M.; Gun'Ko, Y. K.; Boland, J. J.; Niraj, P.; Duesberg, G.; Krishnamurthy, S.; Goodhue, R.; Hutchison, J.; Scardaci, V.; Ferrari, A. C.; Coleman, J. N., High-yield production of graphene by liquid-phase exfoliation of graphite. *Nature Nanotechnology* **2008,** *3*, 563.

48. Stankovich, S.; Dikin, D. A.; Piner, R. D.; Kohlhaas, K. A.; Kleinhammes, A.; Jia, Y.; Wu, Y.; Nguyen, S. T.; Ruoff, R. S., Synthesis of graphene-based nanosheets via chemical reduction of exfoliated graphite oxide. *Carbon* **2007,** *45* (7), 1558-1565.

49. Dikin, D. A.; Stankovich, S.; Zimney, E. J.; Piner, R. D.; Dommett, G. H. B.; Evmenenko, G.; Nguyen, S. T.; Ruoff, R. S., Preparation and characterization of graphene oxide paper. *Nature* **2007,** *448* (7152), 457-460.

50. Wong, C. H. A.; Ambrosi, A.; Pumera, M., Thermally reduced graphenes exhibiting a close relationship to amorphous carbon. *Nanoscale* **2012,** *4* (16), 4972-4977.

51. Terrones, M.; Botello-Méndez, A. R.; Campos-Delgado, J.; López-Urías, F.; Vega-Cantú, Y. I.; Rodríguez-Macías, F. J.; Elías, A. L.; Muñoz-Sandoval, E.; Cano-Márquez, A. G.; Charlier, J.-C.; Terrones, H., Graphene and graphite nanoribbons: Morphology, properties, synthesis, defects and applications. *Nano Today* **2010,** *5* (4), 351-372.

52. Campos-Delgado, J.; Romo-Herrera, J. M.; Jia, X.; Cullen, D. A.; Muramatsu, H.; Kim, Y. A.; Hayashi, T.; Ren, Z.; Smith, D. J.; Okuno, Y.; Ohba, T.; Kanoh, H.; Kaneko, K.; Endo, M.; Terrones, H.; Dresselhaus, M. S.; Terrones, M., Bulk Production of a New

Form of sp2 Carbon: Crystalline Graphene Nanoribbons. *Nano Letters* **2008,** *8* (9), 2773-2778.

53. Chen, L.; Hernandez, Y.; Feng, X.; Müllen, K., From Nanographene and Graphene Nanoribbons to Graphene Sheets: Chemical Synthesis. *Angewandte Chemie International Edition* **2012,** *51* (31), 7640-7654.

54. Qu, L.; Liu, Y.; Baek, J.-B.; Dai, L., Nitrogen-Doped Graphene as Efficient Metal-Free Electrocatalyst for Oxygen Reduction in Fuel Cells. *ACS Nano* **2010,** *4* (3), 1321-1326.

55. Geng, D.; Chen, Y.; Chen, Y.; Li, Y.; Li, R.; Sun, X.; Ye, S.; Knights, S., High oxygen-reduction activity and durability of nitrogen-doped graphene. *Energy & Environmental Science* **2011,** *4* (3), 760-764.

56. Wang, L.; Ambrosi, A.; Pumera, M., "Metal-Free" Catalytic Oxygen Reduction Reaction on Heteroatom-Doped Graphene is Caused by Trace Metal Impurities. *Angewandte Chemie International Edition* **2013,** *52* (51), 13818-13821.

57. Wong, C. H. A.; Sofer, Z.; Kubešová, M.; Kučera, J.; Matějková, S.; Pumera, M., Synthetic routes contaminate graphene materials with a whole spectrum of unanticipated metallic elements. *Proceedings of the National Academy of Sciences* **2014,** *111* (38), 13774.

58. Choi, C. H.; Lim, H.-K.; Chung, M. W.; Park, J. C.; Shin, H.; Kim, H.; Woo, S. I., Long-Range Electron Transfer over Graphene-Based Catalyst for High-Performing Oxygen Reduction Reactions: Importance of Size, N-doping, and Metallic Impurities. *Journal of the American Chemical Society* **2014,** *136* (25), 9070-9077.

59. Lai, L.; Potts, J. R.; Zhan, D.; Wang, L.; Poh, C. K.; Tang, C.; Gong, H.; Shen, Z.; Lin, J.; Ruoff, R. S., Exploration of the active center structure of nitrogen-doped graphene-based catalysts for oxygen reduction reaction. *Energy & Environmental Science* **2012,** *5* (7), 7936-7942.

60. Robertson, J., Preparation and properties of amorphous carbon. *Journal of Non-Crystalline Solids* **1991,** *137–138, Part 2* (0), 825-830.

61. Robertson, J., Properties of diamond-like carbon. *Surface and Coatings Technology* **1992,** *50* (3), 185-203.

62. Robertson, J.; O'Reilly, E. P., Electronic and atomic structure of amorphous carbon. *Physical Review B* **1987,** *35* (6), 2946-2957.

63. Lemoine, P.; Quinn, J. P.; Maguire, P.; McLaughlin, J. A., Comparing hardness and wear data for tetrahedral amorphous carbon and hydrogenated amorphous carbon thin films. *Wear* **2004,** *257* (5-6), 509-522.

64. Gangopadhyay, A., Mechanical and tribological properties of amorphous carbon films. *Tribology Letters* **1998,** *5* (1), 25-39.

65. Bhushan, B.; Kellock, A. J.; Cho, N.-H.; Ager, J. W., Characterization of chemical bonding and physical characteristics of diamond-like amorphous carbon and diamond films. *Journal of Materials Research* **1992,** *7* (02), 404-410.

66. Vojs, M.; Zdravecka, E.; Marton, M.; Bohac, P.; Franta, L.; Vesely, M., Properties of amorphous carbon layers for bio-tribological applications. *Microelectronics Journal* **2009,** *40* (3), 650-653.

67. Oliver, W. C.; Pharr, G. M., An improved technique for determining hardness and elastic modulus using load and displacement sensing indentation experiments. *Journal of Materials Research* **1992,** *7* (06), 1564-1583.

68. Pharr, G. M.; Callahan, D. L.; McAdams, S. D.; Tsui, T. Y.; Anders, S.; Anders, A.; Ager, J. W.; Brown, I. G.; Bhatia, C. S.; Silva, S. R. P.; Robertson, J., Hardness, elastic modulus, and structure of very hard carbon films produced by cathodic-arc deposition with substrate pulse biasing. *Applied Physics Letters* **1996,** *68* (6), 779-781.

69. Logothetidis, S.; Kassavetis, S.; Charitidis, C.; Panayiotatos, Y.; Laskarakis, A., Nanoindentation studies of multilayer amorphous carbon films. *Carbon* **2004,** *42* (5-6), 1133-1136.

70. Dunlop, E.; Haupt, J.; Schmidt, K.; Gissler, W., Hardness and Young's modulus of diamond-like carbon films prepared by ion beam methods. *Diamond and Related Materials* **1992,** *1* (5–6), 644-649.

71. Cho, S.; Chasiotis, I.; Friedmann, T. A.; Sullivan, J. P., Young's modulus, Poisson's ratio and failure properties of tetrahedral amorphous diamond-like carbon for MEMS devices. *Journal of Micromechanics and Microengineering* **2005,** *15* (4), 728-735.

72. Yang, P.; Chen, J. Y.; Leng, Y. X.; Sun, H.; Huang, N.; Chu, P. K., Effect of annealing on structure and biomedical properties of amorphous hydrogenated carbon films. *Surface Coatings Technology* **2004,** *186* (1-2), 125-130.

73. Rodil, S.; Olivares, R.; Arzate, H.; Muhl, S., Biocompatibility, Cytotoxicity and Bioactivity of Amorphous Carbon Films. In *Carbon*, Messina, G.; Santangelo, S., Eds. Springer Berlin Heidelberg: 2006; Vol. 100, pp 55-75.

74. Broitman, E.; Macdonald, W.; Hellgren, N.; Radnoczi, G.; Czigany, Z.; Wennerberg, A.; Jacobsson, M.; Hultman, L., Carbon nitride films on orthopedic substrates. *Diamond and Related Materials* **2000,** *9* (12), 1984-1991.

75. Kinoshita, H.; Kubota, M.; Ohno, G., Deposition of amorphous carbon films using Ar and/or N-2 magnetron sputter with ring permanent magnet. *Thin Solid Films* **2012,** *523*, 52-54.

76. Ahmad, I.; Roy, S. S.; Maguire, P. D.; Papakonstantinou, P.; McLaughlin, J. A., Effect of substrate bias voltage and substrate on the structural properties of amorphous carbon films deposited by unbalanced magnetron sputtering. *Thin Solid Films* **2005,** *482* (1-2), 45-49.

77. Zhang, Y. J.; Liu, X. Y.; Bai, W. Q.; Tang, H.; Shi, S. J.; Wang, X. L.; Gu, C. D.; Tu, J. P., Magnetron sputtering amorphous carbon coatings on metallic lithium: Towards promising anodes for lithium secondary batteries. *Journal of Power Sources* **2014,** *266*, 43-50.

78. Kelly, P. J.; Arnell, R. D., Magnetron sputtering: a review of recent developments and applications. *Vacuum* **2000,** *56* (3), 159-172.

79. Schiller, S.; Goedicke, K.; Reschke, J.; Kirchhoff, V.; Schneider, S.; Milde, F., Pulsed magnetron sputter technology. *Surface and Coatings Technology* **1993,** *61* (1–3), 331-337.

80. Logothetidis, S., Sputtered Amorphous Carbon Films: Micro-Structure, Density, Optical and Mechanical Properties. *International Journal of Modern Physics B: Condensed Matter Physics; Statistical Physics; Applied Physics* **2000,** *14* (2/3), 113.

81. Tay, B. K.; Shi, X.; Cheah, L. K.; Flynn, D. I., Growth conditions and properties of tetrahedral amorphous carbon films. *Thin Solid Films* **1997,** *308*, 199-203.

82. Miyajima, Y.; Henley, S. J.; Adamopoulos, G.; Stolojan, V.; Garcia-Caurel, E.; Drévillon, B.; Shannon, J. M.; Silva, S. R. P., Pulsed laser deposited tetrahedral amorphous carbon with high sp3 fractions and low optical bandgaps. *Journal of Applied Physics* **2009,** *105* (7).

83. Pappas, D. L.; Saenger, K. L.; Bruley, J.; Krakow, W.; Cuomo, J. J.; Gu, T.; Collins, R. W., Pulsed laser deposition of diamond-like carbon films. *Journal of Applied Physics* **1992,** *71* (11), 5675-5684.

84. Kim, D. S.; Kang, T. W., Deposition of amorphous carbon thin films by pulsed RF plasma CVD. *Journal of Chemical Engineering Japan* **2005,** *38* (8), 593-599.

85. Dwivedi, N.; Yeo, R. J.; Goohpattader, P. S.; Satyanarayana, N.; Tripathy, S.; Bhatia, C. S., Enhanced characteristics of pulsed DC sputtered ultrathin (<2nm) amorphous carbon overcoats on hard disk magnetic media. *Diamond and Related Materials* **2015,** *51*, 14-23.

86. Robertson, J., Requirements of ultrathin carbon coatings for magnetic storage technology. *Tribology International* **2003,** *36* (4), 405-415.

87. Cullen, R. J.; Jayasundara, D. R.; Soldi, L.; Cheng, J. J.; Dufaure, G.; Colavita, P. E., Spontaneous Grafting of Nitrophenyl Groups on Amorphous Carbon Thin Films: A Structure–Reactivity Investigation. *Chemistry of Materials* **2012,** *24* (6), 1031-1040.

88. Jayasundara, D. R.; Cullen, R. J.; Colavita, P. E., In Situ and Real Time Characterization of Spontaneous Grafting of Aryldiazonium Salts at Carbon Surfaces. *Chemistry of Materials* **2013,** *25* (7), 1144-1152.

89. Murphy, D. M.; Cullen, R. J.; Jayasundara, D. R.; Doyle, R. L.; Lyons, M. E. G.; Colavita, P. E., Heterogeneous Charge Transfer at the Amorphous Carbon/Solution Interface: Effect on the Spontaneous Attachment of Aryldiazonium Salts. *The Journal of Physical Chemistry C* **2013**.

90. Murphy, D. M.; Cullen, R. J.; Jayasundara, D. R.; Scanlan, E. M.; Colavita, P. E., Study of the spontaneous attachment of polycyclic aryldiazonium salts onto amorphous carbon substrates. *RSC Advances* **2012,** *2* (16), 6527-6534.

91. Jorge Sobrido, A. B.; Dedigama, I.; Mansor, N.; Jervis, R.; Miller, T. S.; Corà, F.; Shearing, P.; Gibbs, C.; McMillan, P. F.; Brett, D. J., Graphitic Carbon Nitride Materials for Energy Applications. *ECS Transactions* **2015,** *64* (38), 13-30.

92. Liebig, J., Ueher Einige Stickstoff - Verbindungen. *Annalen der Pharmacie* **1834,** *10* (1), 1.

93. Franklin, E. C., The Ammono Carbonic Acids. *Journal of the American Chemical Society* **1922,** *44* (3), 486-509.

94. Pauling, L.; Sturdivant, J. H., The Structure of Cyameluric Acid, Hydromelonic Acid and Related Substances. *Proceedings of the National Academy of Sciences of the United States of America* **1937,** *23* (12), 615-620.

95. Lotsch, B. V.; Schnick, W., From Triazines to Heptazines: Novel Nonmetal Tricyanomelaminates as Precursors for Graphitic Carbon Nitride Materials. *Chemistry of Materials* **2006,** *18* (7), 1891-1900.

96. Cohen, M. L., Predicting Useful Materials. *Science* **1993,** *261* (5119), 307-308.

97. Liu, A. Y.; Cohen, M. L., Prediction of New Low Compressibility Solids. *Science* **1989,** *245* (4920), 841-842.

98. Wang, E. G., Research on carbon nitrides. *Progress in Materials Science* **1997,** *41* (5), 241-298.

99. Li, J. J.; Zheng, W. T.; Wu, H. H.; Sung, L.; Gu, G. G.; Bian, H. J.; Lu, X. Y.; Jin, Z. S., Compositional and structural modifications of amorphous carbon nitride films induced by thermal annealing. *Journal of Physics D Applied Physics* **2003,** *36* (16), 2001-2005.

100. Bootkul, D.; Supsermpol, B.; Saenphinit, N.; Aramwit, C.; Intarasiri, S., Nitrogen doping for adhesion improvement of DLC film deposited on Si substrate by Filtered Cathodic Vacuum Arc (FCVA) technique. *Applied Surface Science* **2014,** *310* (0), 284-292.

101. Hayashi, T.; Matsumuro, A.; Muramatsu, M.; Kohzaki, M.; Yamaguchi, K., Wear resistance of carbon nitride thin films formed by ion beam assisted deposition. *Thin Solid Films* **2000,** *376* (1-2), 152-158.

102. Kamata, T.; Kato, D.; Hirono, S.; Niwa, O., Structure and Electrochemical Performance of Nitrogen-Doped Carbon Film Formed by Electron Cyclotron Resonance Sputtering. *Analytical Chemistry* **2013,** *85* (20), 9845-9851.

103. Sidik, R. A.; Anderson, A. B.; Subramanian, N. P.; Kumaraguru, S. P.; Popov, B. N., O-2 reduction on graphite and nitrogen-doped graphite: Experiment and theory. *Journal of Physical Chemistry B* **2006,** *110* (4), 1787-1793.

104. Perini, L.; Durante, C.; Favaro, M.; Perazzolo, V.; Agnoli, S.; Schneider, O.; Granozzi, G.; Gennaro, A., Metal-Support Interaction in Platinum and Palladium Nanoparticles Loaded on Nitrogen-Doped Mesoporous Carbon for Oxygen Reduction Reaction. *ACS Applied Materials & Interfaces* **2015,** *7* (2), 1170-1179.

105. Liu, R. L.; Wu, D. Q.; Feng, X. L.; Mullen, K., Nitrogen-Doped Ordered Mesoporous Graphitic Arrays with High Electrocatalytic Activity for Oxygen Reduction. *Angewandte Chemie International Edition* **2010,** *49* (14), 2565-2569.

106. Zhou, K.; Ke, P.; Li, X.; Zou, Y.; Wang, A., Microstructure and electrochemical properties of nitrogen-doped DLC films deposited by PECVD technique. *Applied Surface Science* **2015,** *329* (0), 281-286.

107. Yang, X. Y.; Hubold, L.; DeVivo, G.; Swain, G. M., Electroanalytical performance of nitrogen-containing tetrahedral amorphous carbon thin-film electrodes. *Abstracts of Papers of the American Chemical Society* **2012,** *244*.

108. Yang, X.; Haubold, L.; DeVivo, G.; Swain, G. M., Electroanalytical Performance of Nitrogen-Containing Tetrahedral Amorphous Carbon Thin-Film Electrodes. *Analytical Chemistry* **2012,** *84* (14), 6240-6248.

109. Durand-Drouhin, O.; Benlahsen, M.; Clin, M.; Bouzerar, R., Deposition mechanism of sputtered amorphous carbon nitride thin film. *Applied Surface Science* **2004,** *223* (4), 269-274.

110. Yang, T. S.; Tsai, T. H.; Lee, C. H.; Cheng, C. L.; Wong, M. S., Deposition of carbon-containing cubic boron nitride films by pulsed-DC magnetron sputtering. *Thin Solid Films* **2001,** *398*, 285-290.

111. Jiang, L. D.; Fitzgerald, A. G.; Rose, M. J., The effect of postdeposition annealing on chemical bonding in amorphous carbon nitride films prepared by dc magnetron sputtering. *Applied Surface Science* **2001,** *181* (3-4), 331-338.

112. Aono, M.; Akiyoshi, H.; Kikuchi, S.; Kitazawa, N.; Watanabe, Y., Effect of substrate temperatures on amorphous carbon nitride films prepared by reactive sputtering. *Journal of Vacuum Science Technology A* **2008,** *26* (4), 966-969.

113. Durand-Drouhin, O.; Lejeune, M.; Clin, M.; Ballutaud, D.; Benlahsen, M., Effect of target self-bias on carbon nitride thin films deposited by RF magnetron sputtering. *Solid State Communications* **2001,** *118* (4), 179-182.

114. Neuhaeuser, M.; Hilgers, H.; Joeris, P.; White, R.; Windeln, J., Raman spectroscopy measurements of DC-magnetron sputtered carbon nitride (a-C : N) thin films for magnetic hard disk coatings. *Diamond and Related Materials* **2000,** *9* (8), 1500-1505.

115. Chen, J. Y.; Wang, X.; Cui, X. Q.; Yang, G. M.; Zheng, W. T., One-step synthesis of N-doped amorphous carbon at relatively low temperature as excellent metal-free electrocatalyst for oxygen reduction. *Catalyis Communications* **2014,** *46*, 161-164.

116. Miller, T. S.; Jorge, A. B.; Suter, T. M.; Sella, A.; Corà, F.; McMillan, P. F., Carbon nitrides: synthesis and characterization of a new class of functional materials. *Physical Chemistry Chemical Physics* **2017,** *19* (24), 15613-15638.

117. Dai, L.; Xue, Y.; Qu, L.; Choi, H.-J.; Baek, J.-B., Metal-Free Catalysts for Oxygen Reduction Reaction. *Chemical Reviews* **2015,** *115* (11), 4823-4892.

118. Zhang, J.; Xia, Z.; Dai, L., Carbon-based electrocatalysts for advanced energy conversion and storage. *Science Advances* **2015,** *1* (7).

119. Maldonado, S.; Stevenson, K. J., Direct Preparation of Carbon Nanofiber Electrodes via Pyrolysis of Iron(II) Phthalocyanine: Electrocatalytic Aspects for Oxygen Reduction. *The Journal of Physical Chemistry B* **2004,** *108* (31), 11375-11383.

120. Wang, D.-W.; Su, D., Heterogeneous nanocarbon materials for oxygen reduction reaction. *Energy & Environmental Science* **2014,** *7* (2), 576-591.

121. Lepesant, M.; Guillet, N.; Mailley, P., Nanostructuring of Catalysts Based on Platinum or Platinum Alloy for PEM Fuel Cell Application. *Meeting Abstracts* **2014,** *MA2014-01* (13), 612.

122. Yarlagadda, V.; Carpenter, M. K.; Moylan, T. E.; Kukreja, R. S.; Koestner, R.; Gu, W.; Thompson, L.; Kongkanand, A., Boosting Fuel Cell Performance with Accessible Carbon Mesopores. *ACS Energy Letters* **2018,** *3* (3), 618-621.

123. Debe, M. K., Electrocatalyst approaches and challenges for automotive fuel cells. *Nature* **2012,** *486* (7401), 43-51.

124. Kongkanand, A.; Mathias, M. F., The Priority and Challenge of High-Power Performance of Low-Platinum Proton-Exchange Membrane Fuel Cells. *The Journal of Physical Chemistry Letters* **2016,** *7* (7), 1127-1137.

125. Prestat, E.; Popescu, R.; Blank, H.; Schneider, R.; Gerthsen, D., Coarsening of Pt nanoparticles on amorphous carbon film. *Surface Science* **2013,** *609*, 195-202.

126. Hansen, T. W.; DeLaRiva, A. T.; Challa, S. R.; Datye, A. K., Sintering of Catalytic Nanoparticles: Particle Migration or Ostwald Ripening? *Accounts of Chemical Research* **2013,** *46* (8), 1720-1730.

127. Shao-Horn, Y.; Sheng, W. C.; Chen, S.; Ferreira, P. J.; Holby, E. F.; Morgan, D., Instability of Supported Platinum Nanoparticles in Low-Temperature Fuel Cells. *Topics in Catalysis* **2007,** *46* (3-4), 285-305.

128. Wang, J.; Yin, G.; Shao, Y.; Zhang, S.; Wang, Z.; Gao, Y., Effect of carbon black support corrosion on the durability of Pt/C catalyst. *Journal of Power Sources* **2007,** *171* (2), 331-339.

129. Maass, S.; Finsterwalder, F.; Frank, G.; Hartmann, R.; Merten, C., Carbon support oxidation in PEM fuel cell cathodes. *Journal of Power Sources* **2008,** *176* (2), 444-451.

130. Reiser, C. A.; Bregoli, L.; Patterson, T. W.; Yi, J. S.; Yang, J. D.; Perry, M. L.; Jarvi, T. D., A Reverse-Current Decay Mechanism for Fuel Cells. *Electrochemical and Solid-State Letters* **2005,** *8* (6), A273-A276.

131. Chen, Y.; Wang, J.; Liu, H.; Li, R.; Sun, X.; Ye, S.; Knights, S., Enhanced stability of Pt electrocatalysts by nitrogen doping in CNTs for PEM fuel cells. *Electrochemistry Communications* **2009,** *11* (10), 2071-2076.

132. Ye, S.; Vijh, A. K.; Dao, L. H., A New Fuel Cell Electrocatalyst Based on Carbonized Polyacrylonitrile Foam: The Nature of Platinum-Support Interactions. *Journal of The Electrochemical Society* **1997,** *144* (1), 90-95.

133. Zhou, Y.; Pasquarelli, R.; Holme, T.; Berry, J.; Ginley, D.; O'Hayre, R., Improving PEM fuel cell catalyst activity and durability using nitrogen-doped carbon supports: observations from model Pt/HOPG systems. *Journal of Materials Chemistry* **2009,** *19* (42), 7830-7838.

134. Kinoshita, H.; Kubota, M.; Ohno, G., Deposition of amorphous carbon nitride films using Ar/N-2 supermagnetron sputter. *Thin Solid Films* **2010,** *518* (13), 3502-3505.

135. Podyacheva, O. Y.; Ismagilov, Z. R., Nitrogen-doped carbon nanomaterials: To the mechanism of growth, electrical conductivity and application in catalysis. *Catalysis Today* **2015,** *249* (0), 12-22.

136. Hu, X.; Wu, Y.; Li, H.; Zhang, Z., Adsorption and Activation of O2 on Nitrogen-Doped Carbon Nanotubes. *The Journal of Physical Chemistry C* **2010,** *114* (21), 9603-9607.

137. Shi, X.; Fu, H.; Shi, J. R.; Cheah, L. K.; Tay, B. K.; Hui, P., Electronic transport properties of nitrogen doped amorphous carbon films deposited by the filtered cathodic vacuum arc technique. *Journal of Physics: Condensed Matter* **1998,** *10* (41), 9293.

138. Ray, S. C.; Mbiombi, W.; Papakonstantinou, P., Electrical and electronic properties of nitrogen doped amorphous carbon (a-CNx) thin films. *Current Applied Physics* **2014,** *14* (12), 1845-1848.

139. Robertson, J.; Davis, C. A., Nitrogen Doping of Tetrahedral Amorphous-Carbon. *Diamond and Related Materials* **1995,** *4* (4), 441-444.

140. Yamada, Y.; Kim, J.; Matsuo, S.; Sato, S., Nitrogen-containing graphene analyzed by X-ray photoelectron spectroscopy. *Carbon* **2014,** *70*, 59-74.

141. Rusop, M.; Soga, T.; Jimbo, T., The bonding properties of amorphous carbon nitride films by the means of X-ray photoelectron spectroscopy studies. *International Journal of Modern Physics B* **2005,** *19* (11), 1925-1942.

142. Yoo, K.; Miller, B.; Kalish, R.; Shi, X., Electrodes of Nitrogen-Incorporated Tetrahedral Amorphous Carbon A Novel Thin-Film Electrocatalytic Material with Diamond-like Stability. *Electrochemical and Solid-State Letters* **1999,** *2* (5), 233-235.

143. Seck, S. M.; Charvet, S.; Fall, M.; Baudrin, E.; Geneste, F.; Lejeune, M.; Benlahsen, M., Functionalization of amorphous nitrogenated carbon thin film electrodes for improved detection of cadmium vs. copper cations. *Journal of Electroanalytical Chemistry* **2015,** *738*, 154-161.

144. Sopchak, D.; Miller, B.; Kalish, R.; Avyigal, Y.; Shi, X., Dopamine and ascorbate analysis at hydrodynamic electrodes of boron doped diamond and nitrogen incorporated tetrahedral amorphous carbon. *Electroanalysis* **2002,** *14* (7-8), 473-478.

145. Brocenschi, R. F.; Rocha, R. C.; Li, L. L.; Swain, G. M., Comparative electrochemical response of estrone at glassy-carbon, nitrogen-containing tetrahedral amorphous carbon and boron-doped diamond thin-film electrodes. *Journal of Electroanalytical Chemistry* **2014,** *712*, 207-214.

146. Medeiros, R. A.; Matos, R.; Benchikh, A.; Saidani, B.; Debiemme-Chouvy, C.; Deslouis, C.; Rocha-Filho, R. C.; Fatibello-Filho, O., Amorphous carbon nitride as an alternative electrode material in electroanalysis: Simultaneous determination of dopamine and ascorbic acid. *Analytica Chimica Acta* **2013,** *797* (1), 30-39.

147. Ye, F. C.; Wen, Z. B.; Wu, H. F.; Wang, C. Y.; Qian, Y., Simultaneous Electrochemical Determination of Ascorbic Acid, Dopamine and Uric Acid Based on Nitrogen Doped Carbon Sphere Modified Glassy Carbon Electrode. *International Journal of Electrochemical Science* **2015,** *10* (2), 1136-1143.

148. Sheng, Z.-H.; Zheng, X.-Q.; Xu, J.-Y.; Bao, W.-J.; Wang, F.-B.; Xia, X.-H., Electrochemical sensor based on nitrogen doped graphene: Simultaneous determination of ascorbic acid, dopamine and uric acid. *Biosensors and Bioelectronics* **2012,** *34* (1), 125-131.

149. Gai, P.; Zhang, H.; Zhang, Y.; Liu, W.; Zhu, G.; Zhang, X.; Chen, J., Simultaneous electrochemical detection of ascorbic acid, dopamine and uric acid based on nitrogen doped porous carbon nanopolyhedra. *Journal of Materials Chemistry B* **2013,** *1* (21), 2742-2749.

150. Ozaki, J.; Tanifuji, S.; Furuichi, A.; Yabutsuka, K., Enhancement of oxygen reduction activity of nanoshell carbons by introducing nitrogen atoms from metal phthalocyanines. *Electrochimica Acta* **2010,** *55* (6), 1864-1871.

151. Ikeda, T.; Boero, M.; Huang, S.-F.; Terakura, K.; Oshima, M.; Ozaki, J.-I., Carbon Alloy Catalysts: Active Sites for Oxygen Reduction Reaction. *The Journal of Physical Chemistry C* **2008,** *112* (38), 14706-14709.

152. Stamatin, S. N.; Hussainova, I.; Ivanov, R.; Colavita, P. E., Quantifying Graphitic Edge Exposure in Graphene-Based Materials and Its Role in Oxygen Reduction Reactions. *ACS Catalysis* **2016,** *6* (8), 5215-5221.

153. Chai, G.-L.; Hou, Z.; Shu, D.-J.; Ikeda, T.; Terakura, K., Active Sites and Mechanisms for Oxygen Reduction Reaction on Nitrogen-Doped Carbon Alloy Catalysts: Stone–Wales Defect and Curvature Effect. *Journal of the American Chemical Society* **2014,** *136* (39), 13629-13640.

154. Guo, D.; Shibuya, R.; Akiba, C.; Saji, S.; Kondo, T.; Nakamura, J., Active sites of nitrogen-doped carbon materials for oxygen reduction reaction clarified using model catalysts. *Science* **2016,** *351* (6271), 361-365.

155. Perini, L.; Durante, C.; Favaro, M.; Agnoli, S.; Granozzi, G.; Gennaro, A., Electrocatalysis at palladium nanoparticles: Effect of the support nitrogen doping on the catalytic activation of carbon-halogen bond. *Applied Catalysis B-Environmental* **2014,** *144*, 300-307.

156. Yang, Z.; Nie, H.; Chen, X. a.; Chen, X.; Huang, S., Recent progress in doped carbon nanomaterials as effective cathode catalysts for fuel cell oxygen reduction reaction. *Journal of Power Sources* **2013,** *236* (0), 238-249.

157. Shao, Y.; Liu, J.; Wang, Y.; Lin, Y., Novel catalyst support materials for PEM fuel cells: current status and future prospects. *Journal of Materials Chemistry* **2009,** *19* (1), 46-59.

158. Shao, Y.; Sui, J.; Yin, G.; Gao, Y., Nitrogen-doped carbon nanostructures and their composites as catalytic materials for proton exchange membrane fuel cell. *Applied Catalysis B: Environmental* **2008,** *79* (1), 89-99.

159. McCreery, R. L., Advanced carbon electrode materials for molecular electrochemistry. *Chemical Reviews* **2008,** *108* (7), 2646-87.

160. Dai, L., Carbon-based catalysts for metal-free electrocatalysis. *Current Opinion in Electrochemistry* **2017,** 18-25.

161. Hu, C.; Dai, L., Carbon-Based Metal-Free Catalysts for Electrocatalysis beyond the ORR. *Angewandte Chemie International Edition* **2016,** *55* (39), 11736-11758.

162. Nitta, N.; Wu, F.; Lee, J. T.; Yushin, G., Li-ion battery materials: present and future. *Materials Today* **2015,** *18* (5), 252-264.

163. Fellinger, T.-P.; Hasché, F.; Strasser, P.; Antonietti, M., Mesoporous Nitrogen-Doped Carbon for the Electrocatalytic Synthesis of Hydrogen Peroxide. *Journal of the American Chemical Society* **2012,** *134* (9), 4072-4075.

164. Liang, C.; Li, Z.; Dai, S., Mesoporous Carbon Materials: Synthesis and Modification. *Angewandte Chemie International Edition* **2008,** *47* (20), 3696-3717.

165. Qiao, Z.-A.; Guo, B.; Binder, A. J.; Chen, J.; Veith, G. M.; Dai, S., Controlled Synthesis of Mesoporous Carbon Nanostructures via a "Silica-Assisted" Strategy. *Nano Letters* **2013,** *13* (1), 207-212.

166. Perazzolo, V.; Durante, C.; Pilot, R.; Paduano, A.; Zheng, J.; Rizzi, G. A.; Martucci, A.; Granozzi, G.; Gennaro, A., Nitrogen and sulfur doped mesoporous carbon as metal-free electrocatalysts for the in situ production of hydrogen peroxide. *Carbon* **2015,** *95*, 949-963.

167. Inagaki, M.; Kang, F., Chapter 1 - Introduction. In *Materials Science and Engineering of Carbon: Fundamentals (Second Edition)*, Butterworth-Heinemann: Oxford, 2014; pp 1-15.

168. Spain, I. L., The Electronic Transport Properties of Graphite, Carbons, and Related Materials. In *Chemistry and Physics of Carbon*, Jr., P. J. W.; Thrower, P. A., Eds. CRC Press: USA, 1981; Vol. 16, p 139.

169. Rusop, M.; Mominuzzaman, S. M.; Soga, T.; Jimbo, T.; Umeno, M., Characterization of phosphorus-doped amorphous carbon and construction of n-carbon/p-silicon heterojunction solar cells. *Japanese Journal of Applied Physics* **2003,** *42* (4S), 2339.

170. Podder, J.; Rusop, M.; Soga, T.; Jimbo, T., Boron doped amorphous carbon thin films grown by r.f. PECVD under different partial pressure. *Diamond and Related Materials* **2005,** *14* (11), 1799-1804.

171. Jiménez, I.; Torres, R.; Caretti, I.; Gago, R.; Albella, J. M., A review of monolithic and multilayer coatings within the boron–carbon–nitrogen system by ion-beam-assisted deposition. *Journal of Materials Research* **2012,** *27* (5), 743-764.

172. Broitman, E.; Furlan, A.; Gueorguiev, G. K.; Czigány, Z.; Tarditi, A. M.; Gellman, A. J.; Stafström, S.; Hultman, L., Water adsorption on phosphorous-carbide thin films. *Surface and Coatings Technology* **2009,** *204* (6), 1035-1039.

173. Chung-Chuan, L.; Cecilia, G.; Esteban, B.; Lars-Åke, N.; Hans, H.; Lars, H.; Gueorgui, K. G.; Johanna, R., Synthesis and properties of CS x F y thin films deposited by reactive magnetron sputtering in an Ar/SF 6 discharge. *Journal of Physics: Condensed Matter* **2017,** *29* (19), 195701.

174. Hellgren, N.; Johansson, M. P.; Broitman, E.; Sandström, P.; Hultman, L.; Sundgren, J.-E., Effect of chemical sputtering on the growth and structural evolution of magnetron sputtered CNx thin films. *Thin Solid Films* **2001,** *382* (1–2), 146-152.

175. Deng, D.; Yu, L.; Pan, X.; Wang, S.; Chen, X.; Hu, P.; Sun, L.; Bao, X., Size effect of graphene on electrocatalytic activation of oxygen. *Chemical Communications* **2011,** *47* (36), 10016-10018.

176. Wang, L.; Yin, F.; Yao, C., N-doped graphene as a bifunctional electrocatalyst for oxygen reduction and oxygen evolution reactions in an alkaline electrolyte. *International Journal of Hydrogen Energy* **2014,** *39* (28), 15913-15919.

177. Maillard, F.; Job, N.; Chatenet, M., Chapter 14 - Approaches to Synthesize Carbon-Supported Platinum-Based Electrocatalysts for Proton-Exchange Membrane Fuel Cells. In *New and Future Developments in Catalysis*, Suib, S. L., Ed. Elsevier: Amsterdam, 2013; pp 407-428.

178. Zhou, Y.; Holme, T.; Berry, J.; Ohno, T. R.; Ginley, D.; O'Hayre, R., Dopant-induced electronic structure modification of HOPG surfaces: implications for high activity fuel cell catalysts. *Journal of Physical Chemistry C* **2009,** *114* (1), 506-515.

179. Holme, T.; Zhou, Y.; Pasquarelli, R.; O'Hayre, R., First principles study of doped carbon supports for enhanced platinum catalysts. *Physical Chemistry Chemical Physics* **2010,** *12* (32), 9461-9468.

180. Pylypenko, S.; Queen, A.; Olson, T. S.; Dameron, A.; O'Neill, K.; Neyerlin, K.; Pivovar, B.; Dinh, H. N.; Ginley, D. S.; Gennett, T., Tuning carbon-based fuel cell catalyst support structures via nitrogen functionalization. I. Investigation of structural and compositional modification of highly oriented pyrolytic graphite model catalyst supports as a function of nitrogen implantation dose. *The Journal of Physical Chemistry C* **2011,** *115* (28), 13667-13675.

181. Favaro, M.; Agnoli, S.; Perini, L.; Durante, C.; Gennaro, A.; Granozzi, G., Palladium nanoparticles supported on nitrogen-doped HOPG: a surface science and electrochemical study. *Physical Chemistry Chemical Physics* **2013,** *15* (8), 2923-2931.

182. Sarapuu, A.; Helstein, K.; Schiffrin, D. J.; Tammeveski, K., Kinetics of Oxygen Reduction on Quinone-Modified HOPG and BDD Electrodes in Alkaline Solution. *Electrochemical and Solid-State Letters* **2005,** *8* (2), E30-E33.

183. Kiuchi, H.; Shibuya, R.; Kondo, T.; Nakamura, J.; Niwa, H.; Miyawaki, J.; Kawai, M.; Oshima, M.; Harada, Y., Lewis Basicity of Nitrogen-Doped Graphite Observed by CO2 Chemisorption. *Nanoscale Research Letters* **2016,** *11* (1), 127.

184. Groves, M. N.; Chan, A. S. W.; Malardier-Jugroot, C.; Jugroot, M., Improving platinum catalyst binding energy to graphene through nitrogen doping. *Chemical Physics Letters* **2009,** *481* (4), 214-219.

185. Wildgoose, G. G.; Wilkins, S. J.; Williams, G. R.; France, R. R.; Carnahan, D. L.; Jiang, L.; Jones, T. G.; Compton, R. G., Graphite Powder and Multiwalled Carbon Nanotubes Chemically Modified with 4-Nitrobenzylamine. *ChemPhysChem* **2005,** *6* (2), 352-362.

186. Zhang, C.; Mahmood, N.; Yin, H.; Liu, F.; Hou, Y., Synthesis of Phosphorus-Doped Graphene and its Multifunctional Applications for Oxygen Reduction Reaction and Lithium Ion Batteries. *Advanced Materials* **2013,** *25* (35), 4932-4937.

187. Kawai, S.; Saito, S.; Osumi, S.; Yamaguchi, S.; Foster, A. S.; Spijker, P.; Meyer, E., Atomically controlled substitutional boron-doping of graphene nanoribbons. *Nature Communications* **2015,** *6*, 8098.

188. Sheng, Z.-H.; Gao, H.-L.; Bao, W.-J.; Wang, F.-B.; Xia, X.-H., Synthesis of boron doped graphene for oxygen reduction reaction in fuel cells. *Journal of Materials Chemistry* **2012,** *22* (2), 390-395.

189. Yang, Z.; Yao, Z.; Li, G.; Fang, G.; Nie, H.; Liu, Z.; Zhou, X.; Chen, X. A.; Huang, S., Sulfur-Doped Graphene as an Efficient Metal-free Cathode Catalyst for Oxygen Reduction. *ACS Nano* **2012,** *6* (1), 205-211.

190. Wang , S.; Iyyamperumal , E.; Roy, A.; Xue, Y.; Yu, D.; Dai, L., Vertically Aligned BCN Nanotubes as Efficient Metal-Free Electrocatalysts for the Oxygen Reduction Reaction: A Synergetic Effect by Co-Doping with Boron and Nitrogen. *Angewandte Chemie International Edition* **2011,** *50* (49), 11756-11760.

191. Paraknowitsch, J. P.; Thomas, A., Doping carbons beyond nitrogen: an overview of advanced heteroatom doped carbons with boron, sulphur and phosphorus for energy applications. *Energy & Environmental Science* **2013,** *6* (10), 2839-2855.

192. Zheng, B.; Wang, J.; Wang, F.-B.; Xia, X.-H., Synthesis of nitrogen doped graphene with high electrocatalytic activity toward oxygen reduction reaction. *Electrochemistry Communications* **2013,** *28* (0), 24-26.

193. Panchakarla, L. S.; Subrahmanyam, K. S.; Saha, S. K.; Govindaraj, A.; Krishnamurthy, H. R.; Waghmare, U. V.; Rao, C. N. R., Synthesis, Structure, and Properties of Boron- and Nitrogen-Doped Graphene. *Advanced Materials* **2009,** *21* (46), 4726-4730.

194. Wu, K.-H.; Wang, D.-W.; Zong, X.; Zhang, B.; Liu, Y.; Gentle, I. R.; Su, D.-S., Functions in cooperation for enhanced oxygen reduction reaction: the independent roles of oxygen and nitrogen sites in metal-free nanocarbon and their functional synergy. *Journal of Materials Chemistry A* **2017,** *5* (7), 3239-3248.

195. Lewis, J.; Redfern, B.; Cowlard, F., Vitreous carbon as a crucible material for semiconductors. *Solid State Electronics* **1963,** *6* (3), 251-254.

196. Cowlard, F.; Lewis, J., Vitreous carbon—a new form of carbon. *Journal of Materials Science* **1967,** *2* (6), 507-512.

197. Gunasingham, H.; Fleet, B., Comparative study of glassy carbon as an electrode material. *Analyst* **1982,** *107* (1277), 896-902.

198. Engstrom, R. C.; Strasser, V. A., Characterization of electrochemically pretreated glassy carbon electrodes. *Analytical Chemistry* **1984,** *56* (2), 136-141.

199. Ranganathan, S.; Kuo, T.-C.; McCreery, R. L., Facile Preparation of Active Glassy Carbon Electrodes with Activated Carbon and Organic Solvents. *Analytical Chemistry* **1999,** *71* (16), 3574-3580.

200. Kiema, G. K.; Aktay, M.; McDermott, M. T., Preparation of reproducible glassy carbon electrodes by removal of polishing impurities. *Journal of Electroanalytical Chemistry* **2003,** *540* (0), 7-15.

201. Chen, P.; McCreery, R. L., Control of Electron Transfer Kinetics at Glassy Carbon Electrodes by Specific Surface Modification. *Analytical Chemistry* **1996,** *68* (22), 3958-3965.

202. Yang, H. H.; McCreery, R. L., Elucidation of the Mechanism of Dioxygen Reduction on Metal-Free Carbon Electrodes. *Journal of The Electrochemical Society* **2000,** *147* (9), 3420-3428.

203. An Wong, C. H.; Ambrosi, A.; Pumera, M., Thermally reduced graphenes exhibiting a close relationship to amorphous carbon. *Nanoscale* **2012,** *4* (16), 4972-4977.

204. Biddinger, E. J.; Deak, D. v.; Singh, D.; Marsh, H.; Tan, B.; Knapke, D. S.; Ozkan, U. S., Examination of Catalyst Loading Effects on the Selectivity of CNx and Pt/VC ORR Catalysts Using RRDE. *Journal of The Electrochemical Society* **2011,** *158* (4), B402-B409.

205. Mayrhofer, K. J. J.; Strmcnik, D.; Blizanac, B. B.; Stamenkovic, V.; Arenz, M.; Markovic, N. M., Measurement of oxygen reduction activities via the rotating disc electrode method: From Pt model surfaces to carbon-supported high surface area catalysts. *Electrochimica Acta* **2008,** *53* (7), 3181-3188.

206. Strano, M. S.; Dyke, C. A.; Usrey, M. L.; Barone, P. W.; Allen, M. J.; Shan, H.; Kittrell, C.; Hauge, R. H.; Tour, J. M.; Smalley, R. E., Electronic Structure Control of Single-Walled Carbon Nanotube Functionalization. *Science* **2003,** *301* (5639), 1519.

207. Nair, N.; Kim, W.-J.; Usrey, M. L.; Strano, M. S., A Structure−Reactivity Relationship for Single Walled Carbon Nanotubes Reacting with 4-Hydroxybenzene Diazonium Salt. *Journal of the American Chemical Society* **2007,** *129* (13), 3946-3954.

208. Libby, W. F., Theory of Electron Exchange Reactions in Aqueous Solution. *The Journal of Physical Chemistry* **1952,** *56* (7), 863-868.

209. Marcus, R. A., On the Theory of Oxidation-Reduction Reactions Involving Electron Transfer. I. *The Journal of Chemical Physics* **1956,** *24* (5), 966-978.

210. Marcus, R. A., Electrostatic Free Energy and Other Properties of States Having Nonequilibrium Polarization. I. *The Journal of Chemical Physics* **1956,** *24* (5), 979-989.

211. Marcus, R. A., On the Theory of Electrochemical and Chemical Electron Transfer Processes. *Canadian Journal of Chemistry* **1959,** *37* (1), 155-163.

212. Pletcher, D., *A first course in electrode processes*. Royal Society of Chemistry, 2009.

213. Swaddle, T. W., Homogeneous versus Heterogeneous Self-Exchange Electron Transfer Reactions of Metal Complexes: Insights from Pressure Effects. *Chemical Reviews* **2005,** *105* (6), 2573-2608.

214. Ford, P. C., Properties and reactions of ruthenium(II) amine complexes. *Coordination Chemistry Reviews* **1970,** *5* (1), 75-99.

215. Peter, L. M.; Dürr, W.; Bindra, P.; Gerischer, H., The influence of alkali metal cations on the rate of the $Fe(CN)_6^{4-}/Fe(CN)_6^{3-}$ electrode process. *Journal of Electroanalytical Chemistry and Interfacial Electrochemistry* **1976,** *71* (1), 31-50.

216. Zahl, A.; van Eldik, R.; Swaddle, T. W., Cation-independent electron transfer between ferricyanide and ferrocyanide ions in aqueous solution. *Inorganic Chemistry* **2002,** *41* (4), 757-764.

217. Beriet, C.; Pletcher, D., A microelectrode study of the mechanism and kinetics of the ferro/ferricyanide couple in aqueous media: The influence of the electrolyte and its concentration. *Journal of Electroanalytical Chemistry* **1993,** *361* (1-2), 93-101.

218. Kitamura, F.; Nanbu, N.; Ohsaka, T.; Tokuda, K., A kinetic and in situ infrared spectroscopic study of the Fe (CN) 63−/Fe (CN) 64− couple on platinum single crystal electrodes. *Journal of Electroanalytical Chemistry* **1998,** *456* (1-2), 113-120.

219. Laviron, E., Electrochemical reactions with protonations at equilibrium: Part XII. The 2 e−, 2 H+ homogeneous isotopic electron exchange reaction (nine-member square scheme). *Journal of Electroanalytical Chemistry and Interfacial Electrochemistry* **1984,** *169* (1), 29-46.

220. Koper, M. T., Thermodynamic theory of multi-electron transfer reactions: Implications for electrocatalysis. *Journal of Electroanalytical Chemistry* **2011,** *660* (2), 254-260.

221. Rossmeisl, J.; Logadottir, A.; Nørskov, J. K., Electrolysis of water on (oxidized) metal surfaces. *Chemical Physics* **2005,** *319* (1-3), 178-184.

222. Nørskov, J. K.; Bligaard, T.; Hvolbæk, B.; Abild-Pedersen, F.; Chorkendorff, I.; Christensen, C. H., The nature of the active site in heterogeneous metal catalysis. *Chemical Society Reviews* **2008,** *37* (10), 2163-2171.

223. Ramaswamy, N.; Mukerjee, S., Fundamental Mechanistic Understanding of Electrocatalysis of Oxygen Reduction on Pt and Non-Pt Surfaces: Acid versus Alkaline Media. *Advances in Physical Chemistry* **2012,** *2012*, 17.

224. Ramaswamy, N.; Mukerjee, S., Influence of Inner- and Outer-Sphere Electron Transfer Mechanisms during Electrocatalysis of Oxygen Reduction in Alkaline Media. *The Journal of Physical Chemistry C* **2011,** *115* (36), 18015-18026.

225. Luo, Z.; Lim, S.; Tian, Z.; Shang, J.; Lai, L.; MacDonald, B.; Fu, C.; Shen, Z.; Yu, T.; Lin, J., Pyridinic N doped graphene: synthesis, electronic structure, and electrocatalytic property. *Journal of Materials Chemistry* **2011,** *21* (22), 8038-8044.

226. Trogadas, P.; Fuller, T. F.; Strasser, P., Carbon as catalyst and support for electrochemical energy conversion. *Carbon* **2014,** *75*, 5-42.

CHAPTER II

Experimental Methods

This chapter introduces the theory behind the main experimental methods employed throughout this thesis. The magnetron sputtering system employed in the preparation of amorphous carbon and nitrogenated amorphous carbon films is described along with a brief discussion of the deposition conditions. The experimental apparatus employed in the electrochemical characterisation is described and the fundamental theory of heterogeneous charge transfer at the electrode-solution interface is discussed in some detail, with specific reference to voltammetric and impedance methods. Finally, other material characterisation techniques applied throughout the work are described including spectroscopic ellipsometry, x-ray photoelectron spectroscopy and atomic force microscopy.

2. Preparation and Characterisation of Amorphous Carbon Model Systems

2.1 Magnetron Sputtering Deposition of Amorphous Carbon (a-C) Based Model Systems

Magnetron sputtering is a method of physical vapour deposition (PVD) commonly used for the deposition of amorphous carbon films.[1-3] The technique involves plasma bombardment of a target surface which causes the ejection – or 'sputtering' – of atoms, which may then condense upon a desired substrate as a thin film. The plasma is generated via the application of a DC[4] or RF voltage[5] depending on the electrical conductivity of the target material.

The technique is distinguished from the basic sputtering process through the use of magnets which are arranged to produce a magnetic field oriented parallel to the target surface.[6] This has the effect of trapping secondary electrons in the vicinity of the target, promoting the formation of a dense plasma which in turn increases the rate of ion bombardment and sputtering.

The plasma is typically generated using an inert gas such as argon, but the incorporation of heteroatoms into the growing carbon film may be accomplished by introducing other gases such as N_2 during deposition.[7-9] Such reactive magnetron sputtering has been employed to produce a variety of nitrogen-incorporated carbon films.[10-12] The use of N_2 in particular is thought to induce bombardment by N^+ and N_2^+ and the subsequent deposition of ejected CN fragments, mainly as radicals, which further react on the surface of the substrate. [11, 13]

There are many factors affecting the properties of sputtered films; the deposition temperature,[10] power,[5] reactive gas composition[14] and substrate bias[15-16] may all potentially be varied in order to produce films with distinctive bulk properties and surface chemistries. In this thesis, amorphous carbon (a-C) and nitrogen-incorporated amorphous carbon (a-C:N) thin films were deposited via DC magnetron sputtering in a vacuum chamber (Torr International Inc) shown in Figure 2.1) at a base pressure $\leq 2\times10^{-6}$ mbar.

The carbon source for both film types was a graphite target (99.999%, Lesker). Importantly, a separate target was used for nitrogenated and non-nitrogenated carbon films in order to avoid cross contamination of the undoped films with residual nitrogen. The nitrogen content of the a-C:N films was varied using an Ar/N_2 plasma with the relative amounts of Ar and N_2 varied using mass flow controllers (Brooks Inc.). A constant total gas

flux of 50 sccm was used for all depositions, yielding deposition pressures in the range $7 \times 10^{-3} - 1 \times 10^{-2}$ mbar. In this thesis, these nitrogenated films will be referred to as a-C:N-X% where X is the percentage flux of N_2 in the vacuum chamber. The carbon source

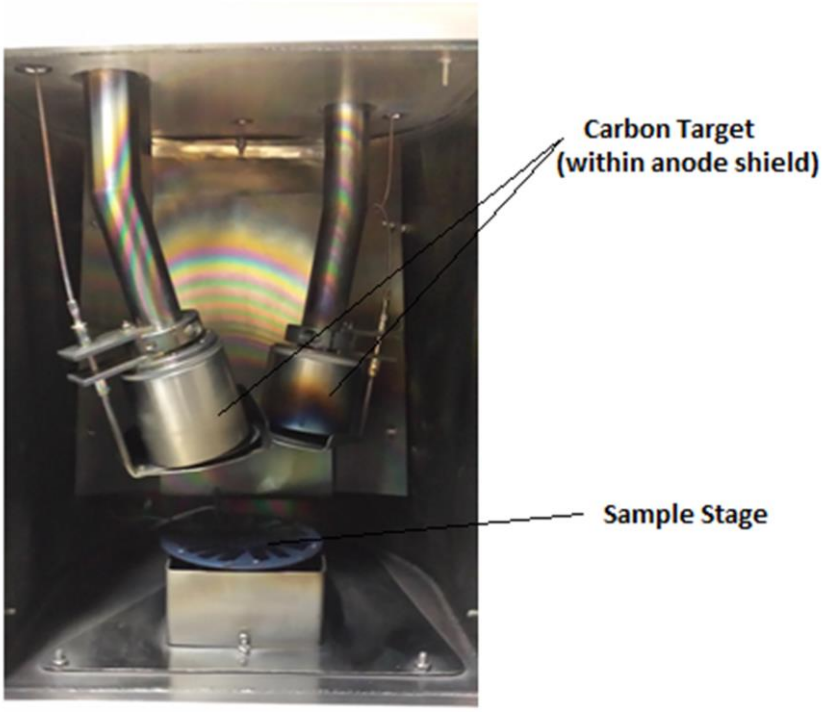

Figure 2.1. Photograph of the inside of the magnetron sputtering chamber used to prepare a-C and a-C:N films described in this thesis. The carbon target is mounted within the anode shield (centre) and the substrates are positioned on the rotating stage at the bottom of the chamber.

for both film types was a graphite target (99.999%, Lesker). Importantly, a separate target was used for nitrogenated and non-nitrogenated carbon films in order to avoid cross contamination of the undoped films with residual nitrogen.

2.2 Electrochemical Characterisation Techniques

Electrochemical Instrumentation

Electrochemical measurements described in this thesis were performed on a Metrohm Autolab AUT50324 potentiostat. Potentiostats may be described as complex electrical circuits based on an operational amplifier[17] which enable the maintenance of a fixed potential at a particular reference point – the reference electrode - over the course of an experiment.

Measurements described in this thesis were obtained using a 3-electrode setup illustrated in Figure 2.2. This arrangement consists of a working electrode (WE), counter electrode (CE) and reference electrode (RE) mounted in a glass cell sealed with a Teflon® cap. The WE is the electrode composed of the material of interest, with its identity depending on the experiment. Unless otherwise specified, all WEs in this work are prepared using glassy

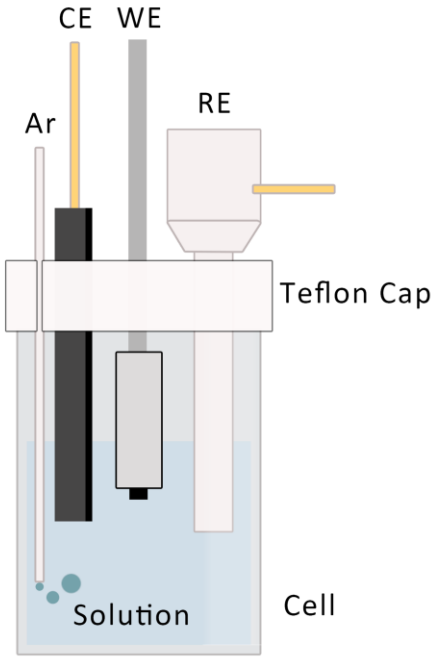

Figure 2.2. Schematic of a typical electrochemical cell used to carry out the work described in this thesis. The WE, CE and RE are all connected to the potentiostat via metal contacts (not pictured). Ar gas is bubbled through the solution to de-aerate via a glass tube, but was normally placed in the headspace above the working solution during experiments to avoid disturbing the concentration profile of redox analytes at the working electrode surface.

carbon (GC) disks (Sigradur, grade K radius 0.25 ± 0.05 cm). These disks were either used directly in electrochemical measurement after being subjected to polishing and/or pre-treatments as described in following chapters, or used as the substrate for the deposition of amorphous carbon and N-doped amorphous carbon thin film electrodes via magnetron sputtering as described in Section 2.1.

Every electrochemical experiment is concerned in some fashion with the measurement of currents and voltages at the WE. As its name suggests, the function of the RE is to serve as a constant reference point for the applied voltage. This reference value is an interfacial voltage associated with the equilibrium point of a particular redox half reaction under specified conditions. For example, under conditions where the activity of H^+ ions is unity and the pressure of H_2 gas bubbling over a Pt electrode is 1 bar, the voltage drop, ΔE, at the electrode-solution interface induced by the following half reaction:

$$H^+ + e^- \rightleftharpoons \frac{1}{2}H_2 \qquad (2.2.1)$$

is known from theoretical calculations to be close to 4.5 V vs Vacuum.[18] A reference electrode constructed under such conditions is termed the Standard Hydrogen Electrode (SHE). In practice, the absolute value of ΔE at the reference is not of much interest to the experimentalist; what is relevant is the ΔE across the WE-electrolyte interface, as indicated relative to the constant potential maintained by the equilibrium at the RE. Hence, by convention, the ΔE produced at the SHE at 25 ^oC is assigned the value of 0.00 V and all applied voltages are reported relative to this value.

Although reaction (2.2.1) is the universal standard reference point for electrochemistry, in practice the SHE is rarely used as a physical RE. This is in part because of pragmatic considerations, such as the hazards and costs associated with a constant bubbling of 1 bar of flammable hydrogen gas, and in part because more convenient reference electrode systems are easily fabricated. An example is the Ag/AgCl reference:

$$AgCl\,(s) + e^- \rightleftharpoons Ag(s) + Cl^-_{(aq,sat)} \qquad E = 0.198\ V\ vs\ SHE$$

Owing to the unit activity of solid AgCl and Ag, this reference electrode has a potential vs the SHE which varies with the chloride concentration as described by the Nernst equation (*vide infra*):

$$E = 0.220 - 0.059[Cl^-] \qquad (2.2.2)$$

An Ag/AgCl RE can be easily prepared using an anodised piece of silver wire immersed in a salt solution such as KCl. The RE internal solution is separated from the working solution by a porous frit which allows for the movement of ions but does not permit the two solutions to mix. Liquid junction potentials across the frit may be avoided by using a similar electrolyte in the working solution to that used in the RE compartment, so as to ensure that there are no differences in the mobilities of the ions on both sides of the frit. For the work described in this thesis, this is accomplished by using an Ag/AgCl reference with a Vycor® porous frit filled with saturated KCl solution and a working electrolyte of KCl.

The Ag/AgCl electrode is not suitable for measurements at high pH, primarily because of the propensity for Ag to form Ag_2O under such conditions, thereby introducing a secondary redox process and imparting an unwanted pH dependence to the reference potential. There are numerous other REs in common use for basic conditions, including the Saturated Calomel Electrode (SCE). One particularly convenient reference system for studies involving a range of pH values, is the Reversible Hydrogen Electrode (RHE). The half-reaction for the RHE is identical to that of the SHE (Equation 2.2.1) except the H^+ activity is not maintained at standard (unit) activity:

$$E = 0.00 + \frac{RT}{F}\ln(\frac{H^+}{H_2}) = 0.0 - \frac{RT}{F}pH = -0.059\times pH \text{ @ } 25\ ^oC \qquad (2.2.3)$$

Instead the reference compartment is allowed to fill with the same filling solution as the working compartment. The H_2 pressure is kept fixed at 1 bar, implying that the reference potential for the RHE is entirely dependent on the pH such that the RHE potential will shift cathodically by 59 mV for every unit increase in pH. While this may appear to be a nuisance, this feature of the RHE is actually convenient for the study of redox processes such as the ORR which have the same first-order dependence on the pH as the H^+/H_2 half reaction. Such processes also shift by -59 mV for each unit increment of pH, allowing for the same fixed potential window vs RHE to be used for a series of measurements of the same redox process at different pH values. The potential values vs RHE can then later be converted back to the SHE scale using Equation (2.2.3), although it is increasingly common for researchers to simply report the potential versus RHE directly, particularly in the ORR literature.

For measurements under acidic and basic conditions, the work described in this thesis makes use of a Hydroflex® RHE system developed by Gaskatel. The electrode consists of a hydrogen source in the form of a disposable cartridge, a Pt mesh and a partially-sealed compartment which takes up the working solution. When not in use, the Hydroflex® was

stored in a solution of the same electrolyte employed during the experiments, as this avoids the need to allow time for the system to equilibrate with the working solution.

The 3-electrode experimental setup is completed through the use of a CE, which has the function of ensuring charge balance by passing a current to match that being passed at the WE. A CE may be constructed from any convenient conducting material provided that it does not introduce additional redox species into the working compartment or otherwise interfere with the working electrode. In practice, this simply means choosing an inert conducting material such as graphite to serve as the counter and placing the CE some distance away from the WE within the working compartment. In order to ensure that the passage of current is not limited by the CE, the counter typically has a significantly larger area than the WE.[17]

The use of a RE and CE in tandem represents a division of the potential and current measurement functions between two separate electrodes. This is done primarily to preserve the set potential of the RE at the Nernstian value specified by its corresponding half reaction. If the RE is also used to pass a significant amount of current it may be itself polarised in the process, thereby shifting the reference point and compromising the RE's function. This is why only the RE only draws an infinitesimal current during normal operation in order to allow for the potential determination. The delegation of macroscopic current flow to the CE prevents this polarization.

Since the leakage of the RE filling solution into the working solution is usually minimised through some form of porous frit separating the two compartments, DC resistance distortions may occur in the RE if the RE input impedance becomes large e.g. due to blockage of the frit by salt deposits, but capacitive distortions introduced into the impedance spectrum by the RE frit at high frequencies can also occur. The capacitive coupling of the RE to a Pt wire can serve as an AC potential source for impedance measurements at frequencies > 100 kHz in order to avoid such distortions. [19]

As a final note on the experimental setup, the electrode arrangement depicted in Figure 2.2 suffers from one practical limitation: the potential difference measured at the RE is not actually the value of ΔE across the WE-solution interface, but rather this value along with a secondary potential drop, which arises due to the resistivity of the electrolyte in the region of solution separating the WE and the RE. This potential drop is usually referred to as the 'iR drop', as its magnitude depends on both i, the current passed between the WE and the CE and the value of R_s, the solution resistance, which varies depending on the placement of the RE. The iR drop may be negligible for experiments passing very small currents, and its

effects on the measurement may also be diminished by using high electrolyte concentrations and placing the WE and RE in close proximity. This is often accomplished using a Luggin capillary, which is a glass tube filled with electrolyte and placed close to the WE surface in order to ensure a well-defined sensing point for the RE and a reduced separation between the RE and the WE.

Regardless of the particular experimental arrangement, in order to report the true values of ΔE, the iR drop must be accounted for in some fashion. In this thesis the iR drop is accounted for using iR compensation through Metrohm's NOVA® software. The solution resistance R_s is determined at the beginning of each experiment via impedance measurements (*vide infra)*. Knowing the value of R_s, it is then possible to correct the reported potential at every stage of the experiment by the value of iR_s using the relation:

$$E_{actual} = E_{measured} - iR_s \tag{2.2.4}$$

It is also possible in principle to correct uncompensated potential data after the fact, if the value of iR_s is known or can be determined from the data. For potentiostatic experiments the correction is trivial to apply using Equation (1.2.4), although the correction may require the use of software packages if the potential varies in a complex fashion with time throughout the experiment, as is the case with voltammetry.

Fundamental Thermodynamics of Electrochemical Systems

A generic redox equilibrium

$$O + e^- \rightleftharpoons R \tag{2.2.5}$$

can be described from the point of view of elementary chemical thermodynamics in terms of an equilibrium constant, K, and the standard Gibbs free energy change for the reaction, ΔG_r^0:

$$K = \frac{a_r(eq)}{a_o(eq)} = \frac{\gamma_r c_r(eq)}{\gamma_o c_o(eq)} \tag{2.2.6a}$$

$$\Delta G_r^0 = -RTlnK \tag{2.2.6b}$$

The thermodynamic quantities should strictly be specified using activities rather than concentrations, however this is rarely applied in electrochemistry because the activity coefficients (γ) are generally unknown quantities (*vide infra*). Changing the composition of

O/R away from the equilibrium composition (i.e. changing the reaction quotient from the equilibrium value K to some other value, Q) may then be described conveniently using the relationship:

$$\Delta G_r = \Delta G_r^0 + RT\ln Q \qquad (2.2.7)$$

Redox equilibria are distinct from chemical equilibria in that they involve charged particles. An electrode at equilibrium with a solution containing O and R in some composition will therefore have a net charge, which may be positive or negative relative to the solution depending on the position of the equilibrium in Equation (2.2.5). This charging of the interface produces the potential difference E across the interface discussed in the previous chapter, which is reported relative to a convenient reference electrode.

The transfer of charge through a potential difference E involves energy transfer as work, w, according to

$$w = -nFE \qquad (2.2.8)$$

where n the number of electrons, F the Faraday constant (i.e. 96,485 J/C) and E is the potential difference

$$E = E_{electrode} - E_{solution} \qquad (2.2.9)$$

Reaction (2.2.5) may be spontaneous in either direction, depending on the chemistry of the O/R redox couple and the ratio of their concentrations. This implies that both a positive and a negative electrode potential, and therefore positive and negative electrical work, may be nonetheless associated with a spontaneous chemical change.

This is distinct from chemical thermodynamics, where $w = \Delta G < 0$ is the signpost of spontaneous change, and it arises from the way in which the potential difference E is specified in equation (2.2.9). To reconcile this apparent incompatibility in notation the typical convention in electrochemistry is to state that a positive value of E corresponds to a spontaneous reaction for which $\Delta G < 0$ in the cathodic direction. If $E < 0$, the reaction proceeds spontaneously in the anodic direction and the positive value of ΔG is then identified with the external work which would be necessary in order to effect the non-spontaneous cathodic process.

The application of this convention to the relation $\Delta G = w$ results in the important equation

$$\Delta G = -nFE \qquad (2.2.10)$$

Using this relation in Equation 2.2.7 leads to the Nernst Equation:

$$E = E^0 - \frac{RT}{nF}\ln Q = E^{0\prime} + \frac{RT}{nF}\ln\left(\frac{C_o}{C_r}\right) \quad (2.2.11)$$

The Nernst equation enables the prediction of the value of E for any half reaction like reaction (2.2.1) under any composition of the reagents. It should be apparent from the Nernst equation that the formal potential, $E^{0'}$, is the value of the potential when $C_o = C_r$, and like ΔG_r^0 it reflects the underlying chemical nature of the O/R couple. The formal potential $E^{0'}$ is always specified in terms of concentrations, rather than activities, with the relationship between $E^{0'}$ and the true thermodynamic potential specified by Equation (2.2.12):

$$E^{0\prime} = E^0 + \frac{RT}{nF}\ln\frac{\gamma_o}{\gamma_r} \quad (2.2.12)$$

In principle if the activity coefficients for O and R are known for the particular experimental conditions it is possible to 'correct' the formal potential using Equation (2.2.12). This thesis follows the more common practice of reporting $E^{0'}$ directly.

The logarithmic term in Equation (2.2.11) reflects the positive entropic contribution of mixing O and R (i.e. $\Delta G_{mix} < 0$) relative to the production of a uniform solution of O or R. The Nernst equation therefore contains entirely thermodynamic information, but it is nonetheless extremely important for the understanding of heterogeneous charge transfer kinetics, the subject of the next section. This is so because any microkinetic theory of charge transfer must produce results consistent with the Nernst equation when describing systems at equilibrium.

The Butler-Volmer Theory of Electron Transfer Kinetics

In Chapter I the Marcus theory of electron transfer was introduced in the discussion of redox probes in order to account for the variation in electron transfer rates observed for different redox-actives species and to emphasise the distinction between outer-sphere and inner-sphere probes. That discussion dealt primarily with the organizational changes undergone by ions in solution during an interfacial charge transfer event. In this section, the Butler-Volmer (BV) theory of electron transfer kinetics is introduced. The application of BV theory to electrochemical systems underpins vast areas of research in electrochemistry, and a good understanding of the axioms underpinning so-called 'Volmerian' systems is essential

for the interpretation of data acquired from numerous experimental techniques applied in this thesis, including voltammetry and impedance spectroscopy.

The Effects of Applied Potential on Activation Energy

Figure 2.3 a) illustrates the potential energy diagram for a generic reduction process O + e = R under standard conditions and with equal concentrations of O and R, similar to that introduced in Chapter I. The potential at the electrode surface under such conditions, E, is by definition equal to the formal potential, $E^{0'}$. The system is at equilibrium, which implies that the rate of reduction of O is equal to the rate of oxidation of R:

$$-\frac{dC_o}{dt} = \frac{dC_r}{dt} \Rightarrow k_c C_o = k_a C_r \quad (2.2.13)$$

The rate constants specified are heterogeneous charge transfer rate constants for the redox reaction (2.2.5). However, under these conditions $C_o = C_r$, which implies that

$$k_c = k_a = k_s \quad (2.2.14)$$

$E^{0'}$ for a redox couple is therefore the unique potential at which the rate constants for the process in both the cathodic and anodic directions are equal in value. This value is termed the standard heterogeneous rate constant, k_s. Also identifiable from the diagram are the activation energies for the cathodic and anodic process, $\Delta G^{\ddagger}_{red}$ and $\Delta G^{\ddagger}_{ox}$ which under these conditions are equal in value to $\Delta G^{\ddagger}_{s}$, the standard activation energy. $\Delta G^{\ddagger}_{s}$ may be related to k_s by an Arrhenius relation:

$$k_s = Ae^{-\frac{\Delta G^{\ddagger}_{s}}{RT}} \quad (2.2.15)$$

Knowing the value of k_s, it is possible to develop a general equation relating the rate constant at any applied potential. The argument is based on the approach adopted in Reference 17. The potential energy diagram in Figure 2.3 b) corresponds to the same O/R system after the electrode has been polarised to a new potential, E, such that $E < E^{0'}$. This potential step represents a destabilisation of the equilibrium situation described by Equations 2.2.14 and 2.2.15, which results in the shifting of the entire reactant (O + e) curve upwards by an amount $\Delta G = -F(E-E^{0'})$. Generally the potential shift will also affect the position of the product curve R, particularly if both O and R are charged species. Figure 2.3 b is valid for uncharged R, such as a metal cation in equilibrium with a solid metal phase.[20]

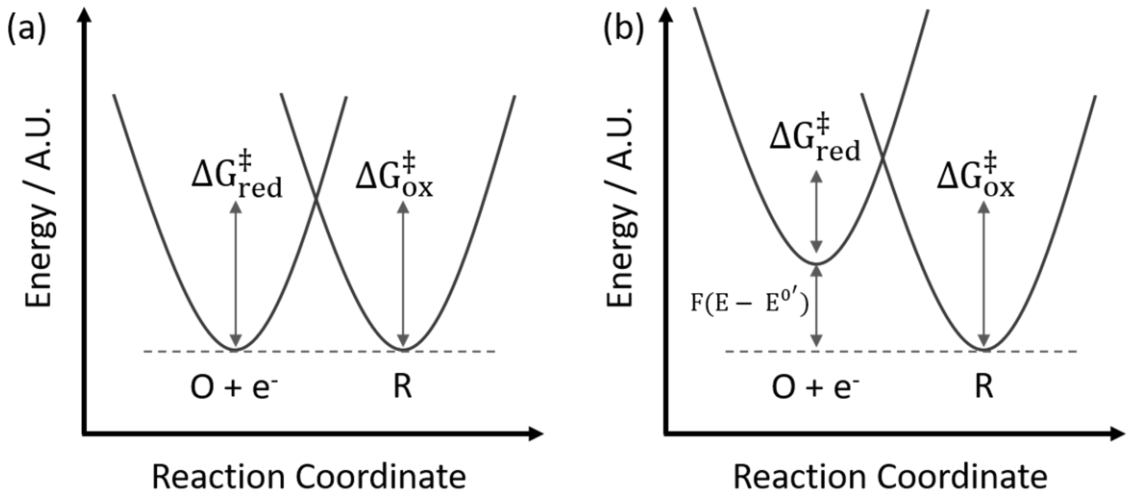

Figure 2.3. Energy-Reactant Coordinate Curves for the O/R system with $c_o = c_R$ a) for $E = E^{0'}$ and b) $E < E^{0'}$.

The shift in the O/R curve is mainly due to the destabilisation of electrons on the electrode relative to the standard value due to the negative shift in potential. This shift in the potential energy curve also results in a change in $\Delta G^{\ddagger}_{red}$ away from its standard value and therefore in a change in the rate constant. By a similar argument, applying a potential $E > E^{0'}$ destabilises the product curve (R) relative to the standard state and reduces $\Delta G^{\ddagger}_{ox}$. This potential-dependence of the cathodic and anodic rate constants may be generalised mathematically as follows:

$$k_c(E) = Ae^{-\frac{\Delta G^{\ddagger}_{red}}{RT}} = Ae^{-\frac{\Delta G^{\ddagger}_{s} + \alpha F(E-E^{0'})}{RT}} = k_s e^{\frac{-\alpha F(E-E^{0'})}{RT}} \qquad (2.2.16a)$$

$$k_a(E) = Ae^{-\frac{\Delta G^{\ddagger}_{ox}}{RT}} = Ae^{-\frac{\Delta G^{\ddagger}_{s} - (1-\alpha)F(E-E^{0'})}{RT}} = k_s e^{\frac{(1-\alpha)F(E-E^{0'})}{RT}} \qquad (2.2.16b)$$

Here a factor α known as the transfer coefficient has been introduced in recognition of the fact that, although the energy of the reactant system has been increased by $F(E-E^{0'})$, the activation energy $\Delta G^{\ddagger}_{red}$ has not changed by this amount. $0 < \alpha < 1$ is therefore a measure of the fraction of the free energy change of the system which alters the activation energy for the charge transfer. Based on purely geometric considerations, for symmetric potential wells like those in Figure 2.3 the amount by which the activation energy for the anodic process is altered by the change in potential must be (1-α).

A common assumption in the theory of BV kinetics is that $\alpha = 0.5$, owing to the symmetry of the potential energy surface cross-sections.[21] Deviations from 0.5 are theoretically expected for large differences in potential from $E^{0'}$; in practice this is difficult to verify experimentally due to mass transport and double layer effects and most experimental studies assume that the transfer coefficient is potential-independent. [20]

The expressions for the heterogeneous rate constants given in Equation 16a and 16b relate to the measured current density for the redox process, *j*, via Equation 2.2.17:

$$\frac{dC_o}{dt} = -k_c(E)C_o + k_a(E)C_r = (jc + ja)/nF = j/nF \ \text{mol/s} \qquad (2.2.17)$$

Note that this expression assumes the convention that cathodic currents are negative and anodic currents are positive. The number of electrons, n, has also been introduced in order to generalise the kinetic equations to include redox processes involving multiple charge transfer events. Equation 2.2.17 can be rewritten using the expressions for the rate constants given on the right hand side of Equations 2.2.16a and 2.2.16b:

$$j = nFk_s(e^{\frac{(1-\alpha)nF\left(E-E^{0'}\right)}{RT}}c_r - e^{\frac{-\alpha nF(E-E^{0'})}{RT}}c_o) \qquad (2.2.18)$$

Equation 2.2.18 illustrates the exponential dependence of the current density for both cathodic and anodic processes, a feature which was observed empirically. The consistency of Equation 2.2.18 with the Nernst equation can be illustrated by allowing C_o and C_r to take on arbitrary values and presuming that E is the equilibrium potential, E_{eq} for that composition. j in Equation 2.2.18 is therefore null by assumption, since the net current density is zero at equilibrium. This rearranges as follows to yield:

$$\frac{j}{nF} = k_s(e^{\frac{(1-\alpha)nF\left(E_{eq}-E^{0'}\right)}{RT}}c_{r*} - e^{\frac{-\alpha nF\left(E_{eq}-E^{0'}\right)}{RT}}c_{o*}) \qquad (2.2.19a)$$

$$\frac{C_{o*}}{C_{r*}} = e^{\frac{nF(E_{eq}-E^{0'})}{RT}} \qquad (2.2.19b)$$

$$E_{eq} = E^{0\prime} + \frac{RT}{nF} ln(\frac{C_{o*}}{C_{r*}}) \qquad (2.2.19c)$$

as predicted by the Nernst equation. It should be stressed that the values of C_o and C_r given in the Equation 2.2.18 describe the concentration profile at the electrode surface, where the charge transfer event is occurring, whereas the asterisked values in Equations 2.2.19a-c specify the bulk concentrations of O and R, because the equilibrium condition applies and the concentration of each reactant is the same at all points in solution. In practical experiments, if C_o and C_r at the surface are also specified by Equation 2.2.19c at any value

of j, the kinetics of electron transfer are so rapid that the system remains in equilibrium at the surface at all times throughout the experiment and the concentrations at the bulk and surface are equal to the Nernstian value.

The overall reaction rate under such conditions is therefore only limited by mass transfer of the species O and R to and from the surface. Such systems are commonly referred to as 'reversible' or 'Nernstian' systems. It should be evident from the dependence of k_s on the activation energy for the process that charge transfer reactions with low activation barriers are most likely to display Nernstian behaviour. In the context of Marcus theory, this corresponds to outer-sphere redox probes with low re-organisation energies.

Further insight can be obtained by examining both terms in Equation 2.2.19a. Since the system is at equilibrium, both of these terms have the same value and can be written as j_0, the exchange current density. Combining Equations 2.2.18 and 2.2.19b yields the relationship:

$$j_0 = nFk_s(C_o)^{(1-\alpha)}(C_r)^{\alpha} \tag{2.2.20}$$

which under the condition $C_o = C_r = C$ reduces to

$$j_0 = nFk_sC \tag{2.2.21}$$

Both j_0 and k_s can be reported as measures of the intrinsic kinetic behaviour for any redox couple. k_s can be seen as a specific reference point for the system, since it pertains to the kinetics at the formal potential where Co = Cr. j_0 is a general reference value for the system at equilibrium with any O/R concentration ratio according to Equation 2.2.20. This suggests that the kinetic performance expressed in terms of j_0 allows the potential to be referenced to the potential at equilibrium, $E\text{-}E_{eq}$, rather than relative to the formal potential. This can be shown by dividing the general j-E relationship (Equation 2.2.18) by j_0 from the right hand side of Equation 2.2.20 and rearranging:

$$\frac{j}{j0} = \left(\frac{c_r}{c_{r*}}\right) e^{\frac{(1-\alpha)nF\left(E-E^{0'}\right)}{RT}} e^{\frac{-(1-\alpha)nF\left(Eeq-E^{0'}\right)}{RT}} - \left(\frac{c_o}{c_{r*}}\right) e^{\frac{(-\alpha)nF\left(E-E^{0'}\right)}{RT}} e^{\frac{-(1-\alpha)nF\left(Eeq-E^{0'}\right)}{RT}}$$

$$= \left(\frac{c_r}{c_{r*}}\right) e^{\frac{(1-\alpha)nF(E-Eeq)}{RT}} - \left(\frac{c_o}{c_{o*}}\right) e^{\frac{(-\alpha)nF(E-Eeq)}{RT}} \tag{2.2.22}$$

The final step leading to Equation 2.2.22 involves Equation 2.2.19c rewritten as

$$\frac{C_r*}{C_o*} = e^{-\frac{nF(E_{eq}-E^{0'})}{RT}}$$

The quantity $(E\text{-}E_{eq})$ is η, the experimental overpotential, and is a measure of the deviation of the electrode potential from the equilibrium value. The ratio of the surface and bulk

concentration of O and R is frequently predicted to be close to unity, particularly at low overpotentials and for low values of the exchange current density. This additional assumption leads to the simplest form of the Butler-Volmer equation:

$$\frac{j}{j0} = e^{\frac{(1-\alpha)nF(\eta)}{RT}} - e^{\frac{(-\alpha)nF(\eta)}{RT}} \quad (2.2.23)$$

At zero overpotential, charge is still crossing the interface at a fixed rate described by the exchange current density, with the anodic and cathodic processes contributing equally. η can then be viewed as a parameter which can be varied in order to favour a net current in the cathodic or anodic direction. Due to the exponential dependence of each of the terms of the BV equation on η, the polarisation of the electrode away from the equilibrium value by a significant amount (|η| > *ca.* 120 mV) will cause the cathodic/anodic term to rapidly approach zero.

Under highly anodic overpotential regions it is possible to neglect the second term on the right hand side in Equation 2.2.23, leading to

$$\frac{j}{j0} = e^{\frac{(1-\alpha)nF(\eta)}{RT}} \quad (2.2.24)$$

Or

$$\ln j = \ln(j_0) + \frac{nF}{RT}(1-\alpha)\,\eta \quad (2.2.25)$$

With a similar relationship obtained for highly cathodic overpotentials:

$$\ln j = \ln(j_0) + \frac{nF}{RT}(-\alpha)\,\eta \quad (2.2.26)$$

Switching the base of the logarithms to base 10 yields the empirical Tafel relationship:

$$\frac{d\log j}{d\eta} = -\frac{\alpha F}{2.303RT} \quad (2.2.27)$$

which verifies that the BV equation yields the empirically-observed dependence of current density on the applied overpotential. This relationship can only be said to hold in the absence of mass transfer effects. Since large values of j_0 and/or large values of η will inevitably lead to contributions of concentration gradients into the system, Tafel relationships are only practically observed for systems with sluggish kinetics. For systems with fast kinetics such as the H_2/H^+ couple on Pt, the influence of mass transport can only be mitigated by using extreme interventions; in this case high overpressures of H_2 are applied via a hydrogen-pump system. [22]

As a final note on Tafel analysis, it is common in the literature for the Tafel behaviour to also be described in terms of the slope of η vs log(j). Tafel slopes reported in this manner are the reciprocal of Equation 2.2.27 reported in mV of overpotential/decade. This convention will be adopted in Chapter VI, where Tafel plots are used in the analysis of the kinetics of the oxygen reduction reaction on nitrogenated carbon systems.

BV Kinetics for Multi-Step Electrochemical Processes

The analysis of BV kinetics just presented applied to a single electron transfer process for a generic redox couple O/R. For many applications this elementary approach is sufficient. However many important electrochemical systems involve multiple charge transfer steps as well as chemical rearrangements, all of which may occur at different rates depending on variables such as the surface chemistry of the electrode material, pH, temperature and concentration of the reactants. The application of BV kinetics to such systems is still possible in principle, as long as certain assumptions are made. As an illustration, consider a hypothetical multi-step process with the following mechanism:

$$A + e^- \rightleftharpoons B \quad (a)$$

$$B \rightleftharpoons C \quad (b)$$

$$C + e^- \rightleftharpoons D \quad (c)$$

Such a process involves two redox couples, A/B and C/D, involved in heterogeneous charge transfer steps, coupled by the homogeneous transformation of B into C. The i-E profile obtained for this system (again assuming that the effects of mass transfer may be neglected or minimised by the design of the experiment) will depend on which of the steps, a), b) or c), has the most sluggish kinetics and hence is rate-determining. If reaction a) is limiting, then the concentrations of the intermediates B and C are both negligible and the overall rate is given by

$$-\frac{dC_A}{dt} = -\frac{j}{F} = k_{s,A} e^{\left(-\frac{aF}{RT}(E-E^{0\prime}A/B)\right)} C_A \quad (2.2.28)$$

If α is assumed to take on the symmetric barrier value of 0.5 the Tafel slope will have a value of 120 mV/dec at 25 ^{o}C. The overall current passed will be twice that of a 1e$^-$ process, but

the Tafel analysis will yield an identical Tafel slope to that expected for a single electron transfer process because the first electron transfer step is rate determining.

If instead reaction b) is rate limiting, it may be assumed that reaction a) occurs rapidly enough for the concentrations of A and B to be equal to the values specified by the Nernst equation:

$$\frac{C_A}{C_B} = e^{-\frac{F}{RT}(E-E^{0\prime}A/B)} \quad (2.2.29)$$

The reaction rate is given by:

$$-\frac{dC_B}{dT} = -k_b C_B = -k_b C_A e^{F/RT(E-E0'A/B)}$$

The log(j) versus E relationship yields a Tafel slope of 60 mV dec^{-1} (or an apparent α, α_{app} of 1) i.e. half the value expected for when the first electron transfer step is rate limiting. The final limiting case, where step c) is rate determining, may be derived under the assumption that all preceding steps are at equilibrium:

$$-\frac{dC_C}{dt} = c_c k_{s,c} e^{-\frac{\alpha F(E-E^{0\prime}C/D)}{RT}} \quad (2.2.30a)$$

$$C_C = K_{BC} C_B = K_{BC} C_a e^{F/RT(E-E0'A/B)} \quad (2.2.30b)$$

Combination of Equations 2.2.30a and 2.2.30b yields the j-E profile:

$$-\frac{j}{F} = K_{BC} C_a e^{-\frac{(1+\alpha)F}{RT}(E-E^{0\prime}A/B-E^{0\prime}C/D)} \quad (2.2.31)$$

The application of Tafel analysis to Equation 2.2.31 yields an α_{app} = 1.5 or a Tafel slope of 40 mV per decade when the 2nd electron transfer is rate limiting. The application of BV theory to complex systems involving multiple electron transfer events enables the determination of the RDS from the j-E profile and provides insights into the reaction mechanism. Such analysis will be applied to the electrochemistry of multi-step mechanisms involving catechol oxidation in Chapters IV and V and oxygen reduction in Chapter VI of this thesis.

Cyclic Voltammetry

Cyclic voltammetry (CV) is among the most commonly applied experimental techniques in electrochemistry, due to the wealth of kinetic and thermodynamic information afforded from a relatively simple experiment. The technique involves the measurement of an i-E profile through the linear ramping of potential at a fixed rate, referred to as the sweep rate, ν. Figure 2.4 illustrates a typical i-E profile for a Nernstian system involving a single e^- transfer. Such traces are referred to as 'voltammograms.' An experiment used to study the oxidation of a generic analyte R is usually carried out in an electrolyte solution containing only R initially. The potential is then ramped from an initial value E to another value according to

$$E = E_i + vt$$

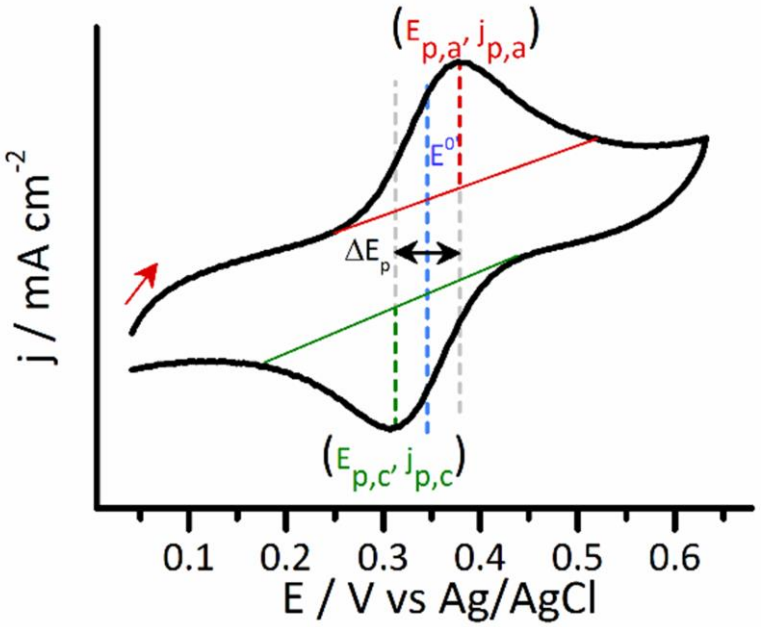

Figure 2.4. Typical voltammogram for a 1-electron redox process showing Nernstian behaviour. Important parameters such as the formal potential, $E^{0'}$, the peak-to-peak separation ΔE_p and the peak current densities $j_{p,a}$ and $j_{p,c}$ are illustrated in the figure. The red arrow indicates the initial potential, E_i.

This half of the voltammogram is termed the 'anodic sweep.' The ramping of potential increases j_a relative to j_c, resulting in a net anodic current as the reduced species R is oxidised. At E_i no net Faradaic current is evident due to the absence of O from solution initially, and because the potential E_i is not sufficiently anodic to effect the oxidation of R. As the potential

increases, the oxidation begins to proceed and R is converted to O in order to satisfy the O/R ratio required by the Nernst equation at each value of potential. The anodic current does not increase exponentially indefinitely, however, as mass transport effects quickly predominate. At the potential $E_{p,a}$, the anodic peak current density $j_{p,a}$ is attained, and increasing the potential beyond this point results in a current which is independent of potential and falls off proportionally to $\frac{1}{t^{1/2}}$.

The fall-off proceeds until the upper limit of potential, E_f, is reached. The value $E_f - E_i$ is referred to as the potential window of the experiment, and it may have an effect on the overall profile of the voltammogram, particularly if E_f is chosen to be too close to $E_{p,a}$. In this thesis, potential windows are always chosen to minimise this issue, which in practice implies that E_F is chosen to be more than *ca.* 250 mV beyond the anodic peak. Once E_f is reached, the potential is then swept cathodically back to E_i, which forces the reduction of O which was formed on the anodic sweep back to R, again to ensure that the O/R ratio at the electrode surface complies with the Nernst equation.

This proceeds until all of the O in the vicinity of the electrode surface is depleted, again manifesting as a peak in the voltammogram at a potential $E_{p,c}$. This is the cathodic peak current density, $j_{p,c}$. The fall-off of the cathodic current density at potentials below $E_{p,c}$ has the same physical origin, *mutatis mutandis*, as for the anodic sweep.

Considering the full voltammogram, it is possible to determine the value of $E^{0'}$ for the O/R couple from the mid-point of the two peaks, $(E_{p,a} + E_{p,c})/2$. This point, marked in Figure 2.4, is the potential value of the experiment where $C_o = C_r$. The coloured baselines in the figure are used to account for the non-Faradaic current which is also passed during the potential sweep, which may be attributed to the behaviour of the electrode-electrolyte interface as a capacitor. Such currents are referred to as 'charging current' or 'capacitive current' and must be subtracted from the total current in order to accurately report the Faradaic contribution only.

Comparison of the capacitance-corrected peak current densities for the anodic and cathodic sweeps in the figure indicates that both have the same value within experimental error, i.e. that $j_{p,c} / j_{p,a} \cong 1$. This reflects the fact that essentially all of the species O produced on the anodic sweep is reduced back to R on the reverse sweep. The O/R couple is therefore reversible in the sense that the O/R ratio is determined by the Nernst equation, but the result also implies that the transformation O-R is chemically reversible. If this were not the case, the ratio $j_{p,c}/j_{p,a}$ might be < 1. Such a result is observed when an irreversible homogeneous

transformation of the product O occurs, which effectively removes O from the electrode surface before it can be reduced back to R. [23]

For a Nernstian system, the separation between the two peaks, $\Delta E_p = E_{p,a} - E_{p,c}$ is equal to 59/n mV, where n is the total number of electrons transferred. Values close to the Nernstian limit are typically referred to as 'quasi-reversible', with significant deviations referred to as 'electrochemically irreversible.' This terminology should not be confused with the question of chemical reversibility discussed above; electrochemical irreversibility implies that k_s for the O/R system is very small, such that the O/R concentration ratio is not described by the Nernst equation but rather by the BV theory of the previous section. An irreversible voltammogram is illustrated in Figure 2.5. Here the ΔE value is approx. 100 mV and the voltammogram is considerably more elongated in shape than the Nernstian case.

In this way, CV experiments offer an immediate qualitative assessment of a redox

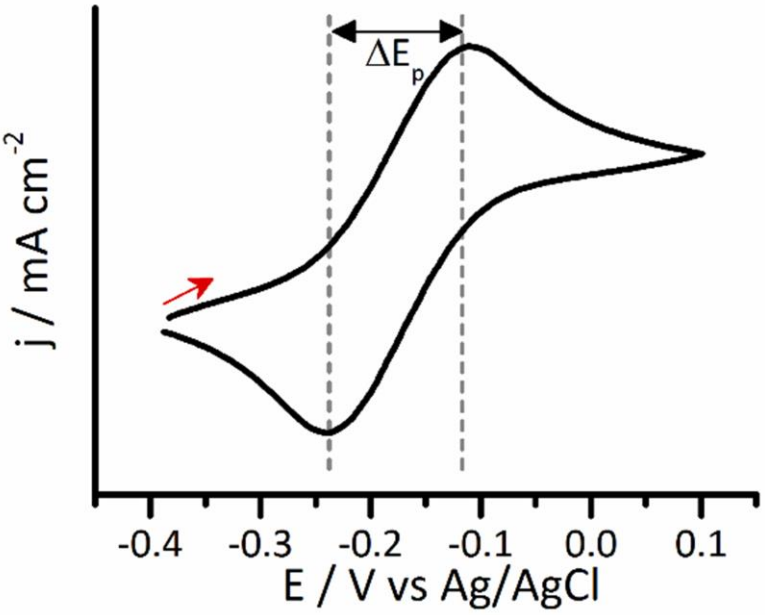

Figure 2.5. Typical CV profile for 1-electron redox process with irreversible charge transfer kinetics. The value of ΔE is illustrated in the figure and is considerably larger in magnitude than the Nernstian value.

system's kinetics. When the charge transfer kinetics are irreversible it is possible to examine the high-overpotential behaviour of the system through Tafel analysis. For voltammograms, this is typically accomplished on capacitance-corrected data in the region of the CV which shows minimal interference from mass-transport effects.

The scan rate, ν, is one of the most important parameters to consider in a CV experiment. Faster scan rates result in higher current densities, since a faster sweep will result in the passage of the same amount of charge in a shorter time period. Fast scan rates also increase

the predominance of mass-transport effects on the system. This is because a faster sweep increases the rate at which the surface concentrations of O/R are altered. A system which displays Nernstian kinetics at a low scan rate of 5 mVs^{-1} may not be able to maintain the Nernstian O/R ratio at ν = 500 mVs^{-1}, because the system may be limited by mass transport of O/R to the electrode surface. 'Electrochemical reversibility' can therefore be said to be a function of the relative rates of charge transfer and mass transport and therefore dependent on ν.

For Nernstian kinetics, the peak current density increase with scan rate shows a square root dependence given by Equation 2.2.32.

$$j_p = 0.446 \times nFC\sqrt{\frac{nF}{RT}}v^{1/2} \qquad (2.2.32)$$

Irreversible systems also have a square root dependence of j_p on ν, but the proportionality between the two is also a function of the charge transfer kinetics due to the non-Nernstian behaviour of the system. The Nernstian system also shows no dependence of ΔE on the scan rate, whilst increasing ν for an irreversible redox couple causes ΔE to also increase.

Voltammetry with Rotating Disk and Rotating Ring Disk Electrodes

The voltammetric experiment introduced in the previous section is carried out with a static working electrode in non-stirred solutions. The only mode of mass-transport of the various redox species is therefore due to diffusion. This presents a limitation in kinetic studies of species with low solubilities, such as O_2 in water for which C_{O2} = 1mM under conditions of saturation. The low solubility of oxygen combined with the very large overpotential values found in oxygen reduction studies results in significant distortions of the i-E curve from mass transport effects. Kinetic studies of oxygen reduction therefore require some method of increasing the rate of mass transport of O_2 to the electrode surface, effectively extending the potential window from which kinetic information may be extracted from the voltammogram.

One methodology for accomplishing this involves the rotating disk electrode (RDE). An RDE consists of an electrode affixed to a cylindrical holder, typically constructed from PTFE, mounted vertically in a rotating shaft capable of rotating the entire working electrode system at several thousand rotations per minute (RPM). The rotation of the electrode in a solution of dissolved redox analyte induces the convective transport of the material to the electrode surface.

This convection is significantly more rapid than the mass transport rate possible through simple diffusion and is a function of the rotation speed, ω, in rpm. CV experiments with an RDE are illustrated in Figure 2.6. The j-E profile with convection no longer has a peak in the polarisation curve at potentials. Instead a steady-state is reached, with a limiting current density j_l determined by the rotation speed according to

$$j_L = 0.201nFD^{2/3}\nu^{-1/6}C\omega^{1/2} \quad (2.2.33)$$

Analysis of the j-E profile in potentials close to the onset of the faradaic process yields kinetic information, whilst the plot of j_L versus $\omega^{1/2}$ can be used to determine the diffusion coefficient, D, for the analyte. This is accomplished in Chapter IV for dopamine in 0.1M sulfuric acid solution.

A more sophisticated experiment involving an RDE is the rotating ring disk electrode (RRDE) setup. The RRDE may be viewed as an RDE which has been mounted within a ring

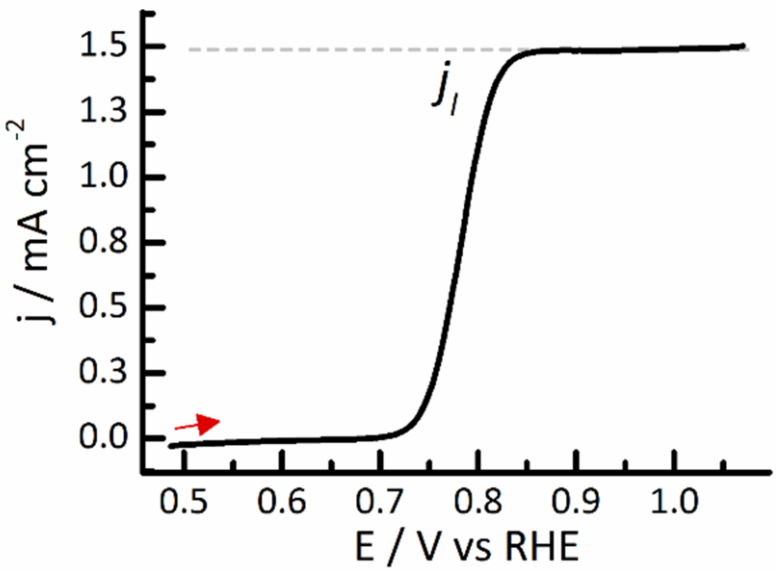

Figure 2.6. Linear sweep voltammogram for a redox process occurring under forced convection conditions with an RDE at a rotation speed of 400 rpm.

electrode which is typically constructed from a noble metal such as platinum or gold. RRDEs are typically applied in experiments involving the study of redox-active intermediates in multi-step processes. This may be understood by examining a generic 2-electron redox process which proceeds according to the following mechanism:

$$O + e^- \rightleftharpoons I_{ads} \quad (a)$$

$$I_{ads} \rightleftharpoons I_{sol} \quad (b)$$

$$I_{ads} + e^- \rightleftharpoons R \quad (c)$$

Here the reduction of O at the disk results in the formation of an intermediate, I_{ads}, which is adsorbed at the electrode surface. Two possible fates for the intermediate are then possible: detachment from the surface to produce solution phase I_{ads}, or further reduction to the final product R. The experimenter would like to understand the extent to which each possible pathway occurs. This can be accomplished via the RRDE method. The experiment proceeds in a similar fashion to that described for the RDE, *viz.* the obtaining of a polarisation curve via voltammetry with rotation of the electrode at some fixed rate.

However, during the course of the experiment, the ring electrode is kept at a fixed potential, E, large enough to guarantee the oxidation of the intermediate I_{ads}. The final product R is assumed to be inactive to further oxidation. The convective transport of an analyte O to the disk electrode may result in the formation of both I and R according to Equations a-c) above, which then travel outwards from the central disk to the ring where I is oxidised back to O. Since R is redox inactive, the current at the ring is therefore proportional to the amount of I produced initially at the disk.

Not all of the material produced at the disk is detected by the ring; each RRDE has a collection efficiency, N, which is determined experimentally using a standard redox probe and specified by the manufacturer. If the production of I from O is the final step in the reaction, the net result is a 1-electron process compared to a 2-electron process if the intermediate is fully reduced to form R. The relative amounts of the $1e^-$ and $2e^-$ process occurring at the surface may be specified as n, the electron transfer number:

$$I_{1e} = Ir/N \tag{2.2.34}$$

$$I_{2e} + I_{1e} = I_D \tag{2.2.35}$$

$$n = \frac{2I_D}{I_D + \frac{I_R}{N}} \tag{2.2.36}$$

Thus, once the ring current is corrected for the collection efficiency, if the process is exclusively 1-electron then $I_r/N = I_D$ (Equations 2.2.34-2.2.35). This results in a value of n = 1 in Equation 2.2.36. By contrast, if $I_r/N = 0$ then I_D in Equation 2.2.35 may be exclusively associated with the 2-electron reduction and Equation 2.2.36 yields n = 2. A real example of the practical use of RRDE studies is in the oxygen reduction reaction, which may proceed with a full $4e^-$ reduction of O_2 to H_2O or a less efficient $2e^-$ reduction to H_2O_2. The RRDE method enables researchers to quantify the relative amounts of $2e^-$ and $4e^-$ reduction using a similar approach to that summarised in Equations 2.2.34-2.2.36. RRDE studies of the ORR on N-doped carbon materials are presented in chapter VI of this thesis. The RRDE shaft and controller applied for these studies were purchased from Pine Instruments.

Electrochemical Impedance Spectroscopy (EIS)

Electrochemical Impedance Spectroscopy (EIS) is a versatile experimental technique for the study of redox systems as well as for the fundamental physico-chemical characterisation of electrode material properties. The technique is based on the perturbation of an equilibrated system with an input, typically a sinusoidal voltage, and measuring the output. Under most conditions the input perturbation is small, with dE < 10 mV, and the output current response is linear:

$$E = E_0 + \Delta E cos(\omega t) = re(E' exp(i\omega t)) \quad (2.2.37)$$

$$I = I_0 + \Delta I cos(\omega t + \varphi) = re(I' exp(i\omega t + \varphi)) \quad (2.2.38)$$

Here the input potential varies sinusoidally with angular frequency ω, and the current output is of the same frequency, but may have a difference in phase from the input of magnitude φ. This is most conveniently specified through the Euler relation as the real part of a complex exponential as shown on the right-hand side of Equations 2.2.37-2.2.38. E is the magnitude of the phasor described by this exponential and may be physically interpreted as the input perturbation. I' is the magnitude of the output phasor and is equivalent to I exp(φ). I' therefore contains both magnitude and phase information for the output.

The quantity of interest in an EIS experiment is the impedance:

$$Z(\omega) = \frac{E'}{I'} = Z_{re} + iZ_{im} \quad (2.2.39)$$

Electrochemical responses to perturbations in the potential include capacitive (charging) responses and resistive responses in the form of charge transfer, which may be further subdivided in to charge transfer resistance due to electrode kinetics and mass transport. Central to the theory of EIS is that such complex electrochemical phenomena may be modelled analogously in the form of electronic circuits composed of resistors and capacitors. The impedance of a resistor may be specified by the well-known Ohm's Law:

$$R = \frac{E}{I} \quad (2.2.40)$$

The phase angle for a resistive component is therefore equal to zero; the current is said to be 'in phase' with the potential change. On the other hand, the fundamental equation governing the behaviour of a capacitor is the ratio of charge Q to voltage E:

$$C = \frac{Q}{E} \quad (2.2.41a)$$

$$Q = CE \quad (2.2.41b)$$

Since $I = dQ/dT$, by Equation 2.2.41b:

$$I' = dQ/dT = CdE/dT \quad (2.2.42)$$

Since $E = Ee^{(i\omega t)}$, $\frac{dE}{dT} = i\omega E\exp(i\omega t) = i\omega E$. This leads to:

$$Z(\omega) = \frac{E'}{I'} = E/i\omega CE = -i/\omega C \quad (2.2.43)$$

The dependence of Equation 2.2.43 above on the imaginary number i may be interpreted as the response of a capacitor being entirely out of phase with the input perturbation. The impedance is also frequency-dependent and dependent upon the magnitude of the capacitance, as shown by the presence of ω in the denominator. The physical interpretation of this fact lies in the timescale involved in charging a capacitor after the application of a voltage. At long timescales (i.e. when ω is very low) the capacitor becomes fully-charged,

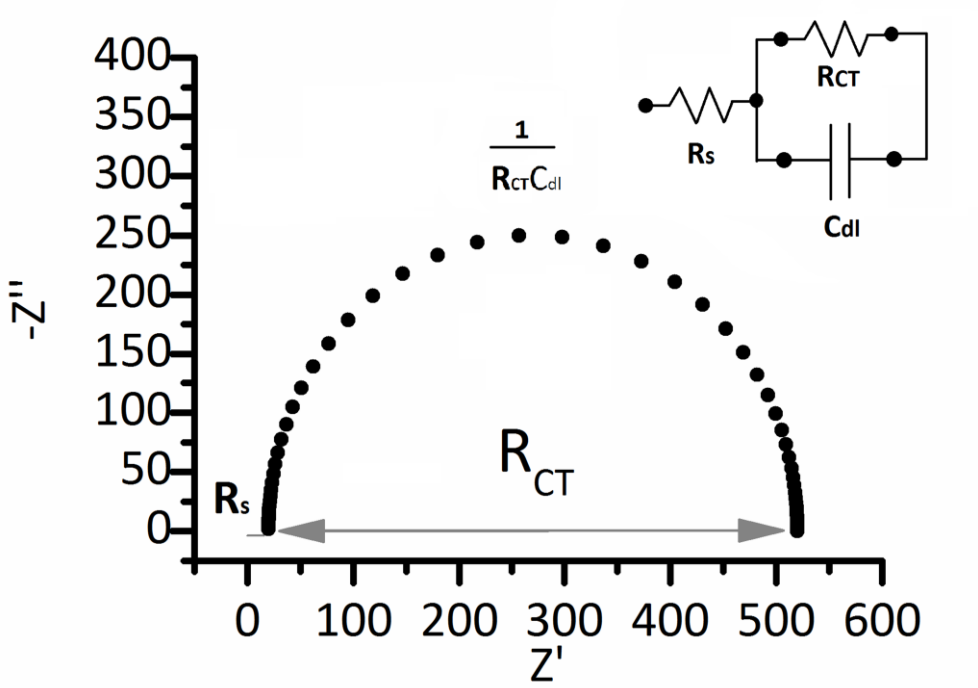

Figure 2.7. Nyquist plot for a generic redox process. The frequency, ω, is chosen to avoid mass transport contributions. Inset is the equivalent circuit describing the system, including the solution resistance, R_s, the charge transfer resistance R_{CT} and the double layer capacitance C_{dl}.

at which point the resulting electric field produced by the charge separation acts as a large impedance to further charge transfer and the capacitor behaves like an open circuit. At short timescales (high frequencies) the impedance has a lower magnitude, because this charge separation has not yet occurred and current may flow freely.

Many electrochemical phenomena can be modelled in terms of combinations of just resistors and capacitors. An example is given in Figure 2.7. Here a uniform electrode material is immersed in a solution containing the O/R redox couple at an applied potential of $E^{0'}$ for the couple, such that the perturbation potential induces charge transfer. At the same time, the input perturbation also induces the flow of a capacitive current according to

Equation 2.2.43. Both charge transfer and double-layer charging events are also occurring in a system where current is being carried by ions in solution. This solution resistance manifests in the impedance spectrum as a resistor. Hence, assuming that only high frequencies are applied, such that mass transfer effects can be neglected, the total output response is modelled by the circuit diagram drawn inset in the figure**.**

From elementary electronics, impedances are summed in series:

$$Z = Z1 + Z2$$

Z is the total impedance, Z1 may be identified with the solution resistance R_s, whilst Z2 is attributed to both the charge transfer resistance for the Faradaic process and the impedance of double-layer charging. The two processes occur in parallel, suggesting that:

$$I2' = \frac{E}{R_{CT}} + i\omega CE \tag{2.2.44}$$

Which leads to:

$$Z2 = \frac{E}{I2'} = \frac{R_{CT}}{1+i\omega CR_{CT}} \tag{2.2.45}$$

The total impedance Z = Z1 + Z2 is therefore given by:

$$R_s + \frac{R_{CT}}{1+i\omega CR_{CT}} \tag{2.2.46}$$

The total impedance is therefore comprised of 'real' components which may be thought of as in-phase elements like resistors and 'imaginary' components which are system components for which the input and output are entirely out of phase. The impedance at any frequency may be represented on the complex plane in Argand form, as in Figure 2.7, which in the field of impedance is termed a Nyquist plot. The R_s and R_{CT} components are illustrated in the x axis (Z') as the high frequency intercept of the semi-circle and the diameter of the semi-circle respectively. The frequency-dependent impedance due to the capacitance is plotted on the y-axis and denoted as Z'; (note that the complex component is plotted as –Z'' in order to avoid negative values). The RC circuit shown Figure 2.7 and specified by Equation 2.2.46 is commonly referred to as an 'RC loop' in the impedance spectrum.

Since the impedance is a complex number, the magnitude and phase information may be obtained from the Nyquist plot in the usual manner using Equations 2.2.47 and 2.2.48:

$$|Z| = \sqrt{Z'^2 + Z''^2} \tag{2.2.47}$$

$$\varphi = \tan^{-1}(-Z''/Z') \tag{2.2.48}$$

The disadvantage of Nyquist plots is that they do not contain frequency information directly. It is therefore common to plot both the magnitude and phase of the impedance as given in Equations 2.2.47 and 2.2.48 as a function of frequency (Figure 2.8) in so-called Bode plots.

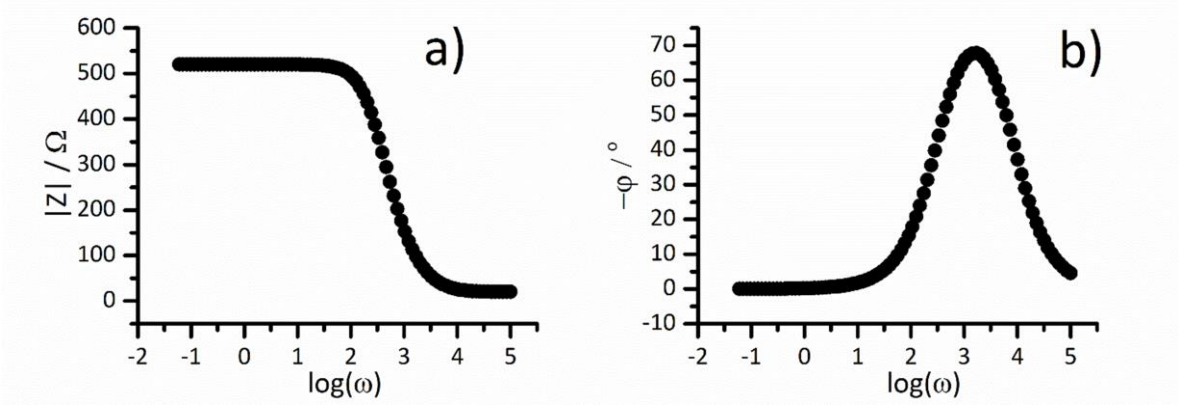

Figure 2.8. a) Bode Magnitude and b) Bode Phase plots of impedance data for the circuit described in Figure 2.7.

In the Bode representation, the high and low frequency values of the impedance in the magnitude plot may be associated with the solution and charge transfer resistance respectively. The phase diagram contains a peak at a particular frequency, referred to as the characteristic frequency, ω_c associated with the RC circuit. It is closely related to the time constant, τ, the time required for the capacitor in the system to be charged to $(1-\frac{1}{e})$ of its asymptotic value:[24]

$$\tau = RC \Rightarrow \omega = 2\pi f = 2\pi(\frac{1}{\tau}) \qquad (2.2.49)$$

Electrochemical Impedance Response of other Important Processes

The use of RC circuits to model impedance spectra is useful for many simple electrochemical responses, but the method is not comprehensive. In order to model other impedances associated with charge transfer phenomena such as mass-transport, and to account for the non-homogeneous nature of many electrodes, additional circuit elements are necessary. The first of these is elements is the Warburg element, W, which is used to model the impedance associated with diffusion of a redox analyte to the electrode surface.

This process can be thought of as a resistance to charge transfer, with a magnitude depending on the value of the diffusion coefficient and solution viscosity. Unlike an R_{CT} value, however, a diffusional impedance also has a time-dependence which is associated with the variation of the magnitude of the concentration gradient at the electrode surface

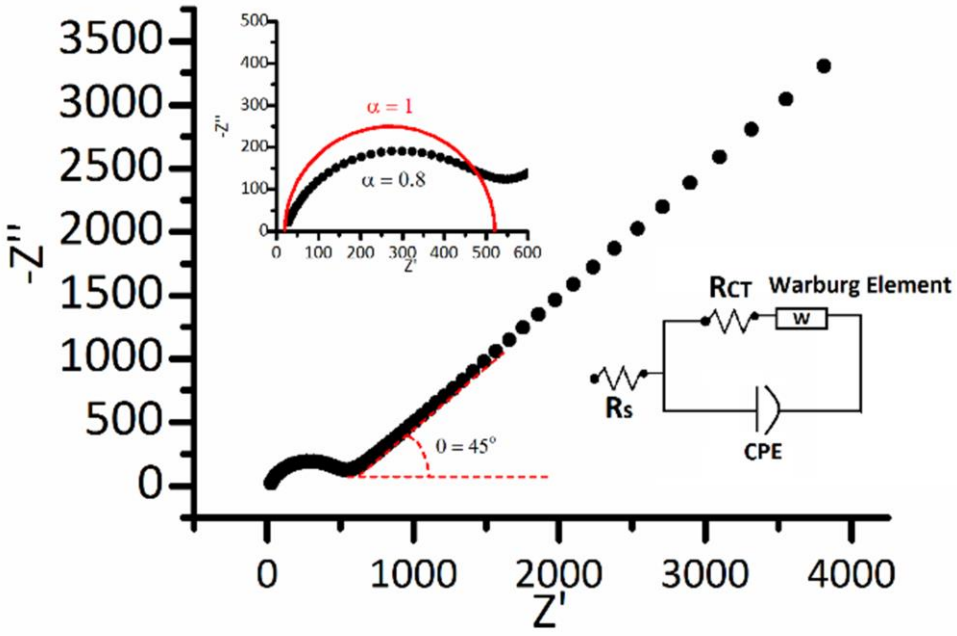

Figure 2.9. Nyquist plot appropriate for the description of a redox process occurring at a real electrode surface including the contributions of mass transport. The high frequency region of the plot (inset) shows a comparison of the semi-circle region for a pure capacitance.

over time. This time dependence manifests as a frequency dependence in the impedance spectra. The Warburg element therefore describes an intermediate behaviour between a purely in-phase and purely out-of-phase phenomenon and thus contributes both real and imaginary contributions to the impedance spectrum:

$$Z_w = \frac{A_w}{\sqrt{\omega}} + \frac{A_w}{j\sqrt{\omega}} \qquad (2.2.50)$$

Here A_w is the Warburg coefficient which is associated with the diffusion of a redox species in solution. Figure 2.9 shows a similar system to that given in Figure 2.7, except the range of ω is low enough to include contributions from mass transport of O/R to the electrode surface. The linear region in the Nyquist plot with slope m = 1 is associated to the Warburg element, and it is also readily identifiable in Bode plots as a phase angle of 45° at low frequencies.

Unlike ideal parallel plate capacitors, the electrode-solution interface often shows heterogeneous properties, which may be attributed to non-uniform chemical composition, roughness and porosity. Figure 2.9 shows a comparison of the Nyquist plot obtained for an ideal capacitor in an RC circuit, similar to that in Figure 2.7, compared to an experimental Nyquist spectrum for a real glassy carbon electrode immersed in KCl solution. The real system shows significant deviations from the purely imaginary response seen in the ideal case, which manifests as a depressing of the high frequency semicircle below the expected value for a pure capacitor.

Accounting for this non-ideal behaviour is usually accomplished by introducing a modified capacitive element known as a constant phase element (CPE). The CPE is so-called because its phase value, although different from that of a pure capacitor, is constant as a function of frequency. As a circuit element it may be considered as a kind of modified capacitor:

$$Z_{CPE} = -i/(\omega^{\alpha})Q \tag{2.2.51}$$

Equation 2.2.51 is similar in form to the impedance of a capacitor, but an exponent alpha has been introduced into the denominator and the pure capacitance C has been replaced with the non-ideal CPE equivalent, Q. There is no consensus in the literature regarding the physical origins of CPE behaviour, and as such in this thesis it will be treated as a capacitor element which has been modified in order to account for non-ideal behaviour.

EIS experiments are liable to suffer from the presence of artefacts in the data unless sufficient care is taken during measurements. As already mentioned, a key assumption underlying the theory of EIS is linearity of the output response with respect to the input. In this thesis, this is ensured by keeping the potential perturbation < 10 mV. There must also be a causal relationship between the input and output, i.e. the response of the system must not occur prior to the input perturbation. Causality may be violated if a system is drifting over time due to non-constant experimental conditions. To avoid this, all experiments described in this thesis were carried out with the temperature controlled to 25^{o}C using a water bath. Additionally, each impedance measurement was replicated under identical conditions a minimum of three times.

As a final point, because impedance data are comprised of real and imaginary contributions, they must satisfy the Kramers-Kronig equations:

$$Z_{im} = \frac{2\omega}{\pi}\int_0^{\infty}\frac{Z_r(x)-Z_r(\omega)}{x^2-\omega^2}\,dx \tag{2.2.52a}$$

$$Z_r(\omega) = Z_r(\infty) + \frac{2\omega}{\pi}\int_0^{\infty}\frac{-xZ_r(x)+\omega Z_r(\omega)}{x^2-\omega^2}\,dx \tag{2.2.52b}$$

A number of methodologies for verifying Kramers-Kronig (KK) consistency exist in the literature. One approach advocated by Orazem et al.[25-26] involves the use of KK consistent equivalent circuit models to fit impedance data. The argument is then that if the model is KK consistent and can be fitted to the data, then the data itself must be KK consistent. All EIS data presented in this thesis were verified to be KK consistent using this approach with Metrohm's NOVA® software, which includes a software package for this purpose.

2.3 Spectroscopic Ellipsometry

Ellipsometry is a non-destructive optical technique that is used to study the bulk optoelectronic properties of a variety of materials. The technique is also commonly employed in thin-film research as a convenient means of measuring film thicknesses without the need for step height experiments with profilometry or atomic force microscopy. The experimental parameters in ellipsometry are the changes induced in the polarisation state of linearly-polarised light upon interaction with a surface. The fundamental equation of ellipsometry is given as:

$$\rho = \frac{|r^p|}{|r^s|} = \tan\Psi\, e^{i\Delta} \tag{2.3.1}$$

Here r_p and r_s refer to the Fresnel coefficients:

$$\mathrm{r_s} = \frac{\mathrm{n_1}\cos\theta_i - \mathrm{n_2}\cos\theta_t}{\mathrm{n_1}\cos\theta_i + \mathrm{n_2}\cos\theta_t} \tag{2.3.2a}$$

$$\mathrm{r_p} = \frac{\mathrm{n_2}\cos\theta_i - \mathrm{n_1}\cos\theta_t}{\mathrm{n_2}\cos\theta_i + \mathrm{n_1}\cos\theta_t} \tag{2.3.2b}$$

The following subsections develop the fundamental optical theory necessary for the understanding of ellipsometry as an experimental technique.

The Polarisation State of Light

Figure 2.10 depicts the interaction of an incident light wave in one medium with another medium with different optical properties. The plane perpendicular to the interface which contains the incident and reflected waves is referred to as the plane of incidence. Some proportion of the incident light wave may be reflected from the interface or transmitted through the material at a point shown by the intersection of the vectors representing the light waves in the figure. The normal drawn through this point is important for the specification of the angles θ_i, θ_r and θ_t corresponding to the angles of the incident, reflected and transmitted wave relative to this normal.

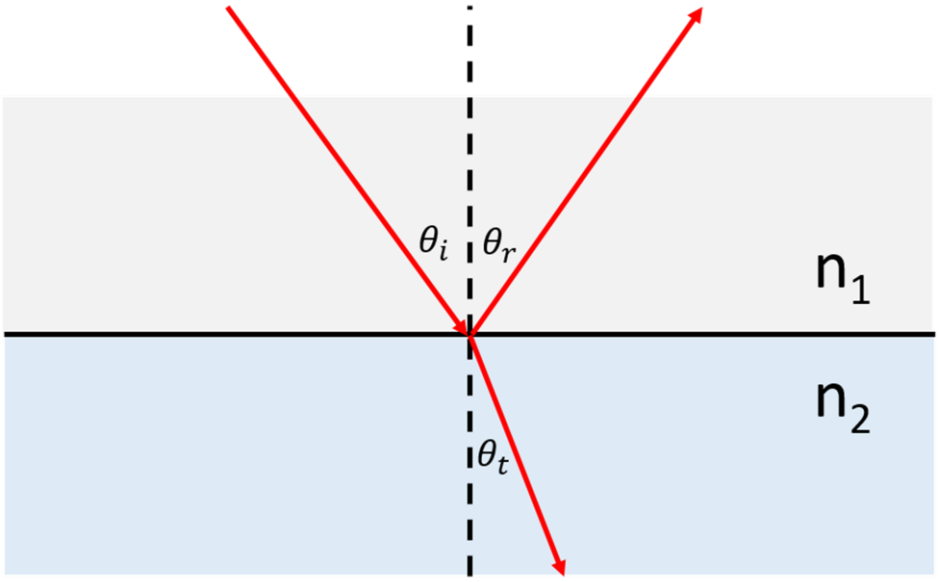

Figure 2.10. Diagram illustrating the interaction of a light wave at an interface between two media with different indices of refraction, n_1 and n_2. The dashed line indicates the normal to the surface.

By the law of reflection, $\theta_i = \theta_r$. The relationship between θ_i and θ_t depends on n_1 and n_2, the respective indices of refraction of the two materials according to the law of refraction:

$$n_1/n_2 = sin(\theta_t)/sin(\theta_i) \qquad (2.3.3)$$

Equation 2.3.3 is often referred to as 'Snell's Law' after the astronomer Willebrord Snell, although it was described independently of Snell's work several years earlier.[27]

The p-s basis set used in this section for describing polarisation states of light can also be described in Figure 2.11. 'p' polarised light is defined as the component of the Electric field

vector E of the light wave which is parallel to the plane of incidence with the surface, which is the plane containing the vectors describing the light wave, whilst ‘s’ polarised light is the component of the field which is perpendicular to this plane and parallel to the interface between the two media. The components of the electric field vector for p and s polarised light are given by Equations 2.3.4a and 2.3.4b.

$$E_p = E_{p0}e^{\mathrm{i}(kx^{-}\omega t^{+}\,\phi p)} \tag{2.3.4a}$$

$$E_s = E_{s0}e^{\mathrm{i}(kx^{-}\omega t^{+}\phi s)} \tag{2.3.4b}$$

Different polarisation states of light are depicted in **Figure 2.11.** Linearly polarised light is described by the relationship

$$\phi_p - \phi_s = n\pi;\ n = (-n, -2, -1, 0, 1, 2 \ldots n)$$

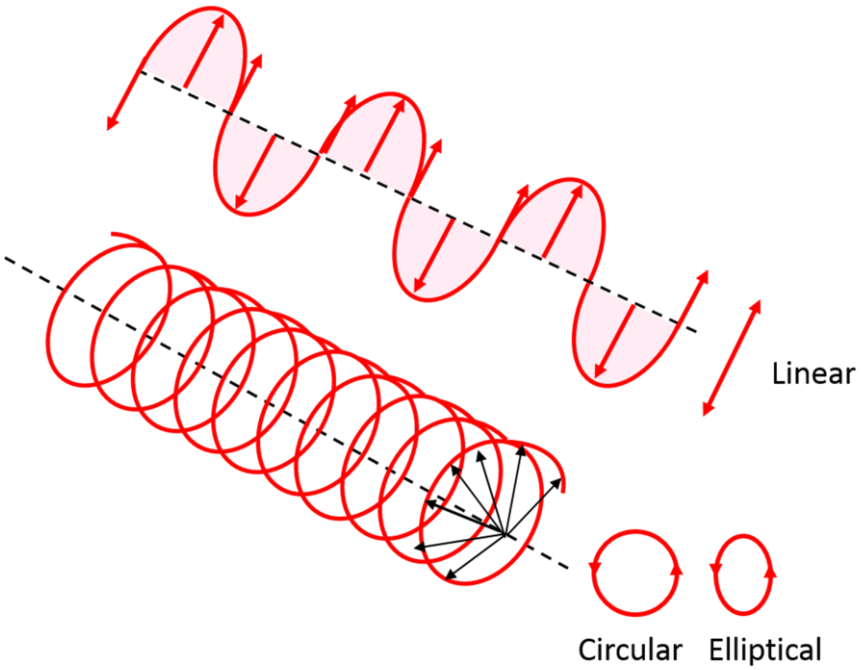

Figure 2.11. Different polarisation states of light.

The polarisation vectors are said to be in phase, resulting in a consistent linear polarisation state corresponding to the vector sum of the p and s components. Circular polarisation is achieved when $E_p = E_s$ and

$$\phi_p - \phi_s = n\pi/2;\ n = (-n, -2, -1, 0, 1, 2 \ldots n)$$

In this case the out-of-phase vector sum of the s and p components results in a polarisation vector which traces out a circular path. If $E_p \neq E_s$ or, alternatively, if ϕ_p and ϕ_s differ by some other fixed constant, the resulting path of the polarisation vector is an ellipse. Elliptical polarisation represents the most general type of coherent polarisation and is the origin of the term 'ellipsometry.' Unpolarised light is composed of contributions from waves with many combinations of s and p polarised light and as such do not display any consistent polarisation state.

In addition to the phase information just described, the variables x and t in Equations 2.3.4a and b describe the spatial and temporal variation of the light wave. Since alterations in the polarisation state are the experimental parameters of interest in spectroscopic ellipsometry, these additional variables may be treated as constant terms. Equations 2.3.5a and b focus only on the polarisation, an approach known as the Jones formalism:

$$E_p = A_p^i e^{i(\phi_p)} \tag{2.3.5a}$$

$$E_s = A_s^i e^{i(\phi_s)} \tag{2.3.5b}$$

E_p and E_s can be considered to be the components of a polarisation vector known as a Jones vector, which specifies the polarisation state of the electric field. Identifying changes in the amplitude (A) and phase (φ) of these components is fundamental to ellipsometry as an optical characterisation technique. Note also that the superscript 'i' has been introduced in Equations 2.3.5 a and b). This indicates the polarisation of the incident light wave, whereas 'r' and 't' will be used to denote the s and p Jones vectors corresponding to the reflected light and transmitted light respectively.

Changes in the Jones vectors are related to the Fresnel Equations 2.3.2a and b, which describe the ratio of the electric field for reflected and transmitted light to the electric field of the incident beam. The ratio is different for s and p polarised light, because the equations are ultimately derived from the application of Maxwell's equations to the interfacial boundary. For example, for an s-polarised incident wave the parallel components of the electric field vector on both sides of the interface must have the same magnitude in order to ensure continuity:

$$E_s^i + E_s^r = E_s^t \tag{2.3.6}$$

In a similar fashion the perpendicular components of the magnetic field vector must also have the same value on both sides of the interface in order to ensure continuity of the magnetic field:

$$B_s^i \cos(\theta_i) - B_s^r \cos(\theta_r) = B_s^t \cos(\theta_t) \tag{2.3.7}$$

Using Snells Law (Equation 2.3.3) and the relationship $B = nE/c$:

$$n_1(E_s^i - E_s^r)\cos(\theta_i) = n_2 E_s^t \cos(\theta_t) \tag{2.3.8}$$

The combination of Equations 2.3.6-2.3.8 may be rearranged to obtain the ratio $\frac{E_s^r}{E_s^i}$:

$$\frac{E_s^r}{E_s^i} = \frac{n_1\cos(\theta_i) - n_2\cos(\theta_t)}{n_1 cos(\theta_i) + n_2 cos(\theta_t)} \tag{2.3.9}$$

Which is equivalent to Equation 2.3.2a. A similar approach for p-polarisation yields the ratio $\frac{E_p^r}{E_p^i}$, which is equivalent to 2.3.2b.

The Fundamental Equation of Ellipsometry

The relationship between the Fresnel equations and the fundamental equation of ellipsometry is derived by first defining a new parameter, $\mu = E_p/E_s$, the ratio of the p- and s-polarised components of the Jones vector.[28] The ratio $|\mu^i/\mu^r|$ is given as:

$$\frac{\left|\frac{E_s^i}{E_p^i}\right|}{\left|\frac{E_s^r}{E_p^r}\right|} = \frac{\frac{A_s^i}{A_p^i} e^{i(\phi_{s,i} - \phi_{p,i})}}{\frac{A_s^r}{A_p^r} e^{i(\phi_{s,r} - \phi_{p,r})}} \tag{2.3.10}$$

The utility of this expression in ellipsometry can be readily seen by making two assumptions: that the amplitudes of the p- and s-components are equal in magnitude, and that the phase difference in the exponentials is that for linear polarisation $\phi_{p,} \pm \phi_{s,} = \pm n\pi$. These assumptions are justified as the polarisation state of the incident wave can be easily adjusted using polarising filters.[29]

Under these conditions $\left|\frac{E_s^i}{E_p^i}\right| = 1$ and, after rearrangement, this leads to:

$$\left|\frac{E_p^r}{E_s^r}\right| = \frac{A_p^r}{A_s^r} e^{i(\phi_{p,r} - \phi_{s,r})} \tag{2.3.11}$$

The ratio is similar in form to Equation 2.3.1 introduced in the previous section. Equation 2.3.11 is typically redefined in terms of the ellipsometric parameter Ψ, such that $\frac{A_p^r}{A_s^r} = \tan(\Psi)$. Similarly the phase difference $\phi_{p,} - \phi_{s,}$ is defined as the second ellipsometric

parameter, Δ. The final step involves the recognition of the relationship between the parameter previously defined as μ and the Fresnel reflection coefficients given by Equations 2.3.2 a and b:

$$\frac{\mu_i}{\mu_r} = \frac{E_s^i}{\frac{E_p^i}{\frac{E_s^r}{E_p^r}}} = \frac{E_p^r}{\frac{E_p^i}{\frac{E_s^r}{E_i^r}}} = \frac{r_p}{r_s} = \rho$$

Where n = $\frac{n2}{n1}$ i.e. the ratio of the indices of refraction of the two media. θ and ϕ are the angles of incidence and transmittance respectively, measured from the normal to the surface. With these terms defined, the fundamental equation of ellipsometry is given finally as

$$\rho = \frac{|r^p|}{|r^s|} = \tan\Psi\, e^{i\Delta}$$

The ellipsometric parameters, Ψ and Δ, are related to the amplitude ratio of the parallel and perpendicular components of the light wave after reflection from the surface and the phase difference between these components. The utility of the technique is that it may be used to determine the complex index of refraction, n + ik of a thin film, as well as the film thickness. Here n is the index of refraction and k is the extinction coefficient, which describes the absorbing properties of the medium. k = Ø implies a transparent medium whilst an absorbing medium has a nonzero k value. Both n and k are functions of the wavelength of the incident light.

Derivation of Thin Film Properties from Ellipsometric Data

The raw Ψ and Δ data obtained via ellipsometry is correlated to the optical properties of the system under study through a modelling procedure which is used to fit the raw data and derive the optical constants of the material as well as the film thicknesses. The modelling procedure used in this thesis has its basis in the literature,[30-31] where it has been used to characterise both amorphous carbon films and hydrogenated amorphous carbon films.

This modelling procedure is a purely mathematical one; it requires no *a priori* knowledge of the material's physical properties to produce a fit with physically accurate information. This approach, known in the literature as a Basis-spline (B-spline) parameterisation,

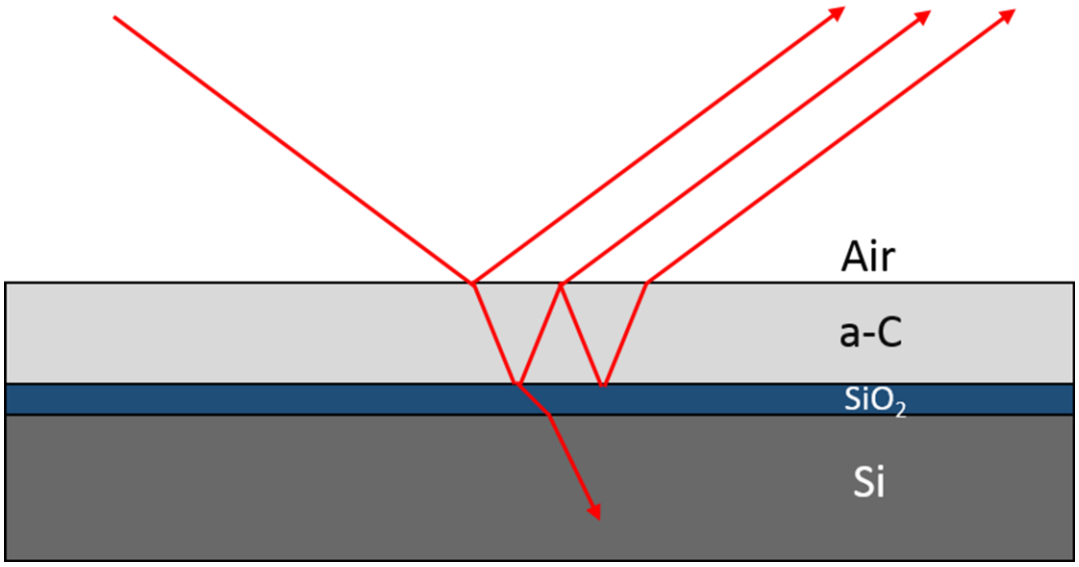

Figure 2.12. Model of the amorphous carbon film deposited on a Si/SiO_2 substrate. The final refracted wave is composed of light due to reflections and refractions from the film as well as the underlying substrate.

involves fitting the raw data measured by the ellipsometer, viz. Ψ and Δ as a function of wavelength, using a model that describes the structure of the film and the underlying substrate. This model is illustrated in Figure 2.12. The film and underlying layers may be modelled as separate media, each with their own value of complex index of refraction. The model therefore includes the optical constants of the Si substrate, a native oxide layer which models the native SiO_2 termination of the Si surface, and a Basis-spline (B-spline) layer for modelling the a-C film. B-splines are piecewise polynomials defined on a particular interval such that the function is continuous at the partitioning points (also known as 'knots') of a given subinterval; they commonly arise in interpolation problems in mathematics.

The Optical (Tauc) Gap in Amorphous Semiconductors

The defining feature of amorphous materials is the absence of long-range order. Disordered materials have significant differences in the organisation of electronic states compared to crystalline solids. Figure 2.13 illustrates the density of states for an amorphous semiconductor material. Similar to in a crystalline semiconductor, the states are delocalised deep within the valence and conduction bands. Within an energy threshold known as the

mobility edge, the electronic states begin to become localised in both bands (shaded area in Figure 2.13). The localisation also has the effect of introducing states in the bandgap (i.e. between E_v and E_c) which manifest in the DOS as tail regions.

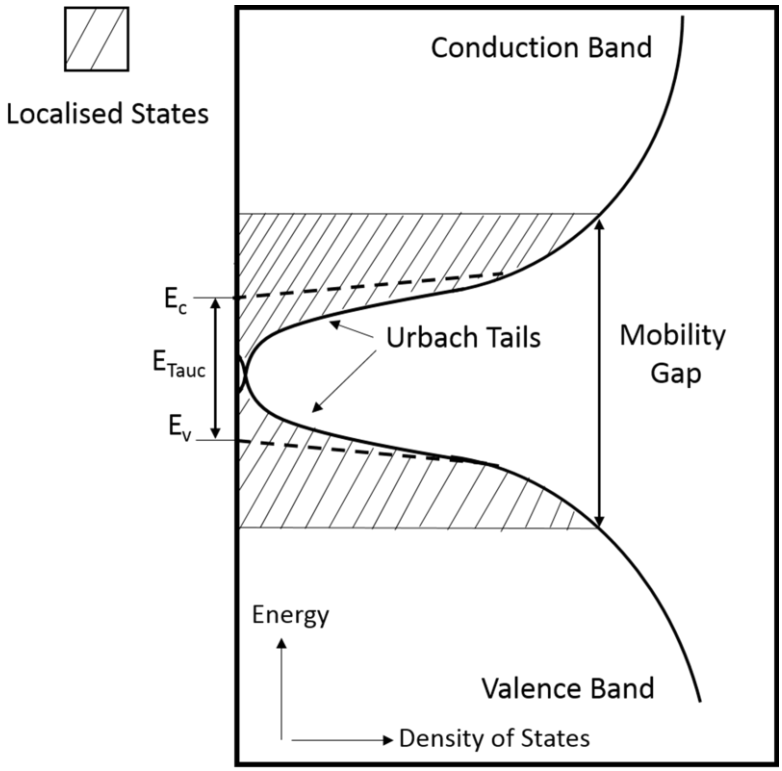

Figure 2.13. Energy-Density of States diagram for an amorphous semiconductor. Redrawn based on Reference 32.

In addition to electronic transitions between delocalised states, the absorption spectrum for an amorphous semiconductor therefore contains contributions from electronic transitions between localised states and localised/delocalised states. Tauc[32] showed that transitions associated with the tail states in the absorption edge can be modelled as an exponential dependence of the absorption coefficient, α, on the energy:

$$\alpha(E) \propto e^{\frac{h\nu}{E_e}} \tag{2.3.12}$$

Whilst transitions associated with the band region display a square root dependence:

$$\sqrt{\alpha h\upsilon} \propto h\upsilon - E_{Tauc} \tag{2.3.13}$$

Here E_{Tauc} corresponds to the gap between the dashed regions in Figure 2.13. The Tauc gap, also referred to as the optical gap, may be viewed as an empirical equivalent to a band gap for amorphous materials. Figure 2.14 shows a plot optical data for a hypothetical amorphous

semiconductor in a form described by Equation 2.3.13. The linear region of the plot can be extrapolated to the abscissa to to obtain the value of the Tauc gap. This procedure is used in this thesis to obtain E_{Tauc} values for a-C and a-C:N materials.

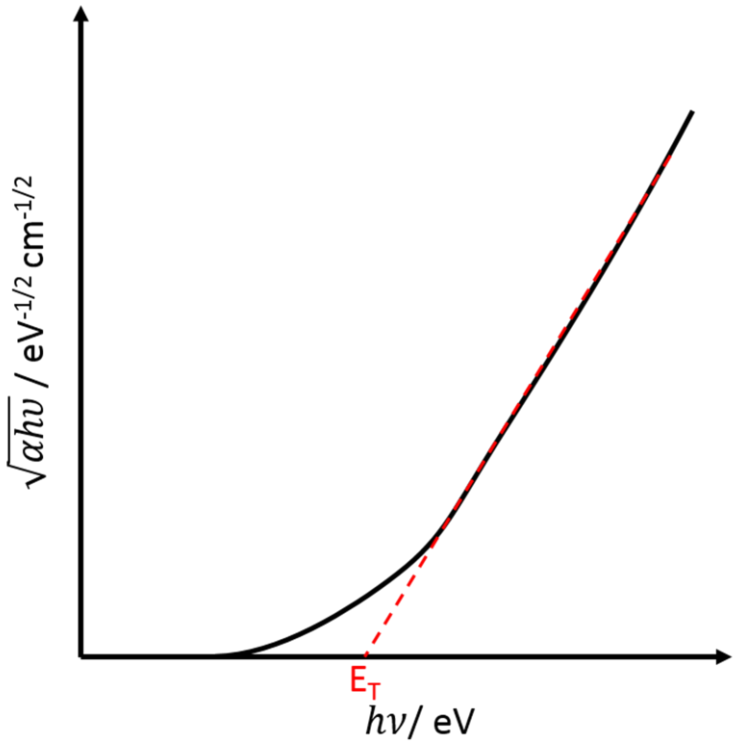

Figure 2.14. Tauc plot for an amorphous semiconductor. The linear region is extrapolated to the abscissa (dashed line) in order to obtain the empirical value of the Tauc gap, E_T.

2.4 X-Ray Photoelectron Spectroscopy (XPS)

XPS is a technique for the determination of surface chemical composition. It is based on the photoelectric effect – the ejection of electrons from atoms following irradiation. X-ray bombardment provides sufficient energy to eject core-shell electrons from the surface with a kinetic energy (KE) given by:

$$KE = h\upsilon - BE - \psi \quad (2.4.1)$$

Where hv is the energy of the incident photon, BE the binding energy of the core electron state and ψ the work function, which measures the energetic input required to transfer an electron from E_F, the Fermi level of the material, to the vacuum. The ejected electrons are

detected using a photomultiplier which may be programmed to select electrons with a specific pass energy. Importantly, it is only electrons which do not lose energy due to collisions that give rise to an appreciable XPS signal at a BE corresponding to that specified by Equation 2.4.1**;** electrons which alter their kinetic energy due to collisions are inelastically scattered and constitute the XPS background. It is possible to calculate λ, the inelastic mean

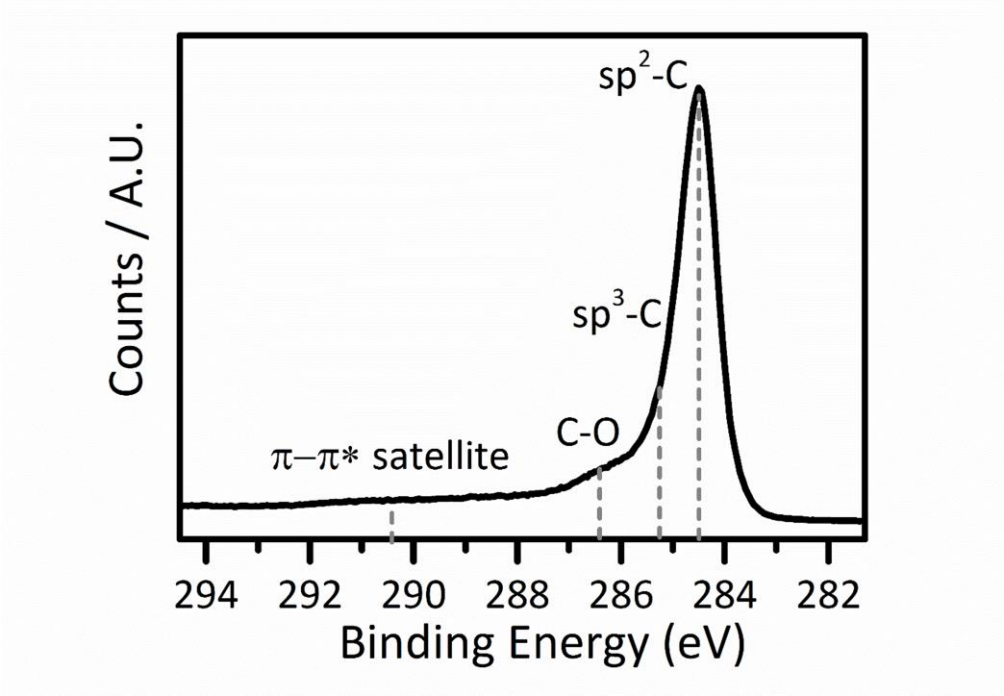

Figure 2.15. XPS spectrum obtained for a C 1s envelope for an amorphous carbon material with *ca.* 80% sp^2 content.

free path, for materials as a function of the photon energy.[33] Comparisons of the value of λ with the crystallographic structure of close-packed metals indicates that inelastically scattered electrons are predicted to arise from a depth of no more than around 3 λ from the surface, assuming normal incidence of the incident light.

This translates into a maximum penetration depth of ca. 10 nm, although the surface sensitivity may be increased by the use of grazing angles of incidence, which reduce the penetration depth and therefore sample a greater proportion of the surface atoms of the material. For the characterisation of many nanomaterials including powders which may have all dimensions < 10 nm in size, XPS is undoubtedly a bulk-characterisation technique. By comparison, for the thin film a-C and a-C:N materials described in this thesis, which have thickness values in the range 60 – 100 nm, XPS measurements may be considered a surface characterisation technique.

Although the photoelectrons detected in XPS experiments arise from the core shells of surface atoms, the measured binding energy value nonetheless provides information about the valence state of the surface atoms, i.e. information about the type and number of chemical bonds and the identity of nearest-neighbour atoms. This information derives from the influence of the bonding environment on the binding energy of the core state. These influences are referred to as 'initial state effects' because they are present in the material prior to the creation of the core hole.

This is illustrated in Figure 2.15 which depicts the XPS spectrum corresponding to photoelectrons ejected from the C 1s orbital in an amorphous carbon material. The envelope contains a number of contributions, primarily arising from sp^2-C and sp^3-C centers between 284-286 eV. The differences in binding energy between sp^2-C and sp^3-C 1s photoelectrons have their origin in the different valence environments of graphite-like and diamond-like carbon. Initial state effects also arise when atoms with significant differences in electronegativity are bonded to one another. The peak above 286 eV in Figure 2.15 is typically assigned to C-O species such as hydroxyl and ether moieties.[34-36]

The uneven electron distribution in the C-O bond results in a polarisation, with the C atom being more positively charged. This polarisation also affects the C 1s electrons, increasing their effective binding energy. The electronegativity effect scales with the number of bonds, implying that a more heavily oxidised atom will eject more photoelectrons with a high BE. C=O moieties have a higher BE of 287-288 eV compared to *ca.* 286 eV for C-O groups.[35]

In addition to initial state effects, the XPS spectrum can also be influenced by events which occur after the creation of the core hole. Such 'final state' effects usually involve interactions between the photoelectron or hole with other electrons in the material. The most obvious final state effect is the inelastic scattering of photoelectrons, which as already discussed manifest as the background signal in the XPS spectrum. However final state effects can also provide chemical information about the material. The broad peak close to 290 eV in Figure 2.15 is commonly referred to as a 'shake-up' feature or a 'π-π^* satellite.'

Shake-up events in XPS refer to interactions between photoelectrons and valence electrons in states with access to a higher energy unoccupied state, such as a filled π state with an unoccupied anti-bonding π^* state (Figure 2.16 a). The ejected photoelectron can transfer some of its kinetic energy to such electrons prior to being detected. The reduction in KE of such photoelectrons manifests in the spectrum as a higher BE contribution, even though the associated photoelectron may have originated in a low BE core state. Depending on the amount of energy transferred by the photoelectron, a 'shake-off' event may also occur, corresponding to the ejection of the excited secondary electron from the surface. Shake up

events are typical of highly conductive samples which have a high density of states at the Fermi level, E_F, as well as a high density of unoccupied states above E_F into which the valence electrons may be excited.

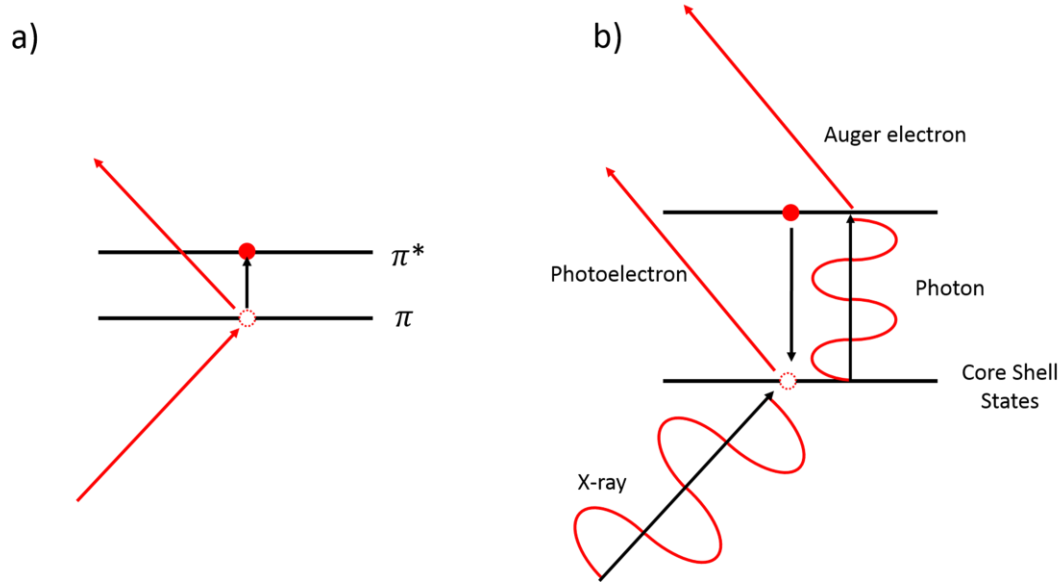

Figure 2.16. a) Schematic illustrating the shake-up effect when an emitted photoelectron interacts with a valence electron, in this case an electron in a π band. b) Schematic illustrating the emission of an Auger electron.

A second final-state effect of relevance to this thesis is the Auger effect, which is illustrated schematically in Figure 2.16 b. The core state formed by ejection of a photoelectron may recombine with an electron from a higher energy state in a different shell, resulting in the emission of a photon corresponding to ΔE, the difference in energy between the two energy states. This photon may in turn excite another electron in a higher energy state to the point that it is ejected from the surface.

The resulting Auger electrons can also be detected in an identical fashion to photoelectrons excited by the incident X-ray. Due to the general fact that these Auger electrons have a generally lower KE compared to primary photoelectrons, they appear as higher BE contributions in the XPS spectrum. Auger electrons may be distinguished from primary photoelectrons by changing the excitation energy of the source. Since their energy is independent of the energy of the incident photon energy, the position of primary photoelectron peaks will be shifted relative to Auger peaks if the source energy is changed.

2.5 Atomic Force Microscopy (AFM)

AFM is a surface imaging technique commonly used for studying surface topography. The technique is based on the interaction of a micrometer-sized tip mounted on a deflectable cantilever with the surface (Figure 2.17). Repulsive and attractive forces between the tip and surface cause its deflection as the cantilever is rastered across the surface. These deflections are monitored by a laser which is focused on the tip. The AFM image may therefore be viewed as a plot of the tip deflections at each position on the area studied during the experiment. This yields a height profile of the surface which can be used to determine the surface roughness and morphology.

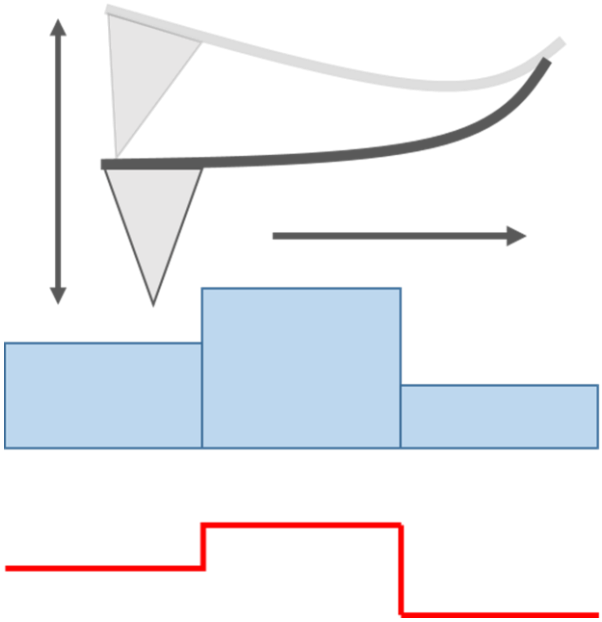

Figure 2.17. Schematic illustrating the interaction between an AFM tip and a surface in tapping mode. The tip position is monitored by tracking the deflection of the cantilever with a laser, resulting in the surface profile plotted at the bottom of the figure.

AFM experiments can be run in so-called contact mode, where the tip remains in contact with the surface, or in tapping mode, where the tip oscillates at a defined AC frequency around the a set point. Contact mode is typically more destructive to the surface, particularly for measurements on biological materials. It may also produce misleading height profiles for the surface if the tip becomes snagged on a surface protrusion. Operating in tapping mode reduces the possibility of damage to both the surface and the tip by making only intermittent

contact with the surface. This also has the effect of reducing the probability of snagging events and is therefore less likely to produce such distorted images. Accordingly, all AFM measurements described in this thesis were obtained in tapping mode using an Asylum Research AFM. Gold-coated silicon cantilevers (NSG01/Au NT-MDT) with a tip height of 14-16 μm, curvature radius of 35 nm and a cantilever length of 125 μm were used in all cases.

2.6 Raman Spectroscopy

Raman spectroscopy is an optical characterisation technique which involves the measurement of inelastically scattered light arising from the interaction of incident photons with a chemical system of interest. The technique is based on the Raman effect, which occurs when some proportion of scattered light from a surface loses a fraction of its energy to excite the vibrational modes of molecules. The energy loss manifests in a Stokes or Anti-Stokes shift in the frequency of the scattered light, which can then be correlated to the surface structure and to the presence of particular chemical species (Figure 2.18).

The selection rule for Raman experiments is that a Raman signal is only observed if the vibrational mode results in a change in molecular polarizability. This is distinct from Infrared Spectroscopy, for which vibrational modes are seen only if they induce a change in the dipole moment. The two techniques are often used in tandem as they offer complementary information. Raman also has numerous advantages over IR spectroscopy, in particular the weak Raman scattering induced by water. IR absorption due to water can obscure large regions of the spectral range which makes structural studies involving biomolecules which incorporate water difficult. The equivalent Raman spectrum is effectively transparent to water in the range 200 – 2000 cm^{-1}.[37]

Raman spectroscopy has been applied in studies of carbon nanomaterials including graphene,[38] and carbon nanotubes.[39] Raman studies of these materials are particularly useful for investigating the carbon scaffold structure i.e. the degree of disorder in the sp^2-C network and the extent of clustering and packing of graphitic carbon domains.[40] This information is particularly relevant to the characterisation of amorphous carbon materials, which depending on the deposition conditions may showcase highly variable sp^2 cluster domain size and organisation.

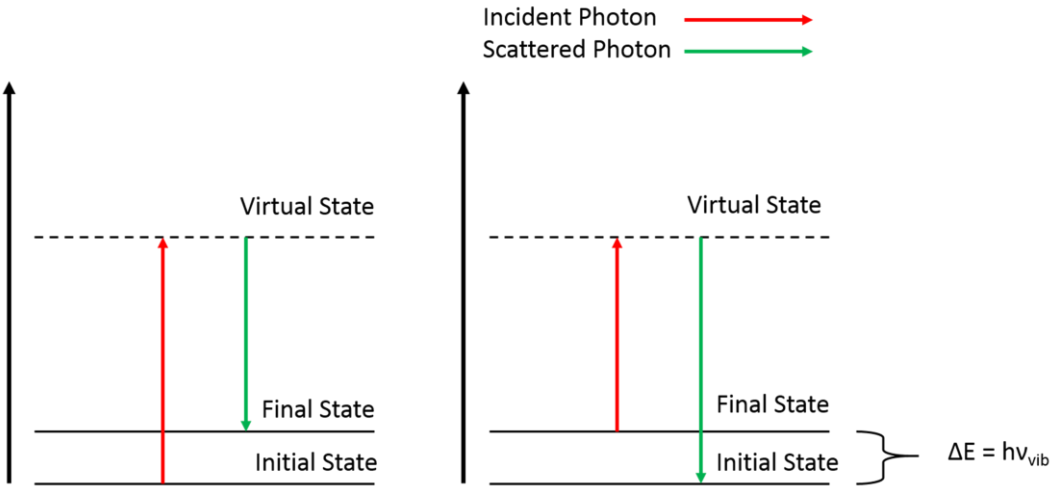

Figure 2.18. Scheme illustrating inelastic scattering with a Stokes (left) and Anti-Stokes (right) energy shift. The energy difference between the incident and scattered photon, ΔE, corresponds to the energy difference in vibrational states of a molecule.

A typical Raman spectrum of an N-free amorphous carbon film similar to those presented in the following chapters of this thesis is illustrated in Figure 2.19. The spectrum is seen to consist of contributions from two broad peaks: the G peak at *ca.* 1580-1600 cm^{-1} and the D peak close to *ca.* 1400 cm^{-1}. The G peak is associated with in plane C-C stretching of sp^2-C whilst the D peak may be attributed to a breathing mode associated with sp^2-C atoms in 6 membered rings. The D peak represents a forbidden mode in perfectly crystalline graphite or graphene layers, but becomes active in the presence of defects and scaffold disorder.

Accordingly, the ratio of peak intensities for the D and G peaks is often used to quantify the degree of disorder in carbon nanomaterials. In highly graphitized materials a higher value of I_D/I_G is generally indicative of increased scaffold disorder, whereas in heavily disordered materials such as sputtered amorphous materials an increasing I_D/I_G may be associated with ordering due to the initial clustering of sp^2 sites into 6-membered rings.[40-42] This theory has also been shown to be applicable to N-doped carbon materials.[41]

In this thesis, Raman spectra were obtained in a backscattering configuration using a Renishaw 1000 micro-Raman system equipped with an Ar^+ laser at 488 nm excitation. The incident beam was focused by a Leica microscope with a 50× magnification objective and short-focus working distance. To avoid damaging the samples, the incident power was always <2 mW.

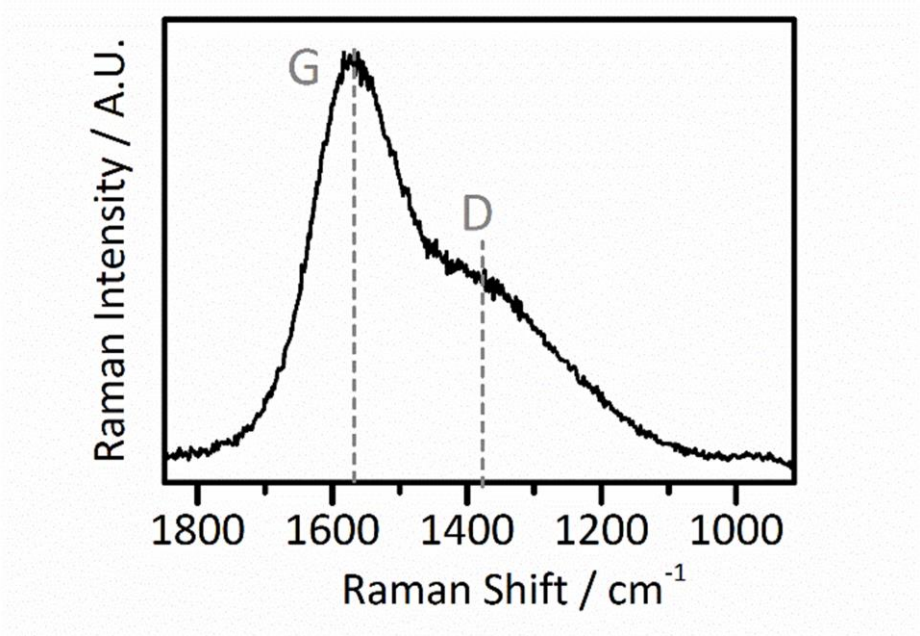

Figure 2.19. Raman spectrum of an amorphous carbon material in the region 1800-1000 cm^{-1}. The dashed lines illustrate the G and D peaks associated with different stretching modes associated with sp^2-C atoms.

2.7 References

1. Cho, N.-H.; Krishnan, K. M.; Veirs, D. K.; Rubin, M. D.; Hopper, C. B.; Bhushan, B.; Bogy, D. B., Chemical structure and physical properties of diamond-like amorphous carbon films prepared by magnetron sputtering. *Journal of Materials Research* **1990,** *5* (11), 2543-2554.

2. Cokun, O. D.; Zerrin, T., Optical, structural and bonding properties of diamond-like amorphous carbon films deposited by DC magnetron sputtering. *Diamond and Related Materials* **2015,** *56,* 29-35.

3. Dai, H. Y.; Zhan, C.; Du, J., Studies on the influence of sputtering power on amorphous carbon films deposited by pulsed unbalanced magnetron sputtering. *Optik - International Journal for Light and Electron Optics* **2016,** *127* (5), 2512-2515.

4. Yang, B. Q.; Feng, P. X., A DC plasma discharge source and its application to synthesis of carbon and carbon nitride thin films. *Surface Review Letters* **2007,** *14* (2), 309-314.

5. Robertson, J., Preparation and properties of amorphous carbon. *Journal of Non-Crystalline Solids* **1991,** *137–138, Part 2* (0), 825-830.

6. Kelly, P. J.; Arnell, R. D., Magnetron sputtering: a review of recent developments and applications. *Vacuum* **2000,** *56* (3), 159-172.

7. Kinoshita, H.; Kubota, M.; Ohno, G., Deposition of amorphous carbon nitride films using Ar/N-2 supermagnetron sputter. *Thin Solid Films* **2010,** *518* (13), 3502-3505.

8. Kinoshita, H.; Kubota, M.; Ohno, G., Deposition of amorphous carbon films using Ar and/or N-2 magnetron sputter with ring permanent magnet. *Thin Solid Films* **2012,** *523*, 52-54.

9. Yasui, T.; Kotani, T.; Fujiuchi, K.; Tahara, H.; Yoshikawa, T., Carbon nitride films deposited by reactive sputtering and pulsed laser ablation. *Thin Solid Films* **2004,** *457* (1), 133-138.

10. Aono, M.; Akiyoshi, H.; Kikuchi, S.; Kitazawa, N.; Watanabe, Y., Effect of substrate temperatures on amorphous carbon nitride films prepared by reactive sputtering. *Journal of Vacuum Science Technology A* **2008,** *26* (4), 966-969.

11. Durand-Drouhin, O.; Benlahsen, M.; Clin, M.; Bouzerar, R., Deposition mechanism of sputtered amorphous carbon nitride thin film. *Applied Surface Science* **2004,** *223* (4), 269-274.

12. Han, L.; Shao, H. X.; He, L.; Chen, X.; Zhao, Y. Q., The effect of nitrogen ion bombarding energy on the bonding structure of nitrogenated tetrahedral amorphous carbon film. *Acta Physica Sinica Chinese Edition* **2012,** *61* (10).

13. Vlček, J.; Rusňák, K.; Hájek, V.; Martinů, L. k., Reactive magnetron sputtering of CNx films: Ion bombardment effects and process characterization using optical emission spectroscopy. *Journal of Applied Physics* **1999,** *86* (7), 3646-3654.

14. Mishra, S. K.; Mahanta, P.; Sen, S.; Pathak, L. C., Effect of Nitrogen on the Growth of Carbon Nitride Thin Films Deposited by RF Plasma Enhanced Chemical Vapor Deposition. *Nanoscience Nanotechnology Letters* **2012,** *4* (1), 90-94.

15. Panwar, O. S.; Khan, M. A.; Satyanarayana, B. S.; Bhattacharyya, R.; Mehta, B. R.; Kumar, S.; Ishpal, Effect of high substrate bias and hydrogen and nitrogen incorporation on density of states and field-emission threshold in tetrahedral amorphous carbon films. *Journal of Vacuum Science Technology B* **2010,** *28* (2), 411-422.

16. Wang, Z.; Wang, C. B.; Zhang, B.; Wang, Q.; Zhang, J. Y., Effects of negative bias on the structural, topological and tribological properties of amorphous carbon films prepared by magnetron sputtering. *Surface Interface Analysis* **2011,** *43* (9), 1218-1223.

17. Bard, A. J.; Faulkner, L. R.; Leddy, J.; Zoski, C. G., *Electrochemical Methods: Fundamentals and Applications*. Wiley New York: 1980; Vol. 2.

18. Trasatti, S., The absolute electrode potential: an explanatory note (Recommendations 1986). *Pure and Applied Chemistry* **1986,** *58* (7), 955-966.

19. Mansfeld, F.; Lin, S.; Chen, Y.; Shih, H., Minimization of High-Frequency Phase Shifts in Impedance Measurements. *Journal of the Electrochemical Society* **1988,** *135* (4), 906-907.

20. Pletcher, D., *A first course in electrode processes*. Royal Society of Chemistry: 2009.

21. Marcus, R. A., Chemical and Electrochemical Electron-Transfer Theory. *Annual Review of Physical Chemistry* **1964,** *15* (1), 155-196.

22. Neyerlin, K.; Gu, W.; Jorne, J.; Gasteiger, H. A., Study of the exchange current density for the hydrogen oxidation and evolution reactions. *Journal of The Electrochemical Society* **2007,** *154* (7), B631-B635.

23. Lin, Q.; Li, Q.; Batchelor-McAuley, C.; Compton, R. G., Two-Electron, Two-Proton Oxidation of Catechol: Kinetics and Apparent Catalysis. *The Journal of Physical Chemistry C* **2015,** *119* (3), 1489-1495.

24. Mark E. Orazem, B. T., *Electrochemical Impedance Spectroscopy*. Wiley, 2008.

25. Esteban, J. M.; Orazem, M. E., On the application of the Kramers-Kronig relations to evaluate the consistency of electrochemical impedance data. *Journal of the Electrochemical Society* **1991,** *138* (1), 67-76.

26. Orazem, M.; Esteban, J.; Moghissi, O., Practical applications of the Kramers-Kronig relations. *Corrosion* **1991,** *47* (4), 248-259.

27. Shirley, J. W., An Early Experimental Determination of Snell's Law. *American Journal of Physics* **1951,** *19* (9), 507-508.

28. Schubert, M., Another century of ellipsometry. *Annalen der Physik* **2006,** *15* (7-8), 480-497.

29. Tompkins, H. G., *A User's Guide to Ellipsometry*. Courier Corporation: New York, 2006.

30. Johs, B.; Hale, J. S., Dielectric function representation by B-splines. *Physica Status Solidi (a)* **2008,** *205* (4), 715-719.

31. Weber, J. W.; Hansen, T. A. R.; van de Sanden, M. C. M.; Engeln, R., B-spline parametrization of the dielectric function applied to spectroscopic ellipsometry on amorphous carbon. *Journal of Applied Physics* **2009,** *106* (12), 145-149.

32. Tauc, J.; Menth, A., States in the gap. *Journal of Non-Crystalline Solids* **1972,** *8*, 569-585.

33. Powell, C.; Jablonski, A., NIST electron inelastic-mean-free-path database. *NIST Standard Reference Database* **2010,** *71*.

34. Gelius, U.; Hedén, P. F.; Hedman, J.; Lindberg, B. J.; Manne, R.; Nordberg, R.; Nordling, C.; Siegbahn, K., Molecular Spectroscopy by Means of ESCA III. Carbon compounds. *Physica Scripta* **1970,** *2* (1-2), 70.

35. Proctor, A.; Sherwood, P. M. A., X-ray photoelectron spectroscopic studies of carbon fibre surfaces—II: The effect of electrochemical treatment. *Carbon* **1983,** *21* (1), 53-59.

36. Yumitori, S., Correlation of C1s chemical state intensities with the O1s intensity in the XPS analysis of anodically oxidized glass-like carbon samples. *Journal of Materials Science* **2000,** *35* (1), 139-146.

37. Wartewig, S.; Neubert, R. H., Pharmaceutical applications of Mid-IR and Raman spectroscopy. *Advanced Drug Delivery Reviews* **2005,** *57* (8), 1144-1170.

38. Ferrari, A. C.; Meyer, J.; Scardaci, V.; Casiraghi, C.; Lazzeri, M.; Mauri, F.; Piscanec, S.; Jiang, D.; Novoselov, K.; Roth, S., Raman spectrum of graphene and graphene layers. *Physical Review Letters* **2006,** *97* (18), 187401.

39. Dresselhaus, M. S.; Dresselhaus, G.; Saito, R.; Jorio, A., Raman spectroscopy of carbon nanotubes. *Physics Reports* **2005,** *409* (2), 47-99.

40. Ferrari, A. C.; Robertson, J., Interpretation of Raman spectra of disordered and amorphous carbon. *Physical Review B* **2000,** *61* (20), 14095-14107.

41. Ferrari, A. C.; Rodil, S. E.; Robertson, J., Interpretation of infrared and Raman spectra of amorphous carbon nitrides. *Physical Review B* **2003,** *67* (15), 155306.

42. Ferrari, A. C.; Robertson, J., Raman spectroscopy of amorphous, nanostructured, diamond-like carbon, and nanodiamond. *Philosophical Transactions of the Royal Society A* **2004,** *362* (1824), 2477-2512.

CHAPTER III

Nitrogenated Carbon Thin Film Electrodes

Herein, a physico-chemical characterisation of nitrogenated carbon thin film electrodes is reported. A combination of optoelectronic characterisation methods, surface analysis and electrochemical measurements is employed in order to correlate the bulk optoelectronic properties of the electrodes to their heterogeneous charge transfer kinetics in simple redox processes.

The data presented in this chapter are part of the following publications:

1. Behan, J. A.; Stamatin, S. N.; Hoque, M. K.; Ciapetti, G.; Zen, F.; Esteban-Tejeda, L.; Colavita, P. E. *The Journal of Physical Chemistry C* **2017,** *121***,** 12, 6596-6604
2. Zen, F.; Angione, M. D.; Behan, J. A.; Cullen, R. J.; Duff, T.; Vasconcelos, J. M.; Scanlon, E.M.; Colavita, P. E. *Scientific reports* **2016,** *6*, 24840.
3. Zen, F.; Karanikolas, V. D.; Behan, J. A.; Andersson, J.; Ciapetti, G.; Bradley, A. L.; Colavita, P. E. *Langmuir* **2017**, *33,* 17, 4198-4206

Co-author contributions to this chapter are as follows: F.Z, G.C and S.N. contributed several of the XPS measurements. L.E-T. contributed SEM images and J.M.V. contributed AFM measurements.

3. Introduction

Nitrogenated carbon materials such as carbon nitrides have been known for more than a century.[1-3] In recent decades interest in the incorporation of nitrogen into carbon scaffolds was reinvigorated due to predictions that graphitic carbon nitride, g-C_3N_4, could be a harder material than diamond[4-5] and numerous investigations into nitrogenated carbons for carbon coating thin-film applications were published.[6-7] More recently, there has been a growing interest in understanding the effects of nitrogenation on the properties of carbon electrode materials, which have electroanalytical applications[8-10] and promising metal-free electrocatalytic performance.[8, 11]

Nitrogen incorporation can significantly affect bulk carbon properties; as reported by several groups,[6-7] substitutional N-sites within a graphitic carbon matrix – often referred to as 'graphitic N' – are said to dope the carbon structure, introducing donor states that can impart n-type conductivity. Nitrogenation also typically introduces a number of other non-doping types of N-site, such as pyridinic- and pyrrolic-N sites, which also have significant effects on the electronic properties.

The presence of N-sites in the carbon surface is particularly relevant for electrochemical processes. In many cases nitrogenation has been shown to accelerate the kinetics of electron transfer, resulting in enhanced peak currents and/or a narrowing of the peak potential separation in voltammetric experiments. The precise mechanism of enhancement is not well understood although it has been speculated that improved electronic properties and/or interactions between the analyte molecules and surface chemical groups may be contributing factors. [12]

These improved charge transfer properties in the doped material relative to N-free carbons have been most prominently studied for multi-step electron-proton coupled reactions, such as hydrogen peroxide production from water[13-14] and the oxygen reduction reaction (ORR).[15-19] Nitrogenated carbons have shown remarkable activity in metal-free ORR, which is the cathode reaction in fuel cells and Li-air batteries. This activity has been attributed to the presence of specific surface sites such as the aforementioned graphitic-N and pyridinic-N sites[15, 20-26] which alter the surface charge density and Lewis basicity.

Heteroatom doping can also result in structural changes in the carbon scaffold such as increased defect and edge-plane exposure, which impact its surface chemistry. Defect creation via nitrogen incorporation has, for instance, been shown to improve Li storage capacity,[27] while greater edge exposure is known to enhance charge transfer rates and

catalytic activity.[25, 28-33] Furthermore, nitrogenation offers a route for increasing the density of states, resulting in higher capacitance, an effect that has been leveraged in the fabrication of supercapacitors.[34]

The effects of nitrogenation on bulk electronic properties, surface chemistry and structural disorder in the carbon network are often interrelated making it challenging to discern or predict the overall effect of nitrogenation on the electrochemical properties of carbon electrodes. Recent studies in the literature have successfully established structure-activity relationships for undoped carbon materials resulting in useful insights on how to predict interfacial redox chemistry based on bulk electronic structure. This has been shown in the case of materials with long range order or high crystallinity, such as nanotubes, graphene and graphite.[35-42] However, less is known about carbon materials which lack long-range order despite them being widely used by the electrochemical community.

Thin film electrodes have recently enabled the study of electrode properties of nitrogenated carbons,[43-46] independently from potentially confounding variables that might affect studies at particle/ink electrodes, such as large differences in topography, porosity, the packing of carbon particles, the presence of binder materials and metal impurities. [47]

In this chapter a detailed physico-chemical characterization of amorphous nitrogenated carbon (a-C:N) thin film electrodes with varying nitrogen content prepared via DC magnetron sputtering is presented. A suite of optical characterization methods including x-ray photoelectron spectroscopy (XPS) and spectroscopic ellipsometry (SE) is employed in order to study the bulk optoelectronic properties and chemical composition of the films. This is combined with electrochemical characterization techniques (cyclic voltammetry (CV) and electrochemical impedance spectroscopy (EIS)) in order to study the interplay between the bulk optoelectronic properties and the performance of the films in heterogeneous charge transfer processes.

It is shown that low levels of nitrogenation produce a-C:N films with greater metallic character than non-nitrogenated materials (a-C), which promotes faster electron-transfer rates to outer-sphere redox species at the carbon-electrolyte interface. High levels of nitrogen incorporation, on the other hand, result in films with characteristics more typical of cluster aggregates than amorphous solids. Electrochemical studies on these materials using both outer-sphere and surface-sensitive redox probes allow for the discrimination of electronic and surface effects resulting from nitrogen incorporation.

3.1 Results and Discussion

Topography of a-C and a-C:N Films

Nitrogen-incorporated amorphous carbon (a-C:N) films were synthesized with different levels of nitrogen incorporation by varying the N_2/Ar ratio of the deposition gas. These films are denoted as a-C:N-X% where X is the percentage of N_2 out of a total flux of 50 sccm N_2/Ar introduced into the deposition chamber during sputtering. N-free films are denoted as a-C. An important feature of a carbon model system for electrochemical studies is a smooth and reproducible topography. In order to verify that the topography of the various a-C:N-X% films was comparable for different levels of nitrogenation, a combination of SEM and AFM techniques were used.

As shown in Figure 3.1, SEM images of a-C and a-C:N films prepared with different N_2/Ar content during the deposition show no distinct morphological differences from one another and are almost entirely featureless. The root mean square (rms) roughness of selected a-C:N

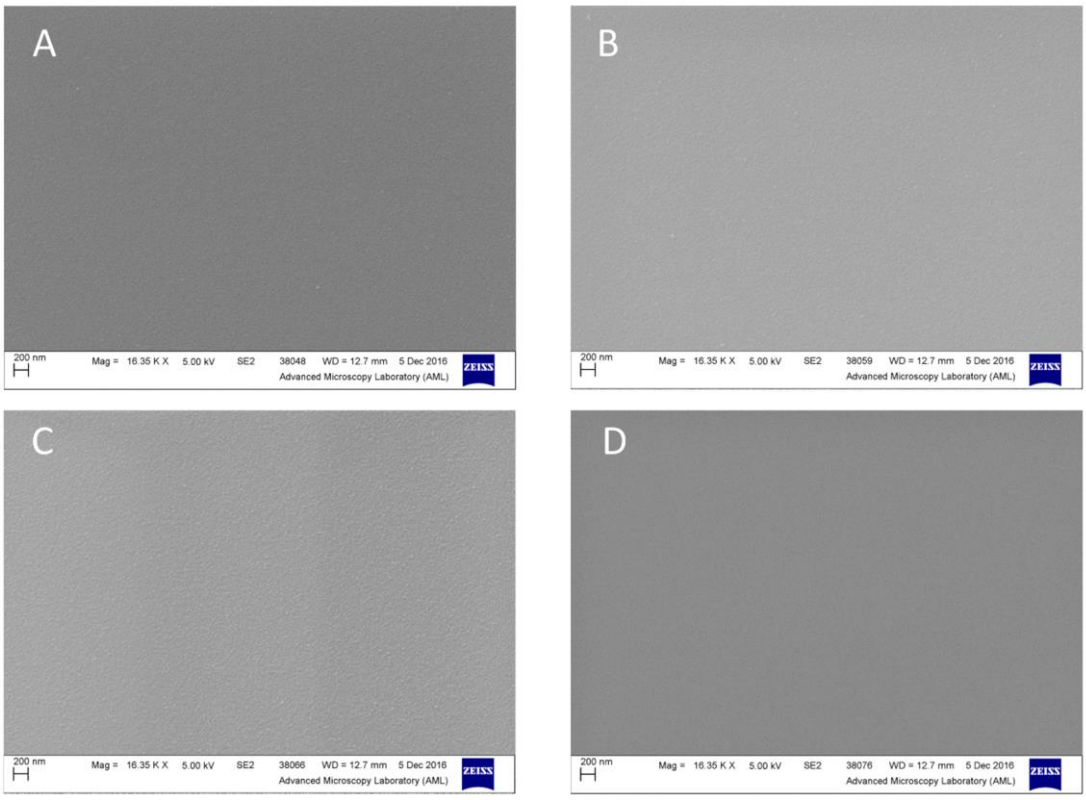

Figure 3.1. SEM images of a) a-C b) a-C:N-2% c) a-C:N-10% d) a-C:N-50% films deposited on Si substrates.

surfaces was determined using AFM measurements as shown in Figure 3.2 with the relevant RMS values reported in Table 2.1. The rms roughness values of both a-C and the a-C:N-X% films are all between 1-1.5 nm, in good agreement with values obtained for sputtered amorphous carbon films by other groups.[48-49] There is no identifiable trend in the roughness values with respect to the N-content and no significant difference in roughness between a-C and a-C:N films. This fact, combined with the generally low absolute values of the rms roughness, implies that the topography may be treated as a constant when comparing the properties of a-C and a-C:N electrodes to one another.

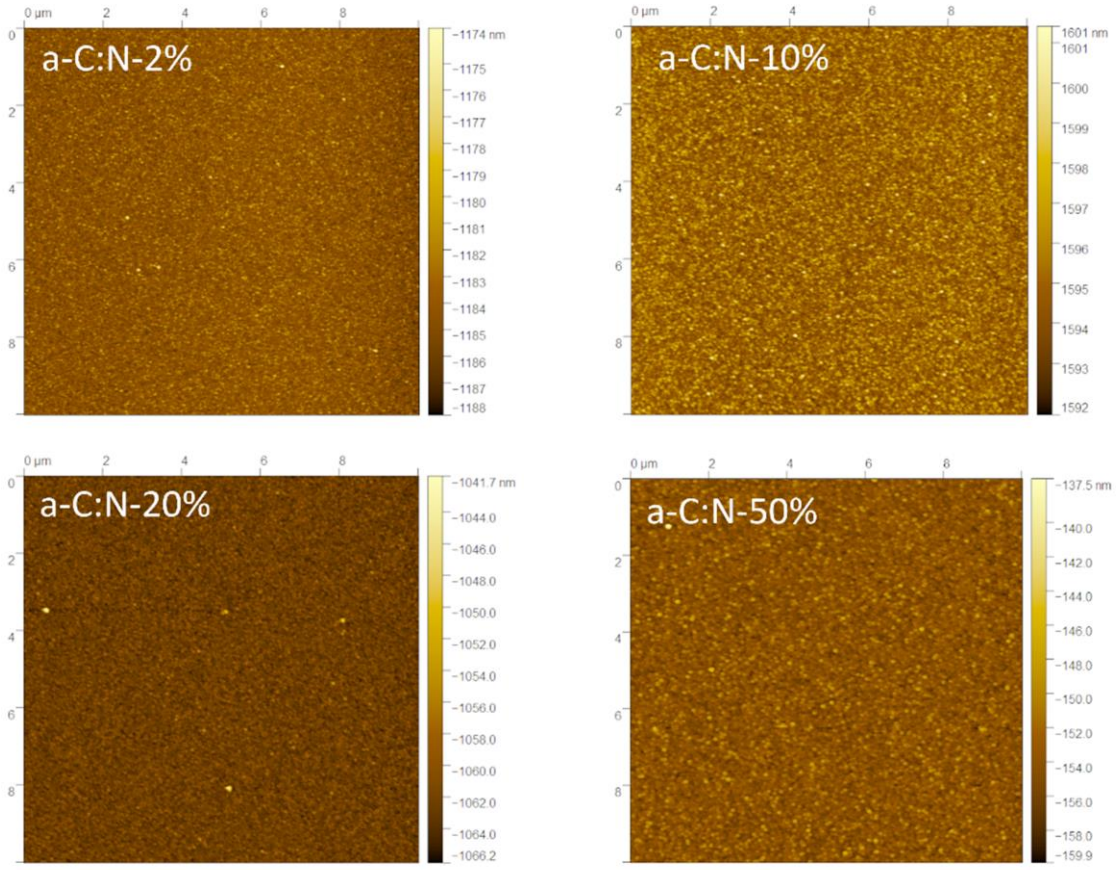

Figure 3.2. 10 x 10 µM AFM images of selected a-C:N films deposited on a Si substrate. These images were used to obtain rms roughness values from the height profiles.

Table 3.1. RMS roughness of a-C and selected a-C:N films

Surface	RMS Roughness (nm)
a-C	1.40 ± 0.07
a-C:N-2%	1.06 ± 0.01
a-C:N-10%	1.02 ± 0.05
a-C:N-20%	1.30 ± 0.03
a-C:N-50%	1.52 ± 0.01

Chemical Composition of a-C:N Films

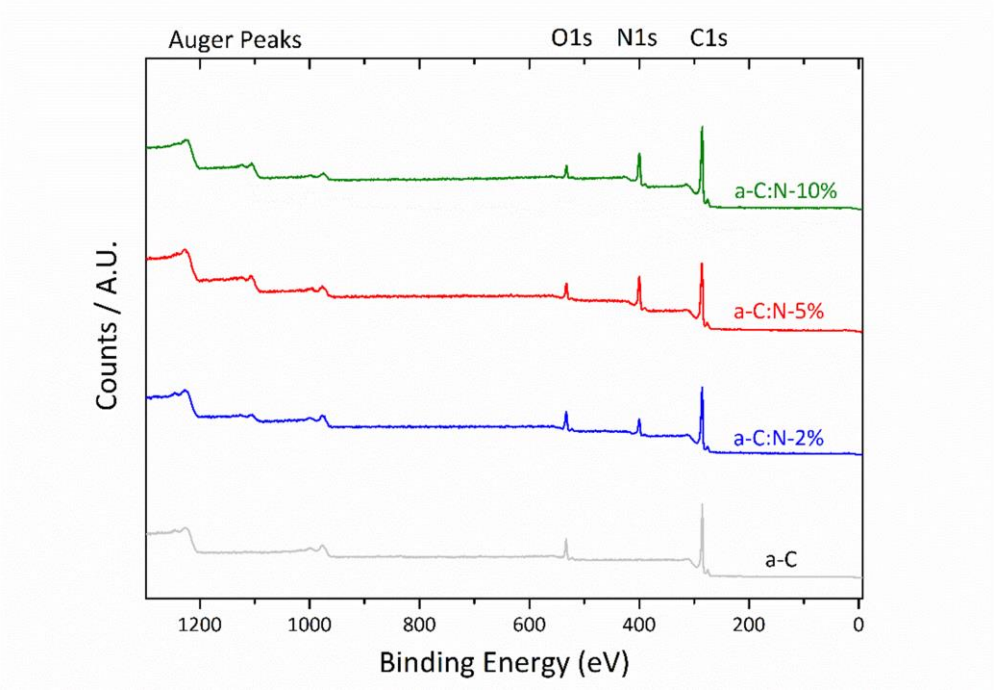

Figure 3.3. Survey scans of a-C and a-C:N-2-10% films.

The chemical composition of the various a-C:N films was investigated using XPS measurements. Survey scans of all a-C:N films show characteristic C 1s, O 1s and N 1s

peaks at 284, 532 and 400 eV, respectively (Figure 3.3). a-C was prepared using exclusively Ar in the deposition gas and contains no nitrogen, as confirmed by the absence of N 1s peaks in the survey spectra. Figure 3.4 a) and Table 3.2 show the changes in N/C% determined via XPS, observed when changing the N_2 % composition in the deposition gas. The plot suggests the presence of two different regimes of nitrogenation. When the N_2 % in the deposition gas is low, (N_2 < 15%) nitrogen atoms are incorporated rapidly into the carbon material, however the rate of incorporation slows considerably for higher N_2 %, in agreement with previous reports by other groups.[50-52]

The elevated N/C at. % values obtained in the slow deposition regime (N_2>15%), suggest that films deposited under such conditions contain N—N bonds and/or incorporate nitrogen gas within their structure.[52-54] Figure 3.4 b) shows the variation of the growth rate of the films with the N_2% in the deposition gas as determined from SE measurements (*vide infra).* The trend in growth rates is similar to the trend in nitrogen content with respect to the N_2 % in the deposition gas, implying that the films with the greatest degree of nitrogen incorporation are also thicker on average.

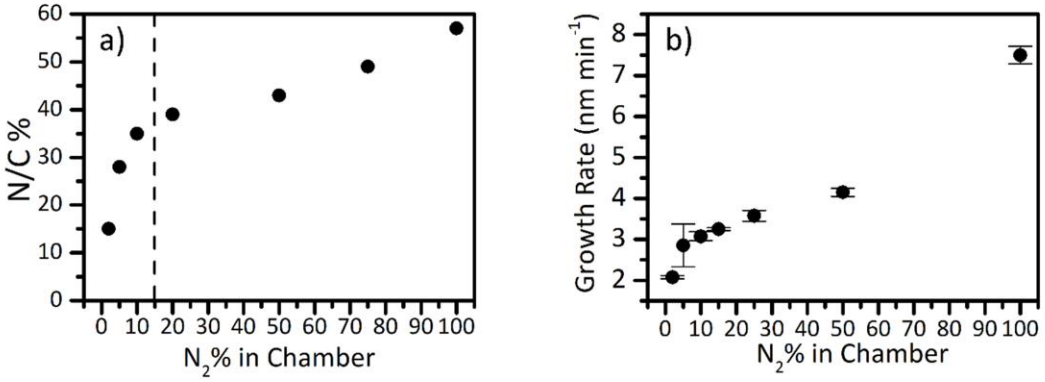

Figure 3.4. a) N/C % of a-C:N films versus the N_2 % in the deposition chamber. The dashed line separates the two different regimes of nitrogen incorporation. b) Growth rate in nm/min of a-C:N films versus the N_2 % flux in the deposition chamber. Error bars represent 95% confidence intervals.

Figure 3.5 a-c shows the N 1s spectra of a-C:N-2%, 5% and 10%, respectively, with similar N 1s envelopes obtained at other N_2 % during deposition. The broad peak envelope indicates the presence of multiple types of N-sites. The N 1s peaks were fitted using five contributions assigned to pyridinic-N (398.2 – 398.8 eV), pyrrolic-N (400 – 400.6 eV), graphitic-N (400.8 – 402.6 eV) and N—O/N—N (403 – 406 eV). The graphitic-N

contribution was further separated into contributions from center- (400.8 – 401.5 eV) and valley-type (402.1 – 402.8) N-sites.[54-55] As noted by several authors, contributions to the envelope above 403 eV could potentially be attributed to the presence of π-π* satellites;[30, 56] These satellites may contribute to our spectra, however they cannot be distinguished from with N—O and N—N contributions due to spectral overlap in this binding energy region.

Pyridinic-N and pyrrolic-N sites were found to dominate the N 1s spectra. Table 3.2 shows that, for all a-C:N films, the increasing N/C % at higher N_2 gas % is mostly explained by an increase in sites attributable to these two types of N site, with comparatively smaller contributions from substitutional and oxide sites. The relative contribution of each type of N-site to the total surface nitrogen content determined from the N 1s deconvolution is reported in Figure 3.5 d and Table 3.2. These show that as the N/C % increases, the

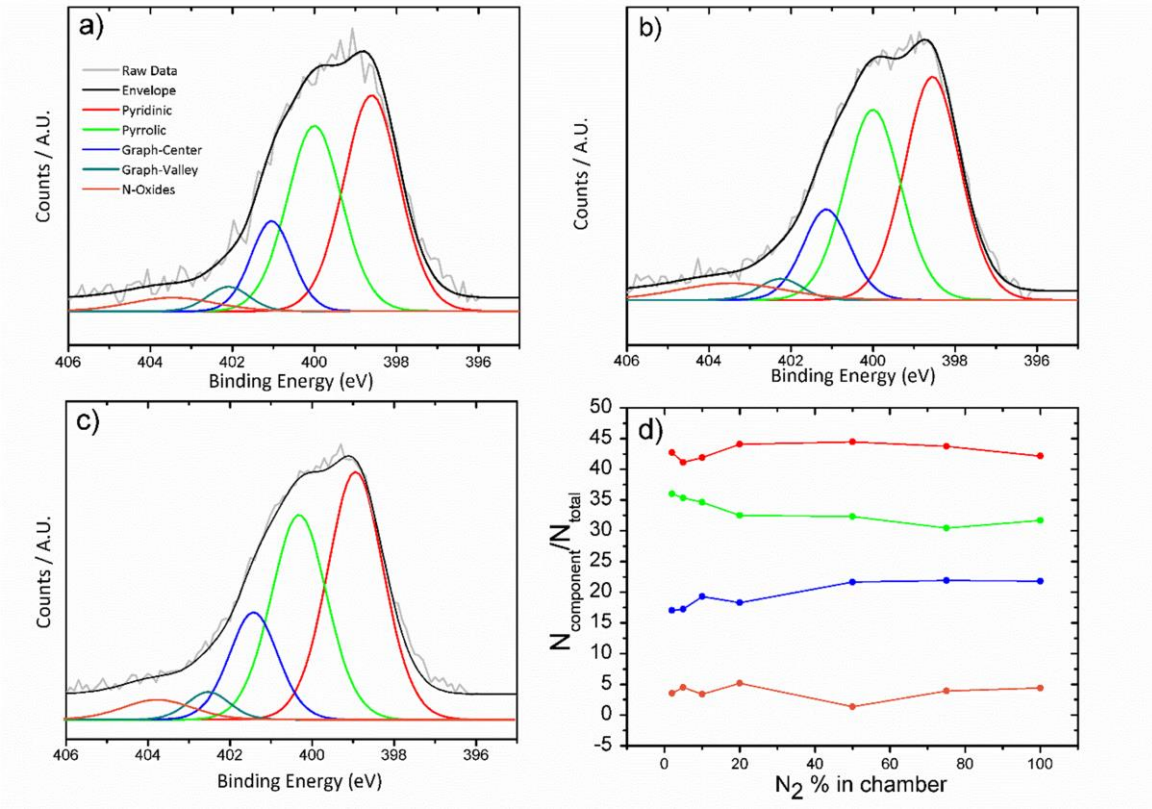

Figure 3.5. a-c) XPS N 1s spectra of a-C:N-2%, 5% and 10% respectively d) Relative contributions of each N component to the total N content as a function of N_2 % present during deposition. The two graphitic-N contributions are considered as one contribution for the analysis.

magnitude of the contribution from each of the nitrogen sites to the overall N content is essentially constant and independent of the total N/C % and growth rate of the film. The differences in the film thickness for the different a-C:N-X % electrodes evident from Figure 3.5 were therefore found to have no significant effect on the N-site chemistry. This result

was further verified by depositing an a-C:N-10% film for half of the normal deposition time of 40 minutes and measuring its XPS spectrum in the N 1s region (405 – 295 eV) as shown in Figure 3.6. As shown in the figure, the differences in the N 1s envelope shape are negligible for the two different deposition times even though there is a difference of *ca.* 50 nm in thickness between the two films. Both films also have a similar calculated N/C *at.* % value of 35 %

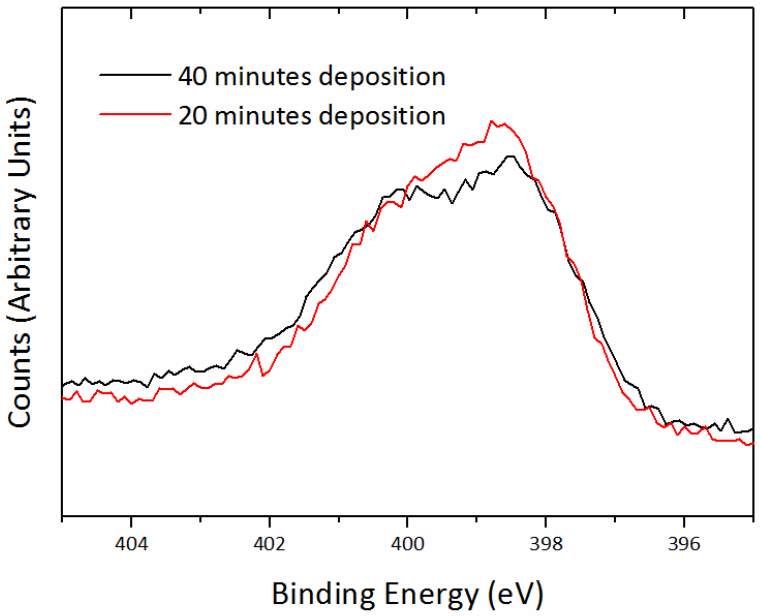

Figure 3.6. N 1s envelope of a-C:N-10% films deposited for 20 minutes (red spectrum) and 40 minutes (black spectrum).

The C 1s spectra obtained for the a-C:N films show a broadening of the envelope with increasing nitrogen content, in agreement with the presence of a range of C-N functional group contributions as shown in Figure 3.7. The N-free a-C films have the typical asymmetric C 1s envelope shape for a carbon film with a high (> 80%) sp^2 content, as reported previously by the group.[57-59] The broadening of this envelope seen in a-C:N-2-10% can be attributed to the formation of C-N bonds in a variety of different configurations. However, the strong spectral overlap between C-O and C-N contributions as well as sp^3-C-C sites observed above 285 eV prevents an unambiguous fitting of individual contributions to the C 1s peak.[30] All of the films possess a comparable O/C close to 8 % (Table 3.2), which may arise from the N_{ox} contributions discussed above and from ambient contamination of the samples due to their exposure to air prior to the XPS studies.

Taken as a whole, the XPS data indicate that larger N_2 fluxes during the deposition of a-C:N films result in increased N-content and film thickness, along with a variety of different types of N-site throughout the bulk of the films. However, no relative differences in the contributions of the various types of N-site to the total N-content were found for depositions carried out at different N_2 %.

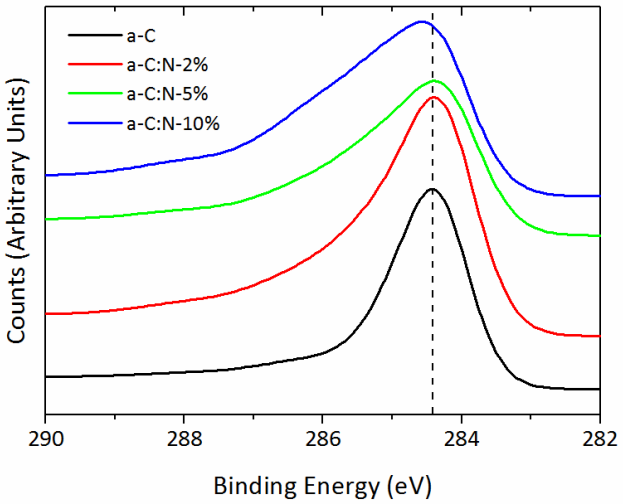

Figure 3.7. C 1s envelopes of a-C and a-C:N-2-10% films. The dashed line around 284.5 eV indicates the position of graphitic carbon (sp^2 sites)

Table 3.2. Composition of a-C and a-C:N-X% samples obtained from XPS spectra.

			$N_{component}/C$%			
N_2 gas%	**N/C %**	**O/C %**	**N_{pyri} %**	**N_{pyrr} %**	**N_{sub} %**	**N_{ox} %**
0%	0	8	0	0	0	0
2%	15	10	6	5	3	1
5%	28	8	12	10	5	2
10%	35	5	16	12	6	1
20%	39	6	17	13	8	1
50%	43	5	18	13	10	2
75%	49	10	21	15	11	2
100%	57	9	24	18	12	3

Optoelectronic Characterization of a-C and a-C:N Films via Spectroscopic Ellipsometry

The bulk optoelectronic properties of a-C:N materials were investigated via spectroscopic ellipsometry measurements. Figures 3.8a and b show representative plots of the optical constants, *n* and *k* for a-C:N-2-20% vs. wavelength in the 400-900 nm range. The real part of the refractive index, *n*, was found to be vary in the range 1.75-2 for all of the samples whilst the trend in the imaginary component, *k*, indicates that the absorptivity of the films in the visible range is generally higher for a-C:N than for a-C. Among the a-C:N films the absorptivity decreases with increasing levels of N-incorporation. Figure 3.8c shows a

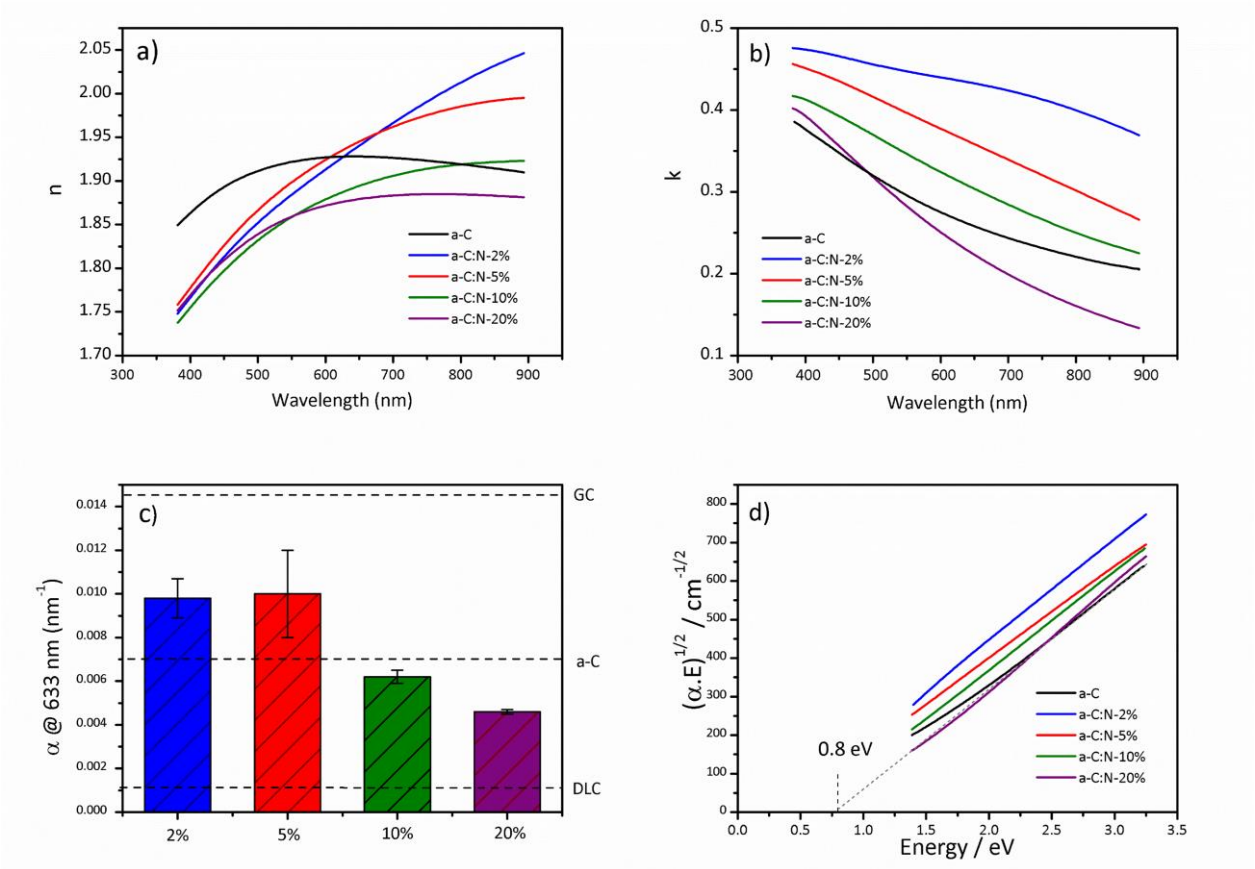

Figure 3.8. (a) Plots of index of refraction (n) derived from SE measurements of a-C and a-C:N-2-20% versus wavelength (nm). **(b)** Plots of extinction coefficient (k) versus wavelength for a-C and a-C:N-2-20%. **(c)** Bar plot of the absorption coefficient, α @ 633 nm for a-C:N-2-20%. Dotted lines refer to a-C films, reported GC absorptivity[60] and sp^3-rich DLC films characterized by Mednikarov et al.[61] **(d)** Tauc plots for a-C and a-C:N-2-20%. The linear region between 2 and 3 eV is extrapolated to the abscissa in order to determine the optical (Tauc) gap as illustrated in the figure for a-C.

comparison of the absorption coefficient α at 633 nm, calculated as $\alpha = \frac{4\pi k}{\lambda}$, for a-C:N-2-20%; values obtained for non-nitrogenated films and literature values for GC[60] and diamond-like carbon (DLC)[61] are also reported as a comparison.

Low levels of nitrogen incorporation (2-5%) produce films with absorptivity similar to or slightly greater than that of N-free a-C, whilst for higher levels of nitrogenation (10-20%) the absorptivity decreases significantly. As described in Chapter II, absorption coefficients as a function of photon energy were used to calculate Tauc plots from which the optical Tauc gap values (E_T) were obtained. The resulting plots are depicted in Figure 3.8 d); values of E_T calculated via extrapolation of the linear region of the plot for a-C and a-C:N films are reported in Figure 3.9. The results show that a-C:N films prepared with low levels (2 – 5%) of N-incorporation have the narrowest optical gaps whilst at higher nitrogen incorporation (a-C:N-10-20%) the optical gap increases. This is consistent with previous reports indicating that low levels of N-incorporation raise the Fermi level of the material and lower its optical gap[24, 62] relative to non-nitrogenated carbons. Based on our results, this effect is observed only for low levels of nitrogen incorporation, whilst carbons with N/C% > 15% display greater semiconductive character.

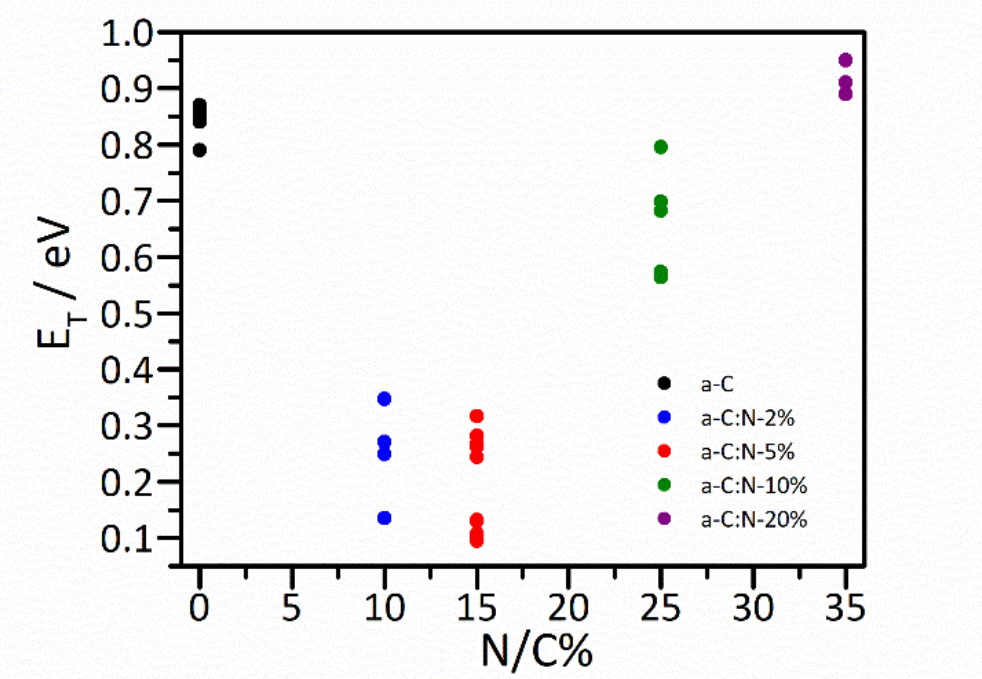

Figure 3.9. Cluster plot of the Tauc gaps (E_T) for a-C and a-C:N-2-20%.

The optoelectronic properties of the a-C:N films were also found to be independent of the film thickness in a similar fashion to the nitrogen surface chemistry (*vide supra*). Figure 3.10 shows plots of the optical constants, n and k, of an a-C:N-10% film prepared at deposition times of 20, 30 and 40 minutes. These films were found to have thickness values of 60 ± 3, 90 ± 5 and 120 ± 5 nm respectively, in good agreement with the values predicted by the growth rate curve in Figure 3.4. As shown in Figure 3.10 both the real and complex components of the refractive index have comparable values across the entire energy range for all three film thicknesses, strongly suggesting that the bulk optical properties of the films are thickness-independent. Indeed, Tauc analysis derived using *k* values for the films in Figure 3.10 yields similar optical gaps close to 0.7 eV for each deposition time, similar to the values obtained for 40 minute depositions only and plotted in Figure 3.9.

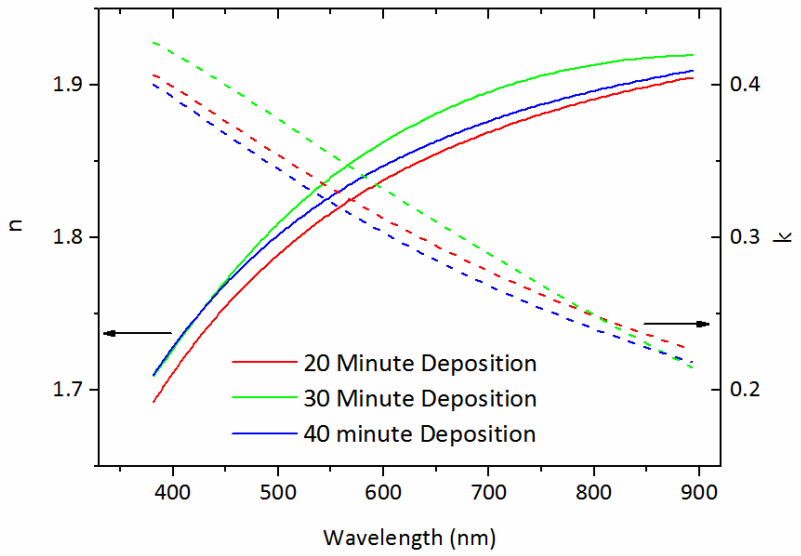

Figure 3.10. Plots of the real and imaginary components of the complex refractive index for a-C:N-10% films with three different deposition times.

At N concentrations found in the a-C:N-20% films and higher, the optical properties of the resulting films significantly depart from those obtained at lower N_2 % values. Figure 3.11 shows plots of the imaginary component of the refractive index versus wavelength for a-C:N samples deposited at high N_2% in the deposition mixture. For these films, the *k* values do not vary smoothly and monotonously as expected of amorphous solids, but display broad

peak-like features. These broad peaks suggest the presence of disordered conjugated clusters in these a-C:N films: the formation of relatively small, poorly-connected graphitic clusters with localized electron density is expected to result in "molecule-like" optical transitions such as those observed for a-C:N-50-100%. Our results are also consistent with work by Rodil et al., who proposed that the increase in E_T values usually observed with increasing N/C% content can be attributed to increased localization of π-electrons.[63]

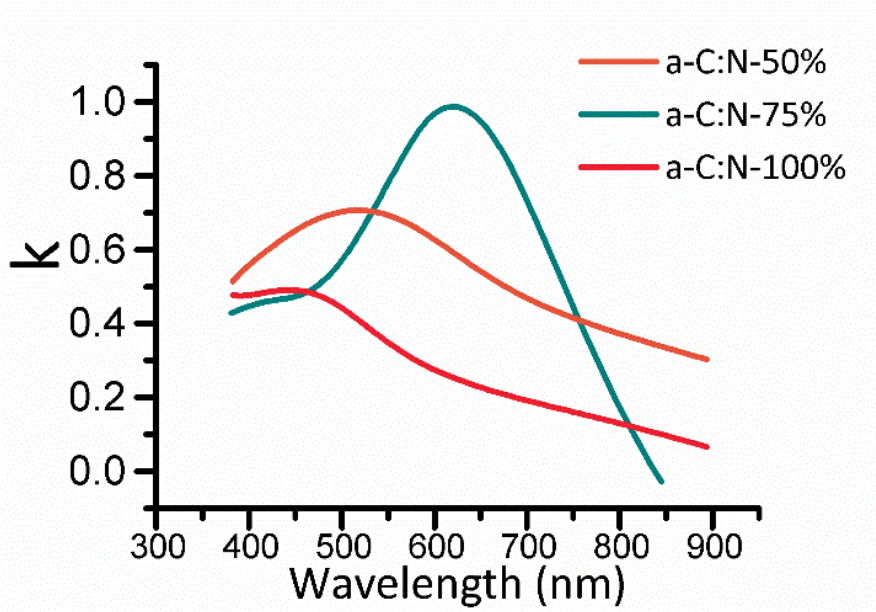

Figure 3.11. Extinction coefficient (k) versus wavelength for a-C:N-50%, 75% and 100% derived from ellipsometry measurements.

Electrochemical Characterization of a-C and a-C:N Films

The electrochemical performance of the a-C and a-C:N films in simple charge transfer experiments to standard redox probes was studied using a combination of cyclic voltammetry and electrochemical impedance measurements. The $Ru(NH_3)_6^{+2/+3}$ redox couple was first chosen as an electrochemical probe. As discussed in Chapter I of this thesis, this complex is an example of an outer-sphere redox species which is relatively insensitive to surface chemistry.[64] Instead the rate of charge-transfer is controlled by the electronic properties of the electrode, *viz.* the Fermi level position (E_F), and density of states (DOS) near E_F.

Figure 3.12 shows CVs obtained for a-C:N-X% electrodes in 1 mM $Ru(NH_3)_6^{+2/+3}$ with 0.1 M KCl. The figure indicates that low levels of nitrogen incorporation result in electrodes with the smallest peak-to-peak separation (ΔE_p) and the highest capacitance-corrected peak current density values (~0.3 mA cm^{-2}). ΔE_p values of 70 – 80 mV obtained for a-C:N-2-5%

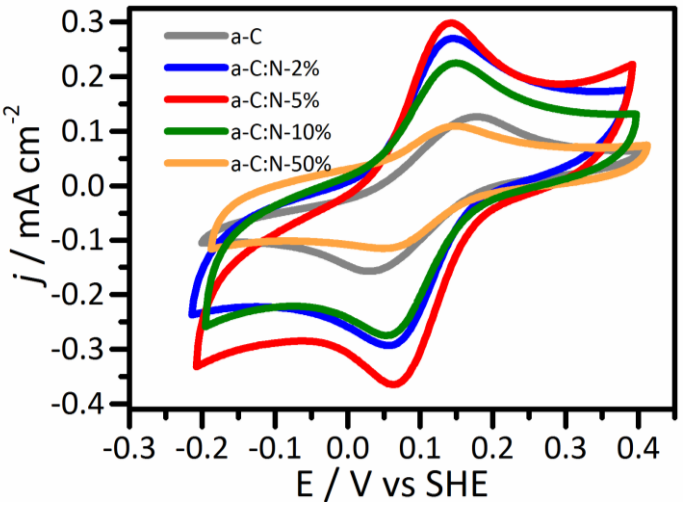

Figure 3.12. Cyclic voltammograms of electrodes of a-C and a-C:N in solutions of 1 mM $Ru(NH_3)_6^{2+/3+}$ in 0.1 M KCl.

at 50 mV s^{-1} (Table 3.3) are close to the reversible limit of 59 mV for a one-electron process, indicating that electron transfer is fast for low levels of nitrogenation. Since each experiment was carried out with the same concentration of $Ru(NH_3)_6^{+2/+3}$, differences in peak current density for different films may possibly be explained by changes in the electroactive area of the sputtered electrodes; this is also consistent with the observed drop in the capacitive contribution to the current for a-C:N-50%. The decrease in peak current density occurs in the absence of a significant change in ΔE_p. This suggests that the electrodes at high N/C content are better described as heterogeneous partially-blocked electrodes, which have been shown to display similar behaviour in their voltammetric response, depending on microdomain size and distribution.[65]

In all cases the ratio of cathodic to anodic peak current densities ($J_{p,c}/J_{p,a}$) is > 0.9 which is close to the theoretical value of 1 for an electrochemically reversible process. Non-nitrogenated a-C yielded a significantly larger ΔE of ~150 mV (Table 3.3) therefore indicating that low levels of nitrogenation result in an enhancement of the electron transfer rate. However, as the N_2% increases in the deposition mixture, this trend reverses and for a-C:N-50%, the peak separation increases to almost 100 mV. This increase is accompanied by a decrease in peak current density to a value comparable to that of a-C. Finally, a-C:N-X% films with X = 75, 100 were found to be too resistive for electrochemical measurements.

In order to quantitatively compare the electron-transfer properties of our films, Electrochemical Impedance Spectroscopy (EIS) was used to determine the resistance to charge transfer (R_{CT}) at the formal potential ($E^{0'}$) of the Ruthenium redox couple.

Table 3.3. Peak current density ratios, peak potential separations and apparent rate constants calculated for nitrogenated and non-nitrogenated carbon electrodes obtained at 50 mV s^{-1} in 1 mM $Ru(NH_3)_6^{+2/+3}$ and 0.1 M KCl. Errors indicate 95% confidence intervals.

Sample	J_{pc}/J_{pa}	ΔE_p (V)	k_{app} (cm s^{-1} x 10^{-3})
a-C	0.9 ± 0.2	0.15 ± 0.02	2.0 ± 0.4
a-C:N-2%	0.9 ± 0.1	0.08 ± 0.01	9.0 ± 0.2
a-C:N-5%	0.91 ± 0.06	0.074 ± 0.007	10 ± 1
a-C:N-10%	0.93 ± 0.09	0.09 ± 0.01	6 ± 2
a-C:N-50%	1.0 ± 0.1	0.095 ± 0.002	5 ± 3

Representative Nyquist plots for a-C:N electrodes in solutions containing 1 mM $Ru(NH_3)_6^{+2}$ and 1 mM $Ru(NH_3)_6^{+3}$ with 0.1 M KCl are shown in Figure 3.13a together with the plot obtained for a-C under the same conditions. Typical features of a mixed kinetic-diffusion process are evident in all complex spectra; a semicircle at high frequency (10^5 – 10^3 Hz) suggests the presence of an impedance to charge-transfer (R_{CT}) in parallel with a capacitive contribution, while at low frequencies (10^3-10^{-1} Hz) a linear behaviour with ~45° slope indicates that the impedance is dominated by diffusion of the redox probe to the electrode surface These EIS spectra were fitted using a Randles circuit (Figure 3.13 b). The model consists of a series connection of a resistor, R_s representing the uncompensated solution resistance and a parallel combination of a double-layer capacitance and a Faradaic impedance. In this case the double-layer capacitance, C_1, was replaced with a constant phase element (CPE 1) which, as discussed in Chapter I, is appropriate in situations where inhomogeneous electrode surfaces are used.[66] The CPE impedance is described by two parameters, Q and α, according to the following equation:

$$Z_{CPE} = \frac{1}{(j\omega)^{\alpha} Q}$$

The Faradaic impedance was modelled as a series combination of a resistor, R_{CT}, representing the resistance to charge transfer, and a second constant phase element (CPE 2) representing the diffusion impedance. Note that, in this case a Warburg element could also have in principle been used, but the resulting CPE exponential (α) values are close to 0.5, which is equivalent to a Warburg impedance. Examples of fits obtained using this circuit are shown in Figure 3.13 c) and d) and a full table of fitting parameters is presented in Table 3.4. In general, the equivalent circuit fits the data well, with some deviations observed in

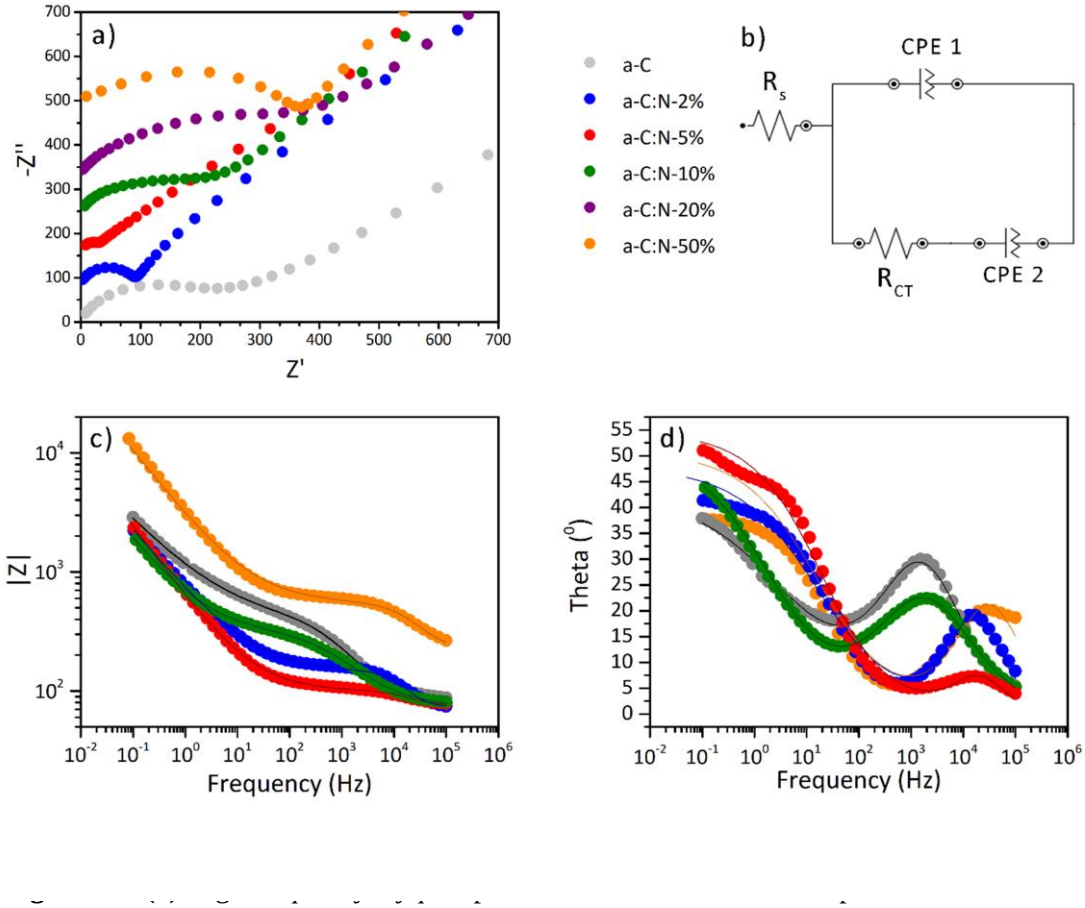

$Ru(NH_3)_6^{+2/+3}$ with 0.1 M KCl. The plots are offset on the y-axis and the solution resistance R_s has been subtracted for ease of comparison. **(b)** Equivalent circuit used to fit EIS data on a-C and a-C:N electrodes. c) Bode magnitude and d) Bode phase plots for a-C and a-C:N electrodes. The fit produced by the equivalent circuit model in each case is shown as a solid line.

particular at low frequencies. The largest of these deviations are obtained for large variations from the expected α value of 0.5 for CPE 2 as shown in Table 3.4. This suggests that the simple Randles equivalent circuit is not entirely applicable in describing the EIS response at these surfaces under mass-transport limiting conditions.

Table 3.4. Summary of parameters obtained from fitting impedance spectra for a-C and a-C:N-X% obtained in solutions of 1 mM $Ru(NH_3)_6^{2+/3+}$ / 0.1 M KCl. The errors presented represent the 95% confidence interval (n = 3-5). The solution resistance, R_s, was found to always have a value of approximately 60 Ω and is omitted from the table for clarity. In the case of CPE Q values the resulting parameter is presented normalised to the geometric area of the glassy carbon disk determined via calipers measurements and verified electrochemically based on the variation of peak current values with the scan rate *(vide infra)*.

Substrate	RCT (Ω)	k_{app} / cm s^{-1} x 10^{-3}	Q1 (cm^{-2})	α(CPE1)	Q2 (cm^{-2})	α(CPE2)
a-C	290 ± 50	4.2 ± 0.09	30 ± 7	0.70 ± 0.09	2000 ± 1000	0.48 ± 0.01
a-C:N-2%	40 ± 30	5.0 ± 0.5	2 ± 2	0.95 ± 0.09	4000 ± 1000	0.56 ± 0.04
a-C:N-5%	23 ± 9	30 ± 1	11 ± 5	0.86 ± 0.06	4000 ± 2000	0.6 ± 0.1
a-C:N-10%	200 ± 200	7 ± 3	100 ± 50	0.67 ± 0.06	3700 ± 300	0.56 ± 0.02
a-C:N-20%	400 ± 300	5 ± 2	400 ± 200	0.59 ± 0.02	4000 ± 2000	0.58 ± 0.05
a-C:N-50%	400 ± 200	5 ± 2	3 ± 2	0.84 ± 0.04	700 ± 200	0.58 ± 0.04

The values for R_{CT} derived from the modelling procedure are plotted vs. N/C % content determined from XPS in Figure 3.13; nitrogenated electrodes a-C:N-2-5% yielded lower R_{CT} values than non-nitrogenated a-C. The values for a-C:N-10% are comparable to those of a-C, whereas those for a-C:N-20% or higher increase progressively. This trend in R_{CT} and k_{app} values agrees with the trend in k_0 values obtained from CV measurements, and suggest that small nitrogen concentrations lead to an enhancement of charge transfer rates, whereas high levels of nitrogen incorporation negatively affect electrochemical performance. Interestingly, by comparing Figure 3.9 and 3.13, R_{CT} values determined via EIS closely parallel E_T vs. N/C % trends determined via ellipsometry. In fact, R_{CT} and E_T appear to be positively correlated (R=0.9458). a-C:N electrodes with the lowest ΔE_p values and largest peak current densities are the a-C:N films with the greatest metallic character, based on E_T determinations. Furthermore, the collapse in peak current density for a-C:N-50% correlates well with the appearance of broad absorption peaks in the imaginary refractive index which are suggestive of greater electronic localization. For both regimes of N-incorporation there is therefore a strong correlation between the bulk optoelectronic properties and electron transfer properties of the films using the $Ru(NH_3)_6^{+2/+3}$ redox probe.

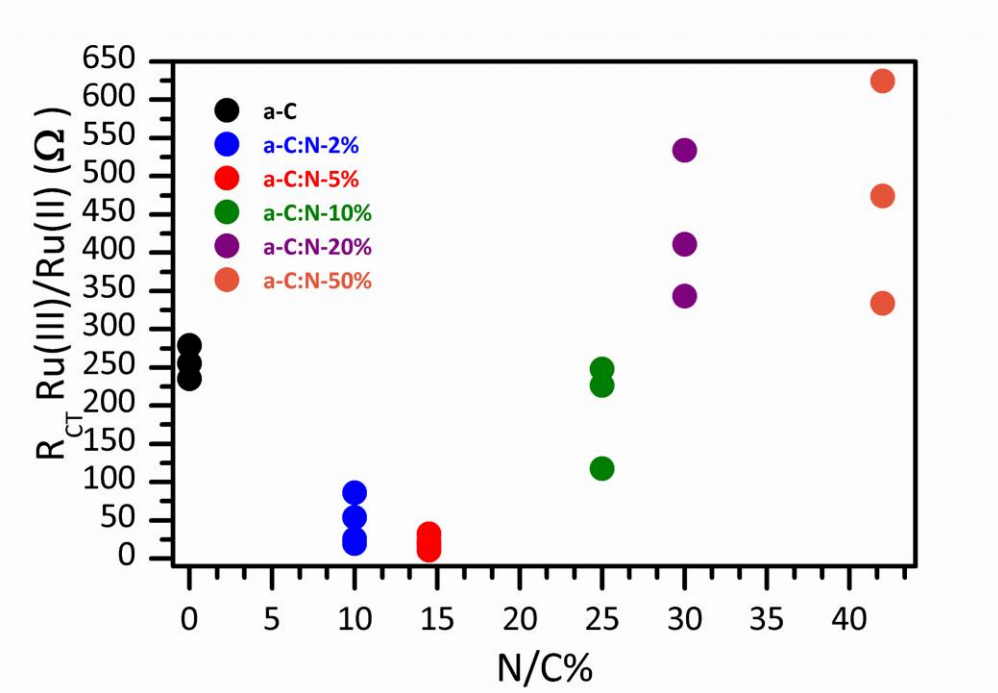

Figure 3.13. Plot of R_{CT} to the Ru(II)/(III) Hexammine redox probe on a-C and a-C:N surfaces obtained via EIS measurements versus N/C % determined from XPS measurements

Electrochemical Characterization using $Fe(CN)_6^{-4/-3}$

Redox couples such as $Ru(NH_3)_6^{+2/+3}$ are in the minority with regards to their relative insensitivity to surface termination in electron transfer processes. In order to understand the effect of nitrogen incorporation on the surface chemistry of carbon electrodes CV and EIS measurements of a-C and a-C:N-X% were carried out in aqueous solutions of $Fe(CN)_6^{-4/-3}$, a redox probe that is known to be sensitive to surface functionalities (e.g. passive layers and charged groups).[64]

Figure 3.14 shows CVs of carbon electrodes in 1 mM $Fe(CN)_6^{-4}$ and 0.1 M KCl for a-C and a-C:N electrodes. Based on the tendency for increasing levels of nitrogenation above 10% to produce insulating surfaces observed in experiments with $Ru(NH_3)_6^{+2/+3}$, the analysis was restricted to a-C:N-2-10% only. As shown in the figure, the ΔE_p for a-C and a-C:N-2% is approximately 80 mV, whilst ΔE_p for a-C:N-5% is slightly higher at 100 mV. The $j_{p,c}/j_{p,a}$ (Table 3.5) is close to 1 for all of these films, indicating that the redox process is reversible for both a-C and a-C:N-2-5% in the case of the $Fe(CN)_6^{-4/-3}$ couple albeit with sluggish electron transfer kinetics compared to the $Ru(NH_3)_6^{+2/+3}$ redox probe. In the case of a-C:N-10% the anodic peak, $E_{p,a}$ is shifted more than 100 mV in the anodic direction and the

cathodic peak $E_{p,c}$ is greatly reduced. This indicates that the charge transfer process is irreversible for $Fe(CN)_6^{-4/-3}$ on a-C:N-10%.

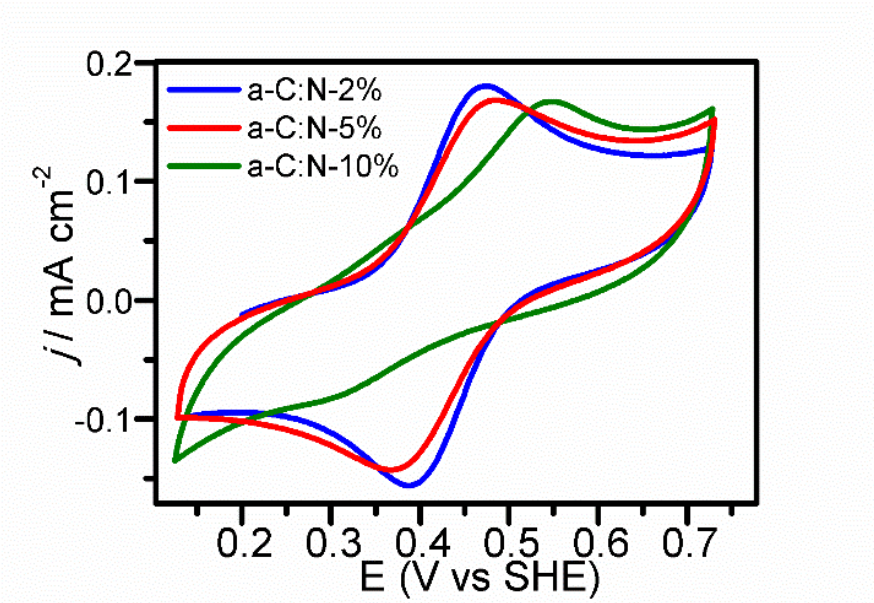

Figure 3.14. CV's of a-C:N-2-10% in solutions of 1 mM $Fe(CN)_6^{-4}$ / 0.1 M KCl at a scan rate of 50 mVs^{-1}.

Table 3.5. Peak current density ratio ($J_{p,c}/J_{p,a}$) and ΔE_p values for a-C and a-C:N-2-10% obtained in 1 mM $Fe(CN)_6^{-4/-3}$ with 0.1 M KCl at 50 mV s^{-1}.

Sample	J_{pc}/J_{pa}	ΔE_p (V)
a-C	0.95 ± 0.05	0.08 ± 0.03
a-C:N-2%	0.8 ± 0.1	0.08 ± 0.02
a-C:N-5%	0.9 ± 0.1	0.1 ± 0.05
a-C:N-10%	0	–

Nyquist plots for a-C and a-C:N films in 1 mM $Fe(CN)_6^{-4}$ in 0.1 M KCl are shown in Figure 3.15. Similar to the results for the $Ru(NH_3)_6^{+2/+3}$ couple, evidence of a mixed kinetic-diffusion controlled electron transfer process can be seen for a-C and a-C:N-2-5%. Due to the irreversibility of a-C:N-10% determined via CV studies, EIS experiments were not attempted on this substrate. For both a-C and a-C:N-2% the semicircle in the high frequency (10^5 – 10^3 Hz) region indicates that the impedance to charge transfer is low for both a-C and

a-C:N-2% with similar magnitudes of R_{CT}. The linear behaviour of the plots in the low frequency region (10^3-10^{-1} Hz) of the figure indicates that ferrocyanide oxidation may proceed rapidly enough to be diffusion-rate limited on both surfaces.

In the case of a-C:N-5%, the broad semicircle in the region from 10^2 to 1 Hz a-C:N-5% plot corresponds to Randles behaviour with a larger contribution of R_{CT} to the impedance. This is in agreement with CV data for a-C:N 5%, which indicate that ΔE_p values for charge transfer to ferrocyanide are slightly larger in the case of a-C:N 5%. The high-frequency region of the impedance plot for a-C:N-5% indicates the appearance of a smaller RC component which is present even in the absence of any redox-active species (Figure 3.16).

This contribution has previously been observed in the EIS of amorphous carbon materials,[67-68] and might be attributed to defects likely to occur in non-crystalline materials, including nanoporosity and mid-gap or surface states.[69-71] It is only observable as a separate

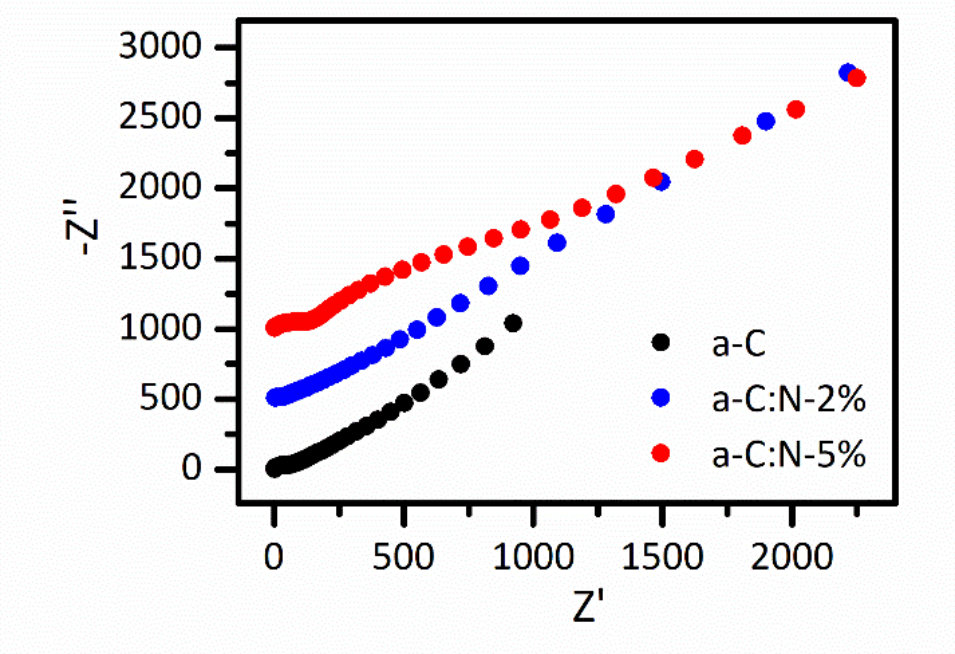

Figure 3.15. Nyquist plots of 1 mM $Fe(CN)_6^{-4/-3}$ in 0.1 M KCl obtained for a-C and a-C:N-2-5%.

time constant when the kinetics of charge transfer to a redox probe in solution are sluggish, which is why only one time constant is observed in EIS spectra for a-C and a-C:N-2% in Figure 3.15.

Both voltammetric and impedance experiments indicate that nitrogen-incorporation into amorphous carbon electrodes results in surfaces which are progressively less amenable to charge transfer to the $Fe(CN)_6^{-4/-3}$ redox couple. The increase in ΔE_p and R_{CT} from a-C to a-C:N-5% and the irreversibility of charge transfer to a-C:N-10% contrasts with the results for $Ru(NH_3)_6^{+2+3}$, which showed lower ΔE_p and R_{CT} values following nitrogenation and

quasi-reversible behaviour for all a-C:N films studied.

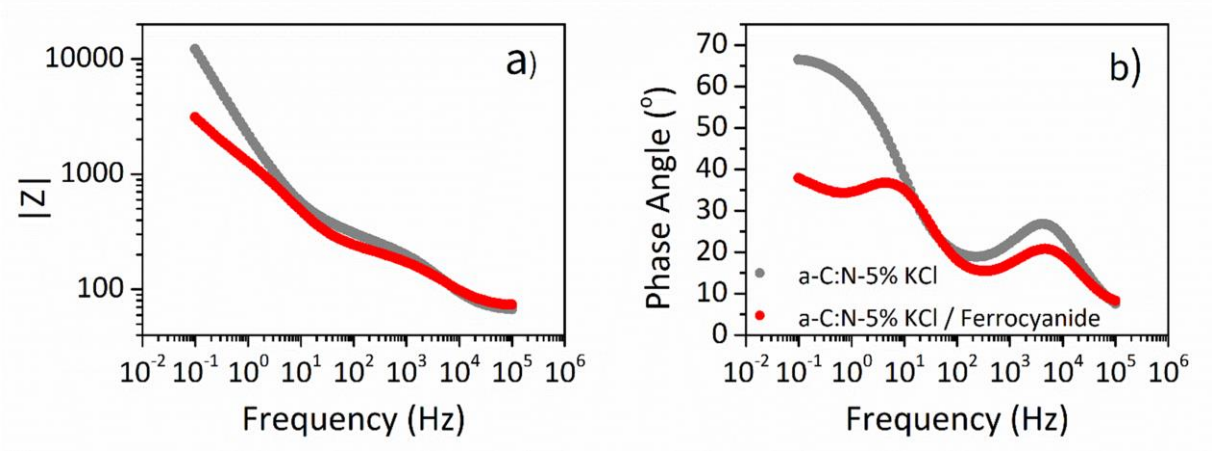

Figure 3.16. a) Magnitude and b) phase plots for an a-C:N-5% electrode in 0.1 M KCl and 0.1 M KCl solution with 1 mM $[Fe(CN)_6]^{2-}$.

Given that the bulk optoelectronic properties of a-C:N-2-10% are known to be more metallic in nature than undoped a-C, this contrasting behaviour is likely to be explained by surface effects on the kinetics of electron transfer. As discussed in Chapter I, the charge transfer to ferrocyanide is catalyzed by the supporting electrolyte, which facilitates the redox process via formation of cationic bridging complexes.[72-75] The availability of specific surface sites is also known to be important in determining the rate of charge transfer of $Fe(CN)_6^{-4/-3}$ at carbon electrodes.[76-77] A recent study by Compton and co-workers[72] showed that ferrocyanide oxidation at graphite electrodes could be rendered almost entirely irreversible by pre-treating the carbon surface with organic solvents such as acetonitrile. Their study concluded that the inhibitory effects of the organic solvent were due to blocking of the active edge sites which in turn prevent the cation bridging required for electron transfer to occur.

It is possible that the incorporation of nitrogen moieties into the carbon matrix of a-C films may produce a similar inhibitory effect which is intrinsic to the surface, rather than induced by the blocking effect of solvent pre-treatment. This result is significant as it underscores the fact that, while the incorporation of nitrogen into the carbon matrix may result in improved bulk electronic properties that typically enhance rates of charge transfer (lower E_T, greater metallic character), it also results in surface nitrogenation that significantly changes interfacial interactions with redox species. Whilst nitrogenation is often associated with improved catalytic properties, as is the case in oxygen reduction, nitrogenation can also result in more sluggish kinetics and an overall inhibitory effect as in the case of charge transfer to the ferrocyanide complex.

3.2 Conclusions

In this chapter, the preparation of nitrogenated amorphous carbon films with varying N/C % was presented along with a detailed characterization of their properties using a combination of optical and electrochemical methods. Results showed that low levels of nitrogenation produce films with greater metallic character when compared to non-nitrogenated amorphous carbon. These films also display the fastest electron-transfer kinetics for the Ruthenium Hexaammine redox couple as measured by a combination of cyclic voltammetry and electrochemical impedance spectroscopy. The resistance to electron transfer, $R_{CT,}$ was shown to be strongly correlated to the Tauc gap, E_T, demonstrating a clear correlation between optoelectronic and electrochemical properties in nitrogenated carbon materials.

Highly nitrogenated amorphous carbon films display properties more consistent with localized and poorly connected arrays of graphitic clusters rather than amorphous solids. These properties were observed both optically, through ellipsometric measurements, and electrochemically based on the inferior electron transfer properties of these materials relative to a-C:N films with lower levels of nitrogenation. An important implication of these results is that ellipsometry emerges as an effective method for the evaluation of defects in carbon electrodes that result from nitrogenation and that the defectiveness evidenced via ellipsometry is straightforwardly reflected in the electrochemical performance.

The response to the outer-sphere redox couple ($Ru(NH_3)_6^{+2+3}$) was contrasted with the surface sensitive $Fe(CN)_6^{-4/-3}$ couple. The introduction of nitrogenated sites facilitates charge transfer in the case of the outer-sphere species, in agreement with an expected increase in charge carriers and metallic character that typically arises from nitrogen doping of carbon materials. The opposite trend is observed for the inner-sphere couple thus indicating that nitrogenation has a profound effect on the surface chemistry and that these effects might dominate the overall electrochemical response of the nitrogenated carbon.

The combined effect of bulk optoelectronic changes and surface modifications that result from nitrogenation, strongly depends on the specific redox species in solution. Results suggest that theoretical predictions of charge transfer rates for ruthenium hexamine based on bulk electronic structure are likely to be accurate at nitrogenated carbons. However, specific models that describe interfacial interactions are required to predict the behavior and trends of inner-sphere redox species which are strongly influenced by the surface chemistry of nitrogenated carbon surfaces.

In the following chapter, the electrochemical response of the a-C and a-C:N materials introduced in this chapter to catechols, another class of inner-sphere redox species, will be studied. These materials will also be used as the basis for other model carbon systems prepared via post deposition treatments of the sputtered films as described in Chapters V and VI.

3.3 Experimental Methods

Chemicals and Materials

Hexaammine Ruthenium (II) Chloride (99.9%, trace metals), Hexaammine Ruthenium (III) Chloride (98%), Potassium Chloride (Bioxtra, >99.0%), Sulfuric Acid (95 – 97%), Hydrogen Peroxide (>30% w/v) Potassium Ferrocyanide (Analar, >99.0%) and methanol (semiconductor grade) were used without further purification.

Substrate Preparation

B-Doped Silicon wafers (MicroChemicals; resistivity 5 – 10 Ω-cm) were used as substrates for carbon deposition; substrates were cleaned with piranha solution (3:1 H_2SO_4:H_2O_2; ***CAUTION:*** *Piranha solution is a strong oxidant which may react explosively with organic solvents – always use in a fumehood*) before rinsing with Millipore water and drying under Ar. Glassy carbon (GC) discs (HTW Sigradur® radius 0.25 ± 0.05 cm) were polished with progressively finer grades of alumina slurry (Buehler). Discs were first polished using 1200 grit sandpaper and 1 μm slurry. After rinsing with copious Millipore water the discs were polished on nylon paper (Buehler) using 1 μm slurry, sonicated for 20 min in Millipore water, then polished on nylon paper using 0.3 μm slurry. Polishing MicroCloths® (Buehler) with 0.3 μm slurry were used for the penultimate step before once again sonicating for 20 min in Millipore water. The final polishing step was 0.05 μm slurry on a fresh microcloth before sonicating the polished discs in Millipore water for 20 min. Clean discs were either used directly in electrochemical experiments or, in the case of a-C and a-C:N depositions, mounted in a custom-made Teflon® holder and placed in the vacuum chamber for coating via magnetron sputtering.

Deposition of carbon electrode materials

Thin film electrodes of amorphous carbon (a-C) and nitrogenated amorphous carbon (a-C:N) were deposited via DC magnetron sputtering in a chamber (Torr International Inc.) with a base pressure ≤ 2 x 10^{-6} mbar and a deposition pressure in the range 2-7 x 10^{-3} mbar. Films with varying Nitrogen percentages were prepared by introducing a nitrogen (N4.5, BOC) and argon (N4.8, BOC) gas mixture into the sputtering chamber using two mass flow controllers (Brooks Instruments). The total gas flow rate was kept at 50 ml min^{-1}, while the mixing ratio was varied to alter the nitrogen content in the films. The deposition time was kept constant at 40 min for all samples.

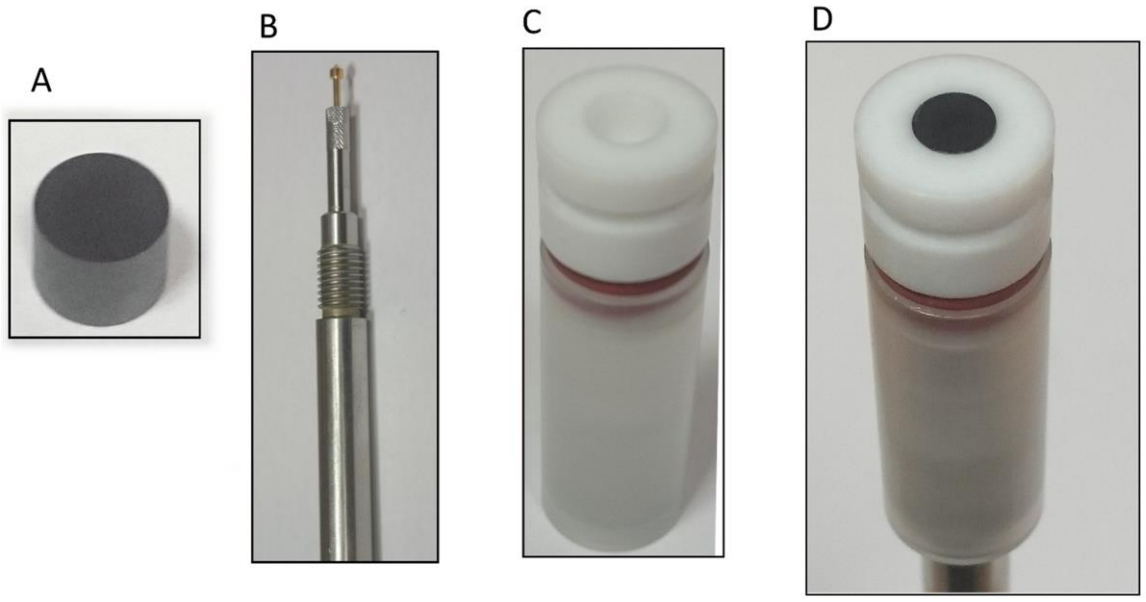

Figure 3.7. (A) Glassy Carbon Disk with sputtered a-C:N film. (B) Static electrode shaft from Pine with gold pyramidal probe. (C) Empty Teflon® cup into which the GC Disk is placed. (D) Fully-assembled working electrode with GC/a-C:N disk, Teflon® Cup and shaft. Contact is established between the gold probe and the rear side of the GC disk; all interfacial contacts were confirmed to be ohmic via i-V plots.

Characterization

Ellipsometry measurements were taken using an alpha-SETM Ellipsometer (J.A. Woolam Co.). The films were deposited on Si wafers and measured at 65º, 70º and 75º incidence. Data were fitted using a 3-layer model which takes into account the substrate, the a-C/a-C:N layer and the air phase, as described in Chapter II. Electrochemical measurements were

carried out using a Metrohm Autolab AUT50324 potentiostat with a Frequency Response Analyser (FRA) module using a 3-electrode setup.

A static disc holder (Pine Instruments) enclosing the a-C/a-C:N sputtered GC disc was used as working electrode (WE, see Figure 3.17); a Hydroflex® hydrogen electrode (Gaskatel) and a Pt wire were used as reference and counter electrodes, respectively. The contact between the film and underlying GC electrode was confirmed to be ohmic through 2-electrode i-V experiments using gold probes. The electrochemical cell consisted of a beaker with a custom-made Teflon® cap. Prior to experiments, the cell was cleaned with piranha followed by rinsing 3 times with Millipore water. Cyclic voltammograms (CVs) in aqueous solutions of 1 mM $Ru(NH_3)_6Cl_2$ or 1 mM Ferrocyanide in deaerated 0.1 M KCl at 25 ^oC were obtained by scanning ± 0.3 V around the Formal Potential, $E^{0'}$ at a scan rate of 50 mV/s; all voltammograms were taken with iR compensation using NOVA software. EIS spectra were obtained at $E^{0'}$ for both redox couples using 100 scans in the frequency range from 100 kHz to 0.1 Hz using an AC amplitude of 8 mV. The resulting spectra were fitted with equivalent circuit models using commercial software (ZView).

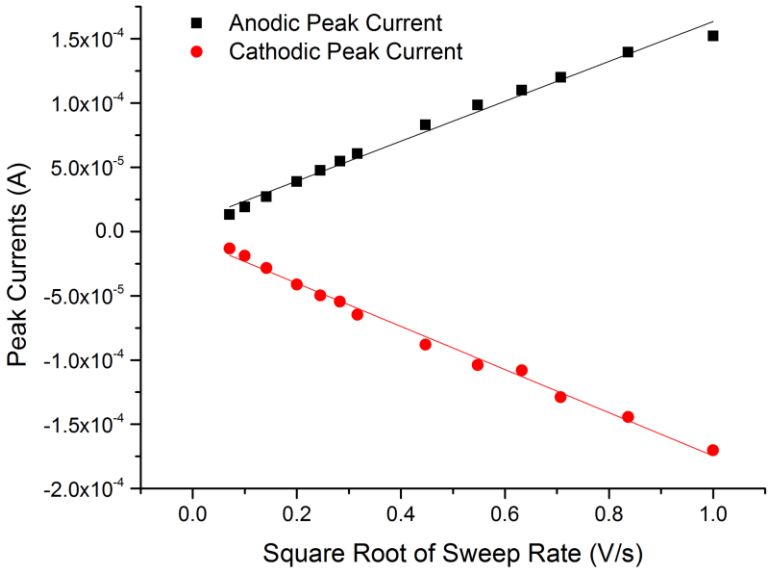

Figure 3.18. Sample plot of peak current versus the square root of the sweep rate used for calculating the area of each glassy carbon disk via the Randles equation.

The geometric area of each disc was determined using calipers and verified via cyclic voltammetry experiments using the $Ru(NH_3)_6^{+2/+3}$ probes at various scan rates using the Randles-Sevcik equation:

$$I_p = 269000.A.D^{1/2}cv^{\frac{1}{2}}.$$

In this equation A is the geometric area of the electrode, D is the diffusion coefficient of the $Ru(NH_3)_6^{2+/3+}$ couple (Ru (III) = 9.1×10^{-6} cm^2 s^{-1} , Ru(II) = 1.19×10^{-5} cm^2 s^{-1}), c is the concentration of the redox couple (1×10^{-6} mol cm^{-3}) and υ is the scan rate in V s^{-1}. Figure 3.17 is an example of a Randles plot for a-C:N-5% deposited on a GC disk with an area of 0.198 cm^2 as found through measurements with calipers. The slopes of the anodic and cathodic peak currents versus $\upsilon^{1/2}$ are 1.55 and 1.61×10^{-4} respectively, giving a a value between 0.191 and 0.197 cm^2 for the geometric area.

In the case of a-C films, X-ray photoelectron spectroscopy (XPS) characterization was performed at 1×10^{-10} mbar base pressure in an ultrahigh vacuum system (Omicron). The X-ray source was a monochromatized Al Kα source (1486.6 eV). Spectra were recorded at 45° takeoff angle with an analyzer resolution of 0.5 eV. In the case of a-C:N films XPS characterization was performed on a VG Scientific ESCAlab Mk II system ($<2 \times 10^{-8}$ mbar), using Al Kα X-rays (1486.6 eV); core-level spectra were collected with analyzer pass energy of 20 eV. Charge compensation, where applicable, was achieved using an electron flood gun and the binding energy scale was referenced to the C 1s core-level at 284.8 eV. Spectra were baseline corrected using a Shirley background and fitted with Voigt functions using commercial software (CasaXPS); atomic percent compositions were determined by calculating peak area ratios after correction by relative sensitivity factors (C 1s = 1.0, N 1s = 1.8, O 1s = 2.93).

3.4 References

1. Liebig, J., Ueher Einige Stickstoff - Verbindungen. *Annalen der Pharmacie* **1834,** *10* (1), 1.

2. Franklin, E. C., The Ammono Carbonic Acids. *Journal of the American Chemical Society* **1922,** *44* (3), 486-509.

3. Pauling, L.; Sturdivant, J. H., The Structure of Cyameluric Acid, Hydromelonic Acid and Related Substances. *Proceedings of the National Academy of Sciences of the United States of America* **1937,** *23* (12), 615-620.

4. Liu, A. Y.; Cohen, M. L., Prediction of New Low Compressibility Solids. *Science* **1989,** *245* (4920), 841-842.

5. Cohen, M. L., Predicting Useful Materials. *Science* **1993,** *261* (5119), 307-308.

6. Robertson, J.; Davis, C. A., Nitrogen Doping of Tetrahedral Amorphous-Carbon. *Diamond and Related Materials* **1995,** *4* (4), 441-444.

7. Silva, S. R. P., *Properties of Amorphous Carbon*. 1st ed.; INSPEC, Inc. The Institution of Electrical Engineers: London, **2003**.

8. Yoo, K.; Miller, B.; Kalish, R.; Shi, X., Electrodes of Nitrogen-Incorporated Tetrahedral Amorphous Carbon A Novel Thin-Film Electrocatalytic Material with Diamond-like Stability. *Electrochemical and Solid-State Letters* **1999,** *2* (5), 233-235.

9. Kamata, T.; Kato, D.; Hirono, S.; Niwa, O., Structure and Electrochemical Performance of Nitrogen-Doped Carbon Film Formed by Electron Cyclotron Resonance Sputtering. *Analytical Chemistry* **2013,** *85* (20), 9845-9851.

10. Yang, X. Y.; Hubold, L.; DeVivo, G.; Swain, G. M., Electroanalytical performance of nitrogen-containing tetrahedral amorphous carbon thin-film electrodes. *Abstracts of Papers of the American Chemical Society* **2012,** *244*.

11. Perini, L.; Durante, C.; Favaro, M.; Agnoli, S.; Granozzi, G.; Gennaro, A., Electrocatalysis at palladium nanoparticles: Effect of the support nitrogen doping on the catalytic activation of carbon-halogen bond. *Applied Catalysis B - Environmental* **2014,** *144*, 300-307.

12. Gai, P.; Zhang, H.; Zhang, Y.; Liu, W.; Zhu, G.; Zhang, X.; Chen, J., Simultaneous electrochemical detection of ascorbic acid, dopamine and uric acid based on nitrogen doped porous carbon nanopolyhedra. *Journal of Materials Chemistry B* **2013,** *1* (21), 2742-2749.

13. Fellinger, T.-P.; Hasché, F.; Strasser, P.; Antonietti, M., Mesoporous Nitrogen-Doped Carbon for the Electrocatalytic Synthesis of Hydrogen Peroxide. *Journal of the American Chemical Society* **2012,** *134* (9), 4072-4075.

14. Perazzolo, V.; Durante, C.; Pilot, R.; Paduano, A.; Zheng, J.; Rizzi, G. A.; Martucci, A.; Granozzi, G.; Gennaro, A., Nitrogen and sulfur doped mesoporous carbon as metal-free electrocatalysts for the in situ production of hydrogen peroxide. *Carbon* **2015,** *95*, 949-963.

15. Guo, D.; Shibuya, R.; Akiba, C.; Saji, S.; Kondo, T.; Nakamura, J., Active sites of nitrogen-doped carbon materials for oxygen reduction reaction clarified using model catalysts. *Science* **2016,** *351* (6271), 361-365.

16. Zhang, J.; Xia, Z.; Dai, L., Carbon-based electrocatalysts for advanced energy conversion and storage. *Science Advances* **2015,** *1* (7).

17. Mamtani, K.; Ozkan, U. S., Heteroatom-Doped Carbon Nanostructures as Oxygen Reduction Reaction Catalysts in Acidic Media: An Overview. *Catalysis Letters* **2015,** *145* (1), 436-450.

18. Ge, X.; Sumboja, A.; Wuu, D.; An, T.; Li, B.; Goh, F. W. T.; Hor, T. S. A.; Zong, Y.; Liu, Z., Oxygen Reduction in Alkaline Media: From Mechanisms to Recent Advances of Catalysts. *ACS Catalysis* **2015,** *5* (8), 4643-4667.

19. Wang, L.; Yin, F.; Yao, C., N-doped graphene as a bifunctional electrocatalyst for oxygen reduction and oxygen evolution reactions in an alkaline electrolyte. *International Journal of Hydrogen Energy* **2014,** *39* (28), 15913-15919.

20. Ikeda, T.; Hou, Z.; Chai, G.-L.; Terakura, K., Possible Oxygen Reduction Reactions for Graphene Edges from First Principles. *The Journal of Physical Chemistry C* **2014,** *118* (31), 17616-17625.

21. Bao, X.; Nie, X.; von Deak, D.; Biddinger, E. J.; Luo, W.; Asthagiri, A.; Ozkan, U. S.; Hadad, C. M., A First-Principles Study of the Role of Quaternary-N Doping on the Oxygen Reduction Reaction Activity and Selectivity of Graphene Edge Sites. *Topics in Catalysis* **2013,** *56* (18), 1623-1633.

22. Wang, Z.; Li, P.; Chen, Y.; Liu, J.; Tian, H.; Zhou, J.; Zhang, W.; Li, Y., Synthesis of nitrogen-doped graphene by chemical vapour deposition using melamine as the sole solid source of carbon and nitrogen. *Journal of Materials Chemistry C* **2014,** *2* (35), 7396-7401.

23. Yasuda, S.; Yu, L.; Kim, J.; Murakoshi, K., Selective nitrogen doping in graphene for oxygen reduction reactions. *Chemical Communications* **2013,** *49* (83), 9627-9629.

24. Lai, L.; Potts, J. R.; Zhan, D.; Wang, L.; Poh, C. K.; Tang, C.; Gong, H.; Shen, Z.; Lin, J.; Ruoff, R. S., Exploration of the active center structure of nitrogen-doped graphene-based catalysts for oxygen reduction reaction. *Energy & Environmental Science* **2012,** *5* (7), 7936-7942.

25. Ikeda, T.; Boero, M.; Huang, S.-F.; Terakura, K.; Oshima, M.; Ozaki, J.-i., Carbon Alloy Catalysts: Active Sites for Oxygen Reduction Reaction. *The Journal of Physical Chemistry C* **2008,** *112* (38), 14706-14709.

26. Favaro, M.; Perini, L.; Agnoli, S.; Durante, C.; Granozzi, G.; Gennaro, A., Electrochemical behavior of N and Ar implanted highly oriented pyrolytic graphite substrates and activity toward oxygen reduction reaction. *Electrochimica Acta* **2013,** *88*, 477-487.

27. Shin, W. H.; Jeong, H. M.; Kim, B. G.; Kang, J. K.; Choi, J. W., Nitrogen-Doped Multiwall Carbon Nanotubes for Lithium Storage with Extremely High Capacity. *Nano Letters* **2012,** *12* (5), 2283-2288.

28. Morcos, I.; Yeager, E., Kinetic studies of the oxygen—peroxide couple on pyrolytic graphite. *Electrochimica Acta* **1970,** *15* (6), 953-975.

29. Stamatin, S. N.; Hussainova, I.; Ivanov, R.; Colavita, P. E., Quantifying Graphitic Edge Exposure in Graphene-Based Materials and Its Role in Oxygen Reduction Reactions. *ACS Catalysis* **2016,** *6* (8), 5215-5221.

30. Maldonado, S.; Morin, S.; Stevenson, K. J., Structure, composition, and chemical reactivity of carbon nanotubes by selective nitrogen doping. *Carbon* **2006,** *44* (8), 1429-1437.

31. Deng, D.; Yu, L.; Pan, X.; Wang, S.; Chen, X.; Hu, P.; Sun, L.; Bao, X., Size effect of graphene on electrocatalytic activation of oxygen. *Chemical Communications* **2011,** *47* (36), 10016-10018.

32. Jeon, I.-Y.; Zhang, S.; Zhang, L.; Choi, H.-J.; Seo, J.-M.; Xia, Z.; Dai, L.; Baek, J.-B., Edge-Selectively Sulfurized Graphene Nanoplatelets as Efficient Metal-Free Electrocatalysts for Oxygen Reduction Reaction: The Electron Spin Effect. *Advanced Materials* **2013,** *25* (42), 6138-6145.

33. Chen, P.; Fryling, M. A.; McCreery, R. L., Electron Transfer Kinetics at Modified Carbon Electrode Surfaces: The Role of Specific Surface Sites. *Analytical Chemistry* **1995,** *67* (18), 3115-3122.

34. Chen, L.-F.; Zhang, X.-D.; Liang, H.-W.; Kong, M.; Guan, Q.-F.; Chen, P.; Wu, Z.-Y.; Yu, S.-H., Synthesis of Nitrogen-Doped Porous Carbon Nanofibers as an Efficient Electrode Material for Supercapacitors. *ACS Nano* **2012,** *6* (8), 7092-7102.

35. Nair, N.; Kim, W.-J.; Usrey, M. L.; Strano, M. S., A Structure−Reactivity Relationship for Single Walled Carbon Nanotubes Reacting with 4-Hydroxybenzene Diazonium Salt. *Journal of the American Chemical Society* **2007,** *129* (13), 3946-3954.

36. Sharma, R.; Nair, N.; Strano, M. S., Structure−Reactivity Relationships for Graphene Nanoribbons. *The Journal of Physical Chemistry C* **2009,** *113* (33), 14771-14777.

37. Strano, M. S.; Dyke, C. A.; Usrey, M. L.; Barone, P. W.; Allen, M. J.; Shan, H.; Kittrell, C.; Hauge, R. H.; Tour, J. M.; Smalley, R. E., Electronic Structure Control of Single-Walled Carbon Nanotube Functionalization. *Science* **2003,** *301* (5639), 1519.

38. Heller, I.; Kong, J.; Williams, K. A.; Dekker, C.; Lemay, S. G., Electrochemistry at Single-Walled Carbon Nanotubes: The Role of Band Structure and Quantum Capacitance. *Journal of the American Chemical Society* **2006,** *128* (22), 7353-7359.

39. Zhong, J.-H.; Zhang, J.; Jin, X.; Liu, J.-Y.; Li, Q.; Li, M.-H.; Cai, W.; Wu, D.-Y.; Zhan, D.; Ren, B., Quantitative Correlation between Defect Density and Heterogeneous Electron Transfer Rate of Single Layer Graphene. *Journal of the American Chemical Society* **2014,** *136* (47), 16609-16617.

40. Batchelor-McAuley, C.; Laborda, E.; Henstridge, M. C.; Nissim, R.; Compton, R. G., Reply to comments contained in "Are the reactions of quinones on graphite adiabatic?", by N.B. Luque, W. Schmickler. *Electrochimica Acta* **2013,** *88*, 895-898.

41. Nissim, R.; Batchelor-McAuley, C.; Henstridge, M. C.; Compton, R. G., Electrode kinetics at carbon electrodes and the density of electronic states. *Chemical Communications* **2012,** *48* (27), 3294-3296.

42. Unwin, P. R.; Güell, A. G.; Zhang, G., Nanoscale Electrochemistry of sp2 Carbon Materials: From Graphite and Graphene to Carbon Nanotubes. *Accounts of Chemical Research* **2016,** *49* (9), 2041-2048.

43. Cachet, H.; Deslouis, C.; Chouiki, M.; Saidani, B.; Conway, N. M. J.; Godet, C., Electrochemistry of Nitrogen-Incorporated Hydrogenated Amorphous Carbon Films. *Journal of The Electrochemical Society* **2002,** *149* (7), E233-E241.

44. Zeng, A. P.; Bilek, M. M. M.; McKenzie, D. R.; Lay, P. A., Correlation of film structure and molecular oxygen reduction at nitrogen doped amorphous carbon thin film electrochemical electrodes. *Diamond and Related Materials* **2009,** *18* (9), 1102-1108.

45. Chen, J. Y.; Wang, X.; Cui, X. Q.; Yang, G. M.; Zheng, W. T., One-step synthesis of N-doped amorphous carbon at relatively low temperature as excellent metal-free electrocatalyst for oxygen reduction. *Cataysisl Communications* **2014,** *46*, 161-164.

46. Chen, J.; Wang, X.; Cui, X.; Yang, G.; Zheng, W., Amorphous carbon enriched with pyridinic nitrogen as an efficient metal-free electrocatalyst for oxygen reduction reaction. *Chemical Communications* **2014,** *50* (5), 557-559.

47. Choi, C. H.; Lim, H.-K.; Chung, M. W.; Park, J. C.; Shin, H.; Kim, H.; Woo, S. I., Long-Range Electron Transfer over Graphene-Based Catalyst for High-Performing Oxygen Reduction Reactions: Importance of Size, N-doping, and Metallic Impurities. *Journal of the American Chemical Society* **2014,** *136* (25), 9070-9077.

48. Dearnaley, G.; Arps, J. H., Biomedical applications of diamond-like carbon (DLC) coatings: A review. *Surface and Coatings Technology* **2005,** *200* (7), 2518-2524.

49. Peng, X.; Barber, Z.; Clyne, T., Surface roughness of diamond-like carbon films prepared using various techniques. *Surface and Coatings Technology* **2001,** *138* (1), 23-32.

50. Alibart, F.; Durand Drouhin, O.; Debiemme-Chouvy, C.; Benlahsen, M., Relationship between the structure and the optical and electrical properties of reactively sputtered carbon nitride films. *Solid State Communications* **2008,** *145* (7–8), 392-396.

51. Alibart, F.; Lejeune, M.; Zellama, K.; Benlahsen, M., Effect of nitrogen on the optoelectronic properties of a highly sp(2)-rich amorphous carbon nitride films. *Diamond and Related Materials* **2011,** *20* (3), 409-412.

52. Hellgren, N.; Johansson, M. P.; Broitman, E.; Hultman, L.; Sundgren, J.-E., Role of nitrogen in the formation of hard and elastic CN_x thin films by reactive magnetron sputtering. *Physical Review B* **1999,** *59* (7), 5162-5169.

53. Hellgren, N.; Johansson, M. P.; Broitman, E.; Sandström, P.; Hultman, L.; Sundgren, J.-E., Effect of chemical sputtering on the growth and structural evolution of magnetron sputtered CNx thin films. *Thin Solid Films* **2001,** *382* (1–2), 146-152.

54. Rodil, S.; Morrison, N.; Robertson, J.; Milne, W., Nitrogen incorporation into tetrahedral hydrogenated amorphous carbon. *Physica Status Solidi (a)* **1999,** *174* (1), 25-37.

55. Sharifi, T.; Hu, G.; Jia, X.; Wågberg, T., Formation of Active Sites for Oxygen Reduction Reactions by Transformation of Nitrogen Functionalities in Nitrogen-Doped Carbon Nanotubes. *ACS Nano* **2012,** *6* (10), 8904-8912.

56. Biniak, S.; Szymański, G.; Siedlewski, J.; Świtkowski, A., The characterization of activated carbons with oxygen and nitrogen surface groups. *Carbon* **1997,** *35* (12), 1799-1810.

57. Cullen, R. J.; Jayasundara, D. R.; Soldi, L.; Cheng, J. J.; Dufaure, G.; Colavita, P. E., Spontaneous Grafting of Nitrophenyl Groups on Amorphous Carbon Thin Films: A Structure–Reactivity Investigation. *Chemistry of Materials* **2012,** *24* (6), 1031-1040.

58. Murphy, D. M.; Cullen, R. J.; Jayasundara, D. R.; Scanlan, E. M.; Colavita, P. E., Study of the spontaneous attachment of polycyclic aryldiazonium salts onto amorphous carbon substrates. *RSC Advances* **2012,** *2* (16), 6527-6534.

59. Jayasundara, D. R.; Cullen, R. J.; Colavita, P. E., In Situ and Real Time Characterization of Spontaneous Grafting of Aryldiazonium Salts at Carbon Surfaces. *Chemistry of Materials* **2013,** *25* (7), 1144-1152.

60. Williams, M. W.; Arakawa, E. T., Optical properties of glassy carbon from 0 to 82 eV. *Journal of Applied Physics* **1972,** *43* (8), 3460-3463.

61. Mednikarov, B.; Spasov, G.; Babeva, T.; Pirov, J.; Sahatchieva, M.; Popova, C.; Kulischa, W., Optical properties of diamond-like carbon and nanocrystalline diamond films. *Journal of Optoelectronics and Advanced Materials* **2005,** *7* (3), 1407-1413.

62. Shi, X.; Fu, H.; Shi, J. R.; Cheah, L. K.; Tay, B. K.; Hui, P., Electronic transport properties of nitrogen doped amorphous carbon films deposited by the filtered cathodic vacuum arc technique. *Journal of Physics: Condensed Matter* **1998,** *10* (41), 9293.

63. Rodil, S. E.; Muhl, S.; Maca, S.; Ferrari, A. C., Optical gap in carbon nitride films. *Thin Solid Films* **2003,** *433* (1-2), 119-125.

64. McCreery, R. L., Advanced carbon electrode materials for molecular electrochemistry. *Chemical Reviews* **2008,** *108* (7), 2646-87.

65. Amatore, C., Savéant, J.M., Tessier, D., Charge transfer at partially blocked surfaces: a model for the case of microscopic active and inactive sites, *Journal of Electroanalytical Chemistry and Interfacial Electrochemistry* **1983,** *147* (1-2), 39-51.

66. Orazem, M. E.; Tribolet, B., *Electrochemical Impedance Spectroscopy*. Wiley: **2008**.

67. Filipe, O. M. S.; Brett, C. M. A., Characterization of Carbon Film Electrodes for Electroanalysis by Electrochemical Impedance. *Electroanalysis* **2004,** *16* (12), 994-1001.

68. Pleskov, Y. V.; Evstefeeva, Y. E.; Krotova, M. D.; Elkin, V. V.; Baranov, A. M.; Dement'ev, A. P., Electrochemical behavior of amorphous carbon films: kinetic and impedance-spectroscopy studies. *Diamond and Related Materials* **1999,** *8* (1), 64-72.

69. Morrison, S. R., *Electrochemistry at Semiconductor and Oxidised Metal Electrodes*. 1st ed.; Plenum Press: **1980**.

70. Mark E. Orazem, B. T., *Electrochemical Impedance Spectroscopy*. Wiley: **2008**.

71. Kobayashi, K.; Takata, M.; Okamoto, S.; Sukigara, M., AC impedance theory for surface states at a semiconductor—liquid junction. *Journal of Electroanalytical Chemistry and Interfacial Electrochemistry* **1985,** *185* (1), 47-60.

72. Xiong, L.; Batchelor-McAuley, C.; Ward, K. R.; Downing, C.; Hartshorne, R. S.; Lawrence, N. S.; Compton, R. G., Voltammetry at graphite electrodes: The oxidation of hexacyanoferrate (II) (ferrocyanide) does not exhibit pure outer-sphere electron transfer kinetics and is sensitive to pre-exposure of the electrode to organic solvents. *Journal of Electroanalytical Chemistry* **2011,** *661* (1), 144-149.

73. Swaddle, T. W., Homogeneous versus Heterogeneous Self-Exchange Electron Transfer Reactions of Metal Complexes: Insights from Pressure Effects. *Chemical Reviews* **2005,** *105* (6), 2573-2608.

74. Peter, L. M.; Dürr, W.; Bindra, P.; Gerischer, H., The influence of alkali metal cations on the rate of the $Fe(CN)_6^{4-}/Fe(CN)_6^{3-}$ electrode process. *Journal of Electroanalytical Chemistry and Interfacial Electrochemistry* **1976,** *71* (1), 31-50.

75. Dogonadze, R. R.; Ulstrup, J.; Kharkats, Y. I., A theory of electrode reactions through bridge transition states; bridges with a discrete electronic spectrum. *Journal of Electroanalytical Chemistry and Interfacial Electrochemistry* **1972,** *39* (1), 47-61.

76. Chen, P.; McCreery, R. L., Control of Electron Transfer Kinetics at Glassy Carbon Electrodes by Specific Surface Modification. *Analytical Chemistry* **1996,** *68* (22), 3958-3965.

77. Granger, M. C.; Swain, G. M., The Influence of Surface Interactions on the Reversibility of Ferri/Ferrocyanide at Boron-Doped Diamond Thin-Film Electrodes. *Journal of The Electrochemical Society* **1999,** *146* (12), 4551-4558.

78. Zen, F.; Angione, M. D.; Behan, J. A.; Cullen, R. J.; Duff, T.; Vasconcelos, J. M.; Scanlan, E. M.; Colavita, P. E., Modulation of Protein Fouling and Interfacial Properties at Carbon Surfaces via Immobilization of Glycans Using Aryldiazonium Chemistry. *Scientific Reports* **2016,** *6*, 24840.

79. Wang, Y.; Limon-Petersen, J. G.; Compton, R. G., Measurement of the diffusion coefficients of [Ru (NH3) 6] 3+ and [Ru (NH3) 6] 2+ in aqueous solution using microelectrode double potential step chronoamperometry. *Journal of Electroanalytical Chemistry* **2011,** *652* (1-2), 13-17.

CHAPTER IV

Electrochemistry of Catechols on Carbon and Nitrogenated Carbon Surfaces

Catechols are a class of biologically-relevant molecules with a rich and complex redox chemistry. The electrochemical response of catechols is known to be highly dependent on the electrode surface preparation and the solution pH. In this Chapter, voltammetric studies of catechol electrochemistry on carbon surfaces are presented. Two different probes are studied: dopamine and 4-methyl catechol. The effect of surface pre-treatment on the response is first investigated using glassy carbon electrodes which are subjected to a number of different surface pre-treatments including electrochemical anodisation and thermal annealing. Experimental results are supported by density functional theory (DFT) calculations on model carbon cluster surfaces. Finally, the response on as-deposited a-C:N surfaces which were previously characterised using outer-sphere redox probes in Chapter III is also presented, in order to contrast the differences in electrochemical behaviour when the surface chemistry is also important.

DFT calculations were accomplished in collaboration with Prof. Max García Melchor and Dr. Laia Vilella-Aribas of the School of Chemistry, TCD. The author is also indebted to Filip Grajkowski, an undergraduate project student who contributed some of the voltammetric data discussed herein.

4. Introduction

Catechols are an important class of biomolecules with particular relevance to neurochemistry. Abnormal levels of catecholamines such as dopamine (DA) have been linked in psychiatric disorders such as depression,[1-2] schizophrenia,[3] and parkinson's disease.[4] The elevation of DA levels in the synapses of dopaminergic neurons by stimulant use has also been implicated in the pathogenesis of addiction. [5] The quantification of catechol concentrations both *in vivo* and through the *ex situ* analysis of biological fluids has often been accomplished electrochemically as reviewed recently by Jacowska and Krysinski.[6]

Carbon materials have been applied as biosensors for catecholamines because of their low cost, biocompatibility, and versatility. Amperometric sensors for DA based on carbon paste electrodes,[7] carbon fibers [8] boron doped diamond [9] and glassy carbon [10] have been prepared. Due to the interference of co-analytes such as ascorbic acid, which has a similar reduction potential to catechols, researchers have employed methodologies such as the immobilization of enzymes at the electrode surface [9] doping the carbon scaffold with nitrogen[11-12] and other pre-treatments of the carbon surface in order to improve selectivity.

Catechol oxidation is complex and has been described according to the 9-membered scheme-of-squares, [13] which involves the net transfer of 2 protons and 2 electrons from the catechol, [14-15] as shown in Figure 4.1**.** The mechanism is pH-dependent; for instance, under basic conditions the pathway involves the transfer of 2 electrons from a deprotonated catechol C^{2-} to form a quinone species C as shown in the top row of the figure. At low pH the catechol is expected to exist predominantly in its monoprotonated CH^{-} form or the diprotonated CH_2 form, implying that proton transfers must occur at some point in the reaction mechanism. The order of the reaction steps at pH 1 is known to be $e \rightarrow H^{+} \rightarrow e \rightarrow H^{+}$.[16]

In addition to the complex reaction scheme, the kinetics of catechol oxidation at carbon surfaces are known to be highly sensitive to the electrode preparation, including the polishing and cleaning steps, exposure to organic solvents and any surface pre-treatments employed. For glassy carbon (GC) the literature is replete with methodologies for surface pre-treatments, both electrochemical and otherwise, which accelerate the charge transfer kinetics. It is difficult to specify which of these protocols (if any) is the most effective, as reports in the literature are often contradictory; for instance, electrochemical oxidation of glassy carbon has been reported to induce catechol adsorption by some groups [17] whilst

others have reported a positive effect on the electron transfer kinetics after oxidative treatments in the absence of adsorption.[18]

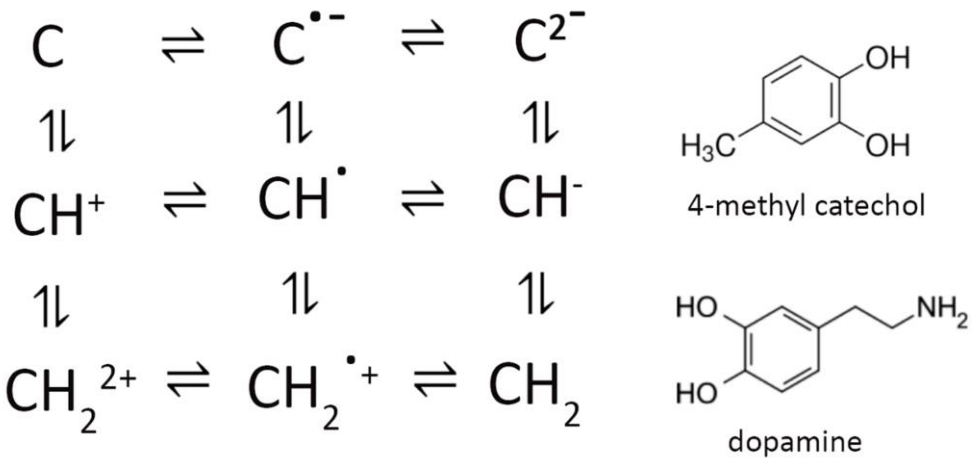

Figure 4.1. Left - 'Scheme of squares' illustrating possible pathways for the 2-electron, 2-proton oxidation of a generic catechol (CH_2). Right – chemical structures of two catechols studied in this chapter: dopamine and 4-methyl catechol.

It is generally thought that adsorption facilitates the inner-sphere redox process via a self-catalytic process which was proposed to involve interactions between adsorbates and solution-phase catechol. Although the precise catalytic mechanism is uncertain, hydrogen-bonding interactions involving the hydroxyl groups of catechol and the C=O of adsorbed quinone were suggested.[17] The chemisorption of blocking organic monolayers which impede catechol adsorption has an inhibitory effect on the kinetics of charge transfer to catechols, an important exception being when the adsorbed species resembles a quinone.[17]

In this case adsorption of the catechol from solution is inhibited but the electron transfer is quasi-reversible. This suggests that it is not adsorption *per se*, but rather the presence of particular surface oxide moieties introduced at the surface by adsorption which facilitate charge transfer to catechols in solution. If this were the case, electrode activation towards catechols through oxidative pre-treatment might be explained if these protocols also introduce these oxide moieties at the electrode surface.

The purpose of this chapter is to provide some clarity regarding the effects of carbon surface pre-treatment on the kinetics of catechol oxidation. This is accomplished by producing GC electrodes with well-defined surface chemistry via simple pre-treatment protocols and correlating the properties of each surface to the kinetics of catechol oxidation. Two catechols were chosen for these studies, 2-(3,4-Dihydroxyphenyl)ethylamine,

henceforth referred to as dopamine (DA), and 4-methyl catechol (4-MC). GC discs subjected to two different pre-treatments, thermal annealing and electrochemical anodisation, were chosen as the model electrodes. These protocols are known to produce surfaces with radically different oxygen contents.[19]

The electron transfer kinetics on each GC surface are evaluated using cyclic voltammetry studies and these results are correlated to the surface composition as determined from XPS measurements. Results indicate that catechol adsorption does not occur on highly oxidised GC surfaces prepared via anodisation although charge transfer occurs quasi-reversibly to both catechols. Thermal annealing produces a low-oxygen content surface on which both DA and 4-MC readily adsorb, resulting in reversible charge transfer kinetics to the catechol in solution.

Based on a careful analysis of the C 1s envelopes of each surface, the tendency for both catechols to adsorb only on the annealed surface is correlated to the graphitization of the GC surface induced by the heat treatment. Conclusions derived from the experimental results are supported by DFT calculations on model carbon clusters. Finally, the redox response of the a-C and a-C:N electrode surfaces introduced in the previous chapter towards DA oxidation is also presented, in order to investigate the effects of nitrogen incorporation on the electrochemical response.

4.1 Results and Discussion

In order to investigate the effects of surface treatments on catechol kinetics, glassy carbon electrodes were prepared using three different methodologies. A polishing protocol using successively finer grades of alumina slurry (1µm, 0.3 µm and 0.05 µm) along with abundant ultrasonication was employed in each case as described in detail in the previous chapter and in the experimental section of this chapter (*vide infra).* GC discs used for electrochemical studies without further treatment are referred to as 'polished GC.'

Two other surface treatments were also employed to induce significant structural and chemical changes in the GC surface. The first of these was an oxidation via electrochemical anodisation at a potential of 1.8 V vs Ag/AgCl (sat) in 0.1 M KOH for 20 s. These GC discs are termed 'anodised GC'. The second treatment employed was a thermal annealing under inert atmosphere in a tube furnace at a temperature of 900 ^{o}C for 1 hr. These GC discs are denoted 'annealed GC'. The chemical composition of all three of these surfaces was studied using XPS, whilst the charge transfer kinetics in catechol solutions were evaluated using cyclic voltammetry experiments.

Cyclic Voltammetry of Dopamine on GC Surfaces

A typical voltammogram obtained in solutions of 1 mM DA / 0.1 M H_2SO_4 is shown in Figure 4.2. A broad waveform with a large value of the peak-to-peak separation, ΔE of 220 mV is obtained even at the low scan rate of 5 mVs^{-1}, suggesting that charge transfer to DA is electrochemically irreversible. CVs obtained in background electrolyte only are devoid of any redox peaks attributable to Faradaic processes occurring at the electrode surface; the current measured can be entirely attributed to the double layer charging current. H_2SO_4 solution was chosen to avoid the fouling of the electrode surface which has been shown to occur under neutral and basic conditions due to the intramolecular cyclisation and subsequent polymerisation of the quinone product. [16]

The broad, asymmetric waveform for DA oxidation and reduction seen in Figure 4.2 on polished GC has been observed previously.[16] Referring to the scheme-of-squares for DA oxidation, it is consistent with a mechanism where the first electron transfer is the rate determining step.[20] This conclusion is supported by Tafel analysis of the rising part of the wave on the anodic sweep as highlighted in Figure 4.2 and plotted in the inset. The Tafel slope of the linear fit to this data results in a value of the effective transfer coefficient, (n + α),

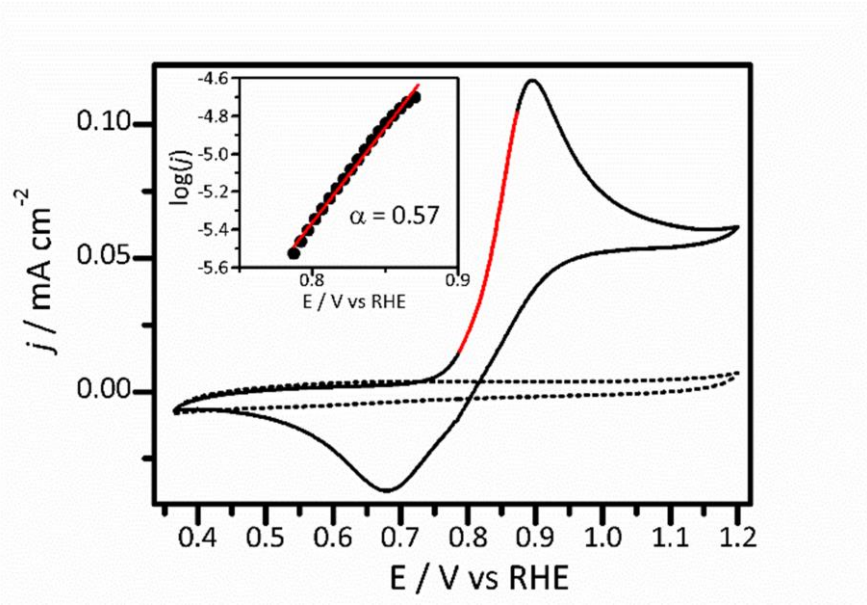

Figure 4.2. Cyclic voltammogram of a polished GC electrode immersed in a solution of 1mM DA in 0.1 M H_2SO_4. Dashed line: CV in background electrolyte, 0.1M H_2SO_4, only. Inset: Tafel plot for the region highlighted in red on the voltammogram. Scan rate: 5 mV s^{-1}

of 0.57, which is close to the value of 0.5 expected for an overall 2 e^- process where the first electron transfer step is rate determining.

The redox response of polished GC in 1mM DA solution at various scan rates is shown in Figure 4.3. As shown in the figure, ΔE increases with increasing scan rate as expected for an irreversible charge transfer process. The peak current density, j_p, increases with the square root of the scan rate, $\nu^{1/2}$ as shown in the inset of the figure. Using the value of 0.1963 cm^2 for the electrode area, $\alpha = 0.5$ and 6.6 x 10^{-6} cm^2 s^{-1} for the diffusion coefficient of DA determined from rotating disk electrode measurements (*vide infra*), the slope of 0.0012 mA cm^{-2} $(Vs^{-1})^{-1/2}$ is consistent with an irreversible charge transfer process resulting in the net charge transfer of 2 electrons according to Equation 4.1: [20]

$$j_p = -0.496\sqrt{n+\alpha}nFc\sqrt{\frac{F\nu D}{RT}} \quad (4.1)$$

The sluggish charge transfer kinetics of DA on polished GC may potentially be attributed to two different factors: the inherent absence of catalytic oxygen moieties at the polished GC surface and the blocking of potentially reactive sites by polishing debris which is not readily removed even by ultrasonication. A methodology for the preparation of a reproducible GC surface with extensive oxygen termination using electrochemical anodisation has been

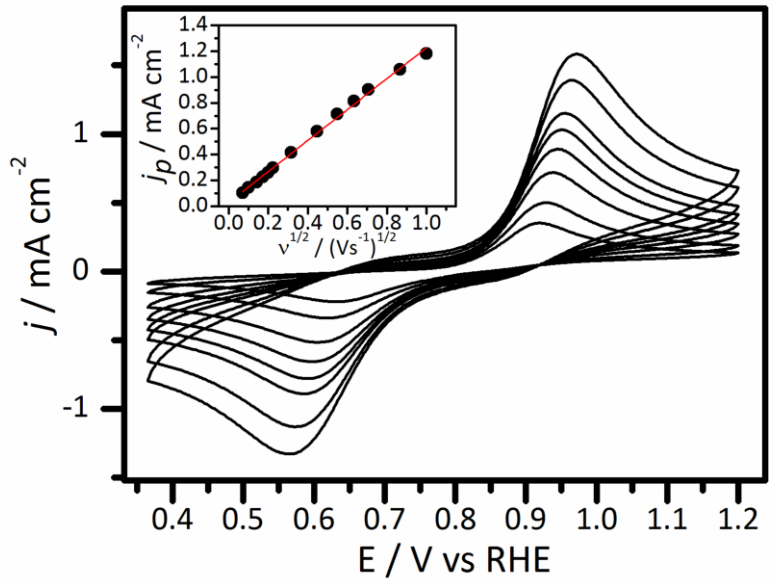

Figure 4.3. Voltammograms for a GC disk in 1 mM DA / 0.1 M H_2SO_4 at scan rates between 5 mV s^{-1} and 1 V s^{-1}. The inset shows a plot of the peak current density, j_p, on the anodic scan versus the square root of the scan rate.

described by McDermott et al. [21] and was shown to expose a fresh GC surface free from the

interference of blocking species and other surface debris which may be introduced by polishing methods.

A representative voltammogram of such an anodised GC disk in 1 mM DA / 0.1 M H_2SO_4 solution is shown in Figure 4.4. The voltammogram has a small ΔE value of 34 mV, which is close to the theoretical value of 59/2 mV for a reversible $2e^-$ charge transfer, suggesting that the anodisation protocol results in a GC surface with quasi-reversible charge transfer kinetics. The peak current densities of the cathodic ($j_{p,c}$) and anodic ($j_{p,a}$) scans are similar, yielding a value of $j_{p,c}/j_{p,a}$ = 0.86, close to the ideal value of 1 for a fully reversible process. Tafel analysis of the rising part of the anodic peak results in a value of (n + α) close to 1.7. Assuming that the α value for each electron transfer step is close to 0.5, this result suggests that n = 1 *i.e.* that one electron is transferred prior to the rate determining step. This implies that the second electron transfer in the scheme-of-squares, the reaction of $CH^{\bullet} \rightleftharpoons CH^+ + e^-$ in Figure 4.1, is the rate determining step on the anodised GC surface.

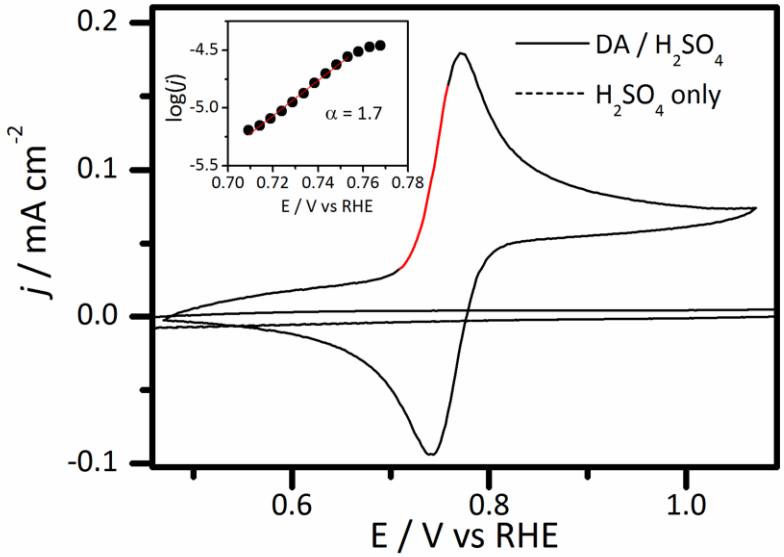

Figure 4.4. CV for an anodised GC disk in a solution of 1 mM DA / 0.1 M H_2SO_4 and background electrolyte, 0.1M H_2SO_4 only. The inset shows a Tafel plot derived from the highlighted region of the voltammogram.

Figure 4.5 a) shows CVs obtained in 1 mM DA / 0.1 M H_2SO_4 with an anodised GC disk at scan rates up to 0.5 V s^{-1}. The ΔE value increases slightly with scan rate but remains generally close to 40 mV. The plot of peak current density versus $v^{1/2}$ shown in Figure 4 b) has a slope of 2.33 x 10^{-3} C $s^{-1/2}$ $V^{1/2}$ which is close to the theoretical value for a reversible

2-electron process as described by Equation 5.2. The anodisation pre-treatment is therefore highly effective at producing a GC surface with rapid charge transfer kinetics.

$$j_p = 0.446nFc\sqrt{\frac{nF\upsilon D}{RT}} \tag{4.2}$$

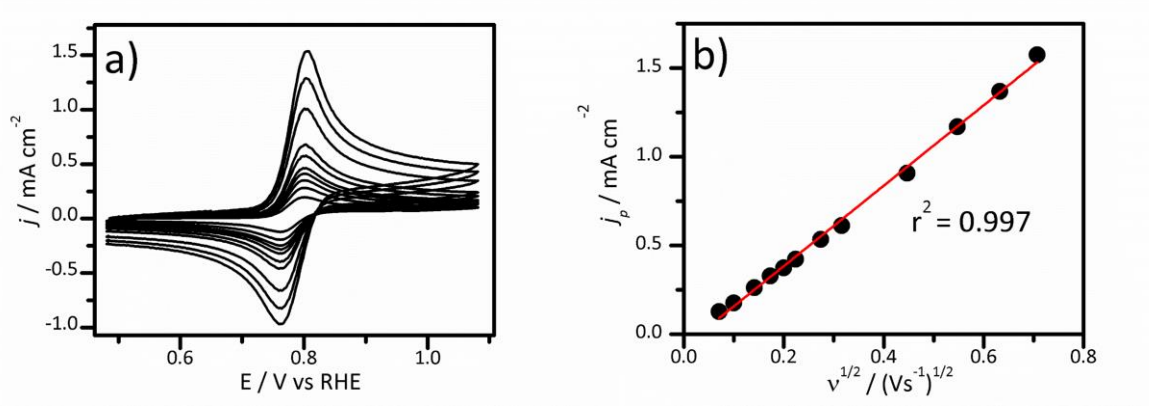

Figure 4.5. a) CVs at scan rates between 5 mVs^{-1} and 500 mV s^{-1} for an anodised GC disk in a solution of 1mM DA / 0.1 M H_2SO_4. b) Peak current density versus $\nu^{1/2}$ derived from the voltammograms in a).

The third surface pre-treatment protocol used in this study involved thermal annealing of a polished GC disk at 900 ^oC. Heat treatments including vacuum annealing and laser activation of GC surfaces have also been employed to prepare a clean surface reproducibly.[22] Figure 4.6 shows a CV at a scan rate of 5 mV s^{-1} for an annealed GC disk in a solution of 1 mM DA / 0.1 M H_2SO_4. The ΔE value of 30 mV s^{-1} is consistent with reversible electron transfer for a 2-electron process, as is the $j_{p,c}/j_{p,a}$ = 0.91. Tafel analysis of the anodic wave yields an effective value of α = 1.2, which is close to the value of α = 1 expected for a Nernstian process. The thermal annealing treatment is therefore the most effective surface preparation method of the three studied in terms of catalysing electron transfer to DA.

Rapid electron transfer to catechols has been attributed to a 'self-catalysis' mechanism[23] whereby adsorption of catechol at the electrode surface facilitates electron transfer to catechols in the solution phase. Adsorbed catechols are themselves redox active[16, 24] and should be detectable via voltammetry at higher scan rates, where the contribution of adsorbed species to the Faradaic current is expected to be maximal.[25] This was investigated for the annealed GC surface in Figure 4.7 a). As shown in the figure, voltammograms obtained at lower scan rates close to 50 mV s^{-1} have a similar form to the CV obtained at

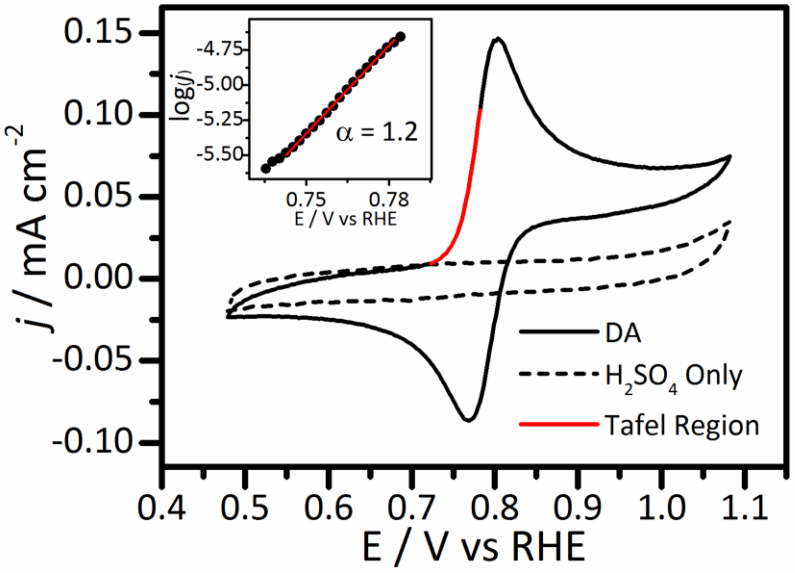

Figure 4.6. CV for an annealed GC disc in a solution of 1mM DA / 0.1 M H_2SO_4 and background electrolyte, 0.1 M H_2SO_4 only. The inset shows the Tafel plot derived from the highlighted region of the voltammogram.

5 mV s^{-1} in Figure 4.6**,** *i.e.* they have ΔE values close to 30 mV. As the scan rate increases, the voltammogram gradually becomes more symmetric in shape around the formal potential, $E^{0'}$ = 0.78 V vs RHE, and ΔE reduces in magnitude to values < 15 mV when the scan rate is 500 mV s^{-1}.

This behaviour is consistent with the presence of surface-bound DA. The peak current densities obtained from the CVs in Figure 4.7 a) are plotted in part b) of the figure. As shown in the figure, the scatter plot is linear with respect to the scan rate, ν, rather than $\nu^{1/2}$, which is the expected result for an adsorbed redox species described by Equation 4.3: [26]

$$i_p = \frac{n^2F^2\,\nu A\Gamma}{4RT} \tag{4.3}$$

Where Γ is the surface coverage of DA in mol cm^{-2} and A is the electrode area in cm^2. The Faradaic current at the annealed GC surface is therefore comprised of contributions from both adsorbed DA and solution-phase DA, with the relative contributions of each distinguished from one another by the scan rate employed during the experiment. This is best illustrated by re-writing Equation 4.3 in logarithmic form:

$$\ln(i_p) = \ln(v) + \ln(\frac{n^2F^2\mathrm{A}\Gamma}{4RT}) \tag{4.4}$$

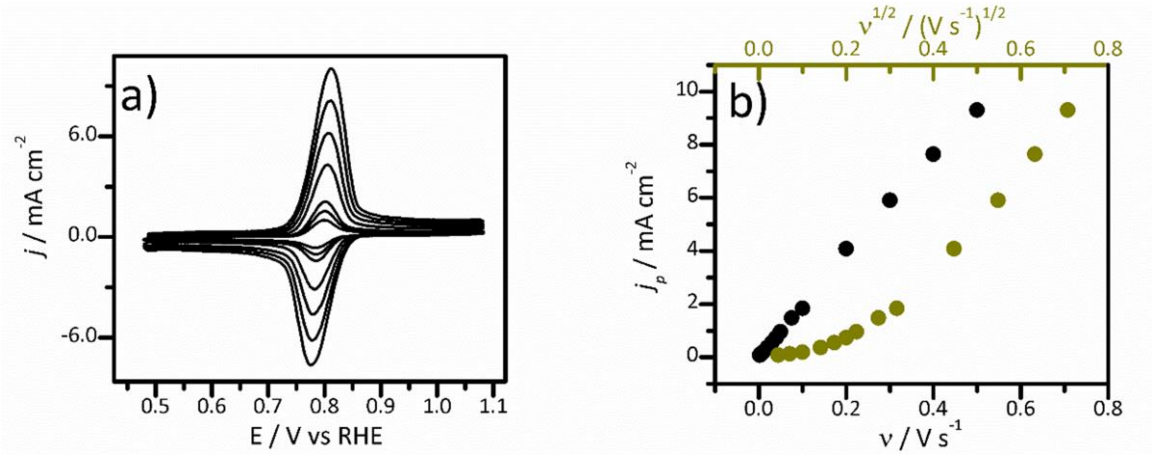

Figure 4.7. a) CVs for an annealed GC disk immersed in 1mM DA / 0.1 M H_2SO_4 at scan rates between 50 mV s^{-1} and 500 mVs^{-1}. b) plots of the peak current densities derived from the voltammograms in a) versus ν (black plot) and $\nu^{1/2}$ (gold plot).

In this format it is clear that a logarithmic plot of the peak currents versus the scan rate is linear with a theoretical slope of m = 1. Equation 4.2 may also be written in terms of the peak current in logarithmic form:

$$\ln(i_p) = 0.5\ln(v) + \ln(0.446n^{\frac{3}{2}}FAD^{\frac{1}{2}}c) \qquad (4.5)$$

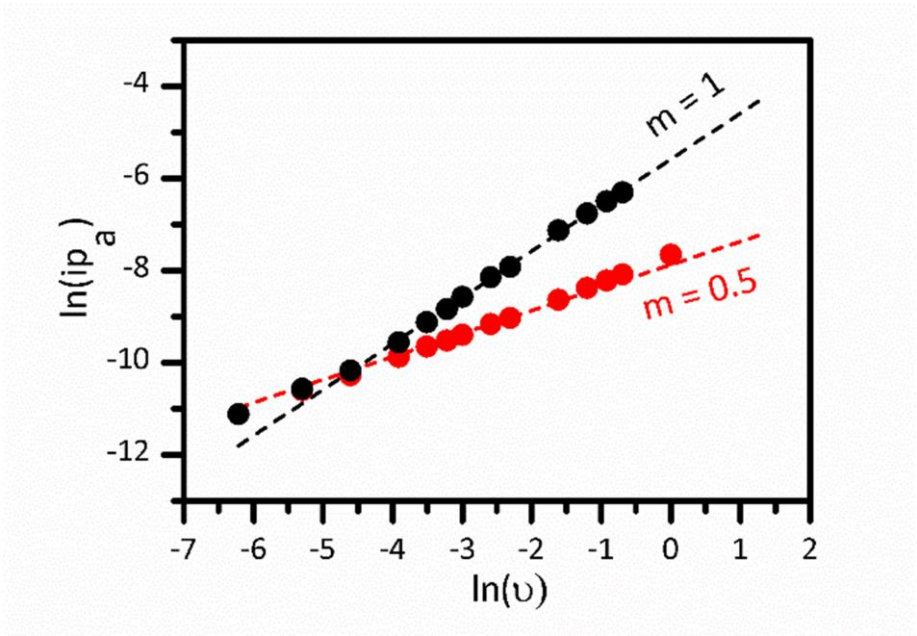

Figure 4.8. Plot of $\ln(i_{p,a})$ versus ln(ν) for annealed GC (black dots) and anodised GC (red dots). The dashed lines represent theoretical lines with slope m = 1 and m = 0.5 respectively and are present only to guide the eye.

Which is also a linear plot with m = 0.5. When the voltammetric response is not complicated by the effects of adsorbed DA, the logarithmic plot of the peak current versus the scan rate should therefore have a slope of m = 0.5. The logarithmic plots of peak current data versus scan rate for annealed and anodised GC are shown in Figure 4.8. For the anodised GC disk, the scatter plot falls on a theoretical line of slope m = 0.5, consistent with a diffusion-controlled process.

For the annealed disk the plot of $\ln(i_p)$ is also on the m = 0.5 line at low scan rates (< 100 mV s^{-1}) but the data points deviate significantly as the scan rate increases, falling instead on a line of m = 1. The crossover point from diffusion to adsorption predominance depends on the concentration of DA in solution as well as the scan rate.[25] Using a low concentration of 25 μM, the peak current is proportional to ν even at lower scan rates (Figure 4.9). There is also no evidence of any solution-phase DA contributing to the voltammogram at this low concentration; the voltammetric response is entirely dominated by adsorbed DA. The voltammetric studies in both 1.0 mM DA and 25 μM DA were carried

Table 4.1. Summary of voltammetric data for the oxidation of 1mM DA in 0.1 M H_2SO_4 on GC electrodes with different surface preparation methods. ΔE and peak current density data are taken from voltammograms carried out at a scan rate of 5 mVs^{-1}.

Surface	ΔE / mV	$j_{p,c}$ / $j_{p,a}$	$d\ln(ip_a)/d\ln(v)$
Polished GC	220	0.32	0.5
Annealed GC	31	0.91	1
Anodised GC	34	0.86	0.5

out after a fixed immersion time of 10 minutes of the electrode, which was the time required for the degassing of the electrolyte solution prior to the experiments. To ensure a fair comparison between polished, annealed and anodised GC electrodes this constant immersion time was maintained across all studies. The DA coverages obtained under different solution concentrations of DA may therefore not be indicative of the equilibrium DA coverages, which would be attained after significantly longer immersion times. Moreover, the equilibration time is expected to be a function of the solution concentration. The reported coverage values are therefore not meant to be indicative of the coverages obtained at equilibrium; they are intended to serve as a relative comparison of the response of the three electrode surfaces to DA solutions with a constant, experimentally amenable immersion time.

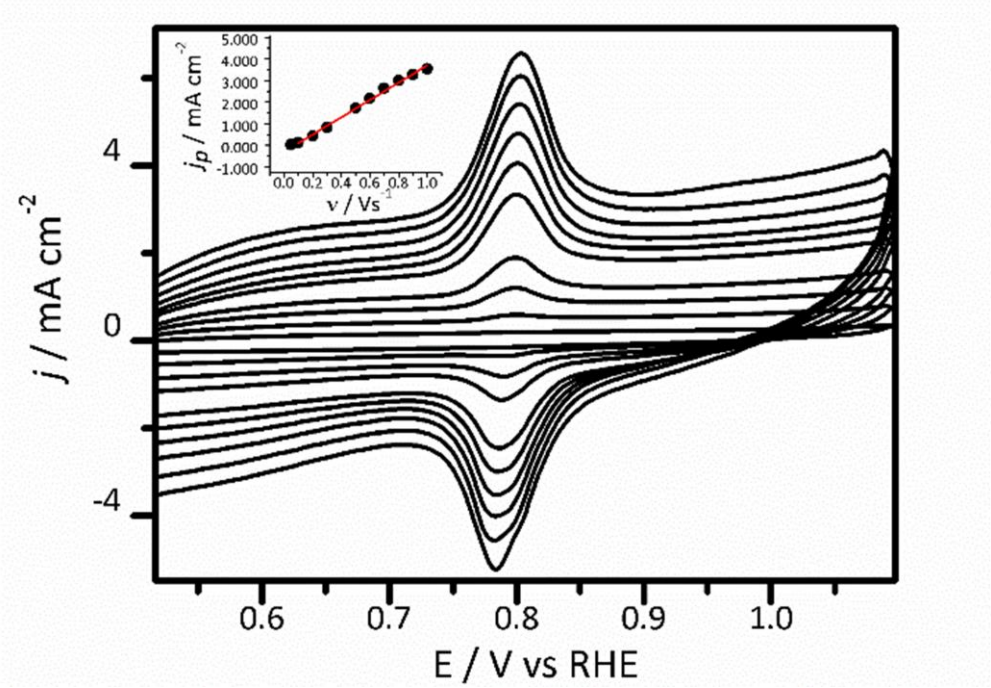

Figure 4.9. CVs for annealed GC in electrodes in solution of 25 µM DA in 0.1 M H_2SO_4. Inset: plot of peak current density of the voltammogram versus ν at scan rates between 100 mV s^1 and 1 V s^{-1}.

The response of the three different types of GC surfaces in solutions of DA is summarised in Table 4.1. Both anodisation and annealing pretreatments are effective in producing surfaces with rapid charge transfer kinetics to DA; however, the mechanism of activation does not appear to be identical on both surfaces. The annealed surface appears to favour the adsorption of DA, which may explain the rapid charge transfer kinetics via a self-catalytic mechanism. The anodised surface also exhibits facile charge transfer to DA with no evidence for the presence of any adsorbed material, suggesting that the improved charge transfer kinetics on the anodised surface compared to polished GC may be explained by differences in the surface chemistry between the two surfaces.

X-Ray Photoelectron Spectroscopy Analysis of GC Surfaces

The differences observed between polished GC and polished GC subjected to surface pre-treatments with respect to charge transfer to DA are the result of the high degree of sensitivity of DA to the surface composition. In order to understand the trends observed in the voltammetric studies of DA, particularly the difference in between the anodised and annealed GC surface, XPS measurements of the surfaces were employed in order to obtain

chemical composition information on the three systems. Survey scans for the three GC electrodes are reported in Figure 4.10. C 1s and O 1s envelopes and Auger peaks associated with carbon and oxygen are present in all three surface types, while no other major contributions from other elements are evident.

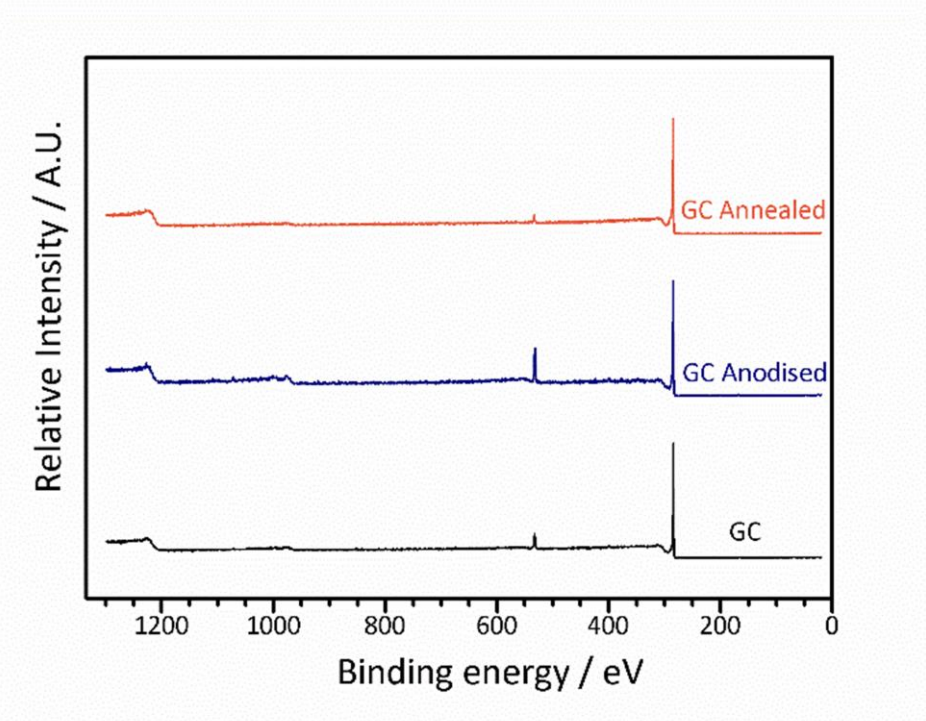

Figure 4.10. XPS Survey scans for polished, anodised and annealed GC.

There are obvious differences in the oxygen content evident in the survey spectra. The O/C at. % derived from the area ratio of high resolution scans of the O 1s and C 1s regions normalised by the respective sensitivity factors is reported in Table 4.2. Both GC and annealed GC have similar O/C % of 3 ± 2 %, whereas the anodised disk has a much higher O/C % of 13 ± 3 %. Although some of the detected oxygen is due to exposure of the samples to the atmosphere prior to the XPS measurement,[27] the high oxygen content in the anodised GC surface may nonetheless be attributed to the introduction of oxide groups into the surface by the oxidative pre-treatment as observed by other authors. [28]

The C 1s envelopes for the three surfaces are plotted in Figure 4.11. All three surfaces show an asymmetric peak centered close to 284.6 eV which is typical for an sp^2 carbon surface. The polished GC surface in particular may be deconvoluted into five main contributions. The main contribution may be assigned to sp^2-bonded carbon atoms centered at 284.6 eV. A second peak close to 285.6 eV is also present and is typically assigned to sp^3-C atoms. Two peaks close to 286.5 and 287.5 eV may be attributed to C-OH and C=O respectively. [29-30] Finally, a broad peak above 288 eV is attributed to the shake-up feature of

the delocalised sp^2-C network of GC, although it may also include contributions from COOH groups. [28]

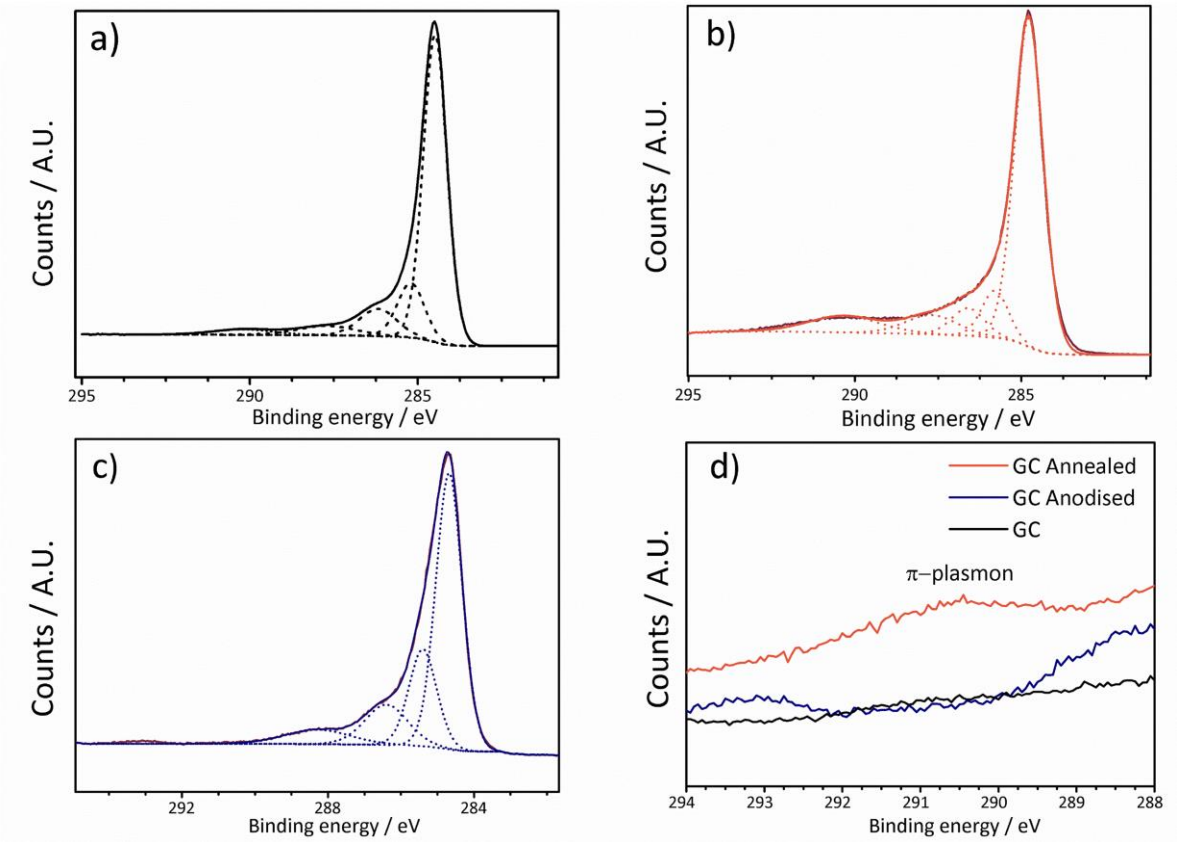

Figure 4.11. Deconvoluted C 1s spectra of a) polished GC b) annealed GC c) anodised GC. The raw data in each case is shown by a continuous gray line, while the envelope resulting from the deconvolution is overlaid in black, orange and navy for polished, annealed and anodised GC respectively. d) shows the C 1s envelopes in the binding energy region between 294 and 288 eV.

The annealed GC (Figure 4.11 b) has a similar deconvolution to the polished surface, although the sp^3-C and oxide peaks are all lower in magnitude and the shake-up feature is considerably more pronounced. This may be explained by an increase in the graphitization of the surface induced by the annealing treatment. Similar results have been observed by laser activation of the GC surface and by the *in situ* fracturing of glassy carbon.[22] The high binding energy side of the C 1s envelope for the anodised GC surface Fig. c) shows considerably larger contributions from sp^3-C at 285.6 eV as well as from the C-oxide peaks between 286-289 eV.

There is also no evidence of a shake-up feature at 290 eV, which implies that the delocalised sp^2 network evident in the polished and annealed GC surfaces may be disrupted by the anodisation treatment. This is supported by the trend in sp^3 / sp^2 % derived from the

area ratios of the peaks at 285.6 eV and 284.5 eV and reported in Table 4.2. The anodised GC possesses the highest sp^3 / sp^2 % of 35 ± 2 whilst the annealed surface has the lowest at 13 ± 1 %.

Table 4.2. Composition data derived from XPS measurements on GC surfaces

Surface	O/C %	C-Oxide %	sp^3 / sp^2 %
Polished GC	3 ± 2	14 ± 3	20 ± 2
Annealed GC	3 ± 2	19 ± 4	13 ± 1
Anodised GC	13 ± 3	28 ± 4	35 ± 2

The differences between the envelopes are most evident in Figure 4.11 d), which shows the high binding energy region of the C 1s envelopes between 295 and 288 eV**.** The region between 288-289 eV is most pronounced for the anodised surface, consistent with the presence of COOH groups introduced by the oxidative treatment, but the π-plasmon peak associated with the shake-up is absent despite being weakly present in polished GC and highly prominent for the annealed surface. The anodised envelope also possesses a small satellite peak close to 293 eV which may be attributed to the intercalation of potassium at the electrode surface introduced during the anodisation treatment in KOH. [31]

The O 1s peaks for the three GC surfaces are plotted in Figure 4.12. There are a number of deconvolutions of the O 1s region of oxidised carbon materials in the literature.[28,30,32] Contributions to the envelope may be divided into two broad regions: O-C in alcohols, ethers and esters between 533.5-535 eV and O=C in ketones, carboxylic acids and esters between 531.5 – 532.6 eV. The envelope shape for both the anodised and polished GC surfaces is similar, suggesting that both of these surfaces possess a mix of various oxide groups. The annealed surface appears to have little to no contributions from O=C groups, which may be removed from the surface by the annealing treatment. A comparison of the O/C % determined from area ratios of the O 1s and C 1s peaks with the collective area of the peaks attributed to C-O and C=O from the C 1s deconvolution in Table 4.2 shows a strong correlation, supporting the assignment of the C 1s peaks to oxide contributions; the increase in O/C % in the anodised GC is accompanied by an increase in the total area associated with C-oxides in the C 1s deconvolution.

Overall, the XPS data suggest significant differences in the surface structure and chemical composition between the three GC surfaces. Anodisation of polished GC results in a significant increase in surface oxides and sp^3 content, both of which are expected to result in

interruptions of the delocalized sp^2 network. This is consistent with the absence of a π-π^* shake-up feature in the C 1s envelope which is only observed on the anodised surface. The thermal annealing treatment apparently results in surface graphitization based on the low value of sp^2/sp^3 observed for annealed GC and the enhancement of the π-π^* shake-up feature.

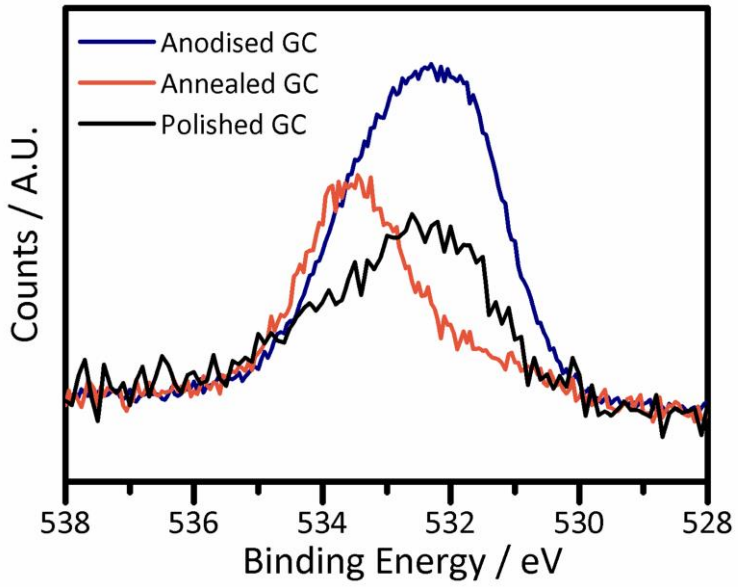

Figure 4.12. O 1s XPS spectra for anodised, annealed and polished GC surfaces.

Examining the surface composition data together with the results of voltammetric studies, the differences in the electrochemical response to DA may be correlated to the unique surface structure and composition of the three GC systems studied. It has been proposed by McCreery et al. that overall surface cleanliness is crucial for the attainment of rapid charge transfer kinetics to DA and to other catechols, [33] the reason being that the chance adsorption of blocking species at the electrode surface serves as a physical barrier to the approach of DA.

Any surface preparation or pre-conditioning which produces an unsullied GC surface is therefore expected to show improved electrochemical performance in catechol oxidation. This partially explains the success of diverse treatments such as *in situ* laser activation, thermal annealing, anodisation and cleaving of GC in producing surfaces with rapid electron transfer kinetics to DA and other catechols (*vide supra*). However, the removal of blocking species from the surface is not a sufficient explanation for the dramatic differences in the electrochemical response evident in this study: both anodization and thermal annealing are extremely effective methods for the removal of blocking species and the behavior of these two surfaces is still highly divergent.

The voltammetric data strongly suggest that DA oxidation at the annealed surface occurs through adsorbed layer of the catechol which self-catalyses electron transfer to DA molecules in the solution phase. The XPS data suggest that the annealing process results in the graphitization of the GC surface to produce a more extensive delocalized sp^2 network than that of polished GC. The binding sites for DA adsorption at the carbon surface could therefore be sp^2 cluster regions of the surface which interact with the catechol via π-interactions with the aryl moiety. By contrast, the anodised GC surface which shows no evidence of adsorbed DA nonetheless displays quasi-reversible DA electron transfer kinetics and has an oxide content which is an order of magnitude larger than the other two surfaces.

In addition to the high proportion of surface oxides, the anodized surface also does not appear to have as extensive of a delocalized π system even compared to polished GC. The electrochemical oxidation pre-treatment also produces a GC surface with the highest apparent sp^3 content of the three surfaces studied. All of these observations are consistent with the disruption of the π system by the anodization process. The introduction of C-O and C=O moieties into the surface likely occurs via the disruption of C=C bonds at the surface. This effectively removes the binding sites for DA adsorption, but the numerous oxide sites introduced also facilitate rapid charge transfer at the surface without the need for DA adsorption to occur.

Computational Studies of DA Adsorption at Model Carbon Surfaces

The experimental result that adsorption of DA is observed only on the annealed GC surface and not on either polished or anodised GC suggested that adsorption could be induced through interactions of the π system of the catechol with exposed graphic cluster regions on the GC surface. In order to investigate this hypothesis, the interaction between DA (Figure 4.13 a) and model surfaces based on graphitized carbon fragments was studied using computations at the DFT-wb97xd level (details are provided in the Experimental section, *vide infra*). The model surfaces used in the study are based on a graphene cluster with a fixed dimension as shown in Figure 4.13. b)

In order to account for the possibility of interruptions in the sp^2 network introduced by polishing or oxidative treatments, graphene surfaces with a vacancy were introduced (Figure 4.13 c), along with graphene surfaces with edges terminated with carbonyl, epoxide, and hydroxyl moieties (Figure 4.13 d-f). The analysis consisted of first optimising all of the structures depicted in Figure 4.13 in isolation and then adsorbing DA at each surface in a

number of different orientations in order to calculate the free energy of adsorption, ΔG_{ads}. The lowest free energy values along with the resulting orientation obtained are summarised in Figure 4.14. All of the orientations attempted along with the initial and final orientations obtained are given in Appendix I.

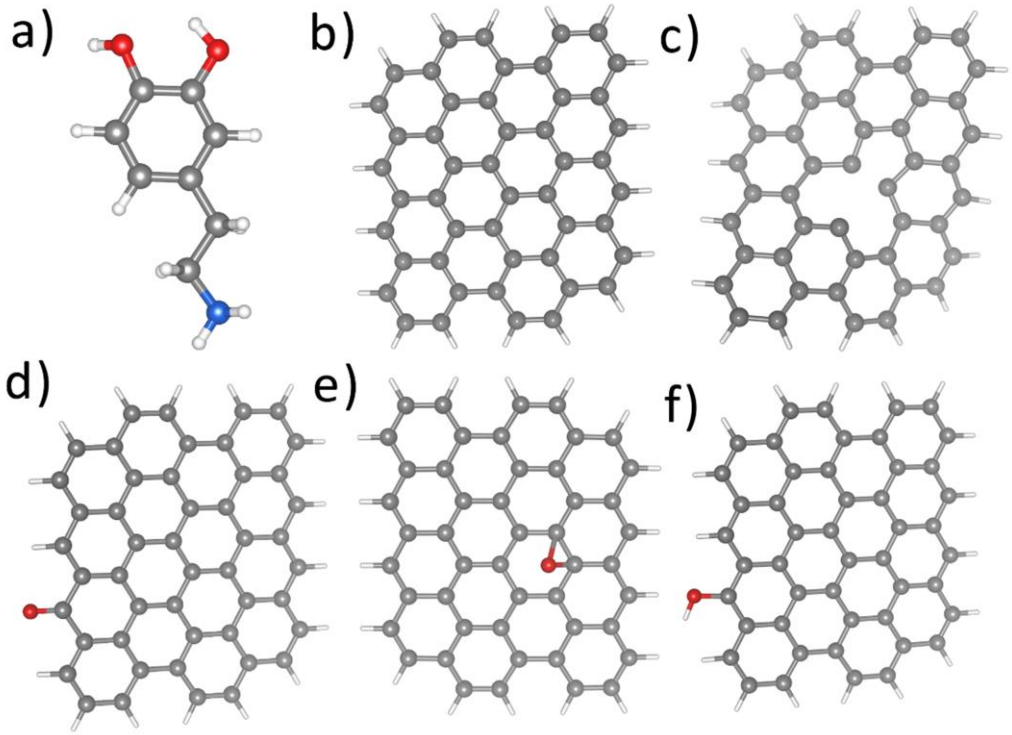

Figure 4.13. Structures used in DFT calculations for DA adsorption. a) DA b) Graphene cluster c) Graphene cluster with a monovacancy d) Graphene cluster with a carbonyl moiety e) Graphene cluster with an epoxide moiety f) graphene cluster with a hydroxyl moiety.

For the interaction of DA with the basal plane of a graphene fragment (DA-BP), the most favourable orientation of the molecule is parallel to the surface at distance of 3.2 Å (Figure 4.14 a). This distance is the expected value for a non-covalent interaction through the π-system and is in agreement with previous theoretical work on DA-graphene adsorption.[34]

The ethylamine chain of DA is oriented away from the aryl moiety with an N-surface distance > 4.5 Å. A similar result was obtained for a DA molecule placed upon a vacancy site (DA-VAC, Figure 4.14 b). The final structure obtained has the DA molecule once again situated on a basal region with the hydrogen atoms on hydroxyl groups of the catechol ring pointing into the vacancy. The DA-VAC interaction is also approximately 2 kcal mol^{-1} more negative than DA-BP, which may be explained by hydrogen bonding between the unsaturated C atoms in the graphene vacancy and the hydroxyl groups of DA.

Interacting the DA molecule with a carbonyl moiety (DA-CO, Figure 4.14 c) results in the DA oriented over the hydrogenated edge of the graphene fragment with the H-atoms of the hydroxyl group pointed towards the C=O group. ΔG_{ads} for this orientation is close to 5 kcal mol^{-1}, which is only slightly weaker than the DA-BP interaction. This result suggests that adsorption of DA at oxidised sites via hydrogen bonding can also occur via attractive interactions comparable to those of the π system with the basal plane. For the interaction with a hydroxyl moiety (DA-OH, Figure 4.14 d) the DA molecule favours the basal plane interaction; indeed, the adsorption free energy for the final state is nearly identical to DA-BP.

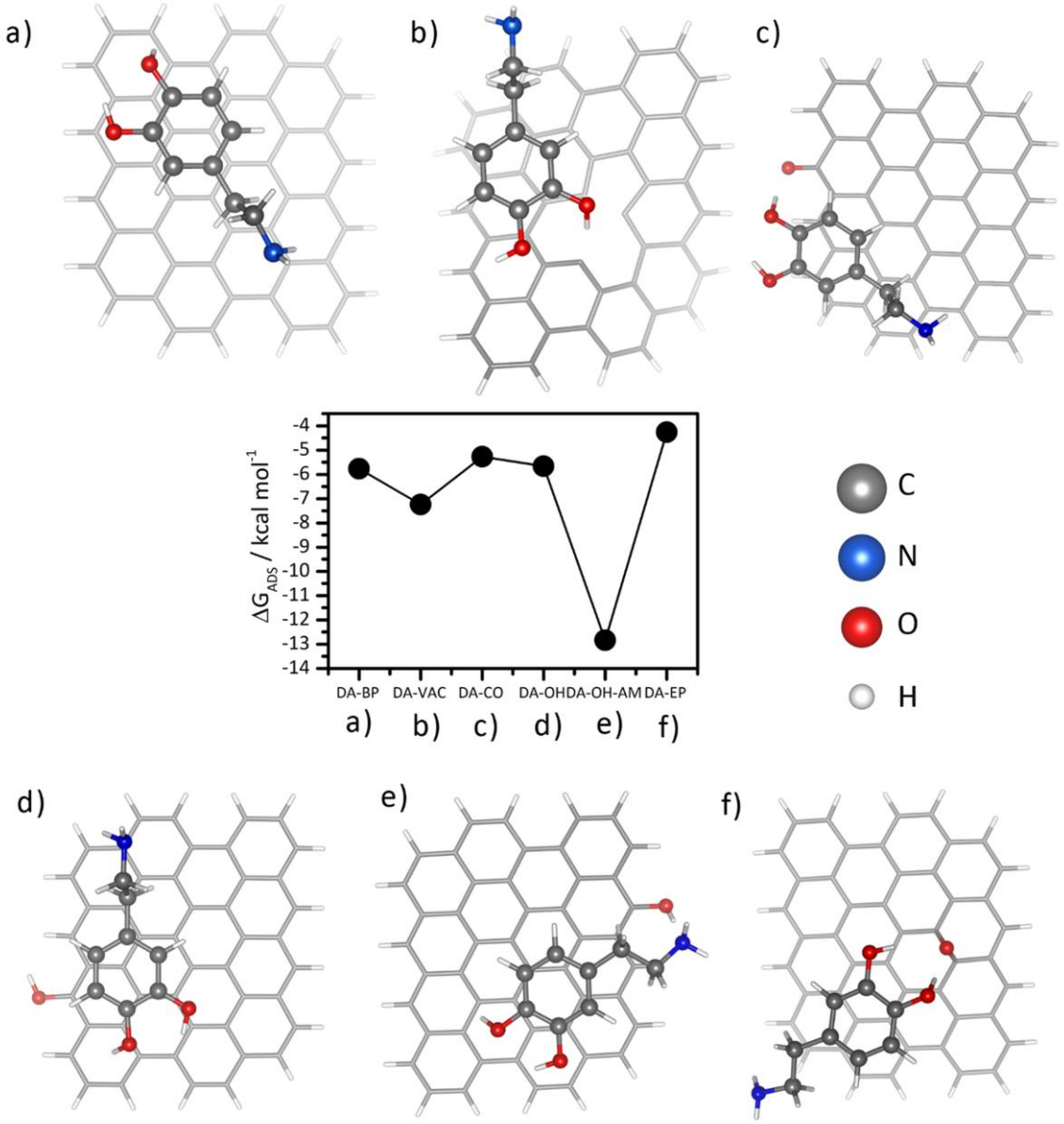

Figure 4.14. ΔG_{ADS} for DA on model surfaces derived from DFT calculations. The corresponding structures for each ΔG_{ADS} values are shown around the graph. a) DA-BP b) DA-VAC c) DA-CO d) DA-OH e) DA-OH-AM f) DA-EP.

The largest absolute magnitude of ΔG_{ads} was instead found for the interaction between the nitrogen atom on the amine of DA and the hydroxyl moiety (DA-OH-AM Figure 4.14 e). A value close to -13 kcal mol^{-1} was found in this case and appears to be the result of favourable interactions both between the aryl moiety and the graphene basal plane and the amine with the hydroxyl group at the graphene edge.

This result strongly suggests that the presence of C-OH edge sites may not interfere with DA adsorption and could in fact enhance it if the molecule is able to interact with both the sp^2 system of the basal plane and a hydroxyl site at an edge simultaneously. The weakest interaction was found for DA at an epoxide site (DA-EP, Figure 4.14 f) for which the DA molecule was found to be oriented slightly further from the basal plane and interacting with the oxygen group of the epoxide through the hydrogen atoms of the hydroxyl groups.

There are two inherent limitations to the computational model applied here, namely that the calculations do not account for the effects of the solvent and treat the adsorption event as though it is occurring in a vacuum, and the calculations do not account for the effect of applied electrode potential on DA adsorption. Despite these limitations, the DFT calculations are overall in good agreement with the results of the voltammetric studies. DA was found to adsorb on an annealed GC surface which is expected to be comprised of numerous uninterrupted sp^2 cluster regions based on the XPS analysis, whilst the computational study predicts a favourable ΔG_{ads} at these basal regions through the π system of the catechol. The introduction of oxide sites such as carbonyl groups and epoxides instead favours interaction with DA through hydrogen-bonding with the hydroxyl moieties of the aryl system rather than through π interactions. The exception to this finding is that hydroxyl moieties at the edge sites of graphitized carbon allow DA to adsorb on the basal plane whilst simultaneously interacting at the edge site through the ethylamine chain.

It is particularly interesting to examine the computational results for DA adsorption at oxidised surfaces together with the O 1s envelopes in Figure 4.12. The envelope for the annealed GC surface is consistent with predominantly C-O moieties such as hydroxyl groups and ethers with very little contribution from C=O groups, whilst both polished GC and anodised GC feature contributions from both broad classes of oxide (*vide supra*). The absence of adsorbed DA in the voltammograms obtained for the latter two surfaces in DA solutions may therefore be attributed to the abundance of C=O groups.

A possible objection to this conclusion is that the DFT studies show a comparable ΔG_{ads} value when DA adsorbs at a carbonyl or epoxide site through hydrogen bonding and when it adsorbs parallel to the basal plane via its π system. Indeed, if the adsorption of DA were accomplished in vacuum the computational results predict that surface-bound DA would be

detectable on all three GC surfaces. The voltammetric studies are however carried out in aqueous 0.1 M H_2SO_4 solution. Accordingly, solutions of DA ≤ 1 mM in concentration are competing with 55.5 M H_2O for hydrogen-bonding sites at oxidised regions of the GC surface, whilst the basal plane regions are predicted to be hydrophobic. This conclusion is supported by water contact angle (WCA) measurements on the two surfaces shown in Figure

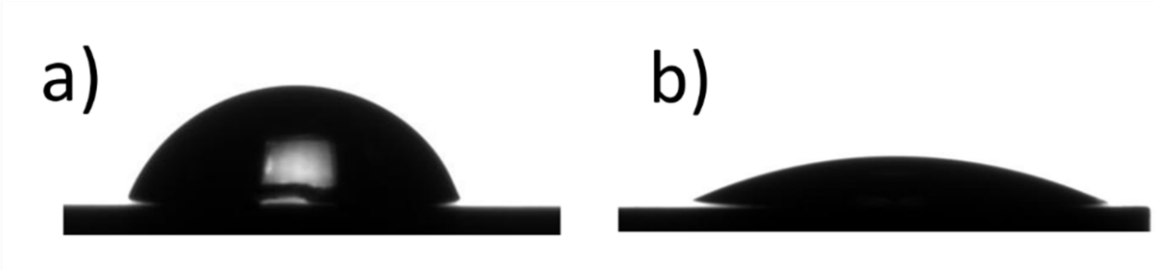

Figure 4.15. Water contact angle of a) annealed GC and b) anodised GC

4.15. The annealed GC surface has a WCA of 72º compared to 74º for polished GC (not shown) and 22º for anodised GC. This confirms that the annealed surface is considerably more hydrophobic than the anodised surface, a fact which may be attributed to the abundance of oxide sites on the anodised surface as well as the graphitization of the annealed surface.

The saturation of existing oxide sites on the anodised surface with water molecules is therefore a plausible explanation for the absence of adsorbed DA. The rapid charge transfer kinetics observed on anodised GC cannot be explained by self-catalysis through adsorbed DA, but it is possible that the large oxide coverage of the anodised surface is itself catalytic towards DA oxidation. McCreery et al. have suggested that the self-catalytic mechanism involves the approach of solution phase DA to the surface by hydrogen bonding to an adsorbed catechol. The numerous oxide sites of the anodised surface may also facilitate the approach of solution-phase DA. This conclusion is supported by the observation of DuVall and McCreery that a chemisorbed quinone layer which impedes DA adsorption entirely is nonetheless catalytic towards DA oxidation, presumably because the quinone moiety is as effective in hydrogen-bonding to DA as DA is itself. [23]

Voltammetric Studies of GC Electrodes Using 4-Methyl Catechol

As outlined in the introduction of this chapter, dopamine is an important biomolecule which has been investigated in particular by the electroanalytical community for the development of new biosensors and probes. The studies presented so far in this chapter are

expected to be highly relevant to researchers working on probes for DA detection. However it is also of interest to investigate if the trends identified for DA voltammetry at GC surfaces may be generalised to other catechols.

Computational studies on DA adsorption at model carbon surfaces identified that the ethylamine moiety could potentially exert a strong influence on the adsorption via H-bonding interactions. 4-methyl catechol (4-MC) was chosen as a second redox probe for voltammetric studies because it does not possess any amine moiety. CVs of 1 mM 4-MC in 0.1 M H_2SO_4 on the three GC surfaces are presented in Figure 4.16. All of the surfaces display voltammograms similar to that observed for DA, although the formal potential for 4-MC, $E^{0'}$ is closer to 0.75 V vs RHE compared to 0.78 V vs RHE observed for DA.

It is clear from the figure that the trends observed in electron transfer kinetics for DA are also evident for 4-MC. The CV on the polished GC surface (Figure 4.16 a) displays a broad asymmetric wave with a ΔE value *ca.* 140 mV, similar to the result for DA in Figure 4.2. Both the annealed (Figure 4.16 b) and anodised (Figure 4.16 c) GC surfaces have CV waveforms with ΔE values close to the theoretical limit of 30 mV for a Nernstian $2e^-$ transfer. The peak current density value on the annealed surface is considerably larger than on polished and anodised surface which is suggestive of the presence of adsorbed 4-MC at the surface. This was confirmed by carrying out experiments at a range of scan rates in 4-MC solutions as shown in Figure 4.17.

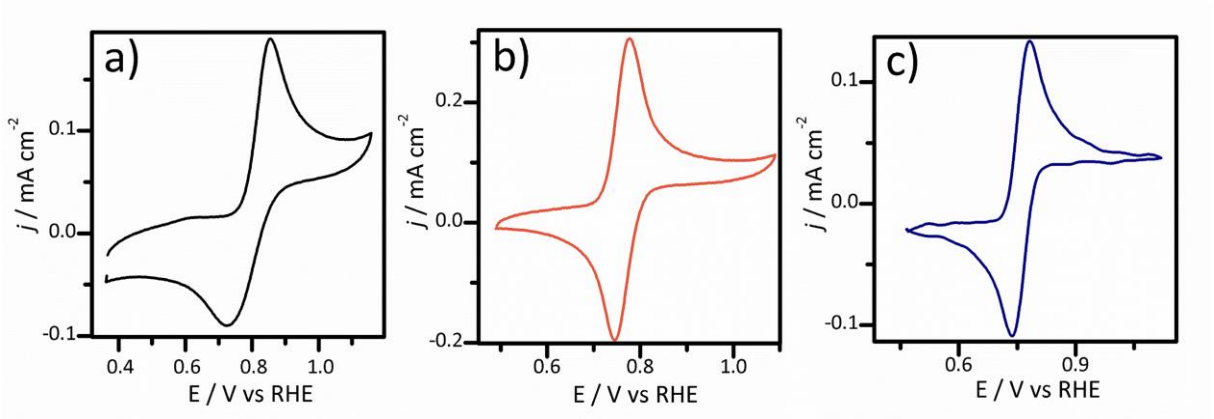

Figure 4.16. CVs of a) polished GC b) annealed GC and c) anodised GC in solutions of 1 mM 4-MC and 0.1 M H_2SO_4. (Scan rate: 5 mVs^{-1})

It is evident in the figure that the measured current densities at annealed GC surfaces in solutions of 4-MC at low concentrations are predominantly due to the oxidation and reduction of surface-bound 4-MC. The ΔE values in the voltammograms taken in the scan range between 10 – 1000 mVs^{-1} in Figure 4.17 a are all < 10 mV and the wave form is symmetric around the formal potential, as expected for a redox-active adsorbate. As was the

case for adsorbed DA, the peak current density j_p obtained from background-corrected voltammograms is linear with respect to the scan rate (Figure 4.17 b). No such evidence for adsorption was observed on either polished or anodised GC. These results support the hypothesis that catechols in general adsorb on graphitized carbon surfaces via the π system, and that an amine moiety is not necessary in order to effect the adsorption. Computational studies of 4-MC on carbon model surfaces carried out in a similar fashion to those for DA were also carried out to support this hypothesis and are discussed in detail in the following chapter.

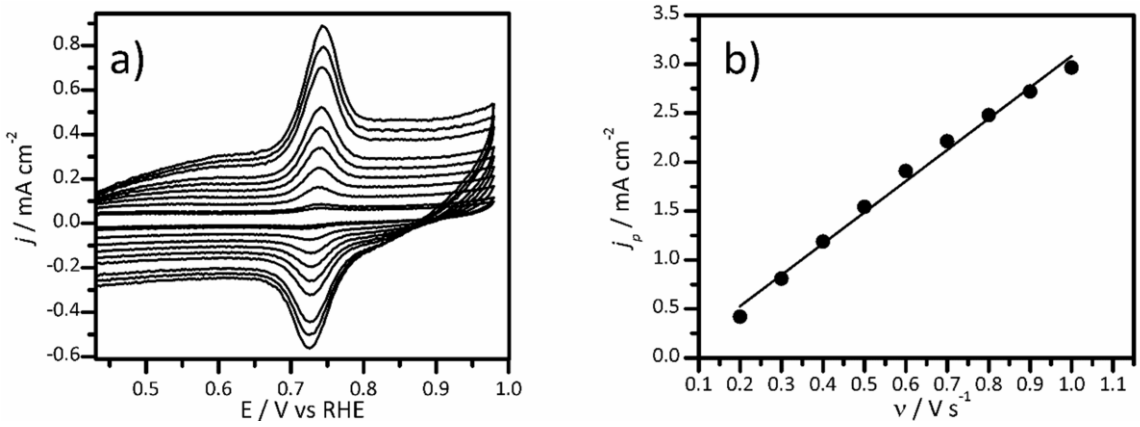

Figure 4.17. a) Voltammograms of annealed GC in 25 μM 4-MC at scan rates between 10 mV s^{-1} and 1 V s^{-1} b) Plot of peak current density versus ν derived from the voltammograms shown in a).

Voltammetric Response of a-C:N Electrodes in Solutions of Dopamine

In the previous chapter, nitrogenated amorphous carbon electrodes (a-C:N) with varying N-content were studied using two redox probes, $Ru(NH_3)_6^{2+/3+}$ and $Fe(CN)_6^{3-/4-}$. Nitrogenation of the amorphous carbon scaffold was shown to influence both the bulk optoelectronic properties and the surface chemistry of the material, which manifested clearly in the electrochemical response to the two redox probes. In particular, electron transfer to the $Fe(CN)_6^{3-/4-}$ probe was found to depend mostly on differences in the surface chemistry whilst the $Ru(NH_3)_6^{2+/3+}$ probe was sensitive only to the bulk properties.

Electrodes based on nitrogen-doped carbon have been applied in electroanalytical applications for the detection of DA, in particular because the simultaneous detection of DA in the presence of co-analytes such as ascorbic acid has been shown to be possible with these materials**.** [11-12. 35-37] However, the effects of nitrogen incorporation on charge transfer to catechols is not well understood at a fundamental level at present. In order to investigate the effects of nitrogenation on the redox response of a-C:N materials to DA, voltammetry studies in solutions of 1mM DA / 0.1 M H_2SO_4 on three of the electrodes described in the previous chapter were carried out as shown in Figure 4.18. with the voltammetric parameters summarised in Table 4.3. The N-free a-C electrode, shown in part a) of the figure, displays

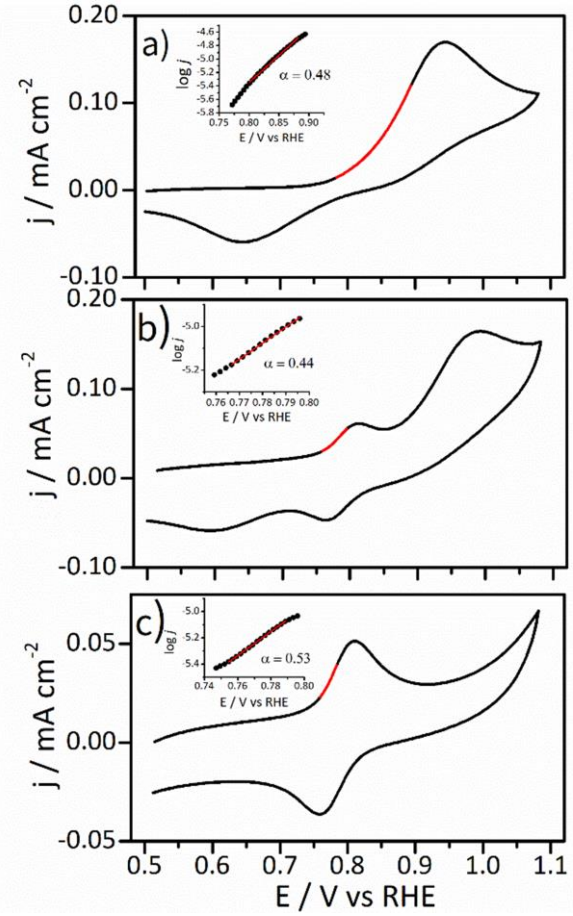

Figure 4.18. Voltammograms of a) a-C b) a-C:N-2% c) a-C:N-10% in solutions of 1mM DA / 0.1 M H_2SO_4 at a scan rate of 5 mV s^{-1}. Inset in each plot is the Tafel plot derived from the highlighted region of the voltammogram.

a very similar redox response to that of polished GC, i.e. a broad, asymmetric voltammogram with > 200 mV peak-to-peak separation, ΔE and an effective transfer coefficient, (n + α) = 0.48. DA oxidation on a-C therefore also occurs through a similar mechanism to that of GC i.e. a $2e^-$ scheme-of-squares mechanism where the 1st electron transfer is the rate

determining step. Figure 4.18 b) shows the voltammogram for an a-C:N-2% electrode under the same conditions. The CV for this electrode has a curious double-humped waveform which can be attributed to a partially-activated surface with some surface sites catalysing electron transfer to DA more rapidly than others. [22,38] This is reflected in the fact that both pairs of peaks have the same formal potential, $E^{0'} = 0.78$ V vs RHE. The larger peak, with a peak current density $j_{p,a} = 9 \times 10^{-5}$ A cm^{-2} has the same broad shape and large ΔE value as seen for a-C, but the smaller peaks ($j_{p,a} = 3 \times 10^{-5}$ A cm^{-2}) have a ΔE value of 43 mV and $j_{p,c} / j_{p,a} = 0.91$ which is consistent with quasi-reversible electron transfer.

The lower value of j_p observed on the small peaks relative to the larger peaks may be explained if only a fraction of the a-C:N-2% surface is activated towards DA. The two processes, one an irreversible charge transfer similar to that which occurs on undoped a-C and the other a quasi-reversible redox process occurring only on the N-doped a-C:N-2%, occur simultaneously at the electrode surface. Analysis of the Tafel region on the small peak is also suggestive of $(n + \alpha) \approx 0.5$, implying that the 1st electron transfer step is still rate-determining even if the kinetics of the overall process are more rapid on the active sites introduced into the surface by nitrogen incorporation.

Table 4.3. Voltammetric parameters for a-C and a-C:N-2-10% electrodes determined at a scan rate of 5 mVs^{-1}

Electrode	ΔE / mV	$j_{p,c} / j_{p,a}$	$j_{p,a}$ / mA cm^{-2}
a-C	250	0.28	9.2×10^{-5}
a-C:N-2%	44, 243	0.91	3.04×10^{-5}
a-C:N-10%	48	0.94	2.04×10^{-5}

Figure 4.18 c) shows a CV of an a-C:N-10% electrode in a solution of 1 mM DA. The most striking feature of the voltammogram is the absence of the large, asymmetric wave seen on a-C and a-C:N-2% in the potential window studied. Only the quasi-reversible peak with a ΔE of 48 mV and a $j_{p,a} = 2 \times 10^{-5}$ A cm^{-2} similar to that observed on the a-C:N-2% surface is evident. In a similar manner to what was observed for the Ferro/Ferricyanide redox couple in the previous chapter, increasing levels of nitrogenation appears to have a deleterious effect on the kinetics of charge transfer to DA. The absence of the irreversible

process in the potential window chosen for the experiment may be because the ΔE value on the a-C:N-10% surface has increased to such an extent that a peak is no longer observed in the range of 0.5-1.1 V vs RHE.

The quasi-reversible process on a-C:N-10% has an identical value of $(n + \alpha) \approx 0.5$ as that on the a-C:N-2% surface. Considering the results obtained on both a-C:N-2% and a-C:N-10% together, nitrogen-incorporation appears to induce the formation of a heterogeneous electrode surface with a small subset of active regions towards DA oxidation. However, this is not the only effect of nitrogenation, which was shown in the previous chapter to also introduce a large number of defects in the carbon scaffold based on spectroscopic ellipsometry results. This disruption of the carbon scaffold structure appears to result in the general inactivation of the majority of the heterogeneous surface towards charge transfer to DA, such that only a small subset of sites remain active for quasi-reversible charge transfer in the a-C:N-10% surface.

The exact nature of the active sites, (i.e. which forms of nitrogen moiety in the a-C:N surfaces facilitate charge transfer to DA) is unclear at this point. It is also of note that none of the voltammograms in Figure 4.18 show any evidence of the presence of adsorbed DA. In the next chapter, experiments and computational studies with DA and 4-MC at model carbon surfaces with a well-defined nitrogen site chemistry will be presented in order to investigate the effects of N-sites on DA electrocatalysis in detail.

4.2 Conclusions

In this chapter, electron transfer to two catechol molecules, DA and 4-MC, was studied using a combination of voltammetry, X-ray photoelectron spectroscopy and DFT calculations. It was shown for both DA and 4-MC that charge transfer kinetics can be improved by pre-treatment of a polished glassy carbon surface using either an electrochemical oxidation or a thermal annealing treatment. Anodisation results in quasi-reversible charge transfer kinetics which, based both the XPS spectra and computational studies, was attributed to catalysis of charge transfer through oxide moieties at the electrode surface. The annealed GC surface was found to have reversible charge transfer to DA despite having an identical oxygen content to polished GC, a feature which was attributed to the self-catalysis of charge transfer through an adsorbed layer of DA.

Based on the XPS studies of the annealed GC surface, the adsorption of both DA and 4-MC was hypothesised to occur through non-covalent interactions between the π system of

the aryl ring of the catechol and graphitized regions of the surface. This hypothesis was supported by computational studies which showed favourable values of ΔG_{ads} at the basal plane of graphene cluster surfaces, whilst the introduction of interruptions in the basal plane in the form of vacancy sites or oxygen moieties instead induces hydrogen bonding interactions with the hydroxyl groups of the catechol ring. It was argued that adsorption interactions at such sites in aqueous media were implausible due to competition from water as a far more abundant H-bond donor, thus explaining why the highly oxidised surface of anodised GC displays no evidence of adsorption for either DA or 4-MC.

Finally, the effects of nitrogen-incorporation on electron transfer to DA was studied by comparing the redox response of N-free a-C to two nitrogenated amorphous carbon surfaces, a-C:N-2% and a-C:N-10%. Nitrogenation was found to activate only a subsection of the electrode, resulting in a heterogeneous redox response in the form of a double-peaked voltammogram in the case of a-C:N-2%.

The a-C:N-10% surface, which was shown in the previous chapter to have a higher N content than a-C:N-2% but also a greater degree of surface heterogeneity in the form of defects, was generally inactive towards DA oxidation except for small active regions of the surface which were presumed to be associated with some of the nitrogen sites. No evidence was found for DA adsorption at either a-C or a-C:N surfaces, which implies that the improved charge transfer kinetics observed on the a-C:N electrodes may be attributed to the effects of particular surface sites rather than the self-catalytic effect of adsorbed DA.

The most important result presented in this chapter is the correlation between the degree of graphitization of the carbon scaffold and the adsorption of DA and 4-MC. In the next chapter, this adsorption will be exploited in order to utilise these catechols as probes of the carbon scaffold nanostructure of graphitized N-doped carbon electrodes.

4.3 Experimental Methods

Chemicals and Materials

Dopamine hydrochloride (98%, Aldrich), 4-Methyl Catechol (98%, Aldrich) Sulfuric Acid (≥95%, Ultratrace) and Methanol (Semiconductor grade) were used without further purification.

Substrate Preparation

Glassy carbon (GC) discs (HTW Sigradur radius 0.25 ± 0.05 cm) were prepared for deposition of a-C and a-C:N films by polishing with progressively finer grades of alumina slurry (Buehler) with particle sizes of 1 μm, 0.3μm and 0.05μm on microcloth (Buehler). Between each round of polishing the disks were rinsed with copious millipore water, then sonicated in methanol and millipore water for 3 minutes each. After the final polishing step this sonication was increased to 10 minutes in each solvent, followed by drying under Ar.

The polished discs were either used immediately for electrochemical and contact angle measurements or subjected to electrochemical/thermal pre-treatments. Annealed GC surfaces were prepared by placing the polished GC discs in a tube furnace at 900 ^{o}C for 1 h. Anodised GC was prepared by mounting the polished GC in a teflon holder as described in the previous chapter and applying a potential of 1.8 V vs Ag/AgCl (sat) in an aqueous solution of 0.1M KOH for 20 s. In the case of a-C and a-C:N depositions, the GC discs were mounted in a custom-made Teflon holder and placed in a vacuum chamber for coating via magnetron sputtering prior to characterisation as reported in Chapter III.

Preparation of a-C and a-C:N

Thin film electrodes of a-C, a-C:N-2% and a-C:N-10% were deposited via DC magnetron sputtering in a chamber (Torr International Inc.) with a base pressure $\leq 2 \times 10^{-6}$ mbar and a deposition pressure in the range $(2–7) \times 10^{-3}$ mbar as described in the Experimental section of the previous chapter.

Electrochemical Characterisation

Electrochemical measurements were carried out using a Metrohm Autolab AUT50324 potentiostat using a 3-electrode setup. A static disc holder (Pine Instruments) enclosing the GC discs was used as working electrode. A Hydroflex hydrogen electrode (Gaskatel) and graphite rod were used as reference and counter electrodes respectively. The electrochemical cell was a five-necked jacketed cell (Pine Instruments) which had its temperature held constant at 25 ^{o}C using a recirculator. Prior to experiments the cell was cleaned using Piranha solution (3:1 H_2SO_4:H_2O_2 **CAUTION:** Piranha solution is a strong oxidant which may react explosively with organic solvents and must always be used in a fumehood) followed by rinsing with copious amounts of Millipore water. The cell was then rinsed three times with the electrolyte solution used during the experiment immediately prior to the analysis.

Cyclic Voltammograms (CVs) were acquired in a potential window of 0.48 – 1.2 V vs RHE in deaerated solutions of 0.1 M H_2SO_4 with and without DA and 4-MC in concentrations ranging from 25 μM to 1 mM. All voltammograms were taken with iR compensation using commercial software (NOVA) with the uncompensated resistance of 18 Ω determined prior to the experiment using Electrochemical Impedance Spectroscopy (EIS). The voltammograms in each case were obtained after immersion of the electrodes in the working solution for approximately 10 minutes.

Determination of the Diffusion Coefficient of DA using Rotating Disk Electrode (RDE) Studies

The diffusion coefficient, D, of DA in 0.1 M H_2SO_4 was determined using an anodised GC disc mounted in a Teflon RDE tip attached to an RDE shaft (Pine Instruments). Linear sweep voltammograms were then performed in 1mM DA / 0.1 M H_2SO_4 solution at rotation speeds of 400, 900, 1600 and 2500 rpm as shown in Figure 4.18. The voltammograms obtained at each rotation rate have the expected form for a steady-state process at potentials > 0.9 V i.e. the limiting current density, j_L, is independent of potential and scales linearly with the square-root of the rotation rate, $w^{1/2}$, according to:

$$j_L = 0.201nFD^{2/3}v^{-1/6}cw^{1/2}$$

Where n = 2 for DA and v = 0.01 cm^2s^{-1} is the kinematic viscosity of water. [317] The plot of j_L versus $w^{1/2}$ is shown inset in Figure 4.19. The value for D was found to be 6.6 x 10^{-6} cm^2 s^{-1}.

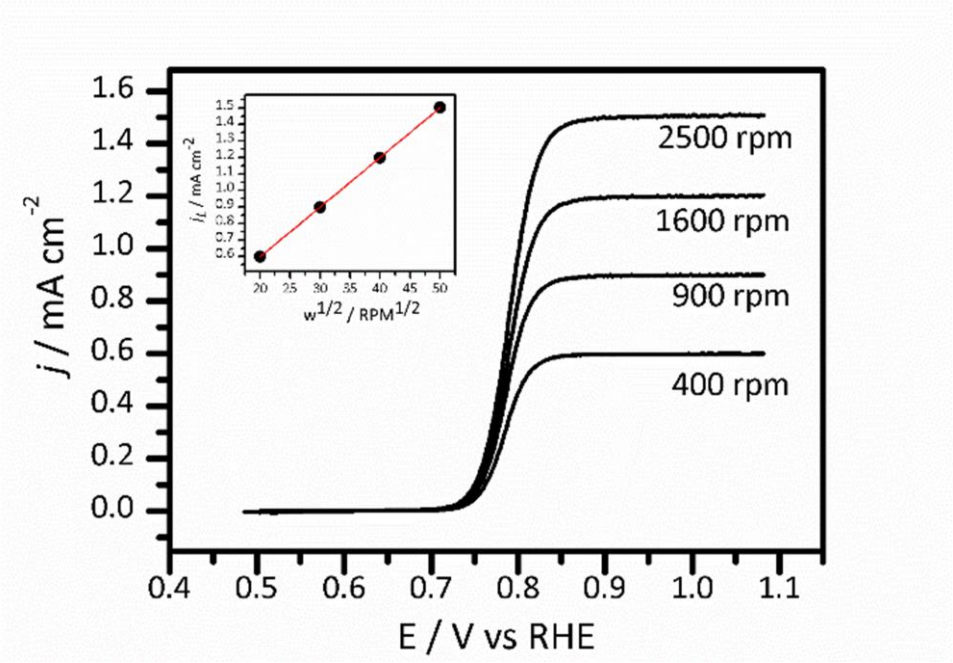

Figure 4.19. Rotating disk electrode experiments on an anodised GC disk in a solution of 1 mM DA / 0.1 M H_2SO_4 at various rotation speeds. Inset: plot of the limiting current j_L versus the square root of the rotation rate, $w^{1/2}$.

X-Ray Photoelectron Spectroscopy Analysis of GC Surfaces

X-ray photoelectron spectroscopy (XPS) characterization was performed at 1 × 10^{-10} mbar base pressure in an ultrahigh-vacuum system (Omicron). The X-ray source was a monochromatized Al Kα source (1486.6 eV). Spectra were recorded at 45° takeoff angle with an analyser resolution of 0.5 eV. Spectra were baseline corrected using a Shirley background and fitted with Voigt functions using commercial software (CasaXPS); atomic percent compositions were determined by calculating peak area ratios after correction by relative sensitivity factors (C 1s = 1.0, N 1s = 1.8, O 1s = 2.93).

Computational Studies

Density functional theory (DFT) calculations reported in this work were carried out using the dispersion corrected hybrid functional ωB97X-D developed by Head-Gordon and Chai,[40] implemented in the Gaussian09 software package.[41] The choice of this level of theory is based on the satisfactory results obtained in previous theoretical studies for thermochemistry and for the description of non-covalent interactions.[42] H atoms were described using the double-ζ basis set 6-31G(d,p), whereas the same basis set plus diffuse functions was employed to describe the more electronegative O and N atoms. Geometry optimizations were performed without imposing any constraints and the nature of all the stationary points was further verified through vibrational frequency analysis. The reported adsorption Gibbs energies (ΔG_{ads}) were calculated at the experimental temperature of 298 K and pressure of 1 atm, according to the following equation:

$$\Delta G_{ads} = G_{surf+DA} - G_{surf} - G_{DA}$$

where $G_{surf+DA}$, G_{surf}, and G_{DA} correspond to the adsorbed DA on the graphene cluster, the clean graphene cluster, and the DA molecule in the gas phase, respectively.

4.4 References

1. Schildkraut, J. J. The catecholamine hypothesis of affective disorders: a review of supporting evidence. *American Journal of Psychiatry* **1965,** *122* (5), 509-522.

2. Dailly, E.; Chenu, F.; Renard, C. E.; Bourin, M. Dopamine, depression and antidepressants. *Fundamental & Clinical Pharmacology* **2004,** *18* (6), 601-607.

3. Howes, O. D.; Kapur, S. The Dopamine Hypothesis of Schizophrenia: Version III—The Final Common Pathway. *Schizophrenia Bulletin* **2009,** *35* (3), 549-562.

4. Lotharius, J.; Brundin, P. Pathogenesis of parkinson's disease: dopamine, vesicles and α-synuclein. *Nature Reviews Neuroscience* **2002,** *3*, 932.

5. Sofuoglu, M.; Sewell, R. A. Norepinephrine and stimulant addiction. *Addiction Biology* **2009,** *14* (2), 119-129.

6. Jackowska, K.; Krysinski, P. New trends in the electrochemical sensing of dopamine. *Analytical and Bioanalytical Chemistry* **2013,** *405* (11), 3753-3771.

7. Forzani, E.; Rivas, G.; Solis, V. Amperometric determination of dopamine on an enzymatically modified carbon paste electrode. *Journal of Electroanalytical Chemistry* **1995,** *382* (1-2), 33-40.

8. Njagi, J.; Chernov, M. M.; Leiter, J.; Andreescu, S. Amperometric detection of dopamine in vivo with an enzyme based carbon fiber microbiosensor. *Analytical Chemistry* **2010,** *82* (3), 989-996.

9. Zhou, Y. L.; Tian, R. H.; Zhi, J. F. Amperometric biosensor based on tyrosinase immobilized on a boron-doped diamond electrode. *Biosensors and Bioelectronics* **2007,** *22* (6), 822-828.

10. Njagi, J.; Ispas, C.; Andreescu, S. Mixed Ceria-Based Metal Oxides Biosensor for Operation in Oxygen Restrictive Environments. *Analytical Chemistry* **2008,** *80* (19), 7266-7274.

11. Sheng, Z.-H.; Zheng, X.-Q.; Xu, J.-Y.; Bao, W.-J.; Wang, F.-B.; Xia, X.-H. Electrochemical sensor based on nitrogen doped graphene: Simultaneous determination of ascorbic acid, dopamine and uric acid. *Biosensors and Bioelectronics* **2012,** *34* (1), 125-131.

12. Gai, P.; Zhang, H.; Zhang, Y.; Liu, W.; Zhu, G.; Zhang, X.; Chen, J. Simultaneous electrochemical detection of ascorbic acid, dopamine and uric acid based on nitrogen doped porous carbon nanopolyhedra. *Journal of Materials Chemistry B* **2013,** *1* (21), 2742-2749.

13. Laviron, E. Electrochemical reactions with protonations at equilibrium: Part XII. The 2 e−, 2 H+ homogeneous isotopic electron exchange reaction (nine-member square scheme). *Journal of Electroanalytical Chemistry and Interfacial Electrochemistry* **1984,** *169* (1), 29-46.

14. Deakin, M. R.; Kovach, P. M.; Stutts, K.; Wightman, R. M. Heterogeneous mechanisms of the oxidation of catechols and ascorbic acid at carbon electrodes. *Analytical Chemistry* **1986,** *58* (7), 1474-1480.

15. Lin, Q.; Li, Q.; Batchelor-McAuley, C.; Compton, R. G. Two-Electron, Two-Proton Oxidation of Catechol: Kinetics and Apparent Catalysis. *The Journal of Physical Chemistry C* **2015,** *119* (3), 1489-1495.

16. Corona-Avendaño, S.; Alarcón-Angeles, G.; Ramírez-Silva, M. T.; Rosquete-Pina, G.; Romero-Romo, M.; Palomar-Pardavé, M. On the electrochemistry of dopamine in aqueous solution. Part I: The role of [SDS] on the voltammetric behavior of dopamine on a carbon paste electrode. *Journal of Electroanalytical Chemistry* **2007,** *609* (1), 17-26.

17. DuVall, S. H.; McCreery, R. L. Control of Catechol and Hydroquinone Electron-Transfer Kinetics on Native and Modified Glassy Carbon Electrodes. *Analytical Chemistry* **1999,** *71* (20), 4594-4602.

18. Deakin, M. R.; Wightman, R. M. The kinetics of some substituted catechol/o-quinone couples at a carbon paste electrode. *Journal of Electroanalytical Chemistry and Interfacial Electrochemistry* **1986,** *206* (1), 167-177.

19. Kundu, S.; Wang, Y.; Xia, W.; Muhler, M. Thermal Stability and Reducibility of Oxygen-Containing Functional Groups on Multiwalled Carbon Nanotube Surfaces: A Quantitative High-Resolution XPS and TPD/TPR Study. *The Journal of Physical Chemistry C* **2008,** *112* (43), 16869-16878.

20. Compton, R. G., Banks, C.E. *Understanding Voltammetry*; 2nd ed.; Imperial College Press, London, 2011.

21. Kiema, G. K.; Aktay, M.; McDermott, M. T. Preparation of reproducible glassy carbon electrodes by removal of polishing impurities. *Journal of Electroanalytical Chemistry* **2003,** *540* (0), 7-15.

22. Hershenhart, E.; McCreery, R. L.; Knight, R. D. In situ cleaning and activation of solid electrode surfaces by pulsed laser light. *Analytical Chemistry* **1984,** *56* (12), 2256-2257.

23. DuVall, S. H.; McCreery, R. L. Self-catalysis by Catechols and Quinones during Heterogeneous Electron Transfer at Carbon Electrodes. *Journal of the American Chemical Society* **2000,** *122* (28), 6759-6764.

24. Chen, L.; Li, X.; Tanner, E. E. L.; Compton, R. G. Catechol adsorption on graphene nanoplatelets: isotherm, flat to vertical phase transition and desorption kinetics. *Chemical Science* **2017,** *8* (7), 4771-4778.

25. Wopschall, R. H.; Shain, I. Effects of adsorption of electroactive species in stationary electrode polarography. *Analytical Chemistry* **1967,** *39* (13), 1514-1527.

26. Laviron, E. Adsorption, autoinhibition and autocatalysis in polarography and in linear potential sweep voltammetry. *Journal of Electroanalytical Chemistry and Interfacial Electrochemistry* **1974,** *52* (3), 355-393.

27. Hellgren, N.; Haasch, R. T.; Schmidt, S.; Hultman, L.; Petrov, I. Interpretation of X-ray photoelectron spectra of carbon-nitride thin films: New insights from in situ XPS. *Carbon* **2016,** *108*, 242-252.

28. Yumitori, S. Correlation of C1s chemical state intensities with the O1s intensity in the XPS analysis of anodically oxidized glass-like carbon samples. *Journal of Materials Science* **2000,** *35* (1), 139-146.

29. Gelius, U.; Hedén, P. F.; Hedman, J.; Lindberg, B. J.; Manne, R.; Nordberg, R.; Nordling, C.; Siegbahn, K. Molecular Spectroscopy by Means of ESCA III. Carbon compounds. *Physica Scripta* **1970,** *2* (1-2), 70.

30. Okpalugo, T.; Papakonstantinou, P.; Murphy, H.; McLaughlin, J.; Brown, N. High resolution XPS characterization of chemical functionalised MWCNTs and SWCNTs. *Carbon* **2005,** *43* (1), 153-161.

31. Estrade-Szwarckopf, H.; Rousseau, B. U.P.S. and X.P.S. studies of alkali-graphite intercalation compounds. *Synthetic Metals* **1988,** *23* (1), 191-198.

32. Proctor, A.; Sherwood, P. M. A. X-ray photoelectron spectroscopic studies of carbon fibre surfaces—II: The effect of electrochemical treatment. *Carbon* **1983,** *21* (1), 53-59.

33. Ranganathan, S.; Kuo, T.-C.; McCreery, R. L. Facile Preparation of Active Glassy Carbon Electrodes with Activated Carbon and Organic Solvents. *Analytical Chemistry* **1999,** *71* (16), 3574-3580.

34. Ortiz-Medina, J.; López-Urías, F.; Terrones, H.; Rodríguez-Macías, F. J.; Endo, M.; Terrones, M. Differential Response of Doped/Defective Graphene and Dopamine to Electric Fields: A Density Functional Theory Study. *The Journal of Physical Chemistry C* **2015,** *119* (24), 13972-13978.

35. Downard, A. J.; Roddick, A. D.; Bond, A. M. Covalent modification of carbon electrodes for voltammetric differentiation of dopamine and ascorbic acid. *Analytica Chimica Acta* **1995,** *317* (1), 303-310.

36. Patel, A. N.; Tan, S.-y.; Miller, T. S.; Macpherson, J. V.; Unwin, P. R. Comparison and Reappraisal of Carbon Electrodes for the Voltammetric Detection of Dopamine. *Analytical Chemistry* **2013,** *85* (24), 11755-11764.

37. Ye, F. C.; Wen, Z. B.; Wu, H. F.; Wang, C. Y.; Qian, Y. Simultaneous Electrochemical Determination of Ascorbic Acid, Dopamine and Uric Acid Based on Nitrogen Doped Carbon Sphere Modified Glassy Carbon Electrode. *International Journal Electrochemical Science* **2015,** *10* (2), 1136-1143.

38. Deakin, M. R.; Kovach, P. M.; Stutts, K. J.; Wightman, R. M. Heterogeneous mechanisms of the oxidation of catechols and ascorbic acid at carbon electrodes. *Analytical Chemistry* **1986,** *58* (7), 1474-1480.

39. Salimi, A.; Eshghi, H.; Sharghi, H.; Golabi, S. M.; Shamsipur, M. Electrocatalytic Reduction of Dioxygen at the Surface of Glassy Carbon Electrodes Modified by Some Anthraquinone Substituted Podands. *Electroanalysis* **1999,** *11* (2), 114-119.

40. Chai, J.-D.; Head-Gordon, M. Long-range corrected hybrid density functionals with damped atom-atom dispersion corrections. *Physical Chemistry Chemical Physics* **2008,** *10* (44), 6615-6620.

41. Frisch, M. J.; Trucks, G. W.; Schlegel, H. B.; Scuseria, G. E.; Robb, M. A.; Cheeseman, J. R.; Scalmani, G.; Barone, V.; Mennucci, B.; Petersson, G. A.; Nakatsuji, H.; Caricato, M.; Li, X. et al. Gaussian 09, Revision E.01. Gaussian Inc. , Wallingford CT, 2009.

42. Penas-Defrutos, M. N.; Bartolome, C.; Garcia-Melchor, M.; Espinet, P. Hidden aryl-exchange processes in stable 16e RhIII [RhCp*Ar2] complexes, and their unexpected transmetalation mechanism. *Chemical Communications* **2018,** *54* (8), 984-987.

CHAPTER V

Catechols as Electrochemical Probes of the Surface Nanostructure of N-Doped Carbon Model Systems

The properties of the electrode surface, including the surface nanostructure of the carbon material and the presence of nitrogen moieties, are of crucial importance in both analytical and catalytic applications. Nitrogenated carbon materials have been investigated by many researchers both as electrochemical sensors for biologically-relevant molecules such as dopamine and as electrocatalysts in the oxygen reduction reaction. This chapter describes the preparation of N-doped carbon model systems based on a-C:N thin film electrodes and their characterization with a series of inner-sphere redox probes. The adsorption of two catechols, dopamine and 4-methyl catechol, at the surface of N-doped carbons is shown to be sensitive to both N-site chemistry and the graphitization of the carbon surface. The experimental work is supported by density functional theory calculations of catechol adsorption on model N-doped carbon surfaces.

The data presented in this chapter are part of the following publication:

> Behan, J. A.; Hoque, M. K.; Stamatin, S.N..; Perova, T.S.; Vilella-Aribas, L.; García-Melchor, M.; Colavita, P. E. *The Journal of Physical Chemistry C* **2018**, *122* (36), 20763-20773.

Co-author contributions to this chapter are as follows: M.K.H. and T.S.P. contributed Raman spectroscopy measurements. S.N. contributed several of the XPS measurements. DFT calculations were carried out in collaboration with L.V.A. and M.G.M. through the use of Trinity College High Performance Computing resources. The author is also indebted to Filip Grajkowski, an undergraduate project student who contributed some of the voltammetric data discussed herein.

5. Introduction

Nitrogenated carbon materials have become important materials in the area of metal-free electrocatalysis for processes including the oxygen reduction reaction (ORR)[1-4] and oxygen evolution reaction (OER).[5-6] Their prominence in the area can be attributed to their facile synthesis from low cost starting materials. To date nitrogen has been successfully incorporated into a variety of different nanocarbons including amorphous carbon,[7-9] graphene,[10-13] and carbon nanotubes.[6, 14]

N-doping is known to induce profound chemical and structural alterations in the carbon scaffold. Nitrogen may be substitutionally incorporated into the carbon scaffold as a so-called graphitic-N site, resulting in the N-doping of the carbon scaffold,[15] or in other chemical forms such as pyridinic-N and pyrrolic-N. Most doping protocols result in a distribution of these sites in varying proportions. Moreover, as discussed in Chapter III, the addition of N-sites into the scaffold also introduces vacancies, defects and edge sites[16] which may also have a significant impact on the material's electrochemical performance.

The co-existence of multiple N-sites poses a particular challenge to researchers carrying out structure-activity studies for electrocatalytic applications. Most of the investigations of N-doped carbons in metal-free ORR have focused on identifying which N-moieties constitute the active sites for oxygen electroreduction. Numerous studies on N-doped carbon model systems have found that the presence of both pyridinic-N and graphitic-N sites result in improved ORR onset potentials and limiting current densities.[8, 17] By contrast, factors such as the degree of graphitization of the carbon scaffold, as well as the size and packing of graphitic clusters and the number of defect sites present at the surface have not been considered in great detail.

This paradoxical lack of focus on the nanostructure of the carbon scaffold in carbon electrocatalysts may be attributed at least in part to the lack of a convenient methodology for probing the carbon nanostructure electrochemically. The purpose of this chapter is to attempt to introduce such a methodology in the form of catechol adsorption at graphitized carbon surfaces.

In the previous chapter, the electrochemical response of both N-free and nitrogenated carbon surfaces in solutions of two catechols, dopamine (DA) and 4-methyl catechol (4-MC) was investigated. It was shown that both DA and 4-MC adsorb at an annealed glassy carbon

electrode, a feature which was attributed to non-covalent interactions between the catechol π system and graphitized domains of the electrode surface regions. This was supported by computational studies of DA on model carbon surfaces based on graphene clusters which confirmed that the interaction between the catecholamine and the sp^2-C network of graphene occurs most favourably through lateral interactions with the phenyl moiety. Results agreed with recent experimental and theoretical investigations of catechol adsorption on graphene and N-graphene surfaces. [18-20]

The oxidation of DA on a-C and a-C:N electrodes was also studied. Nitrogenation was shown to enhance the electron transfer kinetics to DA, though no evidence was found for DA adsorption at either a-C or a-C:N surfaces. This lack of adsorbed DA on a-C:N may be attributed to the carbon scaffold structure of amorphous carbon. Most of the N-doped carbon materials employed in electrocatalysis are graphitized carbon materials with extensive sp^2 networks such as N-graphene, [21] N-HOPG [17] and N-doped carbon nanotubes. [22] By contrast, as-deposited a-C/a-C:N materials are predicted to be highly disordered with L_a, the average lateral dimension of graphitic clusters being no larger than around 1 nm, [23] which may be too small in size to facilitate appreciable levels of DA adsorption.

In order to produce a model system with comparable properties to these materials, graphitized carbon surfaces were prepared by subjecting a-C and a-C:N electrodes to thermal annealing treatments. The resulting surfaces with and without incorporated nitrogen were characterized using a combination of cyclic voltammetry, X-ray photoelectron spectroscopy (XPS) and Raman spectroscopy. Results indicate that both DA and 4-MC adsorb on both nitrogenated and nitrogen-free graphitized carbon surfaces, with both N-site chemistry and carbon nanostructure influencing the DA coverage. DA is found to be a more effective probe than 4-MC for the quantification of graphitization in N-doped carbon due to the propensity of 4-MC for forming multilayer structures at the surface. These results are corroborated by computational studies of DA adsorption on model N-doped graphitic clusters via density functional theory (DFT).

5.1 Results and Discussion

Carbon electrodes with and without the presence of nitrogen were prepared via the DC magnetron sputtering protocol described in Chapter III. a-C and two of the 'as-deposited' nitrogenated carbon thin films, a-C:N-2% and a-C:N-10% were chosen as precursor materials for the preparation of graphitized electrodes. As previously described, the a-C:N-2% and a-C:N-10% electrodes have different N/C at. % ratios of 15% and 35% N/C respectively. The graphitization protocol was an annealing treatment for 1 h under nitrogen at 900 °C, the same protocol which was used to prepare the annealed GC electrodes described in Chapter IV. The N-free annealed carbon films prepared via this method are referred to as a-C a900, whereas the two annealed nitrogenated systems studied are referred to as a-C:N-2% a900 and a-C:N-10% a900. A schematic illustrating the model surface preparation is given in Figure 5.1.

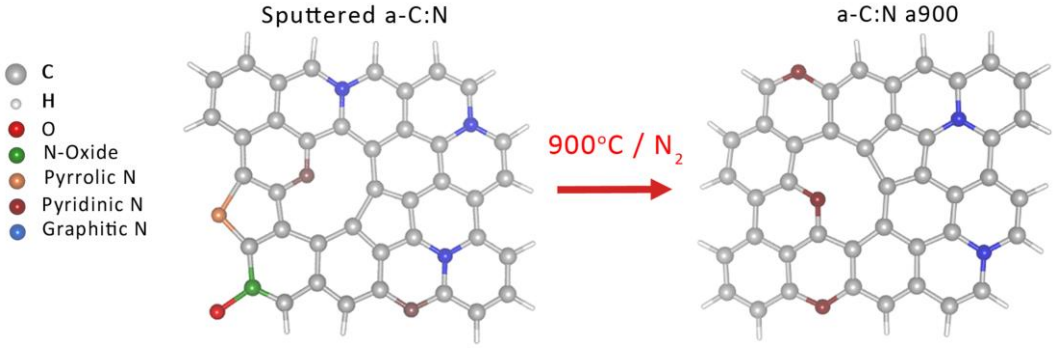

Figure 5.1. Schematic illustrating the preparation of a-C:N a900 electrodes from as-deposited sputtered a-C:N via thermal annealing at 900 °C.

XPS studies of a-C a900 and a-C:N a900 model carbon surfaces

The surface composition of the three graphitized carbon model systems was investigated via XPS. Figure 5.2 a shows survey scans for the carbon electrode materials indicating the presence of C 1s (*ca*. 284 eV) and O 1s (*ca*. 532 eV) peaks. The absence of nitrogen peaks from the a-C a900 surface is evident in the survey and in high resolution scans of the N 1s region between 395 and 405 eV as shown in the inset in Figure 1a, confirming that a-C a900 is a nitrogen-free material. Also shown in the inset is a small peak in the 400 eV region of

the survey spectra for both a-C:N-2% a900 and a-C:N-10% a900, which can be attributed to the presence of nitrogen.[21, 24-25]

High resolution scans of the C 1s region are shown in Figure 5.2 b. The asymmetric

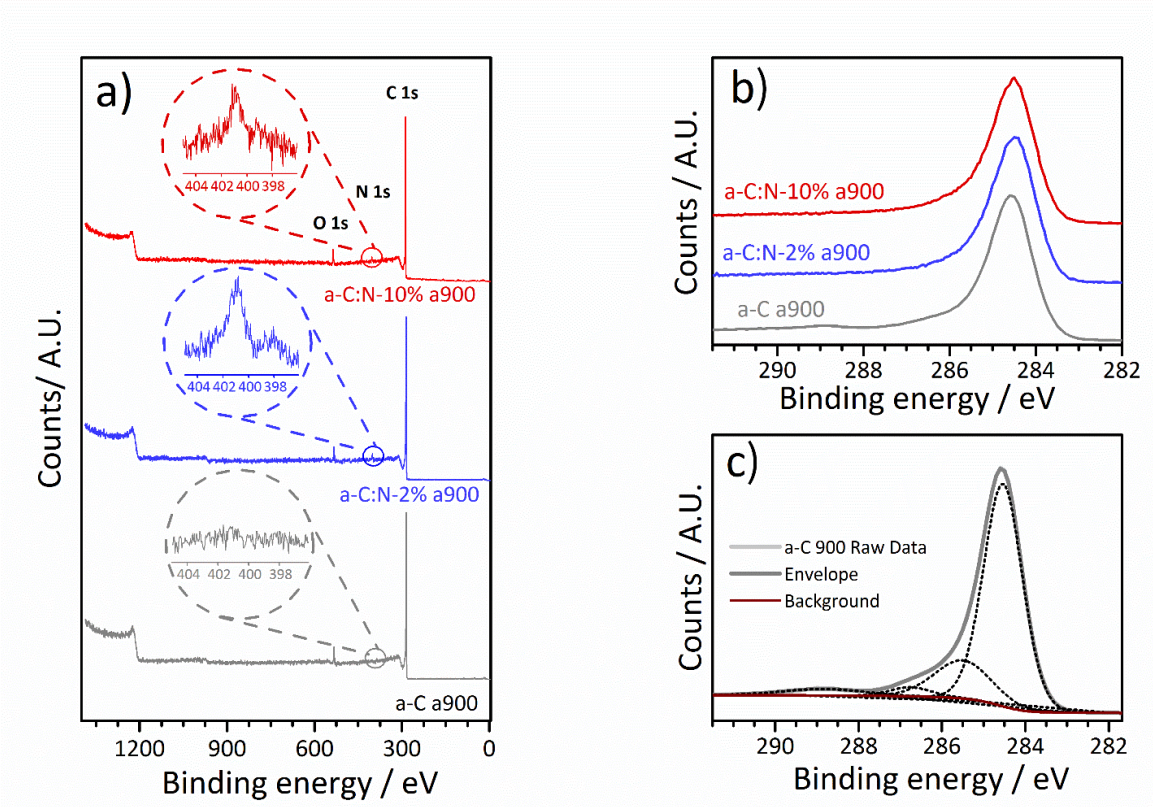

Figure 5.2.(a) Survey scans of a-C a900, a-C:N-2% a900 and a-C:N-10% a900 electrodes. Insets correspond to high resolution scans of the N 1s regions. (b) High resolution C 1s scans of a-C a900 and a-C:N a900 electrodes. (c) Deconvolution of the C 1s envelope of a-C a900; the raw data and envelope are offset relative to the components for clarity. *Redrawn based on Behan, J. A.; Hoque, M. K.; Stamatin, S.N..; Perova, T.S.; Vilella-Aribas, L.; García Melchor, M.; Colavita, P. E. The Journal of Physical Chemistry C* ***2018****, 122 (36), pp 20763-20773. Copyright The American Chemical Society 2018.*

envelope indicates that these carbon materials are predominantly based on sp^2-bonded carbon, as expected for graphitized carbon surfaces. This was further explored by deconvoluting the C 1s envelopes, as shown in Figure 5.2c for the a-C a900 surface, and in Figure 5.3 for a-C:N-2%/10% a900 materials. The peaks at *ca*. 284.5 and *ca*. 285.5 eV present in all deconvolutions are commonly assigned to sp^2 and sp^3 carbon centres, respectively,[26] leading to an estimated sp^3 % of 12 ± 1% in the a-C a900 (see Table 5.1).

Nitrogenation of the carbon scaffold has the effect of increasing the full-width at half maximum (FWHM) of the C 1s envelope (Table 5.1**)** in the a-C:N a900 samples, which is suggestive of the presence of a larger degree of disorder in the carbon sp^2-network.[23] The presence of nitrogen complicates the determination of the sp^3/sp^2 ratio, as the region above *ca*. 285.5 eV includes contributions from both sp^3-C and sp^2-C atoms bonded to nitrogen

moieties.[24-25] The quantitation of the sp^3 content via XPS is therefore limited to the nitrogen-free a-C a900 materials. The peaks at binding energies above *ca*. 286 eV may be assigned to C-O at *ca*. 286.5 eV and C=O at *ca*. 288 eV in the a-C a900 C 1s envelope; however, in the

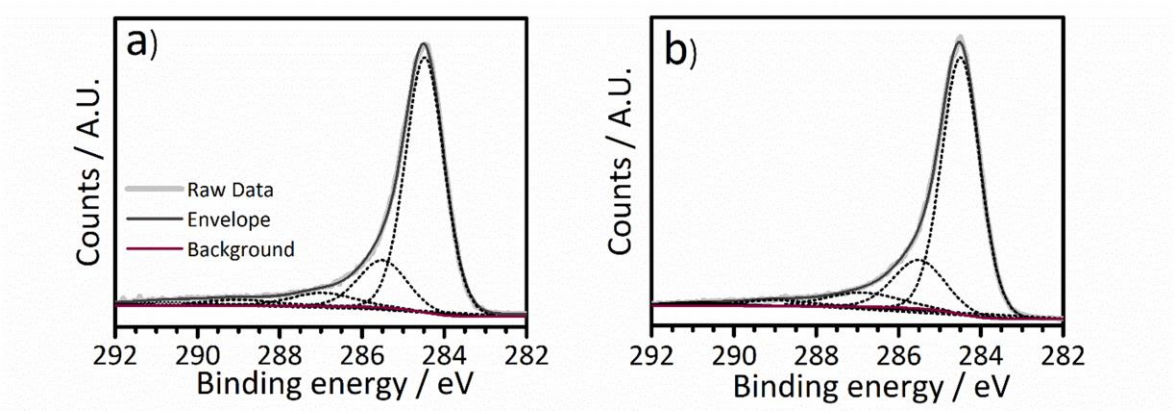

Figure 5.3. Deconvoluted C 1s envelopes of a) a-C:N-2% a900 and b) a-C:N-10% a900

case of the a-C:N a900 envelopes in Figure 5.3, the peaks associated with C-O and C-N bonds cannot be distinguished due to spectral overlap. [27]

The oxygen and nitrogen content present in each film was determined using the area ratios A_{O1s}/A_{C1s} and A_{N1s}/A_{C1s}, respectively, after correction by the sensitivity factors (N = 1.8, C = 1). The resulting O/C and N/C at. % values are reported in Table 5.1. Analysis of variance (ANOVA) on these data indicate that there is no statistically significant difference in O/C at. % among the three surfaces (23 DF, F = 1.70, p = 0.20). The low O/C at. % of *ca.* 3% is consistent with contamination of the surfaces with H_2O and O_2, since the annealed electrodes were exposed to the atmosphere prior to the XPS analysis.[28] Both a-C:N a900 surfaces possess statistically identical N/C at.% close to 2 % (18 DF, t = 1.85, p = 0.083). This is despite the fact that the as-deposited a-C:N-10% surface initially possessed an N/C at. % more than 20% higher than a-C:N-2%, suggesting that the annealing treatment reduces the N content precipitously.

Deconvoluted high resolution N 1s spectra for the a-C:N a900 surfaces are shown in Figure 5.4. For both a-C:N a900 films, best fits to the raw spectrum were achieved using two components. There is a dominant contribution to the envelope at ca. 401 eV which is associated with the presence of graphitic nitrogen (N_G), as well as a smaller shoulder at ca. 398 eV, which is commonly assigned to pyridinic-N (N_P).[21, 24] The ratio of N_P/N_G is approximately 25:75 for both a-C:N-2% a900 and a-C:N-10% a900 (Table 5.1), indicating that both systems possess similar nitrogen site distribution in addition to their similar N/C at. % values.

Table 5.1. C 1s FWHM, sp^3/sp^2 and chemical composition of a-C a900 and a-C:N a900 materials obtained from XPS deconvolutions. Errors reported are 95% confidence intervals.

Sample	C1s FWHM	sp^3 %	O/C %	N/C %	N_G/N_T %	N_P/N_T %
a-C a900	1.00 ± 0.05	12 ± 1	3 ± 2	-	-	-
a-C:N-2% a900	1.7 ± 0.4	-	4 ± 1	1.8 ± 0.3	75 ± 5	25 ± 5
a-C:N-10% a900	2.1 ± 0.6	-	2.6 ± 0.7	2.4 ± 0.6	74 ± 8	26 ± 8

The thermal treatment has a dramatic effect on both the nitrogen content and nitrogen site chemistry of the carbon scaffold in a-C:N a900 electrodes. The as-deposited a-C:N electrodes were previously analysed with XPS in Chapter III, where it was shown that a variety of N-sites including N-oxides and pyrrolic-N sites were present in addition to the N_P and N_G sites. Furthermore, the major component contributing to each of these envelopes was found to be pyridinic N, whilst in the annealed electrodes N_P sites are a minority component. It is well known that annealing of nitrogenated carbon systems at temperatures above 800 °C selects for the most thermally stable N_G sites.[10] Thermal annealing therefore has the effect of reducing the N-content by eliminating all but the most stable of N-sites. This is illustrated

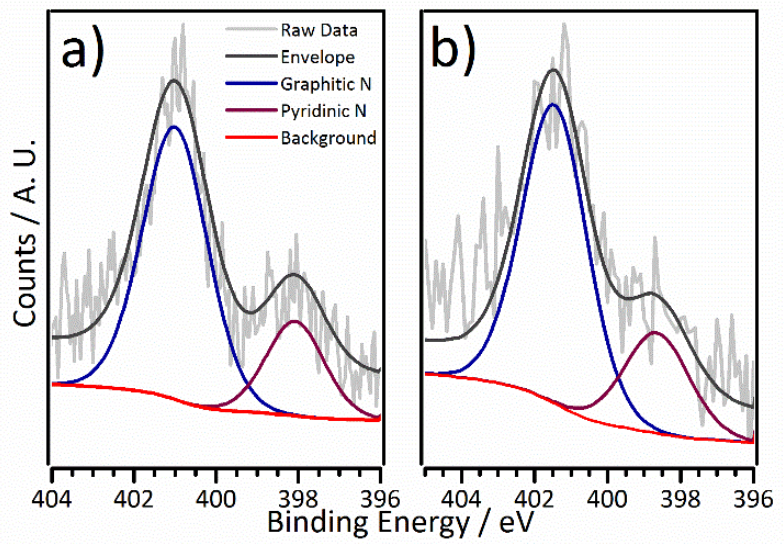

Figure 5.4. High resolution N 1s scans of (a) a-C:N-2% a900, and (b) a-C:N-10% a900, showing their deconvolution into two contributions; raw data and envelope are offset relative to the components for clarity. *Redrawn from Behan, J. A.; Hoque, M. K.; Stamatin, S.N..; Perova, T.S.; Vilella-Aribas, L.; García Melchor, M.; Colavita, P. E. The Journal of Physical Chemistry C 2018, 122 (36), pp 20763-20773. Copyright The American Chemical Society 2018.*

in Figure 5.5 which shows the changes induced in an a-C:N-10% N 1s envelope by thermal annealing at two different temperatures, 700 ºC (a-C:N-10% a700) and 900 ºC (a-C:N-10% a900).

Upon annealing at the lower temperature of 700 ºC for 1 hr, the N-content is also reduced relative to the as-deposited film, but not to the same extent as the thermal treatment at 900 ºC. For the a-C:N-10% a700 there is also a distinctive double-peaked shape in the spectrum centered at 400 eV, which may be attributed to the selective removal of pyrrolic-N sites by the heat treatment. The high binding energy region (> 402 eV) of the a-C:N-10% a700 envelope overlaps almost perfectly with the envelope of the as-deposited a-C:N, suggesting that 700 ºC is not a sufficient temperature for the removal of N-oxide moieties. The high binding energy region of the a-C:N-10% a900 is entirely flat, which implies that the N-oxides have been removed. Based on these results, the apparent trend in thermal stability

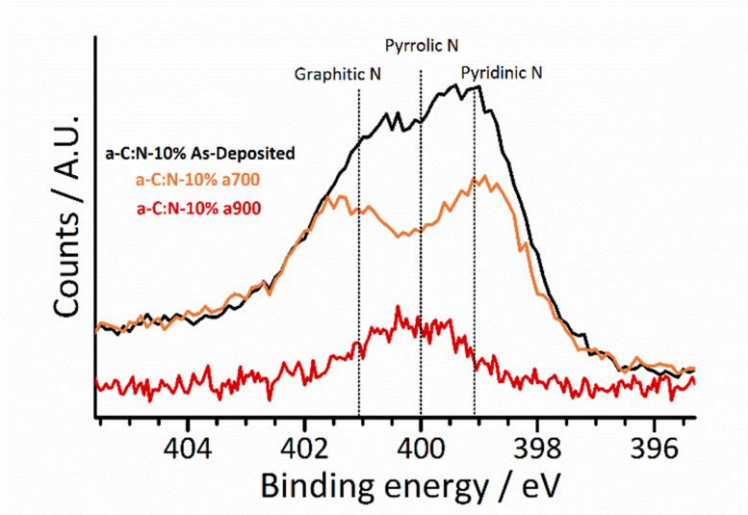

Figure 5.5. N 1s envelope of an a-C:N-10% electrode as-deposited and after annealing at either 700 ºC or 900ºC. Dashed lines show the general positions associated to Graphitic, Pyrrolic and Pyridinic N contributions.

of N-sites in a-C:N is found to be Graphitic-N > Pyridinic-N > N-Oxide > Pyrrolic-N.

In summary, XPS measurements of a-C a900, and a-C:N a900 films indicate that carbon deposition followed by thermal annealing at 900 ºC results in N-free and N-doped graphitized carbon materials. All three carbon materials possess comparable levels of oxygen, whilst the nitrogenated systems have comparable total nitrogen content and similar distribution of surface N-sites. Despite these similarities, the carbon scaffolds differ significantly in their organisation as evidenced by the differences observed in the FWHM of the C 1s envelope.

Raman Spectroscopy Studies of a-C a900 and a-C:N a900 Films

The differences in the structural arrangement in the carbon scaffolds of a-C a900 and a-C:N a900 materials were investigated using Raman spectroscopy measurements carried out at an excitation wavelength of 488 nm. Figure 5.6 shows background-subtracted Raman spectra for the a-C a900 and a-C:N a900 films. All spectra show two maxima at *ca.* 1590 cm^{-1} and 1380 cm^{-1}, commonly referred to as the G and D peaks of sp^2-C centers, respectively.[23, 29-30] The G peak is associated with an in-plane stretching mode of sp^2-C centres present in the carbon scaffold, whereas the D peak is a breathing mode of sp^2-C sites in six-membered rings.[29] In perfectly crystalline graphite, the D peak represents a Raman-forbidden mode, and the peak is only observed in graphitized carbon materials in the presence of disorder/defects. The D peak intensity is therefore highly correlated to the degree of disorder in the carbon scaffold (*vide infra*).

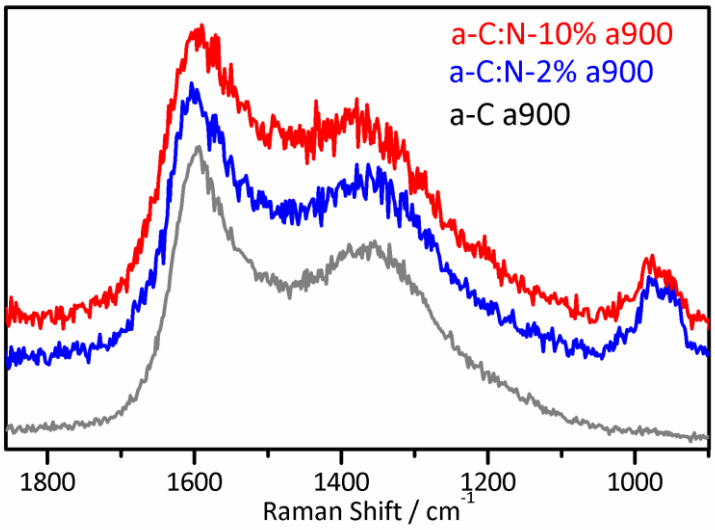

Figure 5.6. Raman spectra of a-C a900 and a-C:N a900 films carbons; spectra are background corrected and offset from one another for clarity.

The best fits for the a-C a900 and a-C:N a900 spectra are presented in Figure 5.7 and were obtained using a 3 peak Gaussian deconvolution involving the aforementioned G and D peaks as well as a third smaller peak close to 1500 cm^{-1} . This component is commonly referred to as the A peak and is associated with C-C stretching vibrations of both three- and four-fold coordinated carbon atoms in the carbon scaffold in the amorphous regions

connecting graphitic crystallites.[31] The small peak close to 1000 cm^{-1} observed in some spectra is associated with the underlying Si substrate on which the films were deposited for Raman characterization.[32] Spectral parameters derived from the fits are reported in Table 5.2.

On the basis of the three-stage model of Ferrari and Robertson for amorphous carbons with and without nitrogen,[23, 29] all three films have properties that are more consistent with nanocrystalline graphite than with amorphous carbon. This is evidenced by a G-peak position at *ca.* 1600 cm^{-1} for all three model systems, which is expected for a graphitized carbon scaffold in both nitrogenated and non-nitrogenated films [23] and a FWHM that is

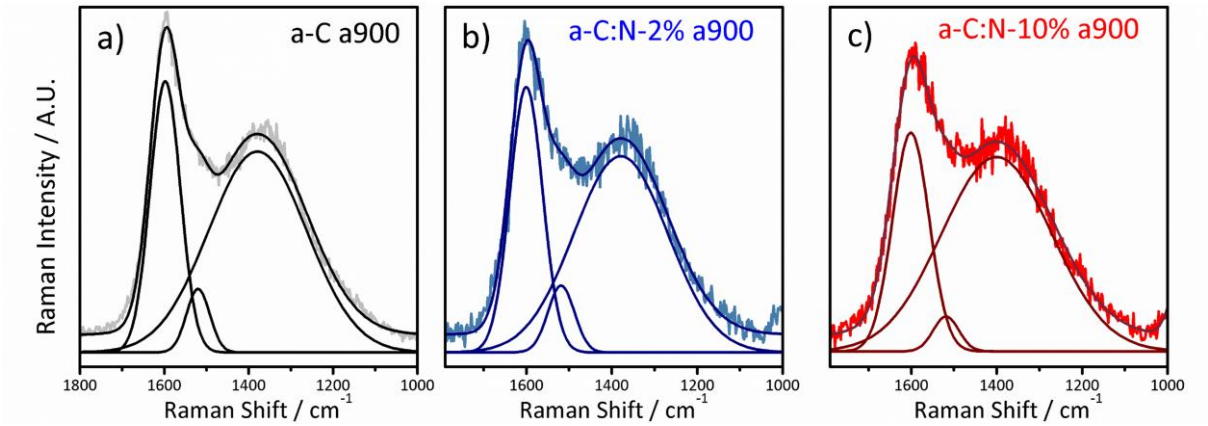

Figure 5.7. Deconvoluted Raman spectra of a-C 900, a-C:N-2% a900 and a-C:N-10% a900.

consistent with a cluster size on the order of 10 nm.[23] For both a-C:N a900 films the G FWHM increases relative to nitrogen-free a-C a900, with a-C:N-10% a900 having the widest FWHM and therefore the greatest disorder. This trend is consistent with the XPS studies which showed a C 1s FWHM trend for the three surfaces in the order of a-C:N-10% a900 > a-C:N-2% a900 > a-C a900. Further insights on the carbon microstructure emerge from an analysis of I_D/I_G and I_A/I_G ratios, also shown in Table 5.2, which are both metrics associated with the level of order/disorder in the carbon scaffold.

The a-C:N-2% a900 has a slightly smaller I_D/I_G and slightly larger I_A/I_G ratios relative to unmodified carbon, although the differences are slight and do not suggest significant differences between a-C a900 and a-C:N-2% a900 in terms of the organization of the carbon scaffold and the density of defects/boundaries. In the case of a-C:N-10% a900, however, the I_D/I_G is significantly larger than for a-C:N-2% a900, which strongly suggests that the graphitic crystallite size is significantly smaller in the a-C:N-10% a900 film. The a-C:N-10% a900 film also shows the smallest I_A/I_G ratio, indicating that graphitized regions

of the scaffold are more closely packed, thus reducing the prevalence of interstitial C-C contributions.

Table 5.2. Raman spectral parameters for a-C a900 and a-C:N a900 carbon materials.

Sample	I_D/I_G	I_A/I_G	G position / cm^{-1}	G FWHM / cm^{-1}	D position / cm^{-1}	D FWHM / cm^{-1}
a-C a900	0.74	0.23	1598	85	1379	274
a-C:N-2% a900	0.73	0.26	1600	91	1379	260
a-C:N-10% a900	0.84	0.16	1603	104	1385	279

Overall, Raman data indicate that a-C:N-2% a900 and a-C:N-10% a900 display significant differences in the organization of their carbon scaffolds, despite these materials possessing an identical N/C at.% and a similar distribution N_G and N_P sites. The fact that the number of N_P sites remains constant between a-C:N-2% a900 and a-C:N-10% a900 is intriguing, since N_P necessarily exists at edge or vacancy sites in the carbon scaffold.

This suggests that the increase in the level of disorder for a-C:N-10% a900 can only be explained on the basis of differences in the organization of the carbon framework around the incorporated N-sites, rather than on the basis of differences in the number density of N_G and N_P sites. These dissimilarities in carbon scaffold structuring likely arise from the use of sputtered precursor films with very different initial N/C contents (15 and 35 at.%), as previously mentioned. This explains the evolution of both a-C:N materials towards an almost identical N-site composition and concentration: the majority of the initial nitrogen content is "annealed-out" by the thermal treatment, resulting in a final concentration < 2.5 at.% of the most stable N_G-sites. However, the initial concentration of edges, defects and N-sites is also what determines the size and packing of graphitic clusters present in the scaffold prior to annealing, which limits the ability to anneal away vacancies and other carbon defects even as the nitrogen sites are removed. Hence, the degree of disorder in the annealed materials is effectively tuned by the amount of disorder present in the precursor carbon.

Voltammetric Studies of a-C a900 and a-C:N a900 Electrodes with DA

Based on XPS and Raman results, a-C a900 and a-C:N-2% a900 films possess similar degrees of graphitization in their carbon scaffold but differ in that a-C:N-2% a900 displays

N_G/N_P functionalities on its surface. At the same time, a-C:N-2% a900 and a-C:N-10% a900 possess indistinguishable N_G/N_P composition but display differences in the nanostructuring of their graphitic clusters. The trio of a-C a900 and a-C:N-2%/10% a900 therefore constitute a useful set of N-doped carbon model systems which in principle allow for the different contributions of N-site chemistry and carbon scaffold organisation to electrochemical behaviour to be distinguished from one another.

To study the effects of surface nanostructuring on the electrochemical response of nitrogenated graphitic carbons, catechols were chosen as redox probes. As discussed in chapter IV, catechols are extremely surface-sensitive probes[33-36] which adsorb onto carbon electrodes through π-stacking interactions at graphitized domains of the scaffold. This behaviour can in principle be exploited to probe the degree of clustering and organization of the carbon scaffold surrounding N-sites.

Figure 5.8 a shows representative CVs in 1.0 mM DA solutions in 0.1 M H_2SO_4 for a-C a900, a-C:N-2% a900 and a-C:N-10% a900 electrodes at a scan rate (v) of 5 mV s^{-1}. For comparison, the voltammogram of a polished glassy carbon (GC) disk is also presented. The oxidation of DA involves a net transfer of two protons and two electrons (n = 2) via a complex 'scheme of squares' mechanism.[34, 37] The CVs in Figure 5.8 a all show the characteristics of a reversible $2e^-$ process, with ΔE values close to the Nernstian value of $\frac{59}{2}$ mV[38] and almost identical anodic and cathodic peak current densities (Figure 5.8 b). By contrast, the DA voltammogram on the GC disk shows a large peak-to-peak separation of 240 ± 60 mV which implies that charge transfer is electrochemically irreversible, as discussed in the previous chapter.[39]

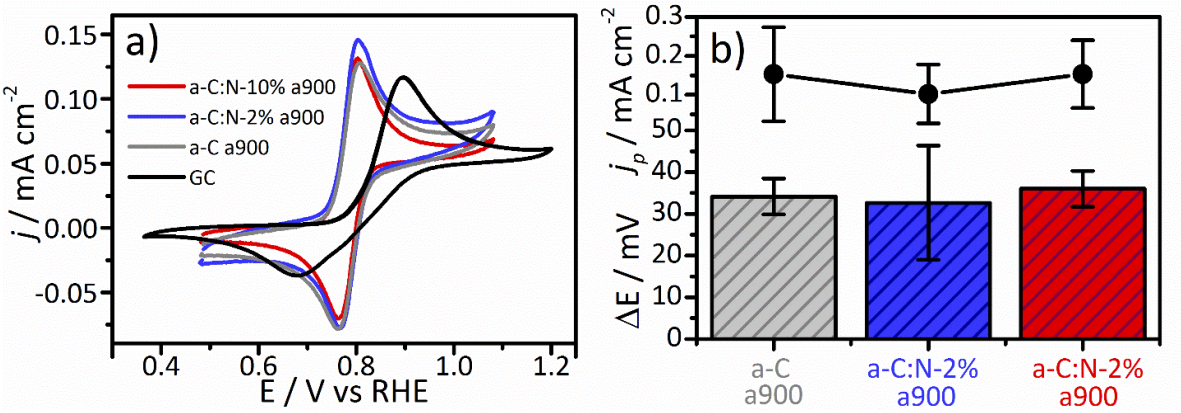

Figure 5.8. a) CVs of GC, anC and anC:N films in solutions of 1.0 mM DA/0.1 M H_2SO_4 at 5 mV s^{-1}. b) Peak current densities (top) and ΔE values (bottom) derived from voltammetric measurements at 5 mV s^{-1} on all annealed electrodes studied. *Redrawn based on Behan, J. A.; Hoque, M. K.; Stamatin, S.N..; Perova, T.S.; Vilella-Aribas, L.; García Melchor, M.; Colavita, P. E. The Journal of Physical Chemistry C 2018, 122 (36), pp 20763-20773. Copyright The American Chemical Society 2018.*

At low scan rates, a-C a900 and a-C:N a900 electrodes all show indistinguishable behaviour towards DA close to the reversible charge transfer limit. However, significant differences emerge among the three materials as the scan rate is increased above 50 mVs^{-1} to 1000 mV s^{-1} (Figures 5.9 a-c). The shape of the voltammetric waves is markedly different from that observed at low scan rates in Figure 5.8 a, becoming more symmetric than expected for a process involving diffusion of a redox analyte to the electrode surface.[39-40] ΔE values in Figures 5.9 a-c are in the range of 10-20 mV, characteristic of an adsorption-controlled process, for which peak-to-peak potential values are expected to approach zero. This result is similar to that obtained on the annealed GC surface described in the previous chapter.

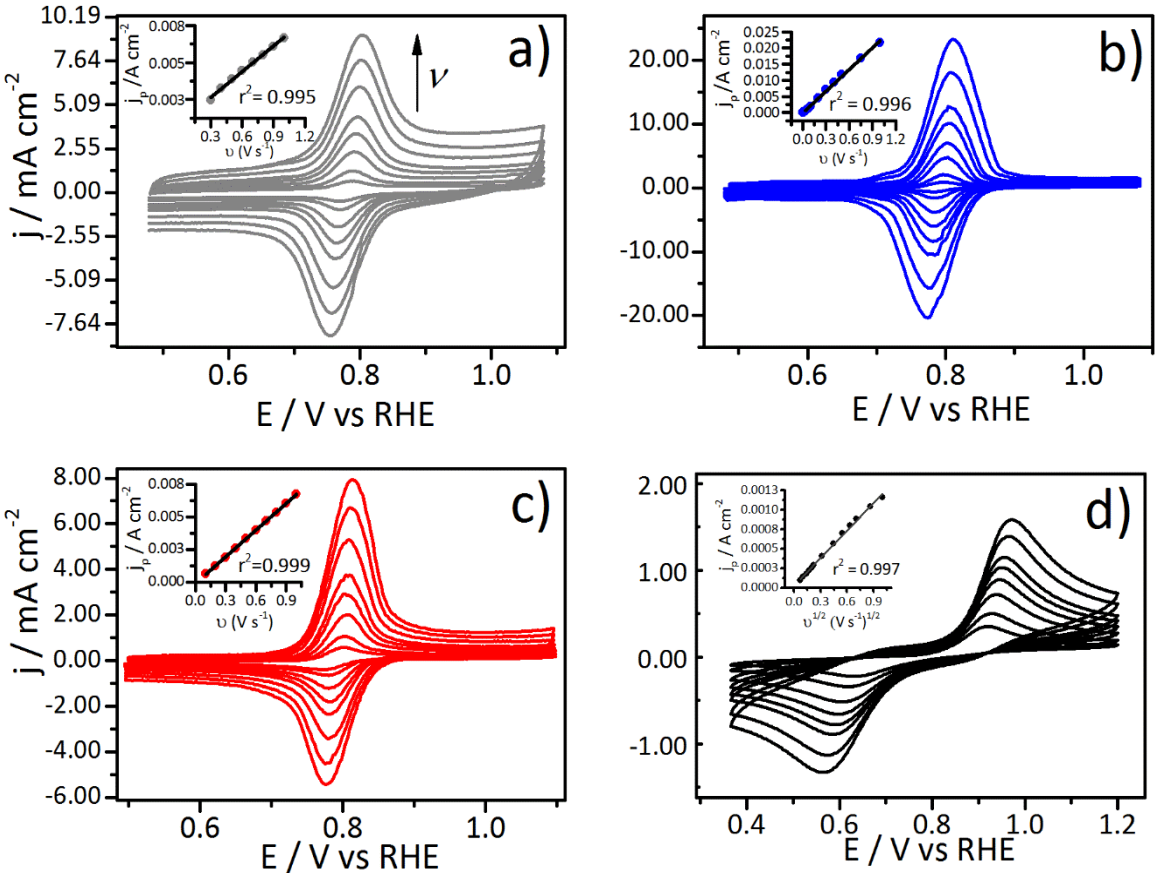

Figure 5.9. CVs of 1.0 mM DA in 0.1 M H_2SO_4 for (a) anC, (b) a-C:N-2% a900, (c) a-C:N-10% a900 and (d) GC electrodes; v = 50-1000 mV s^{-1}. Insets in (a)-(c) are plots of peak current density (j_p) vs. v, showing a linear relationship. The inset in (d) corresponds to a plot of j_p vs. $v^{1/2}$. *Redrawn based on Behan, J. A.; Hoque, M. K.; Stamatin, S.N..; Perova, T.S.; Vilella-Aribas, L.; García Melchor, M.; Colavita, P. E. The Journal of Physical Chemistry C 2018, 122 (36), pp 20763-20773. Copyright The American Chemical Society 2018.*

Plots of the anodic peak current density, j_p, vs. v in the insets of Figures 5.9 a-c show that j_p varies linearly with ν in the range of 50-1000 mV s^{-1}, which is consistent with a surface-adsorbed redox probe. For the bare GC (Figure 5.9 d), there is no evidence of a narrowing of ΔE or an enhancement of j_p, which increases linearly vs. $v^{1/2}$, as expected for a redox process involving only the diffusion of solution-phase DA to the electrode surface.

Changes in waveform and peak separation indicate that both solution-phase and surface-bound DA are redox active at the a-C a900 and a-C:N a900 surfaces, with adsorbed DA contributing more to the overall peak current as the scan rate increases.[41] This is clearly evident from the logarithmic plot of anodic peak current ($i_{p,a}$) vs. scan rate for the a-C a900 and a-C:N a900 electrodes presented in Figure 5.10 a, which shows a slope of m = 0.5 at scan rates of 5-20 mV s^{-1}. This suggests that oxidation of DA in solution dominates the Faradaic current in this range as described by Equation (5.1),

$$\ln(i_p) = 0.5\ln(v) + \ln(2.69.10^5 n^{\frac{3}{2}} A D^{\frac{1}{2}} c) \quad (5.1)$$

where A is the electrode area, D is the diffusion coefficient (6.6 x 10^{-6} cms^{-1}, and c is the concentration of DA. For higher scan rates, there is an enhancement of i_p above the value expected for a Nernstian process such that each of the plots diverges from m = 0.5 and approaches a slope m = 1. This suggests that the response in this scan range is better described by Equation (5.2) and its logarithmic form in Equation (5.3), where the Faradaic current is assumed to originate from a redox species bound at the electrode with a surface coverage Γ.

$$i_p = \frac{n^2F^2\,vA\Gamma}{4RT} \quad (5.2)$$

$$\ln(i_p) = \ln(v) + \ln(\frac{n^2F^2A\Gamma}{4RT}) \quad (5.3)$$

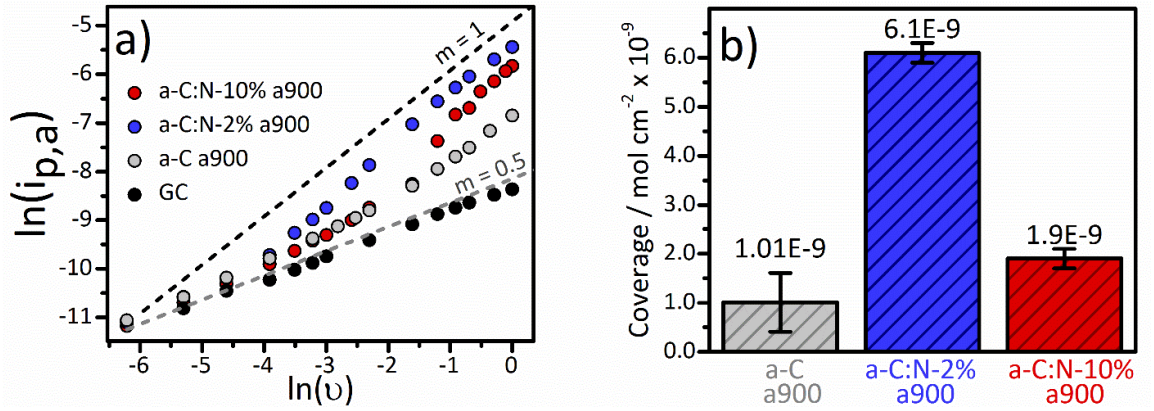

Figure 5.10. (a) Logarithmic plot of the anodic peak current, $i_{p,a}$, vs. v, for a-C a900 and a-C:N a900 electrodes in a solution of 1.0 mM DA in 0.1 M H_2SO_4. The dashed lines represent theoretical slopes of m = 1 and m = 0.5 and are present to guide the eye. (b) Coverage values, Γ, of DA on the electrode surfaces calculated using Equation (5.2) in the text. *Redrawn based on Behan, J. A.; Hoque, M. K.; Stamatin, S.N..; Perova, T.S.; Vilella-Aribas, L.; García Melchor, M.; Colavita, P. E. The Journal of Physical Chemistry C 2018, 122 (36), pp 20763-20773. Copyright The American Chemical Society 2018.*

When both solution-phase and surface-bound redox processes occur simultaneously, the relative contribution of adsorbates is expected to dominate the redox response even at low scan rates, provided that the solution concentration is sufficiently low. [41] This was verified in the case of DA by obtaining voltammograms on an a-C a900 electrode in solutions of 25 µM DA in 0.1 M H_2SO_4 as shown in Figure 5.11 a. It is evident in the figure that the voltammograms obtained at this DA concentration have the distinct features for an adsorbed redox species, *viz.* a wave which is symmetric about the formal potential with a ΔE value *ca.* 5 mV, even at scan rates as low as 10 mV s^{-1}. Figure 5.11 b) shows plots of the peak current densities obtained from the plot in a) versus the scan rate and the square root of the scan rate. The plot is linear with respect to v across the entire range, but non-linear versus $v^{1/2}$, confirming that adsorbed DA at the electrode surface is the predominant contribution to the Faradaic current, when the solution concentration is low.

Using the slopes obtained from the plots in the insets of Figure 5, along with Equation 5.2 with T = 298 K and the electrode geometric area A = 0.1963 cm^2, the DA coverages (Γ_{DA}) at each electrode surface were obtained and are summarized in Figure 6b. From this figure, it is evident that there are significant differences in Γ_{DA} among the three carbon electrodes,

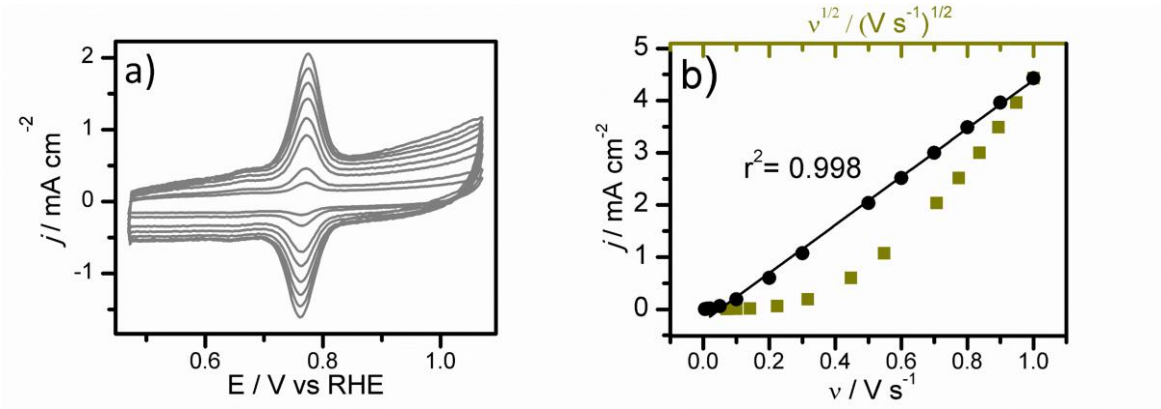

Figure 5.11. a) Voltammograms obtained at an a-C a900 electrode in a solution of 25 µM DA / 0.1 M H_2SO_4 at scan rates between 10 mV s^{-1} and 1 V s^{-1}. b) Plot of the peak current density versus ν and $\nu^{1/2}$, showing that the peak current is linear with respect to the scan rate across the entire scan rate range employed for the experiment.

which display a ratio of 1.0:6.0:1.9 for a-C a900 : a-C:N-2% a900 : a-C:N-10% a900, respectively.

As discussed in the studies of DA adsorption on GC electrodes in the previous chapter, these coverage values are obtained in each case from voltammograms taken for a constant immersion time in DA / H_2SO_4 solution of 10 minutes. This was the time required to degass the electrolyte after assembling the electrochemical cell prior to each experiment. The equilibration time for DA adsorption may be significantly longer than this and as such the

coverages reported in Figure 5.10 are intended to serve as a comparison of the Γ_{DA} value obtained after a constant immersion time and are not intended to be representative of the equilibrium value. Also implicit in these studies is that the adsorption equilibration time does not vary significantly with N-content or with the chemical composition of the surface generally, so that the coverage values obtained for the a-C a900 and a-C:N a900 electrodes are controlled only by the thermodynamics of DA-surface adsorption in each case.

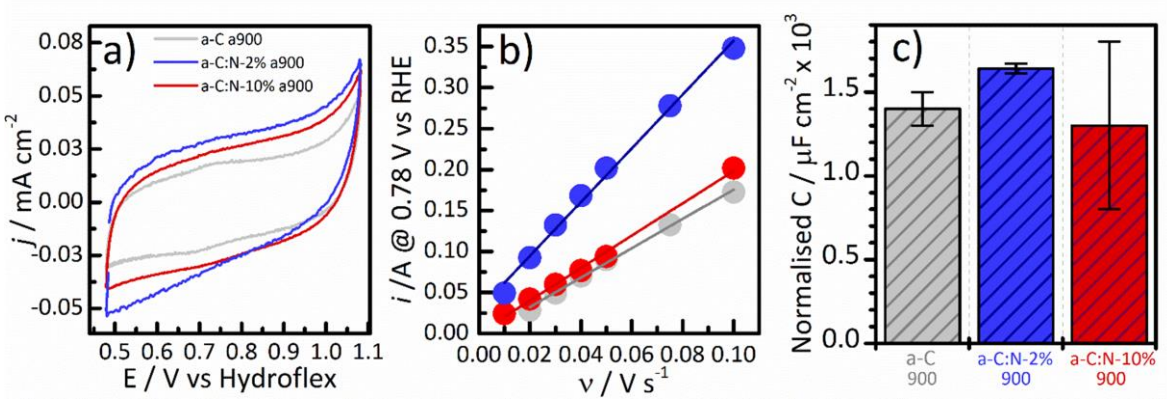

Figure 5.12. a) CVs in 0.1 M H_2SO_4 for annealed electrodes at 10 mV s^{-1}. b) Plots of the capacitive current at 0.78 V vs RHE versus the scan rate for a-C a900 and a-C:N-2-10% a900 c) Calculated area-normalized capacitance values for anC, a-C:N-2% a900 and a-C:N-10% a900. Error bars represent 95% confidence intervals (n = 3).

The differences in Γ_{DA} also cannot be explained based on changes to the electrochemical surface area (ESA) among the three electrodes. This was confirmed based on measurements of specific capacitance in supporting electrolyte solution, shown in Figure 5.12 a). The voltammograms on each surface in the absence of DA show no evidence of any Faradaic processes occuring in the range 0.5 – 1.1 V vs RHE; only the charging current, i_{DL} due to the capacitance of the double layer is evident. The magnitude of i_{DL} is similar for the three surfaces based on the near-overlap of the three voltammograms. By taking the average of the anodic and cathodic currents at the centre of the voltammogram (i.e. at 0.78 V vs RHE) at scan rates between 10 mVs^{-1} and 100 mVs^{-1}, it is possible to produce a plot of the charging current at this potential versus the scan rate, as shown in Figure 5.12 b. Since this plot is linear, according to Equation 5.4:

$$C = (di/dv)_{V=0.78\,V} \tag{5.4}$$

The slope of the best-fit line to this plot is the double-layer capacitance.[42] Resulting values of the capacitance normalised by the geometric area of the electrode are plotted in Figure 5.12 c). The overlap of the error bars in these plots indicate that there is no statistically

significant difference in the capacitance among the three electrodes. Assuming that no surface redox processes contribute to the observed capacitance (i.e. assuming that there are no pseudocapacitive contributions to the charging current), it is possible to obtain an estimate of the roughness factor of the electrode surface by dividing the experimentally-determined capacitance by a standard value of *ca.* 20 μF cm^{-2} which is a value on the lower side of the expected range of 10-60 μF cm^{-2} for a carbon surface.[43] This yields roughness factors of *ca.* 60-70 for the electrodes. This value should be taken as an upper-bound on the roughness contribution, since the large absolute capacitance values found particularly for the a-C:N a900 surfaces may very likely be attributed to some pseudocapacitive contributions arising from the presence of N sites at the surface.

Since the as-deposited a-C and a-C:N electrodes are known to have a roughness in the range of 1-2 nm on Si substrates, the large roughness factors measured here for the annealed surfaces may be attributed in part to the underlying GC substrate which may be heavily scratched during the polishing protocol. It is also possible that the films contain pinholes or nanopores with a dimension too small to be detected via AFM measurements, which would be expected to significantly increase the electrochemically accessible area.

Regardless of the origin of the capacitance values, the estimated value for the double-layer capacitance is similar for all three model surfaces. This suggests that a-C a900 and a-C:N a900 electrodes possess similar values of the ESA. The differences observed in the magnitudes of DA adsorption on the three electrode surfaces therefore arise from specific DA-surface interactions which vary among a-C a900, a-C:N-2% a900 and a-C:N-10% a900 electrodes, thus giving rise to marked differences in adsorption yields.

It is interesting to examine Γ_{DA} results in the light of chemical and structural information obtained via XPS and Raman. Nitrogen incorporation into the a-C:N a900 electrodes in the form of N_G/N_P functional groups results in enhanced Γ_{DA} relative to a-C a900, which likely arises from a combination of chemical and physical effects on DA adsorption at the carbon surface. The similarities between a-C:N-2% a900 and a-C:N-10% a900 in terms of N/C and O/C content and proportion of N_P/N_G functionalities (see Table 5.1) suggest that fundamental physical or structural differences, rather than differences in the nitrogen site chemistry, might better explain the 3-fold enhancement of Γ_{DA} for a-C:N-2% a900 relative to a-C:N-10% a900. Furthermore, the more modest 2-fold enhancement of Γ_{DA} in a-C:N-10% a900 compared to a-C a900 suggests that structural differences in the carbon scaffold can have a stronger effect on DA adsorption than the presence of nitrogen moieties at the electrode surface.

This conclusion is supported by the Raman results, which indicate that a-C a900 and a-C:N-2% a900 are similar in their organization of the carbon scaffold and their degree of graphitization, whilst a-C:N-10% a900 displays the most disordered carbon structure and likely the smallest crystallite size among the three graphitic materials. The introduction of N_G/N_P groups without a significant disruption of the graphitic scaffold results in an enhancement of Γ_{DA} when going from a-C a900 to a-C:N-2% a900. However, this chemical enhancement effect is essentially lost when the degree of graphitization is reduced as shown for the a-C:N-10% a900 electrodes.

These results obtained on the graphitized N-doped carbon surfaces may also offer insight into why the as-deposited a-C and a-C:N electrodes do not show any evidence of DA adsorption despite possessing a much higher N/C at. % than their annealed counterparts: the a-C films produced and previously characterised by the group have small graphitic cluster domains < 1 nm in size[44] which precludes catechol adsorption to the degree observed on graphitized carbon surfaces which possess much larger sp^2 clusters.

Computational studies of DA adsorption on graphene models

Electrochemical results suggest that DA adsorption can track changes in both the surface chemistry and nanostructure of graphitized carbon electrodes. Given the similarities in the degree of graphitization between a-C a900 and a-C:N-2% a900, it appears that probe adsorption is enhanced by the incorporation of N-sites as long as the disruptive effect of nitrogenation does not result in a high concentration of defects in the annealed structure and/or a reduction in the sp^2 domain size. DA adsorption at the carbon surface reflects differences in bulk defect density between a-C:N-2% a900 and a-C:N-10% a900 as observed via Raman spectroscopy, thus suggesting that increased defects in the nitrogenated scaffold can result in reduced probe adsorption.

Hence, the combination of spectroscopic and voltammetric results lead to the hypothesis that DA adsorption may serve as an indicator of the degree of graphitization at the electroactive interface in nitrogenated carbons.

In order to investigate this hypothesis, computational investigations at the DFT-wb97xd level were carried out using the model graphene structures presented in Figure 5.13. DFT-wb97xd functionals are used to investigate both short-range molecular interactions and longer range interactions expected in the case of non-covalent forces.[49] While graphene and N-graphene with vacancies have been studied theoretically,[19-20] DFT calculations have not

been used to evaluate the interaction of DA with graphitic edges, nor have the entropic contributions to the adsorption been investigated by computing the Gibbs free energy of adsorption, $\Delta G_{ads.}$

Computational analysis began in a similar fashion to that described in Chapter IV, by first optimising the structures of the isolated DA molecule and the graphitic model surfaces shown in Figure 5.13, followed by the adsorption of DA on each surface in different possible orientations and at different adsorption sites. The lowest ΔG_{ads} values obtained and the corresponding structures are summarized in Figure 5.14. All of the modelled structures including initial and final states for DA adsorption are illustrated in detail in Appendix I.

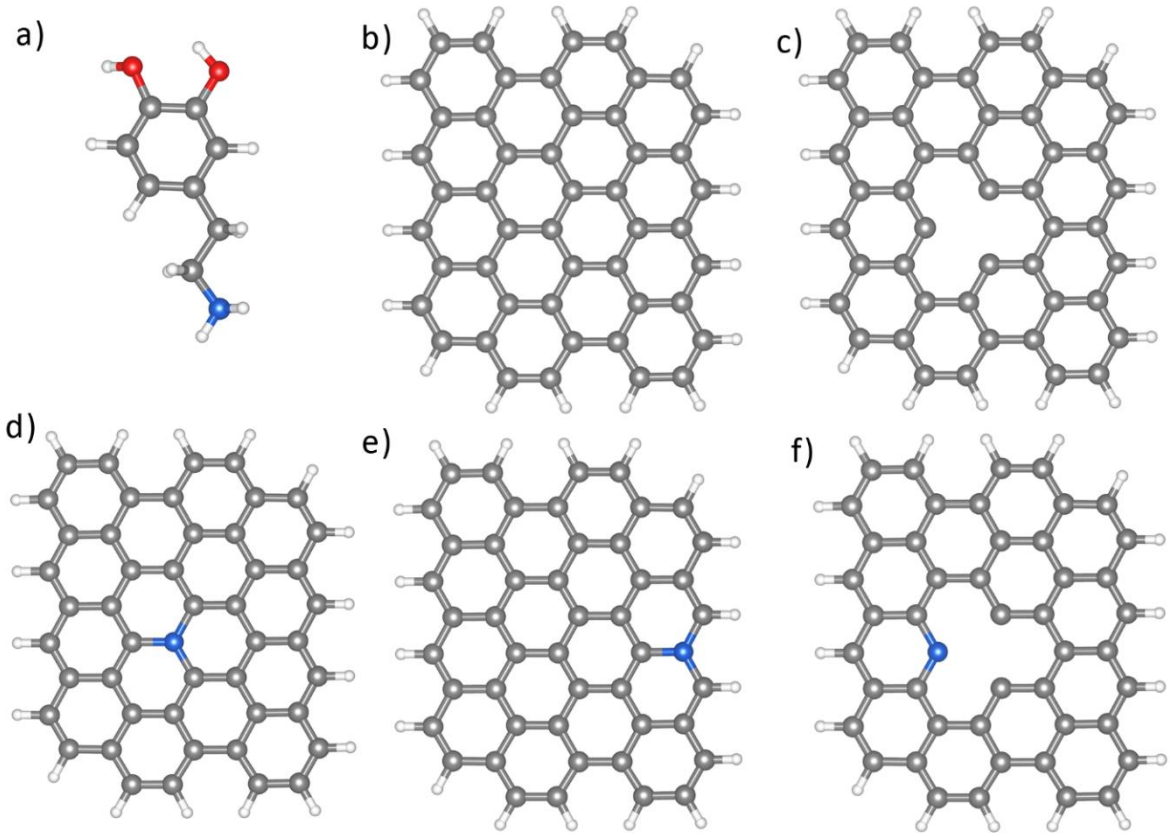

Figure 5.13. Ball and stick representation of the DFT-modelled structures: (a) DA, (b) graphene, (c) graphene with a single carbon vacancy, (d) N-graphene with a graphitic centre site, (e) N-graphene with a graphitic valley site, and (f) N-graphene with a pyridinic vacancy. *Redrawn based on Behan, J. A.; Hoque, M. K.; Stamatin, S.N..; Perova, T.S.; Vilella-Aribas, L.; García Melchor, M.; Colavita, P. E. The Journal of Physical Chemistry C 2018, 122 (36), pp 20763-20773. Copyright The American Chemical Society 2018.*

For the interaction of DA with the basal plane of pristine graphene (DA-BP), it was found that the most favourable orientation of the molecule at the surface is close to parallel, with a ring-surface distance of 3.2-3.6 Å (Figure 5.14 a). This range of bond distances is typical of a non-covalent interactions and are in line with those reported in previous theoretical studies for DA adsorption on graphene.[20]

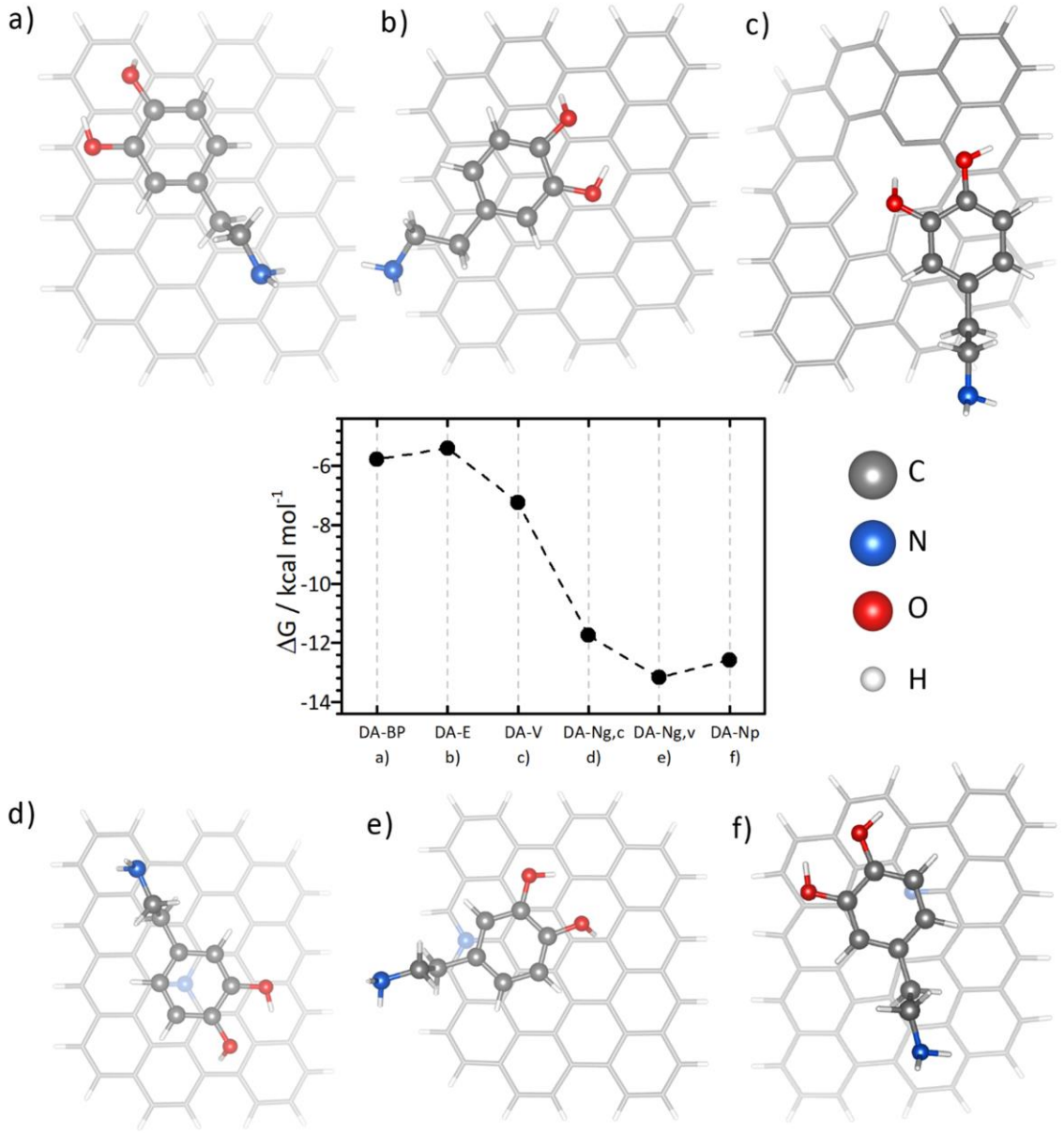

Figure 5.14. Calculated adsorption Gibbs energies (ΔG_{ads}), in kcal mol^{-1} for DA. Top views of the optimized structures for the different adsorption modes and their corresponding ΔG_{ads} values on graphene (a-c) and N-doped graphene (d-f) model systems. *Reproduced from Behan, J. A.; Hoque, M. K.; Stamatin, S.N..; Perova, T.S.; Vilella-Aribas, L.; García Melchor, M.; Colavita, P. E. The Journal of Physical Chemistry C* ***2018****, 122 (36), pp 20763-20773. Copyright The American Chemical Society 2018.*

In this adsorption mode, the ethylamine chain is oriented away from the benzene ring, giving a distance of around 4.6 Å between the N-atom of the amine and the surface. The interaction of DA with the lone pair of the amine pointing to a hydrogenated graphene edge and the aromatic ring facing away from the surface was also considered (DA-E). According to calculations, this adsorption mode is not stable and the DA molecule evolves to an orientation parallel to the basal plane as for DA-BP (Figure 5.14 b). However, unlike DA-BP, the ethylamine group in DA-E is placed in an almost parallel disposition to the surface close to a hydrogenated edge atom, with a N-surface distance of 3.3 Å.

While this might be indicative of a weak interaction between the edge site and the lone pair of the amine, the computed ΔG_{ads} for DA-E is almost identical to DA-BP (-5.4 and -5.5 kcal mol^{-1}, respectively). Hence, for hydrogenated edges no clear preference in the orientation of the amine when the π-system of DA interacts with the basal plane was identified. The DA molecule adsorbed on a carbon vacancy (DA-V) is also oriented parallel to the graphene surface, but in this case the H atoms from the hydroxyl groups point into the vacancy (Figure 5.14 c). The ΔG_{ads} value obtained for DA-V is approximately 2 kcal mol^{-1} lower than DA-BP and DA-E, which may be explained by the favourable interactions arising from the hydrogen bonding between the hydroxyl groups and the unsaturated carbon atoms adjacent to the vacancy.

In the case of the N-doped graphene surfaces (Figures 5.14 d-f), ΔG_{ads} was found to be significantly more negative compared to the aforementioned non-nitrogenated surfaces. In the case of DA-$N_{G,C}$, the orientation of DA is almost identical to that of non-nitrogenated DA-BP, with the π-system of DA sitting on top of the graphitic nitrogen (N_G) and with a N-surface distance of 4.66 Å (Figure 5.14 d). The calculated ΔG_{ads} for DA-$N_{G,C}$ is more than double the value of the DA-BP interaction (-11.7 vs. -5.5 kcal mol^{-1}), thus suggesting that the substitutional N-site enhances adsorption of the DA molecule. The most negative ΔG_{ads} value (-13.4 kcal mol^{-1}), however, was obtained for DA-$N_{G,V}$, where DA sits parallel to the surface over the $N_{G,V}$ site with the amine pointing away from the surface (Figure 5.14 e). A similar adsorption energy was obtained even when the molecule was oriented with the amine pointing at the nitrogenated edge (see Appendix I**)**. Finally, for the interaction of DA with the carbon surface containing a pyridinic vacancy (DA-N_P), the aromatic ring of DA was found to sit on top of the pyridinic nitrogen site (N_P) with the amine group almost parallel to the surface (Figure 5.14 f). The calculated ΔG_{ads} for this structure is only slightly more positive than for DA-$N_{G,V}$, which indicates that DA adsorption at a pyridinic vacancy is also highly favourable.

Overall, the above DFT results are in good agreement with the voltammetric experiments for both a-C a900 and a-C:N a900 surfaces, which are strongly suggestive of a weak adsorption at the carbon surface. This is based on the fact that, for a strong adsorption (ΔG_{ads} in the absence of an applied field, $|\Delta G°_{ads}| > \sim 10$ kcal mol^{-1}), 'pre-peaks' and/or 'post-peaks' are expected to appear in the voltammogram due to the strong interaction of the reactant and/or products with the surface.[41] The DFT-calculated values of ΔG_{ads} for DA-BP, DA-E and DA-V, are either comparable to this threshold value or lower. On the other hand, the computational results also predict that the adsorption at nitrogenated sites has a larger ΔG_{ads}. However, these sites make up a very small proportion of the available binding sites at the surface, as shown from the XPS studies. Therefore, the absence of any pre- or post-peaks in the voltammograms of a-C:N-2% a900 and a-C:N-10% a900 may thus be explained by the low concentration of these sites at the surface.

The more negative values of ΔG_{ads} at nitrogen sites may partially explain why DA coverages are higher for the a-C:N a900 surfaces compared to a-C a900, since adsorption at nitrogen sites is thermodynamically more favourable in N-doped surfaces. However, N-sites alone do not control DA adsorption in general, since a-C:N-10% a900 has a DA coverage which is far lower than for a-C:N-2% a900, despite having an identical N/C at.% and N surface chemistry. This suggests that the mere presence of nitrogen sites is not sufficient to induce DA adsorption and that the organization of the carbon scaffold induced by the annealing is the most important factor. As a-C:N-2% a900 and a-C:N-10% a900 show different coverages of DA despite their similar N/C at.% and N_G/N_P concentration, the differences in graphitic clustering, or more specifically average lateral graphitic cluster size between the two surfaces, are the origin of these variations. This suggests that DA adsorption experiments may be used as an effective probe of the interfacial carbon nanostructure, thus complementing information on defect density derived from bulk methods such as Raman spectroscopy.

Voltammetric Studies of a-C a900 and a-C:N a900 with 4-Methyl Catechol

In the previous chapter it was shown that the voltammetric response of DA and 4-MC at GC surfaces subjected to different surface pre-treatments was similar. Electron transfer to both molecules was found to be sluggish on GC polished with alumina slurry, quasi-reversible on anodised GC electrodes with high values of the O/C at. % and reversible at GC electrodes which were subjected to thermal annealing at 900 ^{o}C. Adsorption of both molecules was

detected voltammetrically at annealed GC and, in the case of DA, was attributed to π-stacking interactions at the graphitized carbon interface based on computational DFT studies.

In this chapter DA was chosen as the first catechol probe of carbon nanostructure for graphitized N-doped carbon surfaces. This choice was motivated in part because of the importance of DA interactions with carbon surfaces to the biosensor community. However, if the conclusions arrived at in Chapter IV and in the preceding four subsections of this chapter are correct, in principle it is possible to apply any catechol species as a surface probe of graphitization, for all catechols share the same 1,2-dihydroxybenzene core which can adsorb at the graphitized domains of the electrode.

A consequence of this principle is that similarly-sized catechols should hypothetically yield similar coverage values at a given surface with a fixed degree of graphitization. In order to test this hypothesis, voltammetric studies of 4-MC with a-C a900 and a-C:N 2%/10% a900 were carried out under similar conditions to those used for DA. Figure 5.15 shows CVs for each of the annealed electrodes in solutions of 1mM 4-MC at a scan rate of 5 mVs^{-1}. The voltammograms for all three electrodes have the characteristics of a

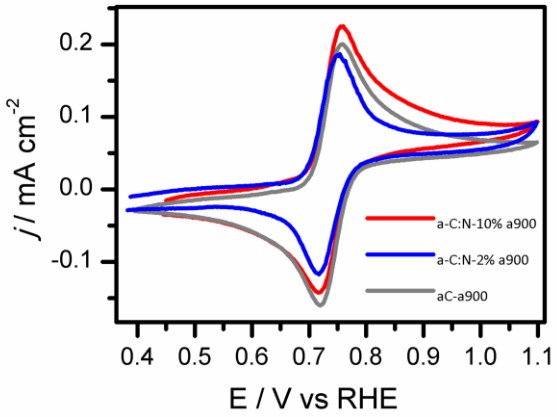

Figure 5.15. CV at 5 mV s^{-1} of a-C a900 and a-C:N-2-10% a900 surfaces in solutions of 1 mM 4-MC / 0.1 M H_2SO_4.

reversible $2e^-$ transfer, i.e. ΔE of 30-35 mV (Table 5.4) indicating that electron transfer to 4-MC is reversible on all three surfaces in a manner similar to that described for DA.

The voltammetric response to 4-MC was also studied as a function of scan rate, *v*, as shown in Figure 5.16. The voltammograms at higher scan rates for 4-MC show a similar response to that seen for DA, i.e. a narrowing of ΔE to values < 10 mV and heightening of the peak current density j_p above that expected for a Faradaic process occurring due to diffusion of the redox probe to the electrode surface. Note that the solution concentration of

4-MC used to obtain the voltammograms in Figure 5.16 is 250 μM, or one quarter of that used for DA in Figure 5.9**,** but the peak current densities obtained in the scan rate range used are comparable. This suggests that $\Gamma_{4\text{-MC}} > \Gamma_{DA}$ on these surfaces, a point which is discussed in more detail further below.

Although the absolute values of 4-MC coverage appear to be different from those of DA, the relative coverage trends for a-C a900, a-C:N-2% a900 and a-C:N-10% a900 on each surface are similar. Figure 5.16 d shows logarithmic plots of the peak currents obtained on each surface. All of the plots are linear with slope m = 1, as expected for adsorbed 4-MC, and the peak currents scale such that $\Gamma_{a\text{-C:N-2\% a900}} > \Gamma_{a\text{-C a900}} > \Gamma_{a\text{-C:N-10\% a900}}$ (Table 5.4). $\Gamma_{4\text{-MC}}$ on the a-C:N-2% a900 surface is once again the highest, but for 4-MC the undoped a-C a900 surface has a larger coverage than N-doped a-C:N-10% a900.

The large differences in $\Gamma_{4\text{-MC}}$ and Γ_{DA} on the a-C a900 surface at higher solution concentrations of the catechols were not anticipated. In order to understand why two molecules with similar structures and generally similar voltammetric behaviour would nonetheless showcase significant differences in adsorbate coverage, $\Gamma_{4\text{-MC}}$ and Γ_{DA} were obtained from voltammetric studies at a range of solution concentrations on the a-C a900

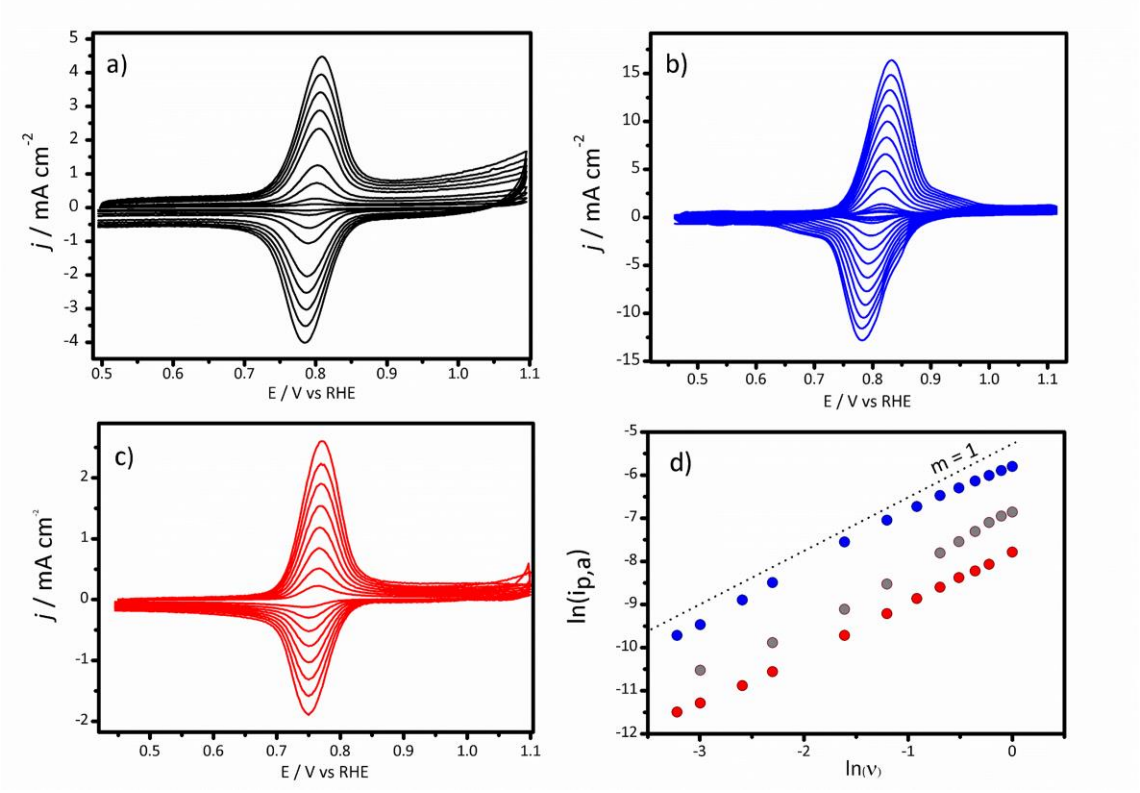

Figure 5.16. Voltammograms of a) a-C a900 b) a-C:N-2% a900 c) a-C:N-10% a900 in solutions of 250 μM 4-MC / 0.1 M H_2SO_4. d) logarithmic plot of peak currents versus scan rate for the voltammograms in a-c.

surface. Figure 5.17 shows CVs at the constant scan rate of 1 V s^{-1} as a function of concentration for each catechol. As shown in the figure, there are significant differences in the peak current densities as well as in the shape of the voltammogram obtained in each case. The FWHM of the voltammogram for 4-MC is significantly wider than that observed for DA at solution concentrations of 500 μM and above (Table 5.4). This suggests that interactions between the adsorbate molecules at the surface are different for 4-MC and DA, with the difference becoming more pronounced at higher solution concentrations where coverages are expected to be highest. [45-46]

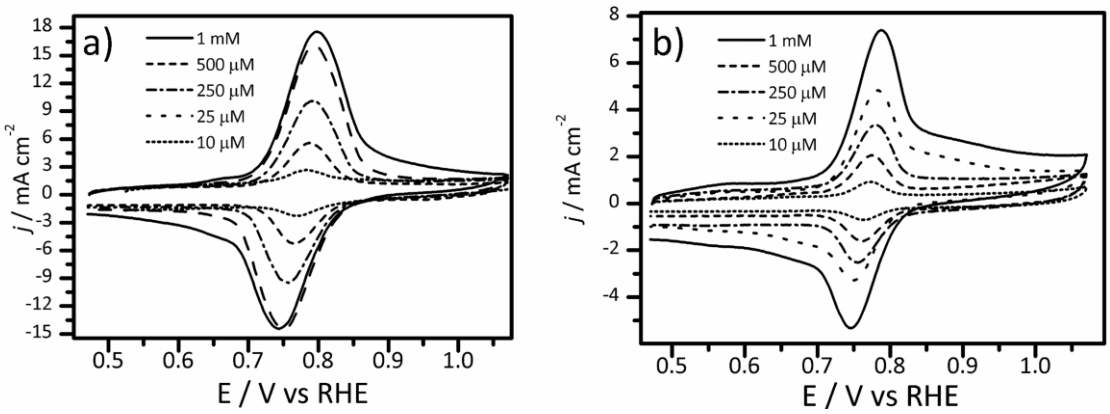

Figure 5.17 CVs of a) 4-MC and b) DA at different solution concentrations in 0.1 M H_2SO_4.

Examining the voltammograms obtained at low solution concentrations, the peak current density values for both catechols are quite similar at concentrations less than 25 μM, suggesting that the apparent enhancement of $\Gamma_{4\text{-MC}}$ relative to that observed for DA is observable only when the concentration of 4-MC exceeds a particular threshold of solution concentration.

Studies of $\Gamma_{4\text{-MC}}$ and Γ_{DA} at the a-C a900 surface determined from voltammetric data as a function of the solution concentration are presented in Figure 5.17 a**.** As shown in the figure, the Γ values for both molecules are identical at a solution concentration of 10 μM and have similar values for a concentration of 25 μM. It is only when the solution concentration is 100 μM and above that significant differences begin to emerge between the molecules. Γ_{DA} begins to level off at around 1 x 10^{-9} mol cm^{-2} at a concentration of 250 μM, whereas $\Gamma_{4\text{-MC}}$ continues to rise in this range up to a value of 4 x 10^{-9} mol cm^{-2}, levelling off only at solution concentrations above 500 μM.

Table 5.4. Average coverages of 4-MC on a-C a900, a-C:N-2% a900 and a-C:N-10% a900 electrodes.

Sample	$\Gamma_{4\text{-MC}}$ / mol cm^{-2} x 10^{-9}
a-C a900	4 ± 1
a-C:N-2% a900	7 ± 2
a-C:N-10% a900	3 ± 1

The profile of the Γ vs c plot for both molecules has the form of a Langmuir isotherm described by Equation 5.5:

$$\frac{\Gamma}{\Gamma_{max}} = \frac{K_{ads}C}{1+K_{ads}C} \tag{5.5}$$

Where c is the solution concentration of the adsorbate and K_{ads} is the equilibrium constant (with units of L mol^{-1}) for the adsorption reaction:

$$A + S \rightleftharpoons AS \tag{5.6}$$

Here A denotes a generic adsorbate, S a surface site and AS the adsorbed molecule. K_{ads} can be derived from a linear regression on the Γ vs C data by rewriting Equation 5.5 in the form:

$$\frac{C}{\Gamma} = \frac{1}{\Gamma_{max}} + \frac{K_{ads}C}{\Gamma_{max}} \tag{5.7}$$

which implies that the plot of C/Γ versus C should be linear with a slope of $K_{ads}/\Gamma_{max.}$ Such plots for 4-MC and DA on a-C a900 are given in Figure 5.17 b) with the associated values of K_{ads} and ΔG^0_{ads} calculated using the relationship $\Delta G^0_{ads} = -RTlnK_{ads}$ after K_{ads} is made dimensionless by multiplying its value by the standard concentration value, $c^0 = 1$ mol L^{-1}. The resulting K_{ads} values are listed in Table 5.5.

Both DA and 4-MC have ΔG^0_{ads} values around 12 kcal mol^{-1} with adsorption being more favourable for 4-MC under standard conditions than for DA. This confirms that, despite the similarities in chemical structure and general electrochemical behaviour of the two

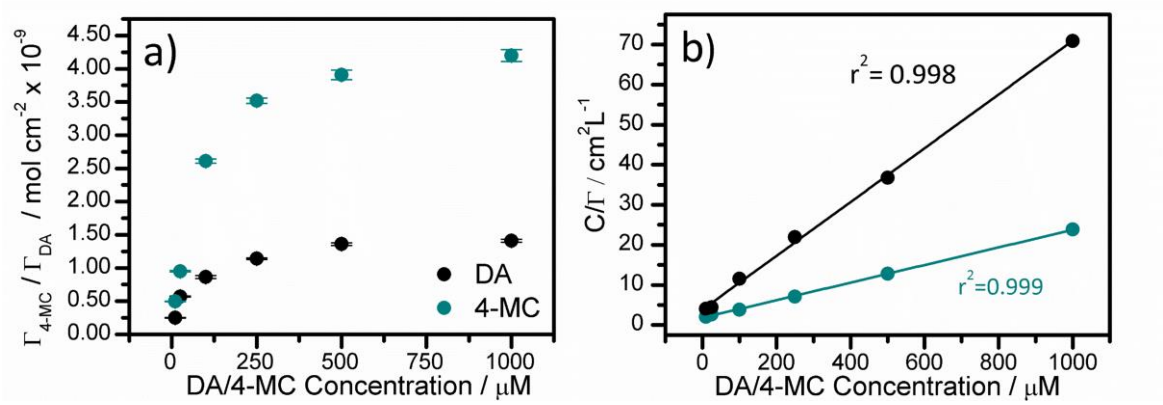

Figure 5.17. a) Coverages of 4-MC and DA at an a-C a900 surface versus solution concentration determined via voltammetry studies. b) Plots of C/Γ versus solution concentration for DA and 4-MC derived from the data in a).

molecules, the thermodynamics governing the adsorption of the two catechols are different. These differences are explored in more detail in the computational study of 4-MC adsorption at model carbon surfaces in the following section.

Table 5.5. Values of K_{ads} and ΔG^0_{ads} for DA and 4-MC on a-C a900 electrodes calculated from adsorption data.

Probe	K_{ads} L mol^{-1}	ΔG^0_{ads} / kcal mol^{-1}
4-MC	4.5 x 10^{-9}	11.37
DA	1.5 x 10^{-9}	12.03

Computational Studies of 4-MC Adsorption at Model Carbon Surfaces

Voltammetric studies of 4-MC on a-C a900 and a-C:N-2%/10% a900 surfaces appear to indicate that the adsorption of 4-MC is thermodynamically more favourable than DA adsorption, with higher coverages obtained for 4-MC on each of the surfaces. In order to

investigate the origin of this surprising difference in adsorption between structurally similar molecules, computational studies of 4-MC on the same N-free and N-doped model surfaces used for DA were carried out.

The results are summarised in Figure 5.18. The calculated value of ΔG_{ADS} for 4-MC at basal and hydrogenated edge sites (4-MC-BP and 4-MC-E, part a and b of the figure) are both comparable to values obtained for DA. This result confirms that adsorption of 4-MC also occurs through π-stacking interactions between the catechol ring and the surface. The interaction between 4-MC and a vacancy in the surface (4-MC-V, part c of Figure 5.18) is more stable than the interaction with the basal plane by *ca.* 4 kcal mol^{-1}. Unlike what was observed for DA, 4-MC also appears to sit directly on the vacancy in the framework rather than evolving towards the basal regions of the surface.

The interactions between 4-MC and $N_{G,C}$ and $N_{G,V}$ sites results in similar ΔG_{ADS} values to those observed for DA, albeit with lower adsorption free energies by *ca.* 2 kcal mol^{-1}. The generally higher ΔG_{ADS} values found for the nitrogenated surfaces is in agreement with the a-C:N-2% a900 surface displaying the highest coverages of both molecules. The strongest interaction found was the interaction between the H atoms of the hydroxyl moiety of 4-MC with the N_P site, which resulted in values of ΔG_{ADS} of -15.5 kcal mol^{-1}.

The DFT calculations offer some insights into the differences in adsorption observed for the two molecules. Although calculations indicate that nitrogenation favours catechol adsorption compared to N-free graphene, interactions at N-sites are generally more favourable for DA than for 4-MC. This may explain why the a-C:N-10% a900 surface shows lower coverages of 4-MC than the a-C a900 surface even though the opposite trend was found for DA. Like DA, 4-MC adsorption may still be disrupted by the presence of excessive defects in the scaffold, and the weaker interactions between 4-MC and N-sites compared to DA may imply that 4-MC is even more sensitive to scaffold disorder than DA is. If this were true, the presence of N-sites in the a-C:N-10% a900 could be more than offset by the increased disorder evident in the carbon scaffold compared to a-C a900 and a-C:N-2% a900, resulting in an inversion of the coverage trend.

The computational results presented so far do not explain the 4-fold increase in $\Gamma_{4\text{-MC}}$ compared to Γ_{DA} on the a-C a900 surface discussed in the previous section. The voltammetric studies appear to indicate that the differences may be explained by interactions between adsorbed molecules. At low concentrations of both solution phase 4-MC and DA, the apparent coverages are extremely similar and are close to the saturation value observed for DA of 1 x 10^{-9}. Assuming a planar interaction with the surface and using tabulated bond length values for adsorbed catechol[20] leads to a rough estimate of 8.5 × 10^{-10} mol cm^{-2} for a close-packed monolayer of DA or 4-MC which agrees well with this result. It is only when the solution concentration is increased that the apparent coverage of 4-MC dramatically increases. This observation, along with the widening of the FWHM of the voltammogram at higher 4-MC concentrations suggests that interactions between 4-MC molecules are

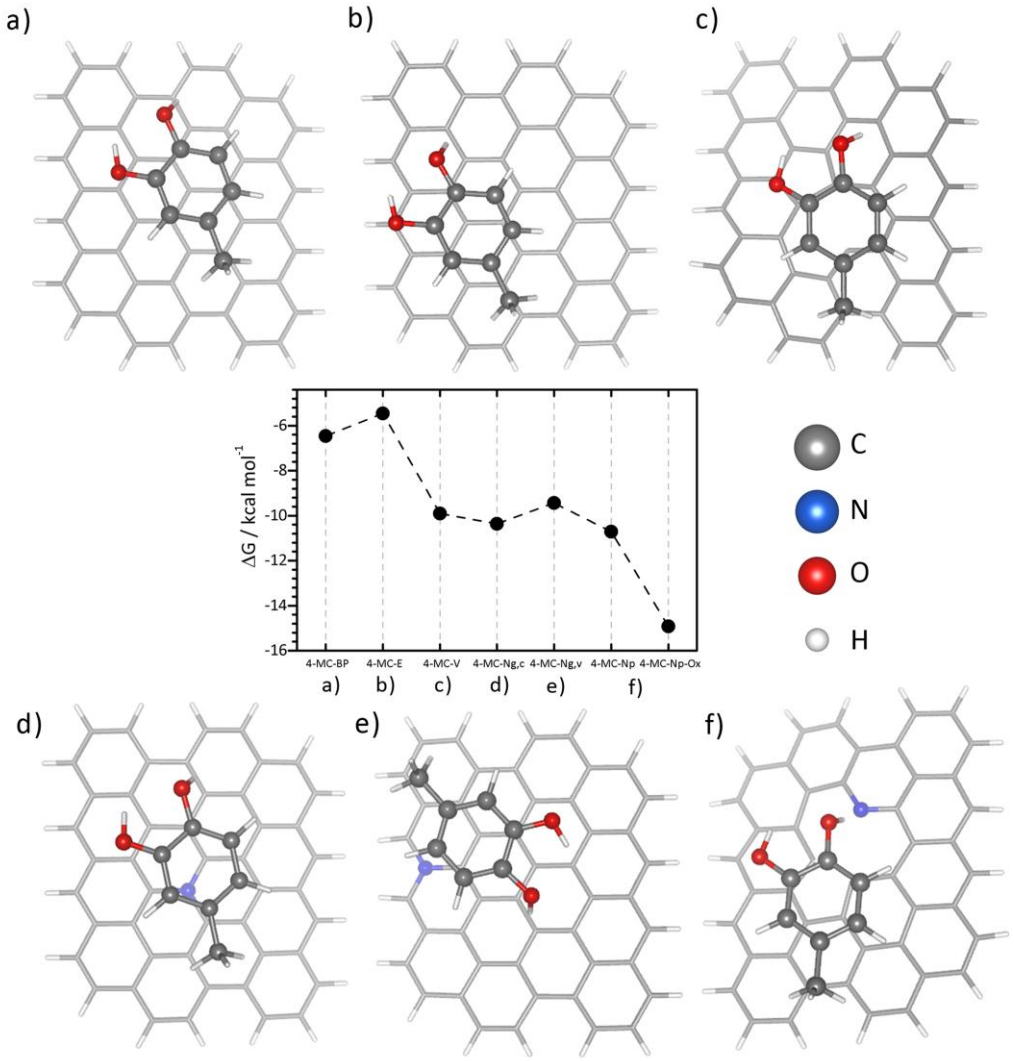

Figure 5.18. Calculated adsorption Gibbs energies (ΔG_{ads}), in kcal mol^{-1} for 4-MC. Top views of the optimized structures for the different adsorption modes and their corresponding ΔG_{ads} values on graphene (a-c) and N-doped graphene (d-f) model systems.

influencing the redox response. To test this hypothesis, calculations were run for a graphene model surface with 2 molecules of 4-MC or DA, as shown in Figure 5.19. The molecules were placed in their optimised geometries and stacked atop one another, with the distance between the two catechols equal to the equilibrium distance between the catechol and the surface determined from previous adsorption calculations.

The initial and final states for 4-MC are extremely similar to one another (Figure 5.19 a), consisting of two 4-MC molecules arrange parallel to one another with their hydroxyl groups oriented opposite one another. Considering the structure of 4-MC, this arrangement corresponds to an antiparallel arrangement of the dipole moments. This suggests that it is possible for a surface bound 4-MC molecule to recruit additional 4-MC molecules from the solution through dipole-dipole interactions. By contrast, attempting to stack DA molecules in a similar fashion is unsuccessful and the stacked structure evolves towards two separate DA molecules interacting with the surface (Figure 5.19 b). This is presumably because steric repulsion between the ethylamine chains prevents the antiparallel arrangment of the phenyl rings which is possible in 4-MC because of the smaller size of the methyl group.

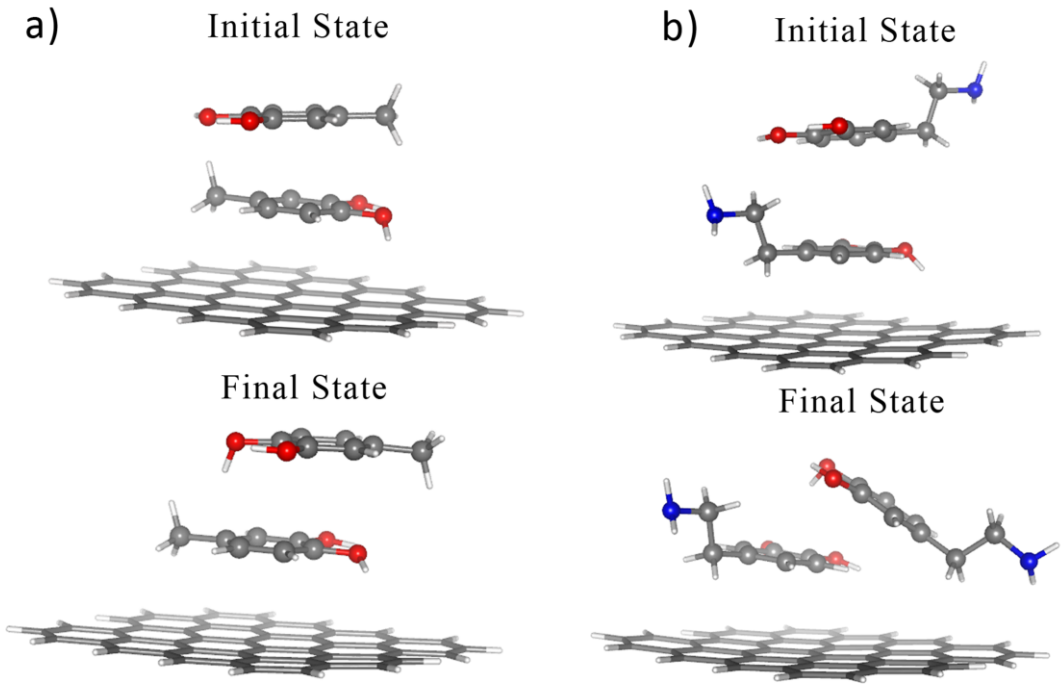

Figure 5.19. Initial and final state structures for a graphene model surface interacting with a stack of two catechol molecules, a) 4-MC and b) DA.

Furthermore, although this was not investigated in the computational study, under the experimental conditions in 0.1 M H_2SO_4 the amine group of DA is expected to be protonated, leading to the possibility of electrostatic repulsion between proximal DA molecules which might also reduce the coverage of DA relative to 4-MC.

These results may explain why the coverages of DA and 4-MC determined from voltammetry are similar only at low concentrations; as the solution concentration increases, the adsorption of additional 4-MC is possible through dipole-dipole interactions with other 4-MC molecules already present at the electrode surface. By contrast, DA molecules may only adsorb at binding sites directly at the electrode surface due to the presence of the ethylamine side chain, which hinders the approach of additional DA molecules even at high concentrations of solution phase DA.

5.2 Conclusions

This chapter has described the preparation of both N-free and N-doped graphitized carbon model systems with and without the presence of nitrogen heteroatoms and the characterization of their surface chemistry and carbon nanostructure using a combination of XPS, Raman spectroscopy, and DFT calculations. It was shown that these graphitic carbon systems exhibit adsorption of two different catechols, dopamine and 4-methyl catechol, with results suggesting that the coverage of both probes is influenced both by the presence of N-sites and by the degree of the graphitization of the carbon surface. Theoretical studies suggested that the adsorption at the surface is controlled by π-stacking interactions between graphitic clusters at the surface and the aryl moiety.

The incorporation of nitrogen sites into the carbon scaffold may enhance adsorption, particularly at graphitic valley sites, but the data do not support the notion that either DA or 4-MC adsorption is controlled primarily by particular N sites, since two model systems with identical N/C % and nitrogen surface chemistry have highly different coverages of both molecules. The chemical effects of N-doping can be counteracted almost entirely by its structurally disruptive effects. This was shown for DA by the dramatic reduction in DA coverage on the a-C:N-10% a900 surface compared to a-C:N-2% a900, and for 4-MC by the reduction in $\Gamma_{4\text{-MC}}$ on a-C:N-10% a900 compared to the undoped a-C a900 surface.

This suggests that the effect of carbon nanostructuring and organization on the adsorption and redox response of catechols should be regarded as of greater significance than the presence of specific N-functional groups. Therefore, it appears important to further explore this interplay between N-functional groups and carbon nanostructuring in their local environment to better understand electrocatalysis at nitrogenated carbon electrodes in general.

It was found that 4-MC and DA display significant differences in the magnitudes of their adsorption despite possessing a similar molecular structure and the same relative trend in coverages on the a-C a900 and a-C:N a900 surfaces. Computational studies simulating 4-MC – 4-MC and DA-DA interactions at graphene surfaces suggested that 4-MC is capable of forming multilayer structures through dipole-dipole interactions, whilst DA is limited to binding only at the electrode surface due to unfavourable steric interactions caused by the bulky ethylamine functionality. This suggests that, while both catechols are effective probes of the carbon surface nanostructure, the coverage of DA is more reflective of the surface properties than the coverage of 4-MC because it is not distorted by multilayer interactions. DA is therefore the more useful probe of the two for making quantitative comparisons between different graphitized carbon nanomaterials.

The results presented herein are expected to generalise to other aryl systems of biological relevance, including other catechols. Non-covalent interactions between aromatic biomolecules may be explored not only in the context of designing biosensors based on graphitic carbons, but also in the use of graphitized amorphous carbon model systems as platforms for the study of structural organization of disordered carbons in general. Finally, it has been shown that, in addition to the effects of heteroatom dopants, the organization of the carbon scaffold is a crucial parameter to consider for the electrocatalysis of inner-sphere redox processes. This concept will also be explored in the next chapter, which details the effects of altering the carbon nanostructure on the performance of different graphitized N-doped carbon model systems in the oxygen reduction reaction.

5.3 Experimental Methods

Chemicals and Materials

Dopamine hydrochloride (98%, Aldrich), Sulfuric Acid (≥95%, Ultratrace) 4-Methyl Catechol (98%, Aldrich) and Methanol (semiconductor grade) were used without further purification.

Substrate Preparation

Glassy carbon (GC) disks (HTW Sigradur radius 0.25 ± 0.05 cm) were prepared by polishing with progressively finer grades of alumina slurry (Buehler) and rinsing with copious

Millipore water. Clean disks were either used immediately for electrochemical and contact angle measurements or, in the case of amorphous carbon and nitrogenated amorphous carbon depositions, mounted in a custom-made Teflon holder and placed in the vacuum chamber for coating via magnetron sputtering prior to characterization, as previously described.[325] In the case of substrates for Raman and XPS measurements, B-doped silicon wafers (MicroChemicals; resistivity 5–10 Ω-cm) were prepared according to the same protocol described in Chapter III

Preparation of Carbon Electrodes

a-C a900 and a-C:N a900 thin film electrodes were prepared by magnetron sputtering followed by a thermal annealing treatment. Briefly, the films were deposited via DC magnetron sputtering in a chamber (Torr International Inc.) with a base pressure $\leq 2 \times 10^{-6}$ mbar and a deposition pressure in the range $(2–7) \times 10^{-3}$ mbar. a-C a900 films with no N-doping were deposited using an Ar plasma; N-doped a-C:N-2% a900 was prepared using 2% N_2 gas in a total flux of 50 sccm Ar/N_2 during the deposition, whilst 10% N_2/Ar was used for a-C:N-10% a900. After deposition, the resulting films were transported directly to a tube furnace and annealed under N_2 atmosphere for 1 h at 900 °C.

Characterization

Electrochemical measurements were carried out using a Metrohm Autolab AUT50324 potentiostat using a 3-electrode setup. A static disk holder (Pine Instruments) enclosing the GC disk with the carbon thin film was used as the working electrode. A Hydroflex hydrogen electrode (Gaskatel) and graphite rod were used as reference and counter electrodes, respectively. The electrochemical cell was a five-necked jacketed cell (Pine Instruments) which had its temperature held constant at 25 °C using a recirculator. Prior to experiments, the cell was cleaned using Piranha solution (3:1 H_2SO_4:H_2O_2 **CAUTION:** Piranha solution is a strong oxidant which may react explosively with organic solvents and must always be used in a fumehood) followed by rinsing with copious amounts of Millipore water. The cell was then rinsed three times with the electrolyte solution used during the experiment immediately prior to the analysis.

Cyclic voltammograms (CVs) were acquired in a potential window of 0.48-1.2 V vs RHE in deaerated solutions of 0.1 M H_2SO_4 with and without DA in concentrations ranging from

25 μM to 1 mM. All voltammograms were taken with iR compensation using commercial software (NOVA) with the uncompensated resistance of 18 ± 1 Ω determined prior to the experiment using Electrochemical Impedance Spectroscopy (EIS).

X-ray photoelectron spectroscopy (XPS) characterization was performed at 1×10^{-10} mbar base pressure in an ultrahigh-vacuum system (Omicron). The X-ray source was a monochromatized Al Kα source (1486.6 eV). Spectra were recorded at 45° takeoff angle with an analyser resolution of 0.5 eV. Spectra were baseline corrected using a Shirley background and fitted with Voigt functions using commercial software (CasaXPS); atomic percent compositions were determined by calculating peak area ratios after correction by relative sensitivity factors (C 1s = 1.0, N 1s = 1.8, O 1s = 2.93).

Raman spectra were measured in backscattering configuration using a Renishaw 1000 micro-Raman system equipped with an Ar+ laser for 488 nm excitation. The incident beam was focused by a Leica microscope with a 50× magnification objective and short-focus working distance; incident power was kept <2 mW to avoid sample damage. Spectra were baseline corrected using commercial software prior to analysis (OriginPro 9.1).

Computational Studies

Density functional theory (DFT) calculations reported in this work were carried out using the dispersion corrected hybrid functional ωB97X-D developed by Head-Gordon and Chai,[47] implemented in the Gaussian09 software package. [48] The choice of this level of theory is based on the satisfactory results obtained in previous theoretical studies for thermochemistry and for the description of non-covalent interactions. [49] H atoms were described using the double-ζ basis set 6-31G(d,p), whereas the same basis set plus diffuse functions was employed to describe the more electronegative O and N atoms. Geometry optimizations were performed without imposing any constraints and the nature of all the stationary points was further verified through vibrational frequency analysis. The reported adsorption Gibbs energies (ΔG_{ads}) were calculated at the experimental temperature of 298 K and pressure of 1 atm, according to the following equation:

$$\Delta G_{ads} = G_{surf+DA} - G_{surf} - G_{DA}$$

where $G_{surf+DA}$, G_{surf}, and G_{DA} correspond to the adsorbed DA on the graphene cluster, the clean graphene cluster, and the DA molecule in the gas phase, respectively.

5.4 References

1. To, J. W. F.; Ng, J. W. D.; Siahrostami, S.; Koh, A. L.; Lee, Y.; Chen, Z.; Fong, K. D.; Chen, S.; He, J.; Bae, W.-G.; Wilcox, J.; Jeong, H. Y.; Kim, K.; Studt, F.; Nørskov, J. K.; Jaramillo, T. F.; Bao, Z., High-performance oxygen reduction and evolution carbon catalysis: From mechanistic studies to device integration. *Nano Research* **2017,** *10* (4), 1163-1177.

2. Siahrostami, S.; Tsai, C.; Karamad, M.; Koitz, R.; García-Melchor, M.; Bajdich, M.; Vojvodic, A.; Abild-Pedersen, F.; Nørskov, J. K.; Studt, F., Two-Dimensional Materials as Catalysts for Energy Conversion. *Catalysis Letters* **2016,** *146* (10), 1917-1921.

3. Dai, L.; Xue, Y.; Qu, L.; Choi, H.-J.; Baek, J.-B., Metal-Free Catalysts for Oxygen Reduction Reaction. *Chemical Reviews* **2015,** *115* (11), 4823-4892.

4. Hu, C.; Dai, L., Carbon-Based Metal-Free Catalysts for Electrocatalysis beyond the ORR. *Angewandte Chemie International Edition* **2016,** *55* (39), 11736-11758.

5. Lin, Z.; Waller, G. H.; Liu, Y.; Liu, M.; Wong, C.-P., Simple preparation of nanoporous few-layer nitrogen-doped graphene for use as an efficient electrocatalyst for oxygen reduction and oxygen evolution reactions. *Carbon* **2013,** *53*, 130-136.

6. Yadav, R. M.; Wu, J.; Kochandra, R.; Ma, L.; Tiwary, C. S.; Ge, L.; Ye, G.; Vajtai, R.; Lou, J.; Ajayan, P. M., Carbon Nitrogen Nanotubes as Efficient Bifunctional Electrocatalysts for Oxygen Reduction and Evolution Reactions. *ACS Applied Materials and Interfaces* **2015,** *7* (22), 11991-12000.

7. Behan, J. A.; Stamatin, S. N.; Hoque, M. K.; Ciapetti, G.; Zen, F.; Esteban-Tejeda, L.; Colavita, P. E., Combined Optoelectronic and Electrochemical Study of Nitrogenated Carbon Electrodes. *The Journal of Physical Chemistry C* **2017,** *121* (12), 6596-6604.

8. Chen, J.; Wang, X.; Cui, X.; Yang, G.; Zheng, W., Amorphous carbon enriched with pyridinic nitrogen as an efficient metal-free electrocatalyst for oxygen reduction reaction. *Chemical Communications* **2014,** *50* (5), 557-559.

9. Chen, J. Y.; Wang, X.; Cui, X. Q.; Yang, G. M.; Zheng, W. T., One-step synthesis of N-doped amorphous carbon at relatively low temperature as excellent metal-free electrocatalyst for oxygen reduction. *Catalysis Communications* **2014,** *46*, 161-164.

10. Ajay, K.; Abhijit, G.; Pagona, P., Thermal stability study of nitrogen functionalities in a graphene network. *Journal of Physics: Condensed Matter* **2012,** *24* (23), 235503.

11. Lai, L.; Potts, J. R.; Zhan, D.; Wang, L.; Poh, C. K.; Tang, C.; Gong, H.; Shen, Z.; Lin, J.; Ruoff, R. S., Exploration of the active center structure of nitrogen-doped graphene-based catalysts for oxygen reduction reaction. *Energy Environmental Science* **2012,** *5* (7), 7936-7942.

12. Li, X.-F.; Lian, K.-Y.; Liu, L.; Wu, Y.; Qiu, Q.; Jiang, J.; Deng, M.; Luo, Y., Unraveling the formation mechanism of graphitic nitrogen-doping in thermally treated graphene with ammonia. *Scientific Reports* **2016,** *6*, 23495.

13. Stamatin, S. N.; Hussainova, I.; Ivanov, R.; Colavita, P. E., Quantifying Graphitic Edge Exposure in Graphene-Based Materials and Its Role in Oxygen Reduction Reactions. *ACS Catalysis* **2016,** *6* (8), 5215-5221.

14. Sharifi, T.; Hu, G.; Jia, X.; Wågberg, T., Formation of Active Sites for Oxygen Reduction Reactions by Transformation of Nitrogen Functionalities in Nitrogen-Doped Carbon Nanotubes. *ACS Nano* **2012,** *6* (10), 8904-8912.

15. Robertson, J.; Davis, C. A., Nitrogen Doping of Tetrahedral Amorphous-Carbon. *Diamond and Related Materials* **1995,** *4* (4), 441-444.

16. Kleinsorge, B.; Ferrari, A. C.; Robertson, J.; Milne, W. I.; Waidmann, S.; Hearne, S., Bonding regimes of nitrogen in amorphous carbon. *Diamond and Related Materials* **2000,** *9* (3–6), 643-648.

17. Guo, D.; Shibuya, R.; Akiba, C.; Saji, S.; Kondo, T.; Nakamura, J., Active sites of nitrogen-doped carbon materials for oxygen reduction reaction clarified using model catalysts. *Science* **2016,** *351* (6271), 361-365.

18. Chen, L.; Li, X.; Tanner, E. E. L.; Compton, R. G., Catechol adsorption on graphene nanoplatelets: isotherm, flat to vertical phase transition and desorption kinetics. *Chemical Science* **2017,** *8* (7), 4771-4778.

19. Fernández, A. C. R.; Castellani, N. J., Noncovalent Interactions between Dopamine and Regular and Defective Graphene. *ChemPhysChem* **2017,** *18* (15), 2065-2080.

20. Ortiz-Medina, J.; López-Urías, F.; Terrones, H.; Rodríguez-Macías, F. J.; Endo, M.; Terrones, M., Differential Response of Doped/Defective Graphene and Dopamine to Electric Fields: A Density Functional Theory Study. *The Journal of Physical Chemistry C* **2015,** *119* (24), 13972-13978.

21. Qu, L.; Liu, Y.; Baek, J.-B.; Dai, L., Nitrogen-Doped Graphene as Efficient Metal-Free Electrocatalyst for Oxygen Reduction in Fuel Cells. *ACS Nano* **2010,** *4* (3), 1321-1326.

22. Gong, K. P.; Du, F.; Xia, Z. H.; Durstock, M.; Dai, L. M., Nitrogen-Doped Carbon Nanotube Arrays with High Electrocatalytic Activity for Oxygen Reduction. *Science* **2009,** *323* (5915), 760-764.

23. Ferrari, A. C.; Rodil, S. E.; Robertson, J., Interpretation of infrared and Raman spectra of amorphous carbon nitrides. *Physical Review B* **2003,** *67* (15), 155306.

24. Titantah, J. T.; Lamoen, D., Carbon and nitrogen 1s energy levels in amorphous carbon nitride systems: XPS interpretation using first-principles. *Diamond and Related. Materials* **2007,** *16* (3), 581-588.

25. Le Normand, F.; Hommet, J.; Szörényi, T.; Fuchs, C.; Fogarassy, E., XPS study of pulsed laser deposited CN_x films. *Physical Review B* **2001,** *64* (23), 235416.

26. Díaz, J.; Paolicelli, G.; Ferrer, S.; Comin, F., Separation of the sp^3 and sp^2 components in the C 1s photoemission spectra of amorphous carbon films. *Physical Review B* **1996,** *54* (11), 8064-8069.

27. Perini, L.; Durante, C.; Favaro, M.; Perazzolo, V.; Agnoli, S.; Schneider, O.; Granozzi, G.; Gennaro, A., Metal–Support Interaction in Platinum and Palladium Nanoparticles Loaded on Nitrogen-Doped Mesoporous Carbon for Oxygen Reduction Reaction. *ACS Applied Materials & Interfaces* **2015,** *7* (2), 1170-1179.

28. Hellgren, N.; Haasch, R. T.; Schmidt, S.; Hultman, L.; Petrov, I., Interpretation of X-ray photoelectron spectra of carbon-nitride thin films: New insights from in situ XPS. *Carbon* **2016,** *108*, 242-252.

29. Ferrari, A. C.; Robertson, J., Interpretation of Raman spectra of disordered and amorphous carbon. *Physical Review B* **2000,** *61* (20), 14095-14107.

30. Waidmann, S.; Knupfer, M.; Fink, J.; Kleinsorge, B.; Robertson, J., Electronic structure studies of undoped and nitrogen-doped tetrahedral amorphous carbon using high-resolution electron energy-loss spectroscopy. *Journal of Applied Physics* **2001,** *89* (7), 3783-3792.

31. Laidani, N.; Guzman, L.; Miotello, A.; Brusa, R. S.; Karwasz, G. P.; Zecca, A.; Bottani, C.; Perrière, J., Nitrogen effects on the microstructural evolution of carbon films under thermal annealing. *Nuclear Instruments and Methods in Phyical Research Section B* **1997,** *122* (3), 553-558.

32. Ferrari, A. C.; Robertson, J., Resonant Raman spectroscopy of disordered, amorphous, and diamondlike carbon. *Physical Review B* **2001,** *64* (7), 075414.

33. DuVall, S. H.; McCreery, R. L., Control of Catechol and Hydroquinone Electron-Transfer Kinetics on Native and Modified Glassy Carbon Electrodes. *Analytical Chemistry* **1999,** *71* (20), 4594-4602.

34. DuVall, S. H.; McCreery, R. L., Self-catalysis by Catechols and Quinones during Heterogeneous Electron Transfer at Carbon Electrodes. *Journal of the American Chemical Society* **2000,** *122* (28), 6759-6764.

35. McCreery, R. L., Advanced carbon electrode materials for molecular electrochemistry. *Chemical Review* **2008,** *108* (7), 2646-87.

36. Patel, A. N.; Tan, S.-y.; Miller, T. S.; Macpherson, J. V.; Unwin, P. R., Comparison and Reappraisal of Carbon Electrodes for the Voltammetric Detection of Dopamine. *Analytical Chemistry* **2013,** *85* (24), 11755-11764.

37. Laviron, E., Electrochemical reactions with protonations at equilibrium: Part X. The kinetics of the p-benzoquinone/hydroquinone couple on a platinum electrode. *Journal of Electroanalytical Chemistry and Interfacial Electrochemistry* **1984,** *164* (2), 213-227.

38. Nicholson, R. S., Theory and Application of Cyclic Voltammetry for Measurement of Electrode Reaction Kinetics. *Analytical Chemistry* **1965,** *37* (11), 1351-1355.

39. Xiong, L.; Batchelor-McAuley, C.; Ward, K. R.; Downing, C.; Hartshorne, R. S.; Lawrence, N. S.; Compton, R. G., Voltammetry at graphite electrodes: The oxidation of hexacyanoferrate (II) (ferrocyanide) does not exhibit pure outer-sphere electron transfer kinetics and is sensitive to pre-exposure of the electrode to organic solvents. *Journal of Electroanalytical Chemistry* **2011,** *661* (1), 144-149.

40. Corona-Avendaño, S.; Alarcón-Angeles, G.; Ramírez-Silva, M. T.; Rosquete-Pina, G.; Romero-Romo, M.; Palomar-Pardavé, M., On the electrochemistry of dopamine in aqueous solution. Part I: The role of [SDS] on the voltammetric behavior of dopamine on a carbon paste electrode. *Journal of Electroanalytical Chemistry* **2007,** *609* (1), 17-26.

41. Wopschall, R. H.; Shain, I., Effects of adsorption of electroactive species in stationary electrode polarography. *Analytical Chemistry* **1967,** *39* (13), 1514-1527.

42. Shrestha, S.; Morse, N.; Mustain, W. E., Effect of surface chemistry on the double layer capacitance of polypyrrole-derived ordered mesoporous carbon. *RSC Advances* **2014,** *4* (87), 47039-47046.

43. Buttry, D.; Bard, A., Electroanalytical chemistry, vol. 17. New York: Marcel Dekker: **1991**.

44. Cullen, R. J.; Jayasundara, D. R.; Soldi, L.; Cheng, J. J.; Dufaure, G.; Colavita, P. E., Spontaneous Grafting of Nitrophenyl Groups on Amorphous Carbon Thin Films: A Structure–Reactivity Investigation. *Chemistry of Materials* **2012,** *24* (6), 1031-1040.

45. Laviron, E., Adsorption, autoinhibition and autocatalysis in polarography and in linear potential sweep voltammetry. *Journal of Electroanalytical Chemistry and Interfacial Electrochemistry* **1974,** *52* (3), 355-393.

46. Angerstein-Kozlowska, H.; Klinger, J.; Conway, B. E., Computer simulation of the kinetic behaviour of surface reactions driven by a linear potential sweep: Part I. Model 1-electron reaction with a single adsorbed species. *Journal of Electroanalytical Chemistry and Interfacial Electrochemistry* **1977,** *75* (1), 45-60.

47. Chai, J.-D.; Head-Gordon, M., Long-range corrected hybrid density functionals with damped atom-atom dispersion corrections. *Physical Chemistry Chemical Physics* **2008,** *10* (44), 6615-6620.

48. Frisch, M. J.; Trucks, G. W.; Schlegel, H. B.; Scuseria, G. E.; Robb, M. A.; Cheeseman, J. R.; Scalmani, G.; Barone, V.; Mennucci, B.; Petersson, G. A.; Nakatsuji, H.; Caricato, M.; Li, X. et al. Gaussian 09, Revision E.01. Gaussian Inc. , Wallingford CT, **2009**.

49. Penas-Defrutos, M. N.; Bartolome, C.; Garcia-Melchor, M.; Espinet, P., Hidden aryl-exchange processes in stable 16e Rh^{III} [RhCp*Ar_2] complexes, and their unexpected transmetalation mechanism. *Chemical Communications* **2018,** *54* (8), 984-987.

CHAPTER VI

Oxygen Reduction Reaction Performance of N-Doped Carbon Model Systems

In this chapter, the performance of nitrogenated carbon electrodes in the oxygen reduction reaction is studied. Nitrogenated carbons prepared via two different methodologies are investigated: bulk-incorporation via DC magnetron sputtering and surface nitrogenation through the thermal treatment of N-free surfaces with ammonia. A combination of XPS and Raman spectroscopy is used to correlate the performance of each material to the N-site chemistry and carbon nanostructure. Rotating ring disk electrode measurements of the materials are used to offer some insight into the mechanism of oxygen reduction.

The data presented in this chapter are part of an upcoming publication from the following authors:

> Behan, J. A.; Stamatin, S.N..; Domínguez, C.; Iannaci, A.; Hoque, M.K.; Perova, T.S.; Vilella-Aribas, L.; García-Melchor, M.; Colavita, P. E.

Co-author contributions to this chapter are as follows: M.K.H. and T.S.P. contributed Raman spectroscopy measurements. S.N. and C.D. contributed several of the RDE measurements on annealed a-C:N electrodes. A.I. contributed two LSV experiments on electrodes in acidic medium. All data were analysed by the author.

6. Introduction

Nitrogen-doped carbons have been under intense study over the previous decade due to their activity in metal-free electrocatalysis of the oxygen reduction reaction (ORR), [1-3] a cathodic process that currently represents the major kinetic limitation in the preparation of commercial devices based on oxygen electrochemistry.[4-7] Numerous studies have focused on understanding the role of N-sites in ORR electrocatalysis, via both experimental and theoretical methods.[8-13] This is a significant challenge, as N-doped carbons typically contain a mix of different nitrogen moieties, thus making it difficult to relate a global electrochemical response to individual active sites.

The uniting factor among many diverse N-doped carbon materials is that they are based on a graphitized carbon material such as cabon nanotubes[1] or graphene.[2] This implies that factors such as the degree of graphitization, graphitic cluster size and the extent of disorder in the graphitic carbon matrix should also be considered in fundamental studies of electrocatalysis, since these factors may also have a large impact on the catalytic performance.

Despite these challenges, researchers have made significant advancements in understanding the electrocatalytic behavior of N-doped carbon materials from fundamental structure-activity studies on well-defined carbon model systems. For example, the 2016 study of Guo et al. [9] utilized nitrogenated carbon model catalysts based on Highly-Oriented Pyrolytic Graphite (HOPG) to demonstrate the correlation between ORR activity and the presence of pyridinic N-sites in acidic media. Both Choi et al. [14] and Li et al. [15] have demonstrated the importance of the size-dependence of the conjugated carbon scaffold for the ORR performance in alkaline conditions, in graphene and carbon dot systems respectively

Although the field has seen significant advancements, much remains poorly understood or controversial. For instance, in addition to the favourable ORR properties of carbon materials doped with pyridinic-N, other research has suggested that graphitic N sites may also be responsible for high ORR activity. [16-17] As noted by Li et al. the vast majority of studies on N-doped carbons have neglected to mention L_a, the average lateral domain size of graphitized regions of the carbon material, even though it may have as strong of an effect on a material's electrocatalytic performance as the presence of particular N-sites.[15] This was illustrated in the studies of catechol adsorption on N-doped carbon model systems described in the previous chapter, where it was shown that alterations to the carbon scaffold in the form

of defects and interruptions in the conjugated sp^2 network can exert a greater influence on catechol adsorption than the introduction of particular nitrogen moieties into the scaffold.

This chapter focuses on fundamental structure-activity studies on different N-doped carbon model catalysts for the ORR under both alkaline and acidic conditions. In contrast to the previous chapters, which all presented amorphous carbon materials doped with nitrogen via the bulk deposition technique of DC magnetron sputtering, this chapter also introduces so-called 'surface doping' of a carbon electrode via annealing under NH_3 flux, which has been employed by many researchers as a methodology for nitrogenating nanocarbons such as graphene [2, 18] and mesoporous carbon. [3] Comparisons of performance between bulk N-doped and surface N-doped carbon materials in the ORR in principle allows the different effects of bulk doping versus surface modification on the electrocatalytic performance to be distinguished.

Similar to the approach in Chapters III and V, the ORR performance of the various N-doped carbons is correlated to both the N-site chemistry and the organization of the carbon scaffold using a combination of X-ray Photoelectron Spectroscopy (XPS) and Raman spectroscopy which afford information about the chemical composition of the materials and the organisation of the carbon scaffold respectively. Results indicate that the ORR on both classes of N-doped carbons under alkaline conditions proceeds through an initial outer-sphere electron transfer to O_2 under alkaline conditions. The activity correlates strongly with graphitic-N content for all of the materials, but graphitic-N sites are almost entirely inactive towards oxygen reduction in acidic media. It is also shown that, for N-doped carbon materials with comparable N-content and N-site chemistry, the material with the lowest degree of disorder in the carbon matrix as determined from Raman studies will have the best ORR performance.

Both bulk and surface doping methodologies are capable of producing N-doped carbon materials with high onset potentials, but if nitrogen incorporation is associated with a significant disordering of the carbon scaffold, the result is a loss of selectivity towards the 4-electron reduction of O_2 to water in favour of the less efficient 2-electron reduction to hydroperoxide. This effect is attributed to the irreversible poisoning of active sites by peroxyl intermediates generated during the ORR.

6.1 Results and Discussion

Characterisation of Nitrogen Doped Carbon Films

XPS Studies of N-doped Carbon Model Systems

This chapter presents studies of the ORR activity of metal-free N-doped carbon model catalysts with well-defined N-site chemistry and a controlled degree of structural disorder in the carbon scaffold prepared from DC magnetron-sputtered amorphous carbon (a-C) and nitrogen-doped amorphous carbon (a-C:N) films. Both a-C and a-C:N thin film electrodes have been used to study the ORR in the past by other groups.[19-20] As described in Chapter I, amorphous carbon films are a class of 2D nanomaterials with comparable properties to reduced graphene oxide which has been rigorously studied in the ORR.[16, 21-24]

An advantage of a-C/a-C:N films is that the conductive N-doped carbon matrix may be directly used as an electrode without the need for a binder material such as Nafion® as is the case for electrocatalytic studies of powder materials immobilized on an electrode via drop-cast inks. [14] The global electrochemical response to powder materials is determined by factors such as the ink composition, electrochemical surface area and the specific properties of the binding agent in addition to the chemical identity of the electrocatalyst and its carbon nanostructure. Thin film electrodes are therefore ideal model electrodes for fundamental structure-activity studies, because they do not require any binder and they may be prepared with varied surface chemistry and nanostructure whilst holding the surface topography constant. Indeed, the model systems presented in this chapter all have comparable roughness values to polished GC, as discussed in the Experimental section.

In this study, nitrogen doped carbon electrodes were prepared via two different methods, as illustrated schematically in Figure 6.1 a). Surface nitrogenation of a-C was accomplished via a thermal annealing treatment using N_2/NH_3 in order to introduce nitrogen moieties into the surface of an undoped carbon material. Two different annealing temperatures, 700 ^oC and 900 ^oC were employed. The materials are therefore denoted a-C-NH_3 a700 and a-C-NH_3 a900. As shown in Figure 6.1 b) and c), the deconvoluted XPS N 1s envelopes of

both NH_3 treated surfaces have two major contributions. The peak at *ca.* 398 eV is typically

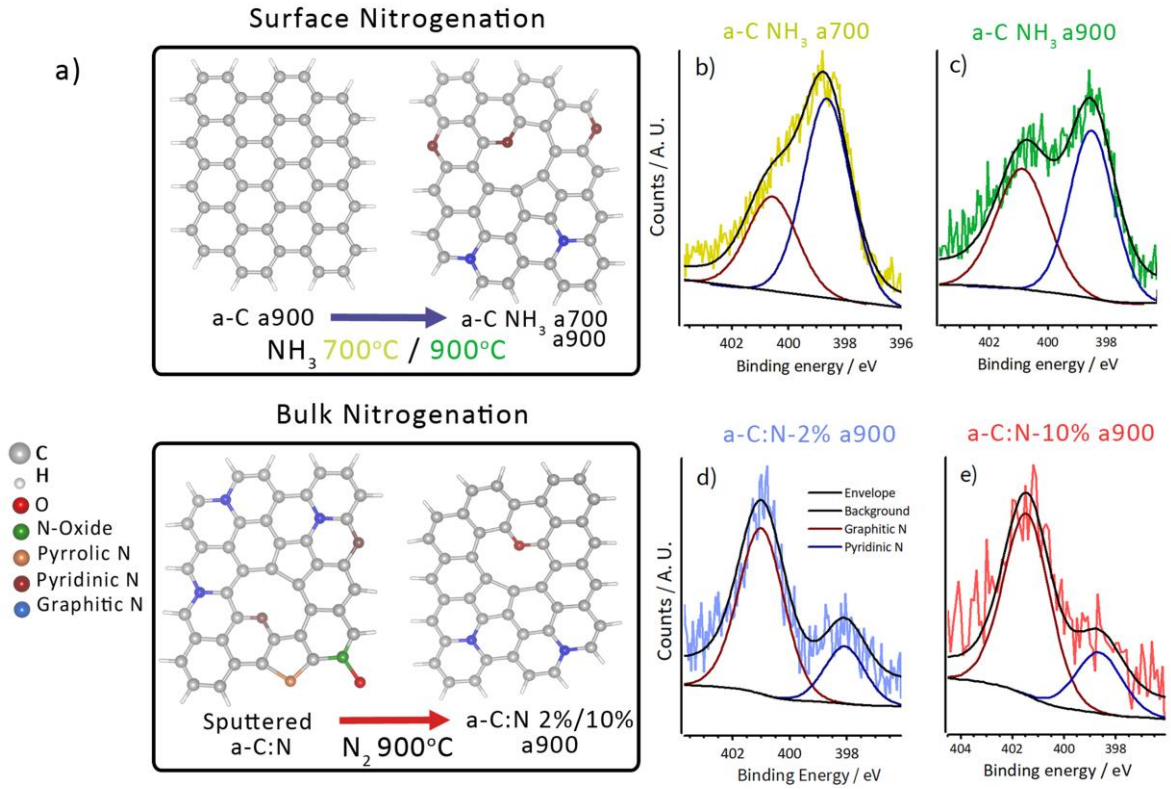

Figure 6.1. a) Schematic illustrating the preparation of a-C NH_3 700/900 (Top) and a-C:N a900 (Bottom) surfaces. N 1s envelopes of b) a-C-NH_3 700 c) a-C-NH_3 900 d) a-C:N-2% a900 and e) a-C:N-10% a900 electrodes. The raw data and envelope are together offset from the components and background for clarity.

assigned to pyridinic N sites (N_P), whilst the smaller peak centered around 401 eV is assigned to graphitic N (N_G).[2, 25]

Bulk nitrogenation was achieved via the use of an N_2/Ar plasma during the film deposition to deposit a-C:N-2% and a-C:N-10% films as described in Chapter III. These films may be described as nitrogenated carbon films with N-sites distributed throughout the entire film as opposed to being localized only at the surface. [26] The as-deposited films also possess a variety of N-sites as shown in the bottom of Figure 6.1 a). The same post-deposition annealing treatment at 900 ^oC in N_2 described in Chapter V was applied in order to produce a-C:N a900 electrodes. As shown in Figure 6.1 d) and e) the resulting electrodes, denoted a-C:N-2%/10% a900, also possess only N_G and N_P sites, however the predominant N sites are N_G. Both bulk N-doping and surface N-doping protocols can therefore be said to produce electrodes with comparable N-site chemistry, but different relative contributions of N_G and N_P sites.

In order to serve as a comparison material, an N-free graphitized carbon electrode was prepared by thermal annealing at 900 ºC under N_2 atmosphere. These films, denoted as a-C a900, were also characterised in Chapter V.

Table 6.1. O/C %, N/C % and N-site composition of a-C a900, a-C NH_3 a700/900 and a-C:N a900 materials obtained from XPS deconvolutions. Errors reported are 95% confidence intervals (n = 3 in each case).

Sample	O/C %	N/C %	N_P %	N_G %
a-C a900	3 ± 2	-	-	-
a-C-NH_3 a700	2.4 ± 0.7	1.9 ± 0.6	64 ± 9	36 ± 9
a-C-NH_3 a900	3 ± 1	1.9 ± 0.5	56 ± 6	43 ± 6
a-C:N-2% a900	4 ± 1	1.8 ± 0.3	25 ± 5	75 ± 5
a-C:N-10% a900	2.6 ± 0.7	2.4 ± 0.6	26 ± 8	74 ± 8

Table 6.1 reports a summary of the data obtained via XPS studies. The O/C and N/C % were determined from the area ratios A_{O1s}/A_{C1s} and A_{N1s}/A_{C1s} respectively after correction by sensitivity factors. Based on the overlap of the 95% confidence intervals for both O/C and N/C %, these values are statistically indistinguishable for all of the nitrogenated electrodes studied. This implies that any differences observed in the resulting

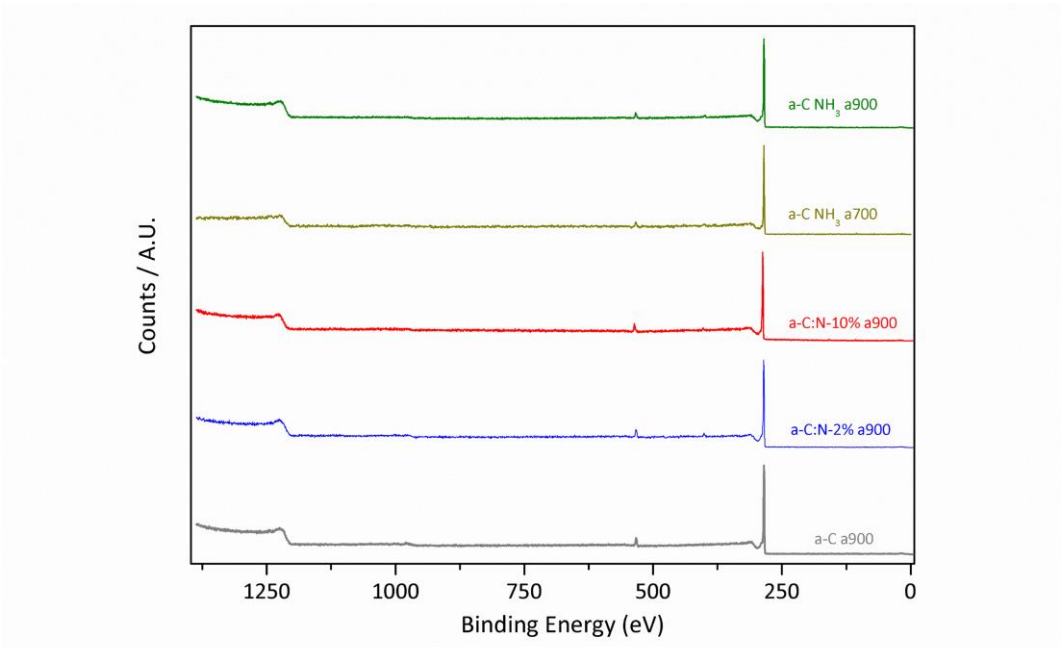

Figure 6.2. XPS survey scans of a-C a900, a-C:N-2/10% a900 and a-C NH_3 700 / 900 electrodes.

electrochemical activity cannot be attributed to differences in the total N- or O-content in the electrode surfaces. The relative proportions of N_G and N_P do differ between the three systems, with a-C:N-2/10% a900 possessing predominantly N_G and a-C-NH_3 a700/a900 predominantly N_P sites. The a-C-NH_3 900 also displays a small enhancement of N_G sites at the expense of N_P sites compared to the a-C-NH_3 700, which may possibly be attributed to the conversion of N_P to N_G at the higher annealing temperature. [13] Additionally, no elements other than C, N and O are evident in the survey scans as shown in Figure 6.2.

Raman Spectroscopy Analysis of N-Doped Carbon Electrodes

Raman spectroscopy measurements at a wavelength of 488 nm were employed in order to study the differences in the bulk nanostructure of each N-doped carbon system. Raman spectra for N-free a-C a900 and nitrogenated amorphous carbon films are plotted in Figure 5.3. All spectra indicate that both the N-doped and N-free materials show the characteristic features of an amorphous carbon material, *viz.* the D peak at *ca.* 1350-1380 cm^{-1} and the G peak centered close to 1600 cm^{-1}.[27-29] Deconvolutions of the Raman envelopes for the four N-doped carbon systems are shown in Figure 6.4. In the case of bulk-doped a-C:N a900 samples, best fits were obtained using a 3-peak deconvolution as described in Chapter V.

Two Gaussian peaks were applied to the aforementioned D and G peaks with a third peak centered close to 1510 cm^{-1} commonly referred to as the A peak. The A peak is characteristic of disordered carbons and has been attributed to the presence of both sp^2- and sp^3-hybridised carbon atoms in the regions between graphitic clusters. [30] For the NH_3-treated samples a small shoulder peak on the D peak around 1100 cm^{-1} is evident in the raw spectra in Figure 6.3, necessitating the use of a fourth Gaussian in the deconvolution. This peak has been referred to as the 'I' peak in the amorphous carbon literature and it has also been associated with disorder in the carbon scaffold. [31]

Raman spectral parameters derived from each of the deconvolutions are reported in Table 6.2. Based on the G peak position close to 1600 cm^{-1} and narrow full width at half maximum (FWHM) values < *ca.* 100 cm^{-1} for all of the materials, all of the electrodes have properties similar to nanocrystalline graphite. [27] This is unsurprising as both the as-deposited a-C and a-C:N electrodes were subjected to high temperature annealing treatments which are expected to promote the graphitization of the carbon scaffold.

In accordance with the three-phase model of Ferrari and Robertson for graphitized N-doped carbons, the intensity ratio of the D and G peak, I_D/I_G, is a measure of disorder in the

carbon scaffold and is inversely proportional to L_a, the average lateral dimension of the graphitic clusters in the graphitized carbon scaffold. [32]

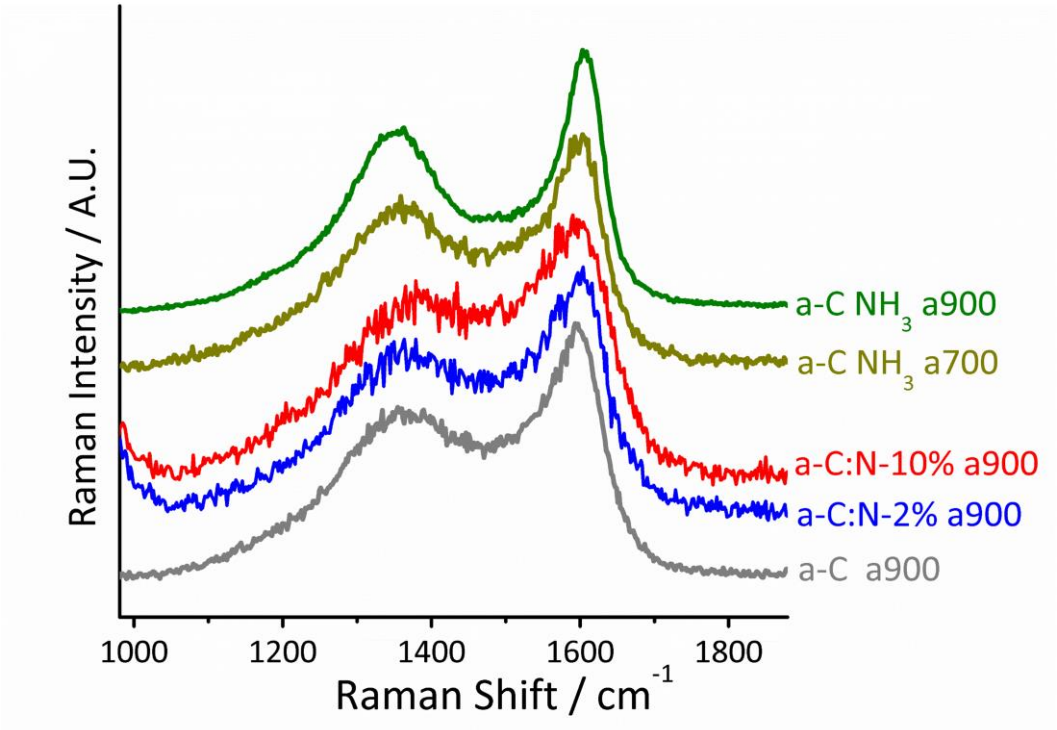

Figure 6.3. Raman spectra of N-free and N-doped amorphous carbon films. The spectra have been background subtracted and plotted offset from one another for clarity.

The a-C a900, a-C:N-2% a900 the a-C NH_3 a700/900 surfaces have similar I_D/I_G values close to 0.74, implying similar L_a values for these three systems on the order of 10 nm.[27] The a-C:N-10% a900 surface has a significantly higher I_D/I_G of 0.84, implying a smaller average clusterite size. This is supported by the low I_A/I_G value of 0.16 for the bulk-nitrogenated system. The I_A/I_G ratio may be taken as a measure of the contributions from amorphous carbon regions in between graphitic clusters. A small value of I_A/I_G is consistent with smaller graphitic clusters which are more efficiently packed. The I_A/I_G is also expected to increase for larger, inefficiently packed clusters which are connected to one another through more extensive amorphous carbon regions. Indeed, the largest value of I_A/I_G of 0.34 was obtained for the a-C NH_3 a900 surface, further suggesting that this material possesses the most extensive graphitized domains of the five systems studied.

This material also displayed the lowest I_D/I_G, highest G peak centre of 1605 cm^{-1} and the narrowest FWHM values for both the G and D peak. All of these results are consistent with a highly-ordered graphitized carbon network with large clusters separated from one another by amorphous regions. By contrast, the a-C NH_3 a700 surface generally has values for each of these parameters intermediate between the a-C-NH_3 a900 and undoped a-C a900. The

differences may be attributed to the higher annealing temperature of 900 °C, which would be expected to induce larger structural rearrangements such as sp^2 clustering and the conversion of sp^3-C to sp^2-C sites.[27] It is also notable that the bulk doped a-C:N-10% a900 displays the highest FWHM values in addition to the highest I_D/I_G, implying that it is the most disordered N-doped system.

In summary, a combination of XPS and Raman spectroscopy measurements indicate that we have prepared three distinct types of metal-free N-doped carbon electrodes using surface and bulk nitrogenation techniques. All three systems possess comparable N-site concentrations despite their different methods of preparation. Two forms of N site, N_G and N_P, were identified in each of the materials in varying proportions. The carbon scaffolds of all three systems are also distinct from one another, with the surface nitrogenated a-C NH_3 a900 surface displaying the greatest degree of nanocrystallinity. All of these results may be attributed to the higher annealing temperature employed during the nitrogenation.

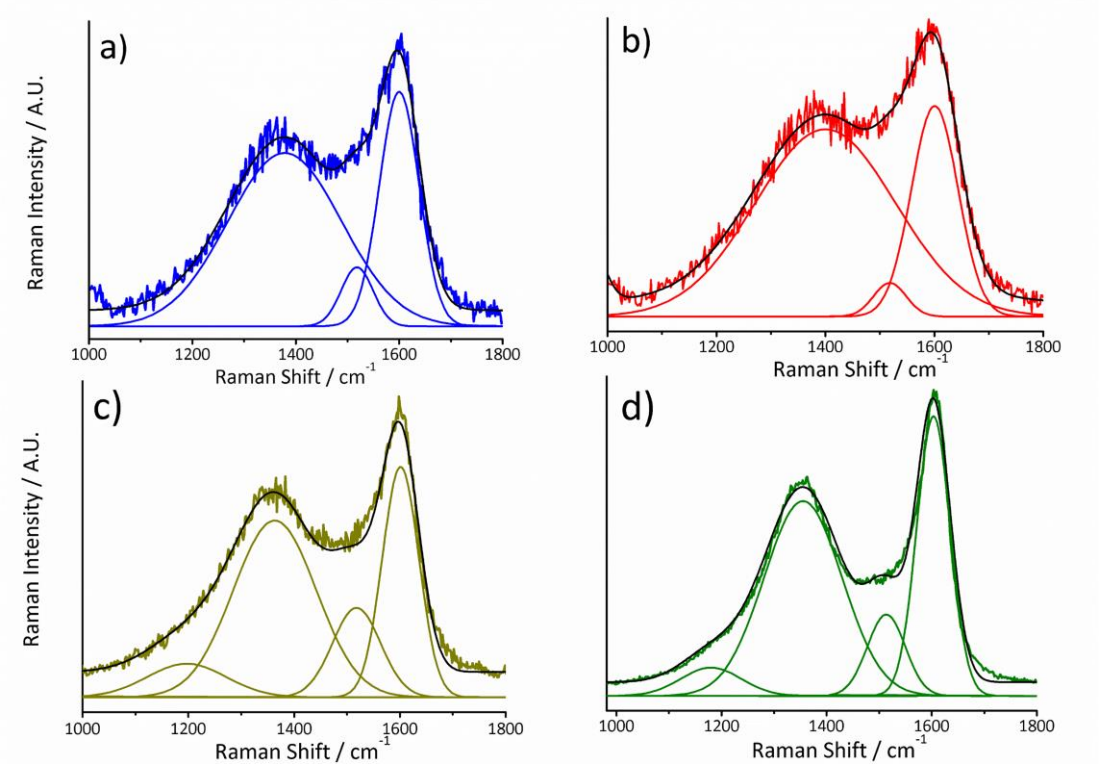

Figure 6.4. a) a-C a900 Raman spectrum and deconvolution b) Comparison of a-C a900 and a-C NH_3 a700 / a900 and a-C:N-10% a900 Raman spectra. c) Deconvolution of a-C NH_3 700 Raman spectrum. d) Deconvolution of a-C-NH_3 900 Raman spectrum e) Deconvolution of a-C:N-10% a900 Raman spectrum. In all deconvolutions the raw data and envelope are offset from the component peaks for clarity.

Table 6.2. Raman Spectral Parameters of N-free and N-doped electrodes derived from the deconvolutions reported in Figure 6.4.

Sample	I_D/I_G	I_A/I_G	G position / cm^{-1}	G FWHM / cm^{-1}	D position / cm^{-1}	D FWHM / cm^{-1}
a-C a900	0.74	0.23	1598	85	1379	274
a-C-NH_3 a700	0.75	0.26	1599	78	1369	255
a-C-NH_3 a900	0.72	0.34	1605	70	1355	186
a-C:N-2% a900	0.73	0.26	1600	91	1379	260
a-C:N-10% a900	0.84	0.16	1603	104	1385	279

ORR Performance of N-doped Carbon Electrodes in Alkaline Medium

The ORR activity of the different N-doped systems in O_2-saturated KOH was evaluated via cyclic voltammetry (CV) experiments using a rotating ring disk electrode (RRDE; Pt ring) at a scan rate of 10 mVs^{-1}. To avoid any potential issues regarding the variation of the collection efficiency at the ring with the rotation speed, all hydrodynamic measurements were obtained at a constant rotation rate of 900 rpm. CVs under identical conditions with N_2-saturated KOH were also obtained in order to evaluate the capacitive contribution to the current. The Faradaic current due to the reduction of oxygen was then obtained by subtraction of the current obtained in N_2/KOH from the current obtained in the oxygenated electrolyte. This is illustrated in Figure 6.5a, which shows a CV for an a-C a900 electrode in both O_2-saturated and N_2-saturated electrolyte. The cathodic sweep of the resulting voltammogram after subtraction of the capacitive charging current is shown in Figure 6 b. The onset potential, E_{on} defined as the value of the potential when j = 0.1 mA cm^{-2}, is 0.65 V vs RHE on the undoped carbon surface, which shows that the undoped carbon material has a low intrinsic activity towards ORR.

ORR Performance of Bulk N-doped Carbon Electrodes

Voltammograms for the bulk N-doped a-C:N-2%/10% a900 electrodes are plotted in Figure 6.6a along with the undoped a-C a900 for comparison. It is evident from the figure that both

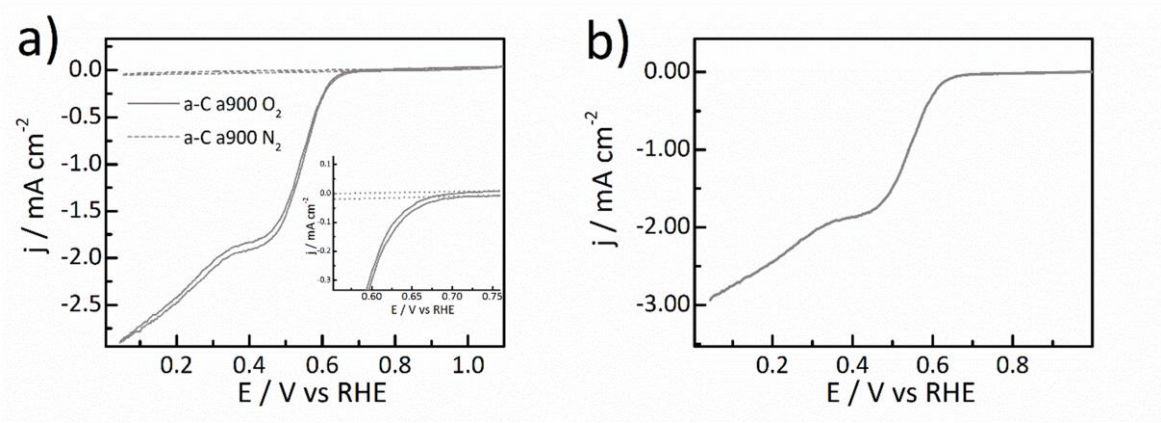

Figure 6.5. a) CV of an a-C a900 electrode in a solution of 0.1 M KOH obtained at a scan rate of 10 mVs^{-1} and a rotation speed of 900 rpm. The inset plot shows the onset region close to 0.65 V vs RHE. b) background-corrected cathodic scan of the a-C a900 electrode.

a-C:N a900 electrodes have an improved E_{on} compared to the undoped a-C a900, suggesting that the incorporation of N sites into the carbon scaffold activates the surface towards the ORR. The results are summarised in Table 6.3. E_{on} for the a-C-N-10% a900 surface is 0.77 V vs RHE, compared to 0.73 V for the a-C:N-2% a900. Both electrodes have absolute values for the limiting current density, $|j_l|$, significantly smaller than the expected value from the Levich equation for a 4-e^- reduction [33], suggesting that the ORR does not proceed as an entirely 4-e^- process on these electrodes.

Tafel plots for both bulk N-doped electrodes are presented in Figure 6.6 b). Depending on the exact region in which the linear fit is performed, both a-C:N-2% a900 and a-C:N-10% a900 have Tafel slopes in the range of 60-70 mV^{-1}, which suggests that the ORR proceeds through a chemical rearrangement step which follows on from an initial rapid electron transfer.[34] This point is discussed further below in the comparison of the ORR performance of bulk N-doped and surface N-doped electrodes.

As discussed in Chapter I, the ORR may proceed via a 4-electron reduction of O_2 to water or a 2-electron reduction producing hydroperoxide HO_2^-, as the final product. The relative amounts of 2e^- and 4e^- reduction can be quantified using Rotating Ring Disk Electrode (RRDE) studies. Figure 6.7 shows plots of the ring current, I_R and disk current I_D for an RRDE experiment on the a-C:N-2% a900 and a-C:N-10% a900 electrodes. The ring currents are highest for a-C:N-10% a900 which are on average almost twice the value as that of the a-C:N-2% a900 (Table 6.3.). The value of the ring current and disk current may be correlated to the yield of hydroperoxide using Equation 6.1:

$$HO_2^- \% = 100 \times 2\left(\frac{\frac{I_R}{N}}{I_D + \frac{I_R}{N}}\right) \quad (6.1)$$

Using the values of I_R and I_D in the plateau region of the ring current (0.3 V vs RHE), the peroxide yield is 33% on a-C:N-2% a900 and 65% on the a-C:N-10% a900 surface, corresponding to a value of n, the average number of electrons transferred in the ORR, of 3.2 and 2.4, respectively. Values of n between 2 and 4 indicate that both the $2e^-$ and $4e^-$ pathway are occurring simultaneously at the electrode surface. Therefore the a-C:N-10% a900 produces hydroperoxide as the final product of ORR through the $2e^-$ pathway almost exclusively, whilst the a-C:N-2% a900 surface shows significantly more $4e^-$ reduction of O_2 to water. This is the case even though the onset potential for the ORR is 30 mV more positive on the a-C:N-10% a900 electrode.

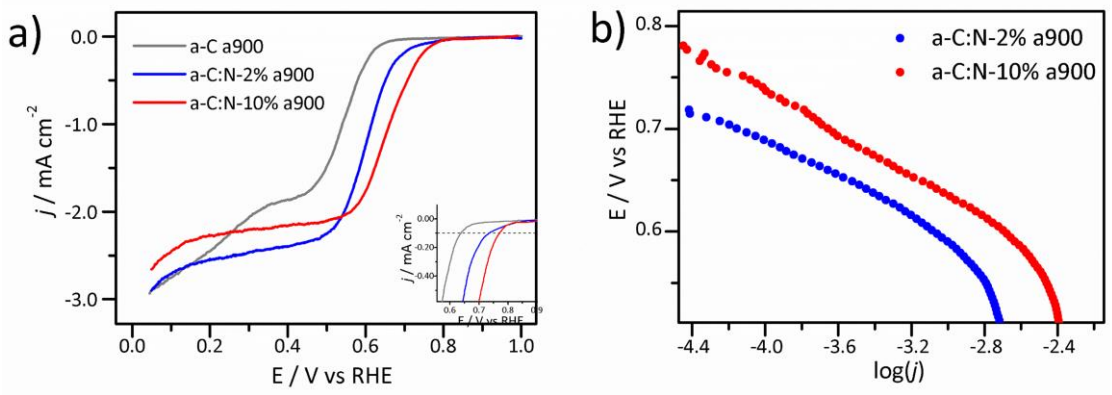

Figure 6.6. a) Voltammograms of a-C a900 and a-C:N-2%/10% a900 in O_2 saturated KOH after background subtraction. The inset figure shows the onset region. b) Tafel plots for a-C:N-2% and 10% a900.

Whilst the RRDE method does not allow a 'true' $4e^-$ pathway to be distinguished from a sequential 2 + 2 e^- pathway with peroxide as an intermediate, the most likely interpretation of this result is that the a-C:N-2% a900 surface is more capable of reducing a peroxide intermediate formed from the first $2e^-$ transfer. This assessment is based on the fact that the true $4e^-$ pathway requires the breaking of both O=O bonds (ΔH = 494 kJ/mol) prior to reduction[35]. Such a feat requires the chemisorption of molecular O_2 which, with the possible exception of certain C atoms adjacent to graphitic-N sites,[23] is not generally feasible on metal-free ORR electrocatalysts in the same manner as is found for Pt/C. In any event, the high peroxide yields evident from the ring currents in Figure 6.7 suggest that if the dissociative $4e^-$ pathway is occurring on the a-C:N a900 surfaces, it is occurring along with a substantial amount of $2e^-$ reduction to peroxide.

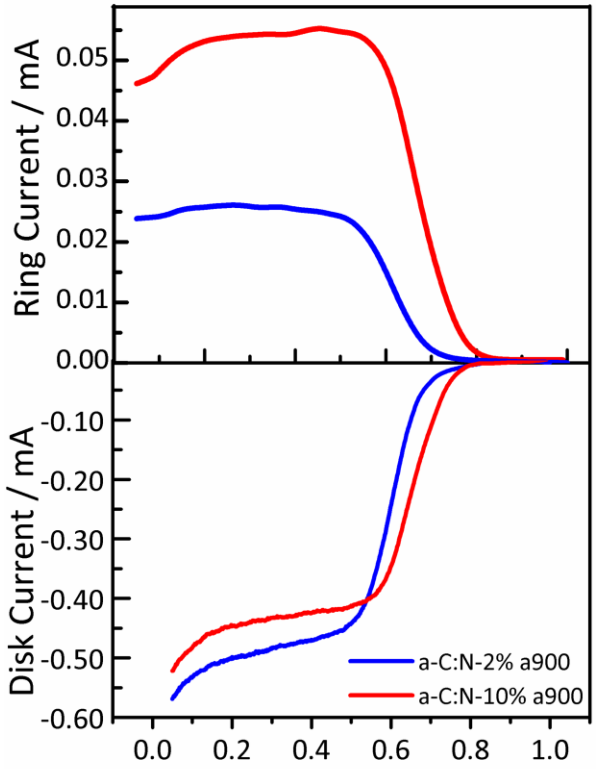

Figure 6.7. RRDE studies (900 rpm) of a-C:N-2% a900 and a-C:N-10% a900 electrodes in O_2 saturated 0.1 M KOH.

ORR Performance of Surface N-doped Carbon Electrodes

The ORR performance of 'surface' N-doped a-C NH_3 a700 and a900 electrodes was studied in an identical fashion to that which was reported for the bulk N-doped systems. Figure 6.8 a shows voltammograms for a-C NH_3 a700 and a900 in O_2-saturated 0.1 M KOH. It is clear from the Figure that the a-C NH_3 900 surface has the highest E_{on}, which at 0.83 V vs RHE is comparable to the most active metal-free N-doped carbons in the literature.[2, 15, 36-38] The a-C NH_3 a700 surface has an onset potential of *ca.* 0.73 V vs RHE, which is similar to the value obtained for a-C:N-2% a900. It is also apparent from Figure 6.8 a and the values tabulated in Table 6.3 that the a-C-NH_3 900 surface has the highest current density in the mass-transport limiting region (*ca.* 0.5 V vs RHE and below). Comparing values at a potential of 0.1 V vs RHE, the a-C-NH_3 900 electrode has a value of $|j|$ close to 4 mA cm^{-2} which is close to the theoretical Levich current for a 4-electron reduction of O_2. The a-C NH_3 a700 displays a significantly lower value of $|j|$ at the same potential, suggesting that the ORR is not proceeding through a full 4 e^- pathway at this surface. Tafel plots for the a-C NH_3 a700 and a900 surfaces are plotted in Figure 6.8 b) with the resulting Tafel slopes given in Table 6.3. Similar to the

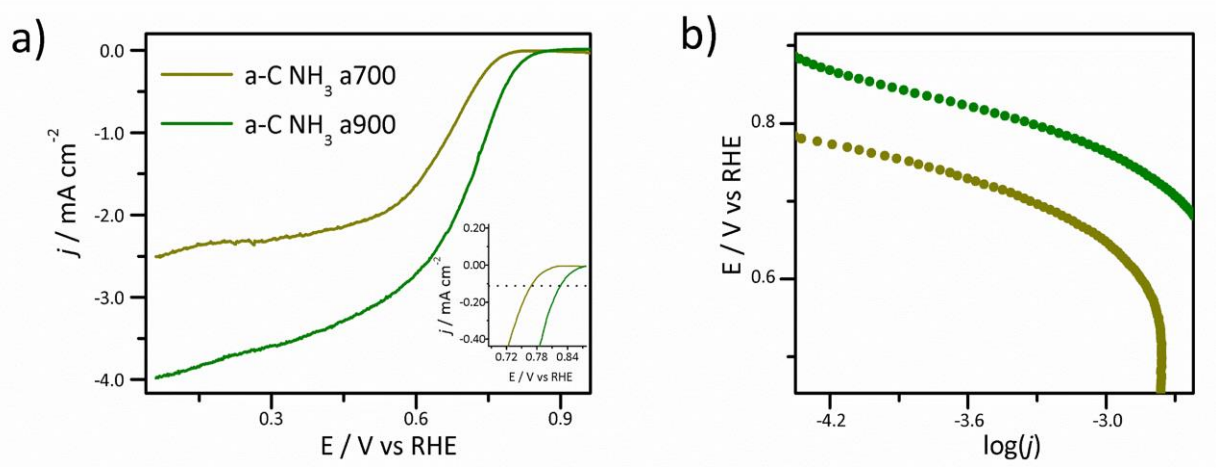

Figure 6.8.a) Voltammograms of a-C NH_3 a700 and a900 electrodes in O_2 saturated 0.1M KOH at a scan rate of 10 mVs^{-1} and a rotation speed of 900 rpm. The inset plot shows the onset region of the ORR. b) Tafel plots for the same electrodes derived from the voltammograms in a).

bulk N-doped surfaces, both of the NH_3-treated electrodes have Tafel slopes of *ca.* 60-70 mV^{-1}. This suggests that both bulk and surface N-doping protocols produce surfaces which catalyze the ORR through a mechanism with a similar rate-determining step.

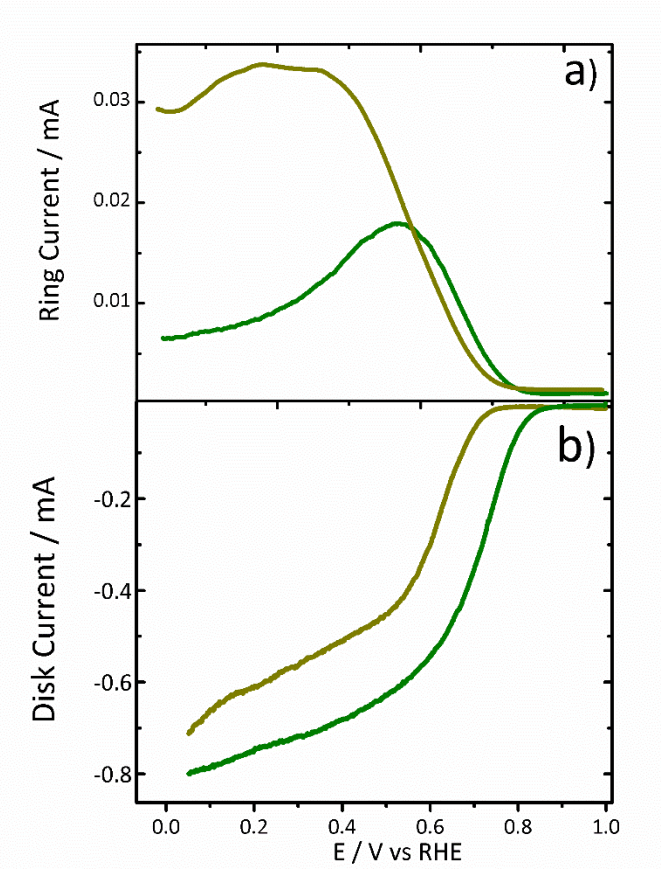

Figure 6.9. RRDE Studies (900 rpm) of a-C NH_3 a700 and a900 electrodes in 0.1 M KOH. a) Rin current

RRDE studies of the a-C NH_3 a700 and a900 surfaces are plotted in Figure 6.9. Immediately apparent in the figure is the unusual peak trace corresponding to the ring current on the a-C NH_3 a900 surface, which is not evident in the a-C NH_3 a700 surface or in any of the a-C:N a900 ring currents plotted in Figurge 6.8. The onset of the ring current for both traces coincides with the onset of ORR, suggesting that the ORR proceeds through a 2-electron pathway to some extent between potentials of 0.8-0.6 V vs RHE. This leads to a plateau in the ring current in the a-C NH_3 a700 surface similar to that observed on bulk N-doped surfaces. For the a-C NH_3 a900 surface the peroxide production begins to decrease at potentials cathodic of *ca.* 0.6 V, suggesting that the 4-electron reduction becomes more favourable at higher overpotentials, such that the average number of electrons transferred becomes close to 4 at E = *ca.* 0.2 V vs RHE.

Comparison of ORR Performance for Bulk N-doped and Surface N-doped Electrodes

The effects of both bulk and surface N-doping on the ORR activity are summarized in Figure 6.10. and Table 6.3. In terms of the usual criteria for high ORR activity, *viz.* high onset potential, large values of |j| in the mass-transport limited region (parts a and b of the figure) and selectivity for the 4-electron pathway (Figure 6.10 c), the surface-nitrogenated a-C NH_3 a900 surface is the best performing electrocatalyst whilst the bulk-doped a-C:N-10% a900 is the worst. As discussed in Section 6.2.1, this difference cannot be associated with the total N content, since all 4 electrodes show comparable N/C %.

The data do not suggest that surface nitrogenation of a graphitized carbon material is preferable to bulk N-doping. This is evident by comparing the results for bulk-doped a-C:N-2% a900 with surface-doped a-C NH_3 a700. Both electrodes have similar onset potentials and ring currents (Figure 6.11 a) and b)) and a similar average electron transfer number close to *n* = 3. Considering the surface composition data from XPS studies, these two electrode surfaces are found to be similar despite possessing different concentrations of N_P sites (a-C:N-2% a900 25% : a-C NH_3 a700 65 %, Table 6.2).

This result implies that, at least in alkaline conditions, the N_P content does not have a dramatic effect on the ORR performance. This is a significant point, since pyridinic-N sites in particular have been suggested as the active sites for the ORR on N-doped carbon. This

point is elaborated upon further below in the comparison of the ORR activity for these materials in acidic medium.

It is interesting to examine the similarities between the ORR activity a-C:N-2% a900 and a-C NH_3 a700 in the context of the Raman data for these materials. Based on the spectral parameters such as I_D/I_G and I_A/I_G, both of these electrodes have very similar carbon nanostructure in terms of the size and distribution of graphitic domains, despite their different routes of preparation. The comparable behavior of these surfaces may therefore be explained by the similarities in the carbon scaffold organization which were produced by the two different nitrogenation methods used in this study.

Considering Table 6.3, it is clear that despite the differences in the ORR activity just discussed, the N-free a-C a900 and all four N-doped carbon surfaces have similar Tafel slopes close to 60-70 mV^{-1} which was associated with a rate-determining chemical step. In

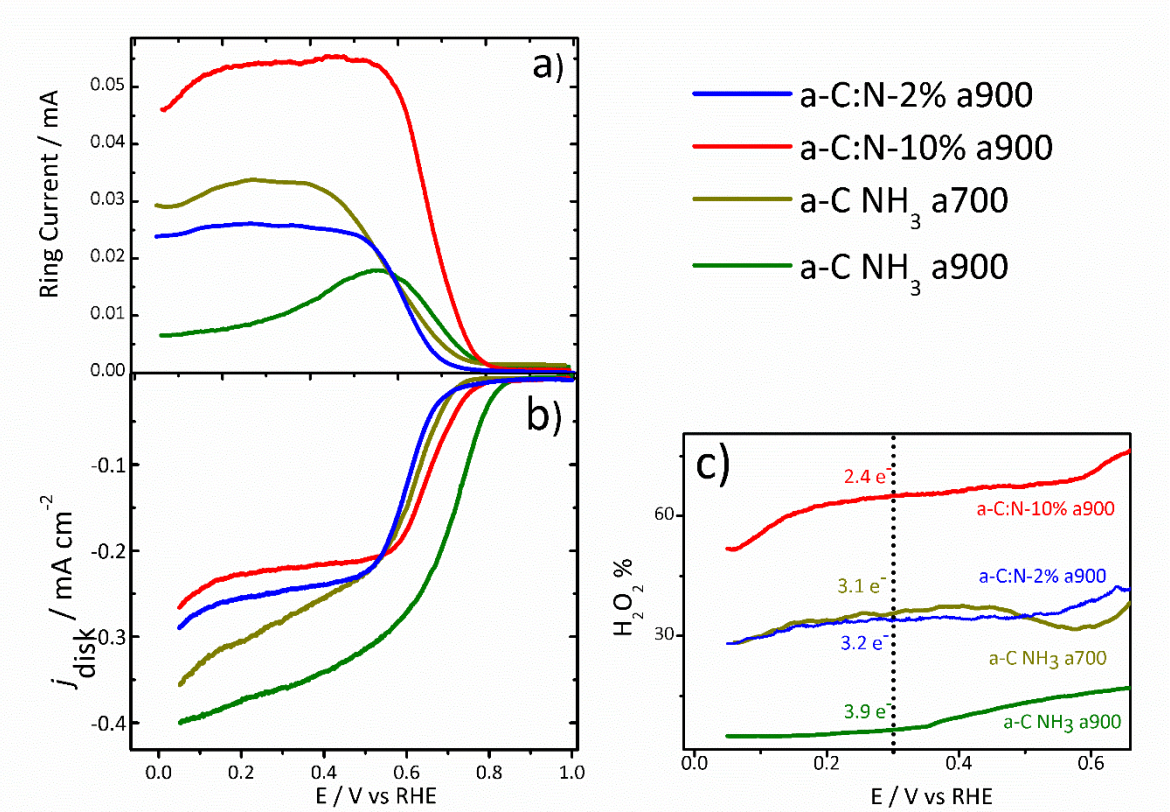

Figure 6.10. Summary of ORR data obtained on all N-doped carbon electrodes in 0.1 M KOH. A) Ring Currents b) disk current densities c) peroxide yields in the potential range 0.6 – 0.05 V vs RHE. The dashed line indicates the peroxide yield corresponding to the value of *n*, the average electron transfer number at 0.3 V vs RHE.

the ORR literature, a Tafel slope of this magnitude on Pt electrodes under identical conditions is associated with the first electron transfer acting as the RDS under conditions

where oxide/hydroxide adsorbates act as blocking species, even though a slope of 120 mV^{-1} is normally expected in the absence of interfering species.[39]

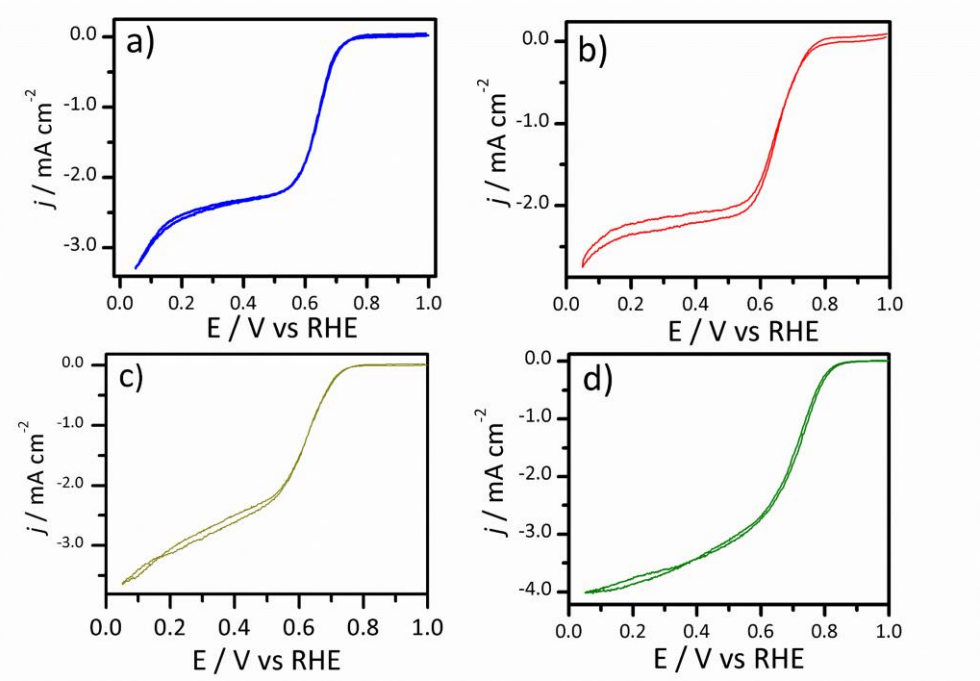

Figure 6.11. Capacitance-corrected cyclic voltammograms of a-C:N a900 and a-C NH_3 a700/a900 surfaces in O_2 saturated 0.1 M KOH. a) a-C:N-2% a900 b) a-C:N-10% a900 c) a-C NH_3 a700 d) a-C NH_3 a900.

The absence of these oxides at higher ORR overpotentials is one of the reasons why the apparent ORR activity on Pt appears significantly better on the anodic sweep of a cyclic voltammogram.[40] Examining the background-subtracted CV's of all four electrodes in 0.1 M KOH (Figure 6.11) there is almost perfect overlap between the cathodic and anodic scans. This strongly suggests that blocking species such as hydroxides in alkaline medium do not interfere with the ORR at the N-doped carbon surface in the same fashion as is observed on Pt. The Tafel slopes obtained on these surfaces are therefore really indicative of a chemical RDS; this point is explored further in the discussion of the ORR mechanism in the following section.

Degradation of the a-C NH_3 a900 ORR Performance

The a-C NH_3 a900 surface is unique among the N-doped carbon electrodes in this study in that it displays remarkable selectivity for the 4e ORR pathway at high overpotentials. The implications of this finding are discussed in detail in the discussion section. The production

of peroxide and other reactive intermediates during ORR can result in the degradation of an N-doped carbon material's performance. [41] It was therefore of interest to examine the effects of exposure to peroxide on the ORR activity of the best-performing electrocatalyst identified in this study.

Figure 6.13 shows a plot of the ring and disk currents of an a-C NH_3 a900 surface obtained after 20 CV's in a potential window between 1V and 0.05 V vs RHE at a scan rate of 10 mVs^{-1} and a rotation rate of 900 rpm. The figure clearly shows a significant degradation in both E_{ON} and $|j|$ at 0.1 V vs RHE after the cycling experiment compared to the initial sweep. Indeed, the ORR onset potential of the degraded a-C-NH_3 900 appears to approach values obtained on the initial scan with the a-C NH_3 a700, which is also plotted in the figure for comparison purposes.

There is also a significant increase in the a-C NH_3 a900 ring current to levels comparable to those found for a-C-NH_3 700, indicating that the selectivity of the a-C-NH_3 900 surface for 4-electron reduction of O_2 at higher overpotentials is lost after cycling. It is important to note that these cycling experiments avoided potentials > 1 V vs RHggE, at which carbon is potentially liable to oxidatively degrade, as is often observed in the Pt/C catalyst layer in fuel cells. [42] Accordingly, this loss in activity may be attributed only to the degradation of the surface by reactive peroxide intermediates.

Table 6.3. Summary of ORR performance on a-C-N_2 900, a-C-NH_3 700/900 and a-C:N-N_2 900 electrodes. All voltages are references relative to RHE.

Sample	E_{ON} / V @ 0.1 mA cm^{-2}	Tafel Slope / mV dec^{-1}	n @ 0.3 V	H_2O_2 % @ 0.3 V	$\|j\|$ / mA cm^{-2} @ 0.1 V
a-C a900	0.65	75	2.6	70	2.3
a-C-NH_3 a700	0.73	66	3.1	35	3.4
a-C-NH_3 a900	0.83	70	3.9	6	3.9
a-C:N-2% a900	0.73	70	3.2	33	2.8
a-C:N-10% a900	0.77	67	2.4	65	2.4

ORR Performance of N-doped Carbon Electrodes in Acidic Medium

The ORR performance of metal-free N-doped carbons has shown a wide variation in the literature, with various claims regarding the desirability of particular N-sites – typically, though not exclusively, N_G and N_P sites – for the ORR performance. It was previously shown

based on the comparison of the a-C:N-2% a900 and the a-C NH_3 a700 surfaces that the density of N_P sites does not appear to have a strong influence on the ORR onset potential or selectivity for the 4-electron pathway, based on the fact that these surfaces have similar performances despite possessing significantly different quantities of pyridinic sites based on the XPS analysis. This result seemed to contradict numerous other studies which correlated the ORR activity to N_P sites. [9, 19]

Many of the studies cited on the role of pyridinic-N were carried out at acidic pH. It was therefore desirable to investigate whether or not the activity of particular N-sites in the ORR is dependent on the pH. This was accomplished by carrying out RDE studies on the four different N-doped carbon model catalyts in O_2-saturated 0.1 M $HClO_4$. The results are reported in Figure 6.13. It is immediately apparent from the figure that all four of the surfaces display vastly inferior performance in acid medium compared to that in 0.1M KOH. The highest E_{on} obtained in $HClO_4$ was 0.37 V vs RHE on the a-C NH_3 a700 surface, some 350 mV more cathodic than the value obtained for the same surface in KOH. Additionally, the a-C:N a900 surfaces display essentially no Faradaic current until potentials < *ca.* 0.1 V vs

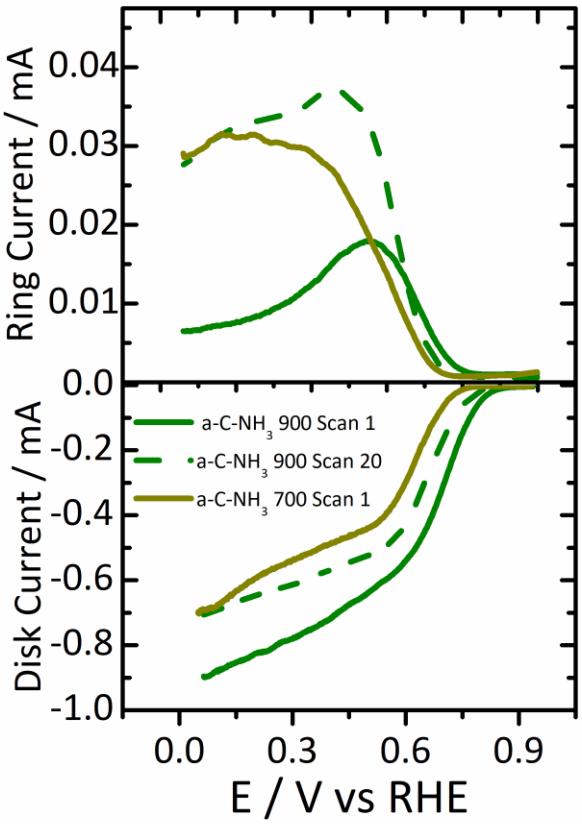

Figure 6.12. RRDE experiments on the a-C-NH_3 900 electrode before (green line) and after cycling (dashed line) between 1 V and 0.05 V vs RHE for 20 scans at 10 mVs^{-1}. The a-C-NH_3 a700 surface is shown as a comparison.

RHE. It is interesting to note that the a-C-NH_3 900 surface has a slightly lower E_{ON} than the a-C NH_3 700, even though the former was shown to be significantly more active in KOH.

The acid ORR results suggest that the ORR performance on N-doped carbons is highly sensitive to the pH, and that both N_p and N_G sites may show different apparent electrocatalytic activity towards the ORR depending on whether the reaction is performed in acid or alkaline conditions.

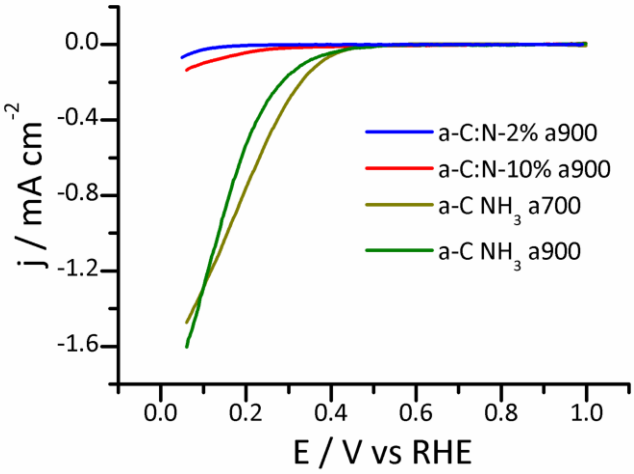

Figure 6.13. Voltammograms of nitrogenated carbon electrodes obtained in O_2 saturated 0.1 M $HClO_4$ (scan rate: 10 mv s^{-1}) using an RRDE at a rotation rate of 900 rpm. All curves are shown following subtraction of the capacitive current obtained from the voltammogram in N_2 saturated electrolyte

Discussion

The literature on metal-free ORR on N-doped carbon surfaces contains a variety of claims regarding the active sites for ORR as well as the ORR mechanism. [9, 11-12. 36-37] Oxygen reduction in both acid and alkaline media is a highly complex process. The full 4 e^- reduction of O_2 to H_2O (Equation 6.1) under alkaline conditions may be achieved via a 'direct' 4e^- - 4 proton pathway, or a 'series' 2 + 2 pathway which may be considered to be the combination of Equations 6.2 and 6.3 where the HO_2^- produced as an intermediate from the first 2e^- process is reduced before it can be detected at the ring. In principle it is not possible to use RRDE measurements to distinguish between the direct and series pathways, as neither pathway would be expected to produce HO_2^- to be detected at the ring. However, the detection of HO_2^- is itself evidence of the series pathway whereby the peroxide intermediate is detectable because it desorbs from the electrode surface before the second 2e^- process (Equation 6.3) has occurred.

$$O_2 + 2H_2O + 4e^- \rightarrow 4OH^- \qquad E° = 1.229 \text{ V vs. RHE} \qquad (6.1)$$

$$O_2 + H_2O + 2e^- \rightarrow HO_2^- + OH^- \qquad E° = 0.695 \text{ V vs. RHE} \qquad (6.2)$$

$$HO_2^- + H_2O + 2e^- \rightarrow 3OH^- \qquad E° = 1.763 \text{ V vs. RHE} \qquad (6.3)$$

Outer-Sphere Electron Transfer to O_2 Under Alkaline Conditions

On Pt and other precious-metal ORR catalysts it has been widely accepted that the adsorption of O_2 is the first step of the ORR and the RDS is the first electron transfer. This is the so-called 'inner sphere electron transfer' (ISET) pathway and it may be followed in both low and high pH conditions. However, under alkaline conditions an outer-sphere electron transfer (OSET) mechanism is also possible as has been highlighted by Markovic et al. on the Ag (111) surface[44] and more generally by Ramaswamy and Mukerjee.[45-46] The OSET mechanism becomes possible due to reaction 6.4, the pH-independent formation of superoxide from dissolved O_2:

$$O_{2\,(aq)} + e^- \rightarrow O_2^{\bullet-}{}_{(aq)} \qquad E^0 = 0.44 \text{ V vs RHE} \qquad (6.4)$$

On the basis of a modified Pourbaix diagram, Markovic et al. [44] argued that the lower absolute potentials of ORR on the SHE scale under alkaline conditions causes the thermodynamic potential for the overall $4e^-$ process (Equation 6.1) to approach the formal potential of Reaction (6.4). The difference in overpotentials is *ca.* 1.5 V in acid conditions compared to *ca.* 0.7 V in base. Ramaswamy and Mukerjee argued[46] that this overpotential difference explains the possibility of using a variety of catalysts for the ORR under alkaline conditions, rather than select precious metal catalysts such as Pt as is the case at low pH: the overpotential of Reaction (6.4) as the first step of ORR is simply too high to be traversed without specific covalent interactions of O_2 with the surface, whereas at high pH non-covalent interactions such as H-bonding and long-range dipole-dipole interactions may be sufficient to overcome the energy barrier.

In this work, the highest onset potential measured for the a-C-NH_3 900 surface is 0.83 V vs RHE which, with reference to Equation 6.4, implies that a potential shift corresponding to a Gibbs energy of adsorption contribution of $-\Delta G_{ads}/F$ = 0.39 V or roughly 38 kJ/mol which may be easily accounted for by non-covalent interactions. Studying superoxide formation on N-free glassy carbon surfaces, Yang and McCreery concluded that superoxide radicals may adsorb even on undoped carbon. [47] This was shown by introducing a covalently-

bound blocking organic methylphenyl layer to the carbon surface, which was shown to prevent the adsorption of superoxide. The end result of Reaction 6.4 on the blocked carbon surface was the degradation of the formed superoxide via homogeneous chemical routes in solution.

The precise nature of the superoxide binding sites on the unblocked GC surface was unknown, though possible candidate adsorption sites mentioned by the authors included oxide moieties and dangling bonds at edge sites. In any case, this paper is good evidence that superoxide generation and adsorption is possible at carbon surfaces even without N-doping.

As discussed in the previous section, the Tafel slopes on each of our surfaces reported in Table 3 are all consistent with a fast electron transfer occurring followed by a rate-determining step which does not involve electron transfer, such as a chemical rearrangement. If an OSET mechanism is assumed with Reaction 6.4 as the initial step, the steps which follow superoxide formation may be adsorption followed by protonation:

$$O_2^{\bullet-}{}_{(aq)} \rightarrow (O_2^{\bullet-})_{ads} \quad (6.5)$$

$$(O_2^{\bullet-})_{ads} + H_2O \rightarrow (HO_2^{\bullet})_{ads} + OH^- \quad (6.6)$$

This has been suggested independently by both McCreery and Mukerjee. [46-47] McCreery in particular showed that, for pH > 12, if adsorption of the superoxide is facilitated by the surface, the rate determining step of the overall reduction process (which in their case was a 2-electron reduction to hydroperoxide, Reaction 6.2) is Reaction 6.6. This step may have two further outcomes: reduction or reaction of the $(HO_2^{\bullet})_{ads}$ with another superoxide:

$$(HO_2^{\bullet})_{ads} + e^- \rightarrow HO_2^- \quad (6.7)$$

$$(HO_2^{\bullet})_{ads} + O_2^{\bullet-}{}_{(aq)} \rightarrow HO_2^- + O_2 \quad (6.8)$$

If superoxide is not adsorbed, or if adsorption is kinetically discouraged, it may instead react with water through a well-established homogeneous pathway[48]:

$$O_2^{\bullet-} + H_2O \rightarrow HO_2^{\bullet} + OH^- \quad (6.9a)$$

$$O_2^{\bullet-} + HO_2^{\bullet} \rightarrow HO_2^- + O_2 \quad (6.9b)$$

which when combining reactions 7a and 7b is equivalent to a disproportionation:

$$2O_2^{\bullet-} + H_2O \rightarrow HO_2^- + O_2 + OH^- \quad (6.10)$$

Reaction 6.10 is expected to be slowed at pH > 12 due to the decrease in water activity as the pH is raised;[46, 49] however, it is not possible in principle rule out contributions from any of the Reactions 6.4-6.10 at the N-doped carbon surfaces presented in this study. HO_2^- may be produced via the homogeneous Reaction 6.9 b, or by reaction of an adsorbed $HO_2^{\bullet}$ (reactions 6.7 or 6.8). Despite this ambiguity, the yield of HO_2^- measured via the RRDE studies indicates that the ORR at both the a-C:N-2% a900 and the a-C NH_3 a700 is primarily a 2-electron process, which is good evidence that the reaction sequence is described by Equations 6.5-6.7.

There is an increased tendency for peroxide production at higher overpotentials on both a-C:N a900 surfaces and on the a-C NH_3 a700 electrode, which is not surprising considering that reaction 6.4 is expected to proceed more rapidly as the applied potential approaches the formal potential of the $O_2/O_2^{\bullet-}$ couple. Since Reaction 6.4 is not the RDS, the HO_2^- detected on the a-C:N-2%/10% a900 and a-C NH_3 a700 surfaces may therefore be explained by desorption of HO_2^- as the final product of an overall 2-electron reduction (Reaction 6.7).

The desorption of weakly-bound HO_2^- has been proposed on Pt due to weak bonding interactions between HO_2^- and the Pt-Oxide substructure as well as the lower absolute potentials of the electrode surface under alkaline conditions. [46] Mayrhofer et al. have also argued that it is the competition between the desorption of the peroxide intermediates from the electrocatalyst surface (H_2O_2 in acid and HO_2^- in base) and the second 2-electron transfer in the 2+2 series ORR pathway which ultimately determines the overall ORR activity.[50] Anything that interferes with the adsorption of the intermediates, including adsorbed spectator ions or the poisoning of reactive sites, is expected to result in increased production of hydroperoxide and a degradation of the ORR activity.

The Influence of the Carbon Scaffold on the ORR Onset Potential

The assumption of a 2 + 2 mechanism which proceeds via an OSET as the first step offers a reasonable interpretation of the trend in ORR onset potentials when considered in conjunction with the XPS and Raman characterisations of each surface. For an OSET, facile kinetics for a cathodic process such as the ORR are predicted for surfaces with higher values of the Fermi level, E_F, which maximises the overlap of occupied states in the surface with the LUMO of the oxidant. This was shown both experimentally and theoretically by Choi et al. on N-graphene surfaces in acid media, for which ball-milling to produce few-layer N-

graphenes with small lateral dimension sizes of at most 2 nm in size modulated E_F upwards and produced materials with higher E_{ON} values for the ORR.[14] A similar size-dependent effect on the ORR in KOH was also observed on N-doped carbon dots by Li et al.[15] although no mechanistic explanation was given.

Considering our results with this literature in mind, the fact that a-C-NH_3 900 displays the highest value of E_{ON} despite possessing a similar N/C % to the other two surfaces may be explained by the high degree of graphitization determined from the Raman analysis, which should correlate to a higher value of E_F and therefore faster electron transfer. The a-C NH_3 900 also has a slight enrichment of graphitic N sites compared to a-C NH_3 a700 as reported in Table 1, which would be expected to raise E_F and also create new states near E_F via the π-doping effect of graphitic N.[51] However based on the XPS analysis, the bulk-deposited a-C:N-2/10% a900 surfaces have the highest amount of N_G sites.

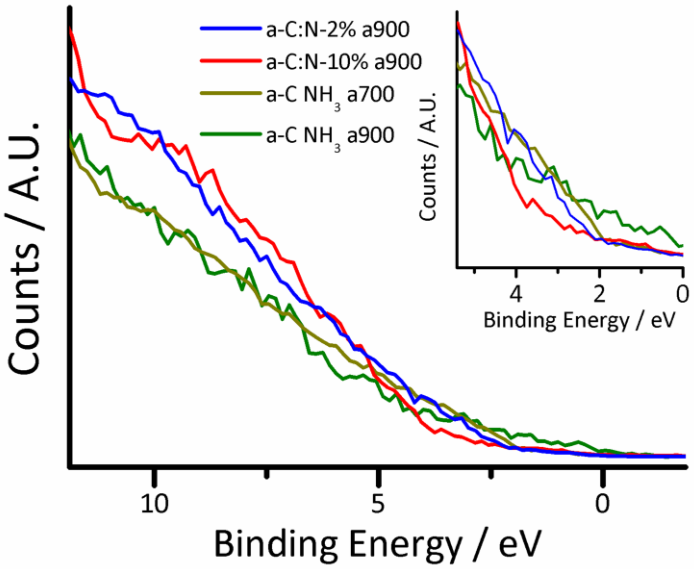

Figure 6.14. Valence studies of N-doped carbon surfaces determined via XPS. The curves in each case are normalized by the cumulative area. The inset shows the binding energy region close to the Fermi edge.

Using the data in Table 6.1, the concentration of N_G sites in both a-C:N a900 carbon scaffolds is close to 1.8 % compared to only 0.8% for a-C NH_3 a900. Thus, the concentration of N_G sites *per se* is not an accurate predictor of ORR activity. The lower activity of the a-C:N-10% a900 may possibly be attributed to the disorder evident in the carbon scaffold based on the Raman analysis. The I_D/I_G and FWHM for a-C:N-10% a900 are consistent with a less graphitized structure, which would in turn be expected to have a lower E_F. These predictions were supported by valence studies of the three surfaces carried out via XPS, reported in Figure 6.15 which indicate that the a-C-NH_3 a900 surface has the highest density of occupied states (DoS) near the Fermi level out of the three surfaces, followed by

a-C:N-10% a900. The a-C NH_3 a700 and a-C:N-2% a900 have a similar DoS in the same region, consistent with their similar values of E_{on}.

In summary, for N-doped carbon model systems with similar N-site chemistry and a comparable concentration of N sites, the ORR onset potential is correlated to the degree of graphitization of the carbon scaffold. More highly graphitized N-doped carbon materials have a greater metallic character (i.e. higher E_F and DoS near E_F) than more disordered nitrogenated materials due to the presence of ordered sp^2-clusters in the graphitized surfaces, which in turn leads to faster electron transfer kinetics in the outer-sphere reduction of O_2 to superoxide.

The Role of N_G Sites and N_P Sites in the ORR on N-doped Carbons

The discussion of the carbon scaffold effect on the ORR performance in our N-doped carbon electrodes shows that the presence of particular N-sites is not in itself a guarantee of high ORR activity. However, for materials with similar concentrations of nitrogen and similar N-site chemistry, trends in the ORR activity may still be correlated to the presence or absence of particular moieties. Since the ORR proceeds via an OSET on these materials, the 'non-local' doping effect[51] of N_G sites in modulating E_F is the most important effect of N-doping in terms of facilitating the first electron transfer. This is why N-free a-C a900 has a poor onset potential compared to the N-doped carbon model systems.

After the generation of superoxide via Reaction 6.4, the binding of intermediates, particularly $HO_2^{\bullet}$ is also crucial for obtaining good ORR activity in through selectivity for the 4-electron pathway. This is the 'local' effect of N-doping. Both N_G and N_P sites have been shown via theoretical calculations[14] to facilitate $HO_2^{\bullet}$ binding, with generally higher values of ΔG_{ads} achieved at pyridinic sites. This may explain why both the a-C:N-2% and 10% a900 have reasonable values of E_{ON} but produce significant amounts of peroxide through the 2 e^- pathway based on the RRDE studies. Both of the bulk N-doped materials possess almost exclusively N_G sites, which help to facilitate the OSET to O_2.

However, subsequently, the dearth of N_P sites to which the $HO_2^{\bullet}$ is predicted to be most strongly bound results in desorption of hydroperoxide, HO_2^- rather than further reduction in the 2 + 2 pathway. This conclusion may appear to be contradicted by the remarkable similarity between the a-C:N-2% a900 and a-C NH_3 a700, which have similar onset potentials and similar average electron transfer numbers based on the RRDE studies. The a-C:N-2% a900 has a comparable selectivity for the 4-electron pathway to the a-C NH_3 a700

despite possessing significantly fewer N_P sites based on the XPS data. It is not possible to definitively explain this inconsistency with the data presented, but a possible explanation may be found in considering the similarities of the carbon scaffold structure for these two model systems as discussed in Section 6.2.4. It may be the case that the selectivity for HO_2^- binding and subsequent reduction instead of desorption is similar for both of these systems owing to the similarities of their nanostructure, whilst the a-C:N-10% a900 surface behaves differently because of the greater degree of disorder in its carbon scaffold. It is clear that further work is needed to investigate the effects of peroxyl intermediate binding at N_G and N_P sites as a function of the degree of graphitization.

The attribution of high ORR onset potentials to the presence of N_G sites may appear to contradict the recent findings of Guo et al. who showed that the the active sites of ORR on N-doped carbons in acidic media are C-atoms adjacent to N_P sites. [9] This contradiction may be resolved by comparing the performance of our model catalysts in alkaline and acid conditions. The OSET mechanism is extremely improbable on N-doped carbons in acidic media (*vide supra*) which implies that the non-local doping effect introduced by N_G sites is unlikely to be the most important factor in facilitating the ORR at low pH. Instead the reaction is most likely to proceed via an ISET involving molecular oxygen, which Guo et al. attributed to the Lewis basicity of C atoms adjacent to N_P sites.

The bulk N-doped a-C:N-2% and 10% a900 surfaces, which have reasonable onset potentials in 0.1M KOH solutions have almost no detectable ORR activity in perchloric acid. This result is consistent with the hypothesis of Guo et al. regarding the importance of N_P sites, since the bulk N-doped electrocatalyst have almost none and therefore are unable to facilitate the ORR at low pH. The higher E_{ON} of the a-C NH_3 a700 compared to the a-C NH_3 a900 in perchloric acid, even though the trend is the opposite in KOH, may also be explained by the higher proportion of N_P sites in the a-C NH_3 a700 based on the XPS studies in Section 6.2.1. The major conclusion of these results, then, is that speaking of a particular type of N-site as 'the' active site does not capture all of the nuances at play in determining the ORR activity. It is clear that both N_G and N_P sites may have roles in the ORR depending on the mechanism, which in turn is highly dependent on the pH.

The Loss of ORR Activity due to Peroxide-induced Degradation of Active Sites: Local vs Non-Local Effects

The degradation of the ORR performance of the a-C-NH_3 a900 after repeated cycling between 1 V and 0.05 V vs RHE (Figure 6.13) illustrates the importance of distinguishing the local effects of N-doping, such as the introduction of charged surface sites or an increase in basicity, from non-local effects such as the raising of E_F and the increase in the DoS near E_F. The a-C NH_3 a900 undergoes a 50 mV cathodic shift in E_{ON} after 20 cycles and also shows a massive increase in the peroxide detected at the ring to values even higher than the a-C NH_3 a700 surface. This dramatic change in the ORR response may be attributed to the degradation of the surface due to the presence of reactive intermediates like peroxyl radicals. The oxidation of the carbon surface due to the presence of bound -OH and -OOH moieties is expected to decrease the conductivity and electron donating capability of the graphitized carbon surface. This is a non-local effect and manifests in the aforementioned cathodic shift of E_{ON}.

Intriguingly, the E_{ON} value of the a-C-NH_3 900 after intentional degradation by repeated cycling is still more positive than the initial scan of a-C-NH_3 700, even though the peroxide yields of the two surfaces are similar. This implies that the non-local changes induced by the degradation, *viz.* decreased conductivity and electron donating capacity, have a less severe impact than the local changes in the surface induced by the oxidative degradation, specifically the blocking of binding sites for intermediates such as $HO_2^{\bullet}$.

The ring currents on the a-C-NH_3 900 display a peak close to 0.5 V in both the initial scan and after cycling, followed by a drop in the peroxide yield at higher overpotentials. This behavior may be explained by considering the relative rates of HO_2^- desorption and dissociation. Mayrhofer et al. demonstrated for Pt surfaces that, if the kinetics of hydrogen peroxide reduction are sluggish and/or desorption of peroxide from the surface is facile, the end product of O_2 reduction is likely to be hydrogen peroxide or its anion. [50] This result also agrees with other observations in the literature that an ORR mechanism proceeding via on OSET has a strong tendency to terminate with peroxide as the final product. [46-47]

At high potentials > 0.7 V vs RHE there is negligible peroxide detected at the ring. The increase in peroxide detected as the potential approaches 0.5 V vs RHE occurs because the rate of peroxide desorption is greater than the rate of further reduction of the adsorbed intermediate in this potential range. After the 0.5 V point is reached, the rate of reduction of

the peroxide intermediate increases such that the rate of further reduction through the 2 + 2 pathway is faster than desorption. On the initial scan, the a-C-NH_3 900 surface is active enough to almost entirely reduce the intermediates via this pathway. However, degradation of the surface by exposure to peroxide on successive scans results in the loss of many of these active sites, possibly due to the formation of oxide species, resulting in a large peroxide yield even at high overpotentials.

6.2 Conclusions

In this chapter, the ORR performance of N-doped carbon model systems prepared via bulk and surface nitrogenation methods was studied in order to compare and contrast the effects of the two N-doping methodologies on the electrocatalytic response. N-doped carbons with constant N-content and two classes of N sites, graphitic N and pyridinic N, in different proportions were prepared by the annealing of DC magnetron sputtered a-C:N surfaces or by treating N-free a-C a900 surfaces under ammonia at 700 ^{o}C or 900 ^{o}C. It was shown that under alkaline conditions, the most likely ORR mechanism on all of the surfaces involves an initial reduction of O_2 to form superoxide, which undergoes further reduction after becoming bound to the surface. Graphitic N sites were strongly correlated to higher onset potentials in alkaline conditions due to their non-local π-dopant effects. Both pyridinic-N and graphitic-N are important for facilitating the 4-electron pathway, as they both modify the carbon scaffold and introduce favourable binding sites for intermediates such as the peroxyl radical. In acidic pH, N-doped carbons with predominantly graphitic N and almost no pyridinic N sites were found to be inactive, which was attributed to the ORR proceeding through an inner-sphere mechanism at low pH for which strong interactions of molecular O_2 with sites associated with pyridinic N are required.

The structural organisation of the carbon scaffold was found to have the greatest influence on the ORR performance in alkaline media. The most active N-doped carbon, a-C NH_3 a900, had activity comparable to other high-performing ORR materials in the literature and was the most graphitized material based on Raman spectroscopy analysis. The activity of this surface was considerably greater than a similar N-doped carbon system, a-C-NH_3 700 with an identical N concentration in the carbon scaffold and very similar N-site chemistry. The model electrode with the lowest selectivity for 4-electron reduction was the bulk-doped a-C:N-10% a900, which was also found to be the most disordered N-doped carbon based on the Raman analysis.

It was also found from the similar ORR responses of the a-C:N-2% a900 and the a-C NH_3 a700 that the precise mechanism of N-doping (bulk or surface nitrogenation) has little effect on the ORR performance. The similarities in the behaviour of these two electrodes were attributed to their comparable carbon scaffold arrangement as identified through the Raman studies. This in turn was a result of the two divergent doping methods fortuitously producing a similar nanostructure in each case. The carbon scaffold structure itself can therefore said to influence the ORR activity to a comparable degree to the dopant sites. In other words, researchers should not consider 'pyridinic N' or 'graphitic N' as isolated chemical entities contributing to the ORR, but rather as particular classes of N site present in a carbon scaffold with a particular sp^2-domain size and organisation.

The combination of both pyridinic N and graphitic N sites and a highly graphitized carbon scaffold was correlated with the highest onset potential and with selectivity for the full 4-electron reduction of O_2 under basic conditions. The precise reasoning for why this particular combination of properties is so favourable to the ORR is unknown at present, but may be speculatively attributed to an increased preference for the 2 + 2 reduction pathway on this surface compared to the production of peroxide followed by its desorption. This hypothesis can be confirmed through further experiments with these model surfaces in the peroxide reduction reaction, as well as through computational studies of the interaction between peroxyl intermediates and N-doped carbon surfaces.

6.3 Experimental Methods

Chemicals and Materials

Potassium Hydroxide (Aldrich, 85%), Perchloric Acid (Fluka, Ultratrace), Methanol (99.9%, Semiconductor grade, Alfa Aesar), Oxygen (Boc Medical, 99.5 %) were used as purchased without further purification.

Substrate Preparation

Glassy carbon (GC) discs (HTW Sigradur radius 0.25 ± 0.05 cm) were prepared for deposition of a-C and a-C:N films by polishing with progressively finer grades of alumina slurry (Buehler) with particle sizes of 1 μm, 0.3μm and 0.05μm on microcloth (Buehler). Between each round of polishing the disks were rinsed with copious millipore water, then sonicated in methanol and Millipore water for 3 minutes each. After the final polishing step this sonication was increased to 10 minutes in each solvent, followed by drying under Ar.

In the case of a-C a900 and a-C:N-2/10% a900 electrodes, the polished discs were then mounted in a custom-made Teflon holder and placed in a vacuum chamber for coating via magnetron sputtering. The resulting electrodes were then transferred into a tube furnace and annealed for 1 h at a temperature of 900 ^{o}C under N_2. The a-C NH_3 700 / 900 surfaces were prepared by taking a-C a900 electrodes and annealing them under NH_3 / Ar in a tube furnace. The annealing treatment was accomplished by ramping the furnace to the desired temperature at a rate of 10 ^{o}C/min under Ar at a flow rate of 200 sccm/min. NH_3 gas was then introduced to the furnace and the flux of N_2 was adjusted to achieve a 50:50 flux of both gases at a total flow rate of 200 sccm/min in total for 30 min. After the ammonia treatment the surfaces were annealed for a further 30 min under 200 sccm of Ar only before cooling to room temperature.

Characterisation

Electrochemical measurements were carried out using a Metrohm Autolab AUT50324 potentiostat using a 3-electrode setup. A Hydroflex hydrogen electrode (Gaskatel) and graphite rod were used as reference and counter electrodes, respectively. The

electrochemical cell was a five-necked jacketed cell (Pine Instruments) which had its temperature held constant at 25 °C using a recirculator. Prior to experiments, the cell was cleaned using Piranha solution (3:1 H_2SO_4:H_2O_2 **CAUTION:** Piranha solution is a strong oxidant which may react explosively with organic solvents and must always be used in a fumehood) followed by rinsing several times with Millipore water.

The cell was then rinsed three times with the electrolyte solution used during the experiment (0.1M KOH or 0.1M $HClO_4$) and then filled with the working solution. Cyclic voltammograms (CVs) were acquired in a potential window of 0.05-1 V vs RHE. All voltammograms were taken with iR compensation using commercial software (NOVA) with the uncompensated resistance determined prior to each experiment using Electrochemical Impedance Spectroscopy (EIS).

The rotating ring-disk electrode experiments were performed using a dismountable RRDE tip (Pine Instruments, Figure 6.15 a) into which the disk electrodes were mounted. The ring inset was made from Pt which was cleaned prior to each experiment by cycling in 0.1 M H_2SO_4 for 50 scans at a scan rate of 50 mV s^{-1}. Contact was established to the rear of the disk using a gold probe (Figure 6.15 b). The tip was attached to a rotating shaft (Pine Instruments, Figure 6.15 c) which could be lowered into the glass cell containing the working solution. Rotation of the shaft at different rpm was accomplished using an RRDE controller also purchased from Pine Instruments.

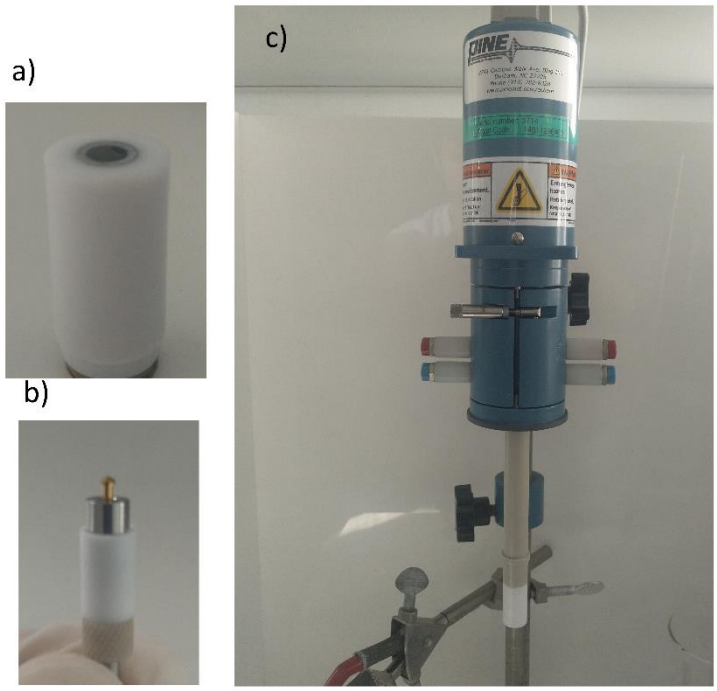

Figure 6.15. a) RRDE tip with Pt ring and mounted GC disk b) gold probe used to establish contact to the GC disk c) RRDE shaft with mounted electrode tip.

X-ray photoelectron spectroscopy (XPS) characterization was performed at 1×10^{-10} mbar base pressure in an ultrahigh-vacuum system (Omicron). The X-ray source was a monochromatized Al Kα source (1486.6 eV). Spectra were recorded at 45° takeoff angle with an analyser resolution of 0.5 eV. Spectra were baseline corrected using a Shirley background and fitted with Voigt functions using commercial software (CasaXPS); atomic percent compositions were determined by calculating peak area ratios after correction by relative sensitivity factors (C 1s = 1.0, N 1s = 1.8, O 1s = 2.93).

Raman spectra were measured in backscattering configuration using a Renishaw 1000 micro-Raman system equipped with an Ar^+ laser for 488 nm excitation. The incident beam was focused by a Leica microscope with a 50× magnification objective and short-focus working distance; incident power was kept <2 mW to avoid sample damage. Spectra were baseline corrected using commercial software (OriginPro 9.1) prior to deconvolution.

The surface roughness of the different model systems was obtained via AFM in tapping mode (Asylum Instruments). Gold-coated silicon cantilevers (NSG01/Au NT-MDT) with a tip height of 14-16 μm and a cantilever length of 125 μm were used in all cases. AFM images of the electrode surfaces are shown in Figure 6.16 and associated rms roughness values are given in Table 6.4. All electrodes are found to have generally similar roughness values which may be attributed to the underlying roughness of the polished GC substrate.

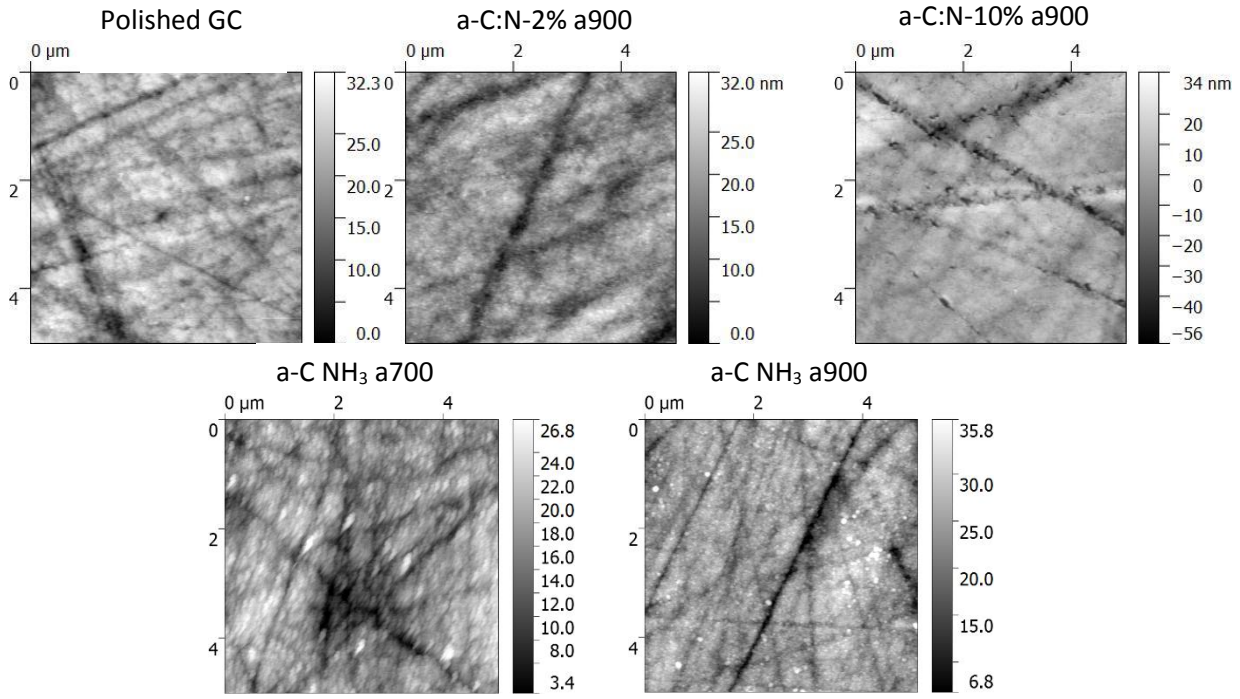

Figure 6.16. AFM height images of polished GC and annealed nitrogenated electrodes deposited on GC substrates. (Size: 5 x 5 μm, 512 lines)

Table 6.4. rms roughness values for polished GC and annealed nitrogenated electrodes.

Sample	rms Roughness (nm)
Polished GC	3.74
a-C:N-2% a900	3.80
a-C:N-10% a900	5.50
a-C NH_3 a700	2.79
a-C NH_3 a900	3.59

6.4 References

1. Gong, K.; Du, F.; Xia, Z.; Durstock, M.; Dai, L., Nitrogen-Doped Carbon Nanotube Arrays with High Electrocatalytic Activity for Oxygen Reduction. *Science* **2009,** *323* (5915), 760-764.

2. Qu, L.; Liu, Y.; Baek, J.-B.; Dai, L., Nitrogen-Doped Graphene as Efficient Metal-Free Electrocatalyst for Oxygen Reduction in Fuel Cells. *ACS Nano* **2010,** *4* (3), 1321-1326.

3. Wang, X.; Lee, J. S.; Zhu, Q.; Liu, J.; Wang, Y.; Dai, S., Ammonia-Treated Ordered Mesoporous Carbons as Catalytic Materials for Oxygen Reduction Reaction. *Chemistry of Materials* **2010,** *22* (7), 2178-2180.

4. Ge, X.; Sumboja, A.; Wuu, D.; An, T.; Li, B.; Goh, F. W. T.; Hor, T. S. A.; Zong, Y.; Liu, Z., Oxygen Reduction in Alkaline Media: From Mechanisms to Recent Advances of Catalysts. *ACS Catalysis* **2015,** *5* (8), 4643-4667.

5. Wang, D.-W.; Su, D., Heterogeneous nanocarbon materials for oxygen reduction reaction. *Energy & Environmental Science* **2014,** *7* (2), 576-591.

6. Wood, K. N.; O'Hayre, R.; Pylypenko, S., Recent progress on nitrogen/carbon structures designed for use in energy and sustainability applications. *Energy & Environmental Science* **2014,** *7* (4), 1212-1249.

7. Dai, L., Carbon-based catalysts for metal-free electrocatalysis. *Current Opinion in Electrochemistry* **2017**.

8. Chai, G.-L.; Hou, Z.; Shu, D.-J.; Ikeda, T.; Terakura, K., Active Sites and Mechanisms for Oxygen Reduction Reaction on Nitrogen-Doped Carbon Alloy Catalysts: Stone–Wales Defect and Curvature Effect. *Journal of the American Chemical Society* **2014,** *136* (39), 13629-13640.

9. Guo, D.; Shibuya, R.; Akiba, C.; Saji, S.; Kondo, T.; Nakamura, J., Active sites of nitrogen-doped carbon materials for oxygen reduction reaction clarified using model catalysts. *Science* **2016,** *351* (6271), 361-365.

10. Iyer, A.; Kaskela, A.; Johansson, L. S.; Liu, X. W.; Kauppinen, E. I.; Koskinen, J., Single walled carbon nanotube network-Tetrahedral amorphous carbon composite film. *Journal of Applied Physics* **2015,** *117* (22).

11. Joucken, F.; Tison, Y.; Lagoute, J.; Dumont, J.; Cabosart, D.; Zheng, B.; Repain, V.; Chacon, C.; Girard, Y.; Botello-Méndez, A. R.; Rousset, S.; Sporken, R.; Charlier, J.-C.; Henrard, L., Localized state and charge transfer in nitrogen-doped graphene. *Physical Review B* **2012,** *85* (16), 161408.

12. McClure, J. P.; Thornton, J. D.; Jiang, R.; Chu, D.; Cuomo, J. J.; Fedkiw, P. S., Oxygen Reduction on Metal-Free Nitrogen-Doped Carbon Nanowall Electrodes. *Journal of The Electrochemical Society* **2012,** *159* (11), F733-F742.

13. Sharifi, T.; Hu, G.; Jia, X.; Wågberg, T., Formation of Active Sites for Oxygen Reduction Reactions by Transformation of Nitrogen Functionalities in Nitrogen-Doped Carbon Nanotubes. *ACS Nano* **2012,** *6* (10), 8904-8912.

14. Choi, C. H.; Lim, H.-K.; Chung, M. W.; Park, J. C.; Shin, H.; Kim, H.; Woo, S. I., Long-Range Electron Transfer over Graphene-Based Catalyst for High-Performing Oxygen Reduction Reactions: Importance of Size, N-doping, and Metallic Impurities. *Journal of the American Chemical Society* **2014,** *136* (25), 9070-9077.

15. Li, Q.; Zhang, S.; Dai, L.; Li, L.-s., Nitrogen-Doped Colloidal Graphene Quantum Dots and Their Size-Dependent Electrocatalytic Activity for the Oxygen Reduction Reaction. *Journal of the American Chemical Society* **2012,** *134* (46), 18932-18935.

16. Geng, D.; Chen, Y.; Chen, Y.; Li, Y.; Li, R.; Sun, X.; Ye, S.; Knights, S., High oxygen-reduction activity and durability of nitrogen-doped graphene. *Energy & Environmental Science* **2011,** *4* (3), 760-764.

17. Sidik, R. A.; Anderson, A. B.; Subramanian, N. P.; Kumaraguru, S. P.; Popov, B. N., O-2 reduction on graphite and nitrogen-doped graphite: Experiment and theory. *Journal of Physical Chemistry B* **2006,** *110* (4), 1787-1793.

18. Li, X.-F.; Lian, K.-Y.; Liu, L.; Wu, Y.; Qiu, Q.; Jiang, J.; Deng, M.; Luo, Y., Unraveling the formation mechanism of graphitic nitrogen-doping in thermally treated graphene with ammonia. *Scientific Reports* **2016,** *6*, 23495.

19. Chen, J.; Wang, X.; Cui, X.; Yang, G.; Zheng, W., Amorphous carbon enriched with pyridinic nitrogen as an efficient metal-free electrocatalyst for oxygen reduction reaction. *Chemical Communications* **2014,** *50* (5), 557-559.

20. Chen, J. Y.; Wang, X.; Cui, X. Q.; Yang, G. M.; Zheng, W. T., One-step synthesis of N-doped amorphous carbon at relatively low temperature as excellent metal-free electrocatalyst for oxygen reduction. *Catalysis Communications* **2014,** *46*, 161-164.

21. Stamatin, S. N.; Hussainova, I.; Ivanov, R.; Colavita, P. E., Quantifying Graphitic Edge Exposure in Graphene-Based Materials and Its Role in Oxygen Reduction Reactions. *ACS Catalysis* **2016,** *6* (8), 5215-5221.

22. Ferre-Vilaplana, A.; Herrero, E., Charge transfer, bonding conditioning and solvation effect in the activation of the oxygen reduction reaction on unclustered graphitic-nitrogen-doped graphene. *Physical Chemistry Chemical Physics* **2015,** *17* (25), 16238-16242.

23. Ikeda, T.; Hou, Z.; Chai, G.-L.; Terakura, K., Possible Oxygen Reduction Reactions for Graphene Edges from First Principles. *Journal of Physical Chemistry C* **2014,** *118* (31), 17616-17625.

24. Luo, Z.; Lim, S.; Tian, Z.; Shang, J.; Lai, L.; MacDonald, B.; Fu, C.; Shen, Z.; Yu, T.; Lin, J., Pyridinic N doped graphene: synthesis, electronic structure, and electrocatalytic property. *Journal of Materials Chemistry* **2011,** *21* (22), 8038-8044.

25. Titantah, J. T.; Lamoen, D., Carbon and nitrogen 1s energy levels in amorphous carbon nitride systems: XPS interpretation using first-principles. *Diamond and Related Materials* **2007,** *16* (3), 581-588.

26. Behan, J. A.; Stamatin, S. N.; Hoque, M. K.; Ciapetti, G.; Zen, F.; Esteban-Tejeda, L.; Colavita, P. E., Combined Optoelectronic and Electrochemical Study of Nitrogenated Carbon Electrodes. *The Journal of Physical Chemistry C* **2017,** *121* (12), 6596-6604.

27. Ferrari, A. C.; Rodil, S. E.; Robertson, J., Interpretation of infrared and Raman spectra of amorphous carbon nitrides. *Physical Review B* **2003,** *67* (15), 155306.

28. Ferrari, A. C.; Robertson, J., Resonant Raman spectroscopy of disordered, amorphous, and diamondlike carbon. *Physical Review B* **2001,** *64* (7), 075414.

29. Ferrari, A. C.; Robertson, J., Interpretation of Raman spectra of disordered and amorphous carbon. *Physical Review B* **2000,** *61* (20), 14095-14107.

30. Laidani, N.; Guzman, L.; Miotello, A.; Brusa, R. S.; Karwasz, G. P.; Zecca, A.; Bottani, C.; Perrière, J., Nitrogen effects on the microstructural evolution of carbon films under thermal annealing. *Nuclear Instruments & Methods in Physics Research, Section B: Beam Interactions with Materials and Atoms* **1997,** *122* (3), 553-558.

31. McEvoy, N.; Peltekis, N.; Kumar, S.; Rezvani, E.; Nolan, H.; Keeley, G. P.; Blau, W. J.; Duesberg, G. S., Synthesis and analysis of thin conducting pyrolytic carbon films. *Carbon* **2012,** *50* (3), 1216-1226.

32. Cançado, L. G.; Takai, K.; Enoki, T.; Endo, M.; Kim, Y. A.; Mizusaki, H.; Jorio, A.; Coelho, L. N.; Magalhães-Paniago, R.; Pimenta, M. A., General equation for the determination of the crystallite size La of nanographite by Raman spectroscopy. *Applied Physics Letters* **2006,** *88* (16), 163106.

33. Mayrhofer, K. J. J.; Strmcnik, D.; Blizanac, B. B.; Stamenkovic, V.; Arenz, M.; Markovic, N. M., Measurement of oxygen reduction activities via the rotating disc electrode method: From Pt model surfaces to carbon-supported high surface area catalysts. *Electrochimica Acta* **2008,** *53* (7), 3181-3188.

34. Pletcher, D., *A First Course in Electrode Processes*. Royal Society of Chemistry: 2009.

35. Katsounaros, I.; Cherevko, S.; Zeradjanin, A. R.; Mayrhofer, K. J. J., Oxygen Electrochemistry as a Cornerstone for Sustainable Energy Conversion. *Angewandte Chemie International Edition* **2014,** *53* (1), 102-121.

36. Lai, L.; Potts, J. R.; Zhan, D.; Wang, L.; Poh, C. K.; Tang, C.; Gong, H.; Shen, Z.; Lin, J.; Ruoff, R. S., Exploration of the active center structure of nitrogen-doped graphene-based catalysts for oxygen reduction reaction. *Energy and Environmental Science* **2012,** *5* (7), 7936-7942.

37. Wu, K.-H.; Wang, D.-W.; Zong, X.; Zhang, B.; Liu, Y.; Gentle, I. R.; Su, D.-S., Functions in cooperation for enhanced oxygen reduction reaction: the independent roles of oxygen and nitrogen sites in metal-free nanocarbon and their functional synergy. *Journal of Materials Chemistry A* **2017,** *5* (7), 3239-3248.

38. Qiu, Y.; Yu, J.; Shi, T.; Zhou, X.; Bai, X.; Huang, J. Y., Nitrogen-doped ultrathin carbon nanofibers derived from electrospinning: Large-scale production, unique structure, and application as electrocatalysts for oxygen reduction. *Journal of Power Sources* **2011,** *196* (23), 9862-9867.

39. Gasteiger, H. A.; Ross, P. N., Oxygen Reduction on Platinum Low-Index Single-Crystal Surfaces in Alkaline Solution: Rotating Ring DiskPt(hkl) Studies. *Journal of Physical Chemistry* **1996,** *100* (16), 6715-6721.

40. Holewinski, A.; Linic, S., Elementary Mechanisms in Electrocatalysis: Revisiting the ORR Tafel Slope. *Journal of the Electrochemical Society* **2012,** *159* (11), H864-H870.

41. Wu, G.; More, K. L.; Johnston, C. M.; Zelenay, P., High-Performance Electrocatalysts for Oxygen Reduction Derived from Polyaniline, Iron, and Cobalt. *Science* **2011,** *332* (6028), 443.

42. Reiser, C. A.; Bregoli, L.; Patterson, T. W.; Yi, J. S.; Yang, J. D.; Perry, M. L.; Jarvi, T. D., A Reverse-Current Decay Mechanism for Fuel Cells. *Electrochemical and Solid-State Letters* **2005,** *8* (6), A273-A276.

43. Zhu, Y.; Lin, Y.; Zhang, B.; Rong, J.; Zong, B.; Su, D. S., Nitrogen-Doped Annealed Nanodiamonds with Varied sp2/sp3 Ratio as Metal-Free Electrocatalyst for the Oxygen Reduction Reaction. *ChemCatChem* **2015,** *7* (18), 2840-2845.

44. Blizanac, B. B.; Ross, P. N.; Markovic, N. M., Oxygen electroreduction on Ag(111): The pH effect. *Electrochimica Acta* **2007,** *52* (6), 2264-2271.

45. Ramaswamy, N.; Mukerjee, S., Fundamental Mechanistic Understanding of Electrocatalysis of Oxygen Reduction on Pt and Non-Pt Surfaces: Acid versus Alkaline Media. *Advances in Physical Chemistry* **2012,** *2012*, 17.

46. Ramaswamy, N.; Mukerjee, S., Influence of Inner- and Outer-Sphere Electron Transfer Mechanisms during Electrocatalysis of Oxygen Reduction in Alkaline Media. *Journal of Physical Chemistry C* **2011,** *115* (36), 18015-18026.

47. Yang, H. H.; McCreery, R. L., Elucidation of the Mechanism of Dioxygen Reduction on Metal-Free Carbon Electrodes. *Journal of The Electrochemical Society* **2000,** *147* (9), 3420-3428.

48. Bielski, B. H.; Allen, A. O., Mechanism of the disproportionation of superoxide radicals. *Journal of Physical Chemistry* **1977,** *81* (11), 1048-1050.

49. Zhang, C.; Fan, F.-R. F.; Bard, A. J., Electrochemistry of Oxygen in Concentrated NaOH Solutions: Solubility, Diffusion Coefficients, and Superoxide Formation. *Journal of the American Chemical Society* **2009,** *131* (1), 177-181.

50. Katsounaros, I.; Schneider, W. B.; Meier, J. C.; Benedikt, U.; Biedermann, P. U.; Cuesta, A.; Auer, A. A.; Mayrhofer, K. J. J., The impact of spectator species on the interaction of H2O2 with platinum – implications for the oxygen reduction reaction pathways. *Physical Chemistry Chemical Physics* **2013,** *15* (21), 8058-8068.

51. Robertson, J.; Davis, C. A., Nitrogen Doping of Tetrahedral Amorphous-Carbon. *Diamond and Related Materials* **1995,** *4* (4), 441-444.

CHAPTER VII

Conclusions and Future Work

7. Conclusions

The aim of this thesis was to prepare carbon model systems based on sputtered amorphous carbon films and study their performance in a variety of electrochemical processes. The main focus of the work was the investigation of charge transfer events at the model carbon interface to redox probes in solution. The effects of N-doping on the optoelectronic properties of amorphous carbon scaffolds were first studied through a combination of x-ray photoelectron spectroscopy and spectroscopic ellipsometry.

It was shown that N-incorporation can produce semi-metallic amorphous carbons, presumably through the doping effect of incorporating substitutional or graphitic N sites into the carbon matrix. However, nitrogenation also results in an increase in structural disorder in the form of vacancies and edge sites which ultimately results in more insulating materials. The bulk effects of N-incorporation were directly correlated to the charge transfer kinetics between the carbon model electrodes and the outer-sphere $[Ru(NH_3)_6]^{2+/3+}$ redox couple using a combination of voltammetric and impedance measurements.

The electrochemical response to surface-sensitive or inner-sphere redox probes was next examined at amorphous carbon and glassy carbon electrode surfaces. It was found that surface chemical modifications including nitrogen incorporation and oxygenation can yield materials with favourable charge transfer kinetics to catechols, whilst structural modification through thermal annealing induces catechol adsorption at graphitized carbon surfaces. N-free and N-doped sputtered amorphous carbon materials were then used as the starting materials for the preparation of annealed carbon model systems with uniform N-site chemistry but different carbon nanostructure as determined from Raman spectroscopy studies.

The adsorption of dopamine and 4-methyl catechol at the electrode surfaces was found to be affected by both the presence of particular N-sites and the availability of graphitic cluster domains which may interact with the catechols through π-π^* interactions. This was supported by computational studies of catechol adsorption at pristine graphene surfaces and graphene surfaces with N and O sites which predicted favourable adsorption free energies for catechols interacting with sp^2 domains via their aryl system.

Heteroatom sites may enhance this response, for instance through H-bonding interactions with the hydroxyl moieties of the catechol or the ethylamine chain of dopamine, but the introduction of excessive defect sites or interruptions in the sp^2-network is not favourable

for adsorption. The adsorption of catechols can therefore be exploited as electrochemical probes of the degree of graphitization in carbon nanomaterials.

Finally, N-doped carbon model systems were studied as electrocatalysts in the oxygen reduction reaction, in order to investigate the different effects of surface nitrogenation and bulk N-doping on the ORR performance. It was found that good ORR performance in terms of the onset potential and selectivity for the 4-electron oxygen reduction pathway can be achieved through both N-doping strategies. N-doping promotes the ORR under basic conditions through the introduction of graphitic-N sites which increase the metallic character of the carbon material and improve the initial outer-sphere electron transfer to O_2, whilst graphitic-N shows no apparent activity under acidic conditions because the outer-sphere charge transfer is not thermodynamically accessible at low pH. The activity under acidic conditions was instead correlated to pyridinic-N sites which promote the ORR through inner-sphere charge transfer to adsorbed O_2.

The role of the carbon scaffold structure in ORR electrocatalysis was also investigated through the correlation of the performance to the nanostructure as determined from Raman studies. The comparable activity of two of the model systems which were prepared via bulk and surface methods was attributed to the similar carbon scaffold arrangement of both electrodes. The degree of graphitization of the carbon scaffold was correlated to both the onset potential and the selectivity for the 4-electron reduction, suggesting that N-doping *per se* is not the only predictor of the ORR performance.

The common theme throughout each chapter of this thesis has been that the preparation of carbon model systems with comparable surface morphology and topography enables the electrochemical performance in a variety of processes to be correlated to specific chemical and surface structural modifications. This has been demonstrated for N-doped carbons in both outer-sphere and inner-sphere redox reactions, but the principle is entirely general and may be applied to other dopants and chemical surface treatments. Significant advances in the area of electrocatalysis with carbon nanomaterials will be seen in the coming years, particularly in the area of electrochemical energy transformation. Fundamental structure-activity studies on carbon model systems, including those based on amorphous carbons, are expected to be at the centre of these developments.

7.1 Future Work

This thesis has identified a number of areas of possible future research on the interactions of nitrogenated carbon electrode materials with inner-sphere redox probes. Chapters IV and V showed that catechols may interact with the basal plane of graphitized carbon surfaces with and without the presence of dopant atoms through π interactions. This was applied in the area of carbon nanostructural characterization, however in principle such interactions may also be useful for electrochemical biosensors based on nitrogenated graphitized carbon materials. Other relevant aromatic biomolecules including other catechols and amino acids such as tyrosine will also be investigated in future projects, as they are expected to produce a similar response to that seen for dopamine and 4-methyl catechol. Voltammetric studies using 4-Nitrobenzylamine, another aromatic redox probe which has previously been used to characterise the graphitic edge content of carbon nanomaterials including graphene, are also currently underway on nitrogenated carbon electrodes. In principle these measurements offer complementary information on the carbon nanostructure to that obtained via dopamine studies.

A second major area of future work identified in the previous chapter involves further studies of the ORR performance of N-doped carbon model systems. The results presented in Chapter VI strongly suggest that subtle differences in carbon nanostructure between the various nitrogenated carbon electrodes affect the binding energy of oxygen reduction intermediates such as peroxyl radicals and the hydroperoxide anion. This results in a large variation in the selectivity towards 2-electron or 4-electron pathways even in model systems with similar N-content and nitrogen surface chemistry.

The selectivity towards the 4-electron reduction at each nitrogenated surface is expected to be correlated to the performance of the electrode in the peroxide reduction reaction (PRR). If the PRR is extremely facile, a full 4-electron reduction of oxygen to water may be expected for the ORR, whilst a sluggish PRR favours the incomplete reduction and subsequent dissociation of hydroperoxide. The performance of these surfaces in peroxide reduction will be investigated in order to confirm this hypothesis. Computational studies of interactions of these ORR intermediates at difference surface sites such as pyridinic-N sites, graphitic-N sites and carbon vacancies are also expected to help explain the effects of both nitrogen site chemistry and carbon scaffold organisation on the ORR performance.

APPENDIX I

Geometrical Structures from Computational Studies of Catechol Adsorption on Graphene Model Surfaces

1. Dopamine

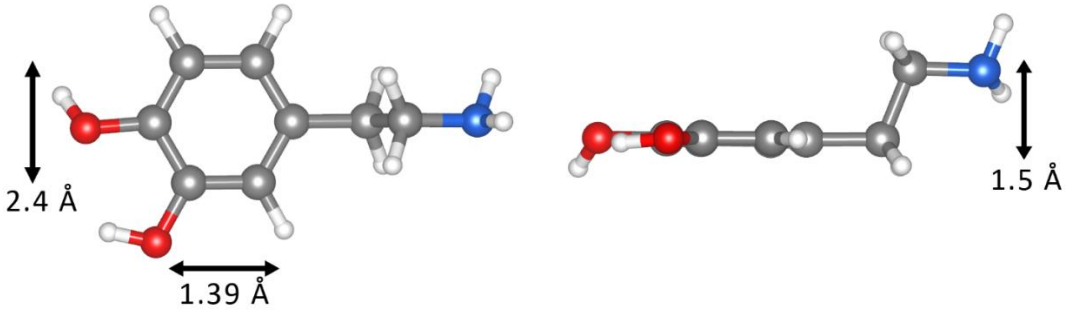

Figure A1. Optimized structure for the dopamine (DA) molecule.

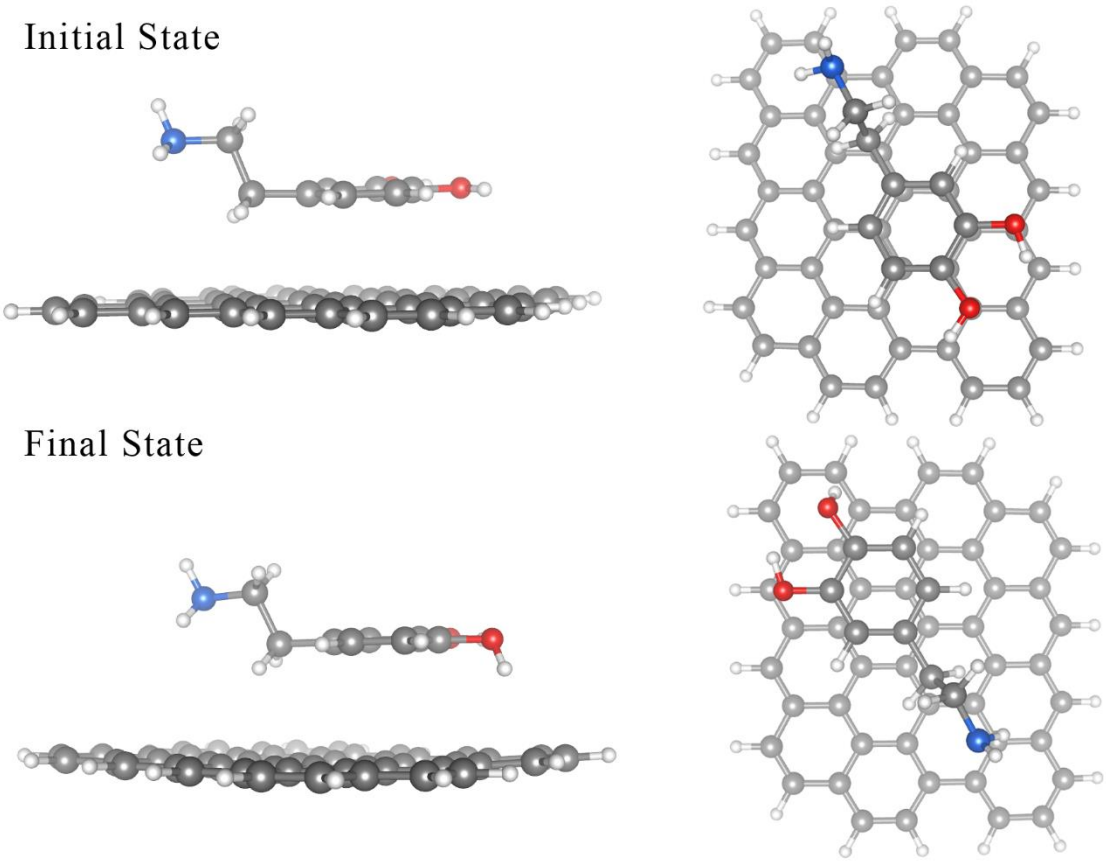

Figure A2. Initial (top) and final (bottom) geometries in the modelling of the DA-BP interaction.

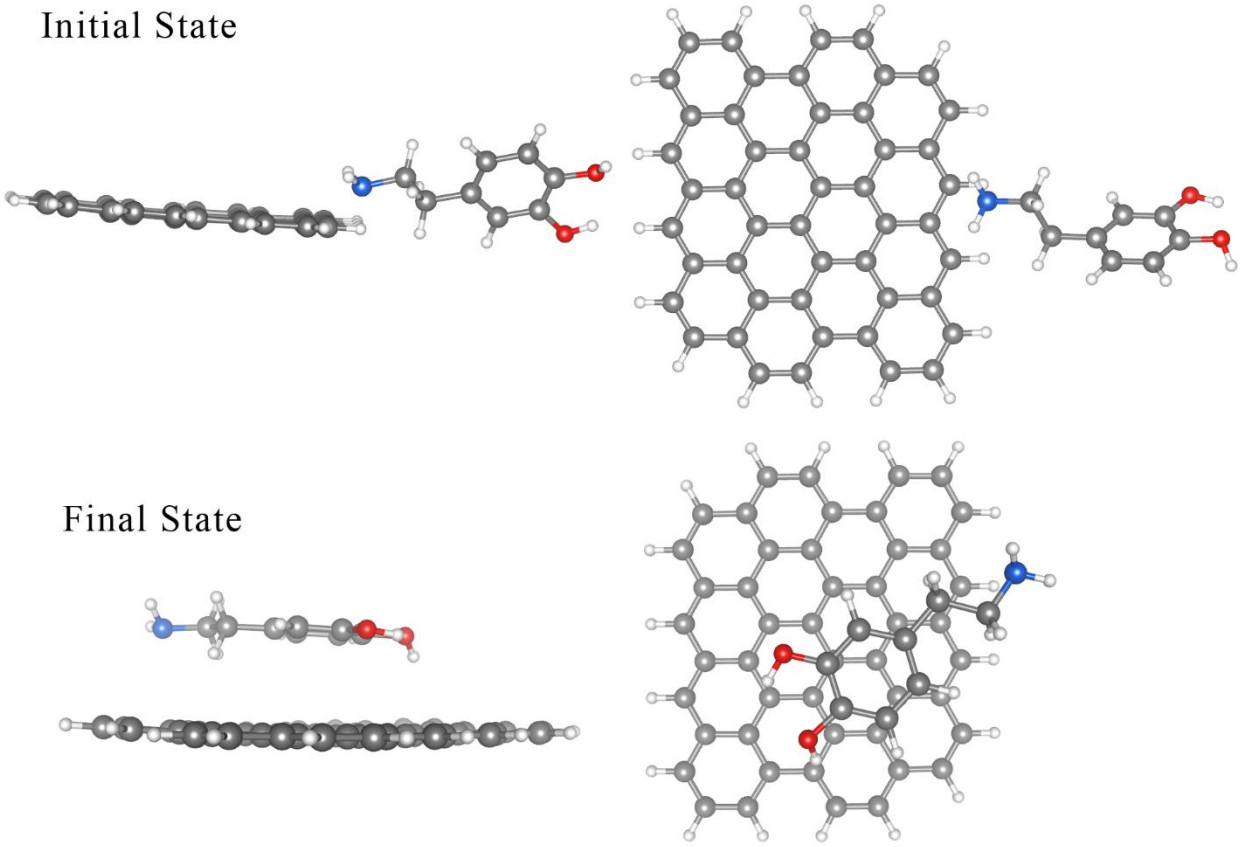

Figure A3. Initial (top) and final (bottom) geometries in the modelling of the DA-E interaction.

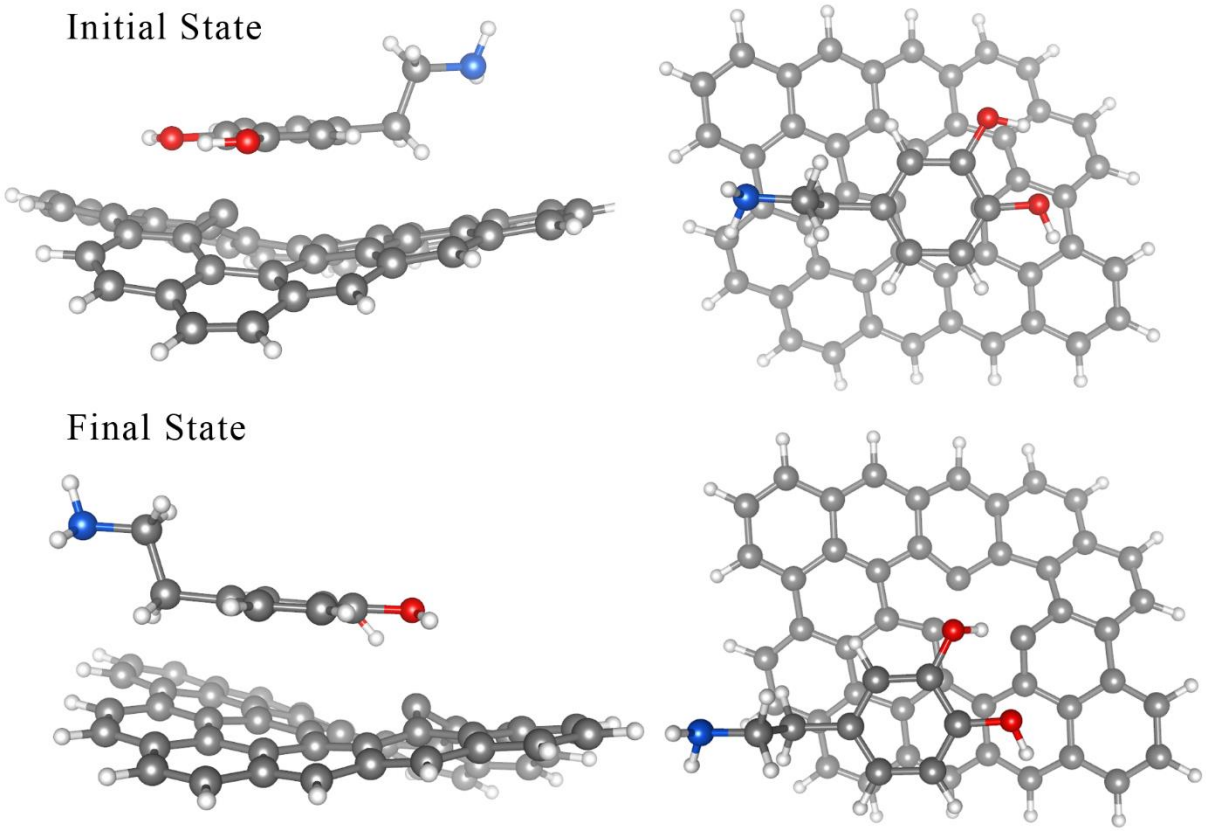

Figure A4. Initial (top) and final (bottom) geometries in the modelling of the DA-V interaction.

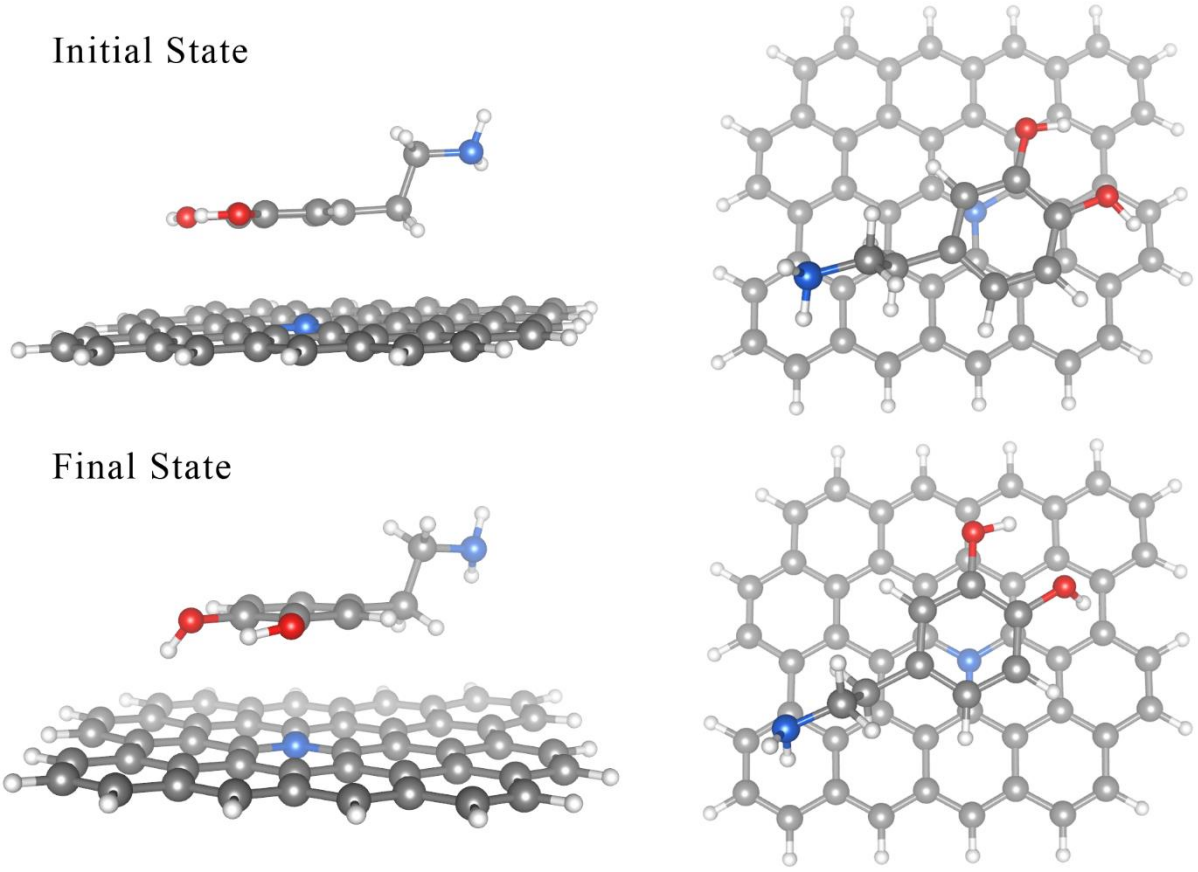

Figure A5. Initial (top) and final (bottom) geometries in the modelling of the DA-$N_{g,c}$ interaction.

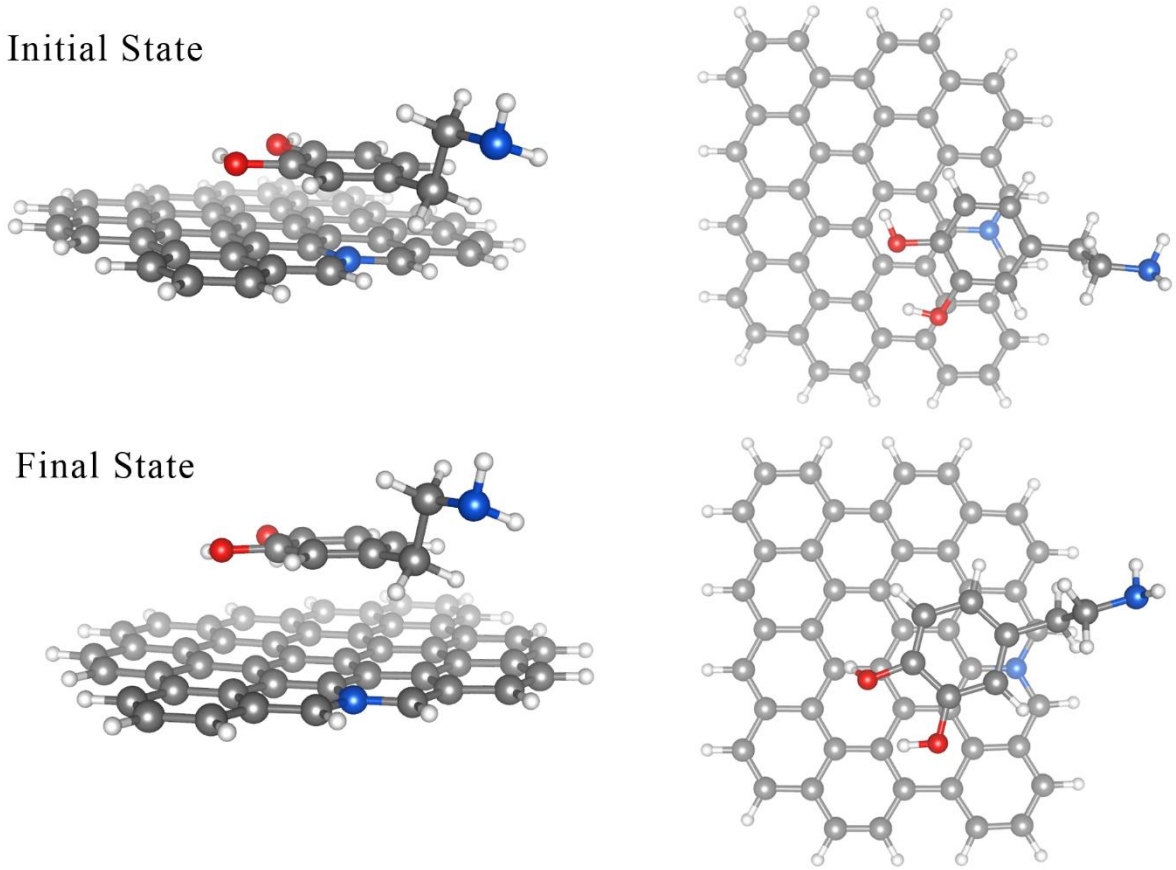

Figure A6. Initial (top) and final (bottom) geometries in the modelling of the DA-$N_{g,v}$ interaction.

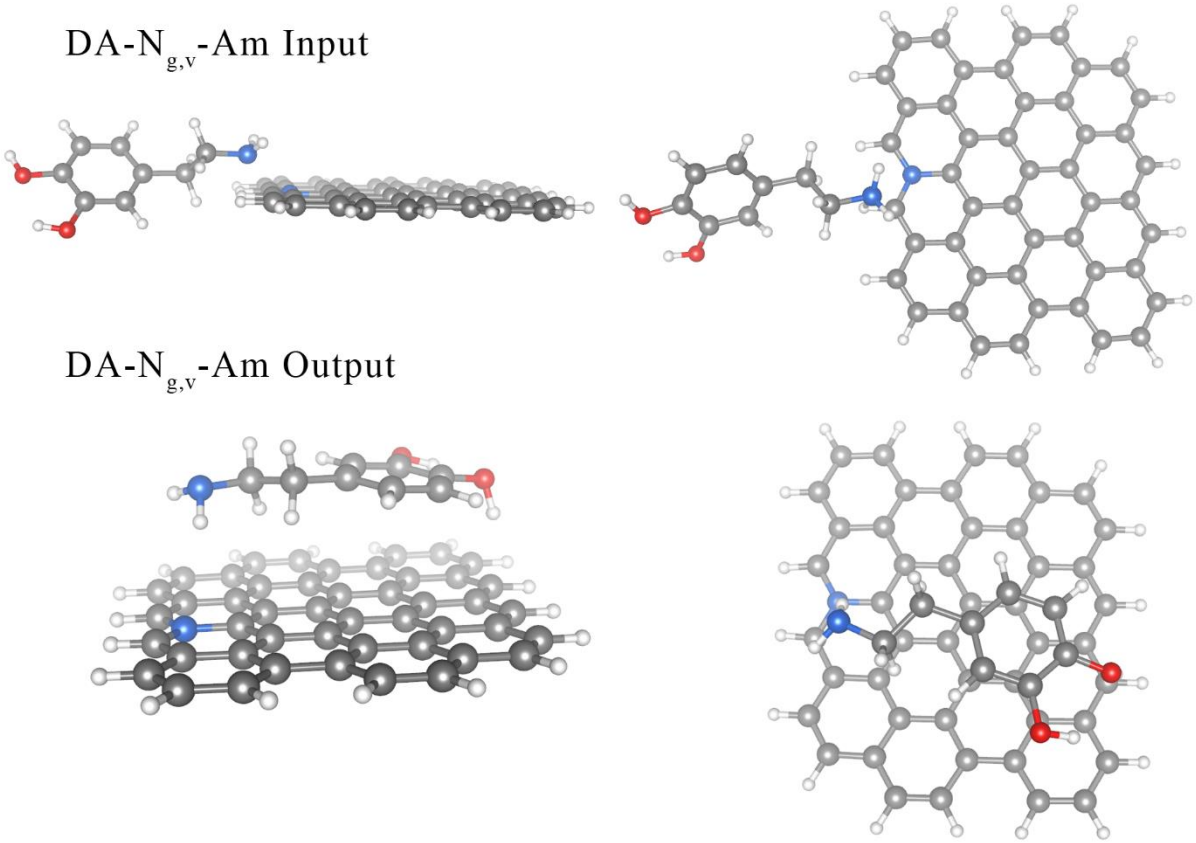

Figure A7. Initial (top) and final (bottom) geometries in the modelling of the DA-$N_{g,v}$-Am interaction

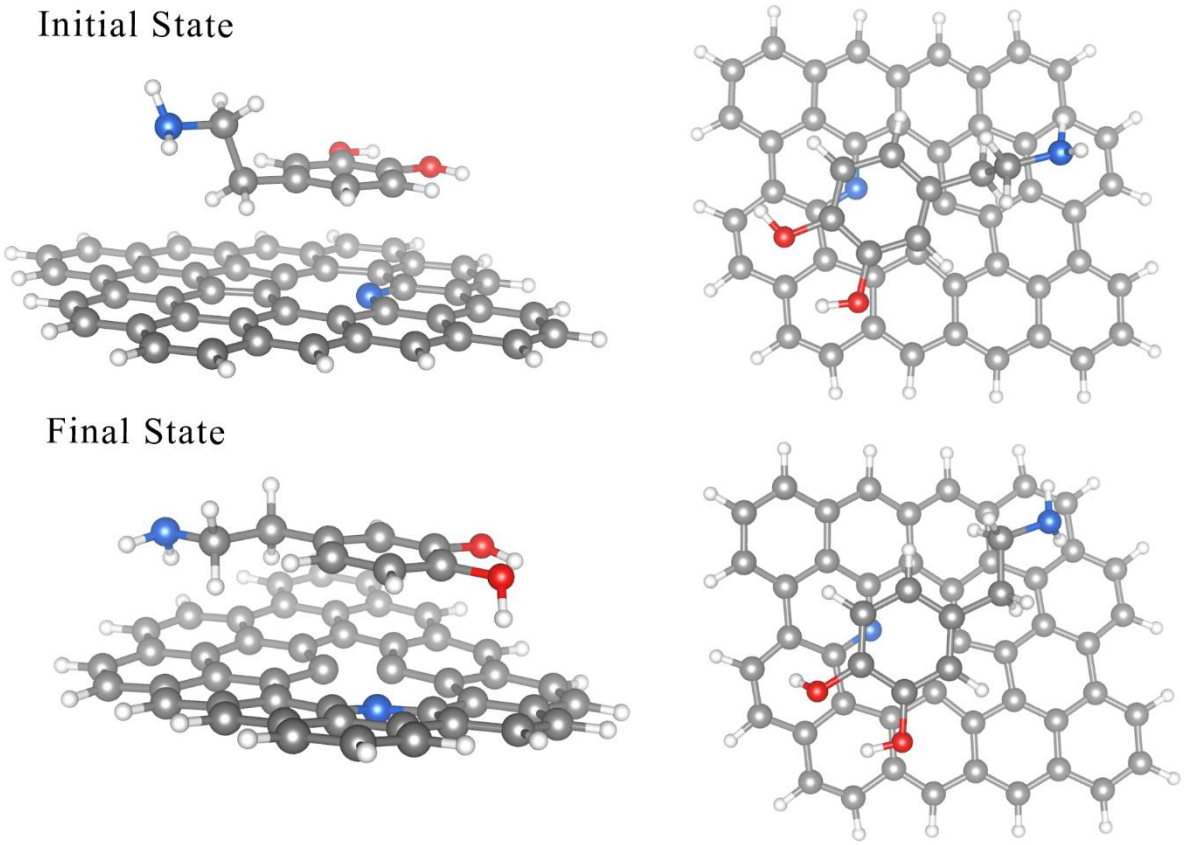

Figure A8. Initial (top) and final (bottom) geometries in the modelling of the DA-N_p interaction.

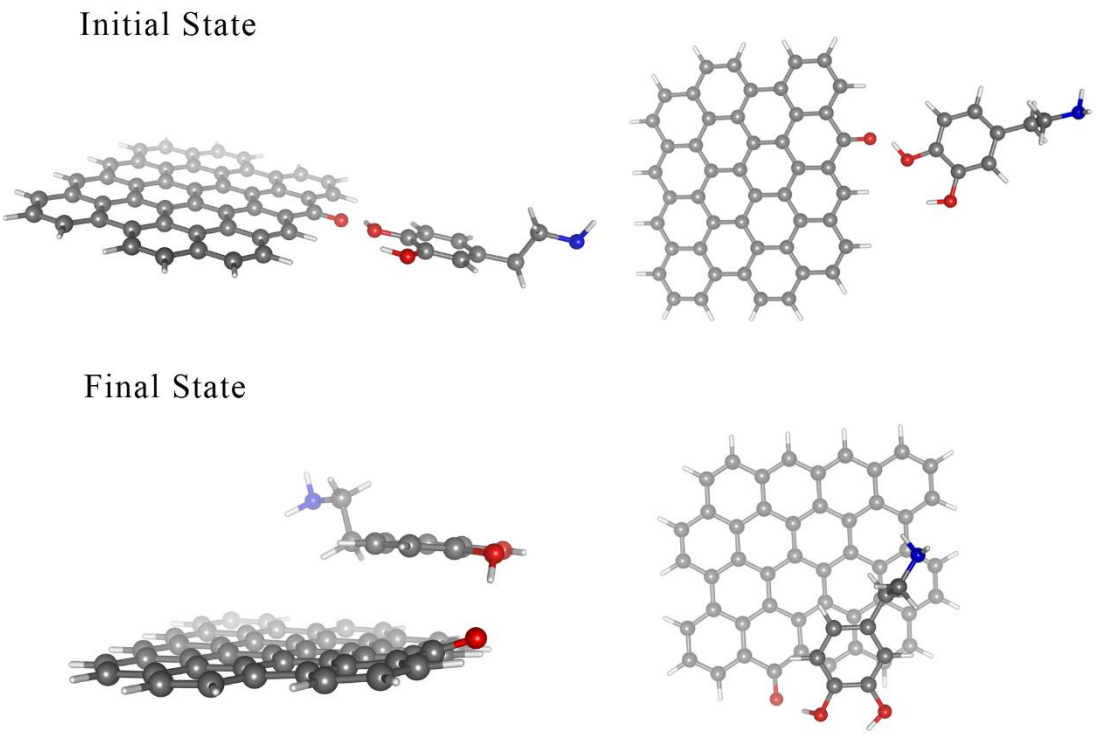

Figure A9. Initial (top) and final (bottom) geometries in the modelling of the DA-Carbonyl interaction.

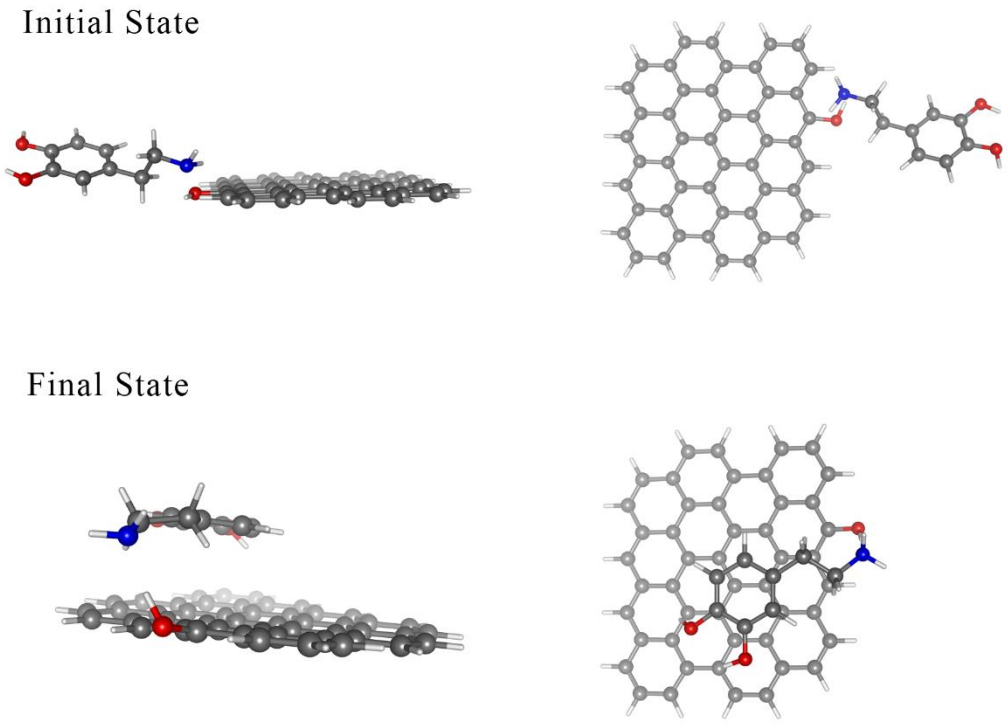

Figure A10. Initial (top) and final (bottom) geometries in the modelling of the DA-hydroxyl-amine interaction.

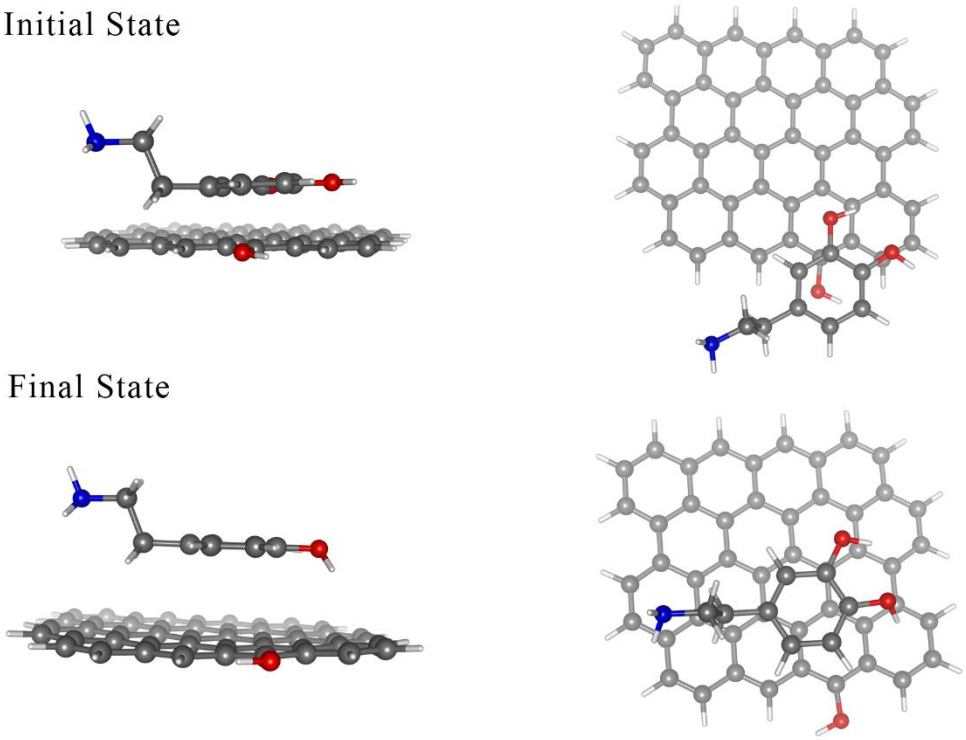

Figure A11. Initial (top) and final (bottom) geometries in the modelling of the DA-hydroxyl-pi interaction.

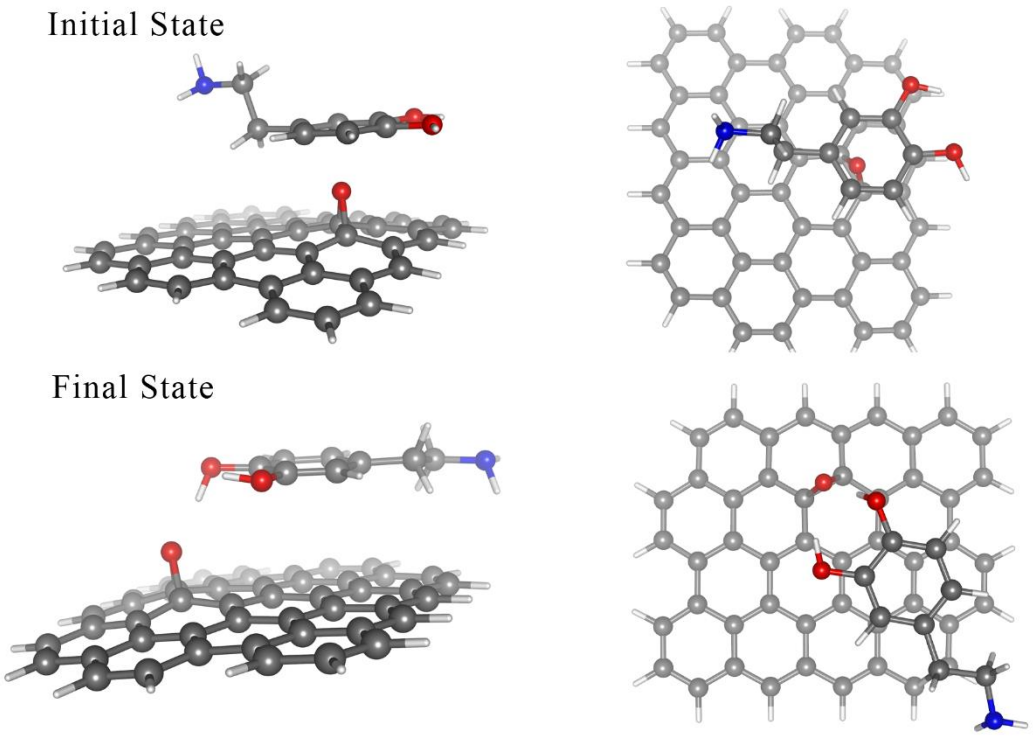

Figure A12. Initial (top) and final (bottom) geometries in the modelling of the DA-epox interaction

1. 4-Methyl Catechol

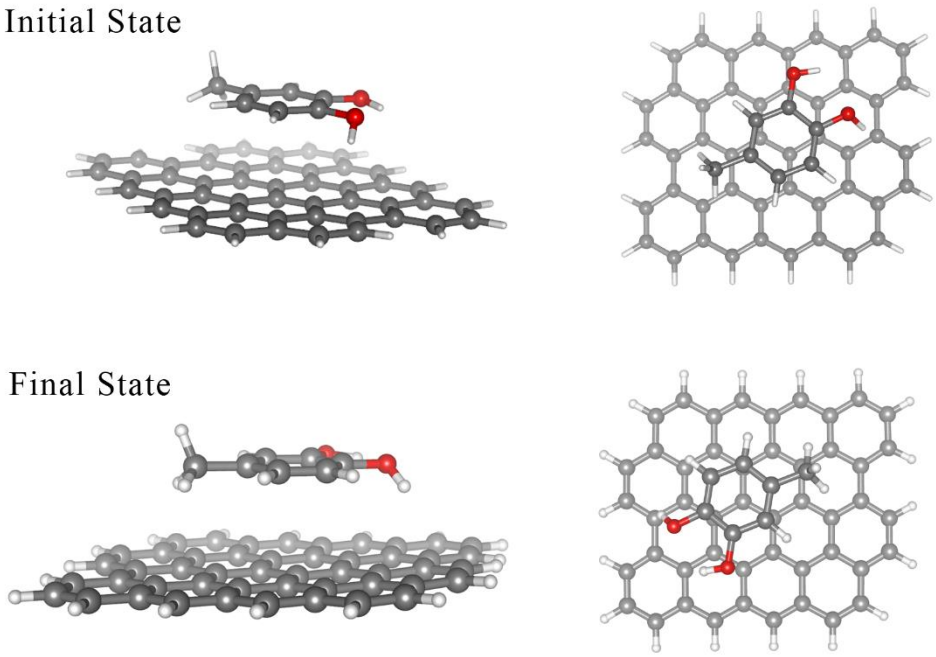

Figure A13. Initial (top) and final (bottom) geometries in the modelling of the MCC-BP interaction.

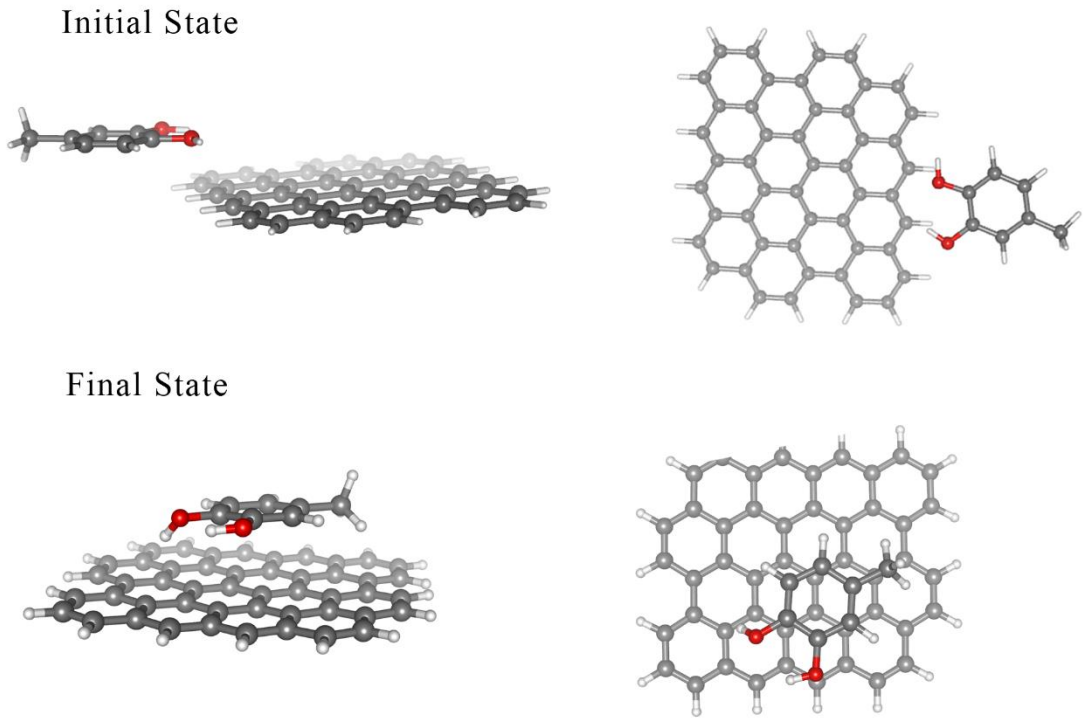

Figure A14. Initial (top) and final (bottom) geometries in the modelling of the MCC-E interaction.

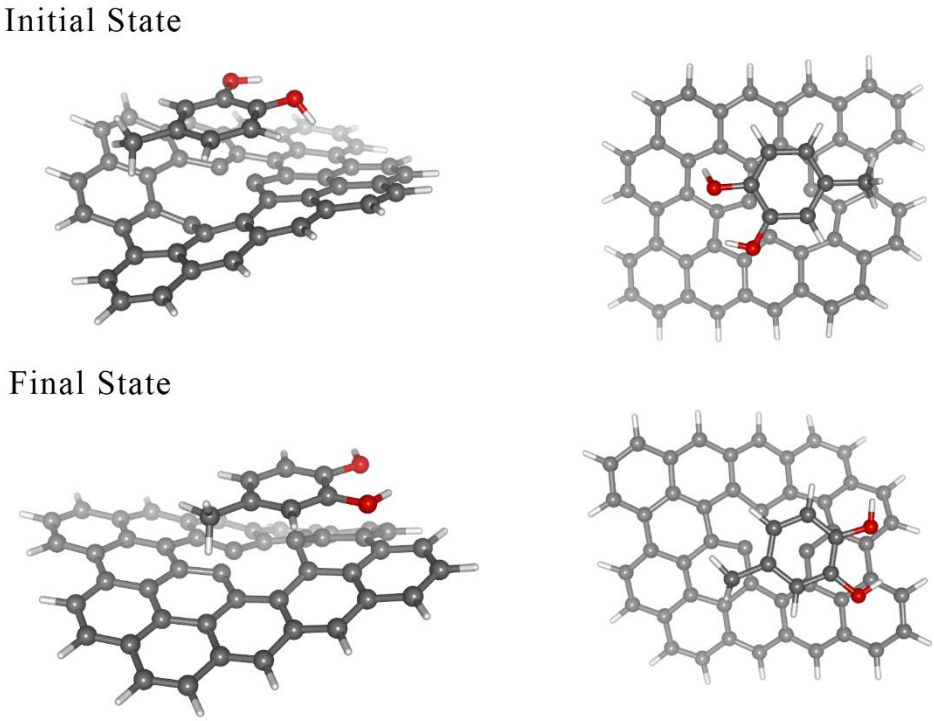

Figure A15. Initial (top) and final (bottom) geometries in the modelling of the MCC-VAC interaction.

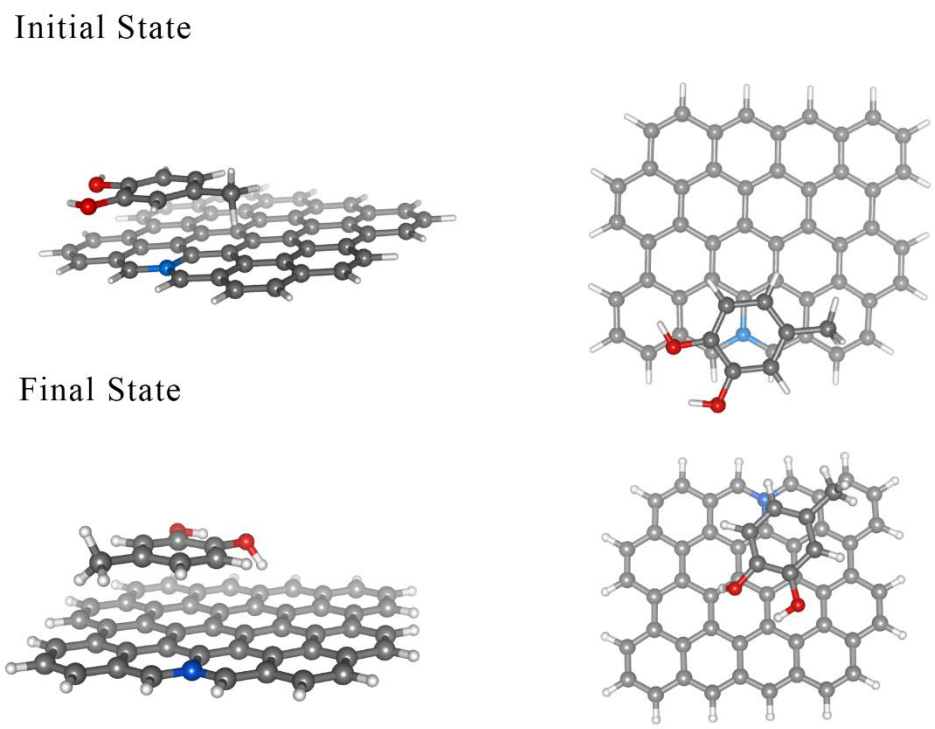

Figure A16. Initial (top) and final (bottom) geometries in the modelling of the MCC-$N_{g,v}$ interaction.

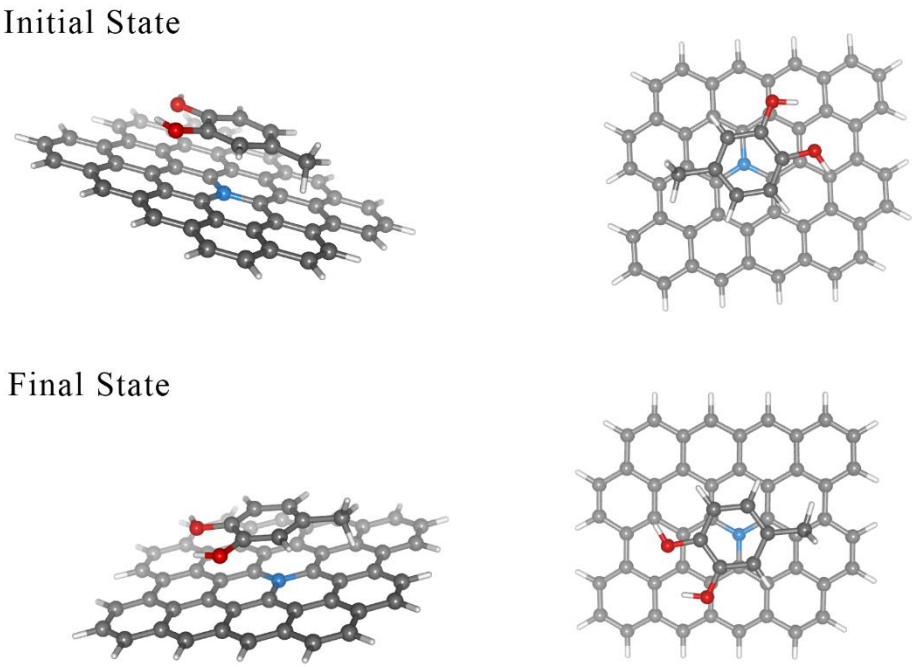

Figure A17. Initial (top) and final (bottom) geometries in the modelling of the MCC-$N_{g,c}$ interaction.

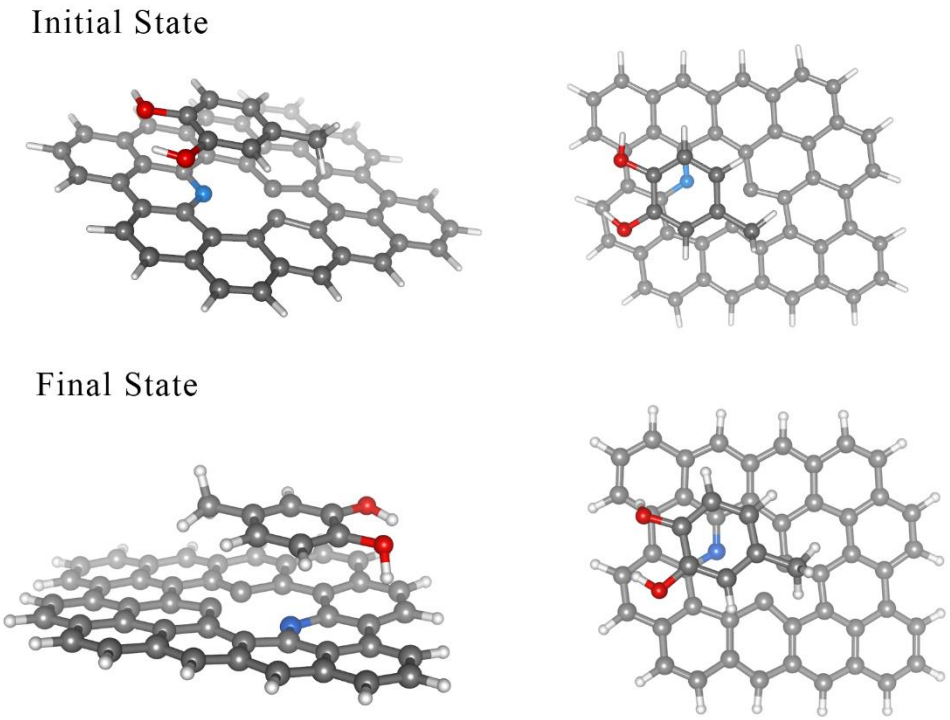

Figure A18. Initial (top) and final (bottom) geometries in the modelling of the MCC-N_{pyr} interaction.

APPENDIX II

Published Work

THE JOURNAL OF PHYSICAL CHEMISTRY C

Article

pubs.acs.org/JPCC

Combined Optoelectronic and Electrochemical Study of Nitrogenated Carbon Electrodes

James A. Behan, Serban N. Stamatin, Md. Khairul Hoque, Guido Ciapetti, Federico Zen, Leticia Esteban-Tejeda, and Paula E. Colavita*

School of Chemistry, CRANN and AMBER Research Centres, Trinity College Dublin, College Green, Dublin 2, Ireland

Supporting Information

ABSTRACT: Modification of carbon materials via incorporation of nitrogen has received much attention in recent years due to their performance as electrodes in applications ranging from electroanalysis to electrocatalysis for energy storage technologies. In this work we synthesized nitrogen-incorporated amorphous carbon thin film electrodes (a-C:N) with different degrees of nitrogenation via magnetron sputtering. Electrodes were characterized using a combination of spectroscopic and electrochemical methods, including X-ray photoelectron spectroscopy, ellipsometry, voltammetry, and impedance spectroscopy. Results indicate that low levels of nitrogenation yield carbon materials with narrow optical gaps and semimetallic character. These materials displayed fast electron-transfer kinetics to hexammine ruthenium(II)/(III), an outer-sphere redox couple that is sensitive to electronic properties near the Fermi level in the electrode material. Increasing levels of nitrogenation first decrease the metallic character of the electrodes, increase the impedance to charge transfer and, ultimately, yield materials with optical and electrochemical properties consistent with disordered cluster aggregates rather than amorphous solids. A positive correlation was found between the resistance to charge transfer and the optical gap when using the outer-sphere redox couple. Interestingly, the use of ferrocyanide as a surface-sensitive redox probe resulted in a monotonic increase of the impedance to charge transfer vs nitrogen content. This result suggests that surface chemical effects can dominate the electrochemical response, even when nitrogenation results in enhanced metallic character in carbon electrodes.

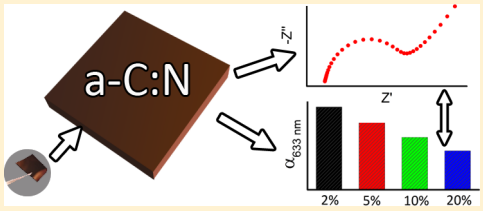

INTRODUCTION

Incorporation of heteroatoms such as nitrogen into carbon frameworks and its effects on carbon properties has received much attention over the past few decades. The initial research mostly focused on the effects of nitrogenation for electronic and mechanical applications of carbon coatings and thin films.[1,2] More recently, there has been growing interest in understanding the effects of nitrogenation on the properties of carbon electrode materials given their importance for applications in electroanalysis[3−5] and electrocatalysis[3,6] and as support materials in fuel cells.[7] Nitrogen incorporation can significantly affect bulk carbon properties; as reported by several groups,[1,2] substitutional N sites within a graphitic carbon matrix introduce donor states that can impart n-type conductivity and enhance overall charge transport, while they can also modulate mechanical stress and defects in the carbon structure. Surface effects of nitrogenation however are also important, particularly for applications in electrochemistry which rely on processes that occur at the carbon interface.

Nitrogenated carbon thin film electrodes have been shown to display large (>3 V) potential windows and low background currents in aqueous solutions, as well as low roughness, which are important requirements for electroanalytical applications.[3−5,8] The above favorable properties have led to applications in the detection of heavy metals in solution, as well as the detection of biomolecules such as estrone, dopamine, and ascorbate.[9−11] Nitrogenation has been shown in many cases to accelerate the kinetics of electron transfer, resulting in enhanced peak currents and/or a narrowing of the peak potential separation. The precise mechanism of enhancement is not well understood, although it has been speculated that improved electronic properties and/or interactions between the analyte molecules and the surface chemical groups contribute to the observed enhancements.[12]

Nitrogenated carbon electrodes are intensely studied for multistep electron−proton coupled reactions, such as hydrogen peroxide production from water[13,14] and the oxygen reduction reaction (ORR).[15−18] Nitrogenated carbons have shown remarkable activity in the ORR, which is the cathode reaction in fuel cells and Li−air batteries. Their activity has been attributed to the presence of specific surface sites such as substitutional and pyridinic nitrogen,[18−25] which alter the surface charge density and Lewis basicity. Heteroatom doping can also result in structural changes in the carbon scaffold that impact its surface chemistry, such as increased defect and edge-plane exposure. Defect creation via nitrogen incorporation has, for instance, been shown to improve Li storage capacity,[26] and greater edge exposure is known to enhance charge transfer rates and catalytic activity.[24,27−32] Furthermore, nitrogenation offers a route for increasing the density of states, resulting in higher

Received: October 7, 2016
Revised: February 23, 2017
Published: March 13, 2017

DOI: 10.1021/acs.jpcc.6b10145
J. Phys. Chem. C 2017, 121, 6596−6604

capacitance, an effect that has been leveraged in the fabrication of supercapacitors.[33]

The effects of nitrogenation on bulk electronic properties, surface chemistry, and structural disorder in the carbon network are often interrelated, making it challenging to discern or predict the overall effect of nitrogenation on the electrochemical properties of carbon electrodes. Recent studies in the literature have successfully established structure−activity relationships for undoped carbon materials, resulting in useful insights on how to predict interfacial redox chemistry based on bulk electronic structure. This has been shown, for instance, in the case of materials with long-range order or high crystallinity, such as nanotubes, graphene, and graphite[34−41] However, less is known about carbon materials which lack long-range order despite them being widely used by the electrochemical community.

Optical characterization methods offer the possibility of discriminating between bulk and surface effects of nitrogenation. However, despite the obvious general interest and wide applications of nitrogen-doped electrodes, their electrochemical properties have not yet been studied in relation to their bulk optoelectronic properties. In this work we present a combined optical and electrochemical characterization study of the interplay between the bulk optoelectronic properties and the electrochemical properties of nitrogenated amorphous carbon (a-C:N) thin film electrodes. Thin film electrodes have recently enabled the study of electrode properties of nitrogenated carbons,[42−45] independently from potentially confounding variables that might affect studies at particle/ink electrodes, such as porosity, packing, binders, and metal impurities. Nitrogenated amorphous carbon (a-C:N) films were synthesized with varying nitrogen content via dc magnetron sputtering. Carbon materials were characterized using a combination of optical and electrochemical techniques, including spectroscopic ellipsometry (SE), X-ray photoelectron spectroscopy (XPS), cyclic voltammetry (CV), and electrochemical impedance spectroscopy (EIS). Results indicated that low levels of nitrogenation produce a-C:N films with greater metallic character than non-nitrogenated materials (a-C), which translates into faster electron-transfer rates at the carbon−electrolyte interface. High levels of nitrogen incorporation, on the other hand, result in films with characteristics more typical of cluster aggregates than amorphous solids. Electrochemical studies on these materials using both outer-sphere and surface-sensitive redox probes allow for the discrimination of electronic and surface effects resulting from nitrogen incorporation

EXPERIMENTAL METHODS

Materials. Hexaammine ruthenium(II) chloride (99.9%, trace metals), hexaammine ruthenium(III) chloride (98%), potassium chloride (Bioxtra, > 99.0%), sulfuric acid (95−97%), hydrogen peroxide (>30% w/v), potassium ferrocyanide (Analar, >99.0%), and methanol (semiconductor grade) were used without further purification.

Substrate Preparation. B-doped silicon wafers (Micro-Chemicals; resistivity 5−10 Ω-cm) were used as substrates for carbon deposition; substrates were cleaned with piranha solution (3:1 H_2SO_4:H_2O_2. ***CAUTION:*** *Piranha solution is a strong oxidant which may react explosively with organic solvents—always use in a fumehood*) before rinsing with Millipore water and drying under Ar. Glassy carbon (GC) discs (HTW Sigradur radius 0.25 ± 0.05 cm) were polished with progressively finer grades of alumina slurry (Buehler). Discs were first polished using 1200 grit sandpaper and 1 μm slurry. After rinsing with copious Millipore water the discs were polished on nylon paper (Buehler) using 1 μm slurry, sonicated for 20 min in Millipore water, and then polished on nylon paper using 0.3 μm slurry. Polishing MicroCloths (Buehler) with 0.3 μm slurry were used for the penultimate step before once again sonicating for 20 min in Millipore water. The final polishing step was 0.05 μm slurry on a fresh microcloth before sonicating the polished discs in Millipore water for 20 min. Clean discs were either used directly in electrochemical experiments or, in the case of a-C and a-C:N depositions, mounted in a custom-made Teflon holder and placed in the vacuum chamber for coating via magnetron sputtering.

Deposition of Carbon Electrode Materials. Thin film electrodes of amorphous carbon (a-C) and nitrogenated amorphous carbon (a-C:N) were deposited via dc magnetron sputtering in a chamber (Torr International Inc.) with a base pressure $\leq 2 \times 10^{-6}$ mbar and a deposition pressure in the range $(2-7) \times 10^{-3}$ mbar. Films with varying nitrogen percentages were prepared by introducing a nitrogen (N4.5, BOC) and argon (N4.8, BOC) gas mixture into the sputtering chamber using two mass flow controllers (Brooks Instruments). The total gas flow rate was kept at 50 mL min^{-1}, while the mixing ratio was varied to alter the nitrogen content in the films; deposition time was kept constant at 40 min for all samples, resulting in smooth films (see Supporting Information) as previously reported.[46]

Characterization. Ellipsometry measurements were taken using an alpha-SETM Ellipsometer (J.A. Woolam Co.). The films were deposited on Si wafers and measured at 65°, 70°, and 75° incidence; data were fitted using a 3-layer model which takes into account the substrate, the a-C/a-C:N layer, and the air phase, as previously reported.[47] Electrochemical measurements were carried out using a Metrohm Autolab AUT50324 potentiostat with a frequency response analyzer (FRA) module using a 3-electrode setup. A static disc holder (Pine Instruments) enclosing the a-C/a-C:N sputtered GC disc was used as working electrode (WE, see Supporting Information); a Hydroflex hydrogen electrode (Gaskatel) and a Pt wire were used as reference and counter electrodes, respectively. The electrochemical cell consisted of a beaker with a custom-made Teflon cap. Prior to experiments the cell was cleaned with piranha followed by rinsing 3 times with Millipore water. Cyclic voltammograms (CVs) in aqueous solutions of 1 mM $Ru(NH_3)_6Cl_3$/$Ru(NH_3)_6Cl_2$ or 1 mM ferrocyanide in deaerated 0.1 M KCl at 25 °C were obtained by scanning ±0.3 V around the formal potential, $E^{0\prime}$, at a scan rate of 50 mV/s; all voltammograms were taken with *iR* compensation using NOVA software. EIS spectra were obtained at $E^{0\prime}$ for both redox couples using 100 scans in the frequency range from 100 kHz to 0.1 Hz using an ac amplitude of 8 mV. The resulting spectra were fitted with equivalent circuit models using commercial software (ZView). The geometric area of each disc was determined using calipers and verified via cyclic voltammetry experiments at various scan rates using the Randles−Sevcik equation (see Supporting Information).

In the case of a-C films, X-ray photoelectron spectroscopy (XPS) characterization was performed at 1×10^{-10} mbar base pressure in an ultrahigh-vacuum system (Omicron). The X-ray source was a monochromatized Al Kα source (1486.6 eV). Spectra were recorded at 45° takeoff angle with an analyzer resolution of 0.5 eV. In the case of a-C:N films XPS characterization was performed on a VG Scientific ESCAlab

DOI: 10.1021/acs.jpcc.6b10145
J. Phys. Chem. C 2017, 121, 6596−6604

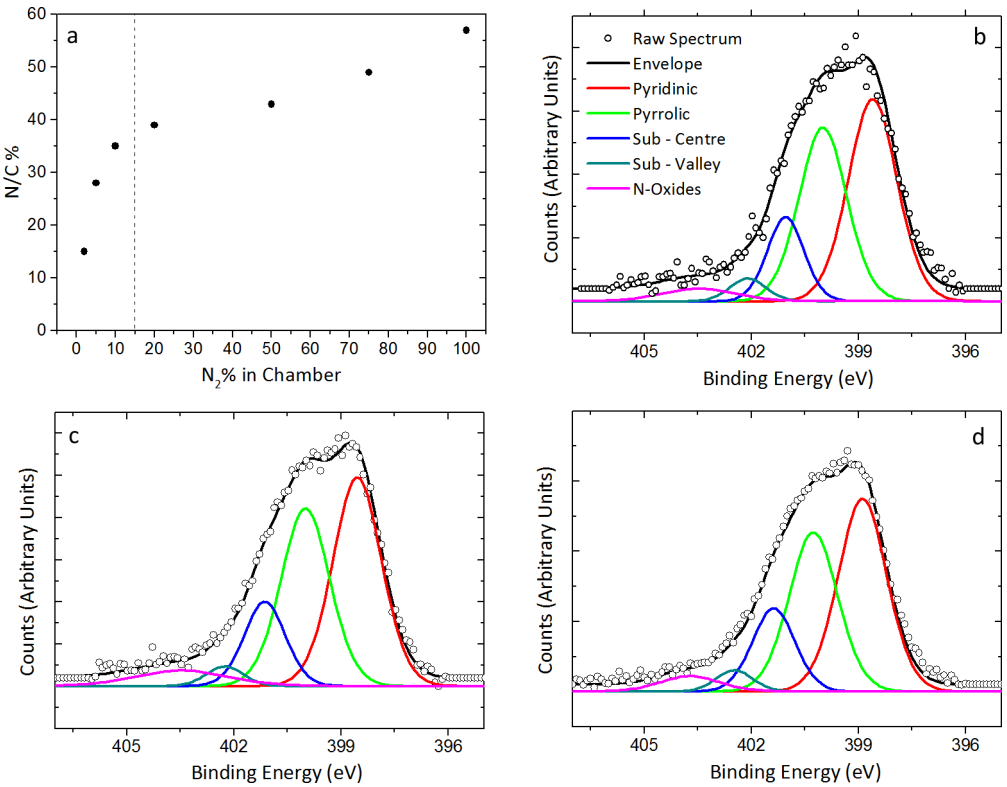

Figure 1. (a) N/C% versus N_2% in the deposition gas. Dotted line delineates the two regimes of nitrogen incorporation. Deconvoluted N 1s XPS spectra for a-C:N-2% (b), a-C:N-5% (c), and a-C:N-10% (d). Raw spectra are shown after Shirley background subtraction and offset for clarity.

Mk II system (<2 × 10^{-8} mbar) using Al Kα X-rays (1486.6 eV); core-level spectra were collected with an analyzer pass energy of 20 eV. Charge compensation, where applicable, was achieved using an electron flood gun, and the binding energy scale was referenced to the C 1s core level at 284.8 eV. Spectra were baseline corrected using a Shirley background and fitted with Voigt functions using commercial software (CasaXPS); atomic percent compositions were determined by calculating peak area ratios after correction by relative sensitivity factors (C 1s = 1.0, N 1s = 1.8, O 1s = 2.93).

RESULTS AND DISCUSSION

Nitrogen-incorporated amorphous carbon (a-C:N) films were synthesized with different levels of nitrogen incorporation by varying the N_2/Ar ratio of the deposition gas; films are denoted as a-C:N-*X*%, where *X* is the percentage of N_2 out of a total flux of 50 sccm N_2/Ar. XPS survey scans of all a-C:N films show characteristic C 1s, O 1s, and N 1s peaks at 284, 532, and 400 eV, respectively. In the absence of N_2 in the deposition gas, non-nitrogenated amorphous carbon (a-C) was prepared, as confirmed by the absence of N 1s peaks in the survey spectra and by the shape of the C 1s envelope (Supporting Information). Figure 1a and Table 1 show the changes in N/C% determined via XPS, observed when changing the N_2% composition in the deposition gas. The plot suggests the presence of two different regimes of nitrogen incorporation. For low N_2 content in the deposition gas (N_2 < 15%) nitrogen atoms are incorporated rapidly into the carbon material; however, the rate of incorporation slows considerably for higher N_2%, in agreement with previous reports by other groups.[48−50] The elevated N/C% values obtained in the slow deposition regime (N_2 > 15%) suggest that films deposited under such conditions contain N−N bonds and/or incorporate nitrogen gas within their structure.[50−52]

Table 1. Surface Composition of a-C and a-C:N-*X*% Samples Obtained from XPS Spectra

			$N_{component}$/C%			
N_2 gas %	N/C%	O/C%	N_{pyri}%	N_{pyrr}%	N_{sub}%	N_{ox}%
0%	0	8	0	0	0	0
2%	15	10	6	5	3	1
5%	28	8	12	10	5	2
10%	35	5	16	12	6	1
20%	39	6	17	13	8	1
50%	43	5	18	13	10	2
75%	49	10	21	15	11	2
100%	57	9	24	18	12	3

Figure 1b, 1c, and 1d shows the N 1s spectra of a-C:N-2%, -5%, and -10%, respectively; similar N 1s envelopes were obtained for a-C:N films deposited with N_2 > 10% (Supporting Information). The broad peak envelope indicates the presence of multiple types of N sites. The N 1s peaks were fitted using five contributions assigned to pyridinic-N (398.2−398.8 eV), pyrrolic-N (400−400.6 eV), substitutional-N (400.8−402.6 eV), and N−O/N−N (403−406 eV). The substitutional-N contribution was further separated into contributions from center- (400.8−401.5 eV) and valley-type (402.1−402.8) N sites.[52,53] As noted by several authors, contributions above 403 eV may also possibly be attributed to the presence of $\pi-\pi^*$ satellites.[29,54] These satellites may contribute to our spectra; however, they would be convoluted with N−O and N−N contributions. Pyridinic-N and pyrrolic-N sites were found to dominate the N 1s spectra; the relative contribution of each type of N site to the total surface nitrogen content is reported

DOI: 10.1021/acs.jpcc.6b10145
J. Phys. Chem. C 2017, 121, 6596−6604

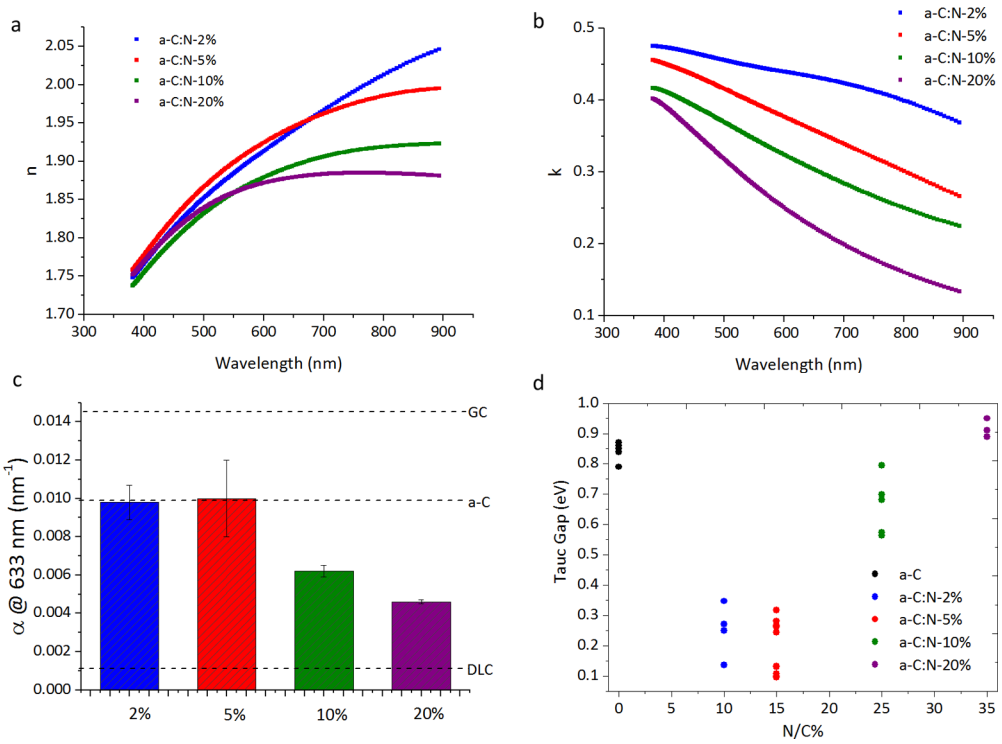

Figure 2. (a) Plots of index of refraction (n) derived from SE measurements of a-C:N-2−20% versus wavelength (nm). (b) Plots of extinction coefficient (k) versus wavelength for a-C:N-2−20%. (c) Bar plot of the absorption coefficient, α, at 633 nm for a-C:N-2−20%. Dotted lines refer to a-C films prepared by our group, reported GC absorptivity,[55] and sp^3-rich DLC films characterized by Mednikarov et al.[56] (d) Cluster plot of Tauc gaps of a-C:N-2−20% versus N/C%. Tauc gaps of a-C films (with N/C% = 0) prepared and previously characterized by the group are also presented for comparison.

in the Supporting Information. The C 1s spectra obtained for the same films also show an increasingly broad envelope with increasing nitrogen content in agreement with the presence of a range of C−N functional group contributions (Supporting Information). However, the strong spectral overlap observed above 285 eV prevents unambiguous fitting of individual contributions to the C 1s peak.[29]

The bulk optoelectronic properties of a-C:N materials were investigated via spectroscopic ellipsometry. Figure 2a and 2b shows representative plots of the optical constants, n and k, for a-C:N-2−20% vs wavelength in the 400−900 nm range. The real part of the refractive index, n, was found to be similar for all samples, while the trend in the imaginary component, k, indicates that the absorptivity of the films in the visible range decreases with increasing levels of N incorporation. Figure 2c shows a comparison of the absorption coefficient α at 633 nm, calculated as $\alpha = (4\pi k)/\lambda$, for a-C:N-2−20%; values obtained for non-nitrogenated films and literature values for GC[55] and diamond-like carbon (DLC)[56] are also reported as a comparison. Low levels of nitrogen incorporation (2−5%) produce films with absorptivity similar to or slightly greater than that of undoped a-C, while for higher levels of nitrogenation (10−20%) the absorptivity decreases significantly. Absorption coefficients as a function of photon energy were used to calculate Tauc plots from which the optical Tauc gap values (E_T) were obtained, as shown in the Supporting Information. Figure 2d reports E_T values as a function of N/C% content in the carbon material; the results show that a-C:N films prepared with low levels (2−5%) of N incorporation have the narrowest optical gaps, while at higher nitrogen incorporation (a-C:N-10−20%) the optical gap increases. This is consistent with previous reports indicating that low levels of N incorporation raise the Fermi level of the material and lower its optical band gap[22,57] relative to non-nitrogenated carbons. On the basis of our results, this effect is observed only for low levels of nitrogen incorporation, while carbons with N/C% > 15% display greater semiconductive character.

Above a-C:N-20% the optical properties of the resulting films significantly depart from those obtained at lower N_2% values. Figure 3 shows plots of the imaginary component of the refractive index versus wavelength for a-C:N samples deposited at high N_2% in the deposition mixture. For these films, the k values do not vary smoothly and monotonously as expected of amorphous solids but display broad peak-like features. These broad peaks suggest the presence of disordered conjugated

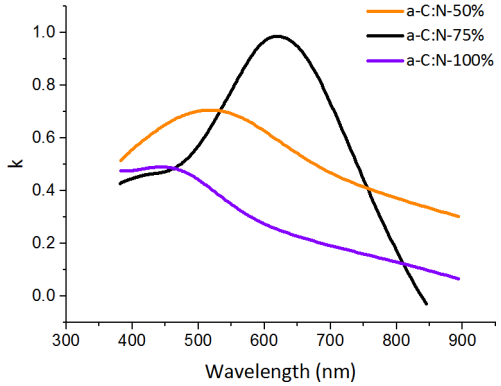

Figure 3. Extinction coefficient (k) versus wavelength for a-C:N-50%, -75%, and -100% derived from ellipsometry measurements.

DOI: 10.1021/acs.jpcc.6b10145
J. Phys. Chem. C 2017, 121, 6596−6604

clusters in these a-C:N films: formation of relatively small, poorly connected graphitic clusters with localized electron density is expected to result in "molecule-like" optical transitions such as those observed for a-C:N-50−100%. Our results are also consistent with work by Rodil et al., who proposed that the increase in E_T values usually observed with increasing N/C% content can be attributed to increased localization of π-electrons.[58]

Electrochemical Characterization of a-C and a-C:N Films. Cyclic voltammetry and electrochemical impedance measurements were carried out to study the effects of nitrogen incorporation on the electron-transfer properties of a-C materials. The $Ru(NH_3)_6^{+2/+3}$ redox couple was first chosen as an electrochemical probe. This complex is an "outer-sphere" redox species which is relatively insensitive to surface chemistry[59] but whose rate of charge transfer is controlled by the electronic properties of the electrode, such as Fermi level position (E_F), and density of states (DOS) near E_F.

Figure 4 shows CVs obtained for a-C:N-X% electrodes in 1 mM $Ru(NH_3)_6^{+2/+3}$ with 0.1 M KCl. The figure indicates that

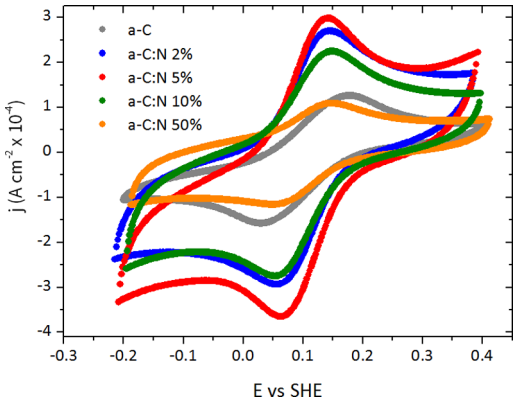

Figure 4. Cyclic voltammograms of selected a-C:N films in solutions of 1 mM $Ru(NH_3)_6^{+2/+3}$ in 0.1 M KCl.

low levels of nitrogen incorporation result in electrodes with the smallest peak-to-peak separation (ΔE_p) and the highest capacitance-corrected peak current density values (~3×10^{-4} A cm^{-2}). ΔE_p values of 70−80 mV obtained for a-C:N-2−5% at 50 mV s^{-1} (Table 2) are close to the reversible limit of 59 mV for a one-electron process, indicating that electron transfer is fast for low levels of nitrogenation. Since each experiment was carried out with the same concentration of $Ru(NH_3)_6^{+2/+3}$, differences in peak current density for different films may possibly be explained by changes in the electroactive area of the sputtered electrodes; this is also consistent with the observed drop in the capacitive contribution to the current for a-C:N-50%. The decrease in peak current density occurs in the absence of a significant change in ΔE_p. This suggests that the electrodes at high N/C content are better described as heterogeneous partially blocked electrodes, which have been shown to display similar behavior in their voltammetric response, depending on microdomain size and distribution.[60]

Table 2. Peak Current Density Ratios and Peak Potential Separations for Nitrogenated and Non-Nitrogenated Carbon Electrodes Obtained at 50 mV s^{-1} in 1 mM $Ru(NH_3)_6^{+2/+3}$ and 0.1 M KCl[a]

sample	J_{pc}/J_{pa}	ΔE_p (V)
a-C	0.9 ± 0.2	0.15 ± 0.02
a-C:N-2%	0.9 ± 0.1	0.08 ± 0.01
a-C:N-5%	0.91 ± 0.06	0.074 ± 0.007
a-C:N-10%	0.93 ± 0.09	0.09 ± 0.01
a-C:N-50%	1.0 ± 0.1	0.095 ± 0.002

[a]Errors indicate 95% confidence interval.

In all cases the ratio of cathodic to anodic peak current densities ($J_{p,c}/J_{p,a}$) is >0.9 which is close to the theoretical value of 1 for an electrochemically reversible process. Non-nitrogenated a-C yielded a significantly larger ΔE of ~150 mV (Table 2), therefore indicating that low levels of nitrogenation result in an enhancement of the electron-transfer rate. However, as the N_2% increases in the deposition mixture, this trend reverses, and for a-C:N-50%, the peak separation increases to almost 100 mV. This increase is accompanied by a decrease in peak current density to a value comparable to that of a-C. Finally, a-C:N-X% films with X = 75 and 100 were found to be too resistive for electrochemical measurements.

In order to quantitatively compare the electron-transfer properties of our films, electrochemical impedance spectroscopy (EIS) was used to determine the resistance to charge transfer (R_{CT}) at the formal potential ($E^{0\prime}$) of the ruthenium redox couple. Representative Nyquist plots for a-C:N electrodes in 1 mM $Ru(NH_3)_6^{+2/+3}$ with 0.1 M KCl are shown in Figure 5a together with the plot obtained for a-C under the same conditions (see also Supporting Information). Typical features of a mixed kinetic−diffusion process are evident in all complex spectra: a semicircle at high frequency (10^5−10^3 Hz) suggests the presence of an impedance to charge transfer (R_{CT})

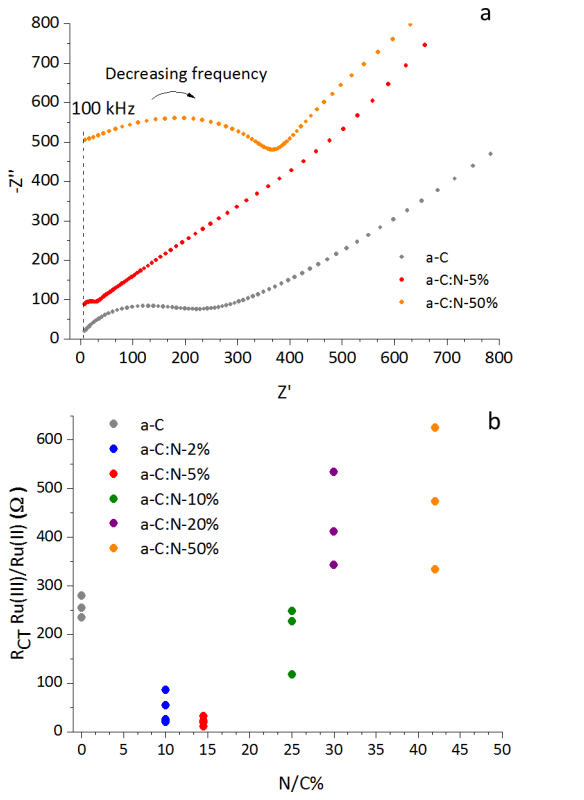

Figure 5. (a) High-frequency Nyquist plots for a-C and selected examples of a-C:N-X% in 1 mM $Ru(NH_3)_6^{+2/+3}$ with 0.1 M KCl. (b) Plot of R_{CT} versus N/C% for the ruthenium redox couple. Legends refer to the N_2/Ar% in the deposition gas during sputtering.

DOI: 10.1021/acs.jpcc.6b10145
J. Phys. Chem. C 2017, 121, 6596−6604

in parallel with a capacitive contribution, while at low frequencies (10^3–10^{-1} Hz) a linear behavior with ~45° slope indicates that the impedance is dominated by mass transport-limited diffusion. EIS spectra for a-C and a-C:N-2–50% in $Ru(NH_3)_6^{+2/+3}$ were fitted using a Randles circuit (Supporting Information); the resulting R_{CT} values are plotted vs N/C% content in Figure 5b; all parameters derived from the fitting procedure and calculated heterogeneous rate constants are reported in the Supporting Information. Nitrogenated electrodes a-C:N-2–5% yielded lower R_{CT} values than non-nitrogenated a-C; the values for a-C:N-10% are comparable to those of a-C, whereas those for a-C:N-20% or higher increase progressively. This trend in R_{CT} values agrees with ΔE and peak-current density values obtained from CV measurements and suggest that small nitrogen concentrations lead to an enhancement of charge transfer rates, whereas high levels of nitrogen incorporation negatively affect electrochemical performance. Interestingly, R_{CT} values closely parallel E_T vs N/C % trends determined via ellipsometry; in fact, R_{CT} and E_T appear to be positively correlated (R = 0.9458) (Supporting Information). a-C:N electrodes with the lowest ΔE_p values and largest peak current densities are the a-C:N films with the greatest metallic character, based on E_T determinations. Furthermore, the collapse in peak current density for a-C:N-50% correlates well with the appearance of broad absorption peaks in the imaginary refractive index which are suggestive of greater electronic localization. For both regimes of N incorporation there is therefore a strong correlation between the bulk optoelectronic properties and the electron-transfer properties of the films using the $Ru(NH_3)_6^{+2/+3}$ redox probe.

Electrochemical Characterization Using $Fe(CN)_6^{-4/-3}$. Redox couples such as $Ru(NH_3)_6^{+2/+3}$ are in the minority with regard to their relative insensitivity to surface termination in electron-transfer processes. In order to understand the effect of nitrogen incorporation on the surface chemistry of carbon electrodes we carried out CV and EIS measurements of a-C and a-C:N-X% in aqueous solutions of $Fe(CN)_6^{-4/-3}$, a redox probe that is known to be sensitive to surface functionalities (e.g., passive layers and charged groups).[59]

Figure 6 shows CVs of carbon electrodes in 1 mM $Fe(CN)_6^{-4}$ and 0.1 M KCl for a-C and a-C:N-2–10%. As shown in the figure, the ΔE_p for a-C and a-C:N-2% is approximately 80 mV, while ΔE_p for a-C:N-5% is slightly higher at 100 mV. The $J_{p,c}/J_{p,a}$ (Table 3) is close to 1 for all of these films, indicating that the redox process is reversible for

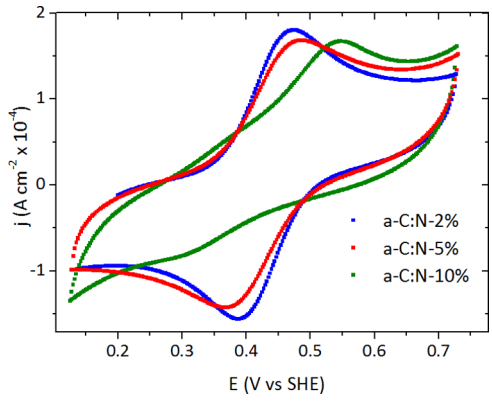

Figure 6. Cyclic voltammograms of 1 mM $Fe(CN)_6^{-4/-3}$ in 0.1 M KCl, obtained at 50 mV s^{-1} for a-C and a-C:N-2–10%.

Table 3. Peak Current Density Ratio ($J_{p,c}/J_{p,a}$) and ΔE_p Values for a-C and a-C:N-2–10% Obtained in 1 mM $Fe(CN)_6^{-4/-3}$ with 0.1 M KCl at 50 mV s^{-1}

sample	J_{pc}/J_{pa}	ΔE_p (V)
a-C	0.95 ± 0.05	0.08 ± 0.03
a-C:N-2%	0.8 ± 0.1	0.08 ± 0.02
a-C:N-5%	0.9 ± 0.1	0.1 ± 0.05
a-C:N-10%	0	

both a-C and a-C:N-2–5% in the case of the $Fe(CN)_6^{-4/-3}$ couple. In the case of a-C:N-10% the anodic peak, $E_{p,a}$ is shifted more than 100 mV in the positive direction and the cathodic peak $E_{p,c}$ is greatly reduced. This indicates that charge transfer is irreversible for $Fe(CN)_6^{-4/-3}$ on a-C:N-10%.

Nyquist plots for a-C and a-C:N films in 1 mM $Fe(CN)_6^{-4}$ in 0.1 M KCl are shown in Figure 7. Similar to the results for the

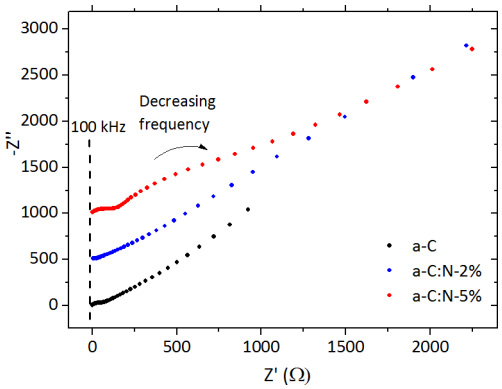

Figure 7. Nyquist plots of 1 mM $Fe(CN)_6^{-4/-3}$ in 0.1 M KCl obtained for a-C and a-C:N-2–5%.

$Ru(NH_3)_6^{+2/+3}$ couple, evidence of a mixed kinetic–diffusion-controlled electron-transfer process can be seen for a-C and a-C:N-2–5%. Due to the irreversibility of a-C:N-10% determined via CV studies, EIS experiments were not attempted on this substrate. For both a-C and a-C:N-2% the semicircle in the high-frequency (10^5–10^3 Hz) region indicates that the impedance to charge transfer is low for both a-C and a-C:N-2% with similar magnitudes of R_{CT}. The linear behavior of the plots in the low-frequency region (10^3–10^{-1} Hz) of the figure indicates that ferrocyanide oxidation may proceed rapidly enough to be diffusion-rate limited on both surfaces. In the case of a-C:N-5%, the broad semicircle in the region from 10^2 to 1 Hz a-C:N-5% plot corresponds to Randles behavior with a larger contribution of R_{CT} to the impedance. This is in agreement with CV data for a-C:N-5%, which indicate that ΔE_p values for charge transfer to ferrocyanide are slightly larger in the case of a-C:N-5%. The high-frequency region of the impedance plot for a-C:N-5% indicates the appearance of a smaller RC component, which is present even in the absence of any redox-active species (i.e., in supporting electrolyte, 0.1 M KCl; Supporting Information). This contribution has previously been observed in the EIS of amorphous carbon materials[61,62] and might be attributed to defects likely to occur in noncrystalline materials, including nanoporosity and midgap or surface states.[63–65]

Both voltammetric and impedance experiments indicate that nitrogen incorporation into amorphous carbon electrodes results in surfaces which are progressively less amenable to

DOI: 10.1021/acs.jpcc.6b10145
J. Phys. Chem. C 2017, 121, 6596–6604

charge transfer to the $Fe(CN)_6^{-4/-3}$ redox couple. The increase in ΔE_p and R_{CT} from a-C to a-C:N-5% and the irreversibility of charge transfer to a-C:N-10% contrasts with the results for $Ru(NH_3)_6^{+2+3}$, which showed lower ΔE_p and R_{CT} values following nitrogenation and quasi-reversible behavior for all a-C:N films studied.

Given that the bulk optoelectronic properties of a-C:N-2–10% are known to be more metallic in nature than undoped a-C, this contrasting behavior is likely to be explained by surface effects on the kinetics of electron transfer. There is evidence that charge transfer to ferrocyanide is catalyzed by the supporting electrolyte, which facilitates the redox process via formation of cationic bridging complexes.[66−69] The availability of specific surface sites is also known to be important in determining the rate of charge transfer of $Fe(CN)_6^{-4/-3}$ at carbon electrodes.[70,71] A recent study by Compton and co-workers[66] showed that ferrocyanide oxidation at graphite electrodes could be rendered almost entirely irreversible by pretreating the carbon surface with organic solvents such as acetonitrile. Their study concluded that the inhibitory effects of the organic solvent were due to blocking of the active edge sites which in turn prevent the cation bridging required for electron transfer to occur. We propose that the incorporation of nitrogen moieties into the carbon matrix of our films may produce a similar inhibitory effect which is intrinsic to the surface. This result is significant as it underscores the fact that while the incorporation of nitrogen into the carbon matrix may result in improved bulk electronic properties that typically enhance rates of charge transfer (lower E_T, greater metallic character), it also results in surface nitrogenation that significantly changes interfacial interactions with redox species. While nitrogenation is often associated with improved catalytic properties, as is, for instance, the case in oxygen reduction, nitrogenation can also result in more sluggish kinetics and an overall inhibitory effect as in the case of charge transfer to the ferrocyanide complex.

CONCLUSIONS

We prepared nitrogenated amorphous carbon films with varying N/C% and characterized them using a combination of optical and electrochemical methods. Our results indicate that low levels of nitrogenation produce films with greater metallic character when compared to non-nitrogenated amorphous carbon. These films also display the fastest electron-transfer kinetics for the ruthenium hexaammine redox couple as measured by a combination of cyclic voltammetry and impedance spectroscopy. We have demonstrated that the resistance to electron transfer, $R_{CT,}$ is strongly correlated to the Tauc gap, E_T, in what we believe is the first demonstration of a clear correlation between optoelectronic and electrochemical properties in nitrogenated carbon materials.

Highly nitrogenated amorphous carbon films display properties more consistent with localized and poorly connected arrays of graphitic clusters rather than amorphous solids. These properties were observed both optically, through ellipsometric measurements, and electrochemically based on the inferior electron-transfer properties of these materials relative to a-C:N films with lower levels of nitrogenation. An important implication of these results is that ellipsometry emerges as an effective method for evaluation of defects in carbon electrodes that result from nitrogenation and that the defectiveness evidenced via ellipsometry is straightforwardly reflected in the electrochemical performance.

It is interesting to note the remarkable difference observed in trends of charge transfer rates obtained when using an outer-sphere redox couple ($Ru(NH_3)_6^{+2/+3}$) vs the surface-sensitive $Fe(CN)_6^{-4/-3}$ couple. Introduction of nitrogenated sites facilitates charge transfer in the case of the outer-sphere species, in agreement with an expected increase in charge carriers and metallic character that typically arises from nitrogen doping of carbon materials. The opposite trend is observed for the inner-sphere couple, thus indicating that nitrogenation has a profound effect on the surface chemistry and that these effects might dominate the overall electrochemical response of the nitrogenated carbon. The combined effect of bulk optoelectronic changes and surface modifications that result from nitrogenation strongly depends on the specific redox species in solution. Our results suggest that theoretical predictions of charge transfer rates for ruthenium hexamine based on bulk electronic structure are likely to be accurate at nitrogenated carbons. However, specific models that describe interfacial interactions are required to predict the behavior and trends of inner-sphere redox species at nitrogenated surfaces. Finally, this study offers clear evidence of the need for both outer- and inner-sphere redox couples to understand the origin of changes in the overall electrochemical response arising from nitrogenation of carbon electrodes.

ASSOCIATED CONTENT

Supporting Information

The Supporting Information is available free of charge on the ACS Publications website at DOI: 10.1021/acs.jpcc.6b10145.

Pictures of the working electrode arrangement, supplemetary XPS results, Tauc plots, Randles–Sevcik analysis, Bode plots, EIS fitting models and parameters, heterogeneous rate constant values, and SEM images of a-C and a-C:N films (PDF)

AUTHOR INFORMATION

Corresponding Author

*E-mail: colavitp@tcd.ie.

ORCID

Paula E. Colavita: 0000-0003-1008-2874

Notes

The authors declare no competing financial interest.

ACKNOWLEDGMENTS

This publication emanated from research conducted with the financial support of Science Foundation Ireland (SFI) Grant No. 13/CDA/2213. F.Z. acknowledges support from SFI Grant No. 12/IP/1273; J.A.B. acknowledges support from the Irish Research Council through Grant No. GOIPG/2014/399; L.E.T. acknowledges support from SFI Grant No. 12/RC/2278. Use of the XPS instrument of I. V. Shvets and C. McGuinness was provided under SFI Equipment Infrastructure Funds.

REFERENCES

(1) Robertson, J.; Davis, C. A. Nitrogen Doping of Tetrahedral Amorphous-Carbon. *Diamond Relat. Mater.* **1995**, *4*, 441–444.

(2) In *Properties of Amorphous Carbon*, 1st ed.; Silva, S. R. P., Ed.; INSPEC, Inc., The Institution of Electrical Engineers: London, 2003.

(3) Yoo, K.; Miller, B.; Kalish, R.; Shi, X. Electrodes of Nitrogen-Incorporated Tetrahedral Amorphous Carbon a Novel Thin-Film Electrocatalytic Material with Diamond-Like Stability. *Electrochem. Solid-State Lett.* **1999**, *2*, 233−235.
(4) Kamata, T.; Kato, D.; Hirono, S.; Niwa, O. Structure and Electrochemical Performance of Nitrogen-Doped Carbon Film Formed by Electron Cyclotron Resonance Sputtering. *Anal. Chem.* **2013**, *85*, 9845−9851.
(5) Yang, X.; Haubold, L.; DeVivo, G.; Swain, G. M. Electroanalytical Performance of Nitrogen-Containing Tetrahedral Amorphous Carbon Thin-Film Electrodes. *Anal. Chem.* **2012**, *84*, 6240−6248.
(6) Perini, L.; Durante, C.; Favaro, M.; Agnoli, S.; Granozzi, G.; Gennaro, A. Electrocatalysis at Palladium Nanoparticles: Effect of the Support Nitrogen Doping on the Catalytic Activation of Carbon-Halogen Bond. *Appl. Catal., B* **2014**, *144*, 300−307.
(7) Zhou, Y.; Neyerlin, K.; Olson, T. S.; Pylypenko, S.; Bult, J.; Dinh, H. N.; Gennett, T.; Shao, Z.; O'Hayre, R. Enhancement of Pt and Pt-Alloy Fuel Cell Catalyst Activity and Durability Via Nitrogen-Modified Carbon Supports. *Energy Environ. Sci.* **2010**, *3*, 1437−1446.
(8) Zeng, A.; Bilek, M. M. M.; McKenzie, D. R.; Lay, P. A.; La Fontaine, A.; Keast, V. J. Correlation between Film Structures and Potential Limits for Hydrogen and Oxygen Evolutions at a-C:N Film Electrochemical Electrodes. *Carbon* **2008**, *46*, 663−670.
(9) Brocenschi, R. F.; Rocha-Filho, R. C.; Li, L. L.; Swain, G. M. Comparative Electrochemical Response of Estrone at Glassy-Carbon, Nitrogen-Containing Tetrahedral Amorphous Carbon and Boron-Doped Diamond Thin-Film Electrodes. *J. Electroanal. Chem.* **2014**, *712*, 207−214.
(10) Sopchak, D.; Miller, B.; Kalish, R.; Avyigal, Y.; Shi, X. Dopamine and Ascorbate Analysis at Hydrodynamic Electrodes of Boron Doped Diamond and Nitrogen Incorporated Tetrahedral Amorphous Carbon. *Electroanalysis* **2002**, *14*, 473−478.
(11) Medeiros, R. A.; Matos, R.; Benchikh, A.; Saidani, B.; Debiemme-Chouvy, C.; Deslouis, C.; Rocha-Filho, R. C.; Fatibello-Filho, O. Amorphous Carbon Nitride as an Alternative Electrode Material in Electroanalysis: Simultaneous Determination of Dopamine and Ascorbic Acid. *Anal. Chim. Acta* **2013**, *797*, 30−39.
(12) Gai, P.; Zhang, H.; Zhang, Y.; Liu, W.; Zhu, G.; Zhang, X.; Chen, J. Simultaneous Electrochemical Detection of Ascorbic Acid, Dopamine and Uric Acid Based on Nitrogen Doped Porous Carbon Nanopolyhedra. *J. Mater. Chem. B* **2013**, *1*, 2742−2749.
(13) Fellinger, T.-P.; Hasché, F.; Strasser, P.; Antonietti, M. Mesoporous Nitrogen-Doped Carbon for the Electrocatalytic Synthesis of Hydrogen Peroxide. *J. Am. Chem. Soc.* **2012**, *134*, 4072−4075.
(14) Perazzolo, V.; Durante, C.; Pilot, R.; Paduano, A.; Zheng, J.; Rizzi, G. A.; Martucci, A.; Granozzi, G.; Gennaro, A. Nitrogen and Sulfur Doped Mesoporous Carbon as Metal-Free Electrocatalysts for the in Situ Production of Hydrogen Peroxide. *Carbon* **2015**, *95*, 949−963.
(15) Zhang, J.; Xia, Z.; Dai, L. Carbon-Based Electrocatalysts for Advanced Energy Conversion and Storage. *Sci. Adv.* **2015**, *1*, e1500564.
(16) Mamtani, K.; Ozkan, U. S. Heteroatom-Doped Carbon Nanostructures as Oxygen Reduction Reaction Catalysts in Acidic Media: An Overview. *Catal. Lett.* **2015**, *145*, 436−450.
(17) Ge, X.; Sumboja, A.; Wuu, D.; An, T.; Li, B.; Goh, F. W. T.; Hor, T. S. A.; Zong, Y.; Liu, Z. Oxygen Reduction in Alkaline Media: From Mechanisms to Recent Advances of Catalysts. *ACS Catal.* **2015**, *5*, 4643−4667.
(18) Wang, D.-W.; Su, D. Heterogeneous Nanocarbon Materials for Oxygen Reduction Reaction. *Energy Environ. Sci.* **2014**, *7*, 576−591.
(19) Ikeda, T.; Hou, Z.; Chai, G.-L.; Terakura, K. Possible Oxygen Reduction Reactions for Graphene Edges from First Principles. *J. Phys. Chem. C* **2014**, *118*, 17616−17625.
(20) Bao, X.; Nie, X.; von Deak, D.; Biddinger, E. J.; Luo, W.; Asthagiri, A.; Ozkan, U. S.; Hadad, C. M. A First-Principles Study of the Role of Quaternary-N Doping on the Oxygen Reduction Reaction Activity and Selectivity of Graphene Edge Sites. *Top. Catal.* **2013**, *56*, 1623−1633.
(21) Yasuda, S.; Yu, L.; Kim, J.; Murakoshi, K. Selective Nitrogen Doping in Graphene for Oxygen Reduction Reactions. *Chem. Commun.* **2013**, *49*, 9627−9629.
(22) Lai, L.; Potts, J. R.; Zhan, D.; Wang, L.; Poh, C. K.; Tang, C.; Gong, H.; Shen, Z.; Lin, J.; Ruoff, R. S. Exploration of the Active Center Structure of Nitrogen-Doped Graphene-Based Catalysts for Oxygen Reduction Reaction. *Energy Environ. Sci.* **2012**, *5*, 7936−7942.
(23) Guo, D.; Shibuya, R.; Akiba, C.; Saji, S.; Kondo, T.; Nakamura, J. Active Sites of Nitrogen-Doped Carbon Materials for Oxygen Reduction Reaction Clarified Using Model Catalysts. *Science* **2016**, *351*, 361−365.
(24) Ikeda, T.; Boero, M.; Huang, S.-F.; Terakura, K.; Oshima, M.; Ozaki, J.-i. Carbon Alloy Catalysts: Active Sites for Oxygen Reduction Reaction. *J. Phys. Chem. C* **2008**, *112*, 14706−14709.
(25) Favaro, M.; Perini, L.; Agnoli, S.; Durante, C.; Granozzi, G.; Gennaro, A. Electrochemical Behavior of N and Ar Implanted Highly Oriented Pyrolytic Graphite Substrates and Activity toward Oxygen Reduction Reaction. *Electrochim. Acta* **2013**, *88*, 477−487.
(26) Shin, W. H.; Jeong, H. M.; Kim, B. G.; Kang, J. K.; Choi, J. W. Nitrogen-Doped Multiwall Carbon Nanotubes for Lithium Storage with Extremely High Capacity. *Nano Lett.* **2012**, *12*, 2283−2288.
(27) Morcos, I.; Yeager, E. Kinetic Studies of the Oxygen—Peroxide Couple on Pyrolytic Graphite. *Electrochim. Acta* **1970**, *15*, 953−975.
(28) Stamatin, S. N.; Hussainova, I.; Ivanov, R.; Colavita, P. E. Quantifying Graphitic Edge Exposure in Graphene-Based Materials and Its Role in Oxygen Reduction Reactions. *ACS Catal.* **2016**, *6*, 5215−5221.
(29) Maldonado, S.; Morin, S.; Stevenson, K. J. Structure, Composition, and Chemical Reactivity of Carbon Nanotubes by Selective Nitrogen Doping. *Carbon* **2006**, *44*, 1429−1437.
(30) Deng, D.; Yu, L.; Pan, X.; Wang, S.; Chen, X.; Hu, P.; Sun, L.; Bao, X. Size Effect of Graphene on Electrocatalytic Activation of Oxygen. *Chem. Commun.* **2011**, *47*, 10016−10018.
(31) Jeon, I.-Y.; Choi, H.-J.; Jung, S.-M.; Seo, J.-M.; Kim, M.-J.; Dai, L.; Baek, J.-B. Large-Scale Production of Edge-Selectively Functionalized Graphene Nanoplatelets Via Ball Milling and Their Use as Metal-Free Electrocatalysts for Oxygen Reduction Reaction. *J. Am. Chem. Soc.* **2013**, *135*, 1386−1393.
(32) Chen, P.; Fryling, M. A.; McCreery, R. L. Electron Transfer Kinetics at Modified Carbon Electrode Surfaces: The Role of Specific Surface Sites. *Anal. Chem.* **1995**, *67*, 3115−3122.
(33) Chen, L.-F.; Zhang, X.-D.; Liang, H.-W.; Kong, M.; Guan, Q.-F.; Chen, P.; Wu, Z.-Y.; Yu, S.-H. Synthesis of Nitrogen-Doped Porous Carbon Nanofibers as an Efficient Electrode Material for Supercapacitors. *ACS Nano* **2012**, *6*, 7092−7102.
(34) Nair, N.; Kim, W.-J.; Usrey, M. L.; Strano, M. S. A Structure-Reactivity Relationship for Single Walled Carbon Nanotubes Reacting with 4-Hydroxybenzene Diazonium Salt. *J. Am. Chem. Soc.* **2007**, *129*, 3946−3954.
(35) Sharma, R.; Nair, N.; Strano, M. S. Structure-Reactivity Relationships for Graphene Nanoribbons. *J. Phys. Chem. C* **2009**, *113*, 14771−14777.
(36) Strano, M. S.; Dyke, C. A.; Usrey, M. L.; Barone, P. W.; Allen, M. J.; Shan, H.; Kittrell, C.; Hauge, R. H.; Tour, J. M.; Smalley, R. E. Electronic Structure Control of Single-Walled Carbon Nanotube Functionalization. *Science* **2003**, *301*, 1519−1522.
(37) Heller, I.; Kong, J.; Williams, K. A.; Dekker, C.; Lemay, S. G. Electrochemistry at Single-Walled Carbon Nanotubes: The Role of Band Structure and Quantum Capacitance. *J. Am. Chem. Soc.* **2006**, *128*, 7353−7359.
(38) Zhong, J.-H.; Zhang, J.; Jin, X.; Liu, J.-Y.; Li, Q.; Li, M.-H.; Cai, W.; Wu, D.-Y.; Zhan, D.; Ren, B. Quantitative Correlation between Defect Density and Heterogeneous Electron Transfer Rate of Single Layer Graphene. *J. Am. Chem. Soc.* **2014**, *136*, 16609−16617.
(39) Batchelor-McAuley, C.; Laborda, E.; Henstridge, M. C.; Nissim, R.; Compton, R. G. Reply to Comments Contained in "Are the Reactions of Quinones on Graphite Adiabatic?", by N.B. Luque, W. Schmickler [Electrochim. Acta XX (2012) YYY]. *Electrochim. Acta* **2013**, *88*, 895−898.

DOI: 10.1021/acs.jpcc.6b10145
J. Phys. Chem. C 2017, 121, 6596−6604

(40) Nissim, R.; Batchelor-McAuley, C.; Henstridge, M. C.; Compton, R. G. Electrode Kinetics at Carbon Electrodes and the Density of Electronic States. *Chem. Commun.* **2012**, *48*, 3294−3296.
(41) Unwin, P. R.; Güell, A. G.; Zhang, G. Nanoscale Electrochemistry of Sp2 Carbon Materials: From Graphite and Graphene to Carbon Nanotubes. *Acc. Chem. Res.* **2016**, *49*, 2041−2048.
(42) Cachet, H.; Deslouis, C.; Chouiki, M.; Saidani, B.; Conway, N. M. J.; Godet, C. Electrochemistry of Nitrogen-Incorporated Hydrogenated Amorphous Carbon Films. *J. Electrochem. Soc.* **2002**, *149*, E233−E241.
(43) Zeng, A. P.; Bilek, M. M. M.; McKenzie, D. R.; Lay, P. A. Correlation of Film Structure and Molecular Oxygen Reduction at Nitrogen Doped Amorphous Carbon Thin Film Electrochemical Electrodes. *Diamond Relat. Mater.* **2009**, *18*, 1102−1108.
(44) Chen, J.; Wang, X.; Cui, X.; Yang, G.; Zheng, W. Amorphous Carbon Enriched with Pyridinic Nitrogen as an Efficient Metal-Free Electrocatalyst for Oxygen Reduction Reaction. *Chem. Commun.* **2014**, *50*, 557−559.
(45) Chen, J. Y.; Wang, X.; Cui, X. Q.; Yang, G. M.; Zheng, W. T. One-Step Synthesis of N-Doped Amorphous Carbon at Relatively Low Temperature as Excellent Metal-Free Electrocatalyst for Oxygen Reduction. *Catal. Commun.* **2014**, *46*, 161−164.
(46) Cullen, R. J.; Jayasundara, D.; Soldi, L.; Cheng, J.; DuFaure, G.; Colavita, P. E. Spontaneous Grafting of Nitrophenyl Groups on Amorphous Carbon Thin Films: A Structure-Reactivity Investigation. *Chem. Mater.* **2012**, *24*, 1031−1040.
(47) Zen, F.; Angione, M. D.; Behan, J. A.; Cullen, R. J.; Duff, T.; Vasconcelos, J. M.; Scanlan, E. M.; Colavita, P. E. Modulation of Protein Fouling and Interfacial Properties at Carbon Surfaces Via Immobilization of Glycans Using Aryldiazonium Chemistry. *Sci. Rep.* **2016**, *6*, 24840.
(48) Alibart, F.; Durand Drouhin, O.; Debiemme-Chouvy, C.; Benlahsen, M. Relationship between the Structure and the Optical and Electrical Properties of Reactively Sputtered Carbon Nitride Films. *Solid State Commun.* **2008**, *145*, 392−396.
(49) Alibart, F.; Lejeune, M.; Zellama, K.; Benlahsen, M. Effect of Nitrogen on the Optoelectronic Properties of a Highly sp^2-Rich Amorphous Carbon Nitride Films. *Diamond Relat. Mater.* **2011**, *20*, 409−412.
(50) Hellgren, N.; Johansson, M. P.; Broitman, E.; Hultman, L.; Sundgren, J.-E. Role of Nitrogen in the Formation of Hard and Elastic CN_x Thin Films by Reactive Magnetron Sputtering. *Phys. Rev. B: Condens. Matter Mater. Phys.* **1999**, *59*, 5162−5169.
(51) Hellgren, N.; Johansson, M. P.; Broitman, E.; Sandström, P.; Hultman, L.; Sundgren, J.-E. Effect of Chemical Sputtering on the Growth and Structural Evolution of Magnetron Sputtered CNx Thin Films. *Thin Solid Films* **2001**, *382*, 146−152.
(52) Rodil, S. E.; Morrison, N. A.; Robertson, J.; Milne, W. I. Nitrogen Incorporation into Tetrahedral Hydrogenated Amorphous Carbon. *Phys. Status Solidi A* **1999**, *174*, 25−37.
(53) Sharifi, T.; Hu, G.; Jia, X.; Wågberg, T. Formation of Active Sites for Oxygen Reduction Reactions by Transformation of Nitrogen Functionalities in Nitrogen-Doped Carbon Nanotubes. *ACS Nano* **2012**, *6*, 8904−8912.
(54) Biniak, S.; Szymański, G.; Siedlewski, J.; Świątkowski, A. The Characterization of Activated Carbons with Oxygen and Nitrogen Surface Groups. *Carbon* **1997**, *35*, 1799−1810.
(55) Williams, M. W.; Arakawa, E. T. Optical Properties of Glassy Carbon from 0 to 82 Ev. *J. Appl. Phys.* **1972**, *43*, 3460−3463.
(56) Mednikarov, B.; Spasov, G.; Babeva, T.; Pirov, J.; Sahatchieva, M.; Popova, C.; Kulischa, W. Optical Properties of Diamond-Like Carbon and Nanocrystalline Diamond Films. *J. Optoelectron. Adv. Mater.* **2005**, *7*, 1407−1413.
(57) Shi, X.; Fu, H.; Shi, J. R.; Cheah, L. K.; Tay, B. K.; Hui, P. Electronic Transport Properties of Nitrogen Doped Amorphous Carbon Films Deposited by the Filtered Cathodic Vacuum Arc Technique. *J. Phys.: Condens. Matter* **1998**, *10*, 9293.
(58) Rodil, S. E.; Muhl, S.; Maca, S.; Ferrari, A. C. Optical Gap in Carbon Nitride Films. *Thin Solid Films* **2003**, *433*, 119−125.
(59) McCreery, R. L. Advanced Carbon Electrode Materials for Molecular Electrochemistry. *Chem. Rev.* **2008**, *108*, 2646−2687.
(60) Davies, T. J.; Compton, R. G. The Cyclic and Linear Sweep Voltammetry of Regular and Random Arrays of Microdisc Electrodes: Theory. *J. Electroanal. Chem.* **2005**, *585*, 63−82.
(61) Filipe, O. M. S.; Brett, C. M. A. Characterization of Carbon Film Electrodes for Electroanalysis by Electrochemical Impedance. *Electroanalysis* **2004**, *16*, 994−1001.
(62) Pleskov, Y. V.; Evstefeeva, Y. E.; Krotova, M. D.; Elkin, V. V.; Baranov, A. M.; Dement'ev, A. P. Electrochemical Behavior of Amorphous Carbon Films: Kinetic and Impedance-Spectroscopy Studies. *Diamond Relat. Mater.* **1999**, *8*, 64−72.
(63) Morrison, S. R. *Electrochemistry at Semiconductor and Oxidised Metal Electrodes*, 1st ed.; Plenum Press, 1980.
(64) Orazem, M. E.; Tribolet, B. *Electrochemical Impedance Spectroscopy*; Wiley, 2008.
(65) Kobayashi, K.; Takata, M.; Okamoto, S.; Sukigara, M. Ac Impedance Theory for Surface States at a Semiconductor—Liquid Junction. *J. Electroanal. Chem. Interfacial Electrochem.* **1985**, *185*, 47−60.
(66) Xiong, L.; Batchelor-McAuley, C.; Ward, K. R.; Downing, C.; Hartshorne, R. S.; Lawrence, N. S.; Compton, R. G. Voltammetry at Graphite Electrodes: The Oxidation of Hexacyanoferrate (II) (Ferrocyanide) Does Not Exhibit Pure Outer-Sphere Electron Transfer Kinetics and Is Sensitive to Pre-Exposure of the Electrode to Organic Solvents. *J. Electroanal. Chem.* **2011**, *661*, 144−149.
(67) Swaddle, T. W. Homogeneous Versus Heterogeneous Self-Exchange Electron Transfer Reactions of Metal Complexes: Insights from Pressure Effects. *Chem. Rev.* **2005**, *105*, 2573−2608.
(68) Peter, L. M.; Dürr, W.; Bindra, P.; Gerischer, H. The Influence of Alkali Metal Cations on the Rate of the $Fe(CN)_6^{4-}/Fe(CN)_6^{3-}$ Electrode Process. *J. Electroanal. Chem. Interfacial Electrochem.* **1976**, *71*, 31−50.
(69) Dogonadze, R. R.; Ulstrup, J.; Kharkats, Y. I. A Theory of Electrode Reactions through Bridge Transition States; Bridges with a Discrete Electronic Spectrum. *J. Electroanal. Chem. Interfacial Electrochem.* **1972**, *39*, 47−61.
(70) Chen, P.; McCreery, R. L. Control of Electron Transfer Kinetics at Glassy Carbon Electrodes by Specific Surface Modification. *Anal. Chem.* **1996**, *68*, 3958−3965.
(71) Granger, M. C.; Swain, G. M. The Influence of Surface Interactions on the Reversibility of Ferri/Ferrocyanide at Boron-Doped Diamond Thin-Film Electrodes. *J. Electrochem. Soc.* **1999**, *146*, 4551−4558.

DOI: 10.1021/acs.jpcc.6b10145
J. Phys. Chem. C 2017, 121, 6596−6604

THE JOURNAL OF PHYSICAL CHEMISTRY C

Article

Cite This: J. Phys. Chem. C 2018, 122, 20763−20773

pubs.acs.org/JPCC

Experimental and Computational Study of Dopamine as an Electrochemical Probe of the Surface Nanostructure of Graphitized N Doped Carbon

James A. Behan,[†] Md. Khairul Hoque,[†] Serban N. Stamatin,[†,‡] Tatiana S. Perova,[§,∥] Laia Vilella-Arribas,[†] Max García-Melchor,*[,†] and Paula E. Colavita*[,†]

[†]School of Chemistry, CRANN and AMBER Research Centres, Trinity College Dublin, College Green, Dublin 2, Ireland

[‡]Faculty of Physics, 3Nano-SAE Research Centre, University of Bucharest, 405 Atomistilor Str., Bucharest-Magurele 077125, Romania

[§]Department of Electronic and Electrical Engineering, Trinity College Dublin, Dublin 2, Ireland

[∥]ITMO University, 49 Kronverskiy pr., Saint Petersburg 197101, Russia

Supporting Information

ABSTRACT: N-doped carbon nanomaterials have received increased attention from electrochemists because of their applications in the metal-free electrocatalysis of important redox processes. In this work, a series of graphitized undoped and nitrogen-doped carbon electrodes prepared by thermal annealing of sputtered amorphous carbon films were prepared and characterized using a combination of X-ray photoelectron spectroscopy and Raman spectroscopy. Adsorption of the surface-sensitive redox probe dopamine at each electrode surface was then studied using cyclic voltammetry and the results correlated to the physicochemical characterization. Results indicate that dopamine adsorption is influenced by both the nitrogen surface chemistry and the degree of graphitization of the carbon scaffold. N-doping, with predominantly graphitic N-sites, was found to increase adsorption of dopamine more than 6-fold on carbon surfaces when the introduction of N atoms did not result in substantial alterations to the sp^2 network. However, when an identical type and level of N-doping is accompanied by a significant increase in disorder in the carbon scaffold, adsorption is limited to levels comparable to those of nitrogen-free carbon. Density functional theory studies of dopamine adsorption on graphene and N-doped graphene model surfaces showed that dopamine interacts via π-stacking at the graphene surface. The Gibbs free energy of adsorption on N-doped graphenes was estimated at 12−13 kcal mol^{-1} and found to be approximately twice that of undoped graphenes. Results suggest that chemical changes resulting from N-doping enhance adsorption; however, high coverage values depend on the availability of sites for π-stacking. Therefore, the structurally disruptive effects of N-incorporation can significantly depress the dopamine response by limiting the availability of basal sites, ultimately dominating the overall electrochemical response of the carbon electrode.

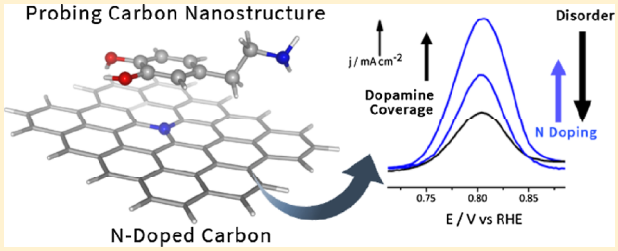

1. INTRODUCTION

Nitrogenated carbon materials have received much attention in recent years, in large part because of the discovery of their activity in the metal-free electrocatalysis of important reactions including the oxygen reduction reaction (ORR)[1,2] and oxygen evolution reaction.[3,4] The synthesis of nitrogenated carbons is facile, versatile, and can be carried out using low-cost reactants, with nitrogen having been successfully incorporated into a variety of different nanocarbons including amorphous carbon,[5−7] graphene,[8−11] and carbon nanotubes.[4,12] The literature has been reviewed recently.[13,14]

Most nitrogenation protocols result in different nitrogen sites incorporated into the material. Nitrogen may be substitutionally incorporated into the carbon scaffold as a so-called graphitic N-site, resulting in the N-doping of the carbon scaffold, or in other chemical forms such as pyridinic-N and pyrrolic-N, both of which are necessarily associated with the formation of vacancies and edge sites within the carbon matrix.[15]

The existence of different N-sites poses a challenge to researchers carrying out structure−activity studies for electrocatalytic applications. A good example is the extensive work done on the ORR at nitrogenated carbon surfaces, which has focused on elucidating active sites for oxygen adsorption or attempting to correlate electrochemical activity to the presence of one or more N-moieties (most commonly pyridinic-N and graphitic-N) in the carbon matrix.[6,16] By contrast, factors such as the degree of graphitization, the size and packing of

Received: June 8, 2018
Revised: August 17, 2018
Published: August 22, 2018

DOI: 10.1021/acs.jpcc.8b05484
J. Phys. Chem. C 2018, 122, 20763−20773

graphitic clusters, and the number of defect sites present at the surface have not been considered in great detail, which may be attributed to the lack of a convenient electrochemical means of probing carbon nanostructures.

The electrochemistry of catechols such as dopamine (DA) is notable for its high degree of sensitivity to the surface chemistry of electrodes. The work by McCreery and co-workers[17,18] on glassy carbon (GC) electrodes shows that catechol adsorption on electrode surfaces may have a dramatic effect on the charge transfer kinetics because of the self-catalysis of one or more of the steps in the "scheme of squares" mechanism often used to describe the 2-electron/2-proton process of catechol oxidation.[19,20] Recently, catechol has been shown to adsorb on graphene nanoplatelets,[21] and the adsorption of DA on graphene, in particular, has been investigated by means of theoretical calculations.[22,23] Because of its biological relevance as an important neurotransmitter, DA has also been intensely studied in the context of electroanalysis and simultaneous detection in the presence of co-analytes such as ascorbic acid.[24−26] DA also has relevance to the nitrogenated amorphous carbon literature in this context[26−28] because these carbons may be engineered to have low background currents and wide potential windows.[29] Interestingly, despite intense focus on tailoring carbon electrode composition and preparation for electroanalytical determinations of DA, comparatively less work has been devoted to investigating the potential application of DA as a probe of surface nanostructuring for N-doped carbons.

In this work, we prepared carbon model systems based on topographically smooth graphitized amorphous carbon with and without incorporated nitrogen, and characterized them using a combination of cyclic voltammetry, X-ray photoelectron spectroscopy (XPS), and Raman spectroscopy. We report what we believe to be the first use of DA as a probe for the surface structure of a disordered nitrogenated carbon material. Results indicate that DA adsorbs on both nitrogenated and nitrogen-free graphitized carbon surfaces, with both the surface chemistry and carbon nanostructure influencing the DA coverage. These results were corroborated by computational studies of DA adsorption on model graphitic clusters via density functional theory (DFT). Our results are expected to have relevance to both the electrochemical detection of DA at nitrogenated carbon surfaces, and the structure−activity characterization of carbon-based materials for surface-catalyzed processes such as the ORR.

2. EXPERIMENTAL METHODS

2.1. Chemicals and Materials. DA hydrochloride (98%, Aldrich), sulfuric acid (≥95%, Ultratrace), hexane (analytical standard), and methanol (semiconductor grade) were used without further purification.

2.2. Substrate Preparation. GC disks (HTW Sigradur radius 0.25 ± 0.05 cm) were prepared by polishing with progressively finer grades of alumina slurry (Buehler), sonicating and rinsing with copious Millipore water as reported previously.[4] Clean disks were either used immediately for electrochemical measurements or, in the case of amorphous carbon and nitrogenated amorphous carbon depositions, mounted in a custom-made Teflon holder and placed in the vacuum chamber for coating via magnetron sputtering prior to characterization, as previously described.[5] In the case of substrates for Raman and XPS measurements, B-doped silicon wafers (MicroChemicals; resistivity 5−10 Ω cm) were prepared via previously reported protocols.[5]

2.3. Preparation of Carbon Electrodes. Undoped and N-doped amorphous carbon thin film electrodes were prepared by magnetron sputtering followed by a thermal annealing treatment. Briefly, the films were deposited via dc magnetron sputtering in a chamber (Torr International Inc.) with a base pressure $\lesssim 2 \times 10^{-6}$ mbar and a deposition pressure in the range $(2-7) \times 10^{-3}$ mbar using a graphite target (99.999%, Lesker) as reported previously.[5] Annealed amorphous carbon films with no N-doping, which will be denoted anC, were deposited using an Ar plasma; N-doped films, denoted as anC:N, were prepared using two different fluxes of N_2 gas in the deposition chamber: anC:N1 was prepared using 2% N_2 gas in a total flux of 50 sccm Ar/N_2 during the deposition, while 10% N_2/Ar was used for anC:N2. After deposition, the resulting films were transported directly to a tube furnace and annealed under N_2 atmosphere for 1 h at 900 °C.

2.4. Characterization. Electrochemical measurements were carried out using a Metrohm Autolab AUT50324 potentiostat using a three-electrode setup. A static disk holder (Pine Instruments) enclosing the GC disk with the carbon thin film was used as the working electrode as reported previously.[5] A Hydroflex hydrogen electrode (Gaskatel) and a graphite rod were used as reference and counter electrodes, respectively. The electrochemical cell was a five-necked jacketed cell (Pine Instruments) which had its temperature held constant at 25 °C using a recirculator. Prior to experiments, the cell was cleaned using Piranha solution (3:1 H_2SO_4/H_2O_2 **CAUTION:** Piranha solution is a strong oxidant which may react explosively with organic solvents and must always be used in a fumehood), followed by rinsing with copious amounts of Millipore water. The cell was then rinsed three times with the electrolyte solution used during the experiment immediately prior to the analysis. Cyclic voltammograms (CVs) were acquired in a potential window of 0.48−1.2 V versus RHE in deaerated solutions of 0.1 M H_2SO_4 with and without DA in concentrations ranging from 25 μM to 1 mM. All voltammograms were taken with iR compensation using commercial software (NOVA) with the uncompensated resistance of 18 ± 1 Ω determined prior to each experiment using electrochemical impedance spectroscopy.

XPS characterization was performed at 1×10^{-10} mbar base pressure in an ultrahigh-vacuum system (Omicron). The X-ray source was a monochromatized Al Kα source (1486.6 eV). Spectra were recorded at a 45° takeoff angle with an analyzer resolution of 0.5 eV. Spectra were baseline-corrected using a Shirley background and fitted with Voigt functions using commercial software (CasaXPS); atomic percent compositions were determined by calculating peak area ratios after correction by relative sensitivity factors (C 1s = 1.0, N 1s = 1.8, O 1s = 2.93).

Raman spectra were measured in backscattering configuration using a Renishaw 1000 micro-Raman system equipped with an Ar^+ laser for 488 nm excitation. The incident beam was focused by a Leica microscope with a 50× magnification objective and short-focus working distance; incident power was kept to <2 mW to avoid sample damage. Spectra were baseline-corrected using commercial software prior to analysis (OriginPro 9.1).

2.5. Computational Studies. DFT calculations reported in this work were carried out using the dispersion-corrected hybrid functional ωB97X-D developed by Head-Gordon and

DOI: 10.1021/acs.jpcc.8b05484
J. Phys. Chem. C 2018, 122, 20763−20773

Chai,[30] implemented in the Gaussian09 software package.[31] The choice of this level of theory is based on the satisfactory results obtained in previous theoretical studies for thermochemistry and for the description of noncovalent interactions.[32] H atoms were described using the double-ζ basis set 6-31G(d,p), whereas the same basis set plus diffuse functions was employed to describe the more electronegative O and N atoms. Geometry optimizations were performed without imposing any constraints, and the nature of all the stationary points was further verified through vibrational frequency analysis. The reported adsorption Gibbs energies (ΔG_{ads}) were calculated at the experimental temperature of 298 K and pressure of 1 atm, according to the following equation

$$\Delta G_{ads} = G_{surf+DA} - G_{surf} - G_{DA} \quad (1)$$

where $G_{surf+DA}$, G_{surf}, and G_{DA} correspond to the adsorbed DA on the graphene cluster, the clean graphene cluster, and the DA molecule in the gas phase, respectively.

3. RESULTS AND DISCUSSION

3.1. Chemical and Structural Characterization of Nitrogen-Free and Nitrogenated Electrodes. Carbon electrodes with and without the presence of nitrogen were prepared via the dc magnetron sputtering protocol described in a previous publication;[5] briefly, sputtering using a N_2/Ar mixture was used to deposit topographically smooth carbon thin films of thickness <120 nm, and the total nitrogen content was varied by changing the proportion of N_2 in the gas mixture. These carbon thin films were prepared as precursor materials for the annealing treatment and contained two different nitrogen concentrations with approximately 15 and 35% N/C at. % ratio, as previously described.[5] The sputtered films were then annealed for 1 h under nitrogen at 900 °C. The nitrogen-free carbon films prepared via this method are referred to as anC throughout this work, whereas the two nitrogenated systems studied are referred to as anC:N1 and anC:N2, which originated from precursors with the lower and higher N-contents, respectively.

The composition of the three different carbon materials was investigated via XPS. Figure 1a shows survey scans for the carbon electrode materials, indicating the presence of C 1s (ca. 284 eV) and O 1s (ca. 532 eV) peaks. The absence of nitrogen peaks from the anC surface is evident in the survey and in high-resolution scans of the N 1s region between 395 and 405 eV shown in the inset in Figure 1a, thus confirming that anC is a nitrogen-free material. Both anC:N electrodes possess a small peak in the 400 eV region, which can be attributed to the presence of nitrogen[33−35] (also shown in the inset).

High-resolution scans of the C 1s region are shown in Figure 1b. The asymmetric envelope indicates that these carbon materials are predominantly based on sp^2-bonded carbon, as expected for graphitized carbon surfaces. This was further explored by deconvoluting the C 1s envelopes, as shown in Figure 1c for the anC surface, and in Figure S1 in the Supporting Information for anC:N materials. The peaks at ca. 284.5 and ca. 285.5 eV (C1 and C2 in Figure 1c) are commonly assigned to sp^2 and sp^3 carbon centers, respectively,[36] leading to an estimated sp^3 % of 12 ± 1% (see Table 1).

Nitrogenation of the carbon scaffold has the effect of increasing the full-width at half maximum (fwhm) of the C 1s (Table 1) in anC:N samples, which is indicative of the presence of a greater amount of disorder in the carbon sp^2 network.[37] Nitrogen incorporation complicates the determination of the sp^3/sp^2 ratio, as the region above ca. 285.5 eV includes contributions from both sp^3-C and sp^2-C bonded to nitrogen.[33,35] Therefore, we limit the analysis of the sp^3 % determined via XPS to the nitrogen-free anC materials. The peaks at binding energies above ca. 286 eV (C3 and C4 in Figure 1c) may be assigned to C−O (ca. 286.5 eV) and C═O (ca. 288 eV) in the case of nitrogen-free anC; however, the introduction of nitrogen precludes an unambiguous assignment between C−O and C−N bonds because of spectral overlap.[38]

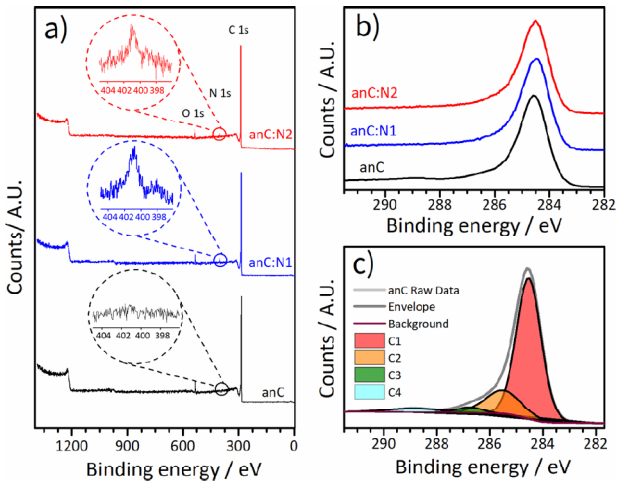

Figure 1. (a) Survey scans of anC, anC:N1, and anC:N2 electrodes. Insets correspond to high-resolution scans of the N 1s regions. (b) High-resolution C 1s scans of anC and anC:N electrodes. (c) Deconvolution of the C 1s envelope of anC; the raw data and envelope are offset relative to the components for clarity.

The amount of oxygen and nitrogen present in the films was determined from area ratios A_{O1s}/A_{C1s} and A_{N1s}/A_{C1s}, respectively, after correction by sensitivity factors, with the resulting O/C and N/C at. % values reported in Table 1. Analysis of variance (ANOVA) on these data indicates that there is no statistically significant difference in O/C at. % among the three carbon materials (23 DF, $F = 1.70$, $p = 0.20$). Additionally, both anC:N1 and anC:N2 possess statistically identical N/C at. % (18 DF, $t = 1.85$, $p = 0.083$).

High-resolution N 1s spectra for the anC:N surfaces are shown along with their deconvolution in Figure 2. For both anC:N films, a deconvolution into two major components yielded the best fits. There is a dominant contribution to the envelope at ca. 401 eV which is associated with the presence of graphitic nitrogen (N_G), as well as a smaller shoulder at ca. 398 eV, which is commonly assigned to pyridinic-N (N_P).[33,34] The ratio of N_P/N_G is approximately 25:75 for both anC:N1 and anC:N2 (Table 1), indicating that both systems possess similar nitrogen site distribution.

In summary, XPS measurements of anC, anC:N1, and anC:N2 indicate that carbon deposition followed by thermal annealing results in graphitized carbon materials with and without nitrogen incorporation. All three carbon materials possess comparable levels of oxygen, while the nitrogenated systems have comparable total nitrogen content and similar distribution of surface N-sites. Despite these similarities, the carbon scaffolds differ significantly as evidenced by the differences observed in C 1s fwhm.

DOI: 10.1021/acs.jpcc.8b05484
J. Phys. Chem. C 2018, 122, 20763−20773

Table 1. C 1s fwhm, sp^3/sp^2, and Chemical Compositions of anC and anC:N Materials Obtained from XPS Deconvolutions[a]

sample	C 1s fwhm	sp^3 %	O/C %	N/C %	N_G/N_T %	N_P/N_T %
anC	1.00 ± 0.05	12 ± 1	3 ± 2			
anC:N1	1.7 ± 0.4		4 ± 1	1.8 ± 0.3	75 ± 5	25 ± 5
anC:N2	2.1 ± 0.6		2.6 ± 0.7	2.4 ± 0.6	74 ± 8	26 ± 8

[a]Errors reported are 95% confidence intervals.

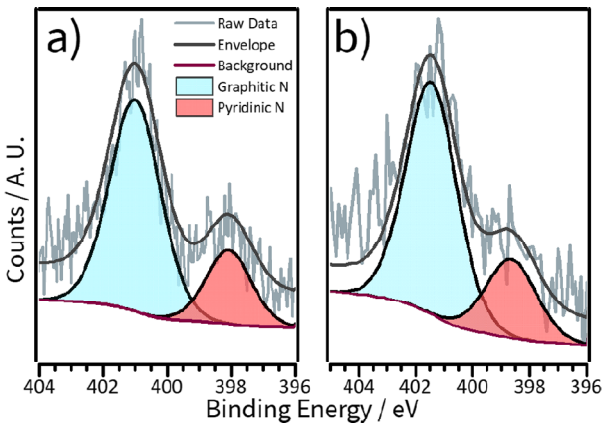

Figure 2. High-resolution N 1s scans of (a) anC:N1 and (b) anC:N2, showing their deconvolution into two contributions; raw data and envelope are offset relative to the components for clarity.

To probe the differences in the carbon scaffolds of anC and anC:N carbon materials, Raman spectroscopy measurements were carried out at an excitation wavelength of 488 nm. Figure 3a shows background-subtracted Raman spectra for the anC and anC:N films. All spectra show two maxima at ca. 1590 and 1380 cm^{-1}, assigned to the G and D peaks of sp^2-C centers, respectively.[37,39,40] The G peak is associated with an in-plane stretching mode of sp^2-C centers present in the carbon scaffold, whereas the D peak is a breathing mode of sp^2-C sites in six-membered rings;[39] the D peak is normally forbidden in perfectly crystalline graphite but is active in the presence of disorder/defects.

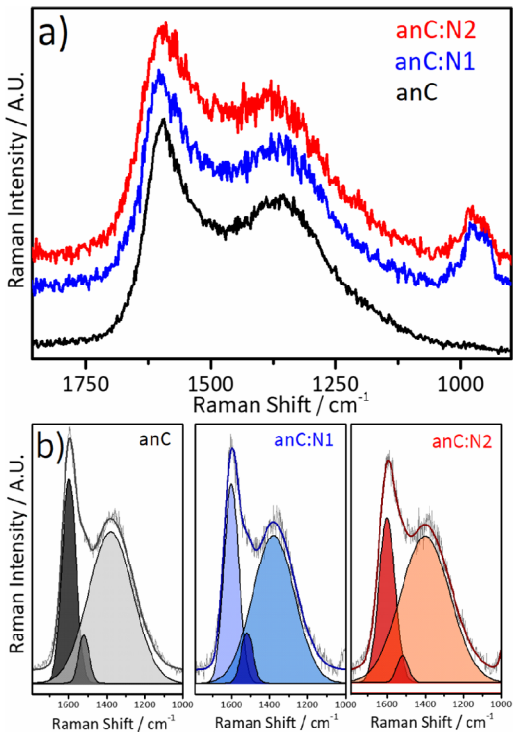

Figure 3. (a) Raman spectra of anC and anC-N carbons; spectra are background-corrected and offset for clarity. (b) Deconvolution of anC, anC:N1, and anC:N2 spectra.

The best fits for the anC and anC:N spectra were obtained using a three-peak Gaussian deconvolution involving the aforementioned G and D peaks as well as a third smaller peak close to 1500 cm^{-1} (Figure 3b). The latter is commonly referred to as the A peak and is associated with C−C stretching vibrations in an amorphous carbon network, where both three- and four-coordinated carbon atoms exist in the regions connecting graphitic crystallites.[41] The small peak close to 1000 cm^{-1} observed in some spectra is associated with the Si substrate on which the films were deposited for Raman characterization.[42] Spectral parameters derived from the fits are reported in Table 2.

On the basis of the three-stage model of Ferrari and Robertson for amorphous carbons with and without nitrogen,[37,39] all three carbon materials have properties that are closer to nanocrystalline graphite than to amorphous carbon. This is evidenced by a G-peak position at ca. 1600 cm^{-1} for all three-model systems and a fwhm that suggests a cluster size <10 nm.[37] For anC:N1 and anC:N2, the G fwhm increases relative to nitrogen-free anC, with anC:N2 having the widest fwhm and therefore the greatest disorder. Further insights on the carbon microstructure emerge from an analysis of I_D/I_G and I_A/I_G ratios, also shown in Table 2, which are diagnostic of the degree of order/disorder. The anC:N1 has slightly smaller I_D/I_G and slightly larger I_A/I_G ratios relative to unmodified carbon, although the differences are relatively small and do not suggest significant differences between anC and anC:N1 in terms of the organization of the carbon scaffold and the density of defects/boundaries. In the case of anC:N2, however, the I_D/I_G is significantly larger than anC:N1, which is strongly suggestive of a smaller average crystallite size for the graphitic clusters. This is consistent with anC:N2, which shows the smallest I_A/I_G ratio, indicating that graphitized regions of the scaffold are more closely packed, thus reducing the prevalence of interstitial C−C contributions.

Overall, Raman data indicate that anC:N1 and anC:N2 display significant differences in the organization of their carbon scaffolds, despite these materials possessing identical N/C at. % and comparable concentration of N_G and N_P sites. The fact that N_P remains constant between anC:N1 and anC:N2 is intriguing because N_P necessarily exists at edge or vacancy sites in the carbon scaffold. The increase in disorder for anC:N2 can therefore only be explained on the basis of differences in the organization of the carbon framework around these N-sites, rather than on the basis of N_G and N_P concentration changes. We believe that dissimilarities in carbon scaffold structuring likely arise from the use of

DOI: 10.1021/acs.jpcc.8b05484
J. Phys. Chem. C 2018, 122, 20763−20773

Table 2. Raman Spectral Parameters for anC and anC:N Carbon Materials.

sample	I_D/I_G	I_A/I_G	G position/cm^{-1}	G fwhm/cm^{-1}	D position/cm^{-1}	D fwhm/cm^{-1}
anC	0.74	0.23	1598	85	1379	274
anC:N1	0.73	0.26	1600	91	1379	260
anC:N2	0.84	0.16	1603	104	1385	279

precursor-sputtered materials that possess different initial N/C contents (15 and 35 at. %), as previously mentioned. It is well known that annealing of nitrogenated carbon systems at temperatures above 800 °C selects for the most thermally stable N_G sites.[8] This explains the evolution of both anC:N materials toward almost identical N-site composition and concentration, that is the majority of the initial nitrogen content is "annealed-out" resulting in a final concentration <2.5 at. % of predominantly N_G-sites. However, the initial concentration of edges, defects, and N-sites determines the level of clustering present prior to annealing, which limits the ability to "anneal-out" carbon defects. Hence, disorder in the precursor carbon seems to influence the final concentration of residual vacancies and the degree of graphitic clustering/ordering achieved post-annealing.

3.2. Voltammetric Studies of anC and anC:N. On the basis of XPS and Raman results, anC and anC:N1 possess similar degrees of graphitization in their carbon scaffold but differ in that anC:N1 displays N_G/N_P functionalities on its surface. On the other hand, anC:N1 and anC:N2 possess indistinguishable N_G/N_P composition but display differences in the nanostructuring of their graphitic clusters. Despite the presence of numerous structure−activity studies on nitrogenated carbons, there has been a disproportionate amount of attention paid to identifying particular N-sites and correlating activities to their presence or absence,[6,16] with less emphasis placed on how the local environment of these sites may be organized. The materials discussed in the previous section offer an opportunity to investigate the effect of graphitic cluster organization on the response of a solid carbon electrode with controlled N-functional group type and concentration, while allowing to discriminate contributions arising from the presence of N-functionalities at the surface. In this context, redox couples have been used as probes of carbon electrode properties by our group and others in the literature.[5,43,44] To probe the effect of surface nanostructuring on the electrochemical response of nitrogenated graphitic carbons, we selected a catechol species as a redox probe, as these are known to be surface-sensitive and adsorb onto carbon electrodes.[17,18,44]

Catechols display redox chemistry that is highly sensitive to surface preparations, ranging from polishing and cleaning protocols to modification with adlayers.[45,46] In particular, recent work by Patel et al.[47] using DA demonstrated a strong dependence of the redox response on carbon electrode edge/plane exposure, while work by Gai et al. and Sheng et al. on nitrogenated carbons showed a range of redox behaviors that suggest high sensitivity to chemical and structural changes.[25,26] These observations led us to speculate that DA redox reactions might be facilitated by π-stacking interactions at amorphous/disordered carbon surfaces, which could in principle be used as a probe for the degree of clustering and organization of the carbon scaffold surrounding N-sites.

Figure 4a shows representative CVs in 1.0 mM DA solutions in 0.1 M H_2SO_4 for anC, anC:N1, and anC:N2 electrodes at a scan rate (ν) of 5 mV s^{-1}. For comparison, the voltammogram

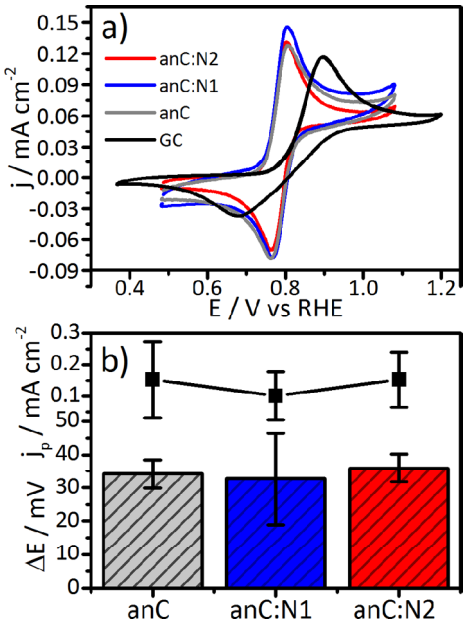

Figure 4. (a) CVs of GC, anC, and anC:N films in solutions of 1.0 mM DA/0.1 M H_2SO_4 at 5 mV s^{-1}. (b) Peak current densities (top) and ΔE values (bottom) derived from voltammetric measurements at 5 mV s^{-1} on all annealed electrodes studied.

of a polished GC disk is also presented. The oxidation of DA involves a net transfer of two protons and two electrons (n = 2) via a complex "scheme of squares" mechanism.[17,48] The CVs in Figure 4a have the characteristics of a reversible 2e$^-$ process, with ΔE values close to the Nernstian value of 59/2 mV[49] and almost identical anodic and cathodic peak current densities (Figure 4b). By contrast, the DA voltammogram on the GC disk shows a large peak-to-peak separation of 240 ± 60 mV which is consistent with irreversible charge transfer kinetics.[50]

anC and anC:N electrodes show indistinguishable behavior toward DA close to the reversible charge transfer limit at low scan rates. However, significant differences emerge among the three materials as the scan rate is increased from 50 to 1000 mV s^{-1} (Figure 5a−c). The shape of the voltammetric waves is markedly different from that observed at low scan rates in Figure 4a, becoming more symmetric in shape, a feature indicative of the presence of an adsorbed redox species at the surface.[46,50] ΔE values in Figure 5a−c are in the range of 10−20 mV, which is characteristic of an adsorption-controlled process, for which peak-to-peak potential values are expected to approach zero. A direct comparison of the current functions at low and high scan rates presented in Figure S2 (see Supporting Information) clearly shows these waveform changes. Plots of anodic peak current density, j_p, versus ν in the insets of Figure 5a−c show that j_p varies linearly in the range of 50−1000 mV s^{-1}, which is consistent with a surface-adsorbed redox probe. For the bare GC (Figure 5d), we found that there is no evidence of a narrowing of ΔE or an

DOI: 10.1021/acs.jpcc.8b05484
J. Phys. Chem. C 2018, 122, 20763−20773

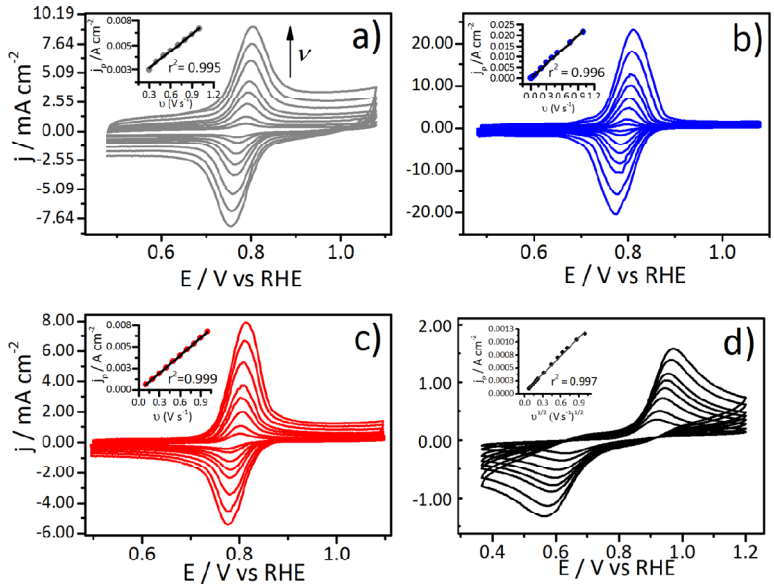

Figure 5. CVs of 1.0 mM DA in 0.1 M H_2SO_4 for (a) anC, (b) anC:N1, (c) anC:N2, and (d) GC electrodes; ν = 50−1000 mV s^{-1}. Insets in (a−c) are plots of peak current density (j_p) vs ν, showing a linear relationship. The inset in (d) corresponds to a plot of j_p vs $\nu^{1/2}$.

enhancement of j_p, which increases linearly versus $\nu^{1/2}$, as expected for a diffusive process which is uncomplicated by the presence of adsorbed reactants.

Changes in waveform and peak separation indicate that both solution-phase and surface-bound DA are redox active, with adsorbed DA contributing more to the overall peak current as the scan rate increases.[51] This is clearly evident from a logarithmic plot of anodic peak current ($i_{p,a}$) versus scan rate for the anC and anC:N electrodes presented in Figure 6a, which shows a slope of m = 0.5 at scan rates of 5−20 mV s^{-1}.

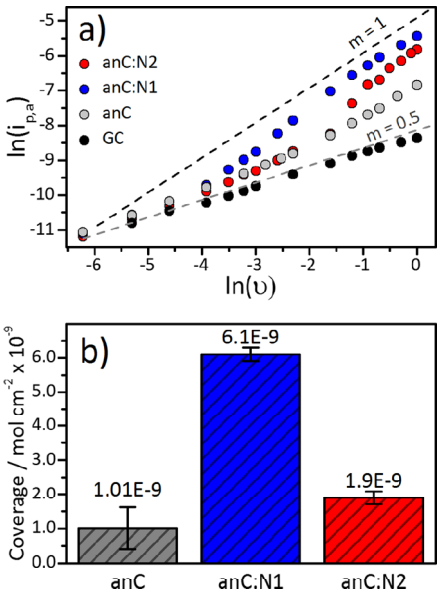

Figure 6. (a) Logarithmic plot of the anodic peak current, $i_{p,a}$, vs ν, for anC and anC:N electrodes in a solution of 1.0 mM DA in 0.1 M H_2SO_4. The dashed lines represent theoretical slopes of m = 1 and m = 0.5 and are present to guide the eye. (b) Coverage values, Γ, of DA on the electrode surfaces calculated using eq 3 in the text.

This suggests that oxidation of DA in solution dominates the Faradaic current in this range as described by eq 2,[52] where A is the electrode area, D is the diffusion coefficient, and c is the concentration of DA. For higher scan rates, there is an enhancement of i_p above the value expected for a Nernstian process such that each of the plots diverges from m = 0.5 and approaches a slope m = 1. This suggests that the response in this scan range is better described by eq 3[53] and its logarithmic form in eq 4, where the Faradaic current is assumed to originate from a redox species bound at the electrode with a surface coverage Γ.

$$\ln(i_p) = 0.5\ln(\nu) + \ln(2.69 \times 10^5 n^{3/2} A D^{1/2} c) \quad (2)$$

$$i_p = \frac{n^2 F^2 \nu A \Gamma}{4RT} \quad (3)$$

$$\ln(i_p) = \ln(\nu) + \ln\left(\frac{n^2 F^2 A \Gamma}{4RT}\right) \quad (4)$$

Using the slopes obtained from the plots in the insets of Figure 5, along with eq 3 with T = 298 K and the electrode geometric area A = 0.1963 cm^2, the DA coverages (Γ_{DA}) at each electrode surface were obtained and are summarized in Figure 6b. From this figure, it is evident that there are significant differences in Γ_{DA} among the three-carbon electrodes, which were found to be in a ratio of 1.0:6.0:1.9 for anC/anC:N1/anC:N2. From the voltammograms, it is also possible to estimate the effects of lateral interactions between adsorbed DA by examining the fwhm of the peaks.[54] The results of this analysis are reported in Table S1 and suggest the presence of only weak lateral interactions.

The differences in Γ cannot be explained based on changes to the electrochemical surface area (ESA) among the three electrodes. This was confirmed based on measurements of specific capacitance in supporting electrolyte solution, which did not afford statistically significant differences in capacitance among the three electrodes (see the Supporting Information). This suggests that differences in the ESA cannot explain the

DOI: 10.1021/acs.jpcc.8b05484
J. Phys. Chem. C 2018, 122, 20763−20773

trend in Figure 6b, and that specific DA-surface interactions vary among anC, anC:N1, and anC:N2, thus giving rise to marked differences in adsorption yields.

It is interesting to examine Γ_{DA} results in the light of chemical and structural information obtained via XPS and Raman spectroscopy. Nitrogen incorporation into the anC:N electrodes in the form of N_G/N_P functional groups results in enhanced Γ_{DA} relative to anC, which likely stems from a combination of chemical and physical effects on DA adsorption at the carbon surface. The similarities between anC:N1 and anC:N2 in terms of N/C and O/C content and proportion of N_P/N_G functionalities (see Table 1) suggest that fundamental physical/structural differences, rather than differences in chemical functionality, might better explain the three-fold enhancement of Γ_{DA} for anC:N1 relative to anC:N2. Furthermore, the more modest two-fold enhancement of Γ_{DA} in anC:N2 compared to anC suggests that physical/structural effects can have a stronger effect on DA adsorption than the presence of N_G/N_P surface functional groups. This conclusion is supported by our Raman results, which indicate that anC and anC:N1 are similar in their organization of the carbon scaffold and their degree of graphitization, while anC:N2 displays the most disordered carbon structure and likely the smallest crystallite size among the three graphitic materials. The introduction of N_G/N_P groups without a significant disruption of the graphitic scaffold results in an enhancement of Γ_{DA} when going from anC to anC:N1. However, this chemical enhancement effect is essentially lost when the degree of graphitization is reduced in anC:N2 materials, that is, because of changes in the carbon nanostructure.

3.3. Computational Studies of DA Adsorption on Graphene Models. Electrochemical results suggest that DA adsorption can track changes in the surface chemistry and the nanostructure of graphitic carbon electrodes. Given the similarities in the degree of graphitization between anC and anC:N1, it appears that probe adsorption is enhanced by the incorporation of N-sites, so long as the disruptive effect of nitrogenation does not result in a high concentration of defects in the annealed structure. Probe adsorption at the carbon surface reflects differences in (bulk) defect density between anC:N1 and anC:N2 as observed via Raman spectroscopy, thus suggesting that increased defects in the nitrogenated scaffold can result in reduced probe adsorption. Hence, the combination of spectroscopic and voltammetric results led us to hypothesize that DA adsorption may serve as an indicator of the degree of graphitization at the electroactive interface in nitrogenated carbons.

With the aim of providing a better understanding of the interaction between DA and the different graphitic surfaces, we carried out a computational investigation at the DFT-wb97xd level (see details in the Supporting Information) using the model graphene structures presented in Figure 7. While graphene and N-graphene with vacancies have been studied theoretically,[22,23] to our knowledge, this is the first time that DFT calculations have been used to evaluate the interaction of DA with graphitic edges, and the first to take into account the entropic contributions to the adsorption by computing the Gibbs free energy of adsorption, ΔG_{ads}.

We started our computational analysis by optimizing the structures of the isolated DA molecule and the graphitic model surfaces shown in Figure 7, followed by the adsorption of DA on the different surfaces taking into account all the possible orientations and adsorption sites. The lowest ΔG_{ads} values

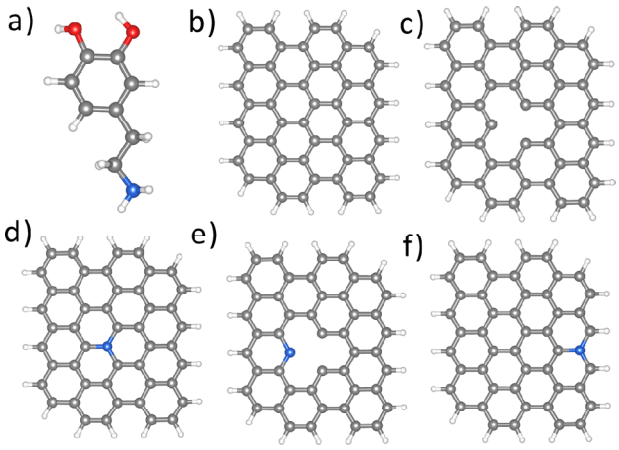

Figure 7. Ball and stick representation of the DFT-modeled structures: (a) DA, (b) graphene, (c) graphene with a single carbon vacancy, (d) N-graphene with a graphitic centre site, (e) N-graphene with a graphitic valley site, and (f) N-graphene with a pyridinic vacancy.

obtained and the corresponding structures are summarized in Figure 8. All the modeled structures showing a less favorable adsorption energy are illustrated in detail in the Supporting Information, Figures S4–S11.

For the interaction of DA with the basal plane of pristine graphene (DA–BP), we found that the most favorable orientation of the molecule at the surface is close to parallel, with a ring-surface distance of 3.2–3.6 Å (Figure 8a). This range of bond distances are typical of noncovalent interactions and are in line with those reported in previous theoretical studies for DA adsorption on graphene.[23] In this adsorption mode, the ethylamine chain is oriented away from the benzene ring, giving a distance of around 4.6 Å between the N-atom of the amine and the surface. The interaction of DA with the lone pair of the amine pointing to a hydrogenated graphene edge and the aromatic ring facing away from the surface was also considered (DA–E). According to our calculations, this adsorption mode is not stable and the DA molecule evolves to an orientation parallel to the basal plane as for DA–BP (Figure 8b). However, unlike DA–BP, the ethylamine group in DA–E is placed in an almost parallel disposition to the surface close to a hydrogenated edge atom, with a N-surface distance of 3.3 Å. While this might be indicative of a weak interaction between the edge site and the lone pair of the amine, the computed ΔG_{ads} for DA–E is almost identical to DA–BP (−5.4 and −5.5 kcal/mol, respectively). Hence, for hydrogenated edges, we conclude that there is no clear preference in the orientation of the amine when the π-system of DA interacts with the basal plane. Likewise, the DA molecule adsorbed on a carbon vacancy (DA–V) is also oriented parallel to the graphene surface, but in this case, the H atoms from the hydroxyl groups point into the vacancy (Figure 8c). The ΔG_{ads} value obtained for DA–V is approximately 2 kcal mol^{-1} lower than DA–BP and DA–E, which may be explained by the favorable interactions arising from the hydrogen bonding between the hydroxyl groups and the unsaturated carbon atoms adjacent to the vacancy.

When moving to the N-doped graphene surfaces (Figure 8d–f), we found that ΔG_{ads} becomes significantly more negative compared to the aforementioned non-nitrogenated surfaces. In the case of DA–$N_{G,C}$, the orientation of DA is

DOI: 10.1021/acs.jpcc.8b05484
J. Phys. Chem. C 2018, 122, 20763–20773

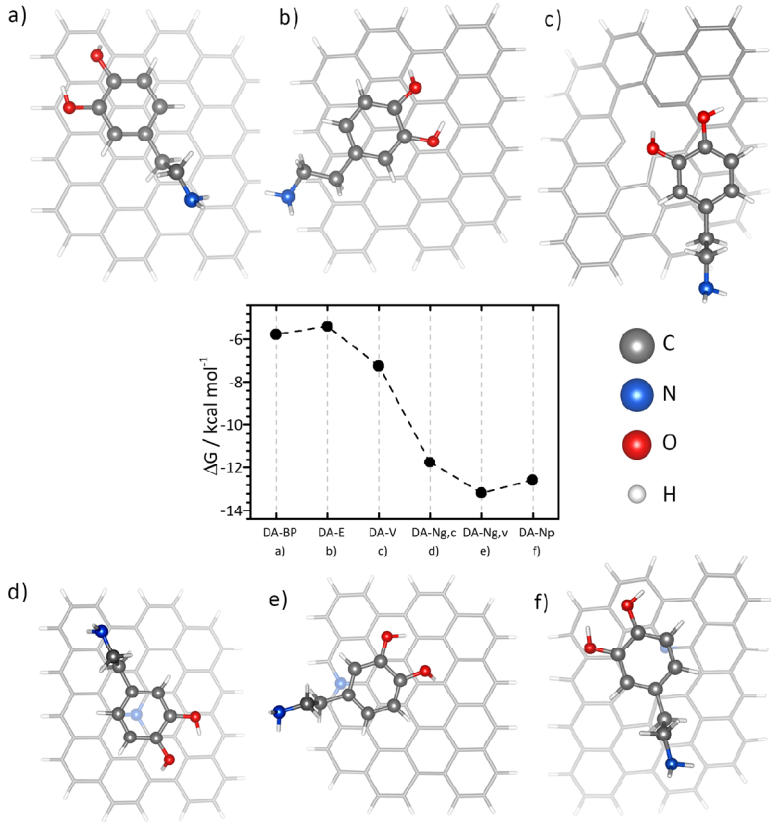

Figure 8. Calculated adsorption Gibbs energies (ΔG_{ads}), in kcal mol^{-1} for DA. Top views of the optimized structures for the different adsorption modes and their corresponding ΔG_{ads} values on graphene (a–c) and N-doped graphene (d–f) model systems.

almost identical to that of non-nitrogenated DA–BP, with the π-system of DA sitting on top of the graphitic nitrogen (N_G) and with a N-surface distance of 4.66 Å (Figure 8d). Interestingly, the calculated ΔG_{ads} for DA–$N_{G,C}$ is more than double the value of the DA–BP interaction (−11.7 vs −5.5 kcal mol^{-1}), thus suggesting that the substitutional N-site enhances adsorption of the DA molecule. The most negative ΔG_{ads} value, however, was obtained for DA–$N_{G,V}$, where DA sits parallel to the surface over the $N_{G,V}$ site with the amine pointing away from the surface (Figure 8e). A similar adsorption energy was obtained even when the molecule was oriented with the amine pointing at the nitrogenated edge (Figure S10). Finally, for the interaction of DA with the carbon surface containing a pyridinic vacancy (DA–N_P), we found that the aromatic ring of DA sits on top of the pyridinic nitrogen site (N_P) with the amine group almost parallel to the surface (Figure 8f). The calculated ΔG_{ads} for this structure is only slightly more positive than for DA–$N_{G,V}$, which indicates that DA adsorption at a pyridinic vacancy is also highly favorable.

Overall, the abovementioned DFT results are in good agreement with the voltammetric experiments for both anC and anC:N surfaces, which are strongly suggestive of a weak adsorption at the carbon surface. This is based on the fact that for a strong adsorption (ΔG_{ads} in the absence of an applied field, $|\Delta G^{\circ}_{ads}| > \sim 10$ kcal mol^{-1}), "pre-peaks" and/or "post-peaks" are expected to appear in the voltammogram because of the strong interaction of the reactant and/or products with the surface.[51] Our DFT-calculated values of ΔG_{ads} for DA–BP, DA–E, and DA–V are either comparable to this threshold value or lower. On the other hand, our DFT results predict the adsorption at nitrogenated sites to be stronger, although these sites make up a very small proportion of the available binding sites at the surface, as shown in the XPS measurements. Therefore, the absence of any pre- or post-peaks in the voltammograms of anC:N1 and anC:N2 may thus be explained by the low concentration of these sites at the surface.

The more negative values of ΔG_{ads} at nitrogen sites may partially explain why DA coverages are higher for the anC:N surfaces compared to anC because adsorption at nitrogen sites is thermodynamically more favorable in N-doped surfaces. However, N-sites alone do not control DA adsorption in general because anC:N2 has a DA coverage which is far lower than for anC:N1, despite having an identical N/C at. % and N surface chemistry. This suggests that the mere presence of nitrogen sites is not sufficient to induce DA adsorption and that the organization of the carbon scaffold induced by the annealing is the most important factor. As anC:N1 and anC:N2 show different coverages despite their similar N/C at. % and N_G/N_P concentration, we conclude that differences in graphitic clustering, or more specifically average lateral graphitic cluster size between the two surfaces, are the origin of these variations. This suggests that DA adsorption experiments may be used as an effective probe of the interfacial carbon nanostructure that is relevant to the electroactive surface, thus complementing information on defect density derived from bulk methods such as Raman spectroscopy.

DOI: 10.1021/acs.jpcc.8b05484
J. Phys. Chem. C 2018, 122, 20763–20773

4. CONCLUSIONS

In this work, we have prepared graphitic carbon model systems with and without the presence of nitrogen heteroatoms and characterized their surface chemistry and carbon nanostructure using a combination of XPS, Raman spectroscopy, and DFT calculations. We have shown that these graphitic carbon systems exhibit adsorption of DA, with results suggesting that the coverage of this probe is influenced both by the presence of N-sites and by the degree of the graphitization of the carbon surface. Theoretical studies suggest that the adsorption at the surface is controlled by π-stacking interactions between graphitic clusters at the surface and the aryl moiety.

The incorporation of nitrogen sites into the carbon scaffold may enhance adsorption, particularly at graphitic valley sites, but the data do not support the notion that DA adsorption is controlled primarily by particular N-sites because two model systems with identical N/C % and nitrogen surface chemistry have highly different coverages of DA. It is clear that the chemical effects of N-doping can be counteracted almost entirely by its structurally disruptive effects. Our results indicate that the effect of carbon nanostructuring and organization on the adsorption and redox response of DA should be regarded as of greater significance than the presence of specific N-functional groups. Therefore, it appears important to further explore this interplay between N-functional groups and carbon nanostructuring in their local environment to better understand electrocatalysis at nitrogenated carbon electrodes in general.

Nitrogenated carbons have been used by the electroanalytical community in general for many years and have been used in DA detection in particular by many groups. We expect that other aryl systems, such as other catechols and molecules with biological relevance, may display similar behavior. Indeed, work is currently underway in our group to explore the interactions of other aryl systems with model carbon systems. These interactions may be explored not only in the context of designing biosensors based on graphitic carbons, but also in the use of graphitic amorphous carbon model systems as platforms for the study of structural organization of disordered carbons. Finally, it is likely that the organization of the carbon scaffold has relevance to other inner-sphere redox processes such as oxygen reduction, for which heteroatom-doped carbons are frequently employed. Work is currently underway in our group to understand the effects of modifying carbon nanostructures of di erent carbon model systems on the ORR.

■ ASSOCIATED CONTENT

Supporting Information

The Supporting Information is available free of charge on the ACS Publications website at DOI: 10.1021/acs.jpcc.8b05484.

C 1s XPS Spectra, comparison of CV waveforms, discussion of fwhm data from voltammetry, capacitance determinations, additional gures of DFT structures, and atomic coordinates of all optimized structures (PDF)

■ AUTHOR INFORMATION

Corresponding Authors

*E-mail: garciamm@tcd.ie (M.G.-M.).
*E-mail: colavitp@tcd.ie (P.E.C.).

ORCID

Max García-Melchor: 0000-0003-1348-4692
Paula E. Colavita: 0000-0003-1008-2874

Notes

The authors declare no competing nancial interest.

■ ACKNOWLEDGMENTS

This publication has emanated from research conducted with the nancial support of Science Foundation Ireland under grant no. 13/CDA/2213 and of the Irish Research Council under grant no. GOIPG/2014/399. Use of the XPS of I. V. Shvets and C. McGuinness provided under SFI Equipment Infrastructure funds. We also acknowledge generous computing allocation time in the Kelvin cluster maintained by the Trinity Centre for High Performance Computing, which was funded through grants from the Higher Education Authority, through its PRTLI program.

■ ABBREVIATIONS

DA, dopamine
CV, cyclic voltammetry
ORR, oxygen reduction reaction
XPS, X-ray photoelectron spectroscopy
anC, amorphous carbon annealed at 900 °C
anC:N, nitrogenated amorphous carbon annealed at 900 °C

■ REFERENCES

(1) To, J. W. F.; Ng, J. W. D.; Siahrostami, S.; Koh, A. L.; Lee, Y.; Chen, Z.; Fong, K. D.; Chen, S.; He, J.; Bae, W.-G.; et al. High-Performance Oxygen Reduction and Evolution Carbon Catalysis: From Mechanistic Studies to Device Integration. *Nano Res.* **2017**, *10*, 1163−1177.

(2) Siahrostami, S.; Tsai, C.; Karamad, M.; Koitz, R.; García-Melchor, M.; Bajdich, M.; Vojvodic, A.; Abild-Pedersen, F.; Nørskov, J. K.; Studt, F. Two-Dimensional Materials as Catalysts for Energy Conversion. *Catal. Lett.* **2016**, *146*, 1917−1921.

(3) Lin, Z.; Waller, G. H.; Liu, Y.; Liu, M.; Wong, C.-p. Simple Preparation of Nanoporous Few-Layer Nitrogen-Doped Graphene for Use as an Efficient Electrocatalyst for Oxygen Reduction and Oxygen Evolution Reactions. *Carbon* **2013**, *53*, 130−136.

(4) Yadav, R. M.; Wu, J.; Kochandra, R.; Ma, L.; Tiwary, C. S.; Ge, L.; Ye, G.; Vajtai, R.; Lou, J.; Ajayan, P. M. Carbon Nitrogen Nanotubes as Efficient Bifunctional Electrocatalysts for Oxygen Reduction and Evolution Reactions. *ACS Appl. Mater. Interfaces* **2015**, *7*, 11991−12000.

(5) Behan, J. A.; Stamatin, S. N.; Hoque, M. K.; Ciapetti, G.; Zen, F.; Esteban-Tejeda, L.; Colavita, P. E. Combined Optoelectronic and Electrochemical Study of Nitrogenated Carbon Electrodes. *J. Phys. Chem. C* **2017**, *121*, 6596−6604.

(6) Chen, J.; Wang, X.; Cui, X.; Yang, G.; Zheng, W. Amorphous Carbon Enriched with Pyridinic Nitrogen as an Efficient Metal-Free Electrocatalyst for Oxygen Reduction Reaction. *Chem. Commun.* **2014**, *50*, 557−559.

(7) Chen, J.; Wang, X.; Cui, X.; Yang, G.; Zheng, W. One-Step Synthesis of N-Doped Amorphous Carbon at Relatively Low Temperature as Excellent Metal-Free Electrocatalyst for Oxygen Reduction. *Catal. Commun.* **2014**, *46*, 161−164.

(8) Kumar, A.; Ganguly, A.; Papakonstantinou, P. Thermal Stability Study of Nitrogen Functionalities in a Graphene Network. *J. Phys.: Condens. Matter* **2012**, *24*, 235503.

(9) Lai, L.; Potts, J. R.; Zhan, D.; Wang, L.; Poh, C. K.; Tang, C.; Gong, H.; Shen, Z.; Lin, J.; Ruoff, R. S. Exploration of the Active Center Structure of Nitrogen-Doped Graphene-Based Catalysts for Oxygen Reduction Reaction. *Energy Environ. Sci.* **2012**, *5*, 7936−7942.

(10) Li, X.-F.; Lian, K.-Y.; Liu, L.; Wu, Y.; Qiu, Q.; Jiang, J.; Deng, M.; Luo, Y. Unraveling the Formation Mechanism of Graphitic

DOI: 10.1021/acs.jpcc.8b05484
J. Phys. Chem. C 2018, 122, 20763−20773

Nitrogen-Doping in Thermally Treated Graphene with Ammonia. *Sci. Rep.* **2016**, *6*, 23495.
(11) Stamatin, S. N.; Hussainova, I.; Ivanov, R.; Colavita, P. E. Quantifying Graphitic Edge Exposure in Graphene-Based Materials and Its Role in Oxygen Reduction Reactions. *ACS Catal.* **2016**, *6*, 5215−5221.
(12) Sharifi, T.; Hu, G.; Jia, X.; Wågberg, T. Formation of Active Sites for Oxygen Reduction Reactions by Transformation of Nitrogen Functionalities in Nitrogen-Doped Carbon Nanotubes. *ACS Nano* **2012**, *6*, 8904−8912.
(13) Dai, L.; Xue, Y.; Qu, L.; Choi, H.-J.; Baek, J.-B. Metal-Free Catalysts for Oxygen Reduction Reaction. *Chem. Rev.* **2015**, *115*, 4823−4892.
(14) Hu, C.; Dai, L. Carbon-Based Metal-Free Catalysts for Electrocatalysis Beyond the Orr. *Angew. Chem., Int. Ed.* **2016**, *55*, 11736−11758.
(15) Kleinsorge, B.; Ferrari, A. C.; Robertson, J.; Milne, W. I.; Waidmann, S.; Hearne, S. Bonding Regimes of Nitrogen in Amorphous Carbon. *Diamond Relat. Mater.* **2000**, *9*, 643−648.
(16) Guo, D.; Shibuya, R.; Akiba, C.; Saji, S.; Kondo, T.; Nakamura, J. Active Sites of Nitrogen-Doped Carbon Materials for Oxygen Reduction Reaction Clarified Using Model Catalysts. *Science* **2016**, *351*, 361−365.
(17) DuVall, S. H.; McCreery, R. L. Self-Catalysis by Catechols and Quinones During Heterogeneous Electron Transfer at Carbon Electrodes. *J. Am. Chem. Soc.* **2000**, *122*, 6759−6764.
(18) DuVall, S. H.; McCreery, R. L. Control of Catechol and Hydroquinone Electron-Transfer Kinetics on Native and Modified Glassy Carbon Electrodes. *Anal. Chem.* **1999**, *71*, 4594−4602.
(19) Jacq, J. Schema Carre: Etablissement Et Discussion De L'equation Generale De La Courbe Intensite-Potentiel En Regime Stationnaire Et Diffusion Convective. *J. Electroanal. Chem. Interfacial Electrochem.* **1971**, *29*, 149−180.
(20) Laviron, E. Electrochemical reactions with protonations at equilibrium. *J. Electroanal. Chem. Interfacial Electrochem.* **1984**, *169*, 29−46.
(21) Chen, L.; Li, X.; Tanner, E. E. L.; Compton, R. G. Catechol Adsorption on Graphene Nanoplatelets: Isotherm, Flat to Vertical Phase Transition and Desorption Kinetics. *Chem. Sci.* **2017**, *8*, 4771−4778.
(22) Fernández, A. C. R.; Castellani, N. J. Noncovalent Interactions between Dopamine and Regular and Defective Graphene. *ChemPhysChem* **2017**, *18*, 2065−2080.
(23) Ortiz-Medina, J.; López-Urías, F.; Terrones, H.; Rodríguez-Macías, F. J.; Endo, M.; Terrones, M. Differential Response of Doped/Defective Graphene and Dopamine to Electric Fields: A Density Functional Theory Study. *J. Phys. Chem. C* **2015**, *119*, 13972−13978.
(24) Deakin, M. R.; Kovach, P. M.; Stutts, K. J.; Wightman, R. M. Heterogeneous Mechanisms of the Oxidation of Catechols and Ascorbic Acid at Carbon Electrodes. *Anal. Chem.* **1986**, *58*, 1474−1480.
(25) Gai, P.; Zhang, H.; Zhang, Y.; Liu, W.; Zhu, G.; Zhang, X.; Chen, J. Simultaneous Electrochemical Detection of Ascorbic Acid, Dopamine and Uric Acid Based on Nitrogen Doped Porous Carbon Nanopolyhedra. *J. Mater. Chem. B* **2013**, *1*, 2742−2749.
(26) Sheng, Z.-H.; Zheng, X.-Q.; Xu, J.-Y.; Bao, W.-J.; Wang, F.-B.; Xia, X.-H. Electrochemical Sensor Based on Nitrogen Doped Graphene: Simultaneous Determination of Ascorbic Acid, Dopamine and Uric Acid. *Biosens. Bioelectron.* **2012**, *34*, 125−131.
(27) Tanaka, Y.; Naragino, H.; Yoshinaga, K.; Nakahara, A.; Kondo, T.; Fujishima, A.; Honda, K. Controllable Electrochemical Activities by Oxidative Treatment toward Inner-Sphere Redox Systems at N-Doped Hydrogenated Amorphous Carbon Films. *Int. J. Electrochem.* **2012**, *2012*, 369130.
(28) Medeiros, R. A.; Matos, R.; Benchikh, A.; Saidani, B.; Debiemme-Chouvy, C.; Deslouis, C.; Rocha-Filho, R. C.; Fatibello-Filho, O. Amorphous Carbon Nitride as an Alternative Electrode Material in Electroanalysis: Simultaneous Determination of Dopamine and Ascorbic Acid. *Anal. Chim. Acta* **2013**, *797*, 30−39.
(29) Yang, X.; Haubold, L.; DeVivo, G.; Swain, G. M. Electroanalytical Performance of Nitrogen-Containing Tetrahedral Amorphous Carbon Thin-Film Electrodes. *Anal. Chem.* **2012**, *84*, 6240−6248.
(30) Chai, J.-D.; Head-Gordon, M. Long-Range Corrected Hybrid Density Functionals with Damped Atom-Atom Dispersion Corrections. *Phys. Chem. Chem. Phys.* **2008**, *10*, 6615−6620.
(31) Frisch, M. J.; Trucks, G. W.; Schlegel, H. B.; Scuseria, G. E.; Robb, M. A.; Cheeseman, J. R.; Scalmani, G.; Barone, V.; Mennucci, B.; Petersson, G. A.; et al. *Gaussian 09*, Revision E.01; Gaussian Inc.: Wallingford CT, 2009.
(32) Peñas-Defrutos, M. N.; Bartolomé, C.; García-Melchor, M.; Espinet, P. Hidden Aryl-Exchange Processes in Stable 16e Rh^{III} [$RhCp^*Ar_2$] Complexes, and Their Unexpected Transmetalation Mechanism. *Chem. Commun.* **2018**, *54*, 984−987.
(33) Titantah, J. T.; Lamoen, D. Carbon and Nitrogen 1s Energy Levels in Amorphous Carbon Nitride Systems: XPS Interpretation Using First-Principles. *Diamond Relat. Mater.* **2007**, *16*, 581−588.
(34) Qu, L.; Liu, Y.; Baek, J.-B.; Dai, L. Nitrogen-Doped Graphene as Efficient Metal-Free Electrocatalyst for Oxygen Reduction in Fuel Cells. *ACS Nano* **2010**, *4*, 1321−1326.
(35) Le Normand, F.; Hommet, J.; Szörényi, T.; Fuchs, C.; Fogarassy, E. XPS Study of Pulsed Laser Deposited CN_x Films. *Phys. Rev. B: Condens. Matter Mater. Phys.* **2001**, *64*, 235416.
(36) Díaz, J.; Paolicelli, G.; Ferrer, S.; Comin, F. Separation of the sp^3 and sp^2 components in the C1s photoemission spectra of amorphous carbon films. *Phys. Rev. B: Condens. Matter Mater. Phys.* **1996**, *54*, 8064−8069.
(37) Ferrari, A. C.; Rodil, S. E.; Robertson, J. Interpretation of Infrared and Raman Spectra of Amorphous Carbon Nitrides. *Phys. Rev. B: Condens. Matter Mater. Phys.* **2003**, *67*, 155306.
(38) Perini, L.; Durante, C.; Favaro, M.; Perazzolo, V.; Agnoli, S.; Schneider, O.; Granozzi, G.; Gennaro, A. Metal-Support Interaction in Platinum and Palladium Nanoparticles Loaded on Nitrogen-Doped Mesoporous Carbon for Oxygen Reduction Reaction. *ACS Appl. Mater. Interfaces* **2015**, *7*, 1170−1179.
(39) Ferrari, A. C.; Robertson, J. Interpretation of Raman Spectra of Disordered and Amorphous Carbon. *Phys. Rev. B: Condens. Matter Mater. Phys.* **2000**, *61*, 14095−14107.
(40) Waidmann, S.; Knupfer, M.; Fink, J.; Kleinsorge, B.; Robertson, J. Electronic Structure Studies of Undoped and Nitrogen-Doped Tetrahedral Amorphous Carbon Using High-Resolution Electron Energy-Loss Spectroscopy. *J. Appl. Phys.* **2001**, *89*, 3783−3792.
(41) Laidani, N.; Guzman, L.; Miotello, A.; Brusa, R. S.; Karwasz, G. P.; Zecca, A.; Bottani, C.; Perrière, J. Nitrogen Effects on the Microstructural Evolution of Carbon Films under Thermal Annealing. *Nucl. Instrum. Methods Phys. Res., Sect. B* **1997**, *122*, 553−558.
(42) Ferrari, A. C.; Robertson, J. Resonant Raman Spectroscopy of Disordered, Amorphous, and Diamondlike Carbon. *Phys. Rev. B: Condens. Matter Mater. Phys.* **2001**, *64*, 075414.
(43) Murphy, D. M.; Cullen, R. J.; Jayasundara, D. R.; Doyle, R. L.; Lyons, M. E. G.; Colavita, P. E. Heterogeneous Charge Transfer at the Amorphous Carbon/Solution Interface: Effect on the Spontaneous Attachment of Aryldiazonium Salts. *J. Phys. Chem. C* **2013**, *117*, 22768−22777.
(44) McCreery, R. L. Advanced Carbon Electrode Materials for Molecular Electrochemistry. *Chem. Rev.* **2008**, *108*, 2646−2687.
(45) Downard, A. J.; Roddick, A. D.; Bond, A. M. Covalent Modification of Carbon Electrodes for Voltammetric Differentiation of Dopamine and Ascorbic Acid. *Anal. Chim. Acta* **1995**, *317*, 303−310.
(46) Corona-Avendaño, S.; Alarcón-Angeles, G.; Ramírez-Silva, M. T.; Rosquete-Pina, G.; Romero-Romo, M.; Palomar-Pardavé, M. On the Electrochemistry of Dopamine in Aqueous Solution. Part I: The Role of [SDS] on the Voltammetric Behavior of Dopamine on a Carbon Paste Electrode. *J. Electroanal. Chem.* **2007**, *609*, 17−26.

DOI: 10.1021/acs.jpcc.8b05484
J. Phys. Chem. C 2018, 122, 20763−20773

(47) Patel, A. N.; Tan, S.-y.; Miller, T. S.; Macpherson, J. V.; Unwin, P. R. Comparison and Reappraisal of Carbon Electrodes for the Voltammetric Detection of Dopamine. *Anal. Chem.* **2013**, *85*, 11755−11764.
(48) Laviron, E. Electrochemical reactions with protonations at equilibrium. *J. Electroanal. Chem. Interfacial Electrochem.* **1984**, *164*, 213−227.
(49) Nicholson, R. S. Theory and Application of Cyclic Voltammetry for Measurement of Electrode Reaction Kinetics. *Anal. Chem.* **1965**, *37*, 1351−1355.
(50) Compton, R. G.; Banks, C. E. *Understanding Voltammetry*, 2nd ed.; Imperial College Press: London, 2011.
(51) Wopschall, R. H.; Shain, I. Effects of Adsorption of Electroactive Species in Stationary Electrode Polarography. *Anal. Chem.* **1967**, *39*, 1514−1527.
(52) Nicholson, R. S.; Shain, I. Theory of Stationary Electrode Polarography. Single Scan and Cyclic Methods Applied to Reversible, Irreversible, and Kinetic Systems. *Anal. Chem.* **1964**, *36*, 706−723.
(53) Laviron, E. Adsorption, Autoinhibition and Autocatalysis in Polarography and in Linear Potential Sweep Voltammetry. *J. Electroanal. Chem. Interfacial Electrochem.* **1974**, *52*, 355−393.
(54) Angerstein-Kozlowska, H.; Klinger, J.; Conway, B. E. Computer simulation of the kinetic behaviour of surface reactions driven by a linear potential sweep. *J. Electroanal. Chem. Interfacial Electrochem.* **1977**, *75*, 45−60.

DOI: 10.1021/acs.jpcc.8b05484
J. Phys. Chem. C 2018, 122, 20763−20773